Blast Performance of Reinforced Concrete Columns Protected by FRP Laminates

By

Bessam Kadhom

Thesis Submitted to the
Faculty of Graduate and Postdoctoral Studies
in partial fulfillment of the requirements
for the Doctorate in Philosophy Degree in Civil Engineering

Department of Civil Engineering
Faculty of Engineering
University of Ottawa

To my Parents

Abstract

Recent terrorist attacks on critical infrastructures using car bombs have heightened awareness on the needs for blast resistance of structures. Blast design of civilian buildings has not been a common practice in structural design. For this reason, there is now an urgent need to mitigate the potentially devastating effects of blast shock waves on existing structures. The current research project, the results of which are reported in this dissertation, aims to expand knowledge on blast resistance of reinforced concrete building columns, while developing a technology and design procedure for protecting critical buildings columns against the damaging effects of impulsive blast loads through the use of externally applied fibre-reinforced polymer (FRP) jackets of different material architecture. The research project has a significant experimental component, with analytical verifications.

A total of thirty two reinforced concrete columns were experimentally investigated under the effects of simulated blast loads using the University of Ottawa Shock Tube. Column dimensions were 150 mm x 150 mm in cross section and 2438 mm in length. Each concrete column was reinforced longitudinally with four 10M rebars which were tied laterally with 6.3 mm closed steel hoops, spaced at 37.5 mm and 100 mm c/c, representing seismic and non-seismic column details, respectively. The experimental research had two phases. Phase-I (sub-study) included blast tests of eight as-built, seismically detailed columns. The behaviour of these columns was explored under single and multiple blast shots, with and without the application of pre-blast axial loads. Phase-II (main-study) included column tests of different carbon FRP (CFRP) designs to investigate the significance of the use of different CFRP column jacket designs on dynamic response of twenty four seismic and non-seismic RC columns.

Analytical investigation was conducted to assess and verify the significance of experimentally investigated parameters on column response. These included the use of Single-Degree-of-Freedom (SDOF) dynamic inelastic analysis, generation of dynamic resistance functions, the effects of variable axial loads, different plastic hinge lengths and the influence of secondary moments (P-Δ moments) on column behaviour.

The results indicate that the loading history has effects on column response, with multiple shots reducing column stiffness, and affecting dynamic response of columns relative to single blast shots of equivalent magnitude. The effect of concrete strength within the normal-strength

concrete range is to increase strength and decrease deformations. Columns with CFRP jackets have considerable improvements in column deformability, with additional increases in column strength. The CFRP laminate design influences performance, with jackets having fibres in $\pm 45^{o}$ orientation especially improving column ductility and increasing plastic hinge lengths, thereby permitting redistribution of stresses and dissipating blast energy. Axial gravity loads vary during blast loads and can affect column strength. It was shown that SDOF dynamic inelastic analysis does capture key structural performance parameters in blast analysis. The consideration of experimentally observed parameters in column analysis; including the influence of CFRP design and associated change in plastic hinge length, variable axial load during response, and secondary moment (P-Δ moments) result in significant improvements in the accuracy of blast analysis. The experimental results and the suggested improvements to the SDOF analysis technique can be used to implement a performance-based design approach recommended as part of the current research project for design of CFRP protection systems for concrete columns.

This research project was conducted jointly by the National Research Council Canada (NRC) and the University of Ottawa.

Acknowledgments

The author would like to express his sincere gratitude to his supervisors Dr. Husham Almansour and Dr. Murat Saatcioglu for their guidance and support throughout all the stages of this investigation.

Special thanks to Dr. Omran Maadani, Mr. Roger Smith and Mr. Jim Margeson for their laboratory assistance over the test phase of this study.

The financial and academic support provided by the National Research Council Canada (NRC) and the University of Ottawa during this research project is greatly acknowledged.

The author's deepest appreciation goes to his family for their understanding and patience.

Table of Contents

List of Tables

Chapter-7

List of Figures

Chapter-2

Chapter-3

Chapter-4

Chapter-5

Chapter-6

Chapter One

Introduction

1-1 General

A large number of civilian structures have been targeted by terrorist attacks worldwide over the last two decades, often using vehicle bombs. The US Department of State reported more than 14,000 global terrorist attacks in 2007, killing more than 20,000 people (Buchan and Chen 2010). This highlights the susceptibility of structures like embassies, commercial centers, governmental buildings, industrial facilities, and residential buildings to the threat of explosions. The substantial dynamic loads generated by explosions can extensively damage critical structural components, such as columns, which are responsible for overall strength and stability of the structure, resulting in high risk of developing progressive collapse. Progressive collapse is defined as the spread of an initial local failure from element to element, eventually resulting in the collapse of the entire structure or a disproportionately large part of it (Sasani et al. 2011, ASCE 2010). Past events showed that preventing progressive collapse can considerably reduce the number of casualties. For example, in Alfred P. Murrah Building in Oklahoma City it was estimated that 87 % of the people died in the collapsed portion of the building, while only 5 % of the people died in the rest of the building (Malvar et al. 2007, ASCE 1996). This illustrates the importance of blast-resistant structural elements and structures in mitigating the effects of bomb blasts and minimizing casualties.

In general, most buildings are not designed against blast loads, although seismically detailed reinforced concrete structures are likely to perform better than structures designed for gravity

loads only (Crawford 2001). This is one reason why there is now a global demand to upgrade existing critical infrastructure to make them blast resistant. One of the blast retrofit strategies considered in the past for existing structures is the application of surface bonded or wrapped fibre reinforced polymer (FRP) sheets. The exceptional engineering properties of FRP composites make them an excellent choice of material for retrofitting. Unfortunately, previous research in this area is very limited (Buchan and Chen 2007). This is due to the high cost of field tests involving live explosives and potential hazards during testing, as well as lack of experience in dealing with live explosives. Video monitoring and data collection during such testing become challenging due to the formation of a fire ball. Therefore, these tests have been limited to military and national security research projects. Furthermore, the results of such tests are often classified information, and are not published. Hence, most structural engineers remain uninformed about the intricacies of blast performance and design of structures subjected to shock waves.

In recent years, new experimental techniques and related facilities have become available for simulated blast testing. These tests can be conducted in a laboratory environment with little potential for experimental hazards. The shock tube available at the structures laboratory of the University of Ottawa is one such example. It provides a safe environment with little operating experience, while generating blast pressures simulating the effects of the actual blast phenomena. Several successful investigations have already been conducted during the last 7 years involving different types of reinforced concrete and masonry elements at the University of Ottawa. Previous studies only focused on investigating the performance of FRP retrofitted RC columns protected by unidirectional fibers placed either in transverse or longitudinal direction (UD 0˚ or UD 90˚). The time history of the axial load degradation during tests and its effect on column behaviour has not been studied comprehensively. Since blast tests are relatively costly, some researchers tested RC components under incrementally increasing blast loads until complete damage. The influence of this repetitive application of blast loads and its effects on column behavior need to be investigated. The present experimental study aims at enriching our understanding of the dynamic response of FRP strengthened reinforced concrete columns under simulated effects of explosions. While the current study focuses on investigating the effect of CFRP laminate design on the structural performance of RC columns, it also adds to the

knowledgebase in this field in terms of overall column behaviour and fills in some of the existing gaps in the literature.

1-2 FRP Retrofitting of Reinforced Concrete Columns

Until the early 1990s, the most common methods used for upgrading RC columns were reinforced concrete and grout-injected steel jackets (Teng 2002, Ballinger et al. 1993). The two strengthening techniques are effective in increasing the column load and deformation capacities. However, both methods are labour intensive and sometimes difficult to apply. The RC jacketing creates the challenge of hoop placement and results in a considerable increase of the member size. Steel jacketing is often difficult to handle, and prone to corrosion when used in bridges. (Abdelrahman and El-Hacha 2012, Teng 2002). FRP jacketing for strengthening deficient RC columns are now being increasingly utilized instead of grout-injected steel jackets. FRPs are a composite material fabricated from long, oriented fibers in the form of glass, carbon or aramid embedded in a polymer matrix such as epoxy (Rodriguez–Nikle et al. 2012). Besides being corrosion resistant and having high strength and stiffness to weight ratios, these materials are easy to handle and apply. The unidirectional FRP retrofitting technique for RC columns (mainly fibers oriented in the hoop direction) was first investigated in Japan in the early of 1980s (e.g Fardis and Khalili 1981, 1982), and a large amount of research on this concept has been carried out since then (Chen et al. 2013).

Shortly after the bombing of the Alfred P. Murrah Building in Oklahoma, fiber reinforced polymer jacketing first emerged as an effective strengthening method against blast loads. Numerical analyses were conducted by Crawford et al. (1995, 1996, 1997b), to investigate the effectiveness of jacketing techniques applied to the ground level load bearing columns of an existing multi-story reinforced concrete building. The findings of the analyses showed that the FRPs jacketing and the steel jacketing systems could prevent column failure and the consequent progressive collapse. The Federal Emergency Management Agency also reported that the jacketing techniques employed to upgrade the seismic resistance of columns could be used in structures exposed to blast (Malvar et al. 2007, ASCE 1996).

FRP jackets can be implemented on site by the wet layup procedure. Concrete column is wrapped laterally by FRP sheets or fabrics impregnated in polymer resin, mostly with fibers oriented in the hoop direction. The hoop wraps greatly increase the axial compressive capacity,

ductility, and the shear resistance of columns. When the flexural strength is not sufficient, additional fibers are provided in the longitudinal direction in the form of FRP strips (Buchan and Chen 2010).

1-3 Reinforced Concrete Columns under Blast Loading

Columns are the primary elements in frame structures. In multi-story buildings, the failure of one single column at the lower level is likely to have an overwhelming effect on the overall structural integrity (Agnew 2007). Column axial loads in tall buildings are considerably high and must be considered in blast analysis. When reinforced concrete columns experience very low lateral deformations, their bending moment capacity is increased due to the presence of axial load. Columns exposed to lateral blast pressures undergo significant shear forces, out of plane deformations, and reflected pressures. The air blast pressure can be adequately approximated as a dynamic load uniformly distributed along the height of the column and characterized by its peak pressure and duration (Rong and Li, 2008). This approximation does not apply to columns that are very close to the explosion. In blast resistant design, a certain level of inelastic deformation of the structural element is permitted in order to dissipate energy. Therefore, column deformability is another aspect of blast-resistance of columns.

1-4 Blast Simulators

Dynamic behaviours of different engineering components subjected to blast loads can be investigated using either actual explosives or blast simulators (Dusenberry 2010). Shock tubes are the most common blast simulators employed by different research organizations. Commonly used shock tubes are air pressure driven tubes, though when higher speeds of shock waves are required internal explosion driven tubes may be used. For such testing, the test specimen is mounted at the front end of a shock tube, at the end of an expansion section, while a driver section located at the other end of the tube is charged with compressed air. Single or double diaphragms are used between the driver and the expansion sections to control the blast pressure. Shock waves similar to those produced by actual explosions are generated when the driver forces air into the specimen at high velocities. Conducting shock tube testing is cost and time effective. Moreover, these tests can be run within an environment subjected to far less restrictions than those in which real blast tests are conducted (Dusenberry 2010).

1-5 Objectives

The primary objective of the current research project is to develop design and analysis methodologies for blast retrofit of existing reinforced concrete columns with externally applied carbon FRP (CFRP) laminates of different fibre architecture and fibre orientations using large-scale tests of columns under simulated blast loading. The objective also includes the generation of test data to establish the residual strength of columns following a blast for mitigation of the adverse effects of progressive collapse, as well as the assessment of the effects of loading history during shock tube testing to address the significance of having a single shot versus multiple shots. The project is intended for far-field bomb blasts that may lead to overloads in columns due to flexure and diagonal tension.

1-6 Scope

The objectives stated in the previous section are fulfilled by executing the following steps, which form the scope of the research project:

1. Experimentally evaluate the effects of different FRP micro-architecture on the structural performance of reinforced concrete (RC) columns retrofitted by FRP laminates when subjected to simulated blast loads.
2. Investigate the effects of loading history on column behaviour by comparing performances of columns subjected to single versus multiple blast shots.
3. Investigate the influence of axial load on behaviour of FRP protected and non-protected columns under blast loads.
4. Assess the residual post-blast axial load capacity of FRP retrofitted RC columns.
5. Examine the suitability of simulating blast response of FRP retrofitted columns using a single-degree-of–freedom (SDOF) model.
6. Develop design and analysis information for FRP retrofitted RC columns under blast induced shock waves.

As can be seen above, the scope of this study consists of experimental and analytical phases. The experimental work consists of design, construction, instrumentation and testing of 32 RC columns designed and detailed either for seismic effects or non-seismic loads. The University of Ottawa Shock Tube is used for simulated blast testing. Eighteen columns are retrofitted with multiple FRP layers of various fiber types and orientations, while the other fourteen columns

represent as-built conditions without any retrofit. Two types of FRPs are employed, consisting of carbon fiber reinforced polymer (CFRP) and aramid (Kevlar) fiber reinforced polymer (AFRP). Unidirectional CFRP, woven [0˚/90˚] CFRP (fibres oriented in transverse and longitudinal directions), and woven [±45˚] CFRP (fibres oriented with 45-degree inclinations) are the three types of carbon fiber reinforced polymer sheets that are considered. Different FRP plies are applied to produce FRP laminates of a specific configuration and strength. The test results are analyzed to assess the effectiveness of the retrofit strategy.

The analytical phase involves dynamic analyses of columns under blast-induced impulsive forcing functions using SDOF analysis. The analysis results are compared with experimentally recorded data to assess the applicability of the analysis techniques. Combined experimental and analytical results are then used to develop a design procedure for FRP retrofitted columns having different FRP architecture and fibre orientation.

1-7 Structure of the Thesis

The thesis is divided into seven chapters. Chapter one contains the introduction, while chapter two provides background and literature review. Chapter three describes the test specimens, materials used, experimental setup, and loading protocol. Chapter four includes a detailed description of the experimental results obtained in this study. Chapter five contains discussion and comparisons of the experimental results. The suitability of simulating blast response of the test columns using SDOF system is presented in chapter six. Finally, chapter seven presents design recommendations while summarizing major findings and conclusions.

1-8 Research Significance

The current research project includes a number of original contributions to blast engineering that pertain to the response of RC columns, with and without FRP protective systems. Although a number of previous research projects were conducted on blast retrofit of concrete columns with externally applied FRP jackets, these were limited to the use of longitudinal and transverse fibres. The use of different FRP architecture, consisting of different types of FRP sheets, especially those that involve laminas with woven fabrics having ±45˚ fibre orientation is unique to this project. The experimental program was designed to make it possible to measure certain key information for the first time, making experimental data invaluable to research and practice in blast engineering. Laser measuring sensors were employed to monitor the mid-height

displacement of columns during blast-induced shock waves. This precise measurement technique made it possible to generate acceleration time histories from which the actual experimental dynamic resistance functions were obtained for the first time in the literature, for comparison against computed resistance functions. Similarly, for the first time, it was possible to capture the axial load time histories experimentally during dynamic impulsive loading, which shed light to the axial load-flexure interaction effects during milliseconds of dynamic response, as the rate at which columns deform laterally happens to be faster than the rate at which the gravity loads could follow columns, until the static equilibrium is restored in the vertical direction. This aspect of blast behaviour was captured and investigated for a potentially significant impact on column design. The effect of CFRP stacking sequence on plastic hinge length was also measured for the first time, providing invaluable experimental data for dynamic inelastic column response, as well as the analysis techniques used for such columns. The experimental data generated is made available to the literature through this thesis.

A number of important analytical verifications were also made in the current research project, which will help researchers and practicing engineers in their future work. While Single Degree of Freedom (SDOF) dynamic analysis is used routinely for blast investigations, certain aspects of this analysis, as affected by experimentally measured parameters were investigated and reported. These include the significance of variable axial load during dynamic blast response, the significance of plastic hinge length as affected by different FRP architecture, the effect of P-Delta effects on column response and the effects of material modelling on dynamic response with emphasis placed on concrete confinement with the additive nature of lateral confinement pressures generated by internal ties and external FRP jackets, as well as the buckling of compression bars during response.

The above contributions paved the way to the formulation of a design procedure for FRP protected RC columns against blast loads. A performance-based design procedure is presented as an additional contribution to the design community.

Chapter Two

Background and Literature Review

This chapter contains three sections. The first section presents a general description of the blast phenomenon, reinforced concrete response to blast loading, and material behaviour under high strain rates. The second section is devoted to the review of FRP external strengthening for both beams (flexural members) and columns (axially loaded members). The third section presents previous research conducted on; i) FRP retrofitted RC columns and as-built RC columns subjected to blast loads and ii) the influence of fiber orientation and ply sequence on the behaviour of confined concrete.

2.1 Blast Effects on Structures

2.1.1 Explosions and blast phenomenon

An explosion is defined as sudden release of energy to the atmosphere forming a blast wave. Based on the type of explosion, it can be classified into physical, chemical, and nuclear (Cormi et al. 2009).

When an explosion is initiated, a blast wave is formed, rapidly travelling away from the explosion epicenter in all directions at supersonic or sonic speeds. This phenomenon is accompanied by an instantaneous increase in the pressure above the ambient atmospheric pressure (P_o). This is referred to as the side-on overpressure, incident overpressure, or merely overpressure (P_{so}). As the wave front propagates further from the explosion center, the peak overpressure gradually decays and within a very short time this pressure falls below normal atmospheric pressure, resulting in negative or suction phase. Generally, the negative phase of a shock wave is lower in magnitude and longer in duration than the positive phase. Consequently,

the negative phase is ignored in blast resistant design of structures (Biggs 1964). Fig. 2.1 shows a detailed pressure – time history for a blast wave in free air.

The impulse of the blast wave is defined as the area under the pressure-time curve. Hence, the positive phase impulse (I_o) can be found as follows:

$$I_o = \int_0^{t_d} P(t)dt \quad (2.1)$$

where,

P(t) is the overpressure function with respect to time

t_d is the duration of positive phase

2.1.2 Prediction of blast pressure

The magnitude of a bomb threat is conventionally identified by the charge weight (*W*) and standoff distance (*R*) between the blast center and the target. Most blast assessments, evaluations and design parameters are primarily expressed in terms of scaled distance $Z = R/W^{1/3}$. Table-2.1 provides commonly used expressions for predicting peak overpressure (P_{so}) as a function of scaled distance.

When a shock wave strikes a solid surface perpendicular to the direction of wave, a reflection occurs, increasing the overpressure applied to the surface (Fig 2.2). The reflected pressure P_r is noticeably larger than the free-field pressure. Equation 2.2 (Cormie et al. 2009) provides an estimate of the magnitude of reflected pressure, $P_{r.}$

$$P_r = 2P_{so}\left(\frac{7P_o + 4P_{so}}{7P_o + P_{so}}\right) \quad (2.2)$$

2.1.3 Structural response to blast loading

Dynamic response analysis of a structure subjected to blast-induced shock wave is a complex process due to the effects of high strain rates, the non-linear behaviour of materials, and the uncertainties in blast load characteristics (Ngo et al. 2007). Blast analysis can be simplified by idealizing both the structure and the loading. These simplifications permit rapid analysis with reasonable accuracy. Fig. 2.3 illustrates a structure subjected to a blast load idealized as a triangular pulse having a peak force of F_o and positive phase duration t_d . The mass-spring model

in the same figure represents a single degree of freedom system (SDOF). The forcing function is described by the following equation:

$$F(t) = F_o(1 - \frac{t}{t_d}) \tag{2.3}$$

The impulse (I) generated by the blast is the area under the force-time curve, and is given by

$$I = \frac{1}{2} F_o t_d \tag{2.4}$$

In blast analysis damping is usually neglected during the forced phase. Neglecting damping, the equation of motion becomes:

$$M\ddot{y} + ky = F_o(1 - \frac{t}{t_d}) \tag{2.5}$$

where,

M is the mass of structure

k is the spring constant

y is the displacement of mass

$\ddot{y}$ is the acceleration of mass

When a structure is exposed to blast effects, large inelastic deformations may be generated in some or all of its structural elements, taking materials beyond their elastic limits. Therefore, inelastic response needs to be computed. Dynamic inelastic response can be obtained using a step-by-step integration technique. A simplified approach is often used in blast analysis for designing elements to obtain an approximate solution. This approach, also known as the graphical solution, involves the use of transformation factors to generate an equivalent idealized elasto-plastic SDOF model that represents the behavior of the structural element. Simple expressions and charts are used to obtain maximum dynamic response of the element for a corresponding resistance function, as shown in Fig. 2.4, and a given blast forcing function.

Charts from (TM 5-1300) are generally used to predict the maximum displacement of structural members. A sample chart is given in Fig. 2.5.

2.1.4 Dynamic reaction

Dynamic reactions are of great importance for designing supporting structures, as well as for computing shear resistance of members under dynamic effects. In fact, the spring force in the equivalent SDOF system is not equal to the dynamic forces generated at the end supports of the real structure. This is because the equivalent SDOF system was originated to have the same deflection of the actual member rather than the same force or stress characteristic (Biggs 1964). The dynamic reaction can only be obtained by solving the equations of dynamic equilibrium of a structural element (Fig. 2.6). For elastic and plastic responses, the results of these solutions give the following equations:

$V(t) = 0.39R(t) + 0.11F(t)$ Elastic Response 2.6

$V(t) = 0.38R(t) + 0.12F(t)$ Plastic Response 2.7

where,

V is the dynamic reaction at the support

R is the dynamic resistance of the structural element

F is the applied blast force

2.1.5 Material behaviour under high strain rates

Fig. 2.7 illustrates distinctive ranges of strain rates associated with different types of loads. It can be seen that blast loads can result in very high strain rates. The high strain rates associated with blast loads alter the mechanical properties of materials. Both steel reinforcement tensile strength and concrete compressive strength are noticeably increased when the structure is under rapidly applied load.

Fig. 2.8 shows typical compressive stress-strain curves of plain concrete tested under fast and slow loading rates. It is observed that the compressive strength of concrete is greater under rapidly applied load. On the other hand, the concrete modulus is less sensitive to high strain rates and its increase can be ignored.

Fig. 2.9 shows typical tensile stress-strain curves for steel coupons tested under standard and rapid loading rates. It can be observed that the fast loading rate results in a significantly higher yield strength, whereas the maximum tensile strength is increased only slightly under a high strain rate. The modulus of elasticity of steel remains the same under slow and high rates of loading.

Enhancement in strength due to high strain rates can be represented by the dynamic increase factor (DIF). Table-2.2 provides design values of DIF for concrete, reinforcing steel, and masonry as recommended by ASCE 2011.

2.1.6 Flexural response of RC members subjected to blast loading

A reinforced concrete beam element subjected to lateral blast pressures exhibits the characteristics of typical flexural response. It deflects under increasing lateral pressure, with increasing deflections until the strain energy in the element balances the applied blast energy. The blast energy is initially consumed by the immediate development of inertia effects. As the deformations increase and the element begins to sustain damage, a significant portion of the applied blast energy is converted into the strain energy.

The response of a reinforced concrete element is characterized by a resistance function, which gives resistance (force or moment) as a function of deformation. Fig. 2.10 shows a typical resistance-displacement function for a flexure-dominant reinforced concrete element subjected to blast loading. It can be seen that the initial curve is linear up to the yielding of tension reinforcement. Thereafter, the curve becomes flat until the crushing of concrete occurs in compression. Usually, the onset of crushing occurs at a deflection corresponding to a support rotation of $\theta = 2^{\circ}$ (Cormie et al. 2009). Concrete is effective in resisting applied moments when θ varies between 0° and 2°. Within this range the section is referred to as "Type-1 Section." Type-1 Section has concrete cover remaining intact on both tension and compression sides, as illustrated in Fig. 2.11. Members that develop Type-1 Sections can be singly or doubly reinforced. Once $\theta > 2^{\circ}$, the compression concrete completely crushes and the compression forces are only resisted by the reinforcement in compression, if present. In the absence of compression reinforcement, the member develops failure as the concrete compression block is not able to sustain applied moments. In order to fully develop the tension reinforcement, an equal amount of steel reinforcement must be provided in the section. Moreover, top and bottom rebars must be

adequately supported by stirrups. A member that experiences total crushing of compression concrete and cracking of the cover concrete in tension is referred to as a Type-2 Section. Fig. 2.11 illustrates a Type-2 Section. This behaviour usually takes place when the support rotation θ is between 2˚ and 5˚ (Cormie et al. 2009). Under higher deformations (θ > 4˚) the resistance may increase due to the strain hardening of tension steel. With further deformations, the element loses its stability and may lose its structural integrity and experience collapse (Cormie et al. 2009).

Full flexural capacity of a member can be developed only if premature brittle shear failure is prevented. The shear capacity of a member must always be higher than the flexural strength if ductile response is to be ensured. This may be possible by adding sufficient shear reinforcement until diagonal compression crushing of concrete occurs.

Equivalent SDOF solution is widely used to obtain dynamic response of reinforced concrete elements subjected to blast loads. Resistance – displacement curve (also called resistance function) is a crucial tool for the SDOF analysis. An idealized resistance function can be established by simply specifying the moment capacity and the corresponding curvature for the section at different load levels, like M_y, and M_u (ASCE 2011) (Fig. 2.12). The corresponding Δ_y and Δ_u are then found using the following expressions:

$$\Delta_y = \emptyset_y \frac{L^2}{3} \qquad 2.8$$

$$\Delta_u = \emptyset_y \frac{L^2}{3} + (\emptyset_u - \emptyset_y) L_p (L - 0.5 L_p) \qquad 2.9$$

where,

M_y is the moment capacity at yield

M_u is the ultimate moment capacity

$\emptyset_y$ is the yield curvature

$\emptyset_u$ is the ultimate curvature

Δ_y is the mid-span deflection at yield

Δ_u is the maximum mid-span deflection

L is the span length

The equivalent plastic hinge length (L_p) used in Eq. 2.9 can be established by using one of the models available in the literature.

2.2 Strengthening of Concrete Structures with FRP

FRP composites, consisting of fibers (main load carrying component) embedded in resin, are used in the construction industry primarily for retrofitting and rehabilitating existing elements. They are often classified into three categories based on the fibres employed; i) carbon fibre reinforced polymer (CFRP), ii) glass fibre reinforced polymer (GFRP) and iii) aramid fibre reinforced polymer (ARFP). The most common resins used are epoxy, polyester, and vinylester (Teng et al. 2003).

External strengthening of concrete structures with FRP is commonly done either by implementing wet lay–up method or by using prefabricated FRP laminates of different forms. The wet lay-up method is the most widely employed method as it is more adaptable to site conditions, especially when bonding on curved surfaces is required, or wrapping around members is to be done. However, prefabricated laminates may result in better quality control. In both methods it is essential to bond the FRP composite on the surface of concrete to achieve the required strengthening function.

In the wet lay-up method also known as laminating, one or successive layers of FRP fabric or sheet, impregnated with liquid resin, is manually applied by hand onto an existing pre-prepared concrete surface. A plastic serrated roller is often used to force out the trapped air from the FRP composite and to evenly distribute the resin all over the fabric. More resin is applied if the fabric is not fully saturated. The FRP composite is then left to cure in ambient temperatures for at least 24 hours.

2.2.1 Flexural strengthening of reinforced concrete components

The application of CFRP plates for enhancing flexural capacity of concrete beams was first investigated in mid-1980s at the Swiss Federal Laboratory for Materials Testing and Research (EMPA) (Teng et al. 2002). Nowadays, surface bonded FRP plates, or layers of FRP fabrics, placed on the tension face of flexural members, is increasingly used as a method of strengthening. De-bonding at the ends of the soffit FRP strip can be avoided by installing FRP

U-strips bonded or mechanically bolted to the ends of the soffit strip as shown in Fig. 2.13. Bonding of FRPs with fibers oriented along the axis of the concrete member can increase the flexural capacity by acting as additional tensile reinforcement (ISIS 2008). This is clearly illustrated in Fig. 2.14.

2.2.2 FRP confinement of axially loaded reinforced concrete columns

Both strength and ductility of axially loaded reinforced concrete columns can be enhanced significantly by providing transverse confinement through the use of FRP jacketing systems. Ductility is defined as the ability of the structural member to develop inelastic deformations without a reduction in load carrying capacity. This is important for members subjected to extreme loads, such as those due to earthquakes and bomb blasts. The amount of transverse FRP reinforcement, as well as the shape of a cross-section affect the efficiency of confinement. FRP confinement is very effective for circular concrete columns where the FRP fibers develop hoop tension. FRP confinement is much less effective in square and rectangular columns. This is because portions of the concrete will remain unconfined by FRP as the lateral confinement pressure is reduced between the section corners (Fig. 2.15). The corners of rectangular concrete columns need to be rounded prior to the application of FRP wraps to prevent stress concentration and tearing of the material in the corners, and to increase the uniformity of confinement pressure.

When a reinforced concrete member is subjected to axial load and bending, longitudinal FRP strips are applied to increase its moment resistance and transverse FRP sheets are applied to enhance the axial load capacity and ductility. A typical application for this dual function is illustrated in Fig. 2.16.

2.3 Previous Studies of Interest

2.3.1 RC columns subjected to blast effects

Dynamic response of reinforced concrete columns under blast effects can be examined using different techniques of load application. These techniques include; i) field blast test (involving detonation of explosives), ii) quasi-static tests simulating blast pressure, and iii) shock wave generated by a shock tube. This section includes previous studies involving unretrofitted and FRP retrofitted RC columns subjected to blast threat using one of the above mentioned test procedures.

Crawford et al. (2001) performed different explosive tests on fifty three bare RC and CFRP wrapped columns. The tests were conducted to validate the design procedure developed by Karagozian and Case, the authors' engineering firm, for blast resistant columns retrofitted with externally applied FRP sheets. Both field and laboratory tests were carried out. The paper reports on very limited data with few comparisons. Two columns; DB6 (as-built) and DB8 (CFRP wrapped) were examined as part of the full-scale field tests. This is depicted in Fig. 2.17. Both columns were subjected to the same blast loads. The four story reinforced concrete office building, shown in Fig. 2.17 was designed for gravity loads only. Column DB8 was retrofitted with six layers of CFRP wraps for shear strength enhancement, and three longitudinal 102 mm CFRP strips on each side for flexural strengthening.

Field tests indicated that Column DB6 failed mainly in shear at the top and bottom. The mid-height region of the column remained intact and vertical. The column's residual mid-height displacement was 250 mm (Fig. 2.18.a). In contrast, Column DB8 remained elastic and no visible damage was observed (Fig. 2.18.b).

The behaviour of CFRP wrapped and unretrofitted columns subjected to blast effects was also investigated by testing 20 full-scale RC columns under controlled lab conditions (quasi-static tests). Blast loading was simulated using a lateral loading system demonstrated in Fig. 2.19. Lateral and axial loads were applied using three and two actuators respectively (Fig. 2.20). The test setup permitted rotational restraints at the top of the test specimen.

The results of the quasi-static test of the columns showed similar behaviour to that obtained by the field tests. The response of unretrofitted column was identical to the companion column tested in the field as shown in Fig. 2.21. Concrete columns retrofitted with two and six layers of CFRP were also tested using the same test set-up shown in Fig. 2.19. The maximum strength of the column wrapped with two layers of CFRP was twice the maximum strength of the unwrapped column. At failure, the mid-height deflection was 114 mm. Two layers of CFRP provided sufficient shear capacity to allow the column to reach its full flexural strength. In this column the failure occurred due to the insufficient strength of CFRP wrap to withstand hoop forces. An excess shear capacity was provided and the ductility was increased when the column was wrapped with six layers of CFRP. No sign of damage was observed even when the deflection at mid-height was developed at 152 mm. The residual lateral deflection was 95 mm.

The above research program also included a corresponding field test using charges of 1000 lbs to 2000 lbs TNT at standoff distances of 10 ft and 20 ft. A special blast chamber designed by Karagozian and Case (K&C) was used to carry out the tests. The columns were subjected to axial loads. A sophisticated set of instrumentation was used including those for lateral displacement and velocity measurements, as well as the measurements of axial load and blast pressure. The instrumentation also included high-speed cameras. Some of the visual results obtained from these tests are shown in Fig. 2.22, illustrating the enhancement obtained in column behavior due to the FRP strengthening.

The authors concluded that retrofitting RC columns with FRP is an effective technique to secure the survivability of reinforced concrete buildings subjected to blast loads. Although significant efforts and resources were devoted to this study, no quantitative relation between the characteristics of the columns and the FRP retrofitting material was developed.

The test data of real blast tests conducted in this study were of limited use because of the noise and the instrument failures, but the importance of the tests was in verifying the effectiveness of the retrofits (Tonatiuh Rodriguez-Nikle 2006).

Gram et al. (2006) indicated that a blast simulator was developed and built in 2005 by the University of California, San Diego and MTS Systems Corporation to test various modified and unmodified RC structural components. Over 20 specimens were successfully investigated by January, 2006 using the blast simulator mentioned above. Test samples included 355 mm x 355 mm x 3000 mm RC columns. The test system generates an impact load to produce 2 ms pulse with a maximum pressure of 35 MPa and impulse of 14 kPa-s over the column surface (Gram et al. 2006). With this technique, visual observation of the test was possible. The results were recorded by successfully implemented instrumentation and a high speed-camera.

The test system was installed on an isolated foundation that provided a fixed reinforced concrete reaction wall at one end and a moveable reinforced concrete reaction wall at the other end (Fig. 2.23). Blast generators (BG) were mounted on the fixed reaction wall through the steel plates embedded in the wall. The positions of BGs could be adjusted as required. The movable reaction wall was a heavy reinforced concrete mass that was built to provide a movable link system to the upper end of the test specimen. The movable wall was post-tensioned to the foundation. Weight of the impacting masses were supported and kept aligned with the specimen by guide rails.

Spacing was allowed between the blast generators for adjustments by attaching the guide rails to the adjustable frame. Test columns were loaded with four blast generators distributed over the full height of the specimens. The simulation of correct boundary conditions and applied load associated with an actual blast event was achieved by the following:

1. In an effort to restrain the column against translation and rotation the footing was post-tensioned to the test floor at the column base.
2. The link system provided at the top of the column allowed vertical movement, while providing lateral and rotational fixity.
3. Three hydraulic jacks with a mechanical lock were used to apply vertical column axial load. The jacks reacted against a steel frame to apply the loads.

Results obtained proved that the live explosive loads can be simulated using the technique explained above. The authors stated in this study that laboratory blast tests represented field tests with acceptable accuracy. It was possible to monitor the specimen failure, time-history and the debris generated in the simulated blast load tests because of the absence of the fire ball associated with live explosives. This study was mainly devoted to describing the testing system, used rather than presenting the results of column tests. The lateral load was applied only in three zones where the impact actuators were rigidly linked to the specimen (see Fig. 2.23) and the relative rotations of the column section across each zone were prevented. Hence, the specimen is divided into five zones: the two end zones, and the three "actuator" zones. The curvatures, rotations, and displacements are not continuous over the column height. On the other hand the authors have not investigated whether fixing the actuators to the column specimens would result in any change of the inertia or the strain energy throughout the test.

Berger et al. (2008) carried out an experiment to test the effectiveness of steel reinforced polymer (SRP) as external strengthening technique for RC columns against blast loads. CFRP retrofitting was also investigated to compare the performance of the two materials. Five unwrapped RC columns and twelve RC columns of various wrapping configurations were exposed to field blast tests. The test parameters included charge and stand-off distance, SRP longitudinal and transverse strengthening, and CFRP strengthening.

Two vertical blast test frames were built to support two RC columns in each test. The column dimensions, transverse reinforcement, SRP sheets, and boundary conditions were identical to those investigated by Carriere et al. (2009). Specimens were reinforced longitudinally with 10M

rebars. Concrete compressive strength was 44 MPa. Yield and ultimate strengths of steel reinforcement were 450 MPa and 630 MPa, respectively. CFRP had a fiber modulus and rupture strain of 228 GPa and 1.67 %, respectively. Outcomes of this study proved that SRP retrofitted columns showed considerably less damage than the control columns. Moreover, it was observed that SRP modified columns showed more ductile behavior than CFRP modified columns. Finally it seemed that the columns wrapped with SRP had better resistance to small projectile impact loads than those wrapped by CFRP. The study did not identify any quantitative comparisons between the amount of retrofitting materials and the application methods, with the levels of damage or the major response parameters.

Williams et al. (2008) evaluated design parameters that have the greatest impact on the performance of bridge columns subjected to severe blast loads. Ten half-scale bridge columns of different designs were subjected to real blast actions. The test variables were cross sectional shape, length-to-depth (L/D) ratio, type of transverse reinforcement, volumetric reinforcement ratio, and splice location. Due to the severity of the blast test carried out in this research project, a unique test setup was required. The reaction structure was specially designed to withstand the repeated large magnitude blast loads (Fig. 2.24). Pressure gauges, steel reinforcement strain gauges, and a high-speed camera were used to fully capture the response during the event. Column end condition was fixed at the base and pinned at the top. Columns were subjected to different charge weight of various standoff distances. In this study only an overview of the basic observation was released due to security restrictions (Williams et al. 2008).

It was observed that in most specimens the base shear clearly dominated response. Little or no flexural cracking was noticed. Even with the extensive shear failure, some columns still retained some axial capacity. Columns provided with adequate shear capacity performed very well as both shear and flexural behaviour were observed. It was also seen that columns with continuous transverse reinforcement behaved better than those reinforced with ties. Finally, this study showed that columns of enhanced level of hoop reinforcement with long hooks performed better than those missing these features.

The authors' recommendations were to increase the volumetric transverse reinforcement ratio and to reduce splices in longitudinal reinforcement at critical regions.

Rodriguez-Nikle et al. (2009) tested ten as-built and CFRP modified non-seismically detailed RC columns using the blast generators shown in the study of Gram et al. 2006 mentioned earlier. The aim of the investigation was to search the effect of different CFRP wrapping schemes on dynamic behaviour of RC columns subjected to blast-like loading. The wrapping design configuration adopted were i) two hoop wraps ii) six hoop wraps and iii) six hoop wraps plus CFRP longitudinal strips. Columns were tested with and without the application of axial loads. It was concluded that all the CFRP strengthening design used highly improved structural performance of the columns when tested by the blast generator. It was noticed that CFRP modified specimens with large mid-height deflection still had enough residual axial capacity to prevent progressive collapse.

Captain (2009) investigated **t**he possibility of representing damage patterns of RC columns observed in a field blast test by an impact generating machine. The researcher also investigated the effectiveness of FRP repair techniques on impact and blast-damaged columns. Eight RC columns, 150 mm x 150 mm in cross section and 2100 mm in length, were tested under impact and live blast loading; four specimens for each type of test. The columns were longitudinally reinforced with four 10M rebars, and transversely with 6.3 mm square closed ties spaced at 100 mm c/c and the concrete compressive strength used was 20 MPa. One specimen from the blast test and four specimens from the impact test were repaired and strengthened using a CFRP jacketing system. Impact tests were conducted using a swing-pendulum impact hammer. Pressure sensors, force sensors, strain gauges, LVDTs, accelerometers, and a high speed camera were used. The author concluded that the rapid application and the short duration of loading created by the impact machine may be appropriate for representing column response under a live blast load. However; for an accurate representation of blast, the load must be distributed uniformly over the entire height of the column. The study showed that the original axial design capacity of damaged columns was recovered by the CFRP wrapping. The impulsive response of the columns tested under zero axial load was well predicted by the SDOF solution.

Carriere et al. (2009) conducted an experimental study to investigate the performance of RC beams and beam-columns transversely wrapped with steel fiber polymers (SRP) and subjected to field blast loading. A total of ten RC specimens were tested under various blast pressures. According to Carriere et al. (2009), SRP sheets have recently been proposed as a potential alternative to CFRP to strengthen reinforced concrete beams. Reinforced concrete specimens

used were 150 mm x 150 mm in cross-section and 2100 mm in length. Unsupported length was 1500 mm. Each test specimen was longitudinally reinforced with four 6 mm rebars, and was laterally reinforced with 6 mm closed steel ties spaced at 100 mm c/c. Average concrete compressive strength was 39 MPa. Yield and ultimate strengths of reinforcing steel were 500 MPa and 600 MPa, respectively. The specified modulus and ultimate strength of the SRP utilized were 78 GPa and 1170 MPa, respectively. Four RC specimens were retrofitted using Hardwire SRP while the other four were left unretrofitted. A special blast test fixture (BTF) was built to hold the RC members in place during the test. When no axial load was applied, two specimens could be tested simultaneously in the BTF, whereas when the specimen was tested as a column, only one specimen could be fitted in the BTF. Fixed-Fixed boundary condition was provided at the specimen ends. Six live blast field tests were carried out. For the first four tests, the RC elements were tested as beams. At each test, two beams were tested at the same time; one beam was SRP retrofitted and the other beam was left unretrofitted, where each test had a different charge weight. For the last two tests, the specimens were tested as columns. One RC column was SRP wrapped and the other column was as-built. Strain gauges, LVDTs, pressure transducers, and a high speed camera were used to record the behaviour of test specimens. The key findings of this study indicated that for the RC members wrapped with SRP, the concrete crushing in the plastic hinge region was reduced. This would likely increase energy absorption by the member and hence, both flexural capacity and ductility were improved. It was also indicated that SRP wraps prevented spalling during the tests.

Lloyd (2010) investigated the dynamic behaviour of fourteen half scale reinforced concrete columns subjected to simulated blast pressures. Twelve columns had dimensions of 100 mm x 150 mm x 2438 mm, and two columns had dimensions of 150 mm x 150 mm x 2438 mm. The Canadian Standard Association CSA23.3-04 for the "Design of Concrete Structures" was followed in design. The columns represented the first floor columns of multi-story buildings located in seismic and non-seismic regions. The University of Ottawa Shock Tube was employed to simulate the blast shock wave. All columns were reinforced longitudinally with 4-10M steel rebars. Columns were reinforced transversely with closed square ties fabricated from 6.3 mm smooth steel rebars. A hydraulic jack was used to apply axial loads on columns. Concrete compressive strength used was 58 MPa for twelve columns. However, two non-seismic column of rectangular cross-section were fabricated from a concrete mix having a compressive strength

of 46 MPa. The lateral supports were placed at each end, spaced 1980 mm apart, providing a near fixed condition against rotation.

The author conducted SDOF analyses to predict maximum displacement at column mid-height and compared the results with test data. The results of the experimental investigation indicated very little or no difference in the blast response between the seismically and non-seismically detailed RC columns. It was also concluded that the SDOF model predicted well the maximum displacement of test specimens for moderate levels of response. For large displacement response the model under-predicted the displacements; though predicted them well when the columns suffered severe damage, approaching the development of collapse mechanism. For future research, the author recommended to investigate the effect of increasing the specimens' cross-sectional dimensions and monitoring the time history of the changes or degradation of the axial load by means of load sensors.

Burrell (2012) experimented 13 half-scale steel fiber reinforced concrete columns (152.4 mm x 152.4 mm x 2468 mm) using the shock tube at the structural lab of the university of Ottawa. Eight normal strength steel fiber reinforced concrete (SFRC) columns and five ultra-high performance fiber reinforced concrete (UHPFRC) columns were subjected to air blasts. Columns were designed following the requirements of CSA A23.3 for both seismic and non-seismic design. Different amounts and types of fibers were used as test variables (Russell 2012).

Longitudinal and transverse reinforcements, end conditions, and clear column height between the supports were identical to those used by Alan Lloyd (2010) in his study. Axial load of 379 kN was applied prior to the application of blast pressure.

The test variables included reinforcement detailing (seismic and non-seismic), amount of steel fibers, type of steel fibers, and concrete type. The blast response of columns was simulated by using a single-degree of freedom dynamic analysis software, RC Blast (Jacques et al. 2013). The software results showed good agreements with test data. The major finding of Burrell's (2012) study was that the addition of steel fibers reduced maximum and residual displacements. The enhancement in column resistance to blast pressure was found to be proportional to the steel fiber added to the concrete mix. The displacements obtained at mid-height for seismic columns were 27% smaller than the corresponding displacements of gravity columns. The author

recommended the adoption of seismic detailing together with steel fibers in concrete to obtain improved blast resistance.

Rodriguez-Nikle et al. (2012) studied the effectiveness of carbon fiber (CFRP) jackets in enhancing the structural behaviour of reinforced concrete columns subjected to blast threats. In their investigation, nine rectangular reinforced concrete columns were subjected to quasi-static loads to mirror the damage patterns obtained in field blast tests in the laboratory. The column specimens were intended to represent columns of mid-rise non-seismic buildings. All columns had the same height of 3267 mm with different cross-sections. Six specimens were 356 mm x 356 mm, one specimen was 305 mm x 305 mm and remaining two were 305 mm x 457 mm.
The test setup is illustrated in Fig. 2.19, which is identical to that used by Crawford et al. (2001) described earlier. Columns with and without CFRP wrapping were tested. The effects of increasing the number of transverse CFRP layers and the addition of longitudinal CFRP strips were evaluated on improving structural response. Static load-deflection relationships (static resistance functions) and CFRP surface strains were measured. The CFRP modified columns failed in a ductile mode rather than experiencing a brittle shear mode of failure. Additional strength gain was observed when CFRP strips were added in the longitudinal direction. This enhancement in strength resulted in an increase in energy absorption capacity and a decrease in mid-height deflection, also reducing the geometric instability of the member. It was noticed that CFRP wrapped columns had enough residual axial load capacity. Findings of this study clearly indicated that columns strengthened with thicker jackets had higher ductility and reduced jacket strains.

Qasrawi (2014) conducted an experimental and analytical study to test the capability of concrete filled FRP tubes (CFFTs) to resist the effects of impact and blast loads. A total of twelve full scale circular RC columns (with 200 mm cross sections and 4.0 m column lengths) were built and tested in the experimental phase of the study. Six columns were CFFTs and the other six were as-built control columns. The columns were subjected to monotonic, impact, and field blast loading. Key findings showed that GFRP tubes confined and protected specimens against severe impulsive loading. Energy absorption was increased by 1223 % in CFFT specimens. Thus both strength and ductility were significantly enhanced. It was also stated that CFFTs are effective systems for impact and blast resistance.

Lloyd (2015) investigated the effect of three different retrofitting methods on blast behaviour of RC columns using a shock tube. Sixteen half scale RC columns were designed and built for this purpose. Retrofitting techniques used were; i) CFRP jacketing ii) transverse steel prestressed confinement (Fig. 2.25 a) iii) compression steel bracing (Fig. 2.25 b) and iv) tension steel bracing (Fig. 2.25 c). FRP retrofitted columns had either transverse CFRP wrapping using unidirectional fibre sheets [0°], longitudinal unidirectional CFRP strips [90°], and a combination of the two [90°/0°]. The columns were subjected to successive multiple blast shots of incrementally increasing magnitude. In general, all three retrofit techniques used were effective in upgrading the blast behaviour of columns. For columns with surface-bonded longitudinal CFRP fibres, the best performance was achieved when the longitudinal fibres were enclosed in transverse FRP sheets. Transverse prestressing increased column ductility, while compression brace retrofit substantially modified column strength. Among the three retrofitting systems employed, the tension brace proved to give the best blast performance. The experimental results were used to develop a SDOF model that predicted the dynamic response of retrofitted columns. A design procedure was recommended for column retrofitting.

2.3.2 Effects of FRP orientation and ply mix on concrete confinement

Mirmiran and Shahawy (1997) tested a total of thirty 152 x 305 mm concrete cylinders to investigate confinement characteristics of FRPs. Twenty four specimens were in the form of a concrete-filled FRP tube and six specimens were plain concrete. The FRP tube was made of unidirectional E-glass fibers at a winding angle $\pm 15^{\circ}$. Jacket thicknesses were 6, 10, and 14 plies. Results of this study indicated that strength and ductility of concrete improved as the number of FRP plies was increased. Only one fiber orientation ($\pm 15^{\circ}$) was examined in the study.

Rochette and Labossiere (2000) studied the effect of FRP wrap thickness and concrete cross-sectional shape on compressive strength of short concrete specimens. The cross-sectional shapes tested were circular, square, and rectangular. Unidirectional CFRP and bi-directional aramid-woven fabrics were utilized to confine the concrete. Fiber orientation used for the entire study was 0° with respect to the transverse direction of the specimen; however one concrete specimen of a square cross-section had a different fiber orientation of $[\pm 15_2{}^{\circ}/0^{\circ}]$. In their conclusions it was stated that the angled-hoop CFRP wrap $[\pm 15_2{}^{\circ}/0^{\circ}]$ should be investigated as a potential orientation to achieve more strength and ductility.

Pessiki et al. (2001) conducted an experimental investigation to explore the axial load behaviour of small scale circular and square plain concrete specimens, and large scale circular and square RC columns wrapped with FRP jacketing systems. Three types of jackets were employed i) woven GFRP [0 ˚, ±45 ˚] jacket ii) unidirectional GFRP [0 ˚] jacket, and iii) unidirectional CFRP [0 ˚] jacket. All concrete specimens were tested under monotonic concentric axial loads. The outcomes of this investigation showed that both the load axial capacity and deformability of the investigated FRP retrofitted specimens were improved compared to unretrofitted concrete. The degree of enhancement in concrete compressive strength and the corresponding strain is related to the FRP jacket strength and stiffness. The properties of FRP materials and the thickness of the jacket highly influence the jacket strength and stiffness.

Parven and Jamwal (2004) examined the effect of wrap thickness and ply configuration on composite-confined concrete cylinders through non-linear finite element analyses. Hoop-angle-hoop and angle-hoop-angle E-glass fiber ply configurations were used. Hoop and angle unidirectional fibers were oriented at 0˚ and [+45˚ / -45˚] with respect to the transverse direction, respectively. For the same laminate thickness, the finite element analysis showed that the hoop-angle-hoop wrap configuration provided a higher compressive strength and ductility when compared with the angle-hoop-angle wrap configuration. The authors recommended the use of the hoop-angle-hoop FRP wrap configuration for the confinement of short circular columns in practice.

Au and Buyukozturk (2005) studied the effects of fiber orientation and ply mix on the load-deformation relationship and failure mode of FRP wrapped concrete cylinders subjected to a uniaxial load. A total of 24 concrete cylinders with dimensions of 150 mm x 375 mm were tested. Concrete compressive strength was 24.2 MPa. Eighteen specimens were FRP-wrapped whereas 6 cylinders were left without any FRP wrapping. Three types of E-glass fabrics were used; i) unidirectional fibers, ii) [0˚/90˚] bidirectional weaved fibers with equal fiber content in both directions, and, iii) [+45˚/ -45˚] bidirectional weaved fibers with equal fiber content in both directions. Wrapping configurations employed were [0˚], [0˚/ 90˚], [+45˚/ -45˚], [90˚/+45˚/ -45˚], [0˚/+45˚/ -45˚], and [+45˚/ -45˚/0˚]. It was concluded that hoop fibers are efficient in providing confinement, however wrapping in this direction leads to brittle failures with sudden release of stored energy. Unlike the hoop confinement, angular FRP confinement tends to fail in a ductile mode owing to the fiber reorientation mechanism and associated energy dissipation mechanism.

Li et al. (2005) tested 27 concrete cylinders (152 mm x 305 mm) to study the effect of fiber orientation on the structural behaviour of FRP wrapped concrete. Six fiber orientations were examined using unidirectional E-glass fabric. Fiber orientations employed were [0˚/0˚], [0˚/90˚], [90˚/90˚], [60˚/30˚], [45˚/45˚], [-45˚/+45˚], [0˚/0˚/0˚/0˚], and [90˚/90˚/90˚/90˚]. Results showed that stress-strain behaviour, strength, ductility, and failure mode are considerably affected by fiber orientation and FRP jacket thickness. It was found that fibers oriented at a certain angle between hoop and axial direction led to the enhancement of concrete compressive strength and ductility in a similar manner as that observed by Ching Au and Oral Buyukozturk (2005).

Sadeghian et al. (2008a) conducted numerical analyses to investigate the effects of various parameters of FRP confinement, including CFRP wrap thickness, fiber orientation, concrete compressive strength, and interfacial bond. The researchers analyzed CFRP jacketed concrete cylinders (150 mm x 300 mm). Fiber orientations adopted in this study were [0˚], [-15˚/+15 ˚], [-30˚/30˚], and [-45˚/+45 ˚]. Concrete compressive strength ranged between 20 and 40 MPa. The findings of the analyses showed a significant enhancement in the strength and ductility of CFRP wrapped cylinders compared with plain cylinders. Concrete compressive strength enhancement decreased and concrete ductility increased as fiber orientation changed form 0˚ to ±45˚. Results also showed that strength and stiffness is highly affected by the jacket thickness. The gain in compressive strength is higher when f_c` (concrete compressive strength) is lower.

Sadeghian et al. (2008b) studied the stress-strain behaviour of slender concrete columns retrofitted with CFRP composites. Thirty concrete cylinders of 100 mm diameter and various heights of 200, 400, 600, and 1000 mm were fabricated and tested under uniaxial compression. CFRP fabric was used to wrap the cylinders. Concrete compressive strength was 20 MPa. Fiber orientations adopted in this investigation were [0˚], [0˚ /0˚], [90˚/0˚], [45˚], and [45˚/0˚]. Key results of this investigation showed the following:

- Hoop fibers modified the failure mode of the concrete and increased the energy absorption capacity.
- [90˚/0˚] wrapping system improved the ultimate strength of slender columns.
- Wrapping with pure angle fiber can reduce the effects of slenderness.
- While [45˚/0˚] system improved the ultimate strength of slender columns, the authors were not able to draw clear observations on column ductility. For this reason more

studies were recommended to understand the behaviour of concrete columns wrapped with angle-hoop fibers.

Sadeghian et al. (2009) conducted an experimental study to explore the effect of fiber orientation on non-linear behaviour of CFRP composites. Twenty four CFRP coupons were subjected to axial tension. Fiber orientations investigated were [0˚], [90˚], [0˚/90˚], [+45˚/ -45˚], [0˚/ +45˚/ -45˚ /0˚], and [+45˚/ -45˚ /0˚+45˚/ -45˚]. Outcomes of this study demonstrated that the stress-strain behaviour of coupons with fiber orientation of 0˚ and 90˚ was perfectly linear with brittle rupture, while those with fiber orientation of ±45˚ were fully nonlinear with high ductility. The behaviour of the combination of 0˚ and ±45˚ was nonlinear up to the maximum strength, followed by nonlinear softening and eventual ductile failure.

Sadeghian et al. (2010) investigated the effect of fiber orientation on compressive behaviour of CFRP confined concrete columns. A total of thirty concrete cylinders were prepared. The 28-day compressive strength of concrete ranged between 35 and 45 MPa. Seven cylinders were unwrapped as control specimens, while twenty three cylinders were wrapped with CFRP having different fiber thicknesses and orientations of [0˚], [90˚], [+45˚/ -45˚]. Significant enhancement in compressive strength, stiffness, and ductility was observed in the CFRP wrapped cylinders compared to those that had plain concrete. It was also stated that the fibers oriented at [+45˚/ -45˚] possessed a larger flat region in the stress-strain relationship. This behaviour can be very useful in cyclic loading and hysteretic damping against seismic loading (Sadeghian et al. 2010).

Hajsadeghi et al. (2011) conducted non-linear finite element analyses to study the behaviour of square/rectangular reinforced concrete columns retrofitted with FRP jackets. Specimens considered were 250 x 250 x 500 mm and 150 x 300 x 500 mm. Square specimens were reinforced with four 14 mm longitudinal rebars, whereas the rectangular specimens were reinforced with four 12 mm rebars. All specimens were reinforced laterally with six 8 mm stirrups. Concrete cover provided was 25 mm. Specimen corners were rounded to a radius equal to 40 mm prior to the bonding of FRP. Each specimen was fully wrapped with unidirectional FRP sheets of a thickness of one, three, and five plies. Fiber orientations considered were [0˚], [+15˚/-15˚], [+30˚/-30˚], and [+45˚/-45˚] with respect to the hoop direction. It was noticed that the stress-strain response is highly affected by the fiber orientation. It was also observed that the highest strength enhancement was obtained with 0˚ fiber wrapping, though [+45˚/ -45˚] fiber orientation gave the highest ductility.

2.4 Summary

The following concluding statements can be made based on the previous research conducted on FRP retrofitted RC columns for improved blast resistance:

1. Most of previous studies were limited to FRP retrofitting of RC columns with two fiber orientations of 0˚ and 90˚. The effects of fiber orientation have not been fully explored and their effects on enhancing strength and ductility of RC columns under blast loads are still not fully understood.
2. There are gaps in the current literature pertaining to the optimal use of FRP ply mix and their effects on dynamic performance of RC columns under blast loads.
3. The variation or degradation of axial load capacity of RC columns during blast events has not been precisely monitored.
4. The dynamic reaction forces at lateral supports of RC columns generated during blast loading have not been measured in earlier tests.
5. No study so far compared the effects of multiple shots on RC members (single versus multiple blast shots).
6. None of the studies assessed post-blast axial load capacity of FRP jacketed RC columns.

Table-2.1: Different equations for estimating peak overpressure (P_{so}) (Ngo et al. 2007)

$P_{so} = \frac{6.7}{Z^3} + 1\ bar\ (P_{so} > 10\ bar)$ $P_{so} = \frac{0.975}{Z} + \frac{1.455}{Z^2} + \frac{5.85}{Z^3} - 0.019\ bar\ (0.1 < P_{so} < 10\ bar)$	Brode (1955)
$P_{so} = 6784\frac{W}{R^3} + 93\left(\frac{W}{R^3}\right)^{\frac{1}{2}}\ (bar)$	Newmark and Hansen (1961)
$P_{so} = \frac{1772}{Z^3} - \frac{114}{Z^2} + \frac{108}{Z}\ (kPa)$	Mils (1987)

Table-2.2: Dynamic increase factor (DIF) for reinforcing bars, concrete, and masonry (ASCE 2011)

Stress Type	DIF			
	Reinforcing Bars		Concrete	Masonry
	F_{dy}/F_y	F_{du}/F_u	f'_{dc}/f'_c	f'_{dm}/f'_m
Flexure	1.17	1.05	1.19	1.19
Compression	1.10	1.00	1.12	1.12
Diagonal Tension	1.00	1.00	1.00	1.00
Direct Shear	1.10	1.00	1.10	1.00
Bond	1.17	1.05	1.00	1.00

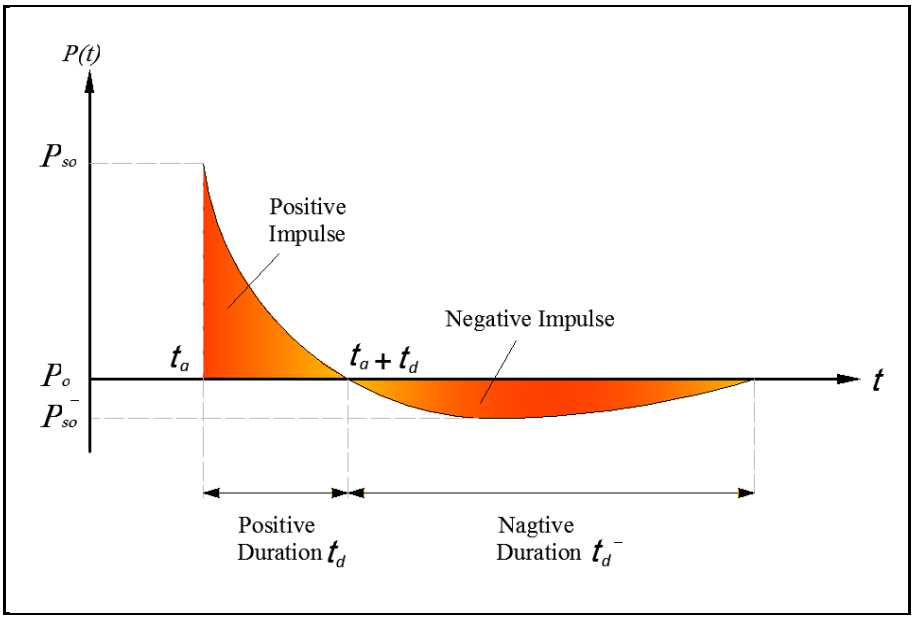

Fig. 2.1 Blast wave pressure-time history

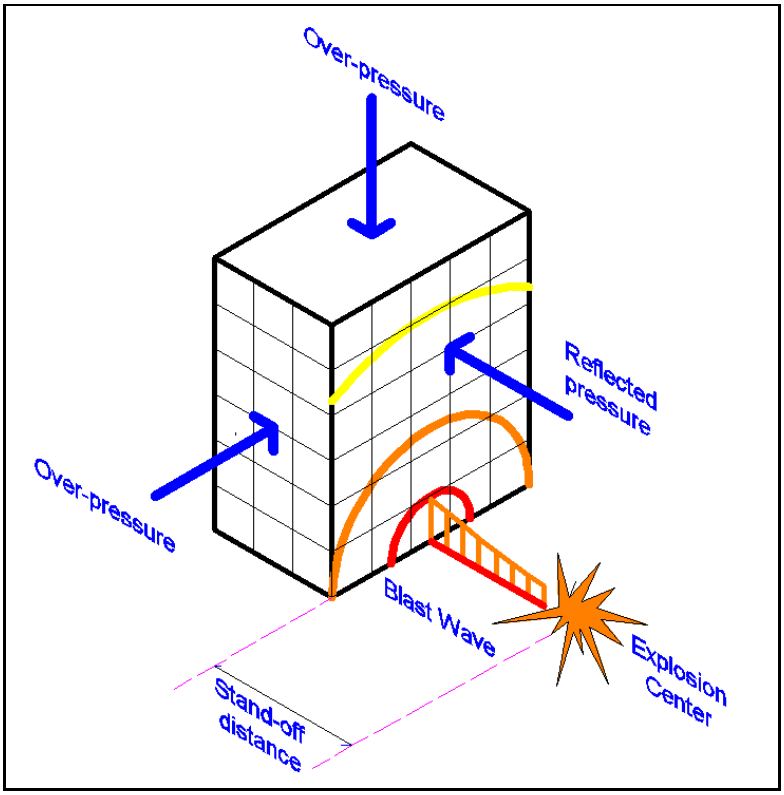

Fig. 2.2 Blast loads on buildings

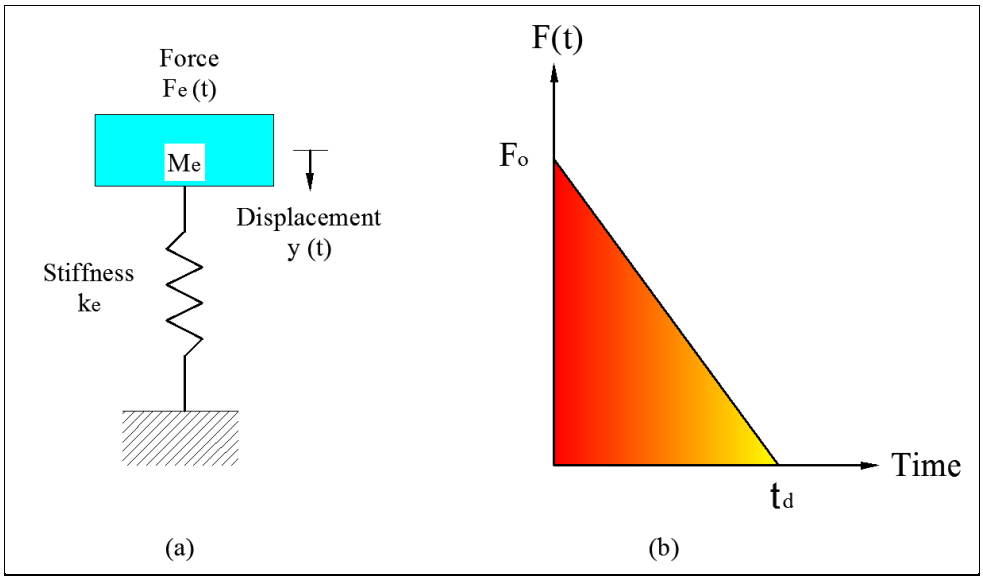

Fig. 2.3 (a) Equivalent SDOF system and (b) Idealized blast loading

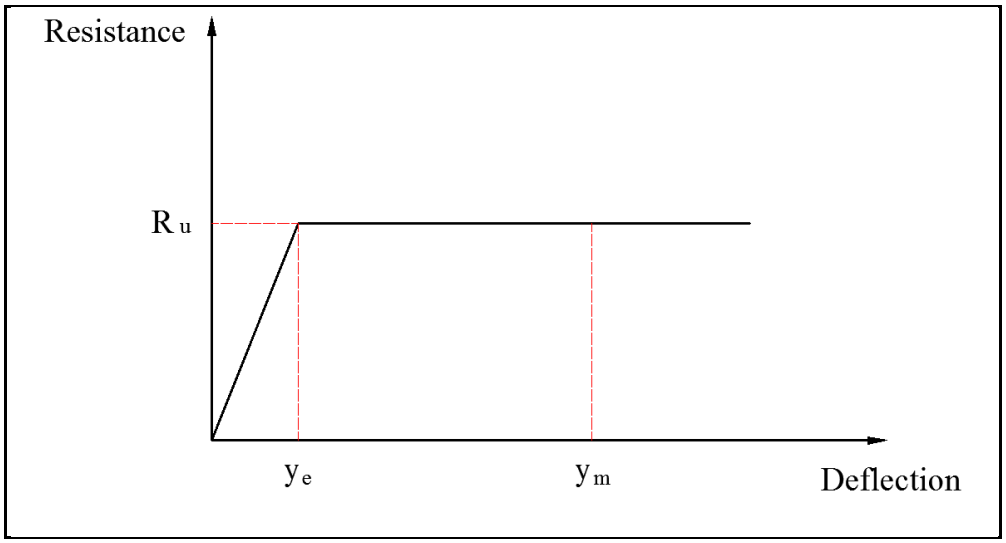

Fig. 2.4 Simplified resistance function of an elasto-plastic SDOF system.

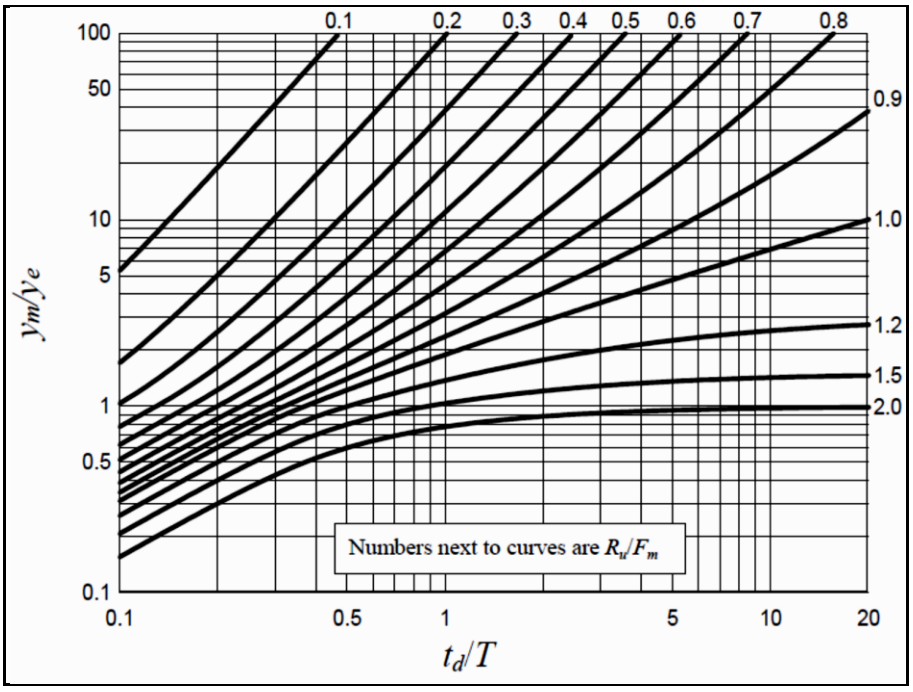

Fig. 2.5 Maximum response of elasto-plastic SDF system to a triangular load (Ngo et al. 2007)

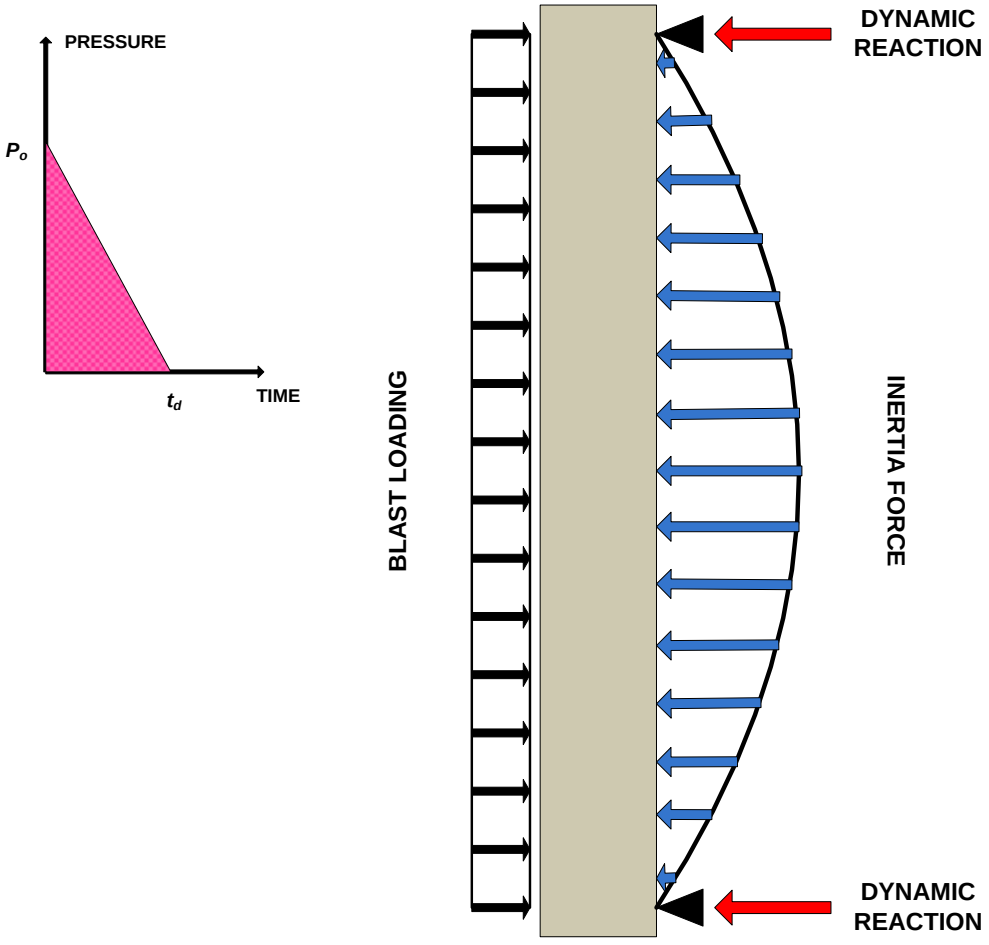

Fig. 2.6 Dynamic equilibrium of a structural component subjected to blast (Biggs 1964-reproduced)

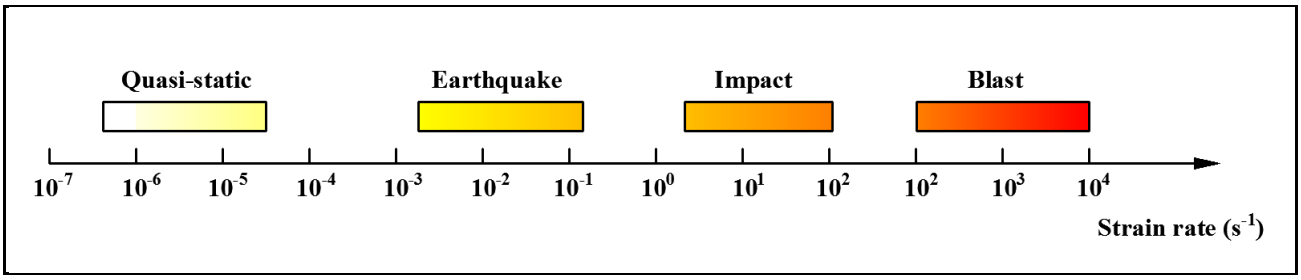

Fig. 2.7 Strain rates associated with different type of loading (Ngo et al. 2007-reproduced)

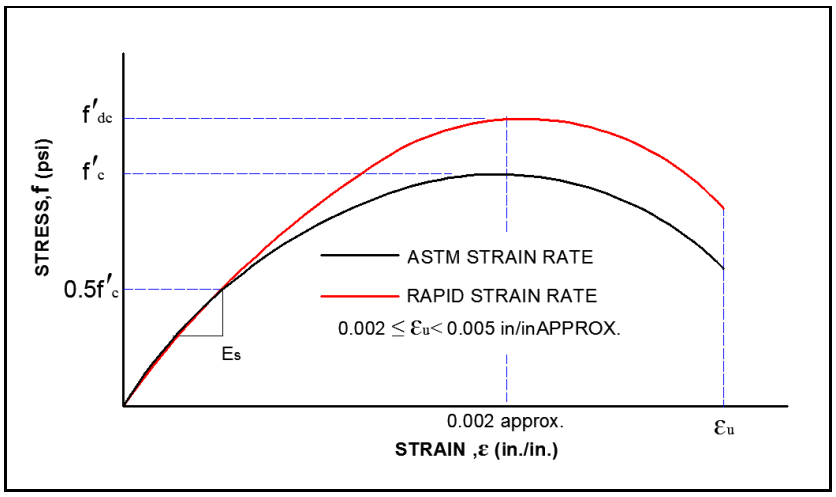

Fig. 2.8 Typical stress-strain curve for concrete under slow and rapid loads

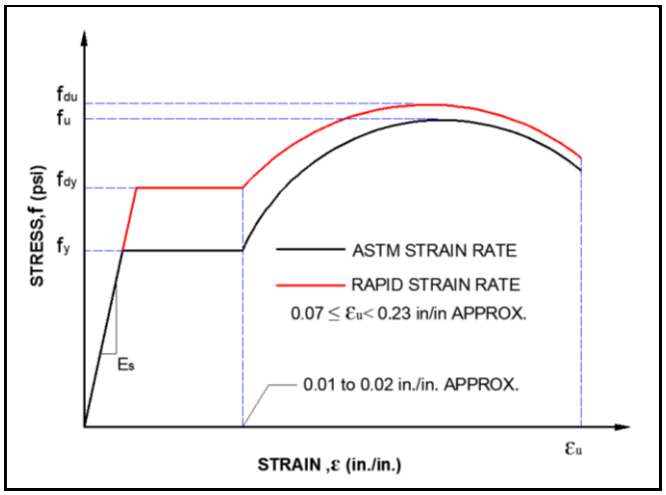

Fig. 2.9 Typical stress-strain curve for steel under slow and rapid loads

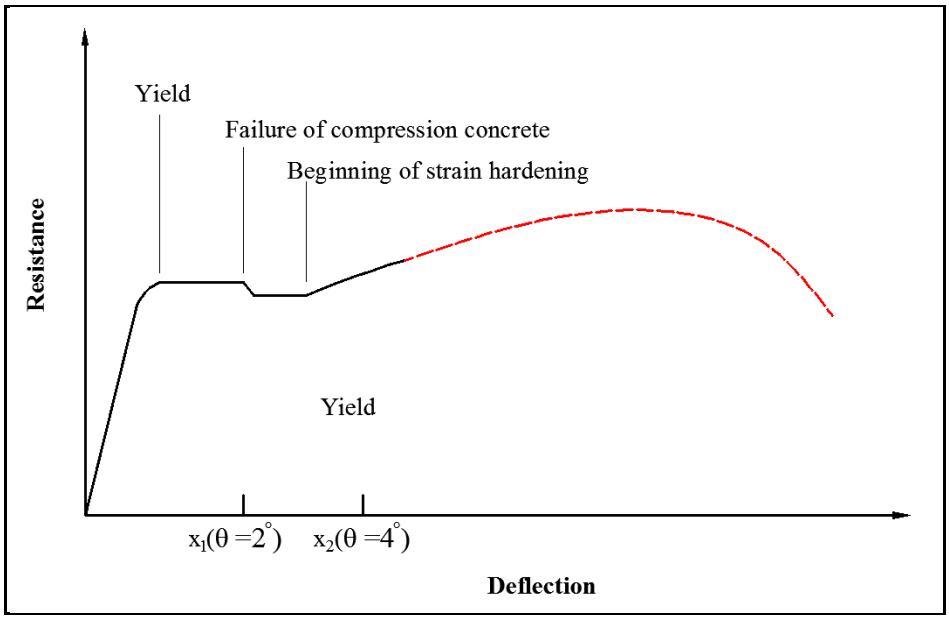

Fig. 2.10 Typical resistance-displacement curve of a reinforced concrete element (Cormie 2009-reproduced)

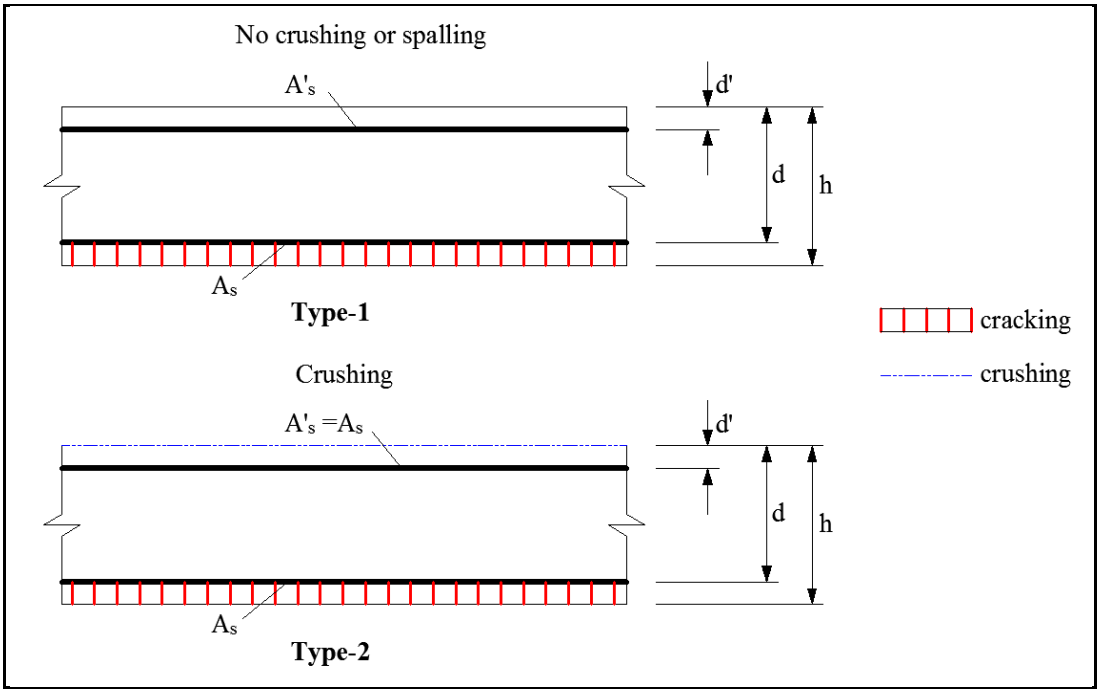

Fig. 2.11 Typical RC cross-section (Cormie 2009-reproduced)

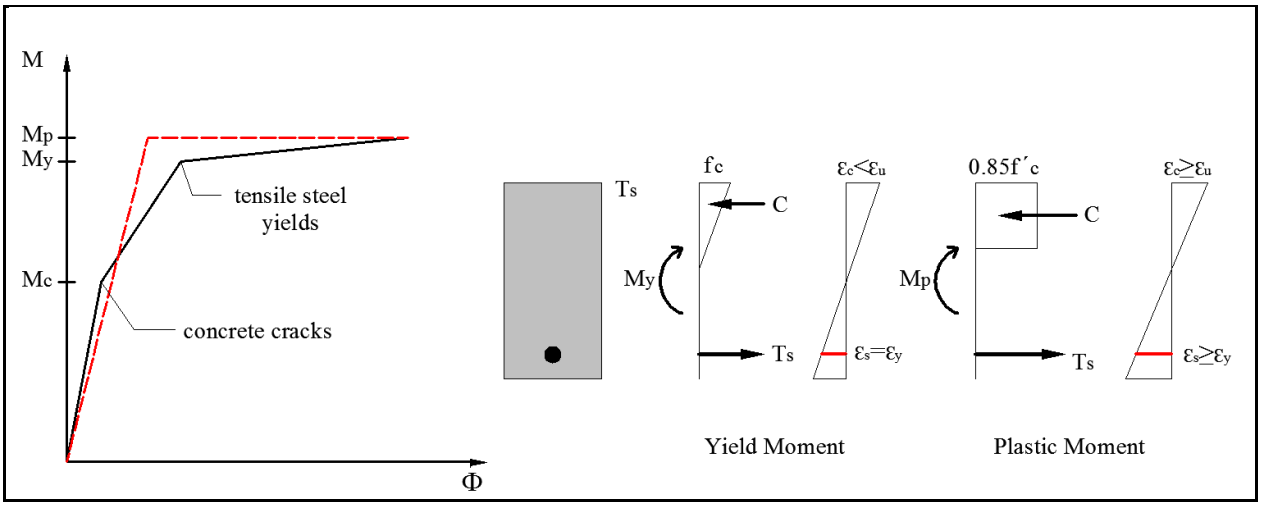

Fig. 2.12 Development of moment-curvature diagram (ASCE 2011-reproduced)

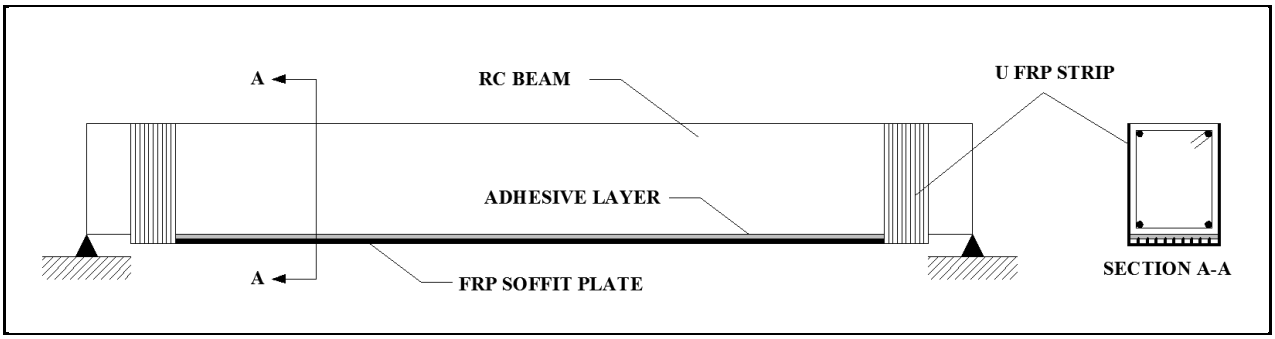

Fig. 2.13 Flexural strengthening using FRP materials (Teng 2002-reproduced)

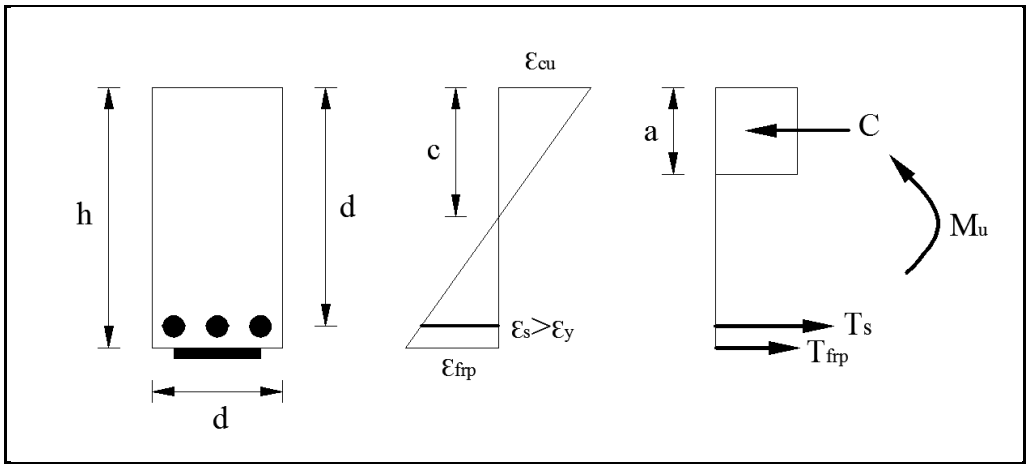

Fig. 2.14 Flexural strengthening of RC section using FRP fabrics

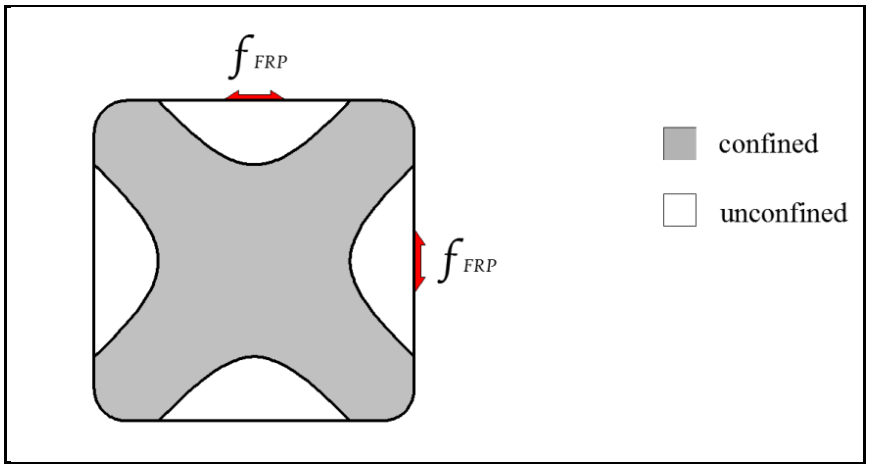

Fig. 2.15 Axial strengthening of a square column using FRP materials

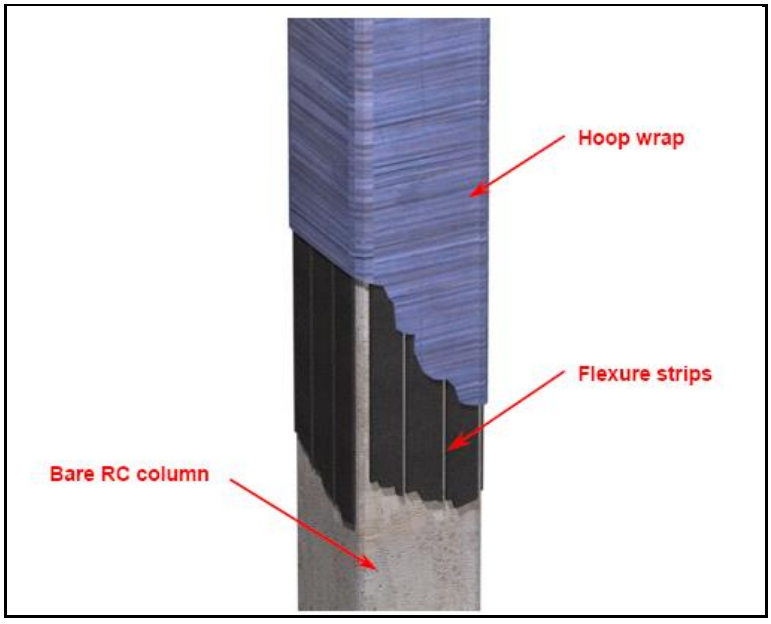

Fig. 2.16 FRP strips for flexural enhancement and FRP hoop wraps for shear enhancement for rectangular concrete column (Crawford et al. 2001)

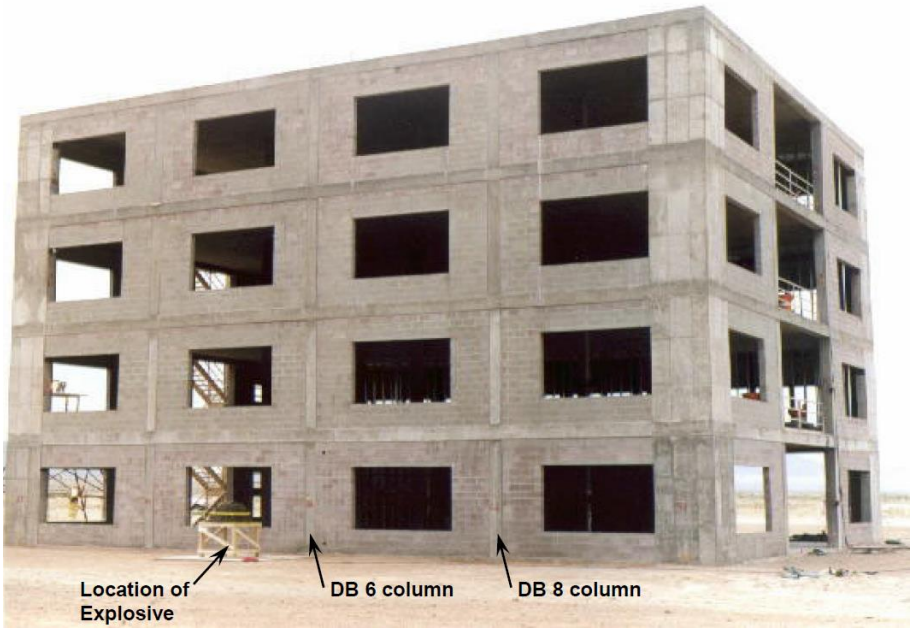

Fig. 2.17 Concrete structure investigated prior to test (Crawford et al. 2001)

(a) (b)

Fig. 2.18 (a) DB6 column after the test (b) DB8 column after the test (Crawford et al. 2001)

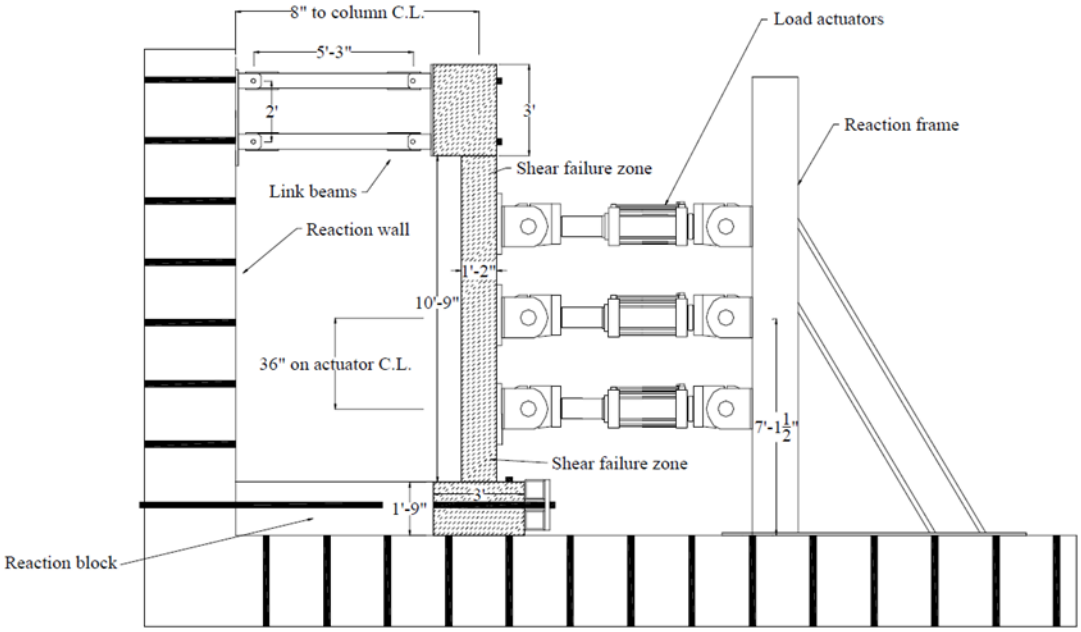

Fig. 2.19 Lateral system used to simulate blast loads (Crawford et al. 2001)

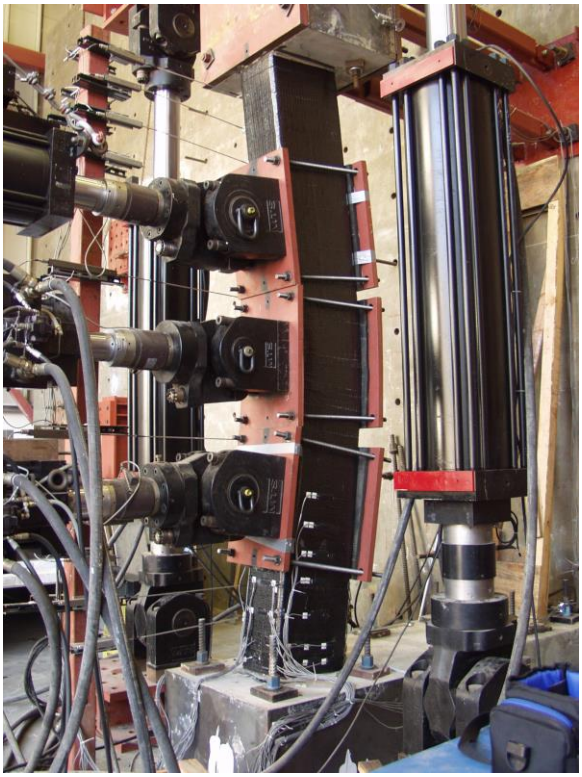

Fig. 2.20 Full scale CFRP RC column tested by lateral loading system (Morril et al. 2004)

(a) (b)

Fig. 2.21 (a) Column from field blast test (b) Column from laboratory test

(Crawford et al. 2001)

(a) (b)

Fig. 2.22 (a) Response of unretrofitted column (a) Response of column with six wraps

(Crawford et al. 2001)

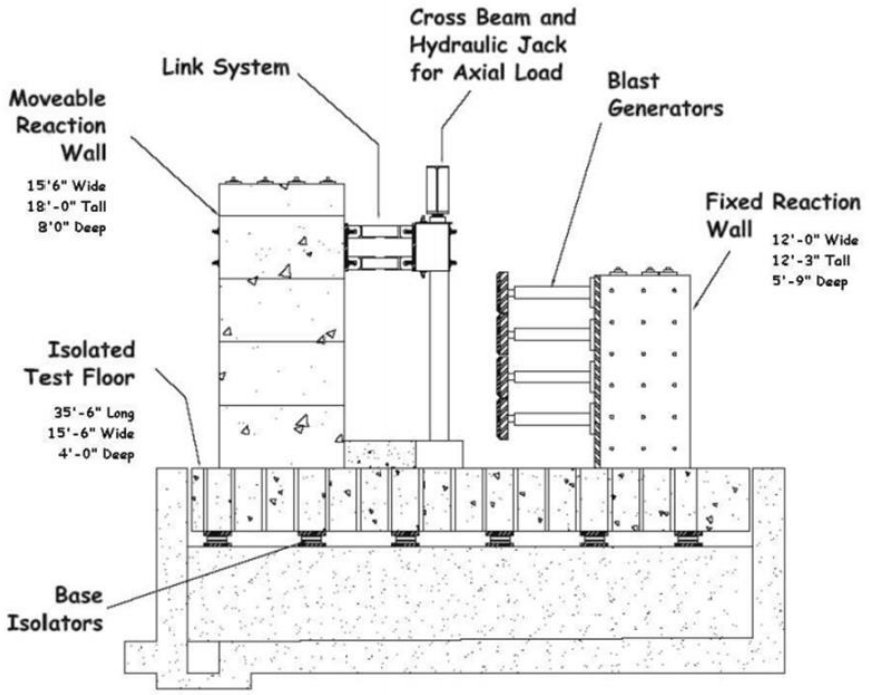

Fig. 2.23 Laboratory blast generator system (T. Rodriguze-Nikle 2006)

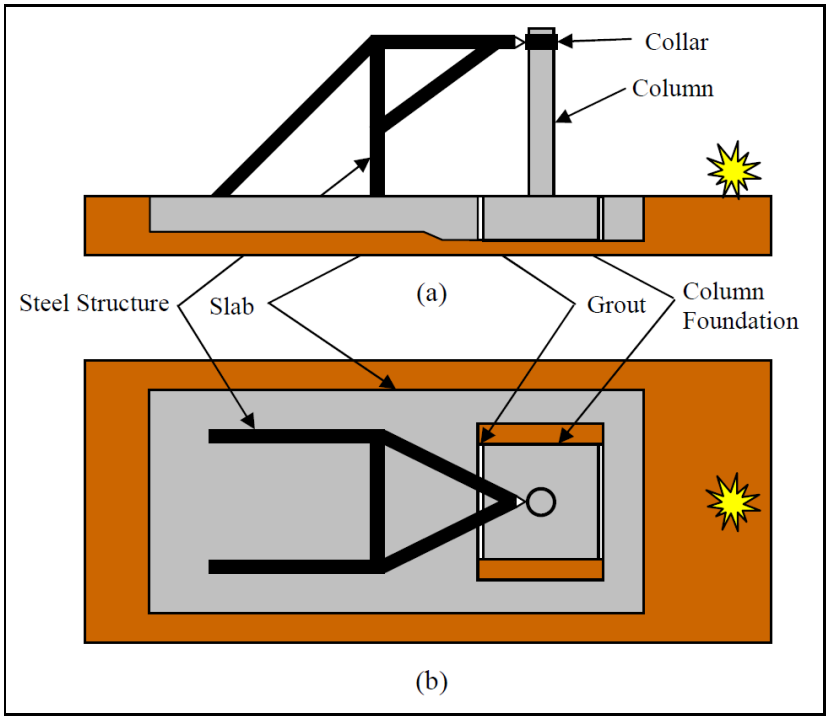

Fig. 2.24 Test Set-up (E. Williamson et al. 2011)

(a) (b) (c)

Fig. 2.25 RC column retrofitting techniques a) steel pre-stressed confinement b) steel bracing-compression c) steel bracing- tension (Alan Lloyd 2015)

Chapter Three

Experimental Program

3.1 Introduction

The experimental program research is aimed at studying the effects of different FRP laminate designs on the structural behaviour of retrofitted reinforced concrete columns subjected to simulated blast loading. A total of thirty two seismically and non-seismically detailed RC columns were tested using the University of Ottawa shock tube (Fig. 3.1). Eighteen columns were retrofitted with FRP laminates of different lay-up, each lamina formed from either a unidirectional fiber with a specified orientation or a woven fiber, while the other fourteen columns were left unprotected. Part of this study was also devoted to investigate the effect of incrementally increasing repetitive blast shots as typically done in experimental research, as opposed to a single shot at the desired level.

The description of test specimens; materials characteristics, including those of the FRP laminates; test setup; and loading protocol are presented in this chapter.

3.2 Description of Test Specimens, Material Properties and the Construction Process

All of the RC columns investigated in this research program had 150 mm x 150 mm x 2438 mm dimensions. Wooden formwork was fabricated to attain the required geometry of the specimens (Fig. 3.2). Each concrete column was reinforced longitudinally with four 10M rebars (reinforcement to gross cross sectional area ratio, ρ = 1.78 %). Columns were also reinforced laterally with 6.3 mm closed steel ties spaced at 37.5 mm and 100 mm c/c for seismic and non-

seismic columns, respectively. Fig. 3.3 clearly illustrates the reinforcement details of the test specimens. Mechanical properties of the steel reinforcement employed in this experimental program are given in Table-3.1. Reinforcement coupon tests were performed according to ASTM E8 Standard - Tension Testing of Metallic Materials. Concrete cover provided was 10 mm, measured to the exterior edge of the ties. A total of 16 strain gauges were placed on steel reinforcement, at various locations, for monitoring the behaviour of columns during testing, as illustrated in Fig. 3.4. Concrete used for column construction was supplied by a local ready-mix concrete company. Concrete was vibrated using an electrical concrete vibrator. Sixty six concrete cylinders (100 mm diameter x 200 mm height) were prepared for standard cylinder tests at different times. The cylinders were prepared and cured according to ASTM C31 Standard for Making and Curing Concrete Test Specimens. Figs. 3.5 through 3.10 show different stages of concrete casting. Two different concrete compressive strengths were used with two different batches of concrete supplied at different times. Thirteen columns had a concrete compressive strength equal to 44 MPa, while nineteen columns had a concrete compressive strength equal to 33 MPa. These concrete strengths were obtained at columns test dates. All concrete cylinders were tested according to ASTM C39 Standard. Once the concrete casting process was over, the specimens were covered with two layers of wet burlap and plastic sheet for curing for 30 days. The formwork was removed after 21 days. When the curing period was over, the columns were kept in the NRC (National Research Council Canada) structure lab until the test date.

All column corners were rounded to a radius equal to 10 mm to avoid stress concentration on externally applied FRP. This is illustrated in Fig. 3.11. Four external strain gauges were placed on the concrete surface at specific locations along the height of the columns to measure compression strains during testing, as depicted in Fig. 3.12.

3.3 CFRP Retrofit System; Description and Application

Eighteen of the 32 columns were retrofitted with selected configurations of multi-layer FRP. These configurations include; i) unidirectional CFRP, ii) woven [0º/90º] CFRP, iii) woven [±45º] CFRP, and iv) woven [0º/90º] Kevlar sheets. In the unidirectional CFRP sheets, the fibers were oriented in one direction, while in the woven [0º /90º] and [±45 º] FRP sheets, the fibers were weaved in two orthogonal directions. The wet lay-up process with wet resin was used to ensure the continuity of the laminas. The column surface was first prepared and vacuumed prior to the

application of FRP layers to ensure proper bond with concrete. FRP sheets were cut to the desired length and dimensions as illustrated in Fig. 3.13. For columns that were longitudinally strengthened with unidirectional CFRP, one strip of 165 mm wide, 2200 mm long FRP sheet was applied on each face. When unidirectional or woven CFRP was applied in the hoop direction, five CFRP rolls of 460 mm width and 610 mm length were needed to cover the entire height of the column with 25 mm overlap. Finally, when kevlar FRP was used, two sheets of 1200 mm width and 1220 mm length were applied in the transverse direction. The application of the wet lay-up procedure is illustrated in Fig. 3.14. The epoxy- hardener ratio used for the resin was 1:3 (Fig. 3.15). The unidirectional fibers in the hoop direction (transverse direction) are symbolized as UD [0º]. The fibres along the longitudinal direction of the column are labelled as UD [90º].

FRP coupon tests were performed according to ASTM D-3039 specifications, as depicted in Fig. 3.16, to establish the mechanical properties of each FRP wrapping system. For this purpose, 450 mm square FRP laminates were fabricated, from which the coupons were cut. For each type of FRP system applied two plates were fabricated to obtain the FRP laminate behaviour in the longitudinal and hoop direction. The FRP type, stacking sequence, number of layers and preparation method were identical to the strengthening laminates wrapped on the columns. Five coupons of 25 mm x 250 mm were cut from each FRP plate using a water jet cutting equipment to ensure a clean cut, and to prevent any FRP damage that might occur along the edges (Fig. 3.17). Table 3.2 gives the properties of FRP for each laminate wrapped around the column specimens. The stress-strain relationships obtained were always linear for all the different types of FRP laminates considered.

3.4 Test Matrix

The experimental program was divided into two parts. The first part was aimed at investigating the effects of multiple shots on dynamic response of un-retrofitted RC columns. The columns were tested under either a single or multiple blast shots. The second part of the experimental program was devoted to the investigation of FRP-retrofitted columns. The test matrix for each part is presented below:

i) Test Matrix-1

A total of eight seismically detailed RC columns were examined under single and repeated blast shots. Table-3.3 lists the column specimens considered in this group. All columns had a concrete

compressive strength of 44 MPa. No axial load was applied on specimens S1-AL0 through S4-AL0. In contrast, an axial load of 400 kN was applied on specimens S1-AL400 to S4-AL400. The columns were labelled with the magnitude of axial load applied. In the multiple-shot protocol, three to four blast shots were applied. The blast pressure for each shot was specified to cause a different level of damage, ranging from elastic to full plastic failure. On the other hand, the single-shot test regime was selected to create full plastic failure in the member.

ii) Test Matrix-2

Eighteen FRP retrofitted RC columns and six unretrofitted RC columns were tested under simulated blast loads. Test specimens were classified into two groups based on the concrete strength. Columns of Group G1 and Group G2 had concrete compressive strength equal to 33 MPa and 44 MPa, respectively. Retrofitted elements were bonded with a range of FRP multilayer protection. Test specimens were named after transverse reinforcement detailing, fiber type, fiber orientation, number of plies, and group number. Test Matrix-2 is given in Table-3.4. Fig. 3.18 to Fig. 3.20 clearly depict the stacking sequence of FRP laminas in the transvers and longitudinal directions of selected columns. The positions of FRP overlap planes are also shown in the same figures.

3.5 Shock Tube Testing Facility

Fig. 3.21 schematically illustrates the shock tube of the University of Ottawa. It can be seen that the shock tube used consists of four main components. The first and second components are the driver and the spool, respectively. These are the components in which the shock energy is built-up in the form of compressed air and the firing action takes place based on the targeted pressure capacity of the diaphragm. The length of the driver section can be adjusted to produce a wide range of pressure-impulse combinations. The blast wave formed in the driver section propagates and expands through the steel nozzle of a truncated square pyramid shape (the expansion section) that ends with a square test area of 2033 mm x 2033 mm. A square steel frame is provided at the end to permit the attachment of test specimens. The expansion section is 7 m long.

3.6 Test Setup

All columns were subjected to lateral pressure simulating a blast-induced shock wave. Tests in this study were conducted using the shock tube available at the Blast Research Laboratory of the

University of Ottawa. The column to be tested was installed at the front of the shock tube. The pressure produced by the shock wave was collected by a steel load transfer assembly covering the entire end of the shock tube, referred to as the "steel curtain" and transferred to the column as uniformly distributed load. The load transfer assembly consists of eight horizontal HSS ribs (76.2 mm x 76.2 mm x 6.3 mm thick) attached to a 2080 mm x 2080 mm x 0.71 mm thick steel sheet. The steel curtain transfers the simulated blast load by accumulating the shock wave pressure generated by the shock tube. Accordingly, the curtain is accelerated and the dynamic pressure is transferred to equally spaced point loads distributed along the entire height of the column. This is illustrated in Fig. 3.22.

A quasi-static axial load system was developed at the NRC, and used to apply the column axial load with appropriate boundary conditions prior to the application of blast loads. The system provides simply supported boundary conditions with a pin support in the lateral direction and a roller at the top and bottom ends of the column. The rollers allow free longitudinal translations, restricting lateral displacements and allowing free rotation in the direction of the load, while the pin restricts the translations but allows a free rotation in the direction of the load. These lateral supports were spaced at 2200 mm c/c, supported by very stiff steel beams, which were attached to the body of the shock tube at the top and bottom. Two load cells were provided, one at the top and the other at the bottom to measure the reaction forces.

Since the main objective of this study is to evaluate the effect of FRP laminate design on the performance of strengthened RC columns, simply supported boundary is selected to allow wide range of lateral load capacities between a lower bound of the capacity of a control column (no FRP strengthening is applied) and the maximum capacity of the shock tube. Columns with pin-pin- axial boundary and simply supported lateral supports requires much lower failure load compared to fixed-fixed or partially fixed boundary.

Axial load was applied by placing two hydraulic jacks with a capacity of 1500 kN each, at the column base. Because of the limited height available to fit the hydraulic axial loading system and the axial load cell, a rigid steel member was designed at the NRC to transfer axial load transferred from the jacks to the column. In order to allow free axial rotation in all directions, NRC spherical low friction pins customized to fit the top and bottom faces of the column were

used. A load cell with a capacity of 2000 kN was mounted on the 910 mm thick reinforced concrete ceiling of the blast-laboratory to monitor the axial load time history.

The shock tube was controlled by a firing system to start the test. A high speed HBM Genesis data acquisition system was employed to collect the data. Lateral displacements at mid-span were accurately monitored by two identical laser displacement sensors (Fig. 3.22). Both a high-speed video camera and a high definition still picture camera were used to capture the progression of the tests. The front view and side view of the test setup are shown schematically in Fig. 3.23 and Fig. 3.24, respectively.

3.7 Test Procedure and Loading Protocol

This section includes the test procedure and the loading protocol for the blast and the post-blast axial capacity tests conducted.

3.7.1 Blast loading protocol

After the column specimen was firmly attached to the shock tube, strain gauges, pressure sensors, laser displacement sensors, and the high speed video camera were connected to the HPM data acquisition system. An axial load of 400 kN was applied prior to the tightening of the lateral supports. Then the driver section of the shock tube was filled with pressurized air up to the required level of pressure. The test started when the air pressure in the spool section was drained, causing an imbalance in pressures on either side of the aluminum diaphragm, causing it to puncture, rushing the pressurized air at supersonic velocities towards the expansion shock tube nozzle.

3.7.2 Testing for post-blast axial capacity

The post-blast axial capacity of selected CFRP retrofitted columns was investigated experimentally. The column axial capacity was determined after a small lateral deflection was imposed on the column through lateral blast loading. Fig. 3.25 illustrates the steps followed in establishing the residual axial load capacity of the column. At the end of the blast loading the column experienced the mid-height displacement shown by “A” in Fig. 3.25. Upon releasing the load, the mid-height displacement bounced back to point “B”. A new axial load was applied monotonically until the maximum capacity of the column was reached at point “C”. The

application of the axial load continued until the column failure point (D) was reached. The test ended by releasing the axial load, at which stage the mid-height deflection reached point “E”.

Table-3.1: Mechanical properties of reinforcement

	10M (Ø 11.3 mm rebar)	Ø 6.3 mm smooth steel wire
Yield Stress, f_y (*MPa*)	572	521
Yield Strain, ε_s (*MPa*)	0.0025	0.0045
Ultimate Stress, f_u (*MPa*)	748	578
Ultimate Strain, ε_u (*MPa*)	0.0771	0.0405

Table-3.2: Mechanical properties of the FRP laminates applied

FRP Stacking Sequence	Thickness (mm)	Longitudinal Direction			Hoop Direction		
		Tensile Strength (MPa)	Modulus of Elasticity (GPa)	Rupture Strain	Tensile Strength (MPa)	Modulus of Elasticity (GPa)	Rupture Strain
UD [0/90/0] W$[\pm 45]_2$	2.86	242.9	20.1	0.013	466.2	32.2	0.013
W $[0/90]_2$ W$[\pm 45]_2$ UD [0]	2.78	137.5	14.5	0.01	430.2	30.4	0.014
W $[0/90]_2$ W$[\pm 45]_2$	2.22	209.3	17.0	0. 012	209.3	17.0	0. 012
UD $[0_2/90_2]$ UD [0]	3.48	326.8	21.4	0.012	475.4	28.5	0.013
UD [0/90] W$[\pm 45]_2$	2.58	300	25.2	0.013	319	25.2	0.02
W[0/90]4	1.99	380.8	29.5	0.012	380.8	29.5	0.012
UD $[0_2/90_2]$	2.65	401.5	32.9	0.012	401.5	32.9	0.012
UD [0/90] W $[\pm 45]_2$ [KEV.]$_2$	3.39	274	22.8	0.013	224.2	20.3	0.012

Table-3.3: Test Matrix-1

Column Name	Column Type	Axial Load (kN)	Type of Shot
S1-AL0	Seismic	0	Multiple
S2-AL0	Seismic	0	Multiple
S3-AL0	Seismic	0	Single
S4-AL0	Seismic	0	Single
S1-AL400	Seismic	400	Multiple
S2-AL400	Seismic	400	Multiple
S3-AL400	Seismic	400	Single
S4-AL400	Seismic	400	Single

Table-3.4: Test Matrix-2

Column Name	Column Type	Number of Columns	FRP Retrofitting	FRP Stacking Sequence	Type of FRP Layer	Number of Plies/Layer
NS1-G1	Non-Seismic	2 (A&B)	As-built	x	x	x
NS2-G1	Non-Seismic	2 (A&B)	✓	UD [0/90/0] W $[\pm 45]_2$	Lamina-1:Unidirectional 0 Lamina-2:Unidirectional90 Lamina-3: Unidirectional 0 Lamina-4: Woven ±45	1 1 1 2
NS3-G1	Non-Seismic	2 (A&B)	✓	W $[0/90]_2$ W$[\pm 45]_2$ UD[0]	Lamina-1:Woven 0/90 Lamina-2: Woven ±45 Lamina-3: Unidirectional 0	2 2 1
NS4-G1	Non-Seismic	2 (A&B)	✓	W $[0/90]_2$ W$[\pm 45]_2$	Lamina-1:Woven 0/90 Lamina-2: Woven ±45	2 2
NS5-G1	Non-Seismic	1	✓	UD $[0_2/90_2]$ UD[0]	Lamina-1:Unidirectional 0 Lamina-2:Unidirectional90 Lamina-1:Unidirectional 0	2 2 1
S1-G1	Seismic	3 (A,B,C)	As-built	x	x	x
S2-G1	Seismic	2 (A&B)	✓	UD $[90_2/0_2]$ W$[\pm 45]_2$	Lamina-1:Unidirectional 90 Lamina-2:Unidirectional 0 Lamina-2: Woven ±45	2 2 2
S3-G1	Seismic	2 (A&B)	✓	W $[0/90]_4$	Lamina-1:Woven 0/90	4
S4-G1	Seismic	2 (A&B)	✓	W $[0/90]_2$ W$[\pm 45]_2$	Lamina-1:Woven 0/90 Lamina-2: Woven ±45	2 2
S5-G1	Seismic	1	✓	UD $[90_2/0_2]$	Lamina-1:Unidirectional 90 Lamina-2:Unidirectional 0	2 2
NS1-G2	Non-Seismic	1	As-built	x	x	x
NS2-G2	Non-Seismic	2(A&B)	✓	W $[0/90]_2$ W$[\pm 45]_2$ UD[0]	Lamina-1:Woven 0/90 Lamina-2: Woven ±45 Lamina-3: Unidirectional 0	2 2 1
KEV.-G2	Non-Seismic	2 (1&2)	✓	UD [90/0] W $[\pm 45]_2$ $[KEV]_2$	Lamina-1:Unidirectional 0 Lamina-2:Unidirectional 90 Lamina-3: Woven ±45 Lamina-4: Woven Kevlar	1 1 2 2

Fig. 3.1 Shock tube

Fig. 3.2 Formworks

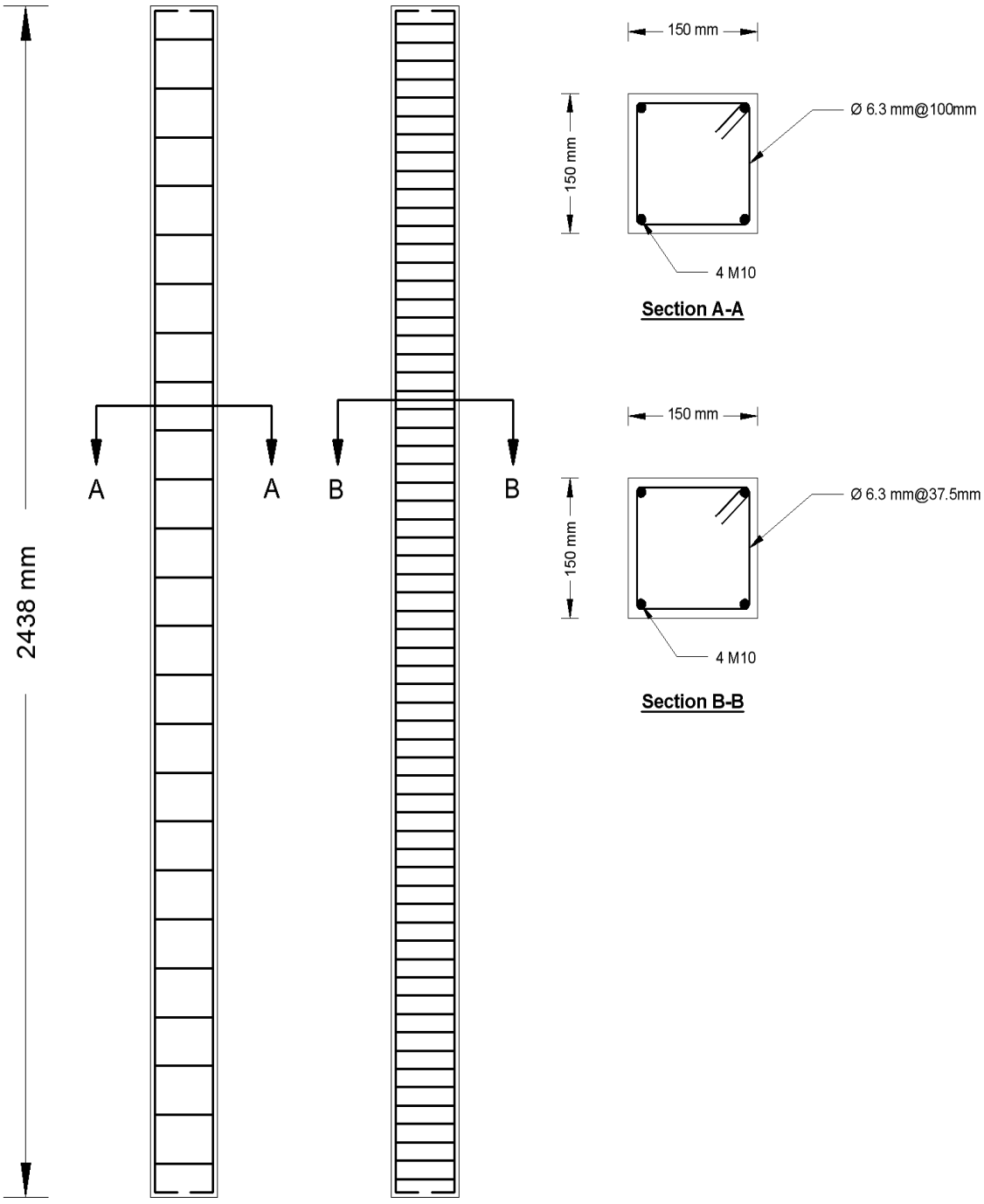

Non-Seismic Column Seismic Column

Fig. 3.3 Column dimensions and reinforcement detailing

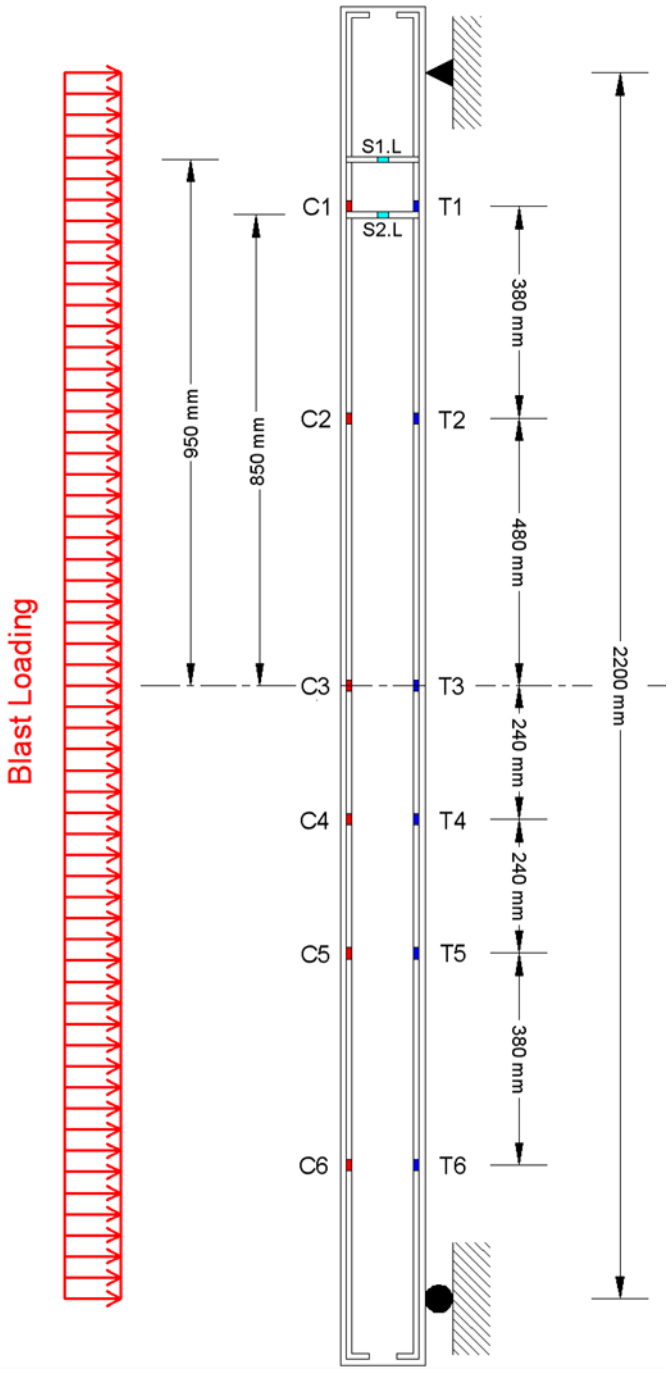

Fig. 3.4 Arrangement of internal strain gauges

Fig. 3.5 Concrete supply and placement

Fig. 3.6 Concrete vibration

Fig. 3.7 Concrete cylinders preparation

Fig. 3.8 Concrete curing by wet burlap

Fig. 3.9 Concrete covered by plastic sheets

Fig. 3.10 Column storing

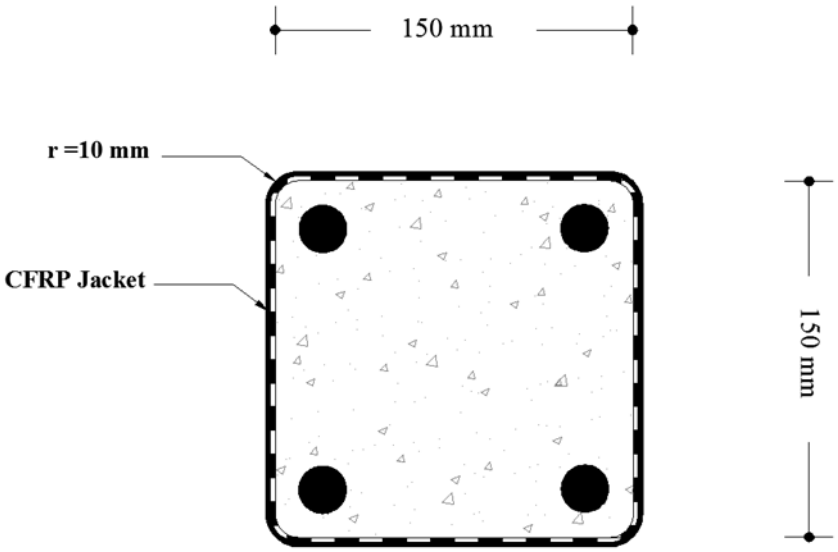

Fig. 3.11 Rounding of column corners

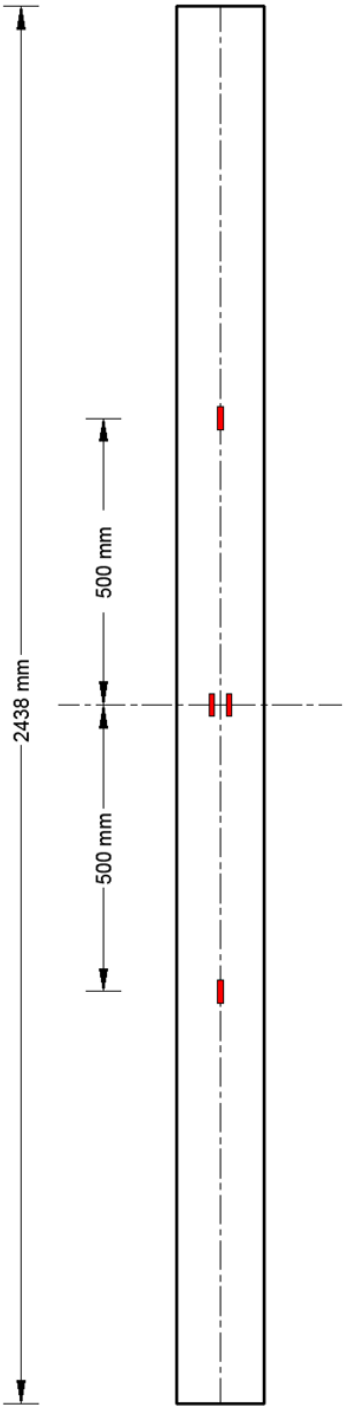

Fig. 3.12 Positions of external strain gauges

Fig. 3.13 CFRP sheets cut to size

Fig. 3.14 Application of CFRP by wet-layup method

Fig. 3.15 Epoxy resin and hardener used

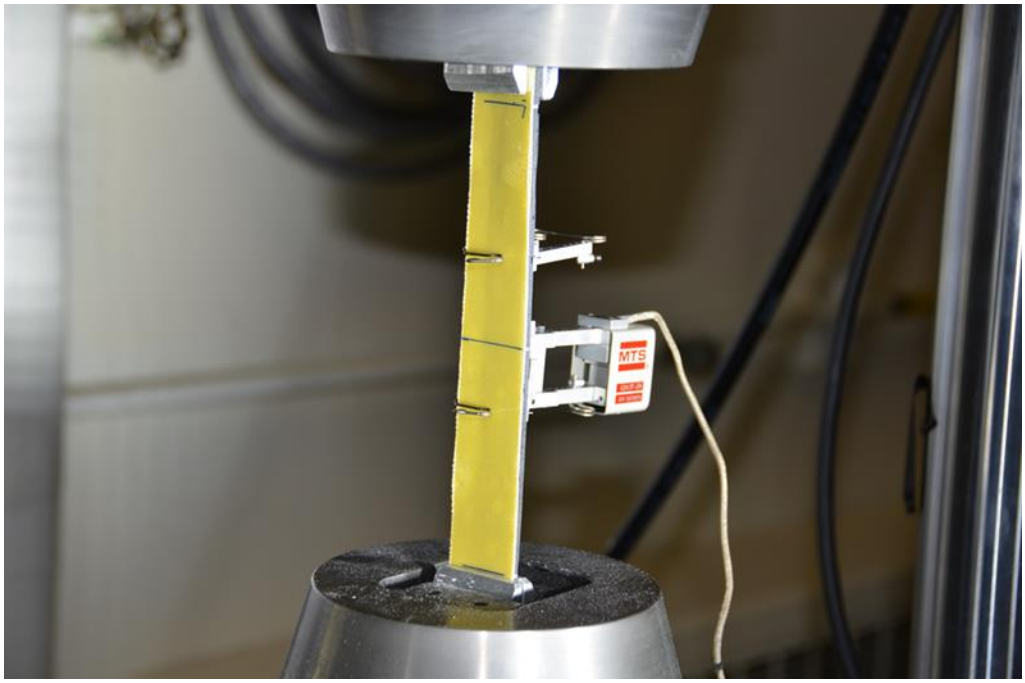

Fig. 3.16 FRP coupon test

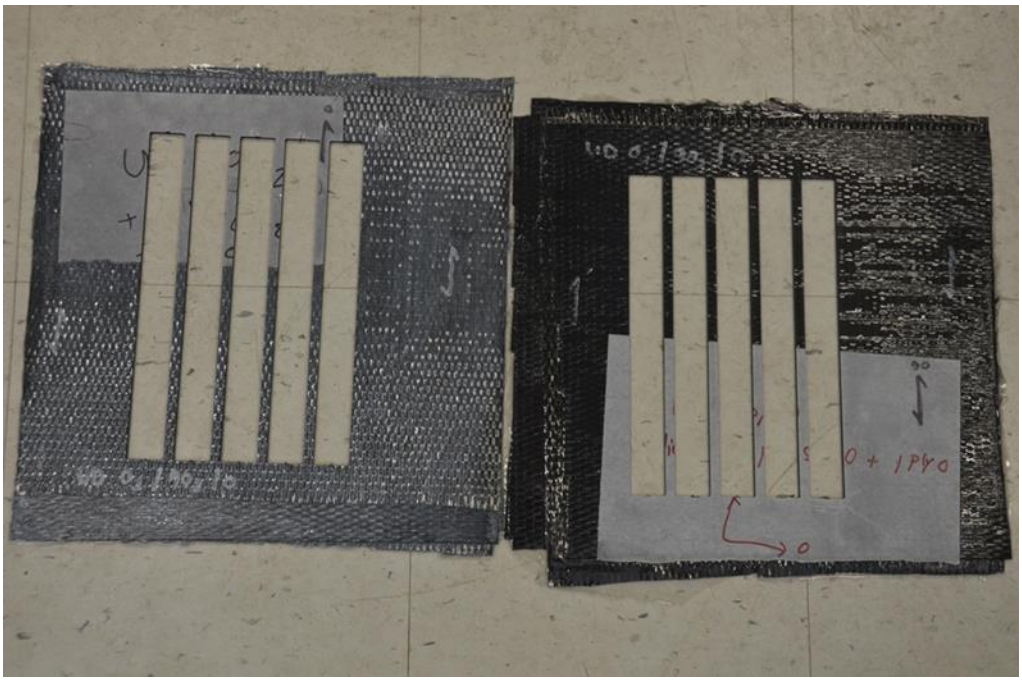

Fig. 3.17 CFRP coupons cut by water jet

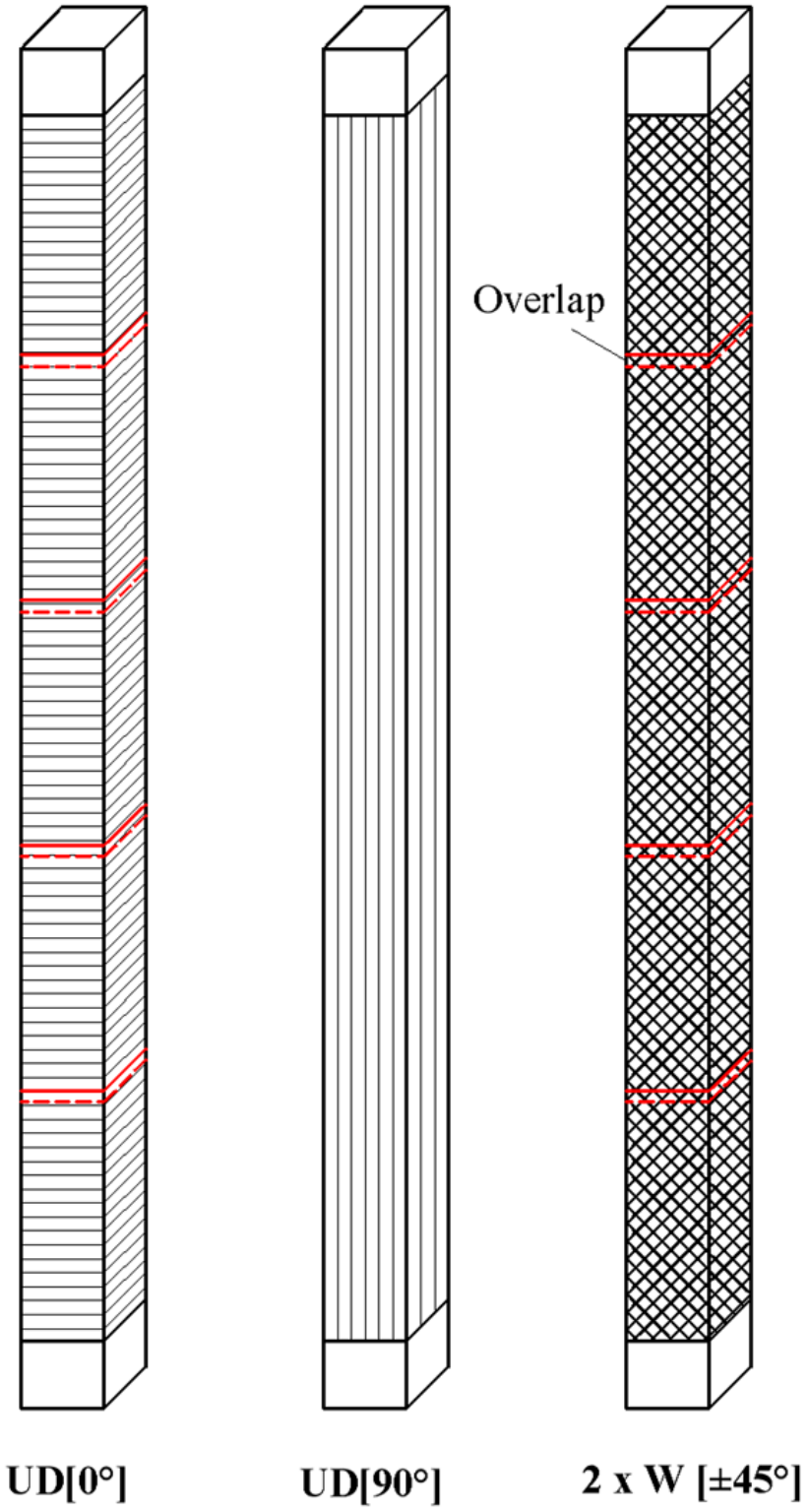

Fig. 3.18 Column S2 protected with UD [0º/90º] W [±45º] $_2$ CFRP laminate

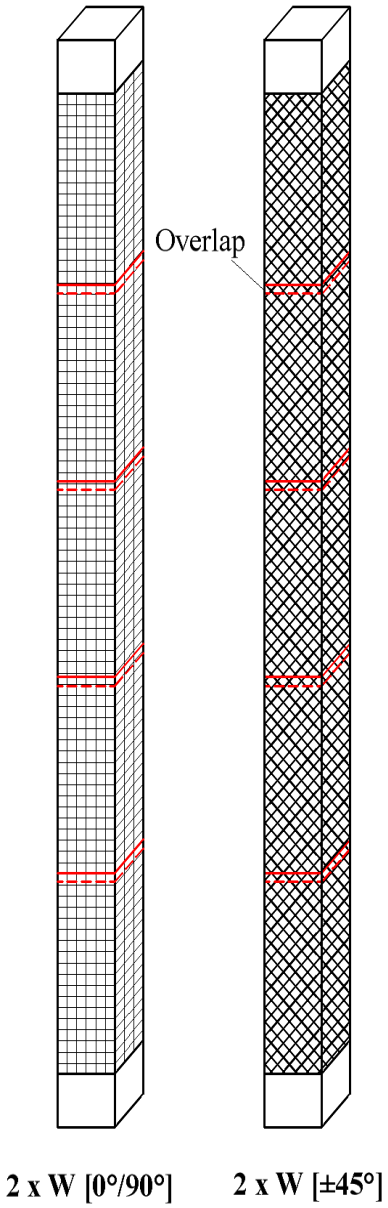

Fig. 3.19 Column S4 protected with W [0º/90º] $_2$ W [±45º] $_2$ CFRP laminate

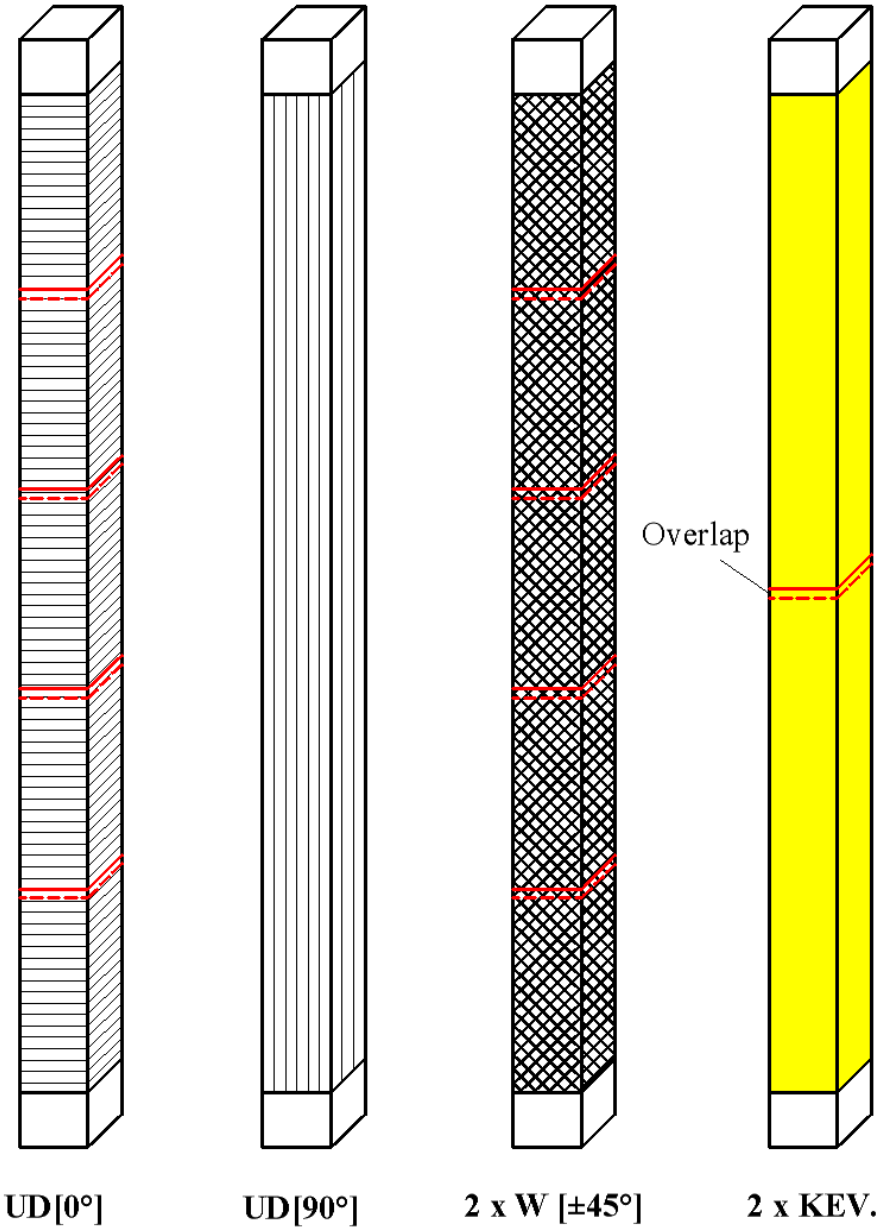

Fig. 3.20 Column S4 protected with UD [0º/90º] W [±45º] $_2$ W [KEV.] $_2$ CFRP laminate

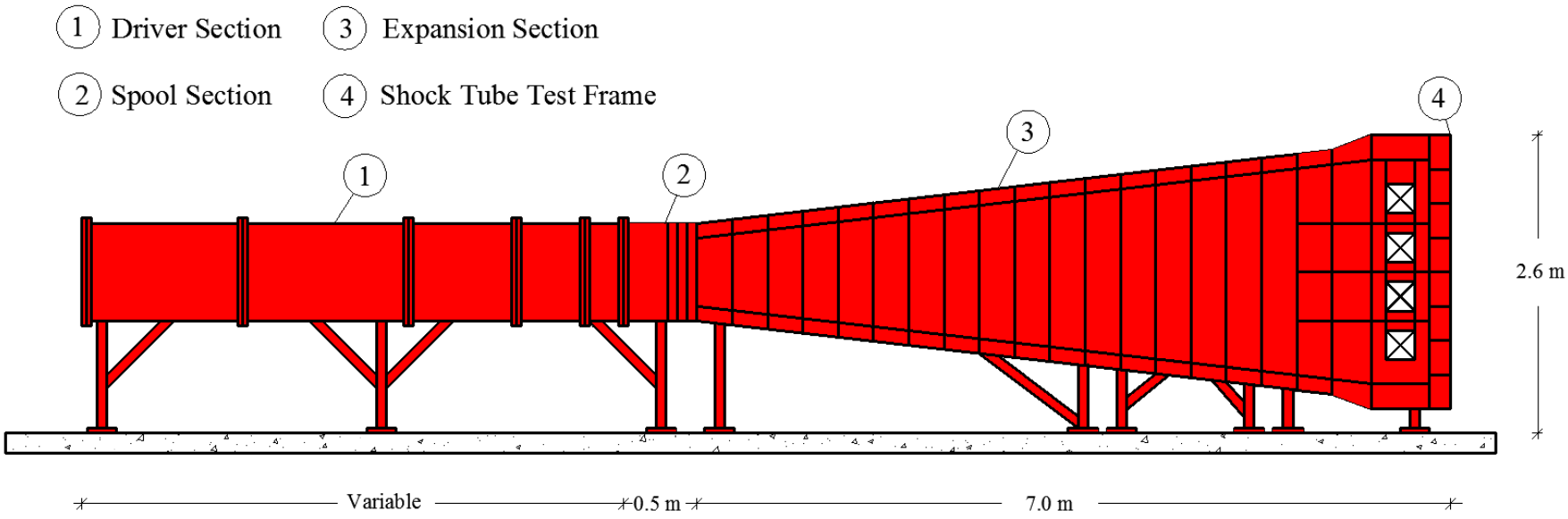

Fig. 3.21 Shock-tube sections (schematic)

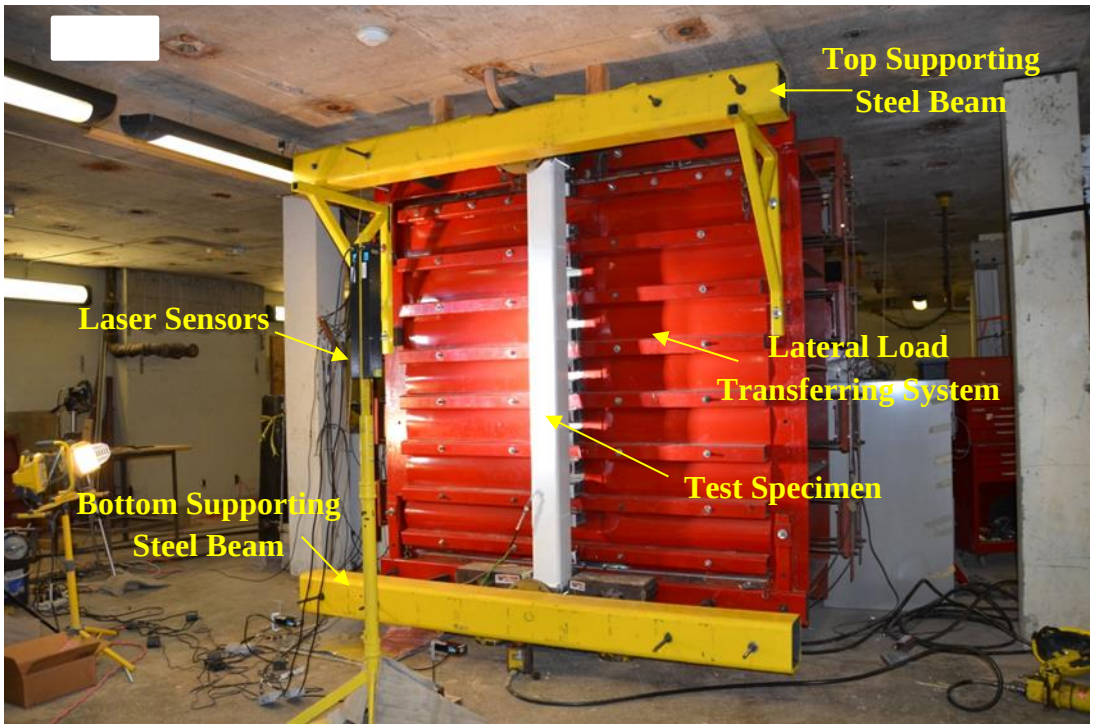

Fig. 3.22 Test Setup

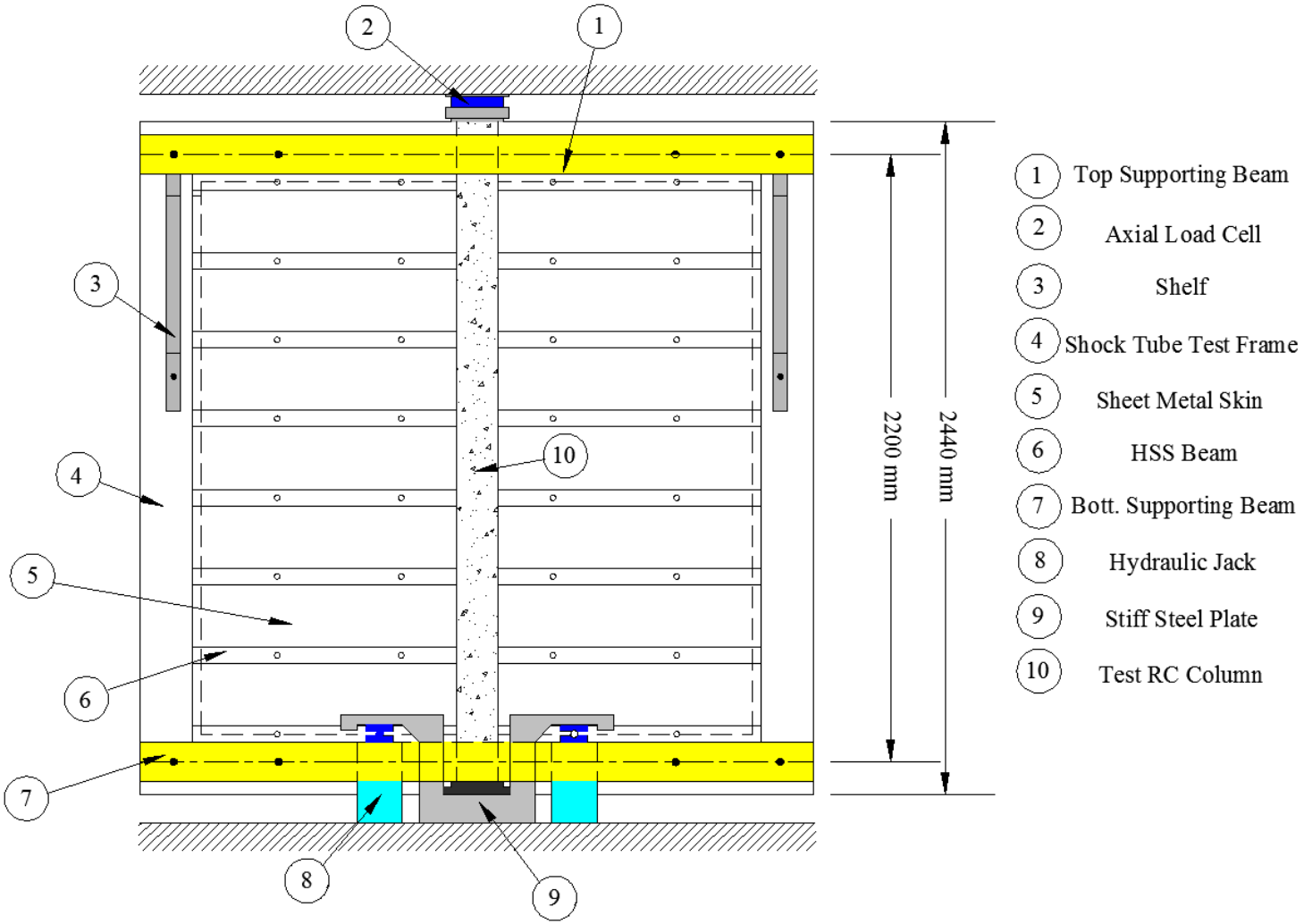

Fig. 3.23 Test setup-front view (schematic)

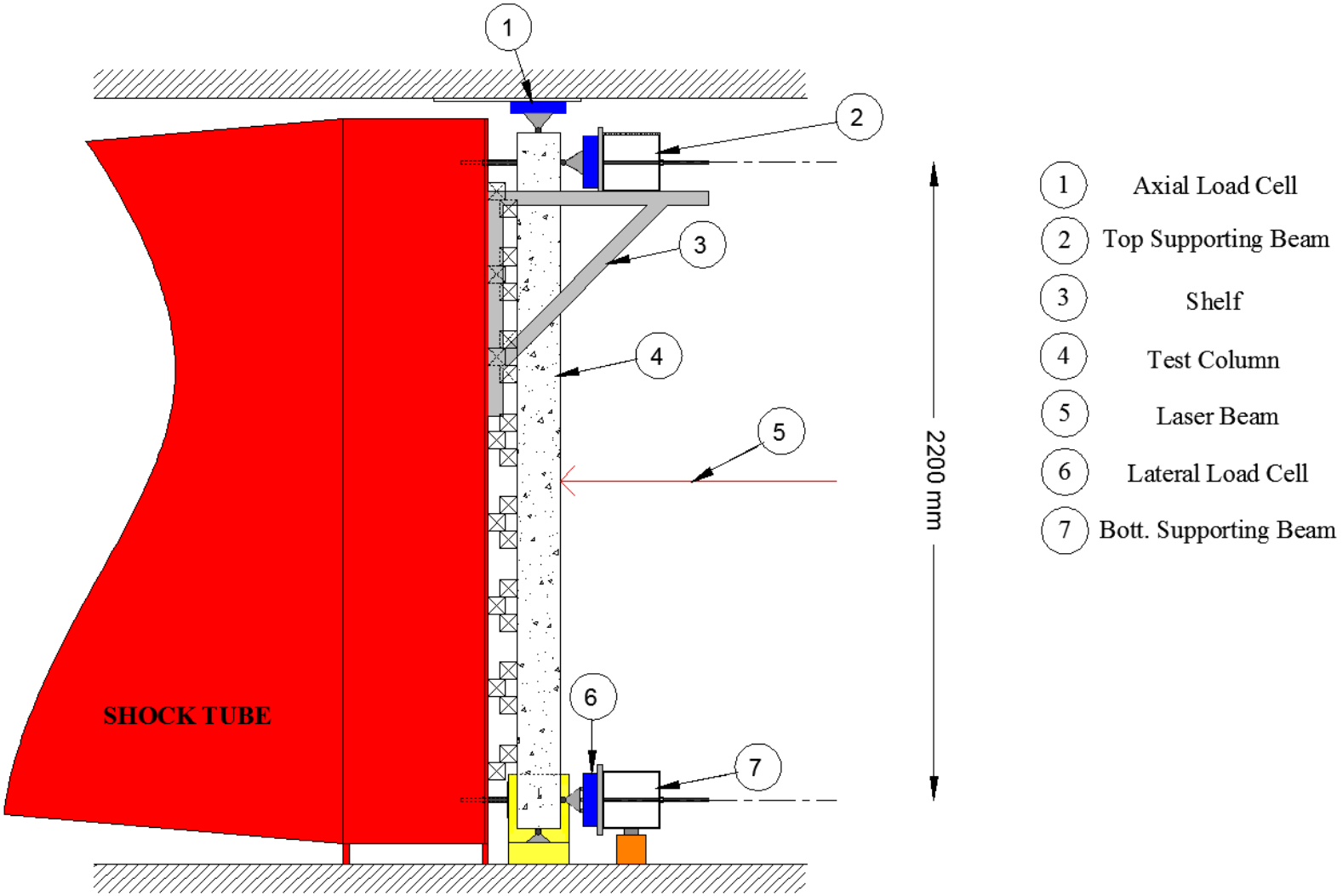

Fig. 3.24 Test setup-side view (schematic)

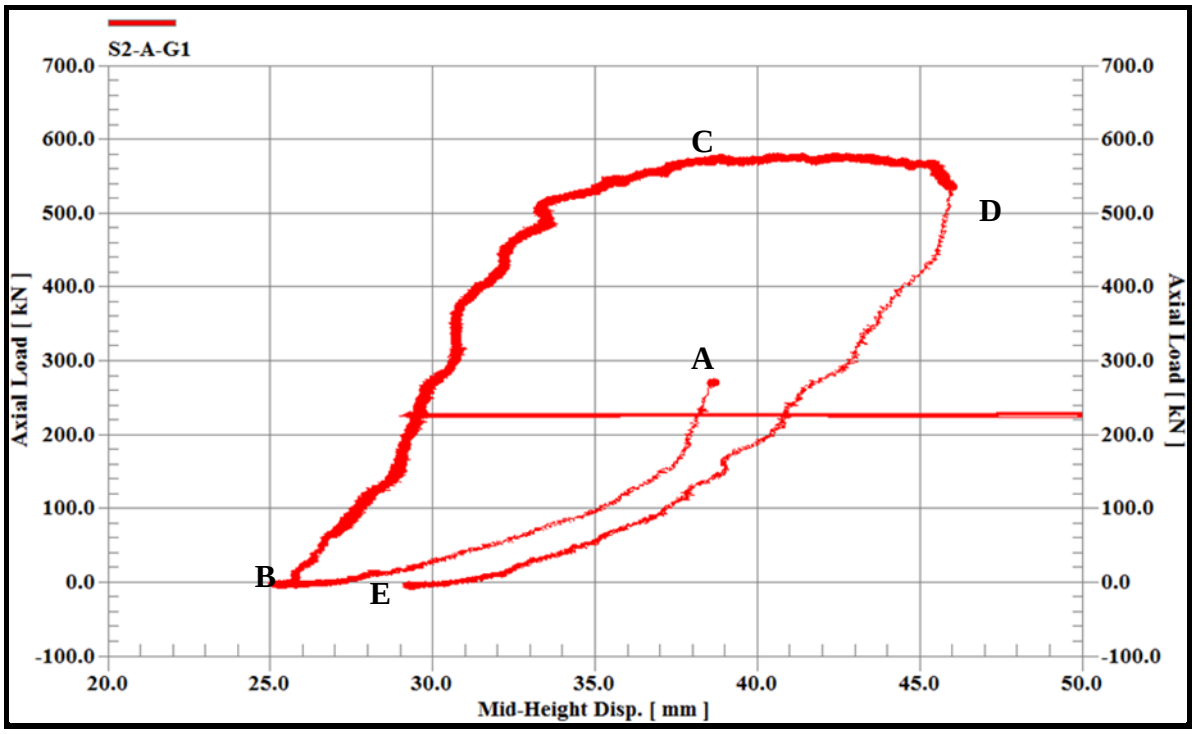

Fig. 3.25 Post-blast axial loading

Chapter Four

Test Results

4.1 Overview

The experimental program of this study is divided into two phases, as described in Chapter 3:

- Phase-I includes shock tube tests for determining the significance of loading history on column performance. These tests are essential for establishing the loading protocol for Phase II tests, which relate to the primary objective of the current research project on FRP protection of blast-resistant columns. They consist of tests indicated in Test Matrix-1 described in Chapter 3; and include 8 un-retrofitted, seismically detailed columns; 4 with axial load and the remaining 4 without axial load.
- Phase-II includes shock tube tests of Test Matrix-2 described in Chapter 3, with a focus on investigating the effects of different FRP laminate design parameters on blast performance of RC columns. They include columns with or without FRP protection under axial load, either with seismic or non-seismic detailing.

The test results are presented in the following sections.

4.2 Test Results of Phase-I

Researchers often use progressively increasing multiple blast shots when they use shock tubes as blast simulators. There is rationale for this practice. Blast testing is often a costly undertaking. Using multiple shots on the same specimen provides more research data to assess the

performance of the same specimen under different levels of blast pressure. The underlining assumption is that the specimen behaviour under high magnitude shots is not affected significantly by previous shots of lower magnitude. Sometimes the use of multiple shots is justified if the investigation focuses on multiple blast attacks on a military facility in a battle field.

In contrast, some researchers believe that even a "small" or a "medium" level of damage and associated residual deformations on structural elements can induce visually unobservable deterioration in the member, affecting its stiffness and integrity under subsequent shots. The early damage caused by previous shots may be especially important for FRP protected columns as they cause partial loss of FRP bond on concrete, microcracking, and FRP interlaminar shear loss. Therefore, it is important to investigate the significance of multiple blast shots, as opposed to a single blast shot at a desired level, before the primary objective of the current study can be pursued.

Phase I tests are also aimed at investigating the effects of pre-applied high axial service loads on column behaviour and their significance on accumulated damage associated with repeated application of blast loads. Phase-I tests also have implications on potential modifications of the test setup and the loading protocol to be used in Phase II.

Phase I consists of eight identical as-built (un-retrofitted) seismically detailed RC columns subjected to single versus multiple blast shots, with and without axial loads. The compressive strength of concrete for the columns was 44 MPa. The firing parameters and the experimental results are summarized in Table 4-1 and Table 4-2. The firing parameters include driver pressure (P_D), reflected pressure (P_r), maximum reflected impulse over the positive phase (I_r), duration of positive phase (t_d), and the pre-blast axial load (A_xL). The experimental results include maximum mid-height deflection ($d_{max.}$), maximum support rotation ($\theta_{max.}$), duration needed to reach maximum mid-height deflection ($t_{max.}$), residual and accumulated mid-height displacements ($d_{residual}$ and $d_{accumulative}$, respectively), maximum applied blast force ($F_o = P_r$ x $4.4m^2$; reflected pressure times the area of the steel curtain load application device), and residual axial load ($A_xL_{residual}$).

The detailed description of all tests, including the observed behaviour, is provided below:

1) Column S1-AL0

This column was subjected to four blast shots. The driver pressures used to generate the shots were 103.5 kPa, 69 kPa, 138 kPa, and 207 kPa for the first, second, third and fourth shots respectively. No pre-blast axial load was applied on the column. Below are the results obtained from the four shots:

a) 1st Blast Shot: Column S1-AL0

The driver pressure selected for this test was 103.5 kPa. Due to some technical difficulties, the data acquisition system was not triggered during the test. Therefore, no useful data was collected. The residual displacement at mid-height was equal to 13.0 mm ($\theta_{residual}$ = 0.68˚). This displacement was measured manually by a measuring tape when the column came to rest. Five tension cracks along the critical mid-height zone were observed at the end of the test. This is depicted in Fig. 4.1.

b) 2nd Blast Shot: Column S1-AL0

The driver pressure selected for this test was 69 kPa. Fig. 4.2 shows that this driver pressure resulted in a maximum reflected pressure of 14.1 kPa and a reflected impulse over the positive phase of 143.5 kPa.ms. The duration of the positive phase was 19.2 ms. Maximum and residual displacements at mid-height were 23.3 mm ($\theta_{max.}$ = 1.21˚) and 2.7 mm ($\theta_{residual}$ = 0.14˚), respectively. The maximum mid-height displacement occurred after 27.3 ms from the start of the test. Fig. A-1 shows that the maximum and residual strains monitored by Strain Gauge T-3 were 0.0054 (t = 26.3 ms) and 0.0002, respectively. The damage observed at the end of this test was identical to that observed in the previous test.

c) 3rd Blast Shot: Column S1-AL0

The driver pressure for this test was 138 kPa. Fig. 4.3 indicates that this driver pressure resulted in a maximum reflected pressure of 22 kPa and a reflected impulse over the positive phase of 236.6 kPa.ms. The duration of the positive phase was 18.65 ms. Maximum and residual displacements at mid-height were 53.3 mm ($\theta_{max.}$ = 2.77˚) and 27.7 mm ($\theta_{residual}$ = 1.44˚), respectively. The maximum mid-height displacement occurred after 30.2 ms from the start of the test. No usable strain readings were collected from this test. There was no concrete crushing at

this load stage. However it was observed that the tension cracks generated by the first blast shot became slightly wider.

d) 4th Blast Shot: Column S1-AL0

The driver pressure for this test was 207 kPa. Fig. 4.4 indicates that this driver pressure resulted in a maximum reflected pressure of 37 kPa and a reflected impulse over the positive phase of 320 kPa.ms. The duration of the positive phase of this test was 18.0 ms. For unknown reasons, the laser sensors did not record the mid-span displacement during this shot. The residual displacement was measured manually at the end of the test as 126 mm ($\theta_{residual} = 6.53^{\circ}$). No strain readings were recorded during this shot. This shot resulted in an extensive tension cracking and concrete crushing in the mid-height region of the column, as shown in Fig. 4.5.

2) Column S2-AL0

This column was subjected to four blast shots. The driver pressures used to generate the shots were 69 kPa, 103.5 kPa, 207 kPa and 207 kPa for the first, second, third and fourth shots, respectively. No pre-blast axial load was applied on the column. Below is the description of the results produced by each shot:

a) 1st Blast Shot: Column S2-AL0

The driver pressure selected for this test was 69 kPa. Fig. 4.6 shows that this driver pressure resulted in a maximum reflected pressure of 13.1 kPa and a reflected impulse over the positive phase of 144 kPa.ms. The duration of the positive phase was 19.4 ms. Maximum and residual displacements at column mid-height were 17.7 mm ($\theta_{max.} = 0.92^{\circ}$) and 3.7 mm ($\theta_{residual} = 0.19^{\circ}$), respectively. The maximum mid-height displacement occurred 25 ms after the start of the test. Fig. A-2 shows that the maximum and residual strains recorded by Strain Gauge T-3 were 0.008 (t =26 ms) and 0.005, respectively. Three minor tension cracks, distributed along the mid-height portion of the test specimen, were observed at the end of this test (Fig. 4.7).

b) 2nd Blast Shot: Column S2-AL0

The driver pressure selected for this test was 103 kPa. Fig. 4.8 shows that this driver pressure resulted in a maximum reflected pressure of 30 kPa and a reflected impulse over the positive phase of 284 kPa.ms. The duration of the positive phase of this test was 19.2 ms. The maximum

and residual displacements at column mid-height were 50.2 mm ($\theta_{max.}$ = 2.6˚) and 27.2 mm ($\theta_{residual}$ = 1.4˚), respectively. The maximum mid-height displacement occurred after 30 ms from the start of the test. Fig. A-3 shows that the maximum and residual strains monitored by Strain Gauge T-3 were 0.0087 (t=36.6 ms) and 0.001, respectively. This shot resulted in seven major tension cracks distributed along the mid-height region of the column. No concrete crushing was observed at the end of this test (Fig. 4.9).

c) 3rd Blast Shot: Column S2-AL0

The driver pressure selected for this test was 207 kPa. The data acquisition system was not triggered during the shot. The residual mid-height displacement produced was 100 mm. This displacement was measured manually using a measuring tape.

d) 4th Blast Shot: Column S2-AL0

The driver pressure selected for this shot was 207 kPa. Fig. 4.10 shows that this driver pressure resulted in a maximum reflected pressure of 30.6 kPa and a reflected impulse over the positive phase of 309.8 kPa.ms. The duration of the positive phase was 18.1 ms. Maximum and residual displacements at column mid-height were 63.4 mm ($\theta_{max.}$ = 3.3˚) and 36.5 mm ($\theta_{residual}$ = 1.9˚), respectively. The maximum mid-height displacement occurred after 36.5 ms from the start of the test. No usable strain readings were collected from this test. This shot resulted in extensive tension cracking and concrete crushing in the mid-height region of the column as shown in Fig. 4.11.

3) Column S3-AL0

In this test, the column was subjected to a single blast shot. The driver pressure used to generate this shot was 207 kPa. No pre-blast axial load was applied on the column. Below is the description of the results obtained from this test:

a) Single Shot: Column S3-AL0

The driver pressure selected for this test was 207 kPa. Fig. 4.12 shows that this driver pressure resulted in a maximum reflected pressure of 35.75 kPa and a reflected impulse over the positive phase equal to 345.2 kPa.ms. The duration of the positive phase was 20 ms. Maximum and residual displacements at column mid-height were 85 mm ($\theta_{max.}$ = 4.42˚) and 64.9 mm ($\theta_{residual}$ =

3.38 ˚), respectively. The maximum mid-height displacement occurred 37.9 ms after the start of the test. Fig. A-4 shows that the maximum strain monitored by Strain Gauge T-3 was 0.0055 (t=12.0 ms). This shot resulted in extensive tension cracking and concrete cover spalling at mid-height. This is shown in Fig. 4.13.

4) Column S4-AL0

The column was subjected to a single blast shot. The driver pressure used to generate this shot was 207 kPa. No pre-blast axial load was applied. Below is the description of the results obtained from this test:

a) Single Shot: Column S4-AL0

The driver pressure selected for this test was 207 kPa. Fig. 4.14 shows that this driver pressure resulted in a maximum reflected pressure of 35.7 kPa and a reflected impulse of 372.1 kPa.ms. The duration of the positive phase in this test was 20 ms. Maximum and residual displacements at column mid-height were 104.9 mm ($\theta_{max.}$ = 5.45 ˚) and 85 mm ($\theta_{residual}$ = 4.42˚), respectively. The maximum mid-height displacement occurred after 42.4 ms from the start of the test. Fig. A-5 shows that the maximum strain monitored by Strain Gauge T-3 was 0.017 (t=12.4 ms). This shot resulted in extensive tension cracking and concrete spalling in the mid-height region of the column. This is illustrated in Fig. 4.15.

5) Column S1-AL400

The column was subjected to two blast shots. The driver pressures of the first and the second shots were 103.5 kPa and 207 kPa, respectively. Below is the description of the two tests conducted on this column:

a) 1st Blast Shot: Column S1-AL400

The driver pressure selected for this shot was 103.5 kPa. Fig. 4.16 shows that this driver pressure resulted in a maximum reflected pressure of 16.9 kPa and a reflected impulse of 179.8 kPa.ms over the positive phase. The duration of the positive phase of this test was 20.4 ms. Maximum and residual displacements at column mid-height were 23.9 mm ($\theta_{max.}$ = 1.25˚) and 6.9 mm ($\theta_{residual}$ = 0.36 ˚), respectively. The maximum mid-height displacement occurred after 26.1 ms from the start of the test. Prior to the blast test, an axial load equal to 400 kN was applied on the

column. However, due to some technical constraints it was not possible to record the axial load time history. Fig. A-6 shows that the maximum and residual strains monitored by Strain Gauge T-3 were 0.0084 (t = 21 ms) and 0.0014, respectively. This shot resulted in few narrow flexural cracks in the mid height region of the column. No concrete crushing was observed at the end of the test as depicted in Fig. 4.17.

b) 2nd Blast Shot: Column S1-AL400

The driver pressure selected for this test was 207 kPa. Fig. 4.18 shows that this driver pressure resulted in a maximum reflected pressure of 31.6 kPa and a reflected impulse of 334.9 kPa.ms over the positive phase. The duration of the positive phase was 20.84 ms. Maximum and residual displacements at column mid-height were 62.5 mm ($\theta_{max.}$ = 3.25 ˚) and 43.7 mm ($\theta_{residual}$ = 2.275˚), respectively. The maximum mid-height displacement occurred after 33.7 ms from the start of the test. It was not possible to record the axial load time history during the shot due to some technical constraints. Fig. A-7 shows that the maximum strain monitored by Strain Gauge T-3 was 0.01 (t=25 ms). This gauge malfunctioned after this reading, and no usable strain data was collected. This shot resulted in extensive tension cracking and concrete crushing in the mid-height region of the column as shown in Fig. 4.19.

6) S2-AL400-Column

This column was subjected to three blast shots. The driver pressures selected were 103.5 kPa, 207 kPa, and 345 kPa for the first, second, and third shot, respectively. Below is the description of the three tests:

a) 1st Blast Shot: Column S2-AL400

The driver pressure selected for this test was 103.5 kPa. Fig. 4.20 shows that this driver pressure resulted in a maximum reflected pressure of 16.9 kPa and a reflected impulse of 188.4 kPa.ms over the positive phase. The duration of the positive phase of this test was 19.3 ms. Maximum and residual displacements at column mid-height were 14.3 mm ($\theta_{max.}$ = 0.745˚) and 3.7 mm ($\theta_{residual}$ = 0.19˚), respectively. The maximum mid-height displacement occurred 22.2 ms after the start of the test. The axial load applied prior to the test was 390 kN, however the residual axial load monitored was 348 kN. No usable strain data was collected from this test. There was no visible damage at the end of the test as shown in Fig. 4.21.

b) 2nd Blast Shot: Column S2-AL400

The driver pressure selected for this test was 207 kPa. Fig. 4.22 shows that this driver pressure resulted in a maximum reflected pressure of 30 kPa and a reflected impulse of 329.5 kPa.ms over the positive phase. The duration of the positive phase was 22.2 ms. The maximum and residual displacements at mid-height were 33.5 mm ($\theta_{max.}$ = 1.74˚) and 20.1 mm ($\theta_{residual}$ = 1.05˚), respectively. The maximum mid-height displacement occurred 24.2 ms after the start of the test. The axial load applied prior to the test was 400 KN, however the residual axial load monitored was 344.5 kN. Fig. A-8 shows that the maximum and residual strains measured by Strain Gauge T-3 were 0.0033 (t = 18.24 ms) and 0.0007, respectively. This shot resulted in two tension cracks at the mid-height of the column. No concrete crushing was observed at the end of the test, as depicted in Fig. 4.23.

c) 3rd Blast Shot: Column S2-AL400

The driver pressure selected for this shot was 345 kPa. Fig. 4.24 shows that the driver pressure resulted in a maximum reflected pressure of 41.4 kPa and a reflected impulse of 435 kPa.ms over the positive phase. The duration of the positive phase of this test was 18.8 ms. The maximum and residual displacements at column mid-height were 130.1 mm ($\theta_{max.}$ = 6.745˚) and 105.6 mm ($\theta_{residual}$ = 5.48˚), respectively. The maximum mid-height displacement occurred after 39.4 ms from the start of the test. The axial load applied prior to the test was 393 kN, however the residual axial load was zero. Fig. A-9 shows that the maximum strain measured by Strain Gauge T-3 was 0.011 (t =15.28 ms). Stain Gauge T-3 was damaged after this reading. This shot resulted in extensive tension cracking and concrete crushing in the mid-height region, as shown in Fig. 4.25.

7) S3-AL400-Test

This column was subjected to a single blast shot. Below is the description of the test conducted on this column:

a) Single Blast Shot: Column S3-AL400

The driver pressure selected for this test was 345 kPa. Fig. 4.26 shows that this driver pressure resulted in a maximum reflected pressure of 48.4 kPa and a reflected impulse of 476.2 kPa.ms

over the positive phase. The duration of the positive phase of this test was 20.6 ms. Maximum and residual displacements at the mid-height of the column were 131.5 mm ($\theta_{max.}$ = 6.82˚) and 113.3 mm ($\theta_{residual}$ = 5.88˚), respectively. The maximum mid-height displacement occurred after 48.4 ms from the start of the test. The axial load applied prior to the test was 389 kN, however the residual axial load was 30 kN. Fig. A-10 shows that the maximum strain measured by Strain Gauge T-3 was 0.0057 (t = 16.45 ms). Strain Gauge T-3 was damaged after this reading. This shot resulted in extensive tension cracking and concrete crushing in the mid-height region of the column as shown in Fig. 4.27.

8) S4-AL400-Test

In this test, the column was subjected to a single blast shot. Below is the description of the test conducted on this column:

a) Single Blast Shot: Column S4-AL400

The driver pressure selected for this test was 345 kPa. Fig. 4.28 shows that this driver pressure resulted in a maximum reflected pressure of 49.1 kPa and a reflected impulse of 481.5 kPa.ms over the positive phase. The duration of the positive phase of this test was 20.5 ms. The maximum and residual displacements at column mid-height were 105 mm ($\theta_{max.}$ = 5.45˚) and 103 mm ($\theta_{residual}$ = 5.35˚), respectively. The maximum mid-height displacement occurred after 41.4 ms from the start of the test. The axial load applied prior to the test was 409.7 kN, however the residual axial load was 49.7 kN. Fig. A-11 shows that the maximum strain measured by Strain Gauge T-3 was 0.0115 (t=15.44 ms). This strain gauge was damaged after this reading. The shot resulted in extensive tension cracking and concrete crushing in the mid-height region as depicted in Fig. 4.29.

4.3 Test Results of Phase-II

The columns tested in Phase II were divided into two groups; Group G1 and Group G2. Group G1 included tests of nineteen columns, either seismically or non-seismically detailed, with or without wrapped CFRP laminates of various designs. All columns of this group had concrete compressive strength equal to 33 MPa. Group G2 included tests of five non-seismic columns, with or without FRP protection of two different laminates. The columns of this group had concrete compressive strength equal to 44 MPa.

Columns of Phase II were prepared in sets, where each set had identical columns. In general, each set had two identical columns, though some sets had three, and yet few others had only a single column. Columns in a given set were subjected to different levels of blast pressure and/or axial load, albeit the difference in load was small, sometimes resulting from unintended experimental variations. The first test was performed using a target blast pressure which was believed to bring the column to its capacity. This target pressure was established based on previous tests and engineering judgement. Subsequent tests on identical columns of the set was conducted under either increased or decreased pressures and/or axial loads to capture the column capacity, while also investigating the effects of change in load on column performance. Often, the difference in test blast pressures and/or axial loads within a set was small. The application of different blast pressures and/or axial loads typically resulted in different levels of column damage, which helped better understand their structural performance. The comparison of column performance among the columns in a given set is provided in subsequent sections, after the presentation of individual column performance.

The results of all Phase II columns are summarized in Table 4.3 to Table 4.6. The firing parameters measured include driver pressure (P_D), reflected pressure (P_r), reflected impulse over the positive phase (I_r), duration of positive phase (t_d), and pre-blast axial load applied (A_xL). The experimental results include maximum and residual mid-height deflections (d_{max} and $d_{residual}$, respectively), maximum support rotations ($\theta_{max.}$), duration needed to reach maximum mid-height deflection ($t_{max.}$), residual axial load ($A_xL_{residual}$), axial load at maximum mid-height deflection ($A_xL_{@d.max.}$), and the maximum applied blast force (F_o) which is equal to P_r x 4.4m^2 (area of the steel curtain of the shock tube).

The following sections provide discussions on test observations, while also presenting the recorded data.

4.3.1 Test results - Group G1

Group G1 included ten sets of blast tests. In general, each set consisted of two identical columns, though some sets had one or three identical columns. Ten columns were seismically detailed whereas nine columns had non-seismic detailing. Below is the description of each set and the results of column tests. Also discussed is the comparison of column behaviour within each set.

1) Column Set NS1-G1

Two identical non-seismic as-built columns were tested in this set. The description of each test, the results recorded and the comparison between the two tests are provided below:

a) Column NS1-A-G1

The maximum axial load applied prior to the test was 411 kN. The designated driver pressure for this test was 345 kPa. Fig.4.30 shows that this driver pressure resulted in a peak reflected pressure of 51 kPa, and a reflected impulse over the positive phase of 477.4 kPa.ms. The positive phase duration was 21 ms. Maximum and residual column mid-height displacements were 125.3 mm ($\theta_{max.} = 6.5^{\circ}$) and 110.2 mm, respectively. The maximum mid-height displacement occurred after 50.8 ms from the start of the test. There was a significant drop in axial load after the test, from 411 kN to a residual axial load of 61.6 kN. The axial load at maximum mid-height displacement was 47 kN. The yield and maximum strain readings captured by Strain Gauge T-3 were 0.0034 (t = 13.96 ms) and 0.017 (t = 16.8 ms), respectively. Strain Gauge T-3 was damaged 16.8 ms after the start of the test (Fig. A-12). This test resulted in complete crushing of the compression concrete and extensive tension cracking at column mid-height, as shown in Fig. 4.31. Outward buckling of the longitudinal compression rebars was also observed at the column critical section.

b) Column NS1-B-G1

The axial load applied prior to the test was 402 kN. The designated driver pressure for this test was about 345 kPa. Fig. 4.32 shows that this driver pressure resulted in a maximum reflected pressure of 53 kPa and a reflected impulse over the positive phase of 488 kPa.ms. The positive phase duration was 20.6 ms. Maximum and residual column mid-height deflections were 156.9 mm ($\theta_{max.} = 8.1^{\circ}$) and 127.3 mm, respectively. The maximum mid-height displacement occurred after 54.8 ms from the start of the test. The residual axial load was only 3.6 kN, a significant drop from 402 kN. The axial load at maximum mid-height displacement was 16.7 kN. The yield and maximum strain readings recorded by Strain Gauge T-3 were 0.0034 (t = 13.7 ms) and 0.0062 (t = 20.8 ms), respectively. This is shown in Fig. A-13. This test resulted in complete crushing of the compression concrete and extensive tension cracking at column mid-height, as depicted in Fig 4.33. Outward buckling of the longitudinal compression rebars was also observed at the column's critical section.

c) Comparisons of Columns in Set NS1-G1

Fig. 4.89 shows that the maximum and residual mid-height displacements originated in Column NS1-B-G1 were 25.2 % and 15.5 %, respectively higher than those of Column NS1-A-G1. This is because Column NS1-B-G1 was subjected to a 4.2 % higher reflected blast force compared to Column NS1-A-G1. The lower part of Fig. 4.89 also shows that while the residual axial load reported in Column NS1-A-G1 was 3.6 kN, the residual axial load observed in NS1-B was 61.6 kN. Both specimens suffered extensive damage near the mid-height region.

2) Column Set NS2-G1

Two identical non-seismic CFRP wrapped RC columns were tested in this set. The laminate design configuration adopted was UD [0˚/90˚/0˚] W $[\pm 45^{\circ}]_2$. The following is a detailed description of each test and the comparison of column behaviour within Set-NS2-G1.

a) Column NS2-A-G1

The axial load applied on the column prior to the test was 410 kN. The designated driver pressure for this test was 345 kPa. Fig. 4.34 shows that this driver pressure resulted in a maximum reflected pressure of 48 kPa and a reflected impulse over the positive phase of 472.9 kPa.ms. The positive phase duration was 20.8 ms. Maximum and residual column mid-height deflections were 53.5 mm ($\theta_{max.} = 2.8^{\circ}$) and 20 mm, respectively. The maximum displacement occurred after 25.6 ms from the start of the test. The residual axial load was 294 kN, which was almost equal to the axial load recorded at maximum displacement. The yield strain, maximum strain, and residual strain readings captured by Strain Gauge T-3 were 0.0032 (t = 13.6 ms), 0.016 (t = 16.4 ms), and 0.0048, respectively. This is shown in Fig. A-14.

After the shot, the column remained intact and no visible damage was observed as shown in Fig. 4.35. Subsequently, it was subjected to monotonically increasing axial compression to establish post-blast axial load capacity. The post-blast axial capacity was found to be 630 kN. The column failed axially due to the crushing of the unwrapped ends of the column. For this reason, all the following (untested) columns were wrapped with FRP at their ends to prevent premature axial failure outside the test region.

b) Column NS2-B-G1

The axial load applied prior to the test was 440 kN. The designated driver pressure for this test was 345 kPa. Fig. 4.36 shows that this driver pressure resulted in a maximum reflected pressure of 54 kPa and a reflected impulse over the positive phase of 503.2 kPa.ms. The positive phase duration of this test was 21.24 ms. Maximum and residual column mid-height deflections were 59.3 mm ($\theta_{max.}$ = 3.1˚) and 18.5 mm, respectively. The maximum displacement took place 26.4 ms after the start of the test. The residual axial load was 334 kN, and this was almost equal to the axial load recorded at maximum mid-height displacement. The yield strain, maximum strain, and residual strain readings captured by Strain Gauge T-3 were 0.0032 (t = 14.16 ms), 0.0059 (t = 15.36 ms), and 0.0007, respectively as shown in Fig. A-15. Similar to Column NS2-A, this column remained intact and no visible damage was observed after the test, as shown in Fig. 4.37. Finally, the post-blast axial capacity was found to be 860 kN.

c) Comparisons of Columns in Set NS2-G1

Fig. 4.90 displays the comparison of the two columns tested in this set. The comparison indicates that both columns behaved semi-elastically. Although Column NS2-B-G1 was exposed to 10.8% higher blast pressure than that of the companion column, the maximum and the residual mid-height displacements for both columns were almost the same. This could be attributed to the larger pre-blast axial load applied on Column NS2-B-G2. This increase in the initial axial load slightly improved the flexural capacity of Column NS2-B-G1. The decay trends of the axial load of the columns were similar.

3) Column Set NS3-G1

Two identical non-seismic CFRP wrapped columns were tested in this set. The laminate design configuration adopted was W $[0^{\circ}/90^{\circ}]_2$ W $[\pm 45^{\circ}]_2$ UD $[0^{\circ}]$. The following is a detailed description of each test and the comparison of column performance in Set-NS3-G1.

a) Column NS3-A-G1

The axial load applied prior to the test was 405 kN. The designated driver pressure for this test was 345 kPa. Fig. 4.38 shows that this driver pressure resulted in a maximum reflected pressure of 49.4 kPa and a reflected impulse over the positive phase of 493.7 kPa.ms. The positive phase duration of this test was 21.3 ms. Maximum and residual column mid-height deflections were

94.7 mm ($\theta_{max.}$ = 4.9˚) and 85.8 mm, respectively. The maximum displacement took place 47.9 ms after the start of the test. The residual axial load was only 218 kN. The axial load recorded at maximum column mid-height displacement was 172.4 kN. The yield and maximum strain readings captured by Strain Gauge T-3 were 0.0037 (t = 13.7 ms) and 0.016 (t = 15.1 ms), respectively. Strain Gauge T-3 was damaged 15.1 ms after the start of the test (Fig. A-16). This test resulted in a single lateral (flexural) wide crack associated with the rupture of the CFRP protection system along the plane of the crack. This crack was located 195 mm above the column mid-height section. This is illustrated in Fig. 4.39.

b) Column NS3-B-G1

The axial load applied prior to the test was 423 kN. The designated driver pressure for this test was 330 kPa. Fig. 4.40 shows that this driver pressure resulted in a maximum reflected pressure of 47 kPa and a reflected impulse over the positive phase of 437.5 kPa.ms. The positive phase duration was 20.76 ms. Maximum and residual column mid-height deflections were 69.1 mm ($\theta_{max.}$ = 3.6˚) and 51.6 mm, respectively. The maximum displacement took place at 32.9 ms from the start of the test. The residual axial load was 329 kN. The axial load recorded at maximum mid-height displacement was 277 kN. The yield and maximum strain readings captured by Strain Gauge T-3 were 0.0038 (t = 14.2 ms) and 0.017 (t = 17.4 ms), respectively. Strain Gauge T-3 was damaged after 17.4 ms from the start of the test (Fig. A-17). This test resulted in a single lateral (flexural) crack associated with the rupture of the CFRP protection system along the plane of the crack. This crack was located 25 mm above the column mid-height section as shown in Fig.4.41.

c) Comparisons of Columns in Set NS3-G1

Fig. 4.91 compares the structural behaviour of Column NS3-A-G1 and Column NS3-B-G1 when investigated under two different levels of blast loads. Although it was externally protected with CFRP laminates, Column NS3-A-G1 experienced significant deflection at mid-height when it was subjected to a blast load of 204 kN. Column NS3-B-G1 was tested under a blast load 9.2 % lower than that applied on Column NS3-A-G1. This reduction in blast load decreased the maximum and the residual mid-height displacements in Column NS3-B-G1 by 27 % and 39.8 %, respectively. The drop in axial load on Column NS3-B-G1 was reduced by 32.1 % compared to Column NS3-A-G1. Both columns depicted poor structural performance under blast loads due to

the rupture of CFRP laminate near the column mid-height. This can be explained by the effect of the laminate lay-up or the stacking sequence of unidirectional and woven laminas. It is observed that having a unidirectional lamina, or UD [0˚], after the woven laminas, or $[\pm 45^{\circ}]_2$, resulted in interruption to the free three-dimensional extensions of the woven fabric. This resulted in high shearing action parallel to the 0˚ angle, which tore down the woven fabric and developed a premature failure of the laminate.

4) Column Set NS4-G1

Two identical non-seismic CFRP wrapped columns were tested in this set. The laminate design configuration adopted was $W[0^{\circ}/90^{\circ}]_2$ $W[\pm 45^{\circ}]_2$. The following provides a detailed description of each test and a comparison of the two columns in Set-NS4-G1.

a) Column NS4-A-G1

The axial load applied prior to the test was 418 kN. The designated driver pressure for this test was 330 kPa. Fig. 4.42 shows that this driver pressure resulted in a maximum reflected pressure of 47 kPa and a reflected impulse over the positive phase of 471.5 kPa.ms. The positive phase duration was 21.8 ms. Maximum and residual column mid-height deflections were 81 mm ($\theta_{max.}$ = 4.2˚) and 75.1 mm, respectively. The maximum displacement occurred at 44.1 ms after the start of the test. The residual axial load was only 172 kN. The axial load recorded at maximum mid-height displacement was 107.6 kN. In this test, Strain Gauge T-3 failed to record the development of tensile strains in tension rebars. Thus, it was not possible to collect the strain data (Fig. A-18). At the end of the test, it was observed that the CFRP system crumbled due to the crushing of the compression concrete in the plastic hinge region. This is shown in Fig. 4.43. Furthermore, a tension crack associated with the rupture of CFRP laminate was observed to occur at 25 mm above the column mid-height.

b) Column NS4-B-G1

The axial load applied prior to the test was 431 kN. The designated driver pressure for this test was 303 kPa. Fig. 4.44 shows that this driver pressure resulted in a maximum reflected pressure of 50.2 kPa and a reflected impulse over the positive phase of 440 kPa.ms. The positive phase duration was 22.2 ms. Maximum and residual column mid-height deflections were 54.1 mm ($\theta_{max.}$ = 2.8˚) and 21.5 mm, respectively. The maximum displacement occurred 26.1 ms after the start of the test. The residual axial load was only 317 kN. The axial load recorded at maximum

mid-height displacement was 299 kN. The yield, maximum, and residual strain readings captured by Strain Gauge T-3 were 0.0037 (t = 16.7 ms), 0.014 (t = 24.8 ms), and 0.0042, respectively (Fig. A-19). This column remained intact and no visible damage was observed after the shot. This is clearly shown in Fig. 4.45. The maximum average dynamic reaction forces measured at the lateral support was 79.5 kN per support, which occurred at 7.9 ms from the start of the test as illustrated in Fig. 4.46. Finally, the post-blast axial capacity of this column was established to be 761 kN.

c) Comparisons of Columns in Set NS4-G1

Two identical non-seismic CFRP wrapped columns were examined in this set. Due to the very large mid-height deflection in Column NS4-A-G1, Column NS4-B-G1 was exposed to 8.3 % lower blast load (note that for this test the driver pressure was reduced from 330 kPa to 303 kPa). This decrease in the applied blast load resulted in a significant reduction of the lateral deflection. Maximum and residual mid-height deflections of Column NS4-B-G1 were reduced by 33.2 % and 71.3 %, respectively compared to those of the companion column. This is illustrated in Fig. 4.92. In addition, the residual axial load recorded for Column NS4-B-G1 was 84.3 % larger than that for Column NS4-A-G1. Both columns behaved in a similar manner until 24 ms when the CFRP laminate ruptured in Column NS4-A-G1. A higher mid-height displacement was developed afterwards. This can be explained by the sensitivity of the "all woven" laminate to the slight increase of the lateral blast load. A sudden tearing of the laminate occurred in the [0˚/90˚] plane. This limited the ability of W [±45˚] plies to hold and distribute successive stresses (see Fig. 4.43).

5) Column Set NS5-G1

One single non-seismic CFRP wrapped column was tested in this set. The laminate design configuration adopted was UD[$0^{\circ}_2/90^{\circ}_2/0^{\circ}$]. The axial load applied prior to the test was 422.5 kN. The designated driver pressure for this test was 330 kPa. Fig. 4.47 shows that this driver pressure resulted in a maximum reflected pressure of 49 kPa and a reflected impulse over the positive phase of 463 kPa.ms. The positive phase duration was 22 ms. Maximum and the residual column mid-height deflections were 51.3 mm ($\theta_{max.} = 2.7^{\circ}$) and 20.5 mm, respectively. The maximum displacement occurred 23.9 ms after the start of the test. The residual axial load was 396.2 kN.

The axial load recorded at maximum mid-height displacement was 267.7 kN. The yield, maximum, and residual strain readings recorded by Strain Gauge T-3 were 0.0037 (t = 14.9 ms), 0.013 (t = 24.9 ms), and 0.0042, respectively (Fig. A-20). This column remained intact after the test and no visible damage was observed as illustrated in Fig. 4.48. The maximum average dynamic reaction forces measured at lateral supports was 64.45 kN, which occurred at 10 ms from the start of the test (Fig. 4.49). The post-blast axial capacity was established to be 882 kN.

6) Column Set S1-G1

This set contains three identical seismically detailed as-built columns; S1-A, S1-B and S1-C. Below is a detailed description of each test in the set:

a) Column S1-A-G1

The axial load applied prior to the test was 419.7 kN. The designated driver pressure for this test was 345 kPa. Fig. 4.50 shows that this driver pressure resulted in a maximum reflected pressure of 53.8 kPa and a reflected impulse over the positive phase of 509.3 kPa.ms. Positive phase duration was 21.52 ms. Maximum and residual deflections at column mid-height were 114.9 mm ($\theta_{max.} = 6^{\circ}$) and 108.5 mm, respectively. The maximum mid-height deflection occurred 69.8 ms after the start of the test. The residual axial load was 160.3 kN. The axial load recorded at maximum mid-height displacement was 140.9 kN. The yield and maximum strain readings captured by Strain Gauge T-3 were 0.0038 (t = 14.9 ms) and 0.021 (t = 24.8 ms), respectively as shown in Fig. A-21. Strain Gauge T-3 was damaged 24.8 ms after the start of the test. This test resulted in complete crushing of the compression concrete and extensive localized tension cracking in the mid-height region of the column, as depicted in Fig. 4.51.

b) Column S1-B-G1

The axial load applied prior to the test was 420 kN. The designated driver pressure for this test was 345 kPa. Fig. 4.52 shows that this driver pressure resulted in a maximum reflected pressure of 56 kPa and a reflected impulse over the positive phase of 499.5 kPa.ms. Positive phase duration was 21.1 ms. Maximum and residual deflections at column mid-height were 130.3 mm ($\theta_{max.} = 6.8^{\circ}$) and 120.6 mm, respectively. The maximum mid-height deflection occurred 54.3 ms after the start of the test. The residual axial load was only 70 kN. The axial load recorded at maximum mid-height displacement was 23.6 kN. The yield and maximum strain readings

captured by Strain Gauge T-3 were 0.003 (t = 13 ms) and 0.0092 (t = 17.7 ms), respectively as shown in Fig. A-22. Strain Gauge T-3 malfunctioned 24.8 ms after the start of the test. This test resulted in complete crushing of the compression concrete and extensive tension cracking at mid-height, as shown in Fig. 4.53.

c) Column S1-C-G1

The axial load applied prior to the test was 426.5 kN. The designated driver pressure for this test was 345 kPa. Fig. 4.54 shows that this driver pressure resulted in a maximum reflected pressure of 50.8 kPa and a reflected impulse over the positive phase of 511 kPa.ms. Positive phase duration was 21.64 ms. Maximum and residual deflections at column mid-height were 148.4 mm ($\theta_{max.} = 8.8^{\circ}$) and 128.3 mm, respectively. The maximum mid-height deflection occurred 47.4 ms after the start of the test. The residual axial load was zero. The yield and maximum strain readings captured by Strain Gauge T-3 were 0.0038 (t = 13.92 ms) and 0.017 (t = 16.9 ms), respectively. Strain Gauge T-3 malfunctioned after 16.9 ms from the start of the test. This test resulted in complete crushing of the compression concrete and extensive tension cracking at mid-height. The maximum average of dynamic reaction forces measured at lateral supports was 96 kN, which occurred 11 ms after the start of the test, as shown in Fig. 4.55.

d) Comparisons of Columns in Set S1-G1

Three seismically detailed as-built columns were tested in this set, but only two columns are presented. Fig. 4.93 compares the time histories of mid-height deflection and axial load for Columns S1-A-G1 and S1-B-G1. Both columns were subjected to equal blast effects. The applied blast load caused a relatively large mid-height deflection in the columns. Nevertheless, the maximum and the residual mid-height deflections which occurred in Column S1-B-G1 were about 12% higher than the corresponding deflections of Column S1-A-G1. This could be attributed to the arching action formed in Column S1-A-G1 caused by the occasional restraining occurred at the top axial support. Note that the lower part of Fig. 4.93 depicts that the pre-blast axial load applied on S1-A-G1 went up from 419.7 kN to 501 kN shortly after the start of the test. This rise in the axial load improved the column flexural capacity and the displacement response of the column. Moreover, the arching action initiated seized the decay in the applied axial load. As a result, the residual axial load of Column S1-A-G1 was 129 % larger than the residual axial load of Column S1-B-G1.

7) Column Set S2 –G1

This set contained simulated blast tests of two identical seismically detailed CFRP jacketed columns. The CFRP design configuration of the protection laminate was UD [0˚/90˚] W[±45˚] $_2$. The following is a description of the results obtained for each column:

a) Column S2-A-G1

The axial load applied prior to the test was 413.8 kN. The designated driver pressure for this test was 355 kPa. Fig. 4.56 shows that this driver pressure resulted in a maximum reflected pressure of 57 kPa and a reflected impulse over the positive phase of 599 kPa.ms. Positive phase duration was 23.9 ms. Maximum and residual column mid-height deflections were 81.3 mm ($\theta_{max.}$ = 4.2˚) and 38.2 mm, respectively. The maximum displacement occurred at 28.7 ms from the start of the test. The residual axial load was 278.5 kN. The axial load recorded at maximum mid-height displacement was 42.5 kN. The yield, maximum, and residual strain readings recorded by Strain Gauge T-3 were 0.003 (t = 12.4 ms), 0.007 (t = 13.5 ms), and 0.0012, respectively as shown in Fig. A-23. The column remained intact at the end of the test, and no visible damage was observed. This is shown in Fig. 4.57. The maximum average of dynamic reaction forces measured at lateral supports was 65.2 kN, which occurred 5.6 ms after the start of the test (Fig. 4.58). The post-blast axial load capacity was found to be 560 kN.

b) Column S2-B-G1

The axial load applied prior to the test was 412.7 kN. The designated driver pressure for this test was 390 kPa. Fig. 4.59 shows that this driver pressure resulted in a maximum reflected pressure of 61 kPa and a reflected impulse over the positive phase of 561.4 kPa.ms. Positive phase duration was 21.3 ms. Maximum and residual column mid-height deflections were 100.3 mm ($\theta_{max.}$ = 5.2˚) and 90.9 mm, respectively. The maximum displacement occurred at 43.7 ms from the start of the test. The residual axial load was 157 kN. The axial load recorded at maximum mid-height displacement was 42.5 kN. The yield and maximum strain readings captured by Strain Gauge T-3 were 0.003 (t = 13.5 ms), 0.016 (t = 25.5 ms), respectively. Strain Gauge T-3 malfunctioned 25.5 ms after the start of the test, as shown in Fig. A-24. This test resulted in tension cracks associated with rupturing of the CFRP protection system in the critical region (Fig. 4.60). The maximum average of dynamic reaction forces measured at lateral supports was 59.8 kN, which occurred 8.1 ms after the start of the test, as indicated in Fig. 4.61.

c) Comparisons of Columns in Set S2-G1

Fig. 4.94 compares the time history of the mid-height displacement and axial load of Columns S2-A-G1 and S2-B-G1. To attain the maximum capacity of the retrofitted RC member, Column S2-B-G1 was exposed to 5.2 % larger blast force compared to Column S2-A-G1. Whilst Column S2-A-G1 remained intact with minor residual damage at the end of the event, Column S2-B-G1 suffered 138 % higher residual mid-height displacement associated with the rupture of the CFRP protection system. The responses of both columns were identical until maximum deflection, when rupturing of the CFRP laminate at 100 mm below the mid-height occurred in Column S2-B-G1. Immediately after this incident, a larger un-restorable mid-height deflection was generated. The residual axial load of Column S2-A-G1 was 77.4 % larger than that of Column S2-B-G1. The failure of the CFRP laminate in Column S2-B-G1, and the failure of other columns at 5 to 15% increase in lateral load indicates that the initial target load is selected to be just below the expected blast failure load.

8) Column Set S3-G1

This set contained tests of two identical seismically detailed CFRP jacketed columns. The CFRP design configuration of the protection laminate used was $W[0^{\circ}/90^{\circ}]_4$. The following is a description of the results recorded in each test of this set:

a) Column S3-A-G1

The axial load applied prior to test was 402 kN. The designated driver pressure was 380 kPa. Fig. 4.62 shows that this driver pressure resulted in a maximum reflected pressure of 58.8 kPa and a reflected impulse over the positive phase of 586.5 kPa.ms. Positive phase duration was 23.2 ms. Maximum and residual column mid-height deflections were 172.1 ($\theta_{max.} = 8.89^{\circ}$) mm and 145.3 mm, respectively. The maximum displacement occurred at 50.6 ms from the start of the test. The residual axial load was zero. The yield and maximum strain readings recorded by Strain Gauge T-3 were 0.0032 (t = 13.9 ms), and 0.0156 (t = 18.7 ms), respectively. Strain Gauge T-3 malfunctioned 18.7 ms after the start of the test as shown in Fig. A-25. The very large deflection associated with this test resulted in a single wide tension crack situated at 50 mm below the column mid-height section as shown in Fig. 4.63. The formation of this crack ruptured the CFRP protection system at the crack level. Crushing of compression concrete was also observed upon

the complete rupture of the CFRP sheet in that region. Maximum average dynamic reaction force measured at lateral supports was 67.0 kN, which occurred at 9.1 ms after the start of the test. This is shown in Fig. 4.64.

b) Column S3-B-G1

The axial load applied prior to the test was 413 kN. The designated driver pressure was 305 kPa. Fig. 4.65 shows that this driver pressure resulted in a maximum reflected pressure of 47 kPa and a reflected impulse over the positive phase of 456.1 kPa.ms. Positive phase duration was 21.9 ms. Maximum and residual column mid-height deflections were 54.7 mm ($\theta_{max.}$ = 2.85˚) and 20.2 mm, respectively. The maximum displacement occurred at 28.4 ms from the start of the test. The residual axial load was 326 kN. The axial load recorded at maximum mid-height displacement was 233.4 kN. The yield, maximum, and residual strain readings recorded by Strain Gauge T-3 were 0.003 (t = 14.76 ms), 0.015 (t = 16.4 ms), and 0.0028, respectively as shown in Fig. A-26. At the end of the test, the column remained intact and no visible damage was observed (Fig. 4.66). The maximum average dynamic reaction forces measured at lateral supports was 59.5 kN, which occurred at 11.4 ms from the start of the test (Fig. 4.67). Finally, the post-blast axial capacity of this column was determined to be 776 kN.

c) Comparisons of Columns in Set S3-G1

Two seismically detailed CFRP protected RC columns were investigated in this set. Column S3-A-G1 experienced severe damage associated with very large maximum and residual mid-height deflections when subjected to blast force of a magnitude equal to 222.5 kN (Fig. 4.95). To prevent this level of damage in Column S3-B-G1, the blast load applied was reduced by 17.6%. The drops in the maximum and residual mid-height deflections of Column S3-B-G1 were 68.2 % and 86.1 %, respectively. The residual axial load measured in S3-A-G1 was nil, while it was 326 kN in Column S3-B-G1.

9) Column Set-S4

This set contained two identical seismically detailed CFRP jacketed columns. The CFRP design configuration of the protection laminate was W$[0^{\circ}/90^{\circ}]_2$ W$[\pm 45^{\circ}]_2$. The following is a description of the results recorded in each test of this set:

a) Column S4-A-G1

The designated driver pressure for this test was about 345 kPa. Fig. 4.68 shows that this driver pressure resulted in a maximum reflected pressure of 55 kPa and a reflected impulse over the positive phase of 486.6 kPa.ms. Positive phase duration was 20.4 ms. The maximum and residual column mid-height deflections were 111.3 mm ($\theta_{max.}$ = 5.8˚) and 103 mm, respectively. The maximum displacement occurred at 47.3 ms from the start of the test. The axial load applied prior to the test was 411.3 kN; however the residual axial load was only 88 kN. The axial load recorded at mid-height maximum displacement was 47 kN. The yield and maximum strain readings captured by Strain Gauge T-3 were 0.0032 (t = 14.1 ms) and 0.019 (t = 15.6 ms), respectively. Strain Gauge T-3 malfunctioned 15.6 ms after the start of the test as shown in Fig. A-27. The very large column deflection associated with this test resulted in a single wide tension crack situated at 100 mm below the column mid-height section as shown in Fig. 4.69. The formation of this crack ruptured the CFRP protection system at the crack plane. The maximum average of dynamic reaction forces measured at lateral supports was 64.7 kN, which occurred at the instant of 10.6 ms from the start of the test (Fig. 4.70).

b) Column S4-B-G1

The axial load applied prior to the test was 409 kN. The designated driver pressure was 305 kPa. Fig. 4.71 shows that this driver pressure resulted in a maximum reflected pressure of 50 kPa and a reflected impulse over the positive phase of 462.5 kPa.ms. Positive phase duration was 21.8 ms. Maximum and residual column mid-height deflections were 62 mm ($\theta_{max.}$ = 3.2˚) and 54.6 mm, respectively. The maximum displacement occurred at 31.8 ms and the residual axial load was 234 kN. The axial load recorded at maximum mid-height displacement was 110 kN. The yield and maximum strain readings recorded by Strain Gauge T-3 were 0.0036 (t = 16 ms), and 0.0155 (t = 26.76 ms), respectively as shown in Fig. A-28. Strain Gauge T-3 malfunctioned 20.4 after the start of the test. The relatively large column deflection associated with this test resulted in a single wide tension crack situated at 75 mm below the column mid-height section, as depicted in Fig. 4.72. The formation of this crack ruptured the CFRP protection system at the crack plane. The maximum average dynamic reaction force measured at lateral supports was 54.3 kN, which occurred at 9.0 ms after the start of the test as shown in Fig. 4.73.

c) Comparisons of Columns in Set S4-G1

Two seismically detailed CFRP retrofitted RC columns were tested in this set. The comparison shown in Fig. 4.96 shows that Column S4-A-G1 was exposed to a blast load of 210 kN. This load resulted in the fracture of CFRP laminate, coupled with a large mid-height deflection. On the other hand, Column S4-B-G1 was subjected to 11% lower blast load. This reduction in the load produced maximum and residual mid-height deflections of smaller amounts by 44.3 % and 47 %, respectively. Yet, decreasing the blast load in the second test did not prevent the rupture of the CFRP laminate of Column S4-B-G1. The residual axial load in Column S4-B-G1 was 165.9 % higher than the residual axial load observed in Column S4-A-G1.

10) Column Set-S5-G1

This set contained one single seismically detailed CFRP jacketed columns. The CFRP design configuration of the protection laminate used was UD [$90^{\circ}_2/0^{\circ}_2$]. The axial load applied prior to the test was 417.5 kN. The designated driver pressure was 345 kPa. Fig. 4.74 shows that this driver pressure resulted in a maximum reflected pressure of 49 kPa and a reflected impulse over the positive phase of 499 kPa.ms. The duration of the positive phase of this test was 20.7 ms. Maximum and residual deflections at the mid-height of the column were 58.7 mm ($\theta_{max.} = 2.7^{\circ}$) and 26.5 mm, respectively. The maximum displacement occurred at 26.7 ms and the residual axial load was only 327.1 kN. The axial load recorded at maximum mid-height displacement was 203.1 kN. The yield, maximum and residual strain readings recorded by Strain Gauge T-3 were 0.0038 (t = 15.2 ms), 0.0124 (t = 18.7 ms) and 0.0034, respectively as shown in Fig. A-29. This column remained intact after the test with no visible damage. This is illustrated in Fig. 4.75. The maximum average dynamic reaction force measured at lateral supports was 64.1 kN, which occurred 10.2 ms after the start of the test (Fig. 4.76). Finally, the post-blast axial load capacity of this column was established by test to be 765 kN.

4.3.2 Test results - Group G2

Group G2 included three sets of columns. Typically, two identical columns were tested in each set, except for one set, in which a single test was performed. All the specimens in this set were non-seismic columns. A detailed description of the tests is provided in the following sections:

1) Column NS1-G2

A single as-built column was tested in this set. The axial load applied prior to the test was 411 kN. The designated driver pressure was 330 kPa. Fig. 4.77 shows that this driver pressure resulted in a maximum reflected pressure of 50 kPa and a reflected impulse over the positive phase of 431.5 kPa.ms. The positive phase duration was 19.85 ms. Maximum and residual column mid-height displacements were 110.9 mm ($\theta_{max.} = 5.8^{\circ}$) and 97.5 mm, respectively. The maximum mid-height displacement occurred 46.4 ms after the start of the test. The residual axial load was 64 kN, whereas the axial load recorded at maximum mid-height displacement was 28 kN. The yield and maximum strain readings captured by Strain Gauge T-3 were 0.0032 (t = 15.9 ms) and 0.0148 (t = 17.4 ms), respectively, as indicated in Fig. A-30. Strain Gauge T-3 was damaged 17.4 ms after the start of the test. This test resulted in complete crushing of the compression concrete and extensive tension cracking in the mid-height region of the column as shown in Fig. 4.78.

2) Column Set NS2-G2

Two identical CFRP wrapped columns were tested in this set. The laminate design configuration adopted was W $[0^{\circ}/90^{\circ}]_2$ W$[\pm 45^{\circ}]_2$ UD $[0^{\circ}]$. Below is a description of the test results in this set:

a) Column NS2-A-G2

The axial load applied prior to the test was 401 kN. The designated driver pressure for this test was about 503 kPa. Fig. 4.79 shows that this driver pressure resulted in a maximum reflected pressure of 61 kPa and a reflected impulse over the positive phase of 625.2 kPa.ms. The positive phase duration was 19.88 ms. Both maximum and residual column mid-height deflections were 257 mm ($\theta_{max.} = 13.2^{\circ}$). The maximum mid-height displacement occurred 51.9 ms after the start of the test.; however the residual axial load was zero. All the strain gauges were damaged during the test; therefore no usable strain data was available. The large lateral displacement associated with the application of the intense blast shot herein developed a lateral fracture at 157 mm above the column mid-height section, as illustrated in Fig. 4.80. The rebars and the CFRP protection laminate were ruptured at the plane of fracture, on the tension side. Concrete crushing and CFRP jacket rupturing were observed on the compression side.

b) Column NS2-B-G2

Axial load applied prior to the test was 402 kN. The designated driver pressure for this test was about 345 kPa. Fig. 4.81 shows that this driver pressure resulted in a maximum reflected pressure of 56 kPa and a reflected impulse over the positive phase of 569.5 kPa.ms. The positive phase duration was 23.5 ms. Maximum and residual column mid-height displacements were 76.25 mm ($\theta_{max.}$ = 2.85˚) and 69 mm, respectively. The maximum mid-height displacement occurred 49.4 ms after the start of the test. The residual axial load was 288 kN. The axial load recorded at maximum mid-height displacement was 252.5 kN. The yield and maximum strain readings recorded by Strain Gauge T-3 were 0.0029 (t = 14.7 ms) and 0.01 (t = 17.3 ms), respectively, as shown in Fig. A-31. Strain Gauge T-3 was damaged after 17.3 ms from the start of the test. This test resulted in a single lateral tension crack associated with the rupture of CFRP laminate along the plane of the crack. This crack was located 125 mm below the column mid-height section. This is shown in Fig. 4.82.

c) Comparisons of Columns in Set NS2-G2

Two CFRP retrofitted RC columns were tested in this set. Column NS2-A-G2 was tested first under a blast load of 277 kN. This load was relatively high; as a result, the dynamic response measured was extremely large (Fig. 4.97). The pre-test axial load applied on the test specimen dropped to zero once the mid-height deflection reached 92 mm. Due to the extensive damage developed in Column NS2-A-G2, a smaller blast load was applied on Column NS2-B-G2. Despite the major reduction in blast load, Column NS2-B-G2 underwent a permanent deflection combined with the rupture of the CFRP laminate at mid-height. However, the applied axial load on Column NS2-B-G2 only dropped to 290 kN at the end of the test. This can be attributed to the premature failure associated with the use of CFRP lamina UD [0˚] after the application of four woven laminas (W [0˚/90˚] $_2$ / W [±45˚] $_2$).

3) <u>Column Set KEV-G2</u>

Two identical FRP wrapped columns were tested in this set. The laminate design configuration adopted was U [0˚/90˚] W [±45˚] $_2$ W[KEV]. Below is the description of the tests in this set:

a) Column KEV-1-G2-Test

The axial load applied prior to the test was 412 kN. The designated driver pressure for this test was 350 kPa. Fig. 4.83 shows that this driver pressure resulted in a maximum reflected pressure of 58 kPa and a reflected impulse over the positive phase of 579 kPa.ms. The positive phase duration was 23.72 ms. Maximum and residual column mid-height displacements were 131.7 mm ($\theta_{max.} = 6.8^{\circ}$) and 120.8 mm, respectively. The maximum mid-height displacement occurred 50 ms after the start of the test. The residual axial load was 94 kN. The axial load measured at maximum mid-span displacement was 16.7 kN. The yield and maximum strain readings recorded by Strain Gauge T-3 were 0.0035 (t = 12.8 ms) and 0.017 (t = 14.4 ms), respectively. This is indicated in Fig. A-32. Strain Gauge T-3 was damaged 14.4 ms after the start of the test. This test resulted in a primary rupture of the FRP system located at 75 mm above the column mid-height section, and a secondary rupture of the FRP system located at 240 mm below the mid-height section of the column. This is shown in Fig. 4.84. The maximum average dynamic reaction force measured at lateral supports was 69.6 kN, which occurred 8 ms after the start of the test (Fig. 4.85).

b) Column KEV-2-G2

The axial load applied prior to the test was 420 kN. The designated driver pressure for this test was about 345 kPa. Fig. 4.86 shows that this driver pressure resulted in a maximum reflected pressure of 55 kPa and a reflected impulse over the positive phase of 531.7 kPa.ms. The positive phase duration was 23.4 ms. Maximum and residual column mid-height deflections were 96.6 mm ($\theta_{max.} = 5^{\circ}$) and 89.7 mm, respectively. The maximum mid-height displacement occurred 46.3 ms after the start of the test. Residual axial load was only 240 kN. The axial load monitored at maximum mid-height displacement was 149 kN. The yield and maximum strain readings recorded by Strain Gauge T-3 were 0.0035 (t = 13.7 ms) and 0.015 (t = 18.9 ms), respectively as shown in Fig. A-33. Strain gauge T-3 was damaged 18.9 ms after the start of the test. Debonding between the Kevlar plies at the overlap region was noticed at the end of the test. The overlap plane was located 40 mm below the column mid-height section, which is illustrated in Fig. 4.87. No other damage was observed along the height of the column. The maximum of average dynamic reaction forces measured at lateral supports was 69.4 kN, which occurred 8.5 ms after the start of the test (Fig. 4.88).

c) Comparisons of Columns in Set KEV-G2

The structural performance of Columns KEV.1-G2 and Column KEV-2-G2 are compared in Fig. 4.98. Maximum and residual mid-height deflections recorded in KEV-1-G2 were relatively large, while the residual axial load recorded was relatively low when the column was subjected to 215 kN blast force. Column KEV-2-G2 on the other hand, was subjected to a blast load of smaller magnitude. In this test, only 200 kN blast force was applied. This is about 6.9 % less than the blast force applied on KEV-1-G2. Due to the reduction in applied load, the maximum and residual mid-height deflections originated in Column KEV-2-G2 were lower by 26.65 % and 25.75 %, respectively. The residual axial load observed in Column KEV-2-G2 increased by 155.3 % as compared to Column KEV-1-G2.

4.4 Shock Tube Displacements

The effects of the movement and vibration of the shock tube on column mid-height displacement were measured. Fig. 4.99 and Fig. 4.100 display the displacements monitored for the center and edge of the bottom supporting steel frame, fastened to the body of the shock tube, during tests of Columns S2-B-G1 and S2-A-G, respectively. The blast shock pressure applied in these tests was very high; hence the associated shock tube displacements are expected to be the highest.

It is clear from Fig. 4.99 and Fig. 4.100 that the maximum displacement of the centre and the edge of the bottom supporting steel frame were very small (less than 2 mm). Therefore the movement of the shock tube during testing was assessed to be negligible, with little or no effect on measured column mid-height displacements.

Table-4.1: Firing parameters and experimental results for S-AL0 columns

Column	A_xL *(kN)*	*Shot No.*	P_D *(kPa)*	P_r *(kPa)*	I_r *(kPa.ms)*	t_d *(ms)*	$d_{max.}$ *(mm)*	$\theta_{max.}$ *(degrees)*	$t_{max.}$ *(ms)*	$d_{residual}$ *(mm)*	$d_{accumlative}$ *(mm)*	F_o *(kN)*
S1-AL0	0	1st	103.5	-	-	-	-	-	-	13*	13*	-
	0	2nd	69	14.1	143.5	19.2	23.3	1.21	27.3	2.7	15.7	65.8
	0	3rd	138	22	236.6	18.65	53.3	2.77	30.2	27.7	43.4	112
	0	4th	207	37	320	18	-	-	-	126*	126*	156.4
S2-AL0	0	1st	69	13.1	144	19.4	17.7	0.92	25	3.7	3.7	65
	0	2nd	103.5	30	284	19.2	50.2	2.61	30	27.2	30.9	129.8
	0	3rd	207	-	-	-	-	-	-	100*	100*	-
	0	4th	207	30.6	309.8	18.1	63.4	3.3	36.5	36.5	136.5	150.7
S3-AL0	0	1st	207	35.75	345.2	20	85	4.42	37.9	64.9	64.9	151.8
S4-AL0	0	1st	207	35.7	372.1	20	104.9	5.45	42.4	85.5	85.5	163.9

* measured manually

Table-4.2: Firing parameters and experimental results for S-AL400 columns

Column	A_xL *(kN)*	*Shot No.*	P_D *(kPa)*	P_r *(kPa)*	I_r *(kPa.ms)*	t_d *(ms)*	$d_{max.}$ *(mm)*	$\theta_{max.}$ *(degrees)*	$t_{max.}$ *(ms)*	$d_{residual}$ *(mm)*	$d_{accumlative}$ *(mm)*	$A_xL_{residual}$ *(kN)*	F_o *(kN)*
S1-AL400	400	1st	103.5	16.9	179.8	20.4	23.9	1.24	26.1	6.9	6.9	-	77.6
	-	2nd	207	31.6	334.9	20.84	62.5	3.25	33.7	43.7	50.6	-	141.5
S2-AL400	390	1st	103.5	16.9	188.4	19.3	14.3	0.745	22.2	3.7	3.7	348	85.9
	400	2nd	207	30	329.5	22.2	33.5	1.74	24.2	20.1	23.8	344.5	130.6
	393	3rd	345	41.4	435	18.8	130.1	6.745	39.4	105.6	129.4	0	203.5
S3-AL400	389	1st	345	48.4	476.2	20.6	131.5	6.82	48.4	113.3	113.3	30	203.5
S4-AL400	409.7	1st	345	49.1	481.5	20.5	105	5.45	41.4	103	103	49.7	206.8

Table-4.3: Firing parameters and experimental results for non-seismic columns in Group-G1

Column	A_xL *(kN)*	P_D *(kPa)*	P_r *(kPa)*	I_r *(kPa.ms)*	t_d *(ms)*	F_o *(kN)*	$d_{max.}$ *(mm)*	$\theta_{max.}$ *(degrees)*	$t_{max.}$ *(ms)*	$d_{residual}$ *(mm)*	$A_xL_{residual}$ *(kN)*	$A_xL_{@d.max.}$ *(kN)*
NS1-A-G1	411	345	51	477.4	21	200	125.3	6.5	50.8	110.2	61.6	47
NS1-B-G1	402	345	53	488	20.6	208.5	156.9	8.1	54.8	127.3	3.6	16.7
NS2-A-G1	410	345	48	472.9	20.8	200	53.5	2.8	25.6	20	294	294
NS2-B-G1	440	345	54	503.2	21.24	208.5	59.3	3.1	26.4	18.5	334	334
NS3-A-G1	405	345	49.4	493.7	21.3	204	94.7	4.9	47.9	85.8	218	172.4
NS3-B-G1	423	330	46.85	437.5	20.76	185.5	69.1	3.6	32.9	51.6	329	277
NS4-A-G1	418	330	47	471.5	21.8	190.4	81	4.2	44.1	75.1	172	107.6
NS4-B-G1	431	303	50.2	440	22.2	174.5	54.1	2.8	26.1	21.5	317	299
NS-5-G1	422.5	330	49	463	22	185	51.3	2.7	23.9	20.5	396	267.7

Table-4.4: Firing parameters and experimental results for seismic columns in Group-G1

Column	A_xL *(kN)*	P_D *(kPa)*	P_r *(kPa)*	I_r *(kPa.ms)*	t_d *(ms)*	F_o *(kN)*	$d_{max.}$ *(mm)*	$\theta_{max.}$ *(degrees)*	$t_{max.}$ *(ms)*	$d_{residual}$ *(mm)*	$A_xL_{residual}$ *(kN)*	$A_xL_{@d.max.}$ *(kN)*
S1-A	419.7	345	53.8	509.3	21.52	208	114.9	6	69.8	108.5	160.3	140.9
S1-B	420	345	56	499.5	21.1	208	130.3	6.8	54.3	120.6	70	23.6
S1-C	426.5	345	50.8	511	21.64	208	148.8	8.8	47.4	128.3	0	0
S2-A	413.8	355	57	599	23.9	221	81.3	4.2	28.7	38.5	278.5	42.5
S2-B	412.7	390	61	561.4	21.3	232	100.3	5.2	43.7	90.9	157	90
S3-A	402	380	58.8	586.5	23.2	222.5	172.1	8.89	50.6	145.3	0	0
S3-B	413	305	47	456.1	21.9	183	54.7	2.85	28.4	20.2	326	233
S4-A	411	345	55	486.6	20.4	210	111.3	5.8	47.3	103	88	47
S4-B	409	305	50	462.5	21.8	187	62	3.2	31.8	54.6	234	110
S-5	417.5	345	49	499	20.7	212	58.7	2.7	26.7	26.5	327	203

Table-4.5: Firing parameters and experimental results for non-seismic columns in Group-G2

Column	A_xL *(kN)*	P_D *(kPa)*	P_r *(kPa)*	I_r *(kPa.ms)*	t_d *(ms)*	F_o *(kN)*	$d_{max.}$ *(mm)*	$\theta_{max.}$ *(degrees)*	$t_{max.}$ *(ms)*	$d_{residual}$ *(mm)*	$A_xL_{residual}$ *(kN)*	$A_xL_{@\ dmax.}$ *(kN)*
NS1-G2	411	330	50	431.5	19.85	191	110.9	5.8	46.4	97.5	64	28
NS2-A-G2	401	503	61	625.2	19.88	277	257	13.2	51.9	257	0	0
NS2-B-G2	402	345	56	569.5	23.5	213	76.25	2.85	49.4	69	288	252.5
KEV.1-G2	412	350	58	579	23.72	215	131.7	6.8	50	120.8	94	16.7
KEV.2-G2	420	345	55	531.7	23.4	200	96.6	5	46.3	89.7	240	149

Table-4.5: Measured dynamic reactions

Column	*Dynamic Reaction (V) (kN)*	t_v *(ms)*
NS4-B	79.5	7.9
NS5	64.45	10.1
S1-C	96	11
S2-A	65.2	5.6
S2-B	59.8	8.1
S3-A	67	9.1
S3-B	59.5	11.4
S4-A	64.7	10.6
S4-B	54.3	9.4
S-5	64.1	10.2
KEV.1	69.6	7.56
KEV.2	69.4	8.7

t_v is the duration to maximum dynamic reaction

(a) (b)

Fig. 4.1 Level of damage in Column S1-AL0 after the 1st shot: a) front view; b) side view

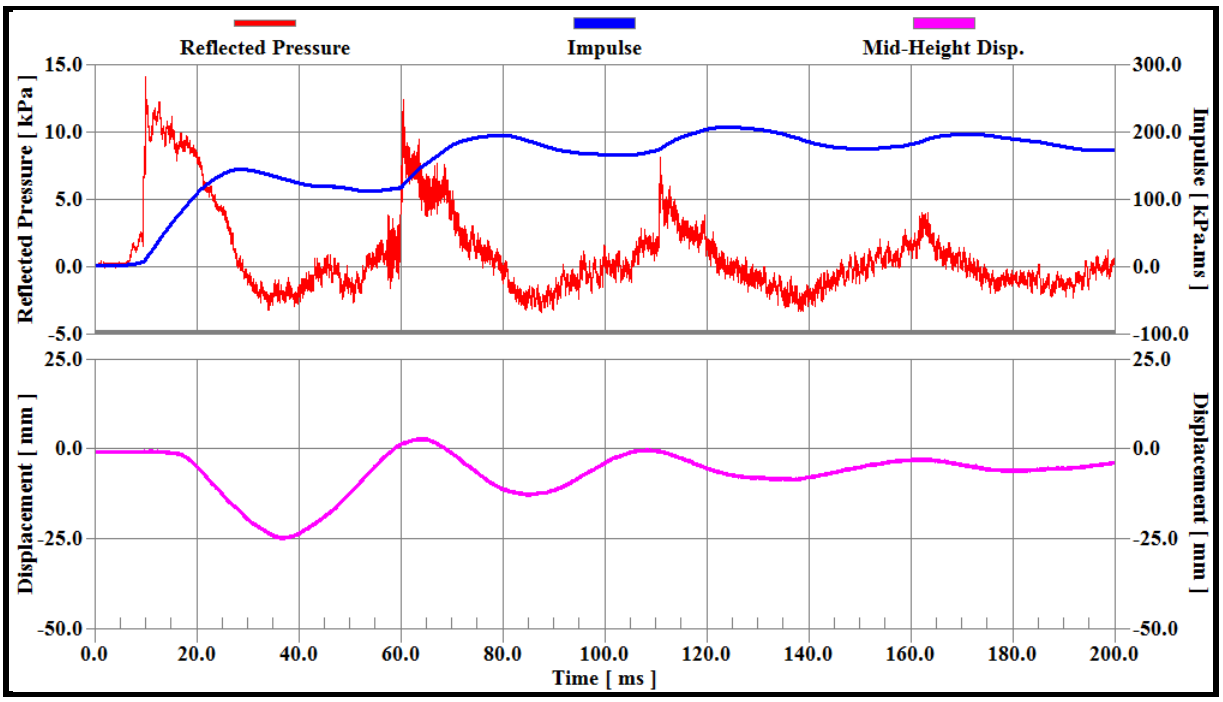

Fig. 4.2 Time history of reflected pressure, positive impulse, and mid-height displacement resulted by the 2nd blast shot applied on S1-AL0

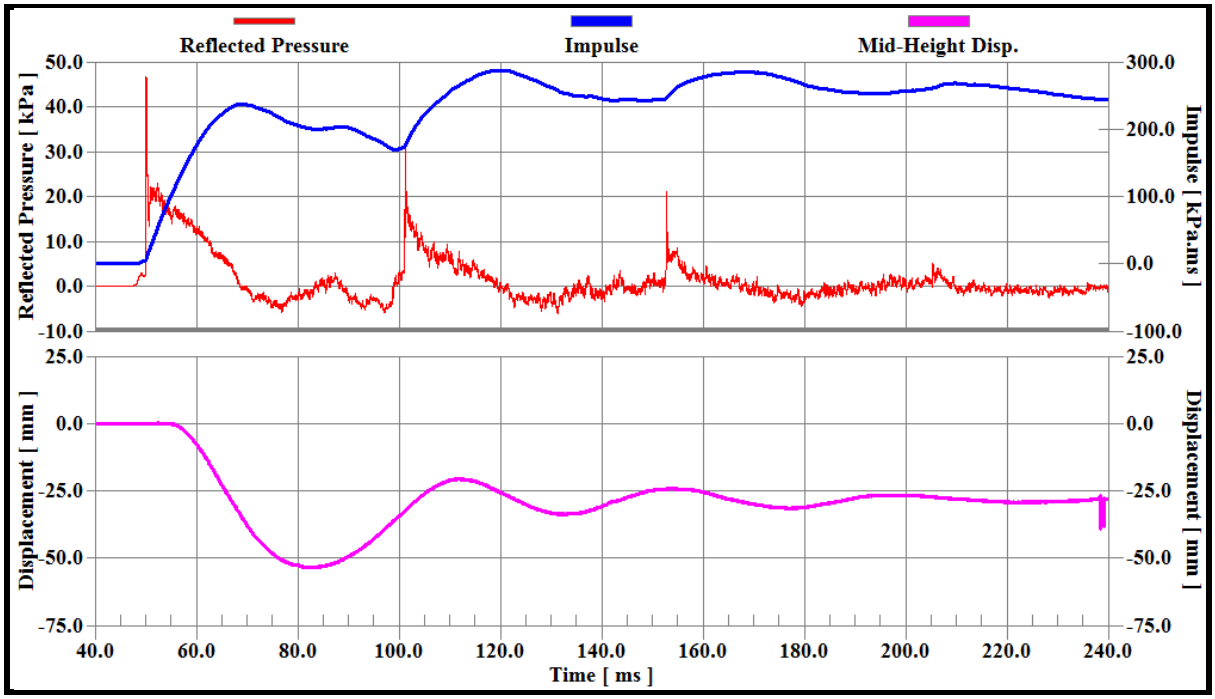

Fig. 4.3 Time history of reflected pressure, impulse, and mid-height displacement resulted by the 3rd blast shot applied on S1-AL0

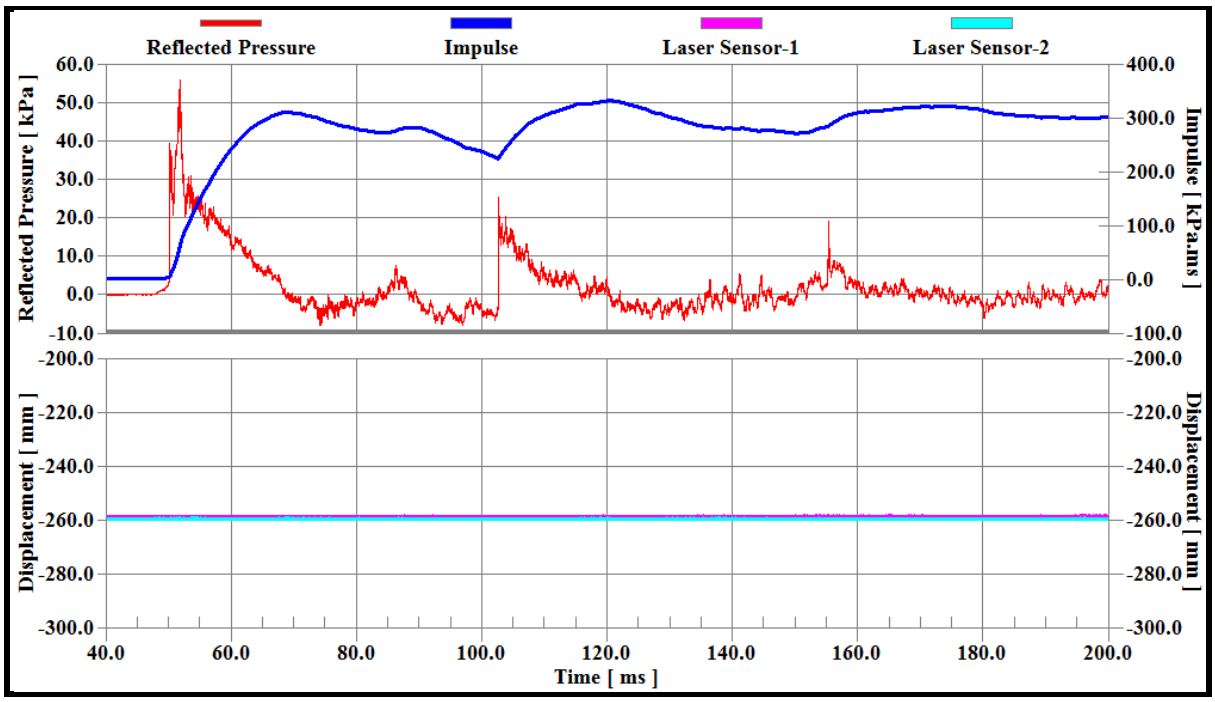

Fig. 4.4 Time history of reflected pressure, impulse, and mid-height displacement resulted by the 4th blast shot applied on S1-AL0

(a) (b)

Fig. 4.5 Level of damage in Column S1-AL0 after the 4th shot: a) front view; b) side view

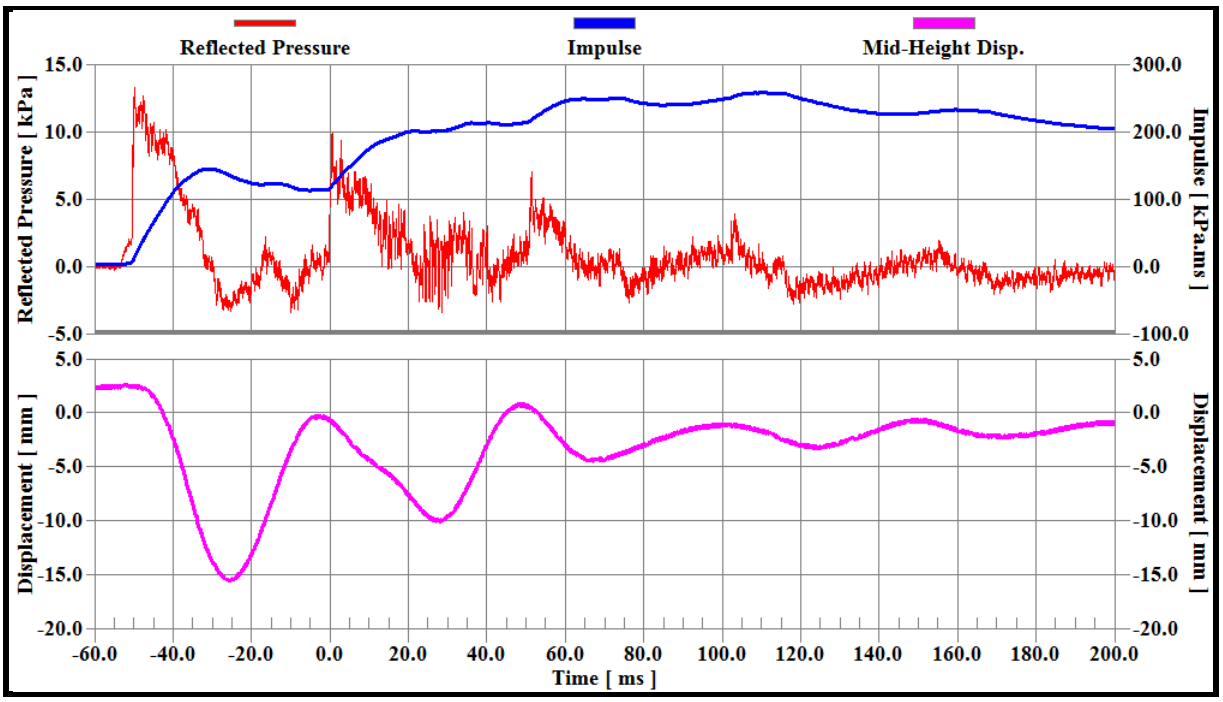

Fig. 4.6 Time history of reflected pressure, impulse, and mid-height displacement resulted by the 1st blast shot applied on S2-AL0

(a) (b)

Fig. 4.7 Level of damage in Column S2 -AL0 after the 1st shot: a) front view; b) side view

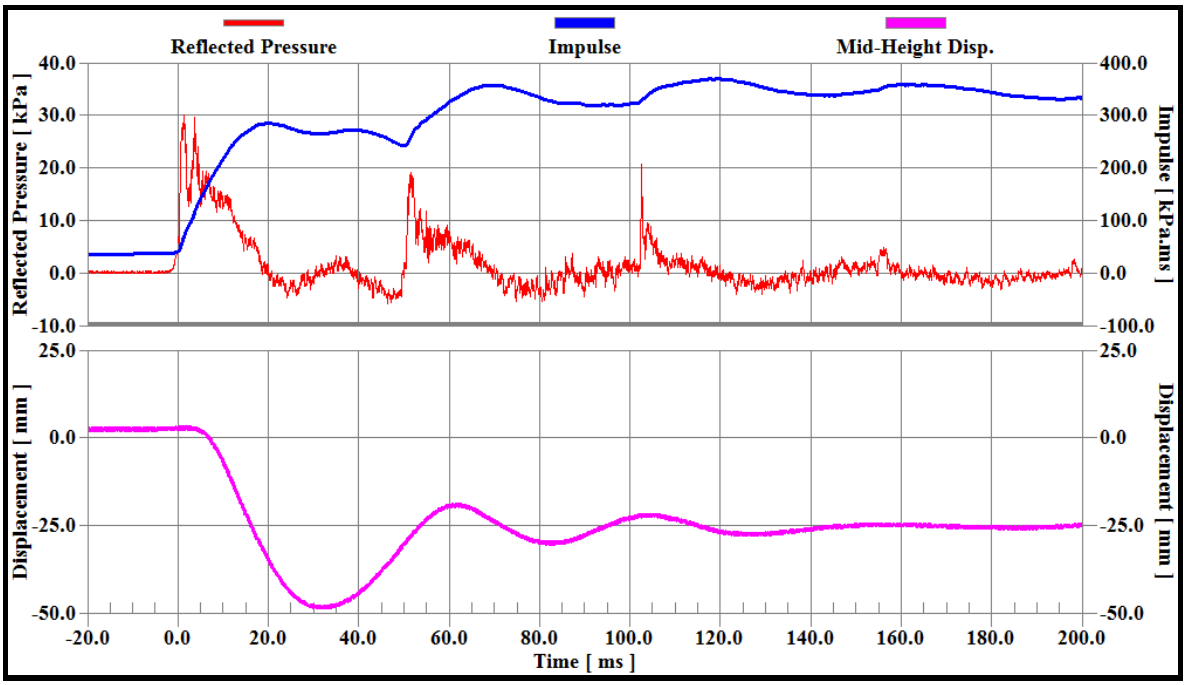

Fig. 4.8 Time history of reflected pressure, impulse, and mid-height displacement resulted by the 2nd blast shot applied on S2-AL0

(a) (b)

Fig. 4.9 Level of damage of Column S2-AL0 after the 2nd shot: a) front view; b) side view

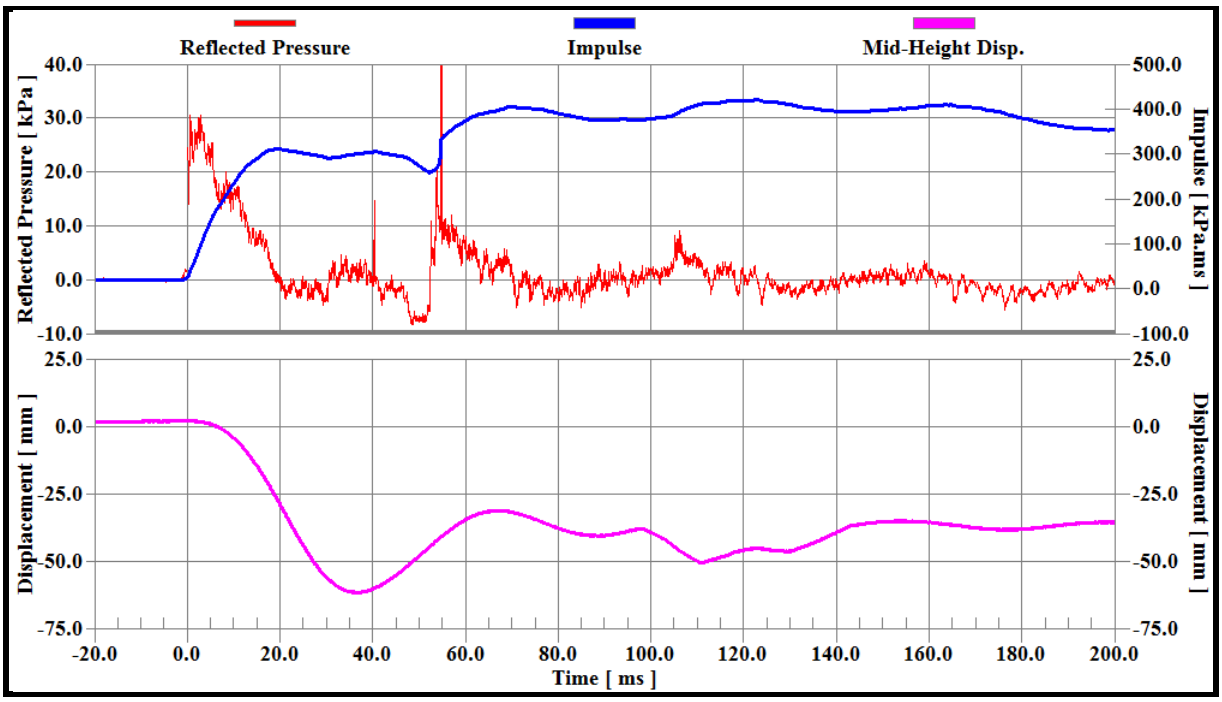

Fig. 4.10 Time history of reflected pressure, impulse, and mid-height displacement resulted by the 4th blast shot applied on S2-AL0

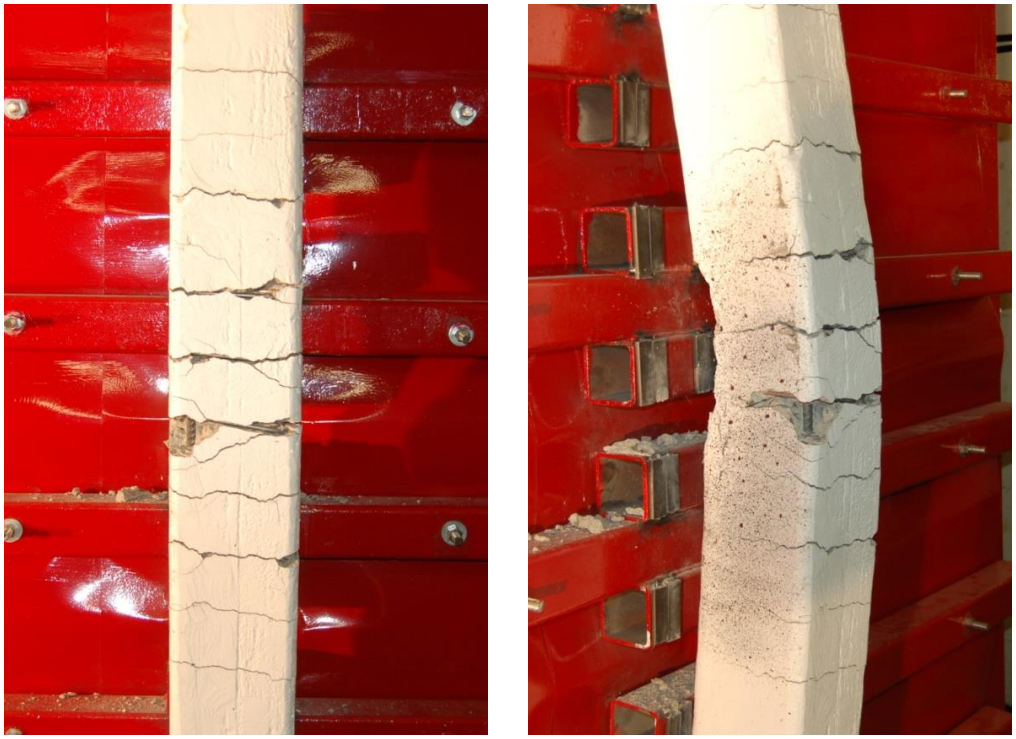

(a) (b)

Fig. 4.11 Level of damage in Column S2-AL0 after the 4th shot: a) front view; b) side view

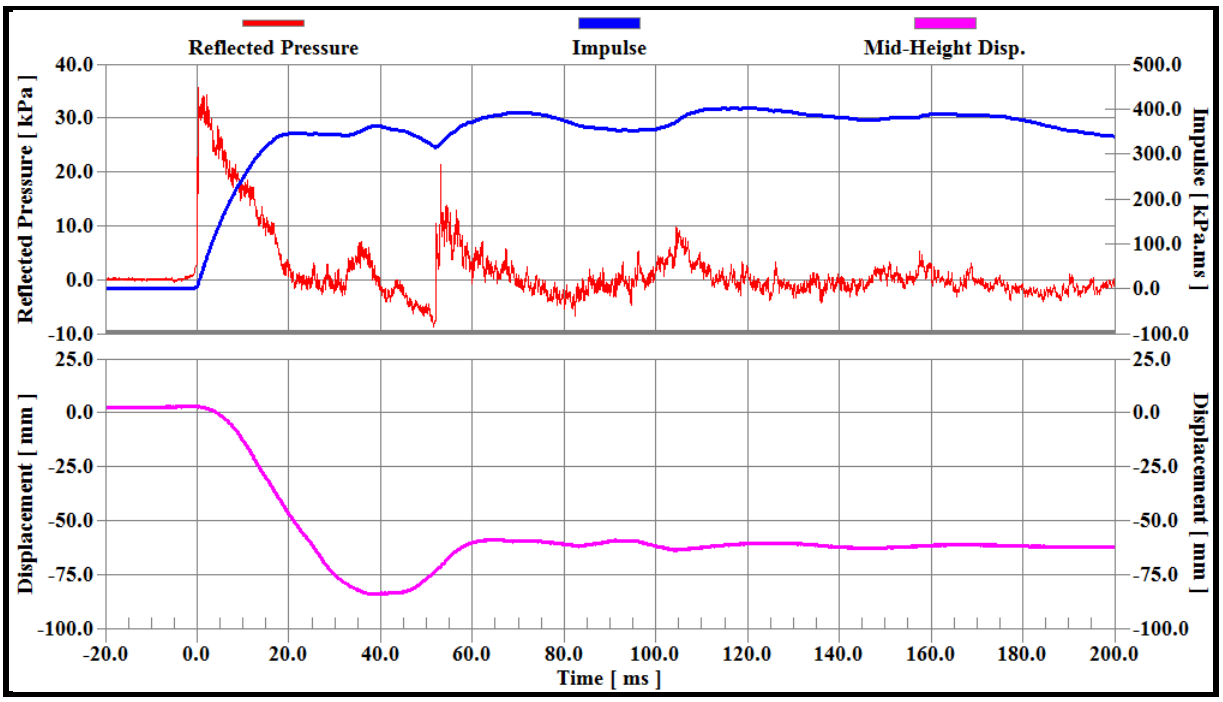

Fig. 4.12 Time history of reflected pressure, impulse, and mid-height displacement resulted by a single blast shot applied on S3-AL0

(a) (b)

Fig. 4.13 Level of damage in Column S3-AL0 (single shot): a) front view; b) side view

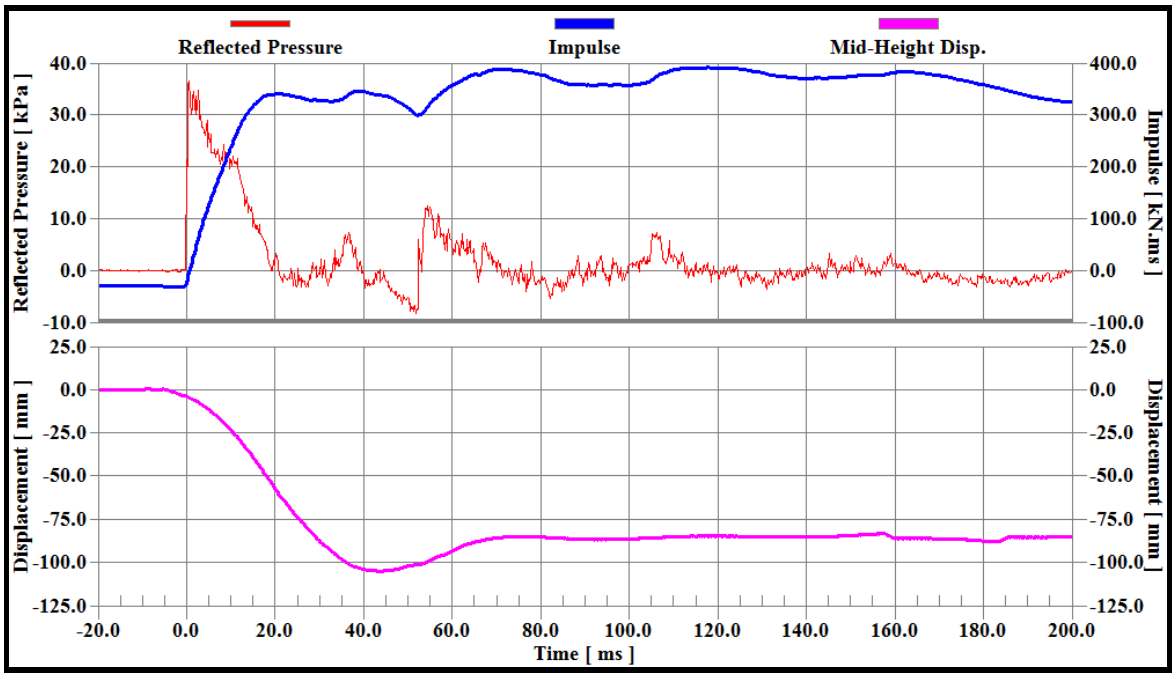

Fig. 4.14 Time history of reflected pressure, impulse, and mid-height displacement resulted by a single blast shot applied on S4-AL0

(a) (b)

Fig. 4.15 Level of damage in Column S4-AL0 (single shot): a) front view; b) side view

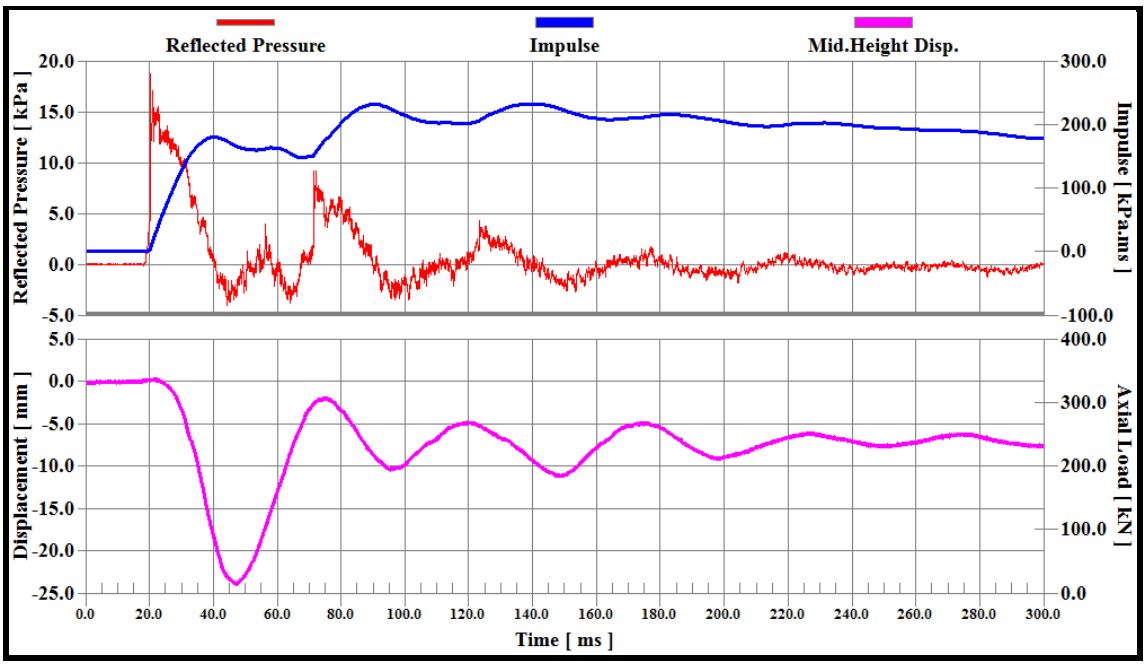

Fig. 4.16 Time history of reflected pressure, impulse, and mid-height displacement resulted by the 1st blast shot applied on S1-AL400

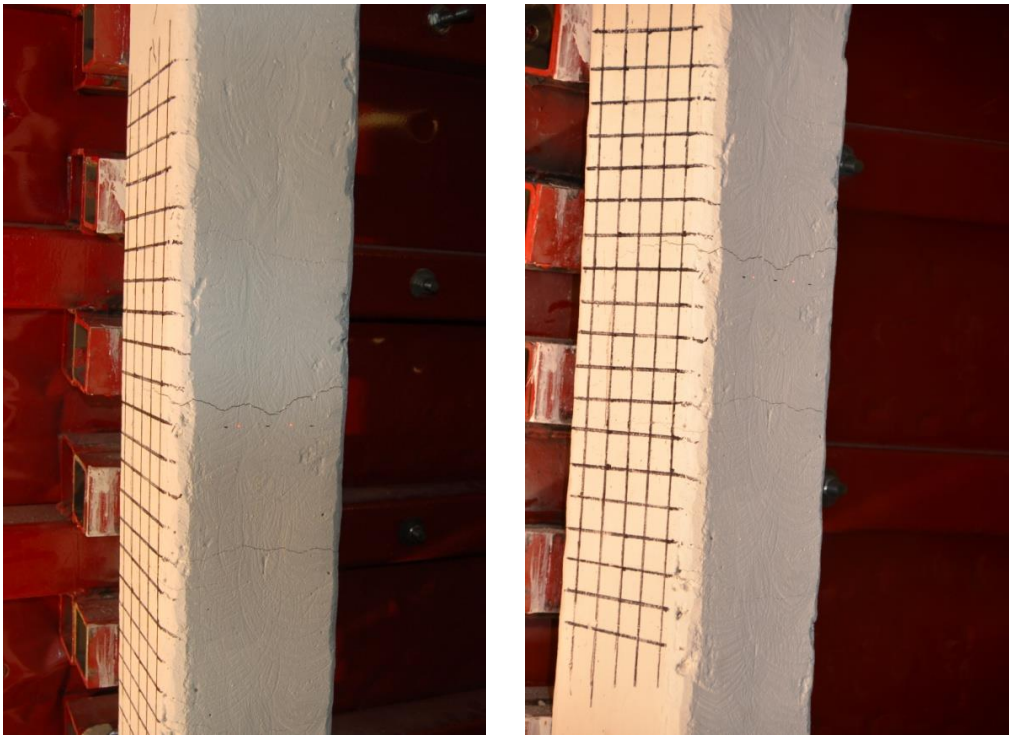

(a) (b)

Fig. 4.17 Level of damage in Column S1-AL400 after the 1st shot: a) front view; b) side view

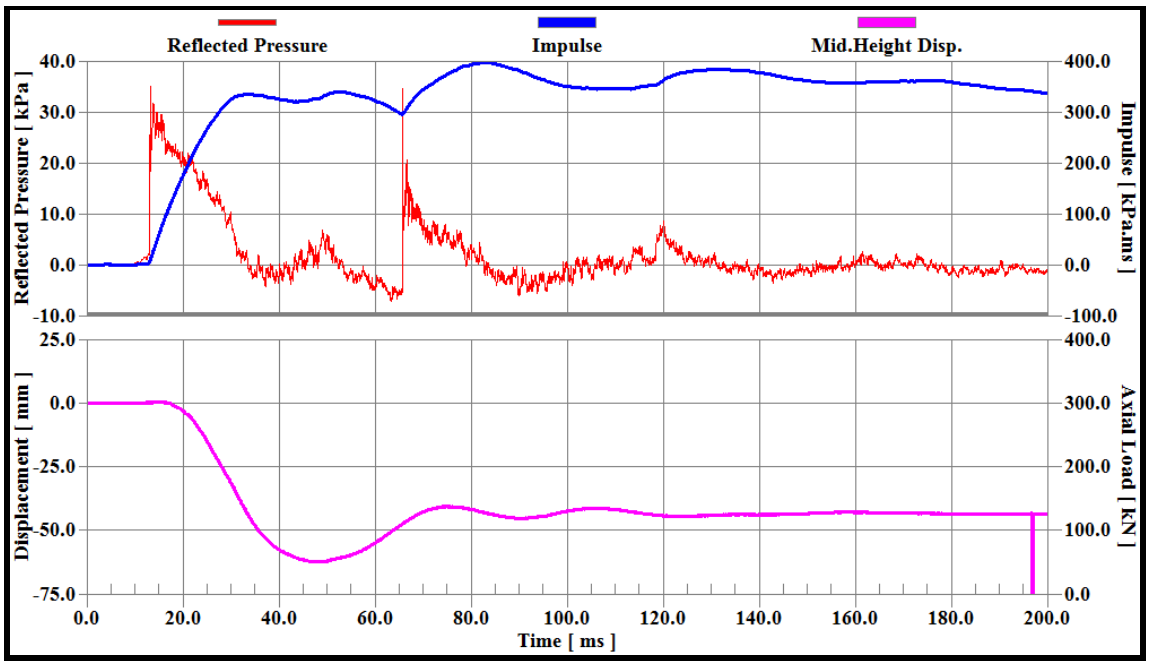

Fig. 4.18 Time history of reflected pressure, impulse, and mid-height displacement resulted by the 2nd blast shot applied on S1-AL400

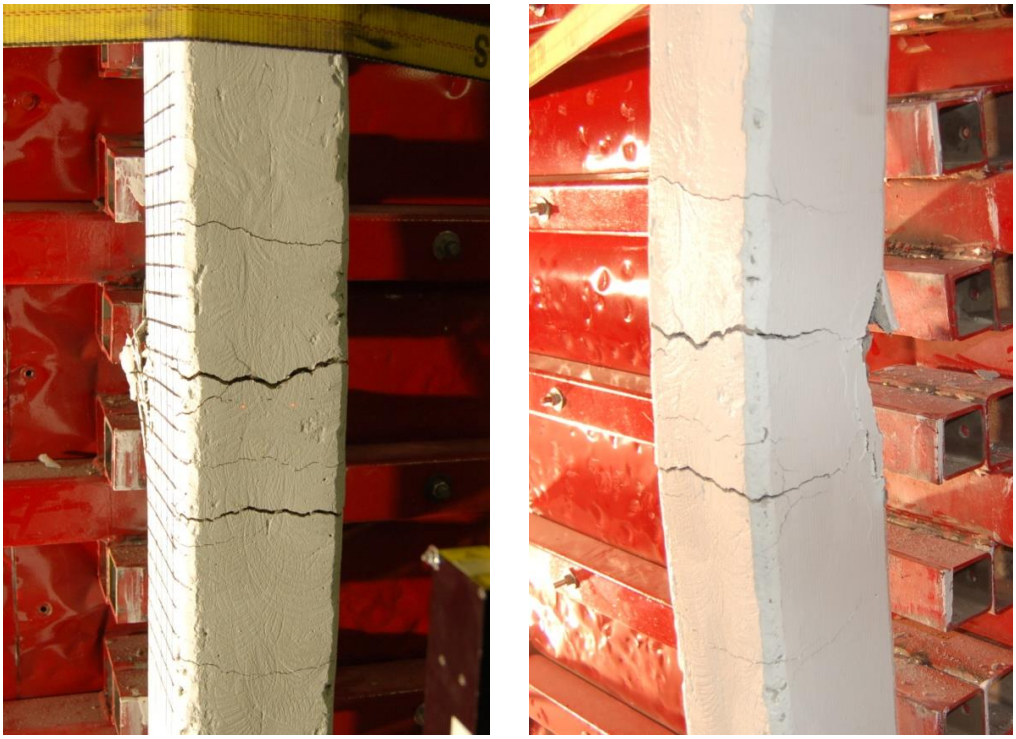

(a) (b)

Fig. 4.19 Level of damage in Column S1-AL400 after the 2nd shot: a) front view; b) side view

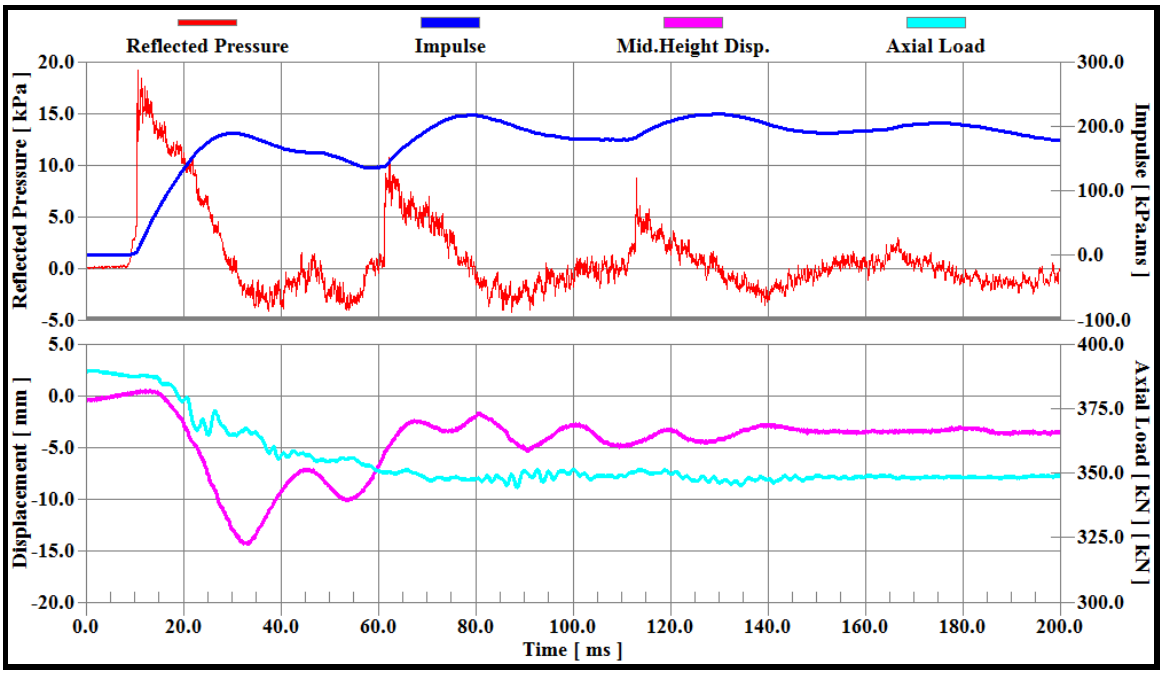

Fig. 4.20 Time history of reflected pressure, impulse, axial load, and mid-height displacement resulted by the 1st blast shot subjected to S2-AL400

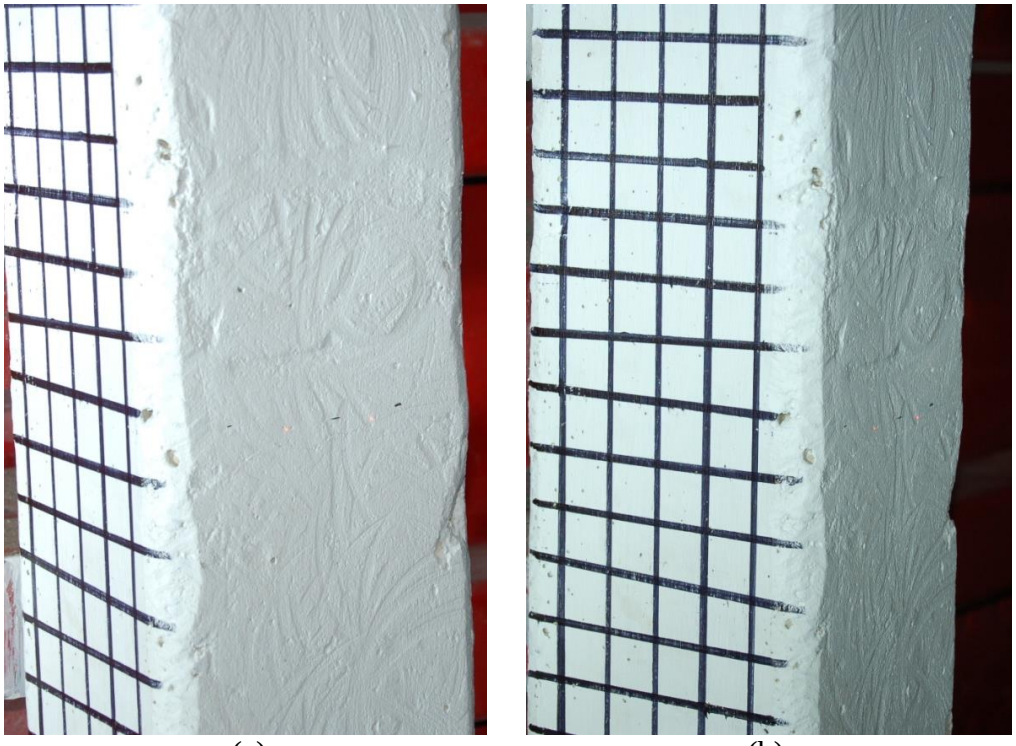

(a) (b)

Fig. 4.21 Level of damage in Column S2-AL400 after the 1st shot: a) front view; b) side view

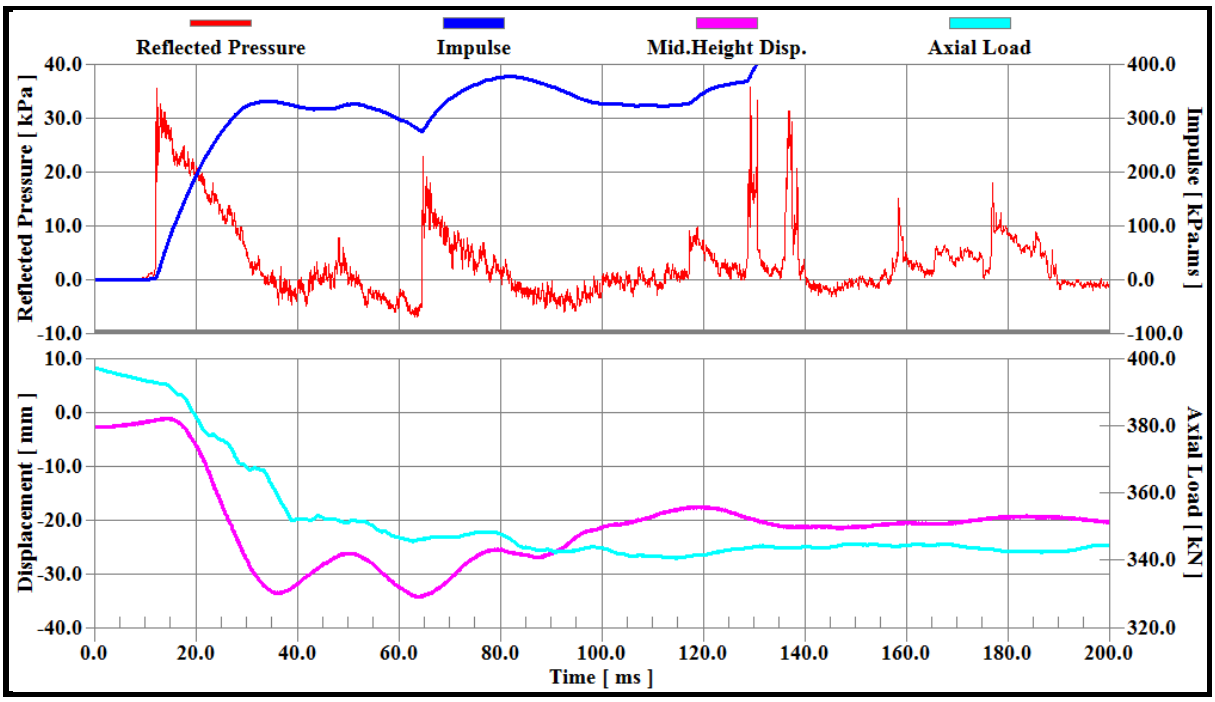

Fig. 4.22 Time history of reflected pressure, impulse, axial load, and mid-height displacement resulted by the 2nd blast shot applied on S2-AL400

(a) (b)

Fig. 4.23 Level of damage in Column S2-AL400 after the 2nd shot: a) front view; b) side view

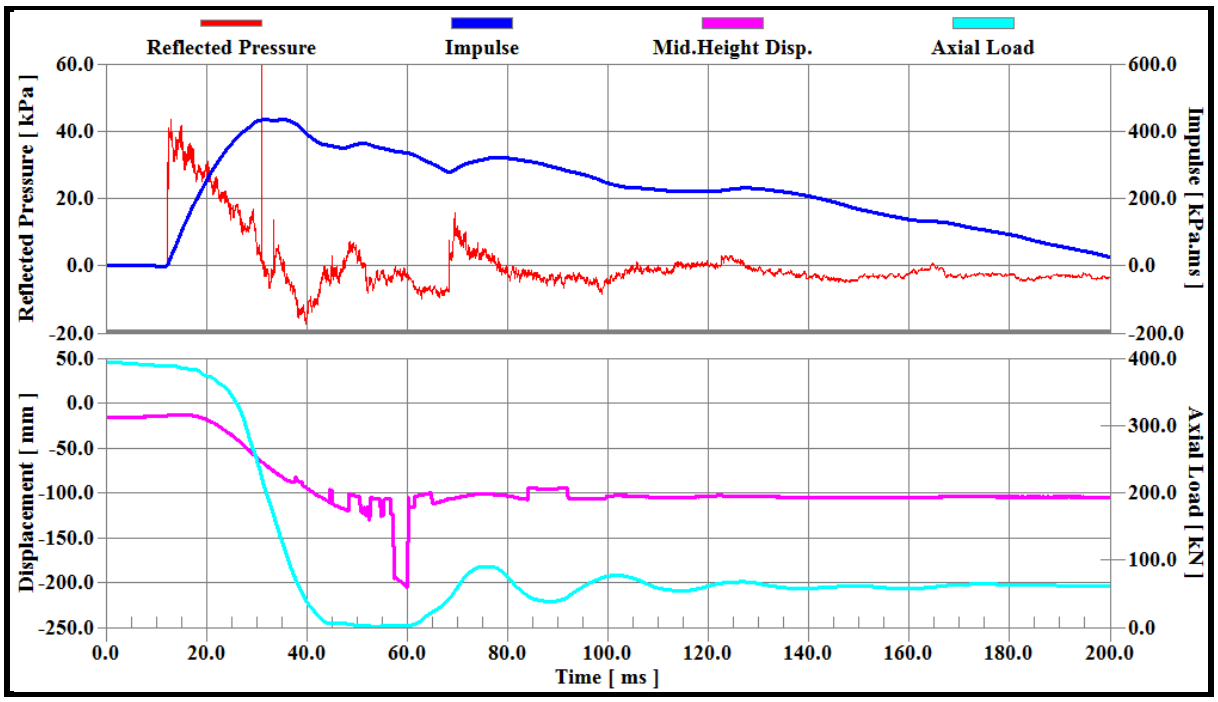

Fig. 4.24 Time history of reflected pressure, impulse, and mid-height displacement resulted by the 3rd blast shot applied on S2-AL400

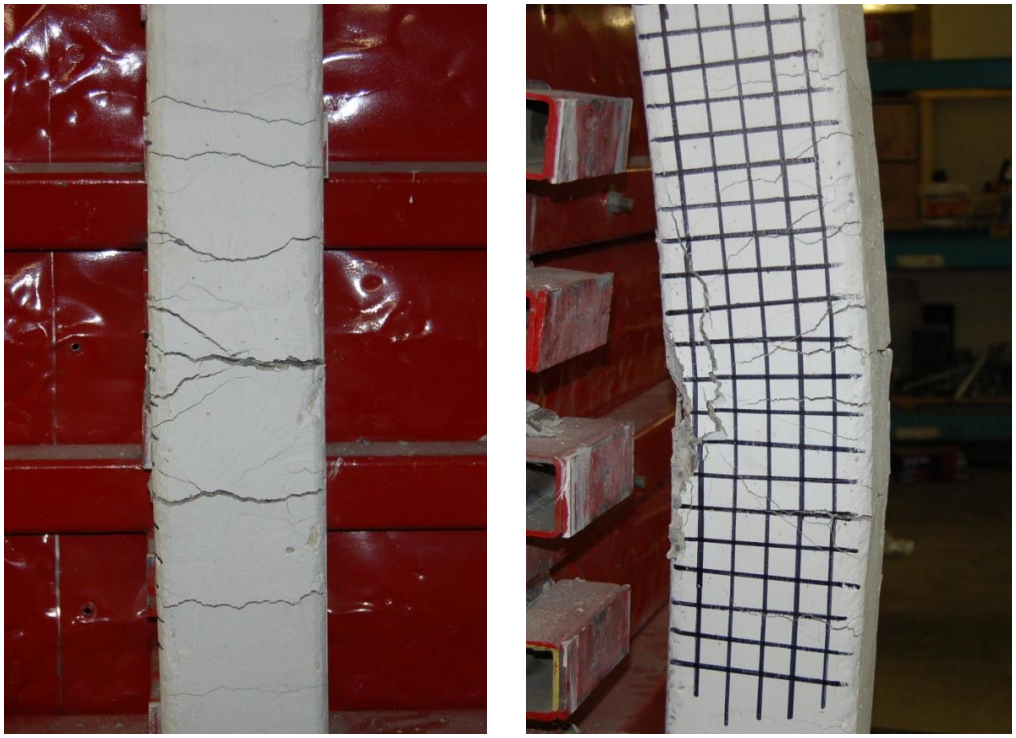

(a) (b)

Fig. 4.25 Level of damage in Column S2-AL400 after the 3rd shot: a) front view; b) side view

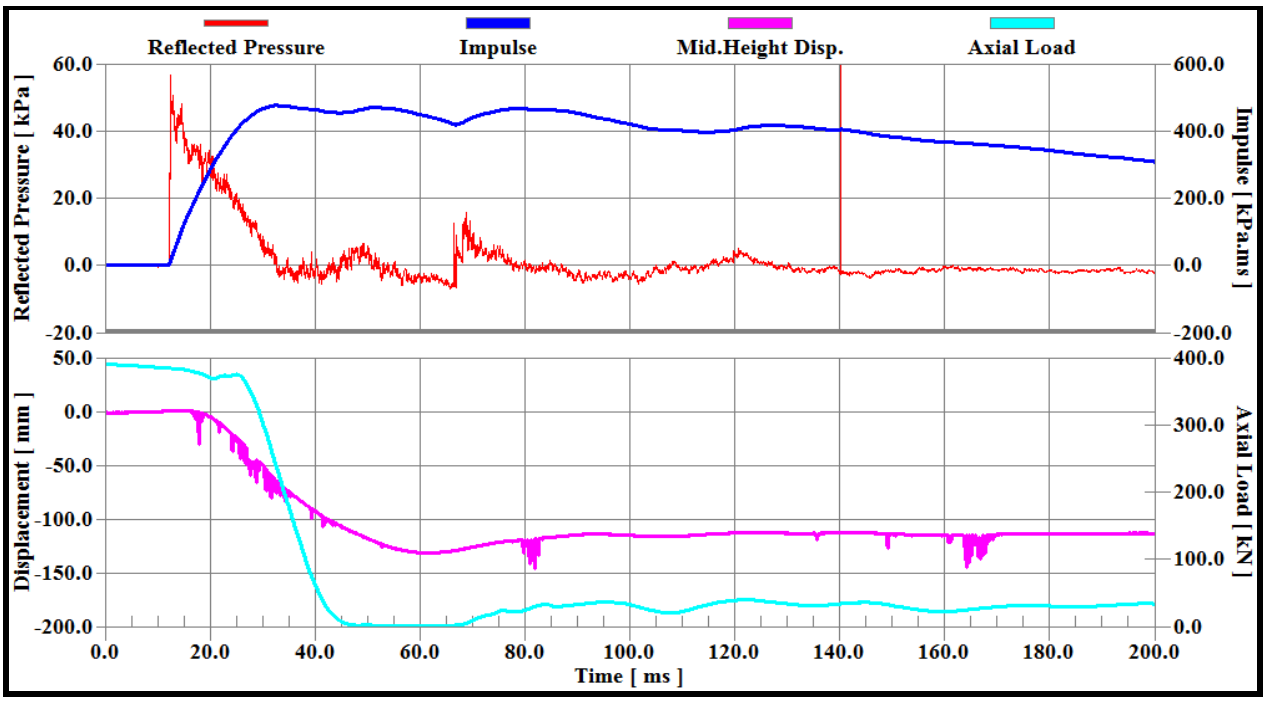

Fig. 4.26 Time history of reflected pressure, impulse, and mid-height displacement resulted by a single blast shot applied on S3-AL400

(a) (b)

Fig. 4.27 Level of damage in Column S3-AL400 after a single shot: a) front view; b) side view

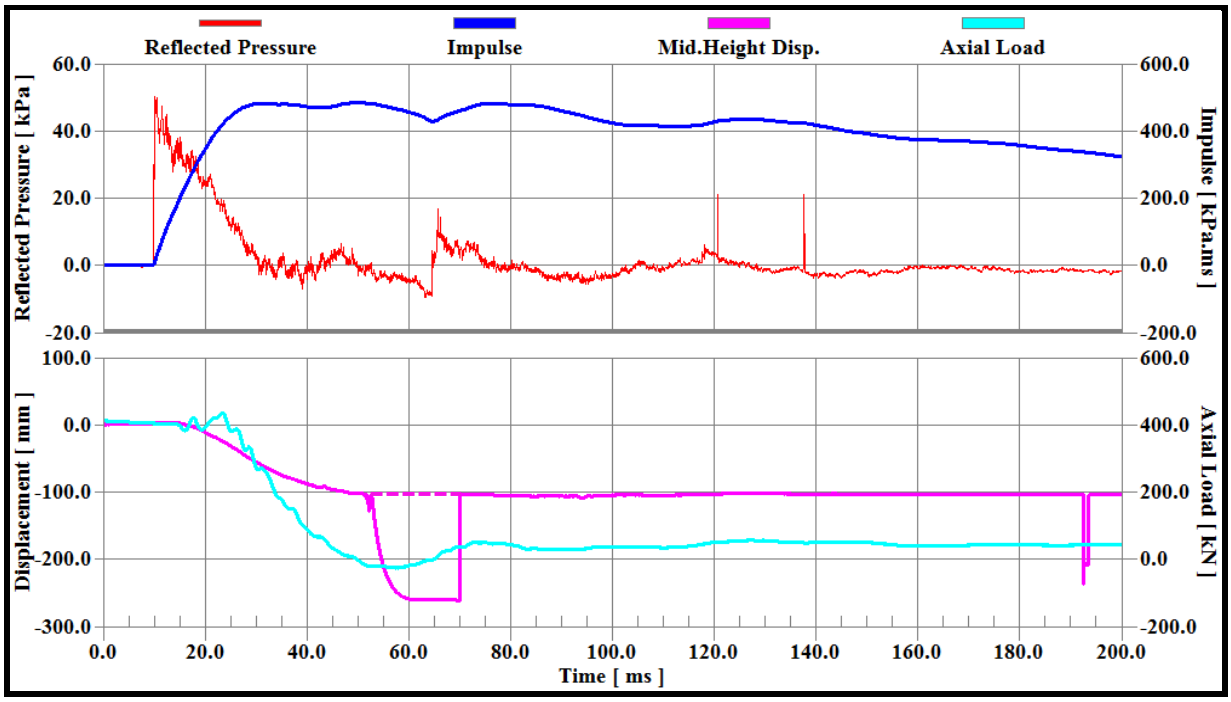

Fig. 4.28 Time history of reflected pressure, impulse, and mid-height displacement resulted by a single blast shot applied on S4-AL400

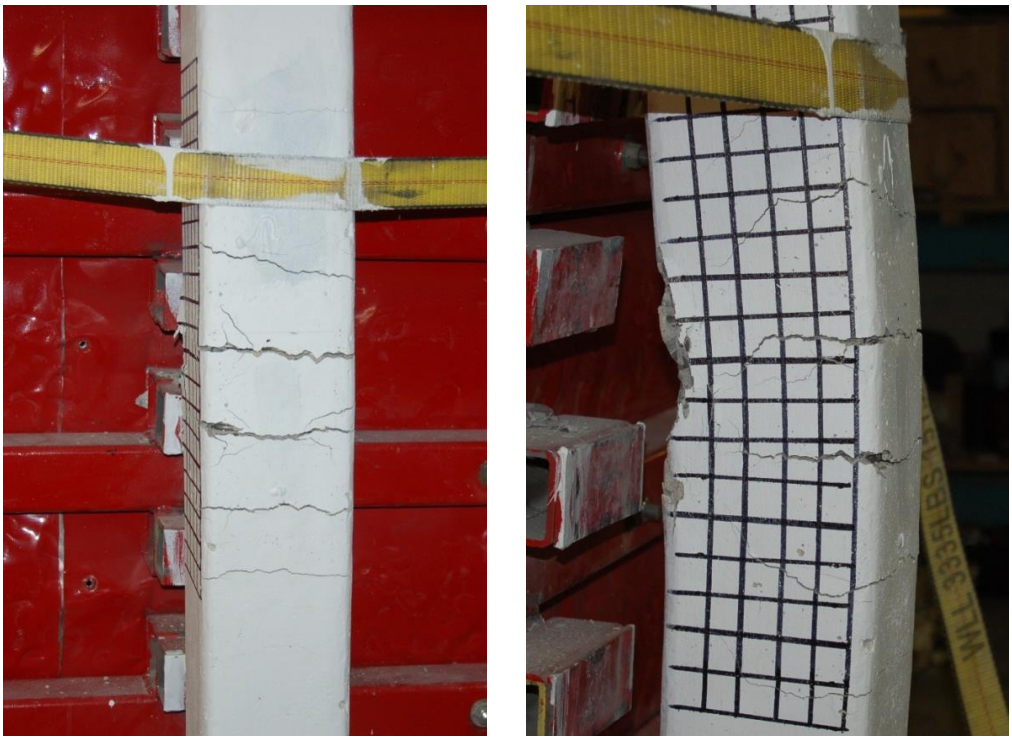

(a) (b)

Fig. 4.29 Level of damage in Column S4-AL400 after a single shot: a) front view; b) side view

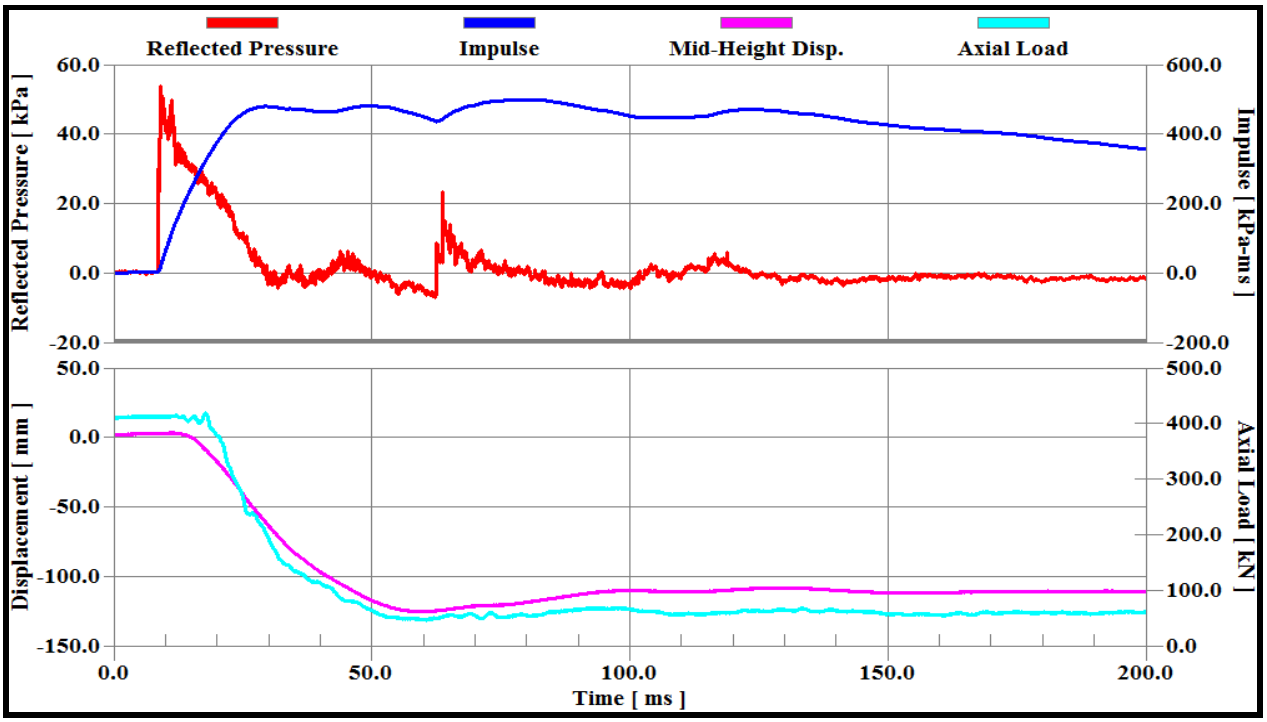

Fig. 4.30 Time history of reflected pressure, Impulse, mid-height displacement, and axial load for Column NS1-A-G1

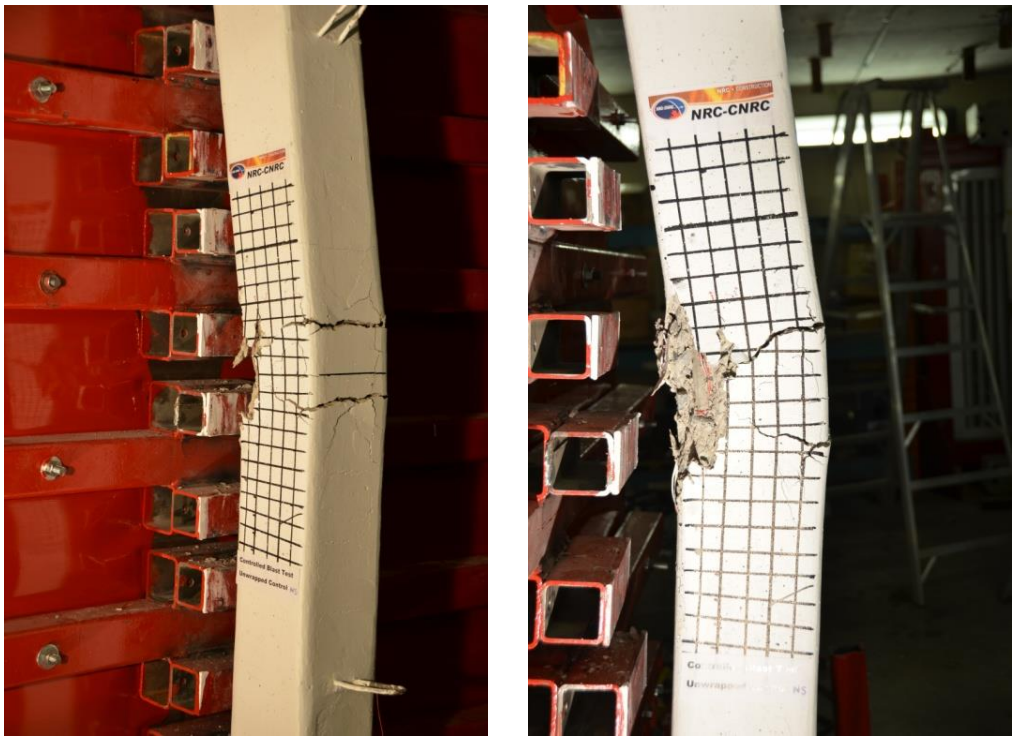

(a) (b)

Fig. 4.31 Level of damage in Column NS1-A-G1: a) front view; b) side view

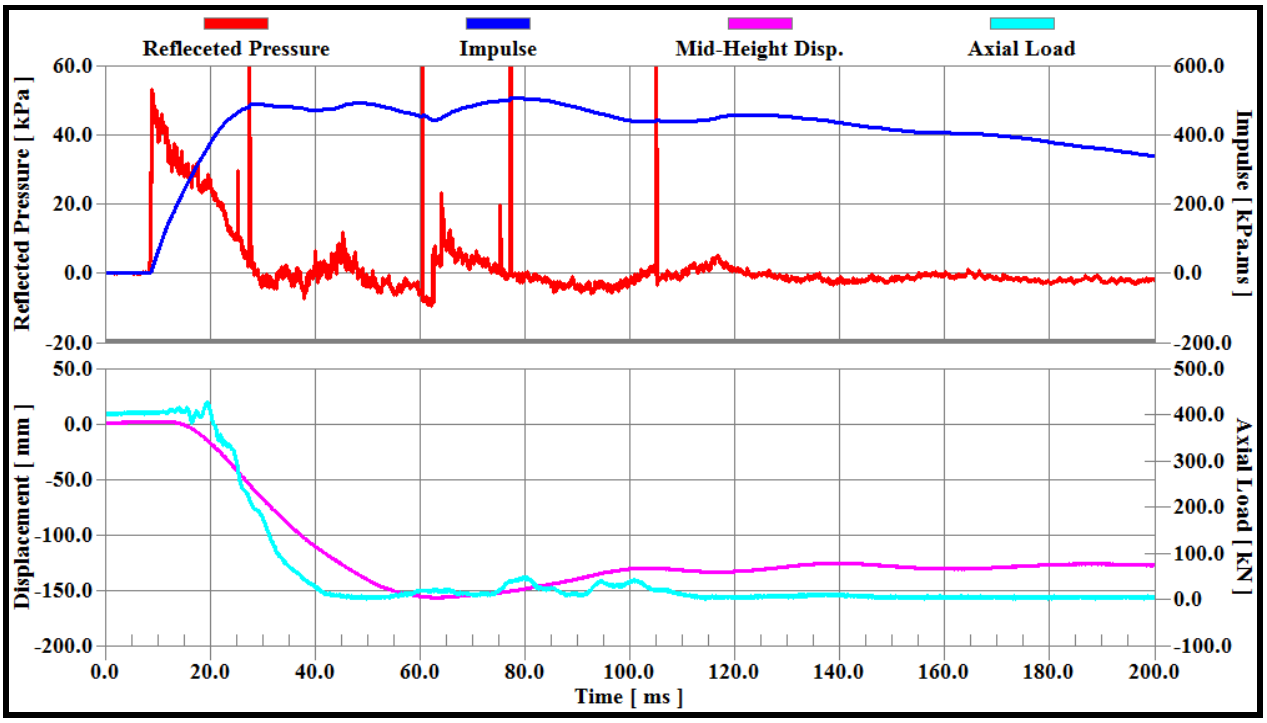

Fig. 4.32 Time history of reflected pressure, Impulse, mid-height displacement, and axial load for Column NS1-B-G1

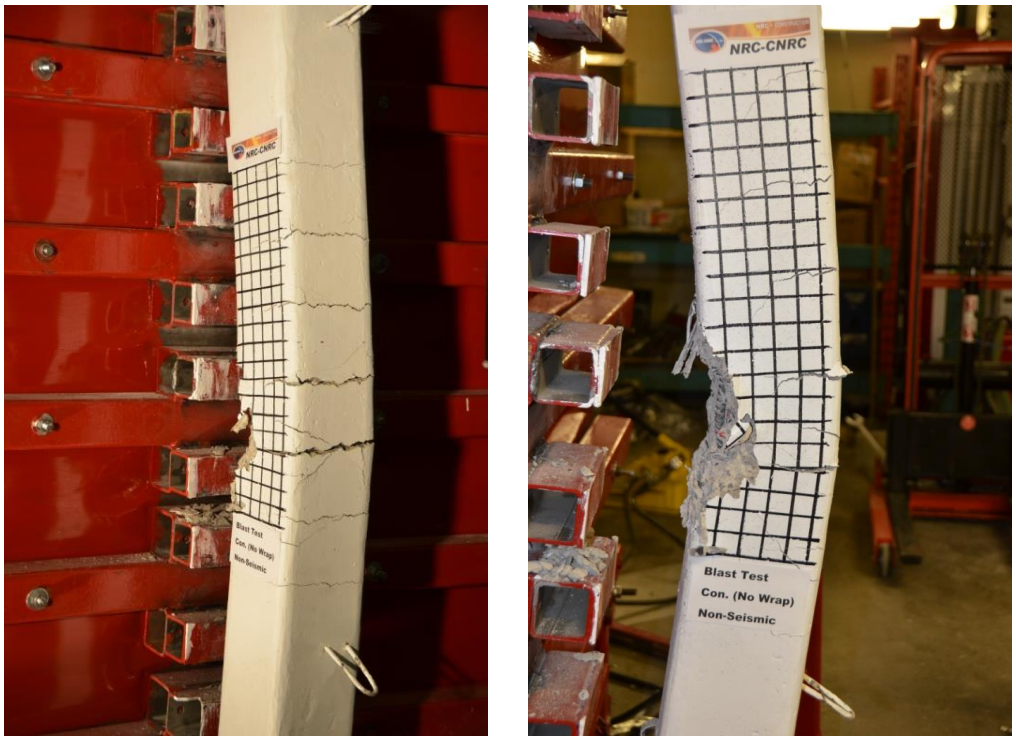

(a) (b)

Fig. 4.33 Level of damage in Column NS1-B-G1: a) front view; b) side view

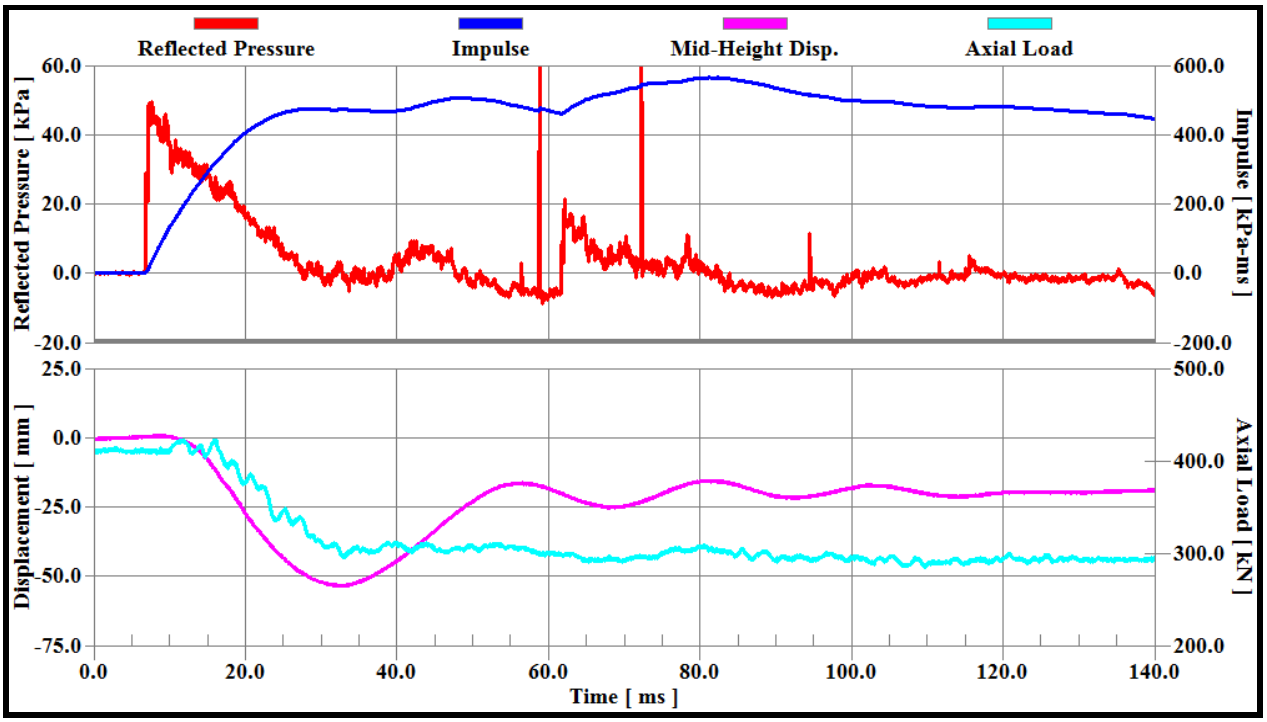

Fig. 4.34 Time history of reflected pressure, Impulse, mid-height displacement, and axial load for Column NS2-A-G1

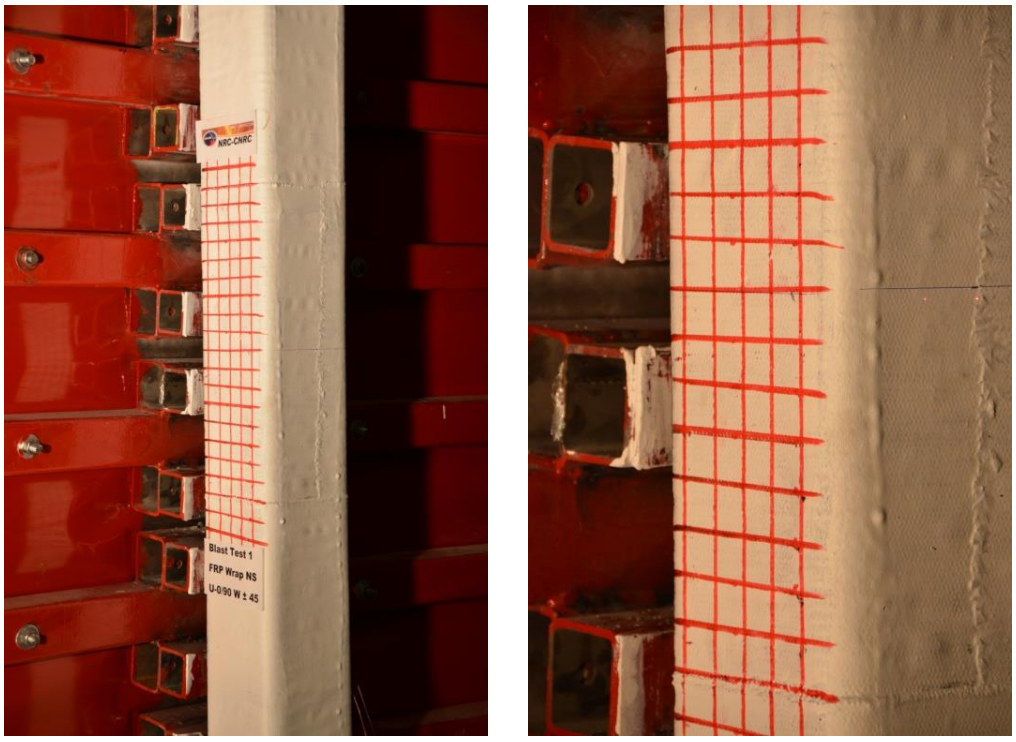

(a) (b)

Fig. 4.35 Level of damage in Column NS2-A-G1: a) front view; b) side view

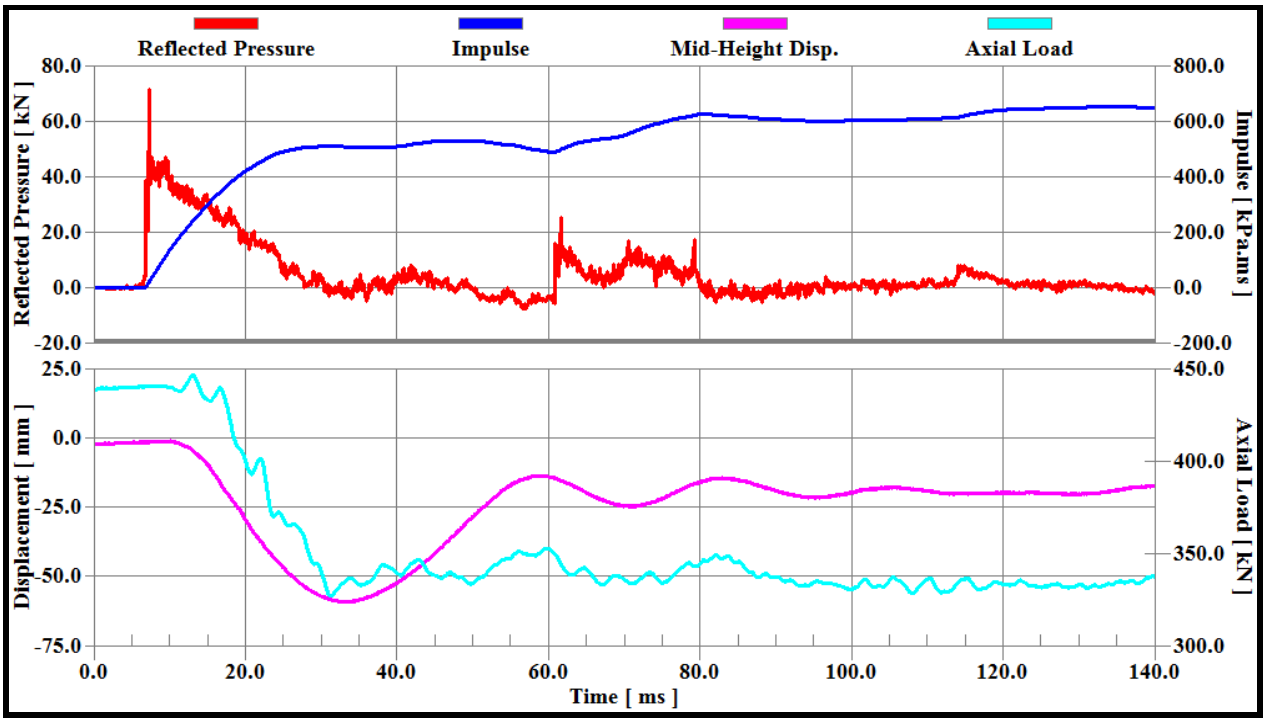

Fig. 36 Time history of reflected pressure, Impulse, mid-height displacement, and axial load for Column NS2-B-G1

(a) (b)

Fig. 4.37 Level of damage in Column NS2-B-G1: a) front view; b) side view

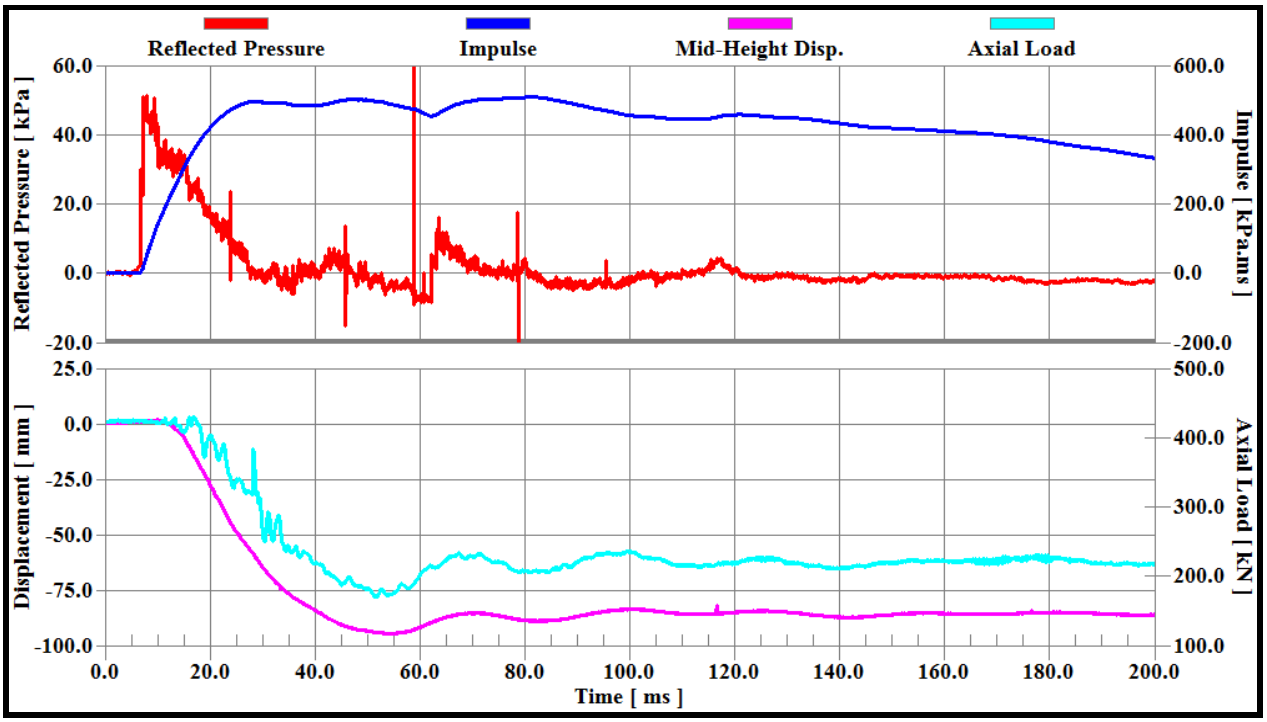

Fig. 4.38 Time history of reflected pressure, Impulse, mid-height displacement, and axial load for Column NS3-A-G1

(a) (b)

Fig. 4.39 Level of damage in Column NS3-A-G1: a) front view; b) side view

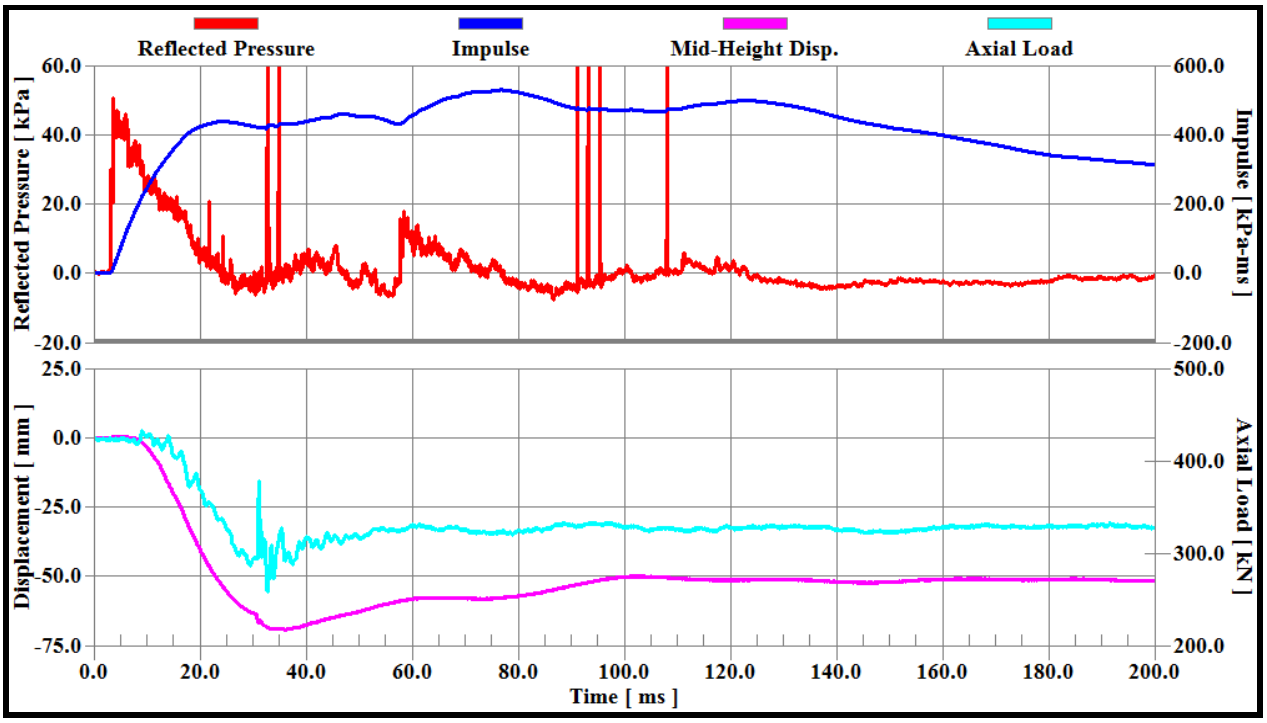

Fig 4.40 Time history of reflected pressure, Impulse, mid-height displacement, and axial load for Column NS3-B-G1

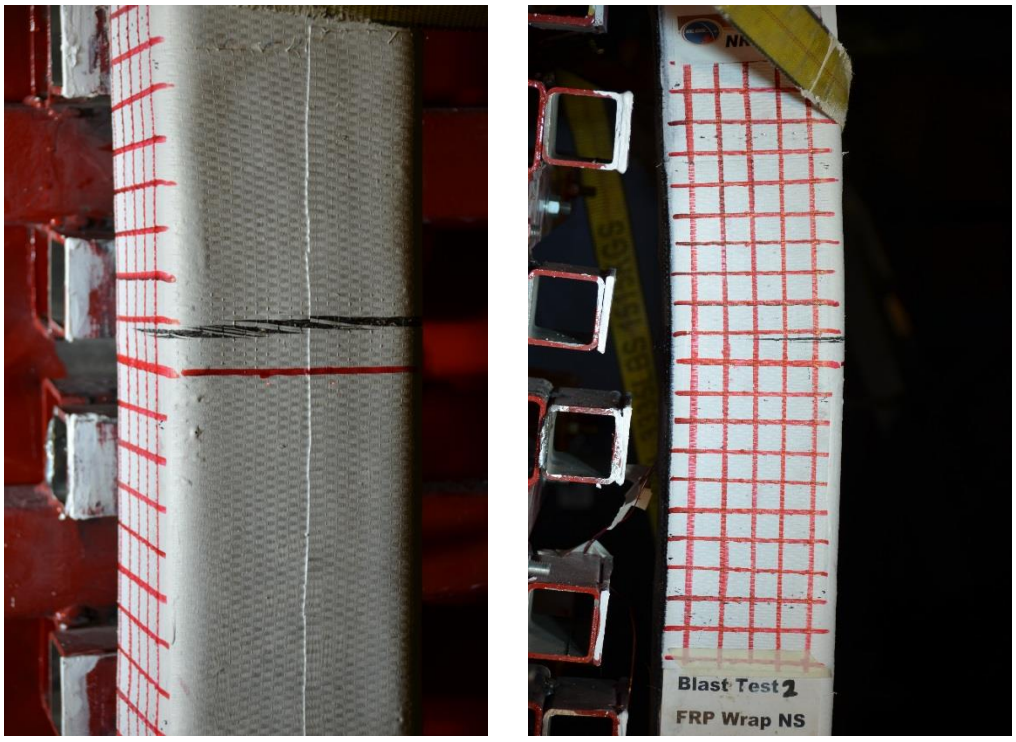

(a) (b)

Fig. 4.41 Level of damage in Column NS3-B-G1: a) front view; b) side view

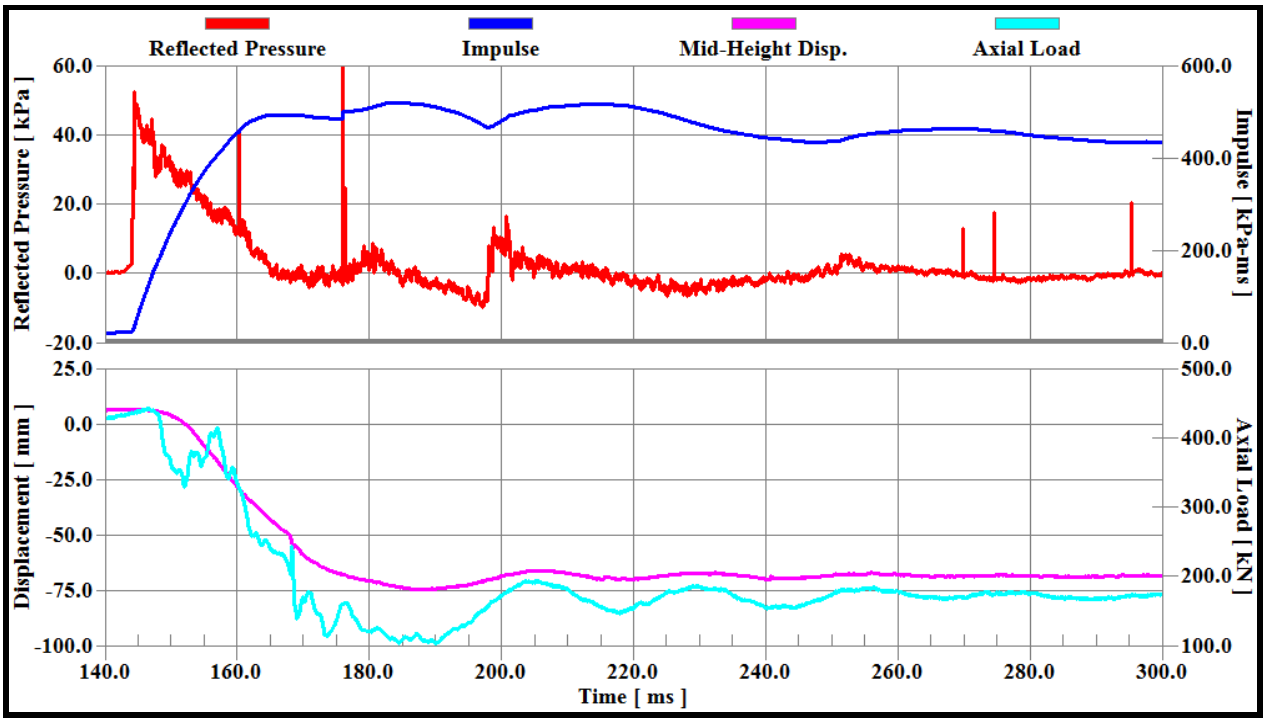

Fig. 4.42 Time history of reflected pressure, Impulse, mid-height displacement, and axial load for Column NS4-A-G1

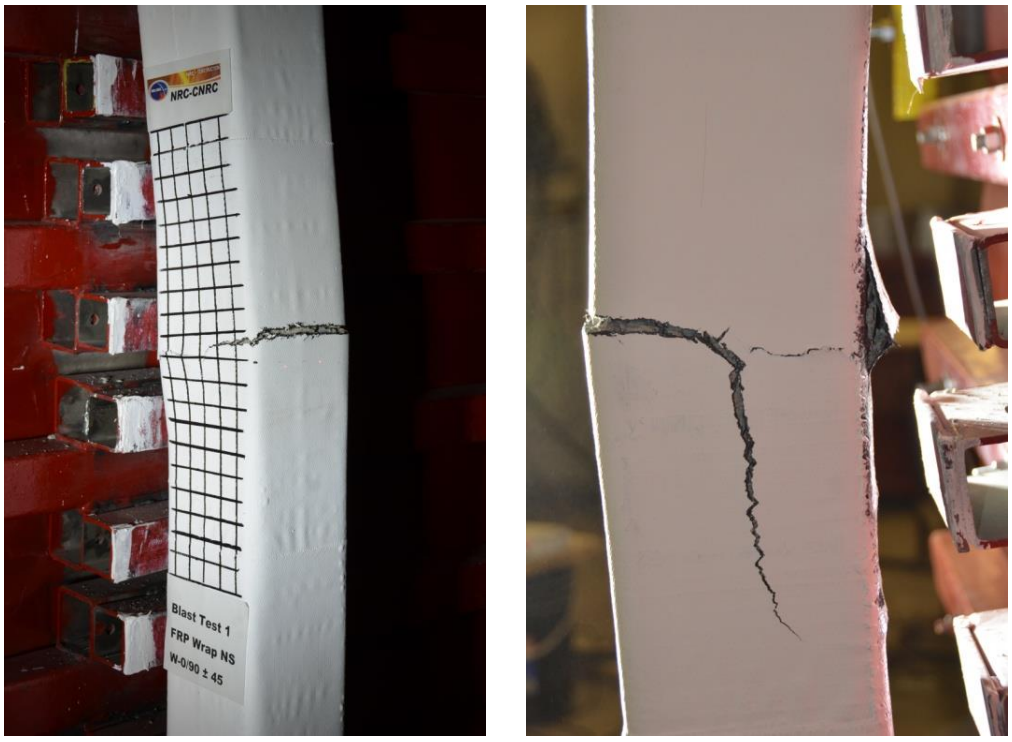

(a) (b)

Fig. 4.43 Level of damage in Column NS4-A-G1: a) front view; b) side view

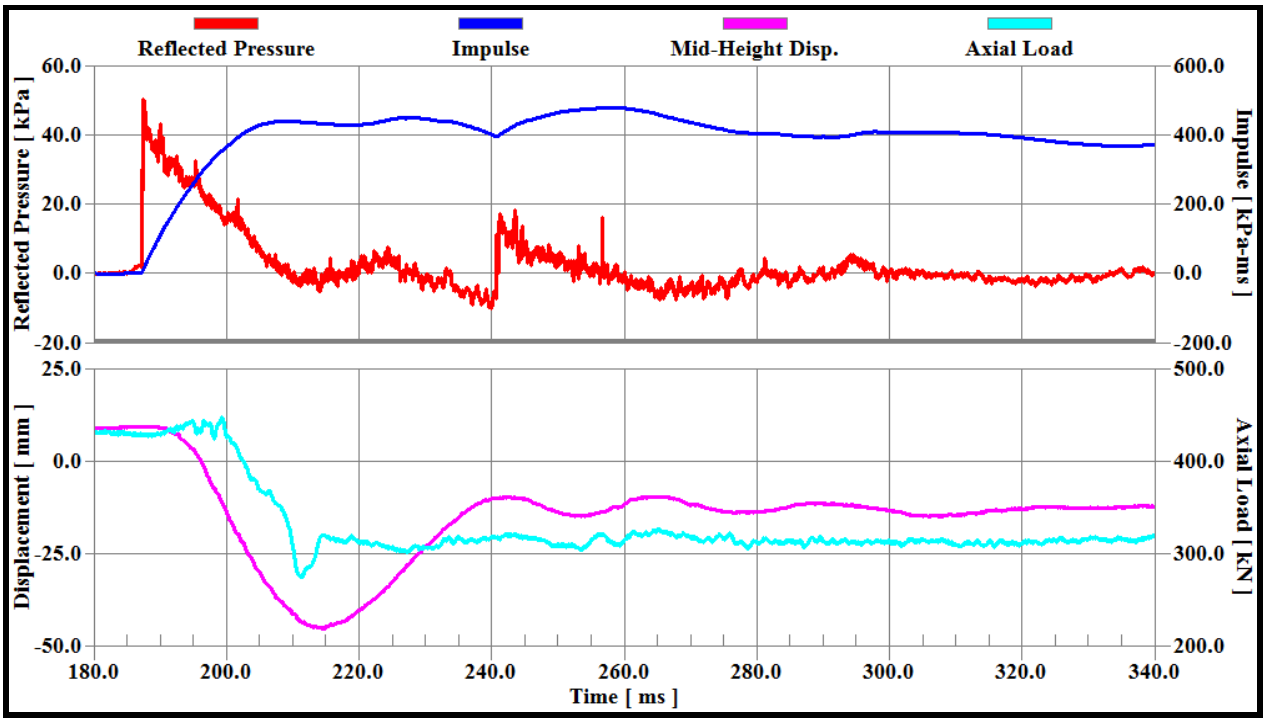

Fig. 4.44 Time history of reflected pressure, Impulse, mid-height displacement, and axial load for Column NS4-B-G1

(a) (b)

Fig. 4.45 Level of damage in Column NS4-B-G1: a) front view; b) side view

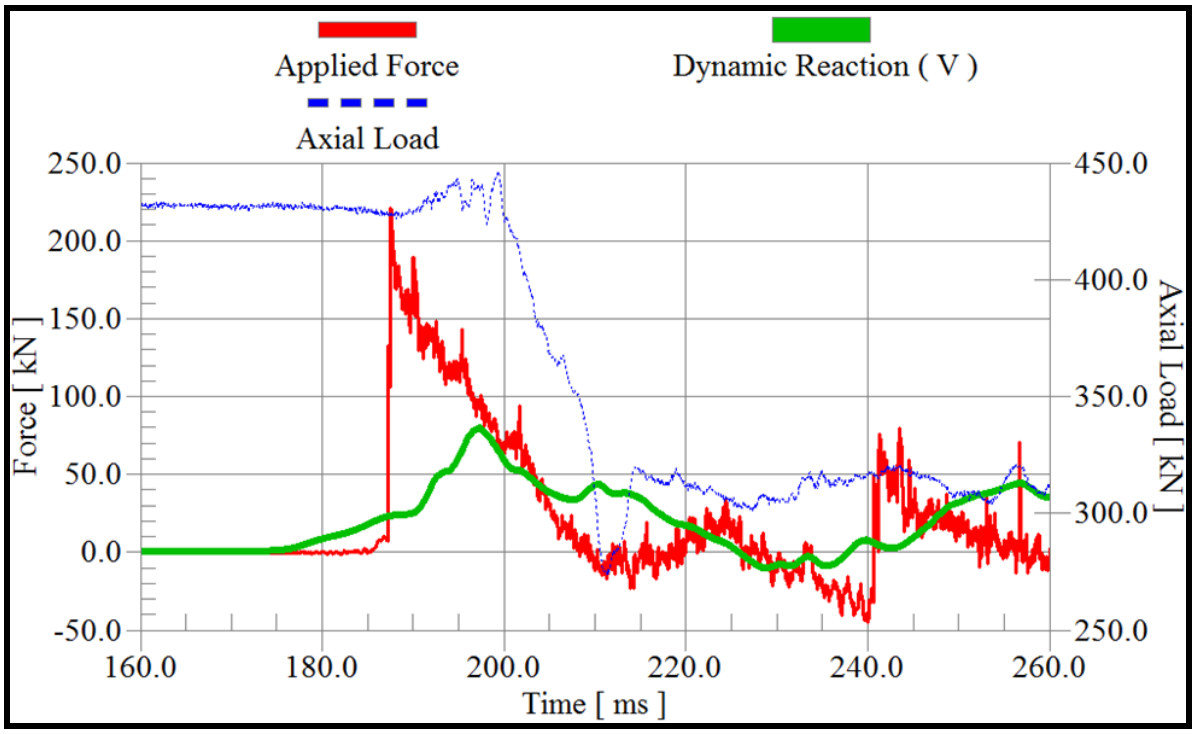

Fig. 4.46 Time history of dynamic reaction of Column NS-4B-G1

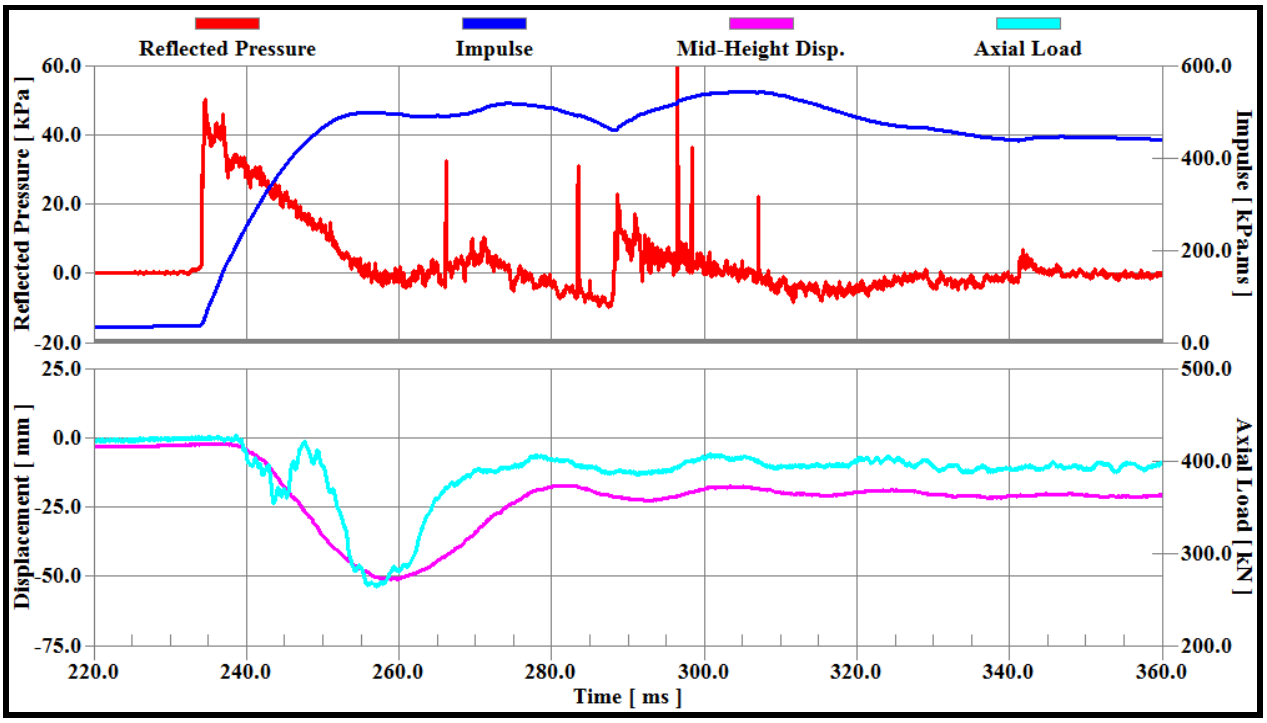

Fig. 4.47 Time history of reflected pressure, Impulse, mid-height displacement, and axial load for Column NS5-G1

(a) (b)

Fig. 4.48 Level of damage in Column NS5-G1: a) front view; b) side view

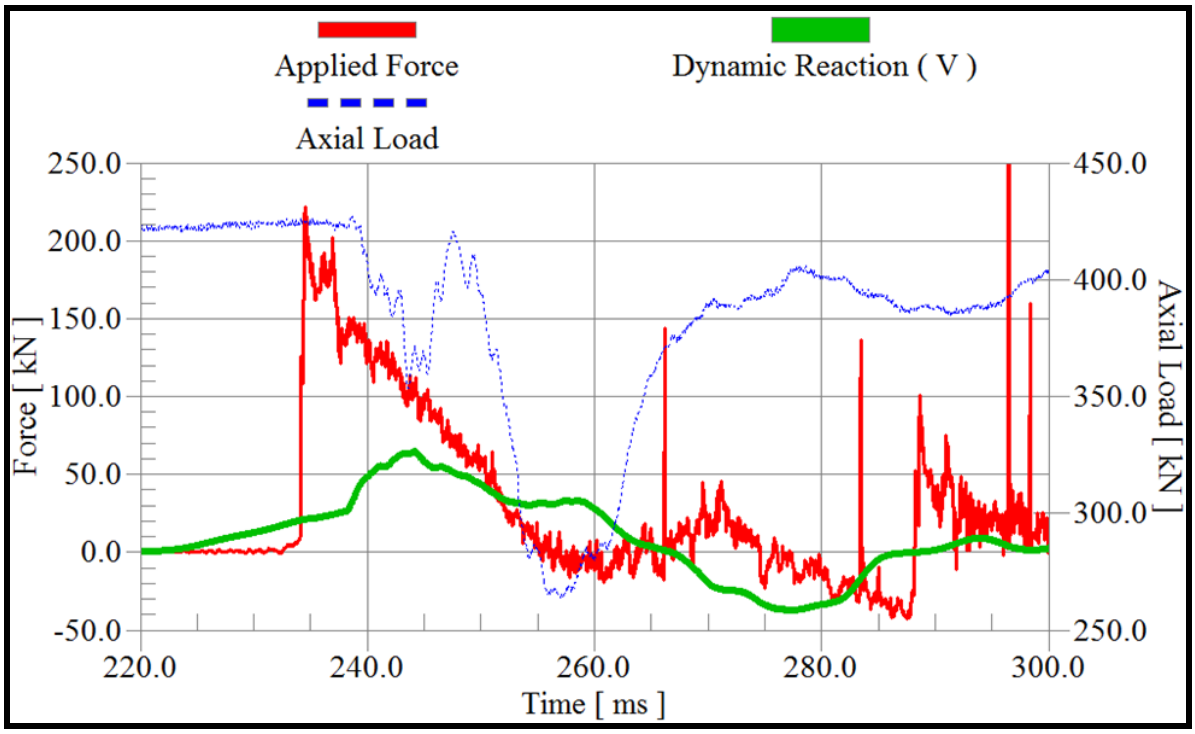

Fig. 4.49 Time history of dynamic reaction of Column NS-5-G1

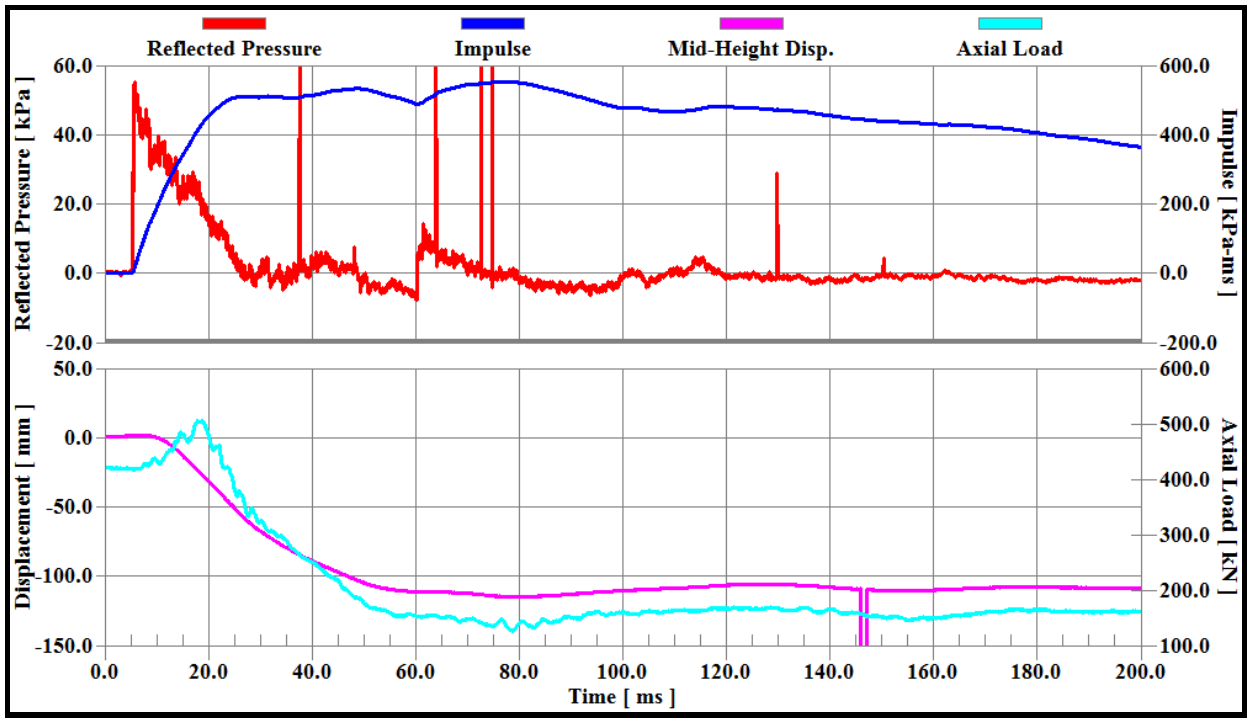

Fig. 4.50 Time history of reflected pressure, Impulse, mid-height displacement, axial load for Column S1-A-G1

(a) (b)

Fig. 4.51 Level of damage in Column S1-A-G1: a) front view; b) side view

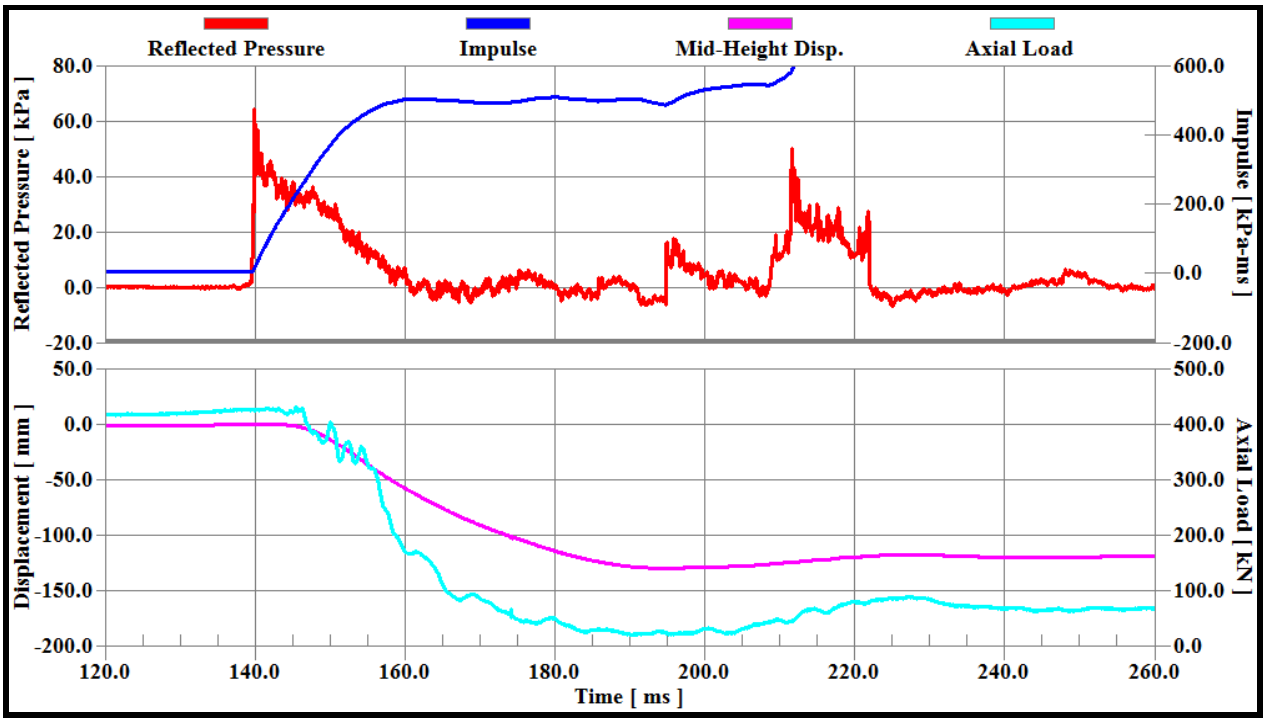

Fig. 4.52 Time history of reflected pressure, Impulse, mid-height displacement, axial load for Column S1-B-G1

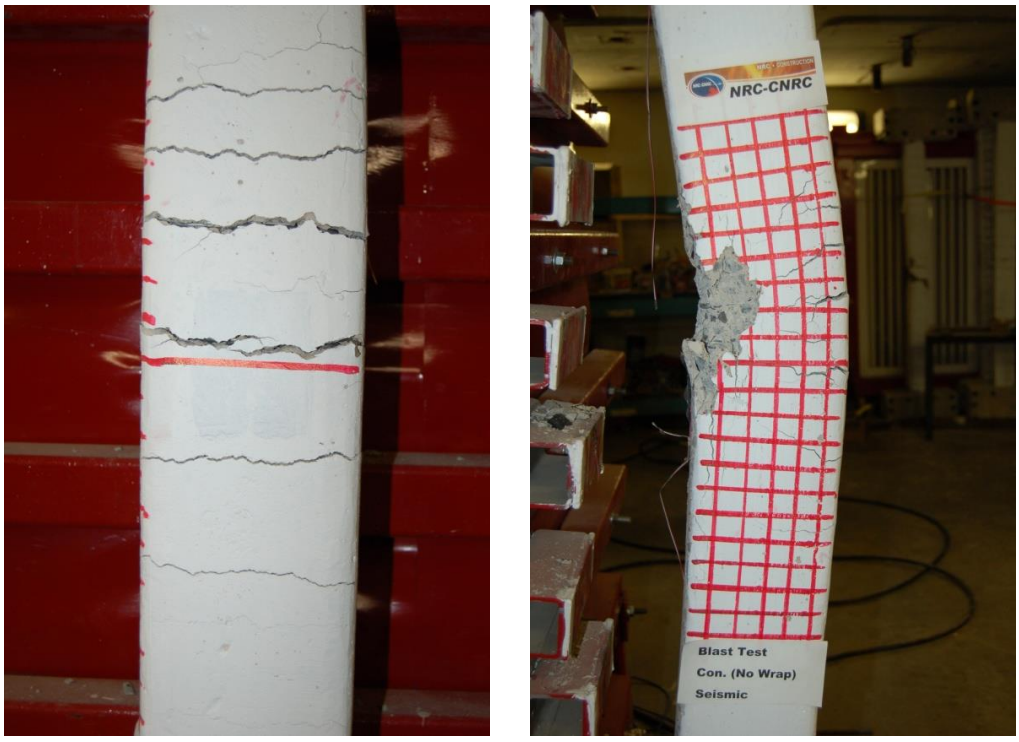

(a) (b)

Fig. 4.53 Level of damage in Column S1-B-G1: a) front view; b) side view

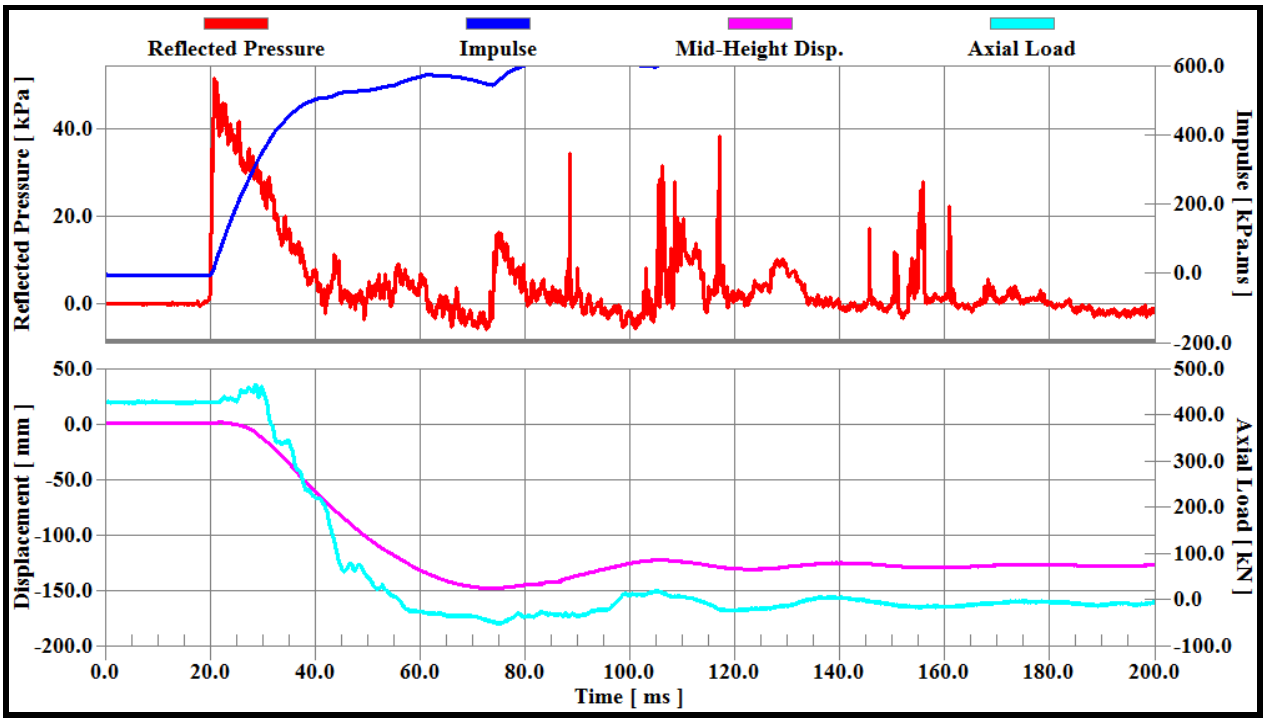

Fig. 4.54 Time history of reflected pressure, Impulse, mid-height displacement, axial load for Column S1-C-G1

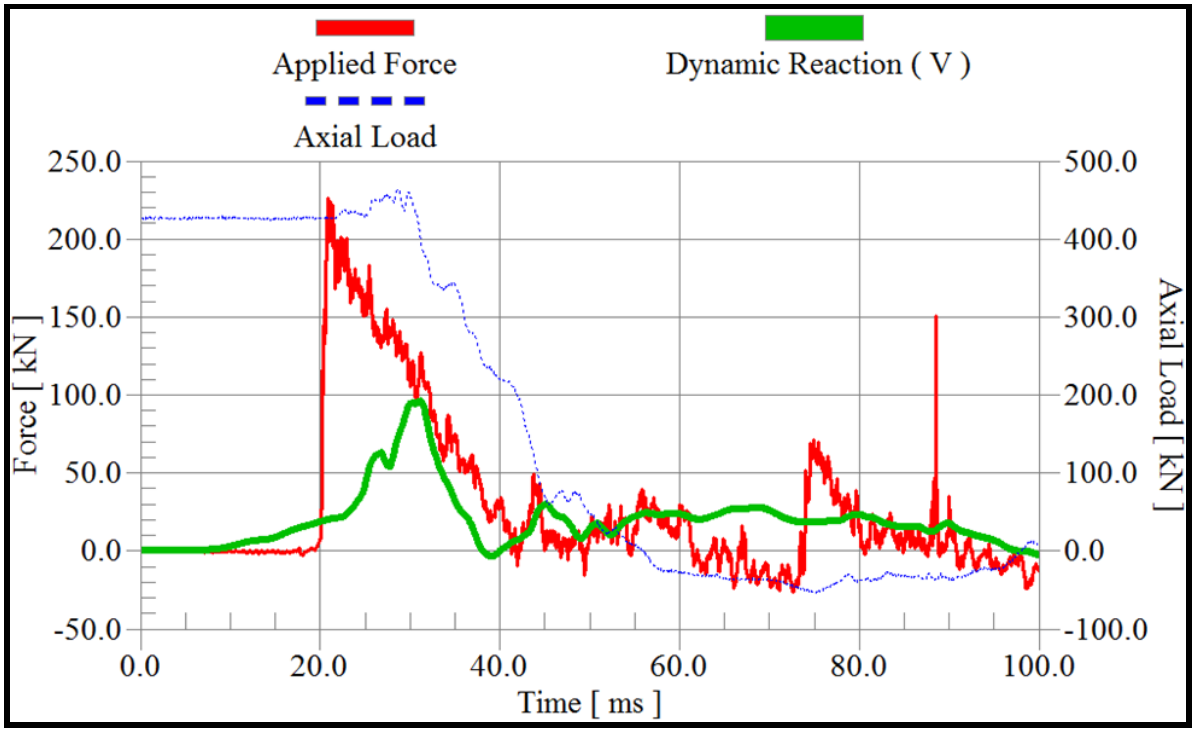

Fig. 4.55 Time history of dynamic reaction of Column S1-C-G1

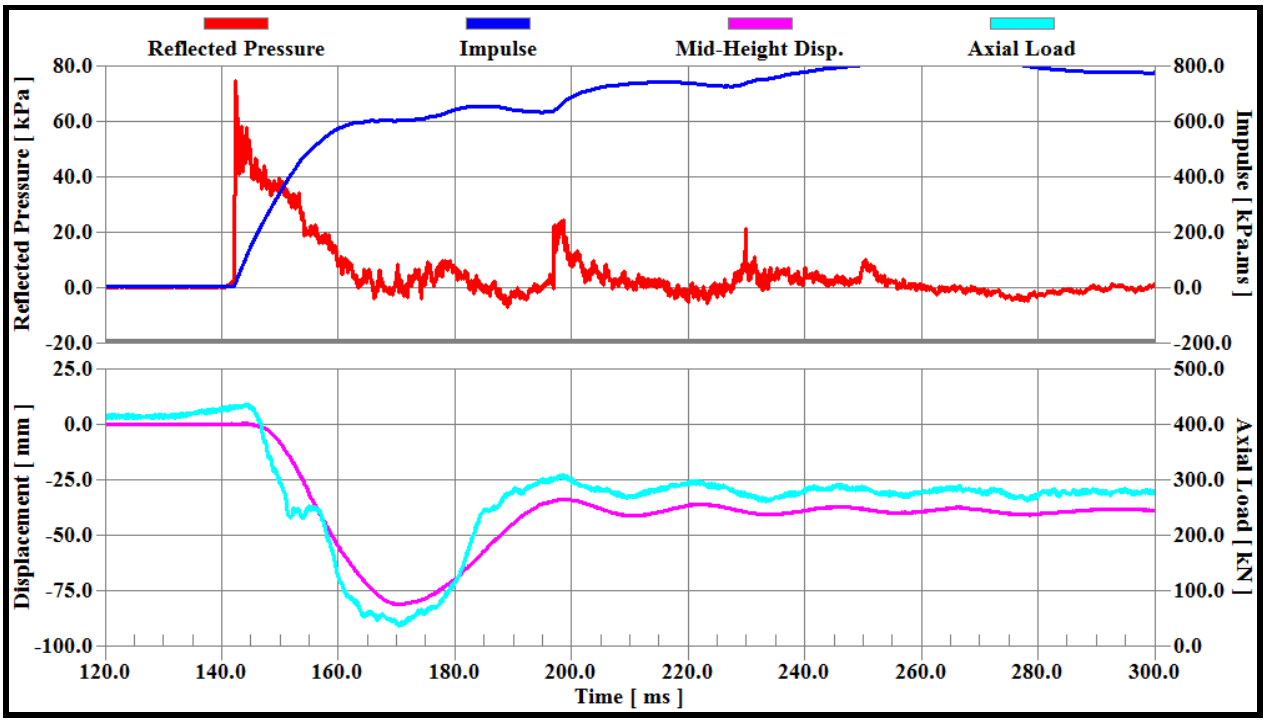

Fig. 4.56 Time history of reflected pressure, Impulse, mid-height displacement, axial load for Column S2-A-G1

(a) (b)

Fig. 4.57 Level of damage in Column S2-A-G1: a) front view; b) side view

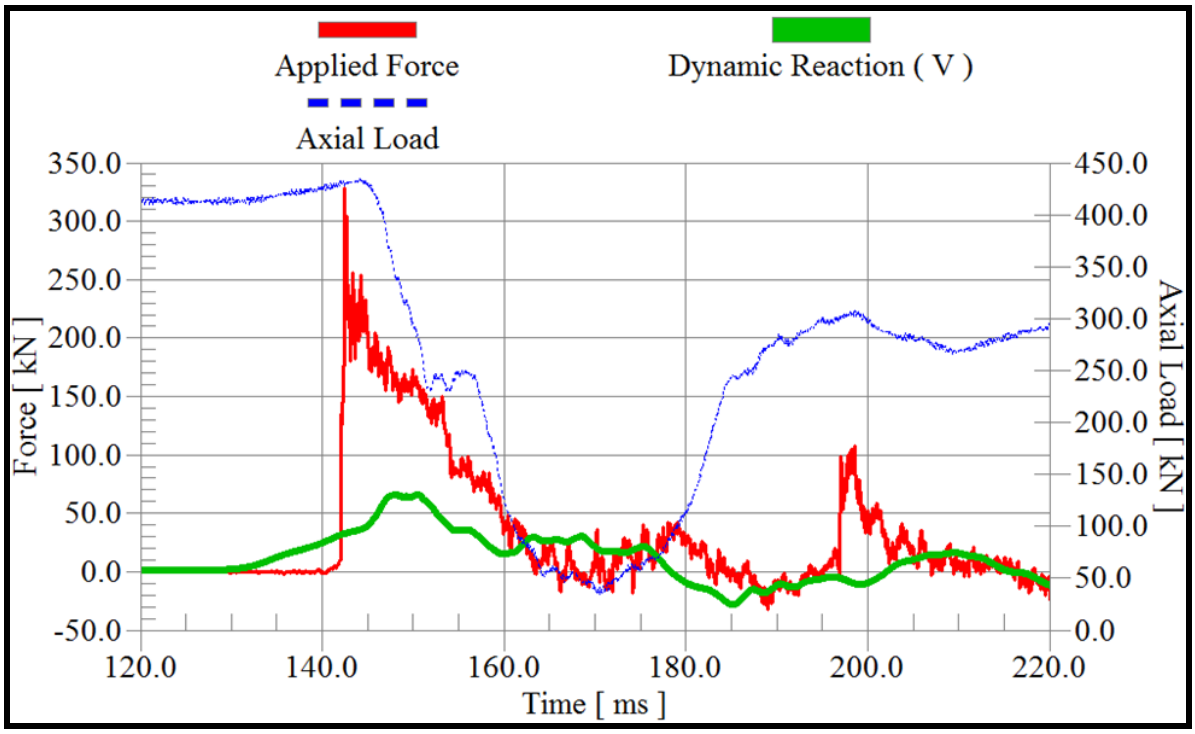

Fig. 4.58 Time history of dynamic reaction of Column S2-A-G1

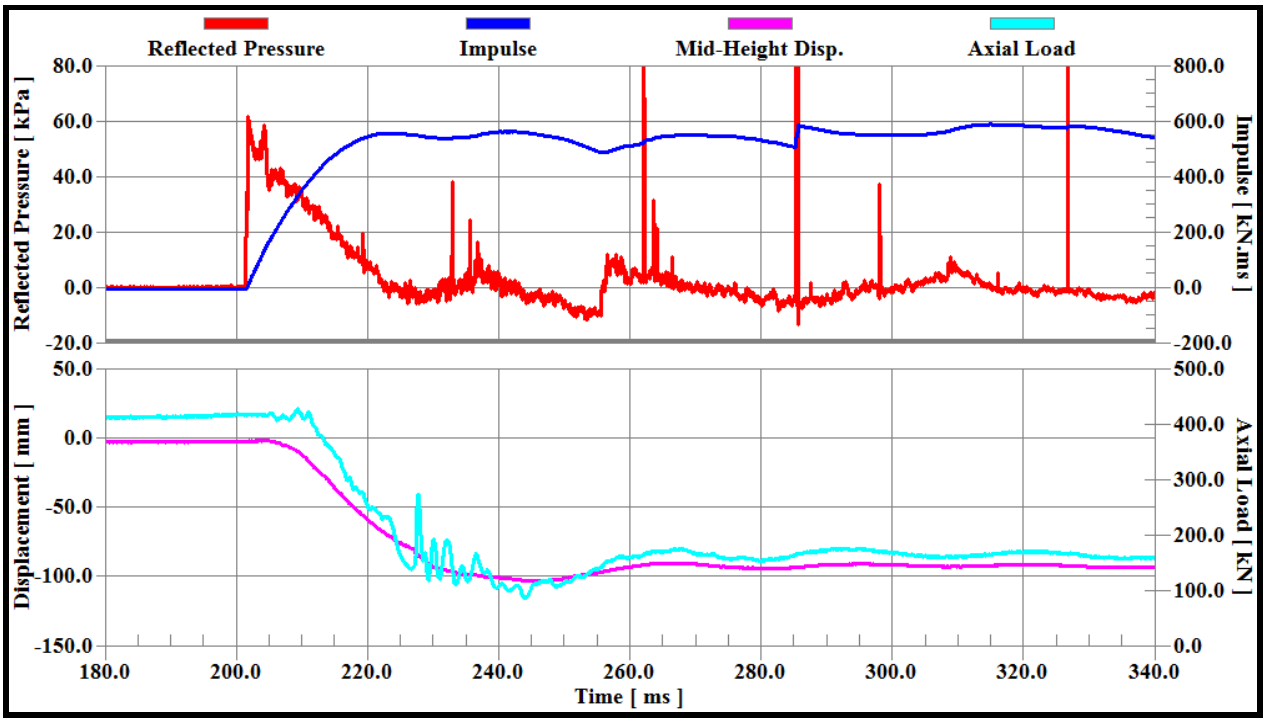

Fig. 4.59 Time history of reflected pressure, Impulse, mid-height displacement, axial load for Column S2-B

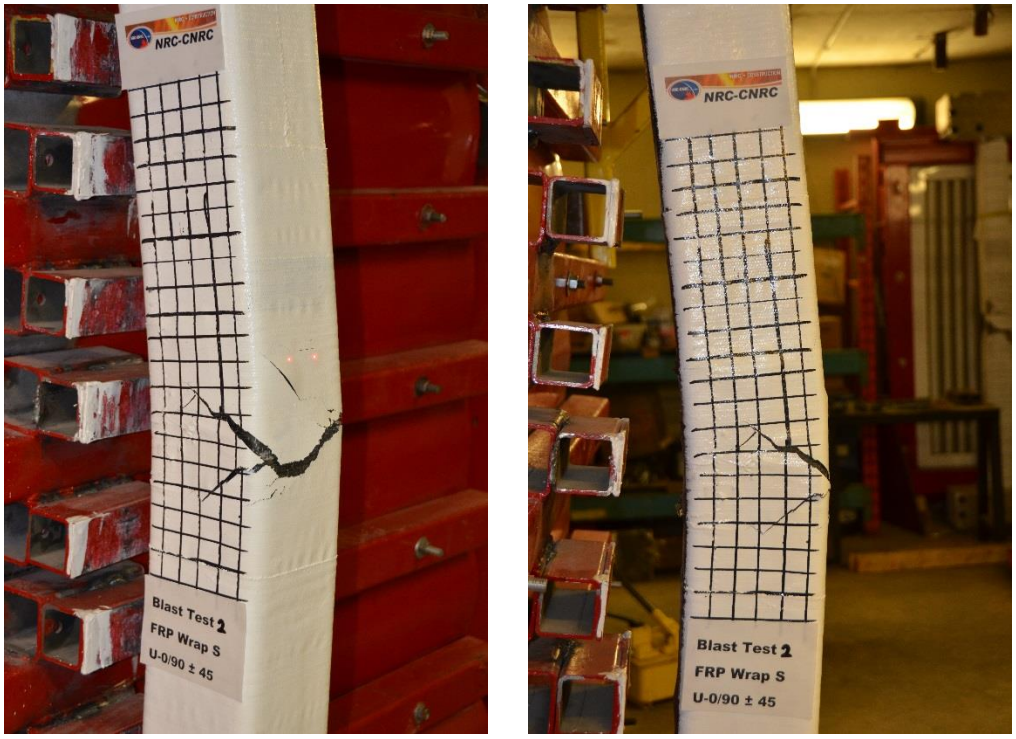

(a) (b)

Fig. 4.60 Level of damage in Column S2-B: a) front view; b) side view

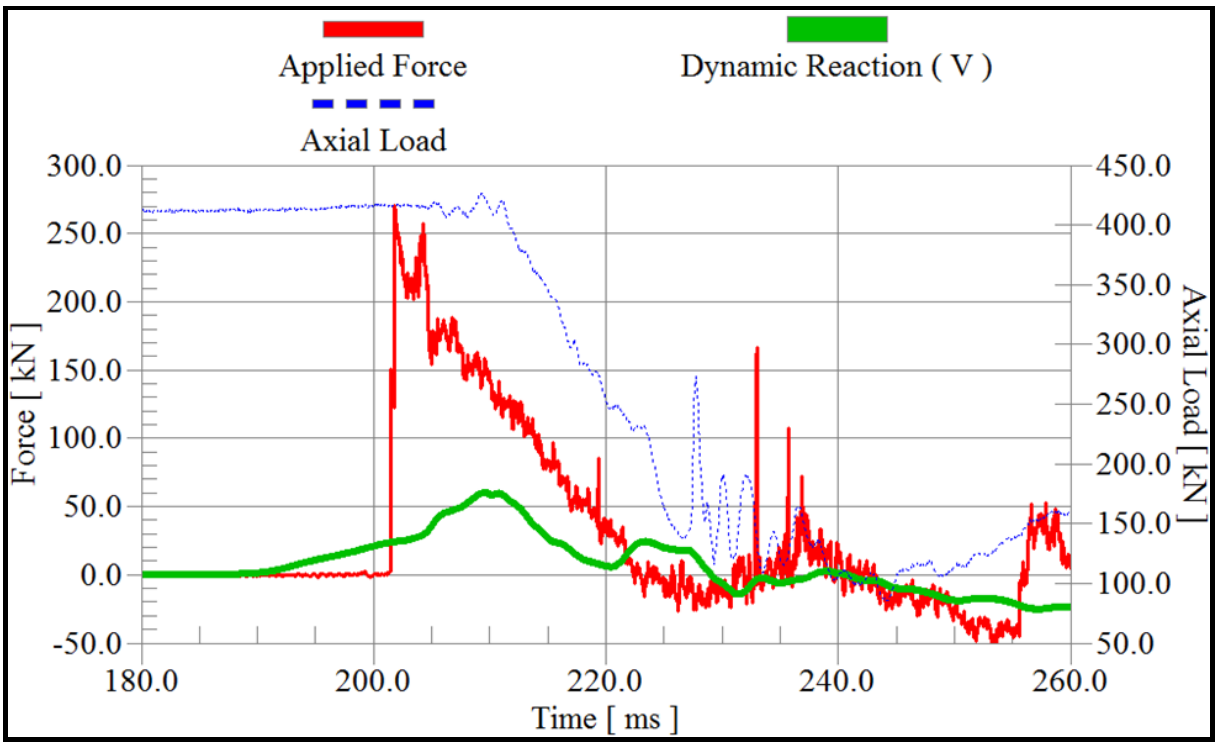

Fig. 4.61 Time history of dynamic reaction of Column S2-B-G1

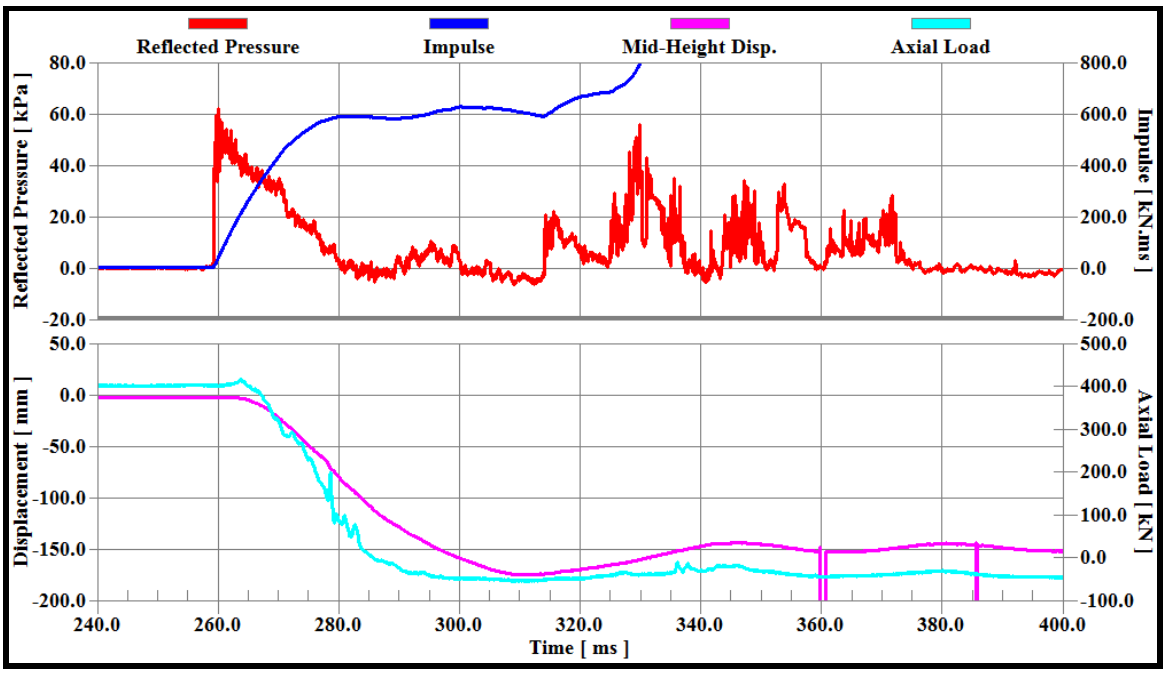

Fig. 4.62 Time history of reflected pressure, Impulse, mid-height displacement, axial load for Column S3-A-G1

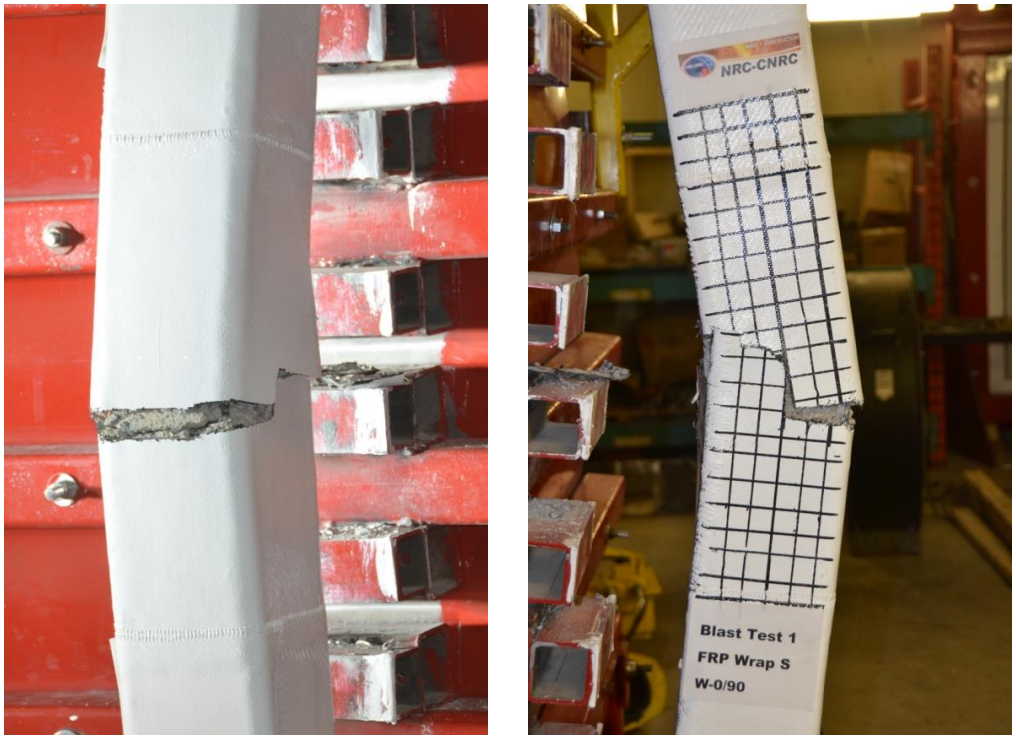

(a) (b)

Fig. 4.63 Level of damage in Column S3-A-G1: a) front view; b) side view

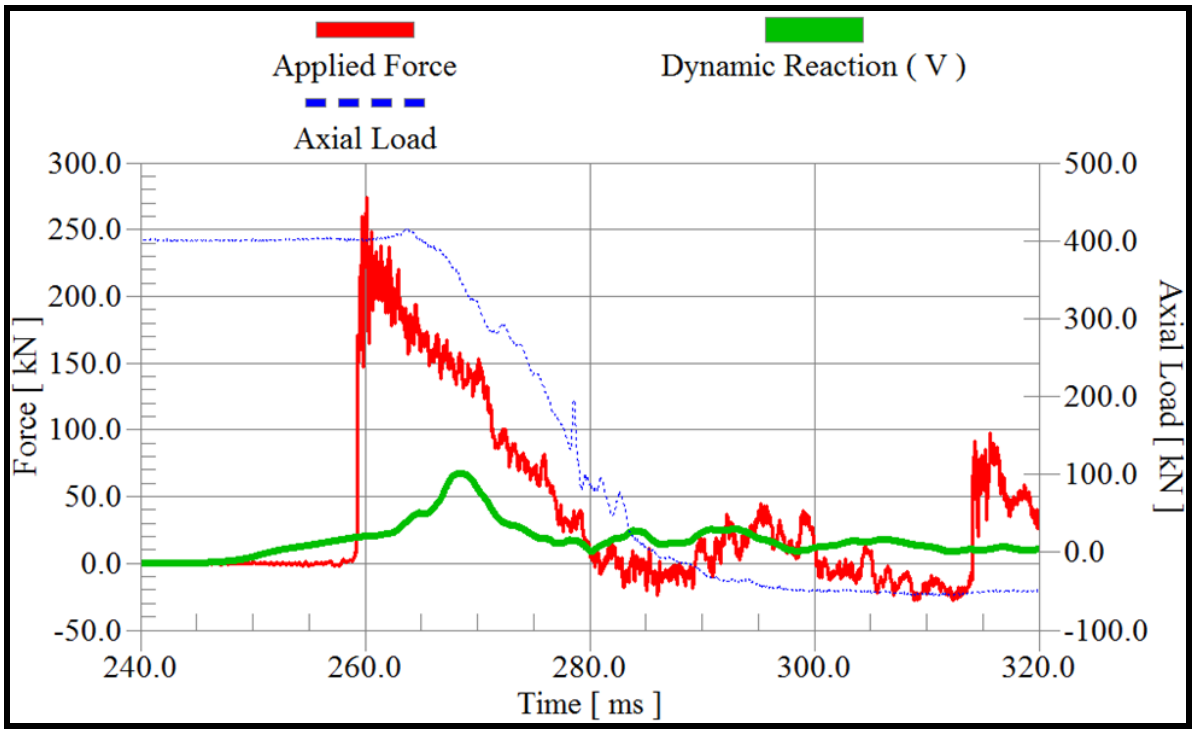

Fig. 4.64 Time history of dynamic reaction of Column S3-A-G1

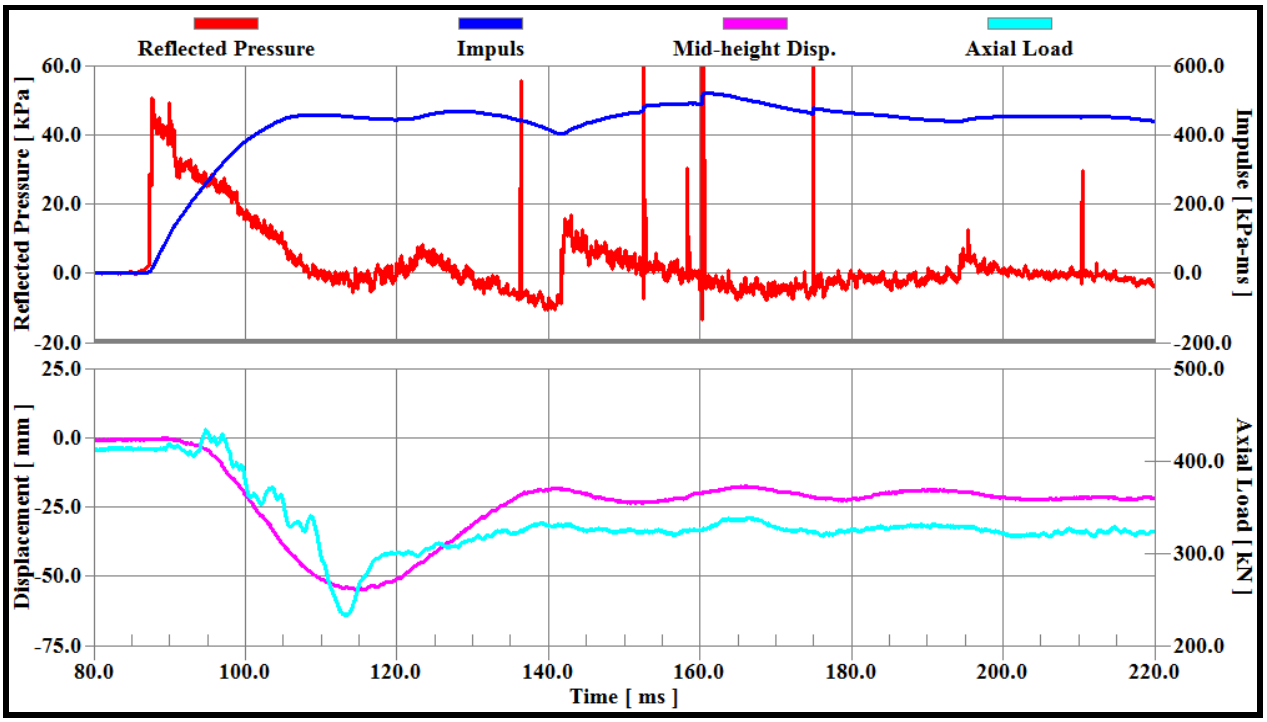

Fig. 4.65 Time history of reflected pressure, Impulse, mid-height displacement, axial load for Column S3-B-G1

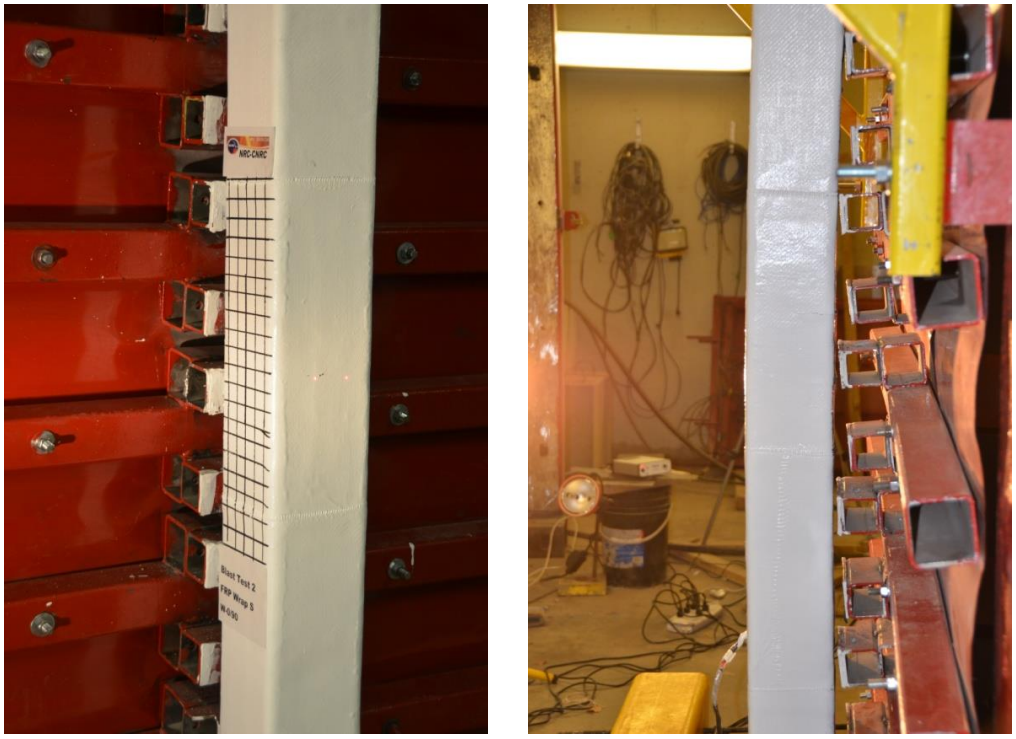

(a) (b)

Fig. 4.66 Level of damage in Column S3-B-G1: a) front view; b) side view

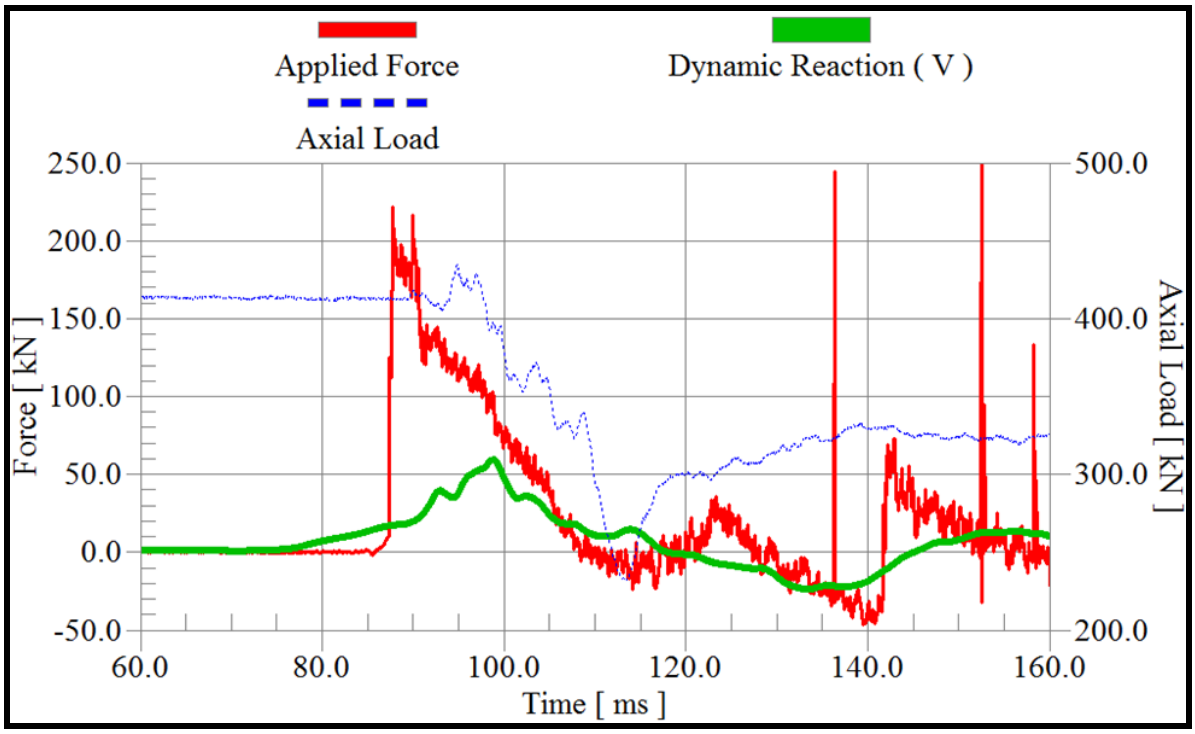

Fig. 4.67 Time history of dynamic reaction of Column S3-B

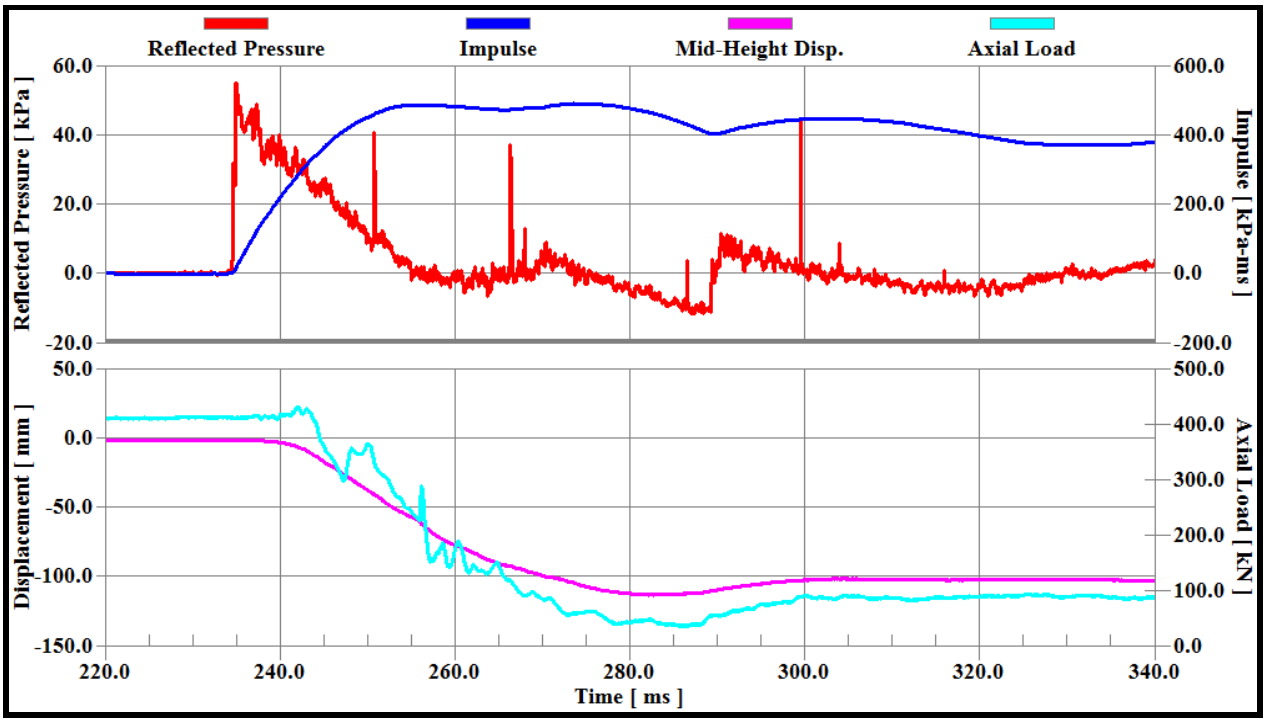

Fig. 4.68 Time history of reflected pressure, Impulse, mid-height displacement, axial load for Column S4-A-G1

(a) (b)

Fig. 4.69 Level of damage in Column S4-A-G1: a) front view; b) side view

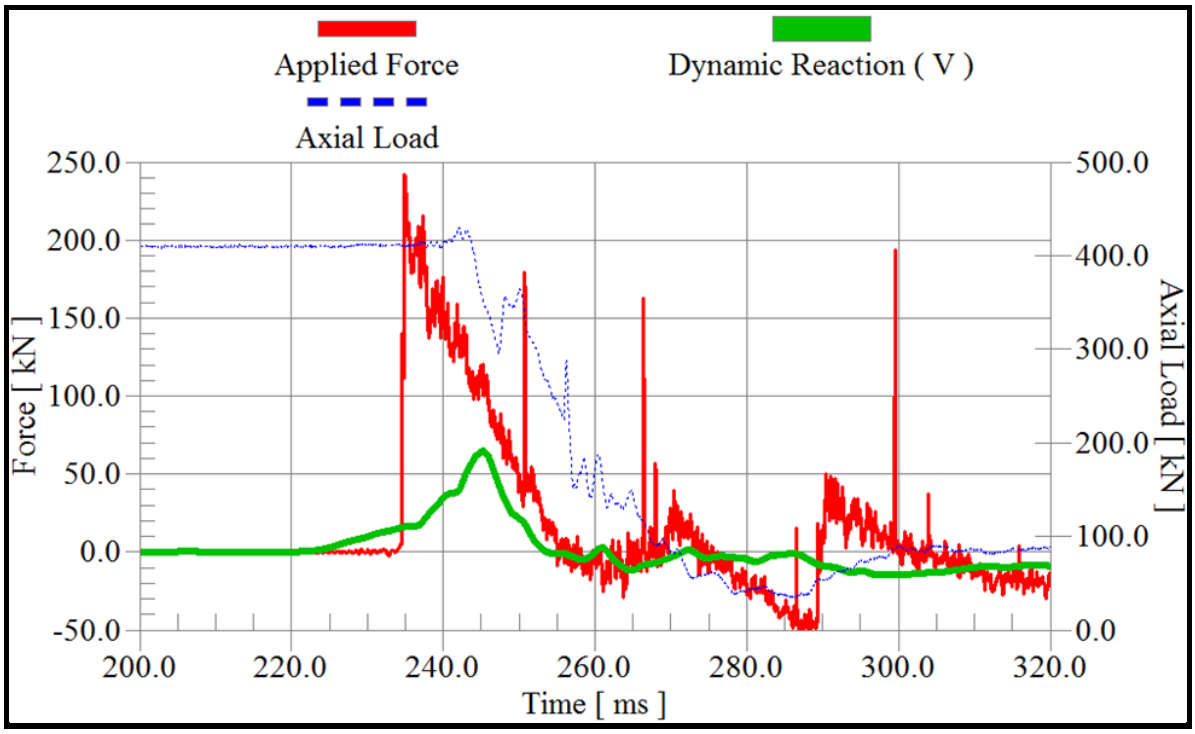

Fig. 4.70 Time history of dynamic reaction of Column S4-A-G1

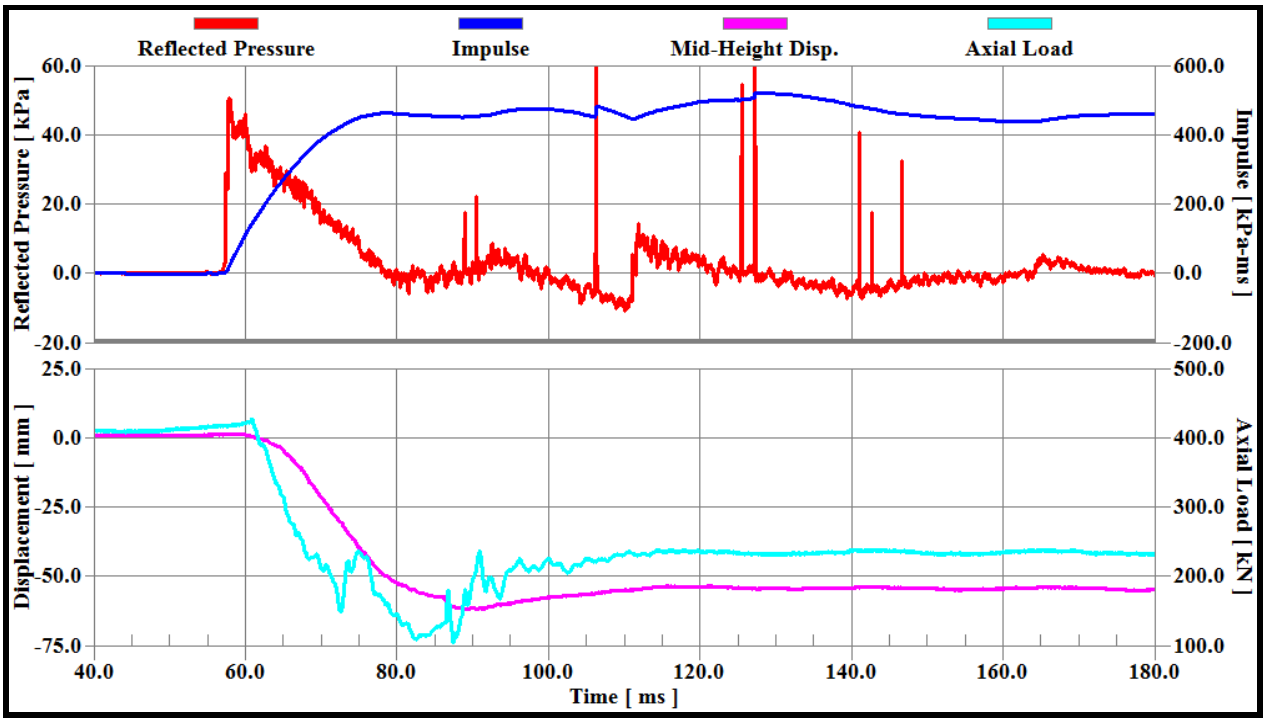

Fig. 4.71 Time history of reflected pressure, Impulse, mid-height displacement, axial load for Column S4-B-G1

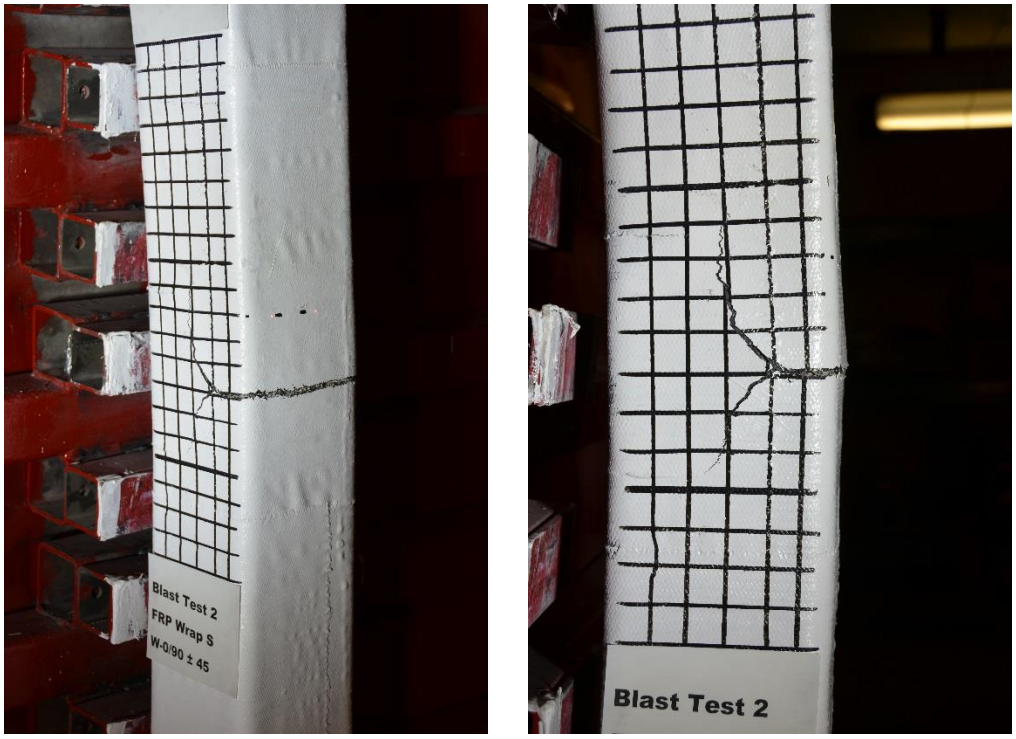

(a) (b)

Fig. 4.72 Level of damage in Column S4-A-G1: a) front view; b) side view

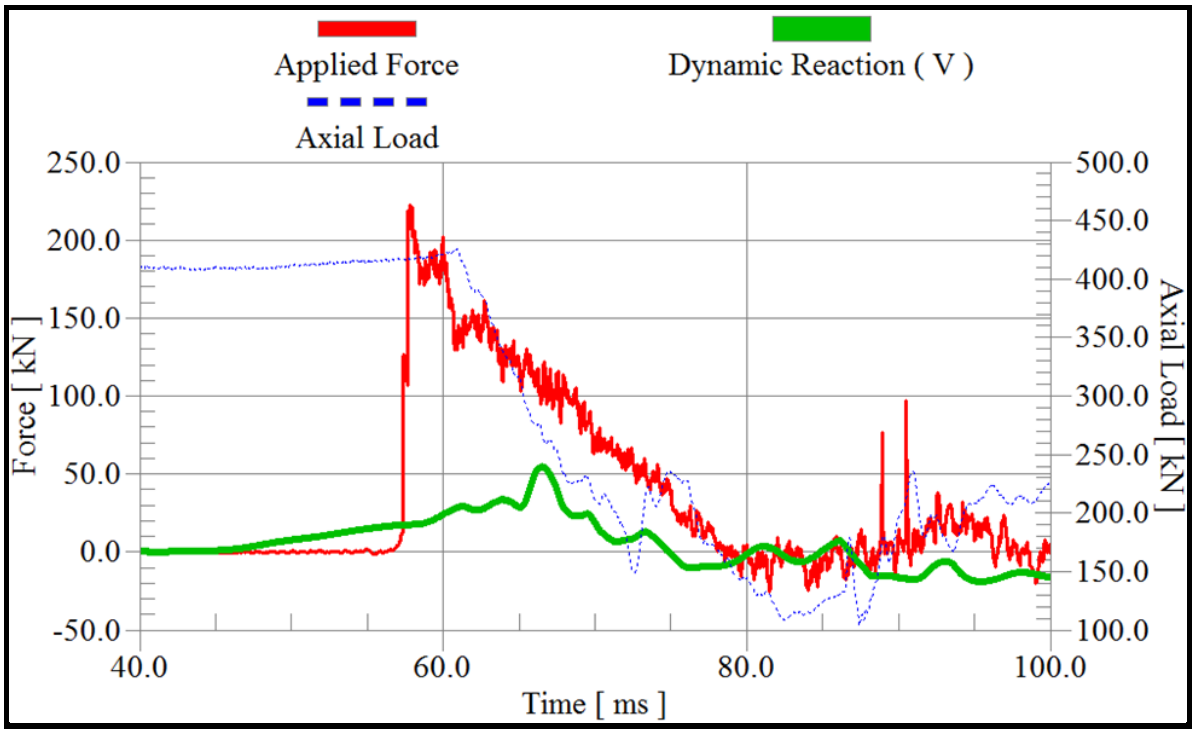

Fig. 4.73 Time history of dynamic reaction of Column S4-B

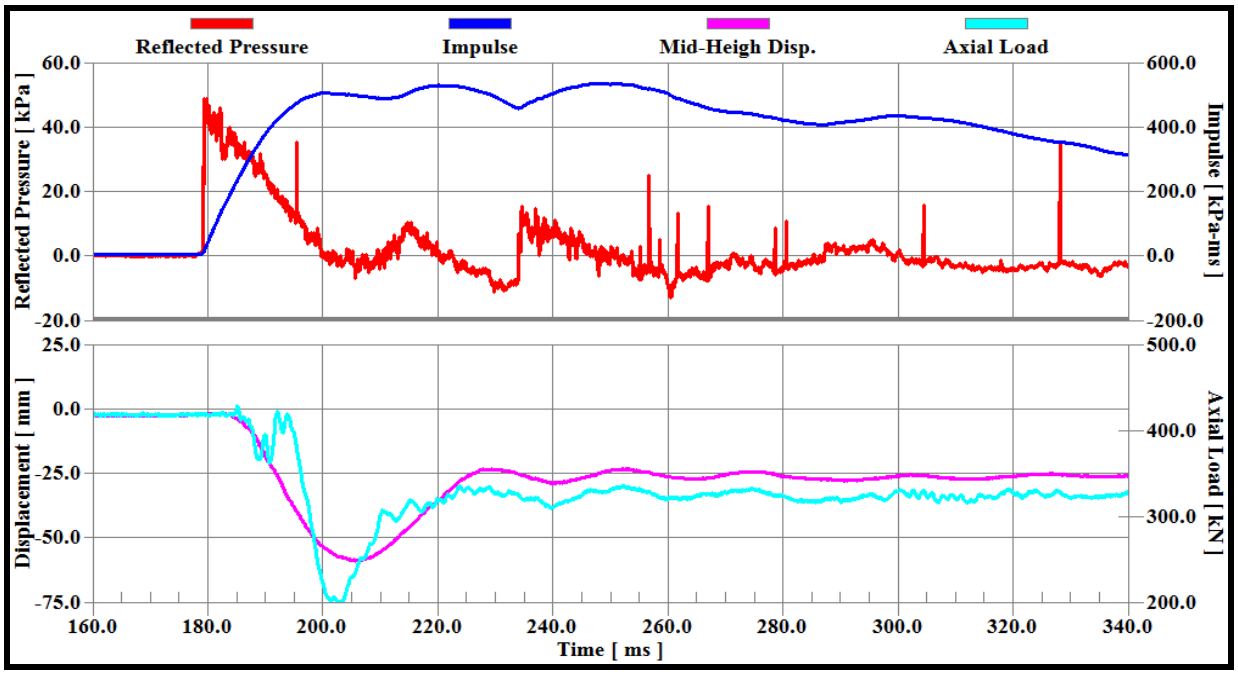

Fig. 4.74 Time history of reflected pressure, Impulse, mid-height displacement, axial load for Column S5-G1

(a) (b)

Fig. 4.75 Level of damage in Column S5-G1: a) front view; b) side view

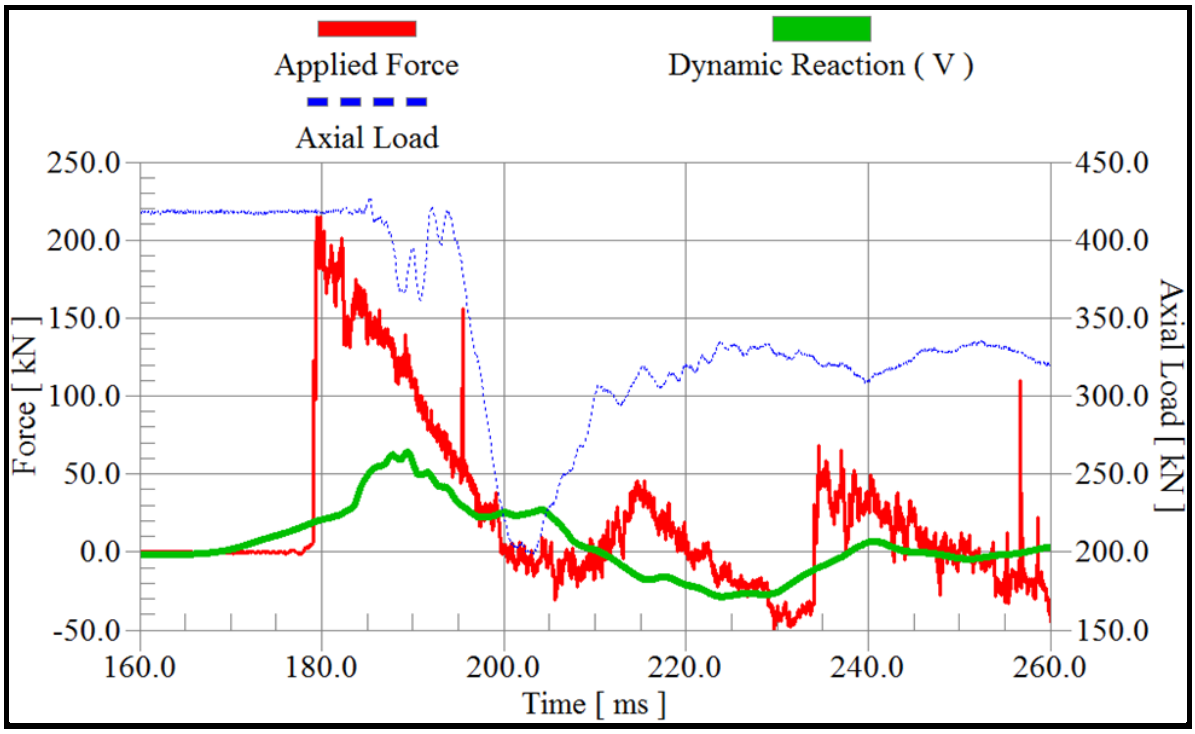

Fig. 4.76 Time history of dynamic reaction of Column S5-A-G1

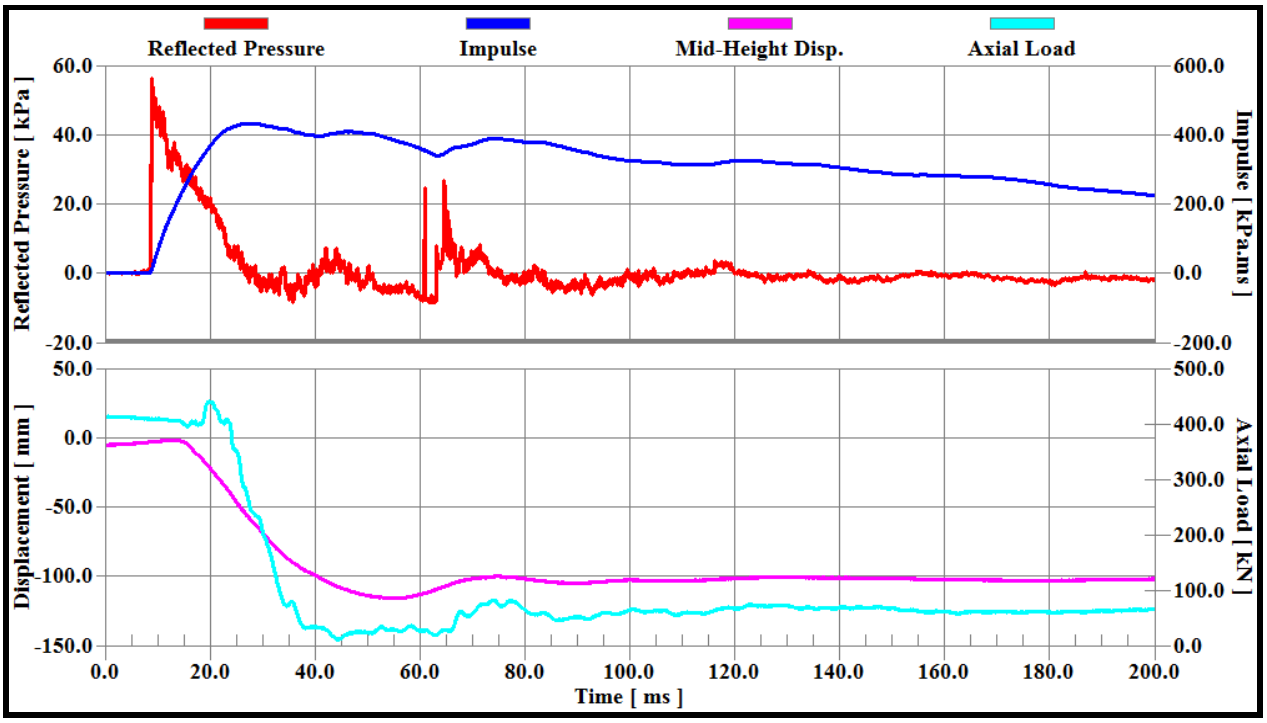

Fig. 4.77 Time history of reflected pressure, Impulse, mid-height displacement, and axial load for Column NS1-G2

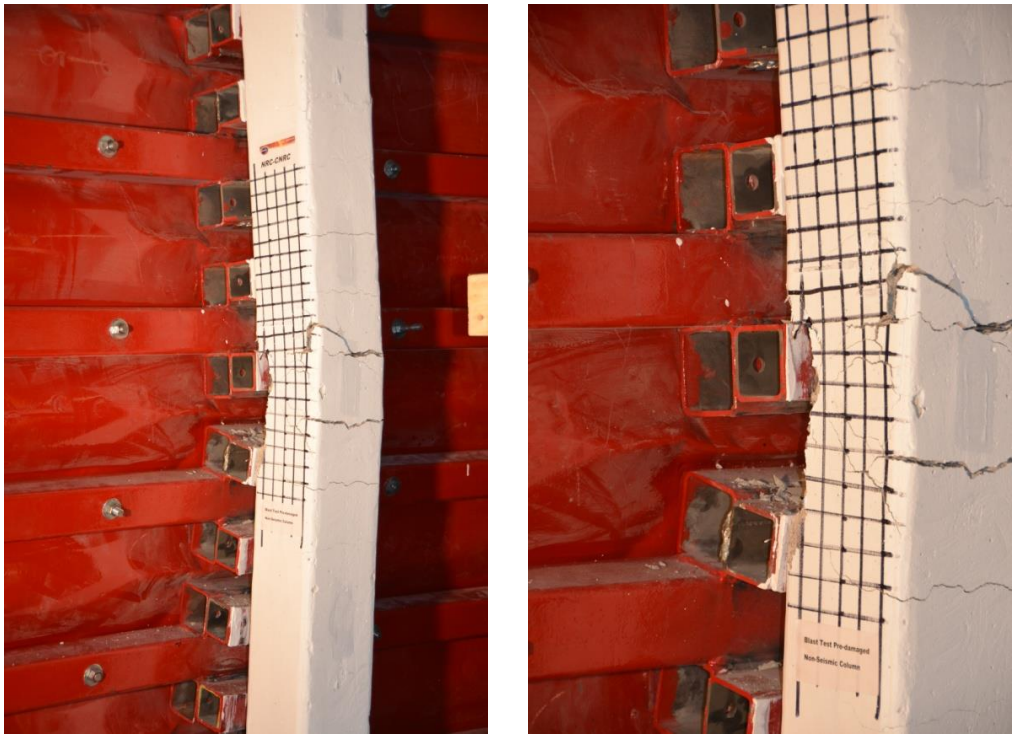

(a) (b)

Fig. 4.78 Level of damage in Column NS1-G2: a) front view; b) side view

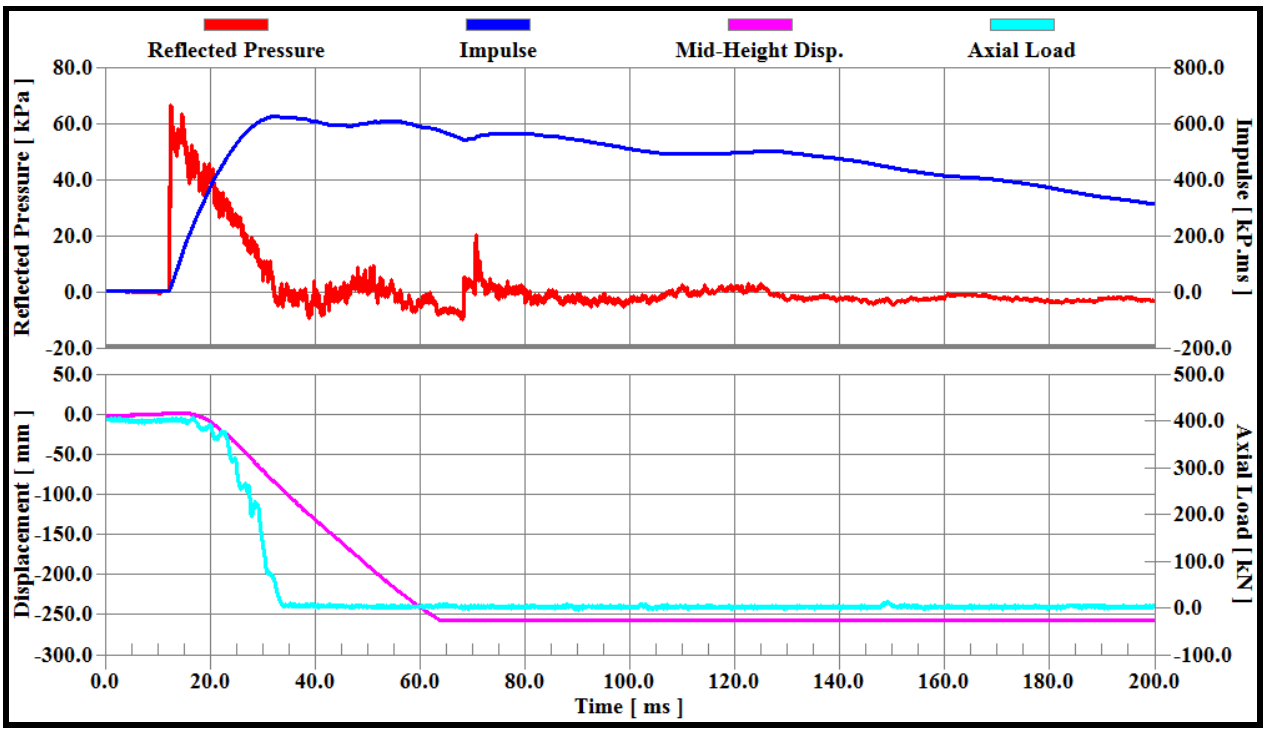

Fig. 4.79 Time history of reflected pressure, Impulse, mid-height displacement, and axial load for Column NS2-A-G2

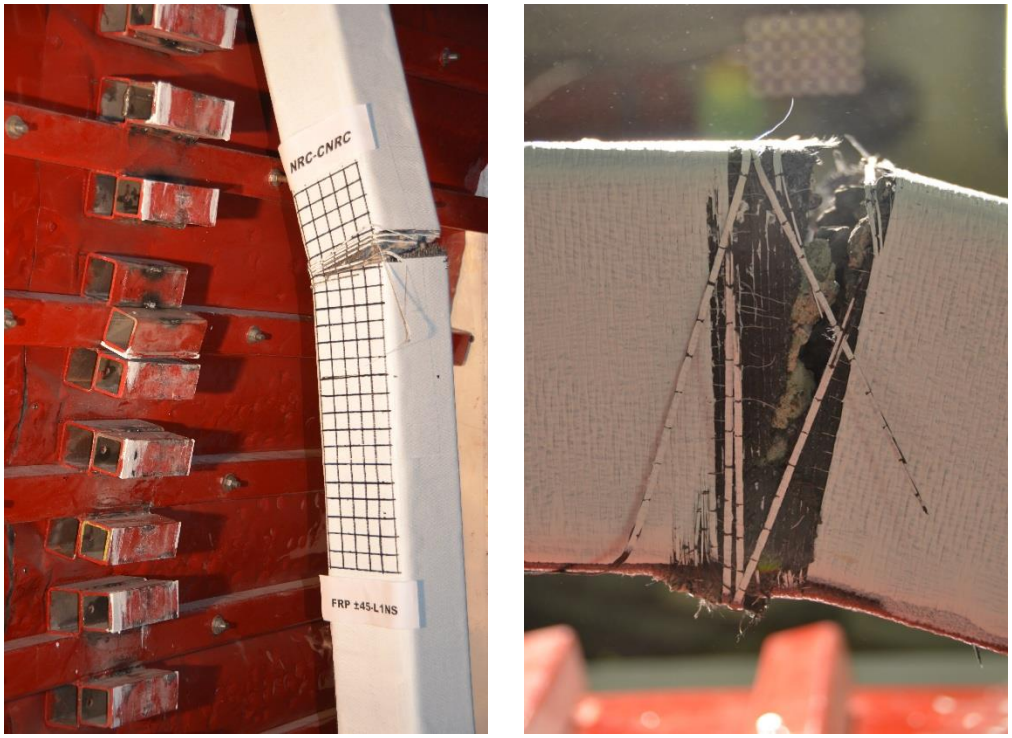

(a) (b)

Fig. 4.80 Level of damage in Column NS2-A-G2: a) front view; b) side view

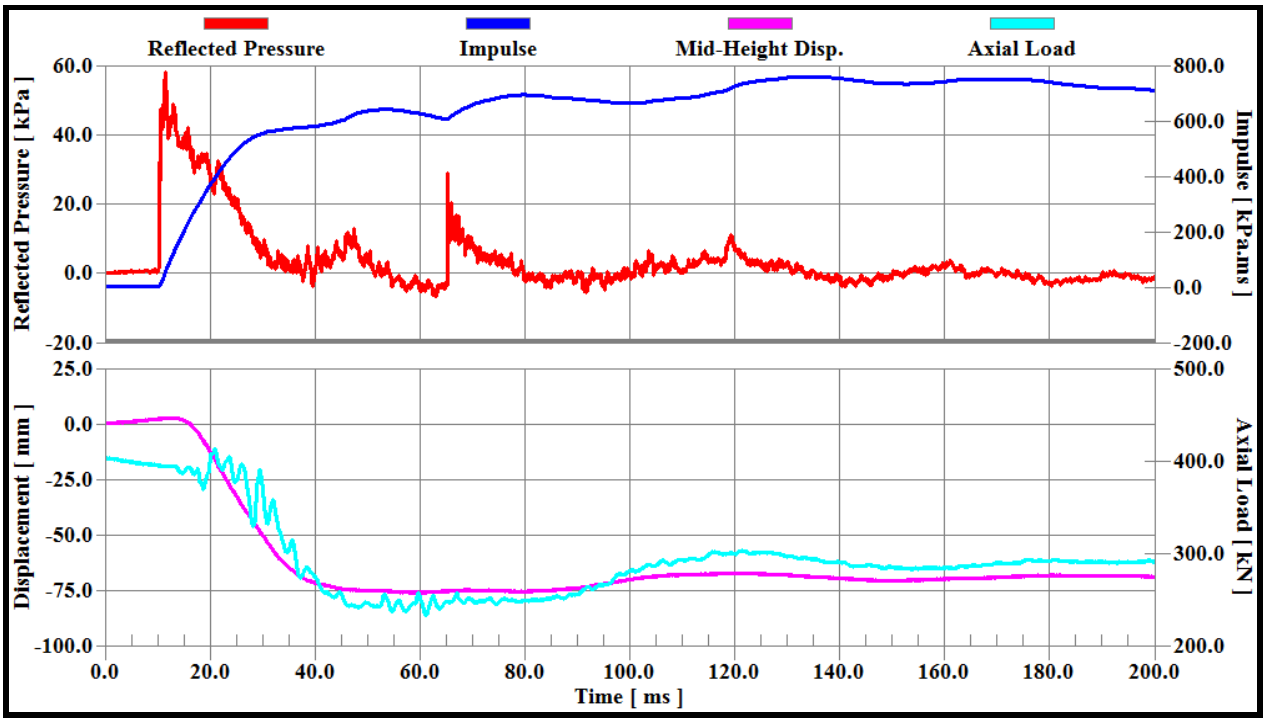

Fig. 4.81 Time history of reflected pressure, Impulse, mid-height displacement, and axial load for Column NS2-B-G2

(a) (b)

Fig. 4.82 Level of damage in Column NS2-B-G2: a) front view; b) side view

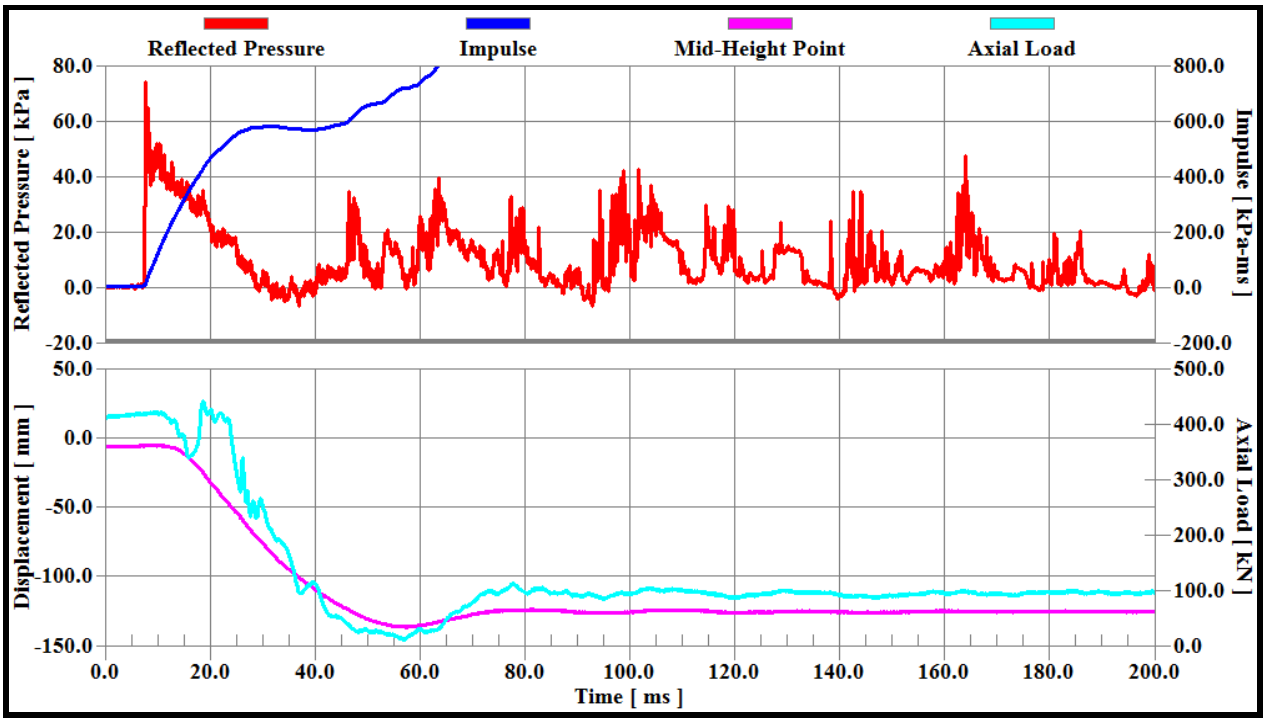

Fig. 4.83 Time history of reflected pressure, Impulse, mid-height displacement, and axial load for Column KEV-1-G2

(a) (b)

Fig. 4.84 Level of damage in Column KEV-1-G2: a) front view; b) side view

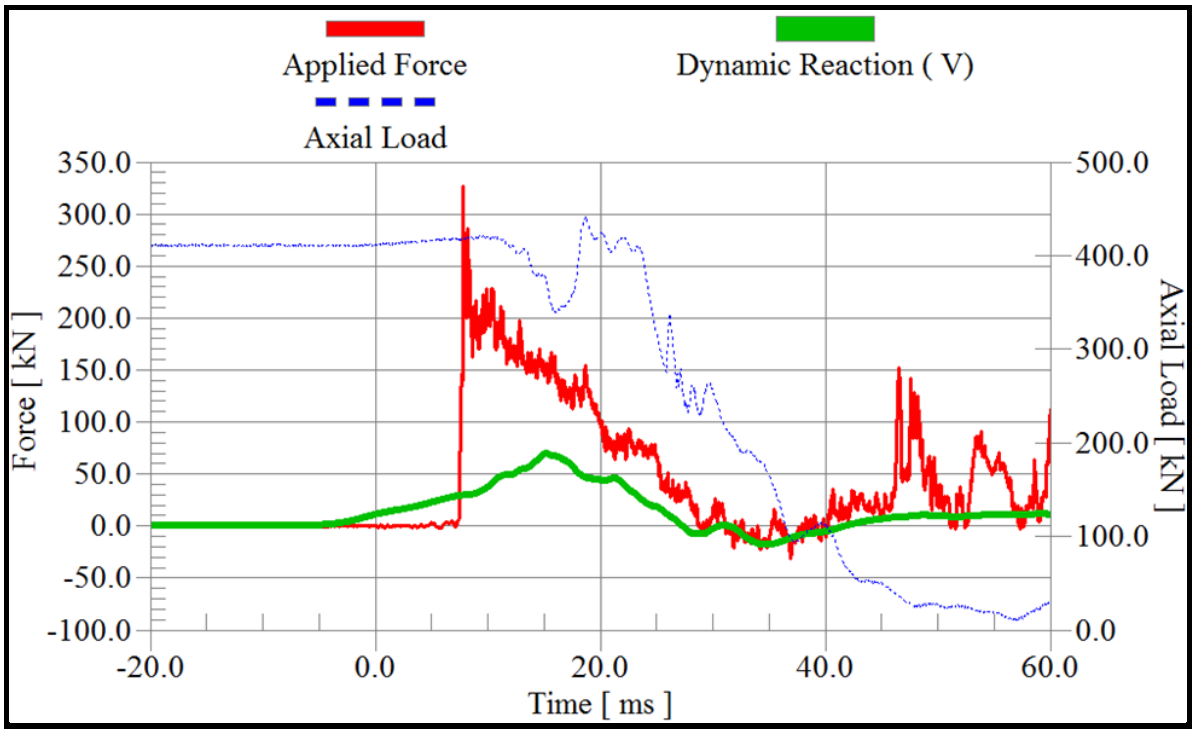

Fig. 4.85 Time history of dynamic reaction of Column KEV-1-G2

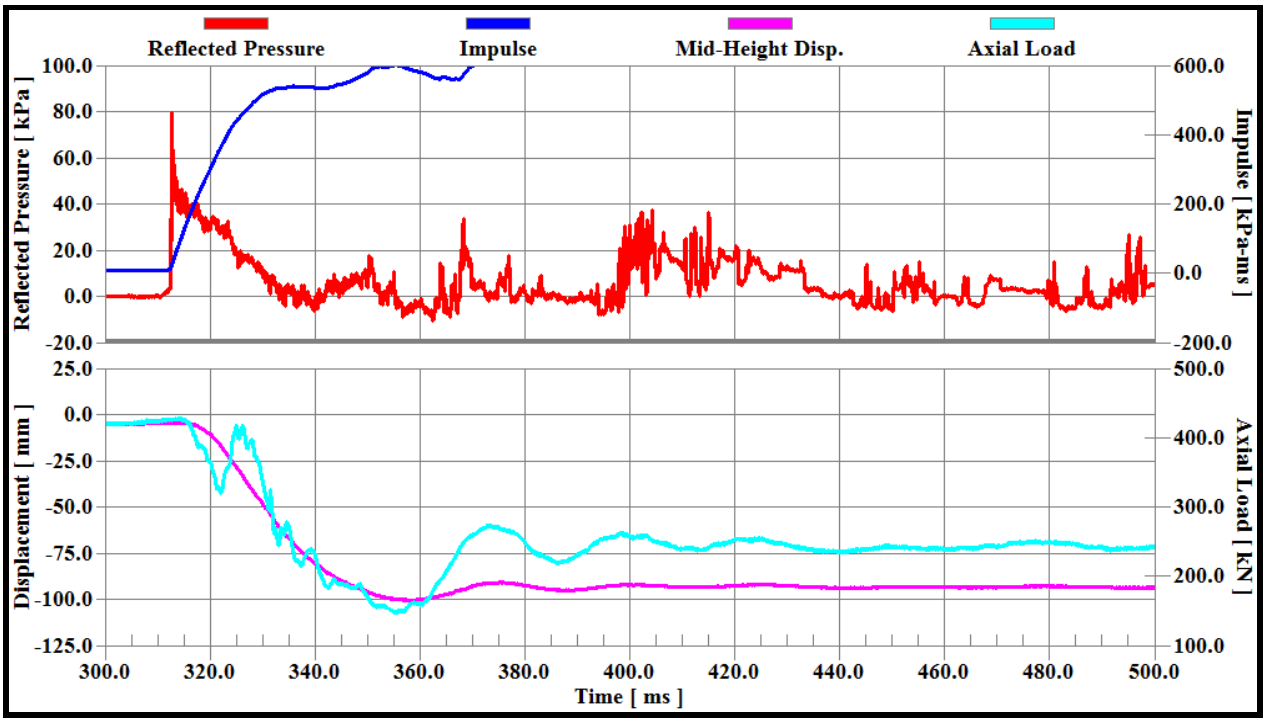

Fig. 4.86 Time history of reflected pressure, Impulse, mid-height displacement, and axial load for Column KEV-2-G2

(a) (b)

Fig. 4.87 Level of damage in Column KEV-2-G2: a) front view; b) side view

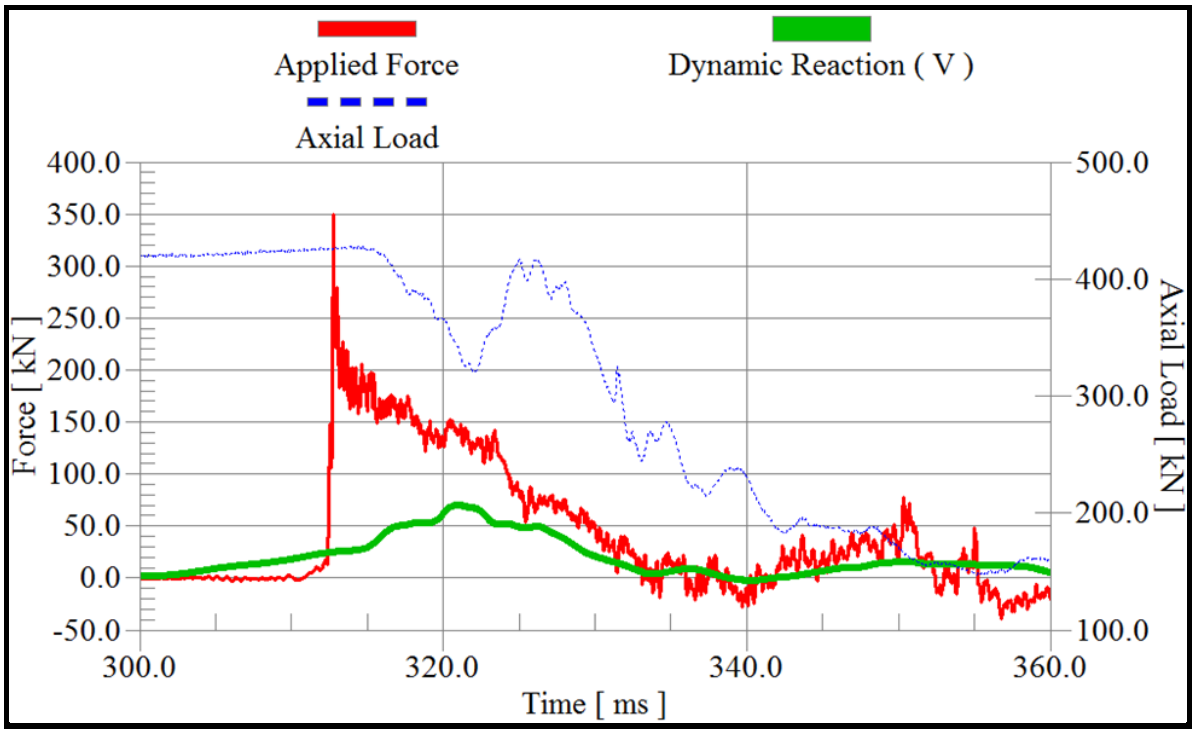

Fig. 4.88 Time history of dynamic reaction of Column KEV-1-G2

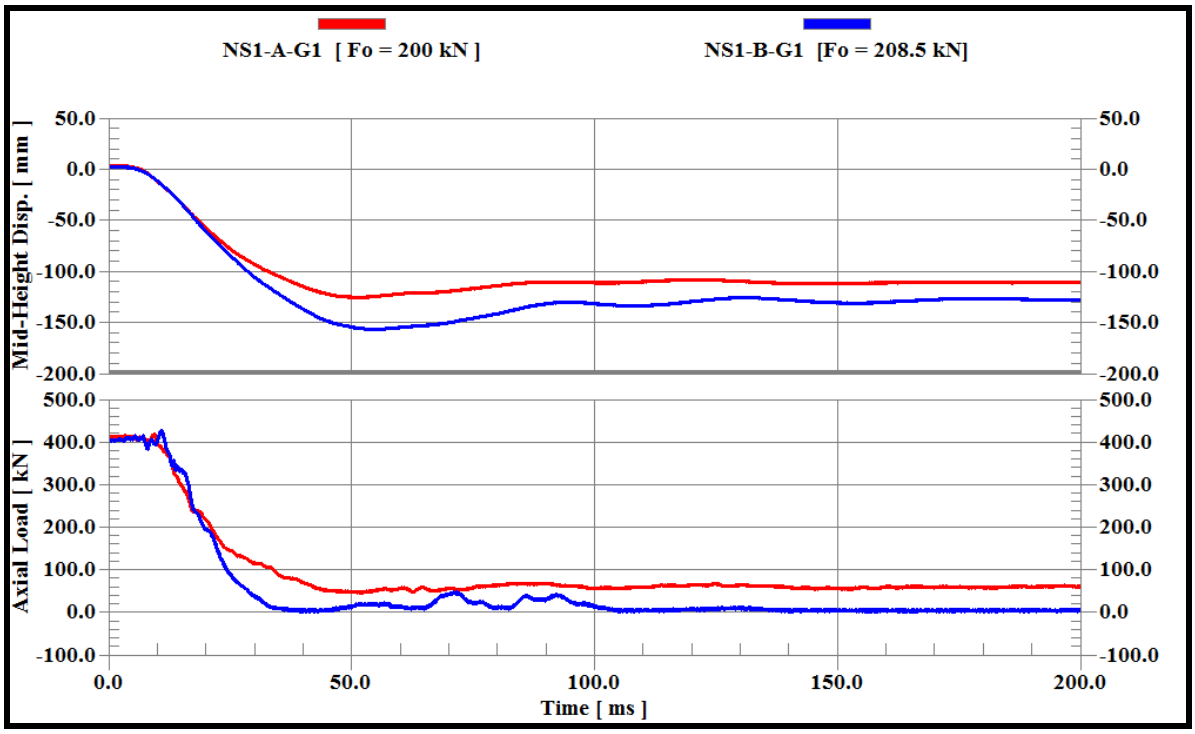

Fig. 4.89 Mid-height deflection and axial load time history for NS1-A-G1 and NS1-B-G1

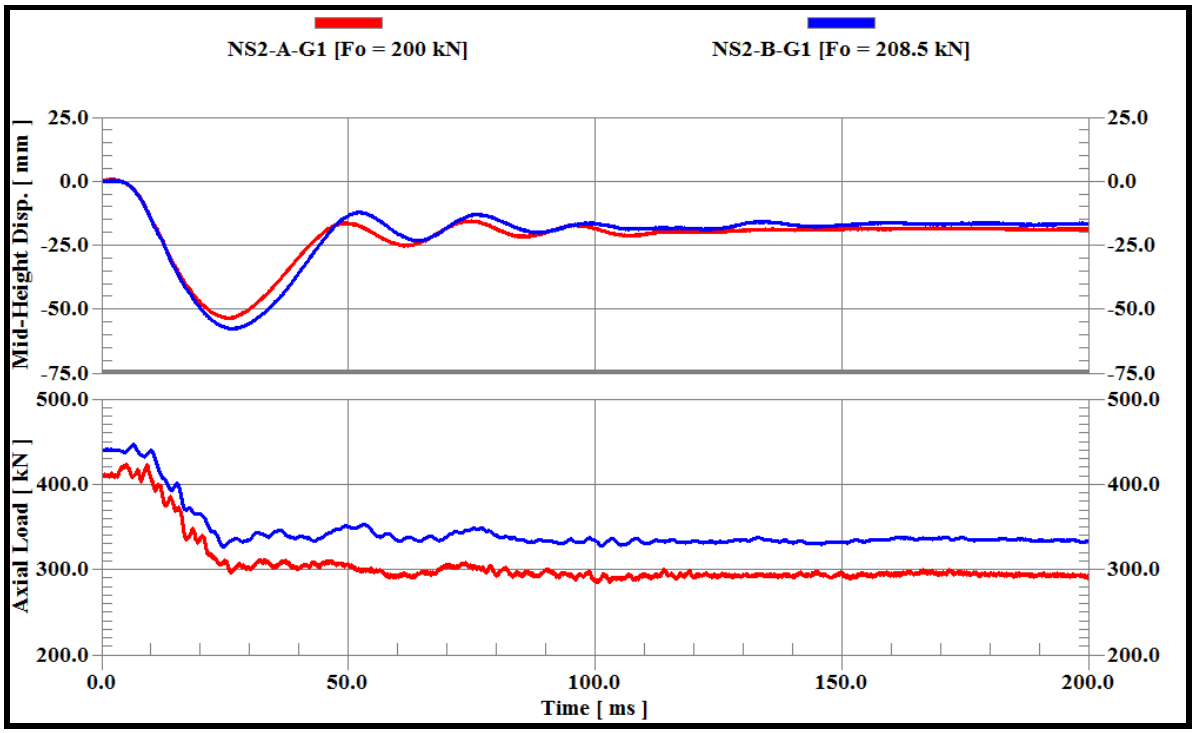

Fig. 4.90 Mid-height deflection and axial load time history for NS2-A-G1 and NS2-B-G1

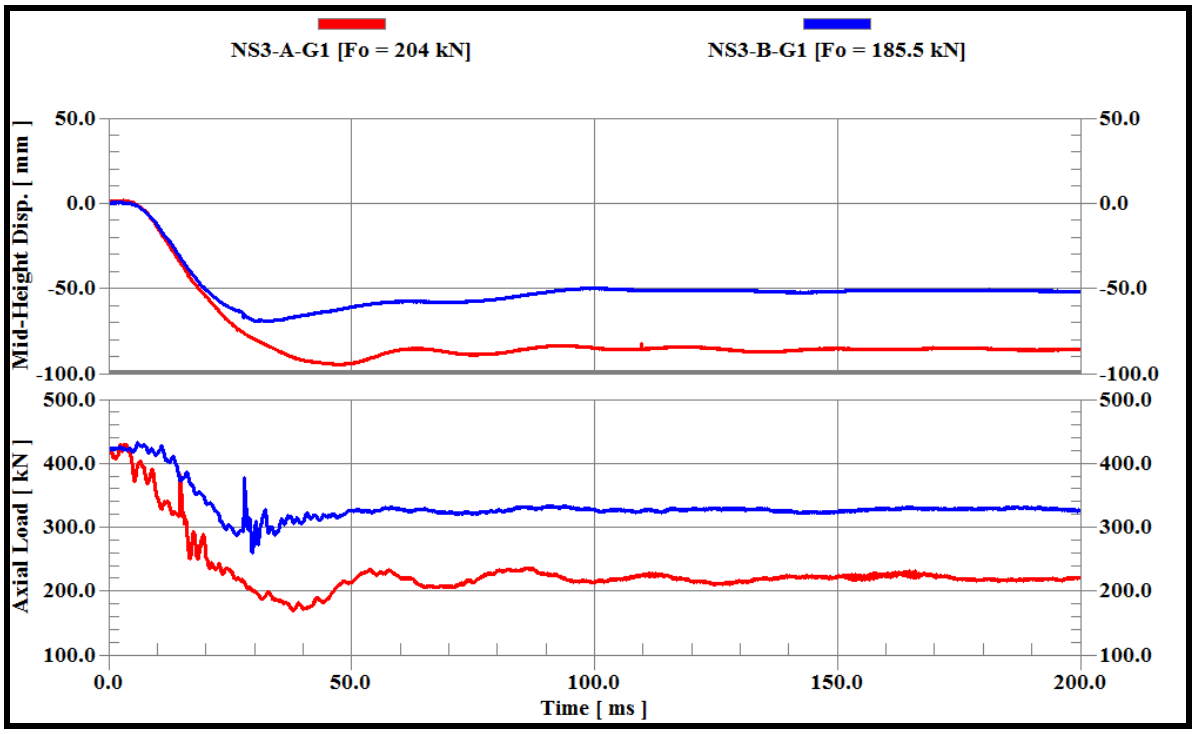

Fig. 4.91 Mid-height deflection and axial load time history for NS3-A-G1 and NS3-B-G1

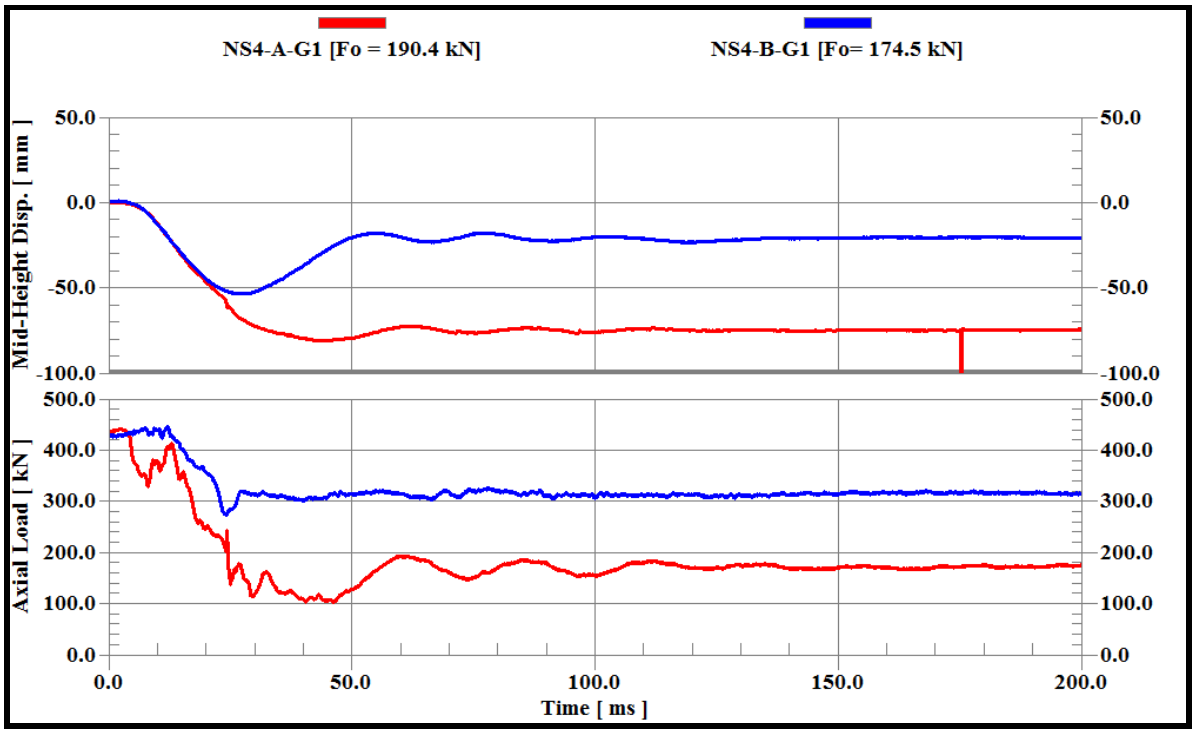

Fig. 4.92 Mid-height deflection and axial load time history for NS4-A-G1 and NS4-B-G1

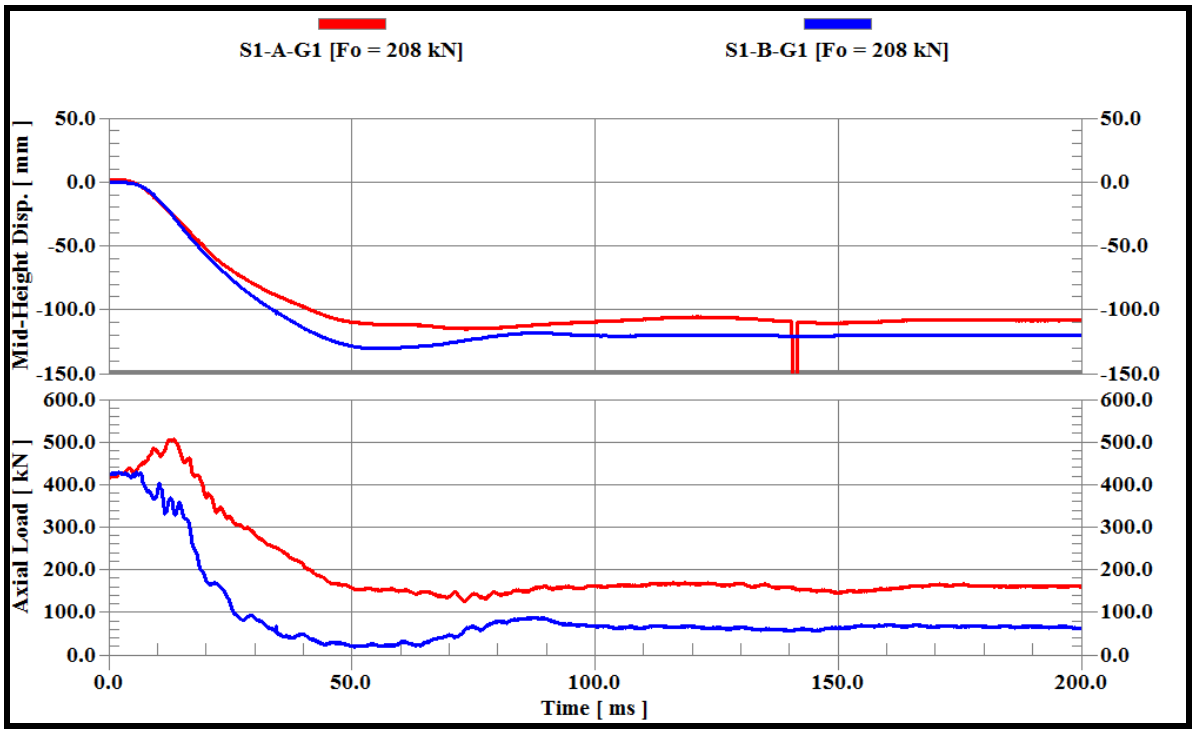

Fig. 4.93 Mid-height deflection and axial load time history for S1-A-G1 and S1-B-G1

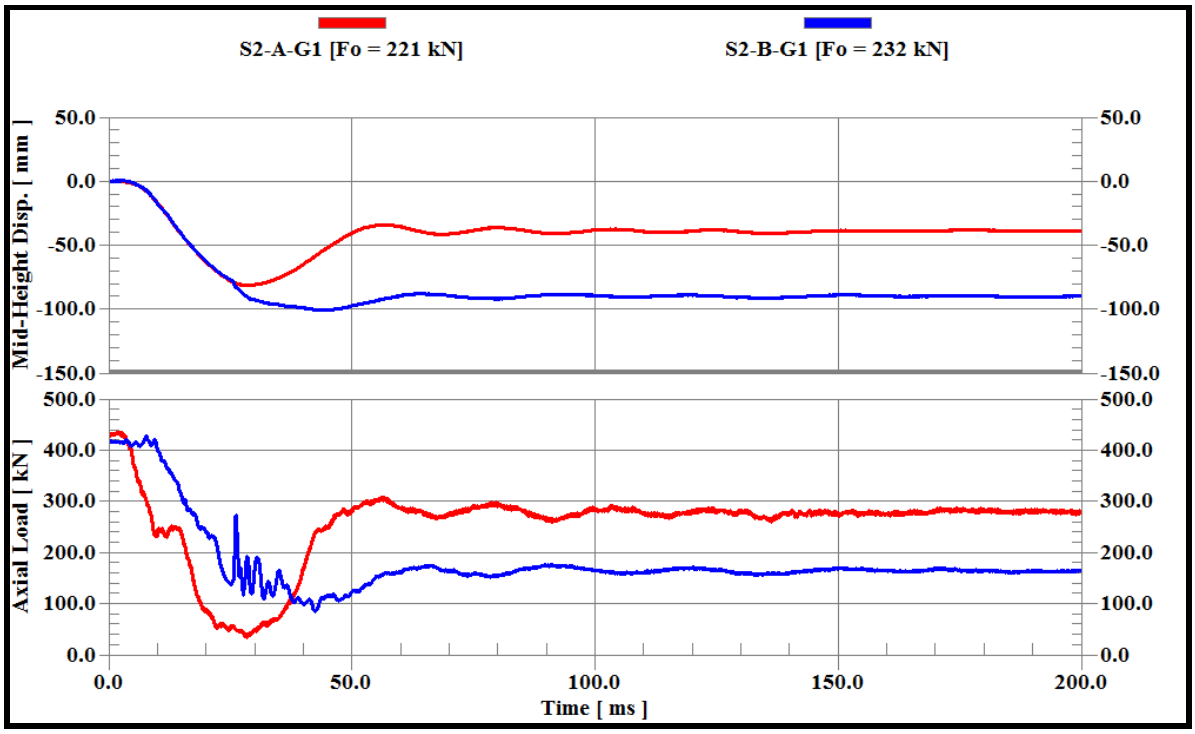

Fig. 4.94 Mid-height deflection and axial load time history for S2-A-G1 and S2-B-G1

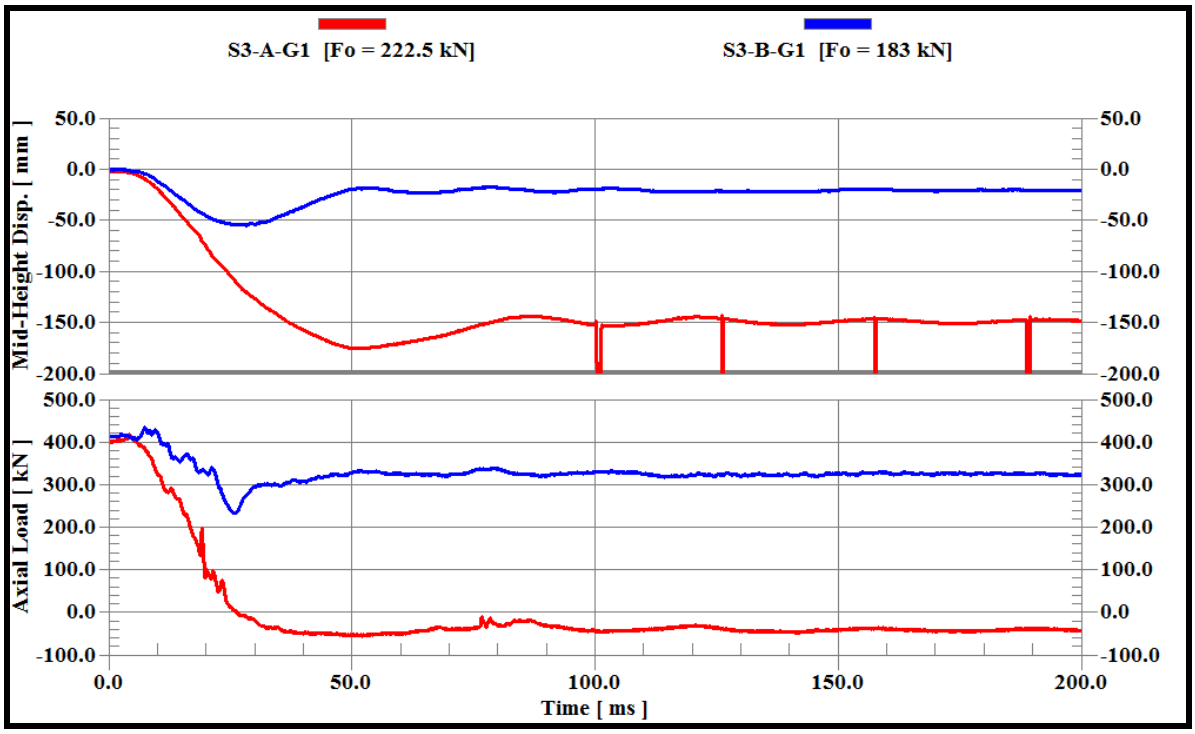

Fig. 4.95 Mid-height deflection and axial load time history for S3-A-G1 and S3-B-G1

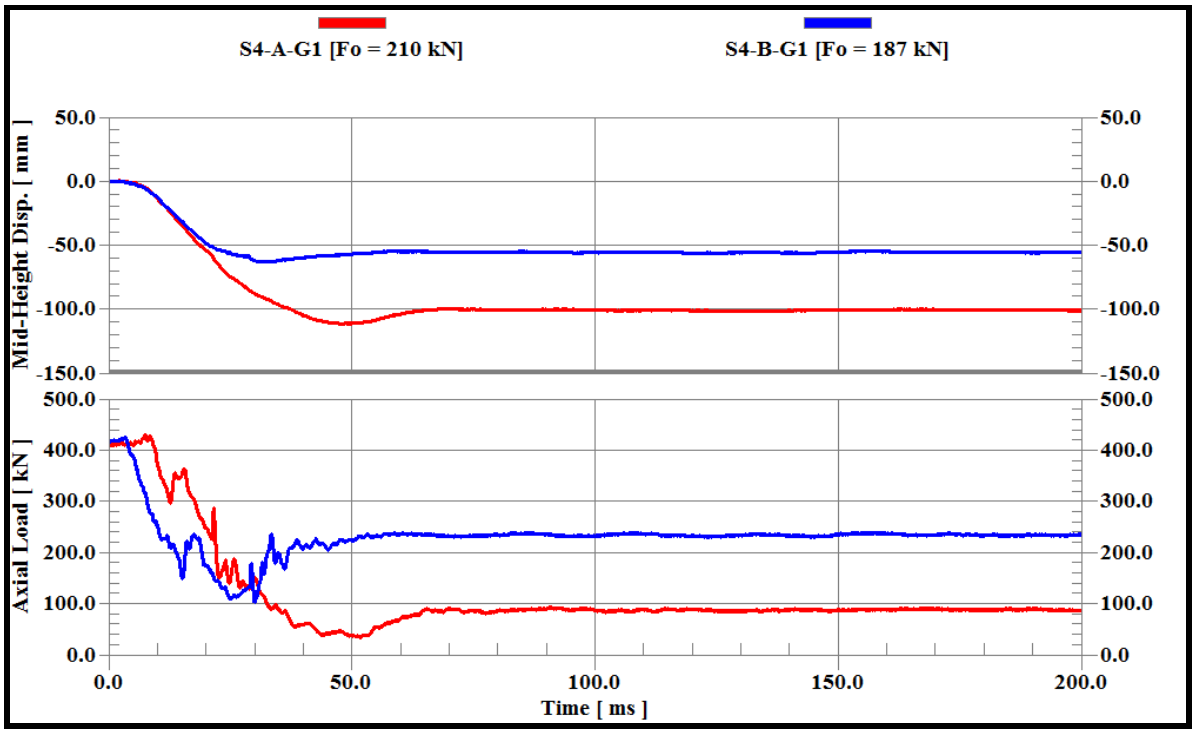

Fig. 4.96 Mid-height deflection and axial load time history for S4-A-G1 and S4-B-G1

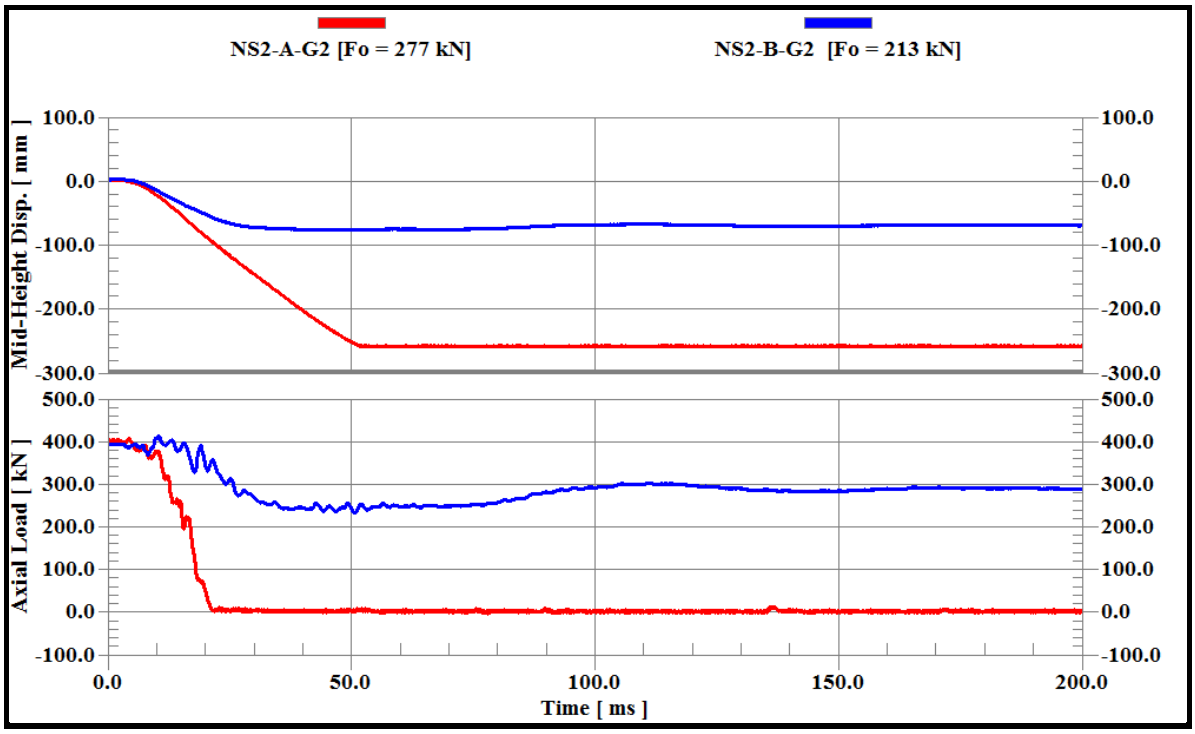

Fig. 4.97 Mid-height deflection and axial load time history for NS2-A-G2 and NS2-B-G2

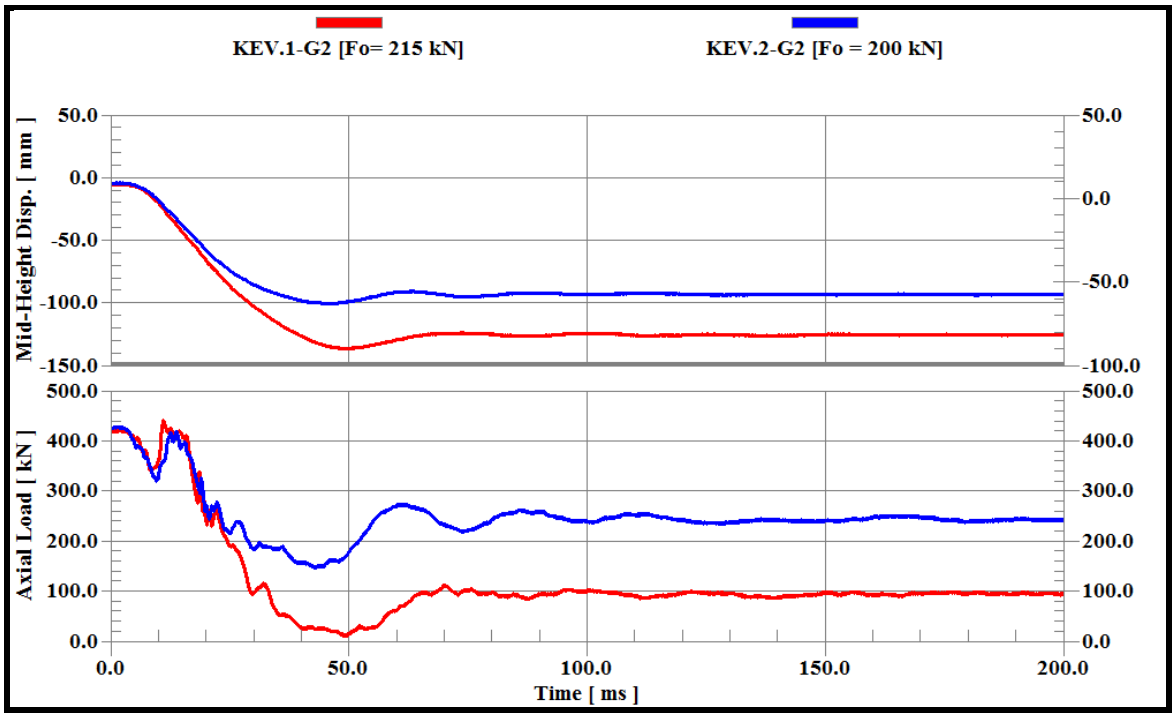

Fig. 4.98 Mid-height deflection and axial load time history for KEV-1 and KEV-2

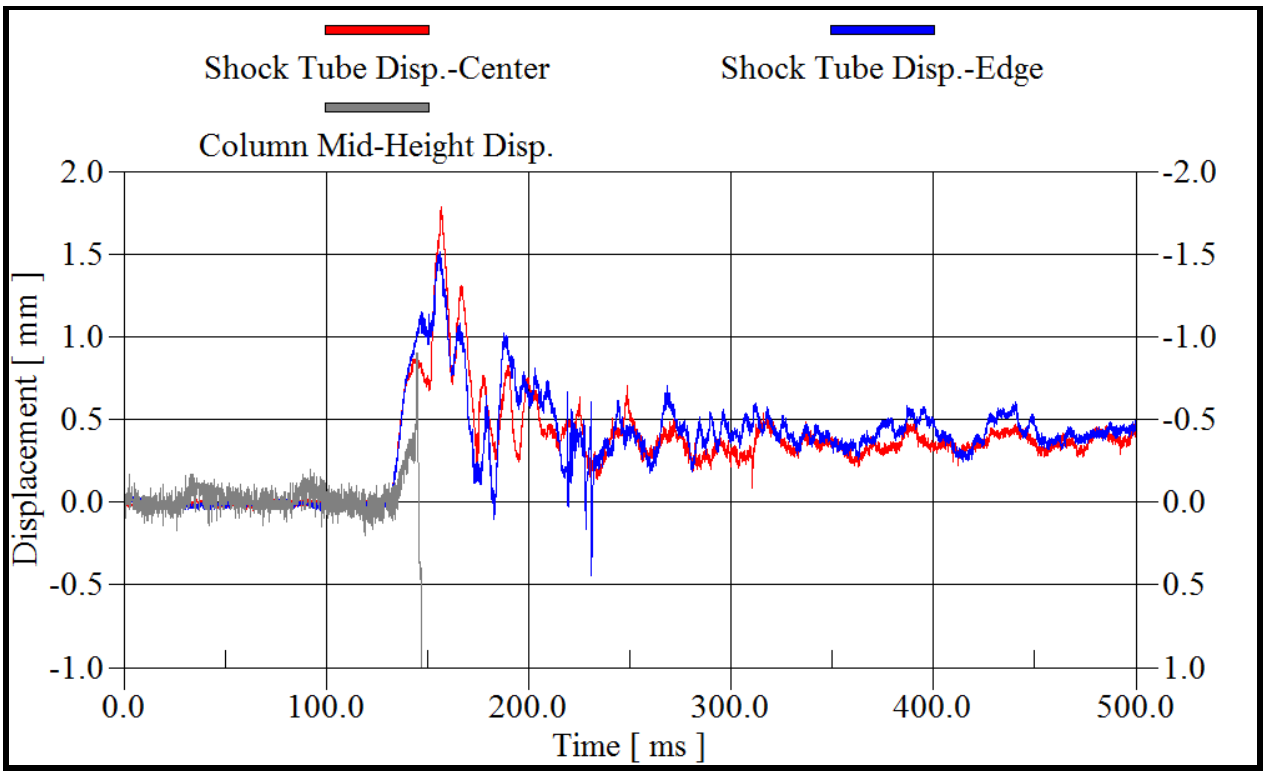

Fig. 4.99 Shock tube displacement-S2-A-G1-Test

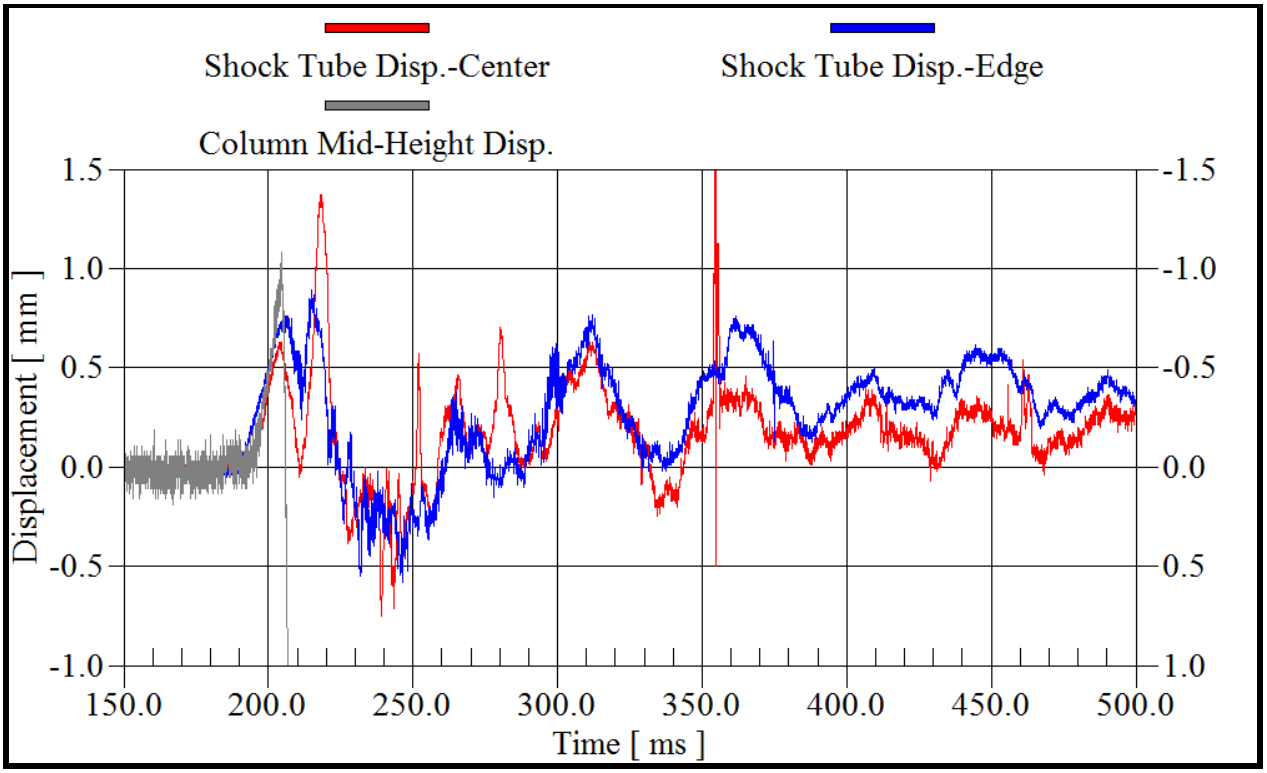

Fig. 4.100 Shock tube displacement-S2-B-G1-Test

Chapter Five

Structural Performance Study

The experimental results of Phase-I and Phase-II, presented in Chapter 4, are assessed in this chapter to establish the effects of the test parameters. The assessment of Phase-I test results reveals the effect of single versus multiple blast shots on the dynamic behaviour of as-built RC columns, with and without the application of pre-blast axial loads. The assessment of Phase-II test results gives the effects of different FRP laminate designs on dynamic response. Experimentally derived resistance functions (load-deformation relationships), plastic hinge lengths, and post-blast axial load capacity of seismically detailed and non-seismic columns are established. The influence of concrete compressive strength on blast performance of columns is also evaluated. The dynamic resistance-displacement relationships of test columns are generated and compared with corresponding static relationships. Finally, the dynamic reaction forces generated from experimental data are compared with corresponding theoretical values.

5.1 Structural Performance of RC Columns in Phase-I Test Program

5.1.1 Performance of RC members under single and multiple blast effects

The effect of single versus multiple applications of blast shots on dynamic response of columns is presented in this section. This was essential to establish the blast shock load protocol used in Phase II tests.

Fig. 5.1 compares the mid-height displacements of Columns S2-AL0, S3-AL0, and S4-AL0. Column S2-AL0 was subjected to multiple blast loads while Column S3-AL0 and Column S4-AL0 were tested under single blast shots. The reported peak blast forces applied were 151 kN, 152 kN, and 164 kN for Columns S2-AL0, S3-AL0, and S4-AL0, respectively (Table-4.1). No pre-blast axial load was applied on these columns.

It can be noticed that the accumulated residual mid-height displacement produced by the last blast shot applied on Column S2-AL0 is 110.3 % larger than the residual mid-height displacement of Column S3-AL0, and 59.65 % larger than the residual mid-height displacement of Column S4-AL0.

Similarly, the structural performance of columns with pre-blast axial load is also compared under single and multiple blast shots. The last blast shot applied on Column S2-AL400 and the single blast shot applied on Column S3-AL400 were equal to 203.5 kN. It can be seen in Fig. 5.2 that the residual mid-height displacement of Column S2-AL400 was 14.2 % larger than the residual mid-height displacement of Column S3-AL400.

The above comparison suggests that columns experience lower lateral displacements at column mid-height when exposed to single shots compared to those under multiple shots. This is due to the repeated yielding and successive degradation of materials used when several shots are applied. It was also observed that the damage in critical regions of test specimens was more severe under multiple shots. The axially loaded columns exhibited reduced effects of multiple shots relative to those under zero axial load. This can be explained by the improvements attained in flexural and diagonal tension capacities by the presence of axial compression.

5.1.2 Blast performance of RC members with and without the application of axial load

The columns were tested either under zero axial load or under 400 kN of axial compression. The axial load was applied by two hydraulic jacks as described in Chapter 3, and the oil pressure in the system was kept constant. When the lateral shock wave was applied, the columns developed lateral displacements, and experienced large support rotations, which resulted in the axial shortening of columns. This in turn caused an extension of the stroke of the jack that applied axial compression with an instantaneous drop in the hydraulic pressure. Thus, the axial force dropped to lower values. This setup is believed to represent the loading mechanism for a column of a typical multi-storey building subjected to far field blast. The self-weight and service gravity loads applied on the column are under gravitational acceleration. When subjected to blast shock waves with extremely high accelerations, the gravitational load cannot follow the sudden change in column deformation at the same rate, resulting in the loss of axial load instantaneously, which is expected to recover significantly after the blast, depending on the remaining integrity and continuity with the attached members. The drop in axial compression is proportional to the

increase in lateral displacement. On the other hand, the second order effects of axial load (or P-Δ effect) become more significant as displacements increase. However, the axial load drop slows down the increase in the P-Δ effect. While the significance of this phenomenon depends on the continuity and redundancy that exist in the framing system, a drop in column axial load is expected to occur momentarily during response to blast loads.

Fig. 5.3 compares the mid-height displacements of Columns S4-AL0, S3-AL400, and S4-AL400. All columns were tested under single blast shots. No pre-blast axial load was applied on S4-AL0, whereas Columns S3-AL400 and S4-AL400 were axially loaded to 389 kN and 409.7 kN, respectively. The blast forces applied to S4-AL0, S3-AL400, and S4-AL400 were 164 kN, 203.5 kN, and 207 kN, respectively. Fig. 5.3 shows that the maximum and residual mid-height displacements of Column S3-AL400 are noticeably higher than the corresponding displacements of S4-AL400, though the blast forces applied on the columns were very similar. This is predominantly due to the fact that the initial axial load applied on S4-AL400 is larger than that applied on S3-AL400. In the same figure, it can be seen that the maximum mid-height displacement of Column S4-AL0 and Column S4-AL400 are equal, although the latter column was subjected to a blast load that is 26 % higher than that for the former column.

The resistance-displacement functions for S3-AL0 and S4-AL400 were generated from experimental data. The strains at column mid-span at different levels of mid-height displacements were used for this purpose. The recorded strains are shown in Figs. 5.4 and 5.5. Column yield moment and maximum moment capacity were computed through sectional analysis using the strain values recorded. This resulted in the lateral force-lateral displacement relationship by connecting the two computed points with smooth curves. The resulting resistance function is shown in Fig. 5.6. Column S4-AL400 with axial compression exhibited 98% higher resistance than that for Column S3-AL0 without any axial compression. The increased resistance can be attributed to the enhanced flexural capacity, as well as the activation of the concrete confinement mechanism under axial load, with more concrete in the compression zone.

5.1.3 Conclusions of Phase-I tests

The results of Phase-I columns, presented in the above sections, indicate that multiple shots with incrementally increasing pressures resulted in increased strength and stiffness decay in columns, in comparison with a single shot having the same maximum level of pressure. There was a clear

effect of the loading history. Therefore, it was decided that it would be more appropriate to conduct the Phase-II tests using a single shot at a pre-determined pressure level to simulate a single blast effect on columns. The use of single shot becomes important in Phase-II where the effects of multiple shots on CFRP laminate design, in term of microcracking, deterioration of steel-concrete bond strength, and FRP interlaminar shear damage, are avoided. Furthermore, it was observed in Phase I tests that the presence of axial compression increased flexural strength and played an important role on column behaviour. Therefore, it was also decided to conduct the Phase-II tests under an appropriate level of initial axial load, and monitor the change in axial load during response. This would help establish the effects of flexure-axial load interaction on column response.

5.2 Effects of CFRP Design on Dynamic Response of Non-Seismic Columns

5.2.1 Group G1

Columns NS1-A-G1(as-built), NS2-A-G1(UD[0˚/90˚/0˚]W[±45˚]$_2$), NS3-A-G1(W[0˚/90˚]$_2$ W[±45˚]$_2$UD[0˚]), NS4-A-G1 (W[0˚/90˚]$_2$W[±45˚]$_2$) and NS5-G1 (UD[0_2/90_2/0]) were subjected to blast loads of 200 kN, 200 kN, 204 kN, 190.4 kN and 185 kN, respectively. Since these columns were tested under almost the same blast load, the comparison of their mid-height displacements would indicate the effects of different laminate designs on column response. This comparison is made in Fig. 5.7. The figure clearly shows that Columns NS2-A-G1 and NS5-G1 provided the best performance and their dynamic behaviours were nearly alike, though Column NS2-A-G1 was subjected to a blast pressure 7.45 % higher than that for Column NS5-G1. In the same figure, it is depicted that Columns NS3-A-G1 and NS4-A-G1 experienced relatively high maximum and residual mid-height deflections, and their structural performance was not significantly enhanced by the CFRP protection.

Another comparison was conducted between Columns NS3-B-G1 and NS4-A-G1 in Fig. 5.8. Column NS3-B-G1 was wrapped by W [0˚/90˚] $_2$ W [±45˚] $_2$ UD [0˚] CFRP laminate, whereas Column NS4-A-G1 was wrapped with W [0˚/90˚] $_2$ W [±45˚] $_2$. The difference was the absence of the last UD [0˚] ply in the hoop direction on Column NS4-A-G1. The rest of the plies were identical for both columns. Fig. 5.8 compares the time history of mid-height response and axial load for the two columns. They were subjected to blast pressures of nearly the same magnitude. Both columns suffered permanent damage at the end of the test and the extra unidirectional layer

added in the hoop direction had a negligible effect. It did affect, however the CFRP rupture pattern, developing a rupture that was parallel to the hoop direction (see Fig. 4.41), unlike the CFRP rupture of NS4-A-G1, which was initiated horizontally on the column tension side before it propagated towards the sides with an angle close to 90˚, parallel to the column longitudinal axis (see Fig. 4.43).

The reduced maximum and residual mid-height displacements of Column NS3-B-G1 is due to the lower blast load applied rather than the extra CFRP layer added (the reflected impulse over the positive phase of 437.5 kPa.ms for Column NS3-B-G1 versus 471.5 kPa.ms for Column NS4-A-G).

5.2.2 Group G2

The time history of mid-height displacement and axial load for Columns NS1-G2 (as-built), NS2-B-G2 (W $[0^{\circ}/90^{\circ}]_2$ W $[\pm 45^{\circ}]_2$ UD $[0^{\circ}]$) and Kev.2-G2 are compared in Fig. 5.9. It can be observed that all three columns suffered very high permanent deflections. The highest blast load was applied on Columns NS2-B-G2; nevertheless, Column NS2-B-G2 showed the best dynamic performance among the three. Contrary to the expectations, Column Kev.2, despite being wrapped with six plies of various FRP fabrics, showed relatively poor performance. It was noted during the Kevlar layup application that the fabric could not be fully saturated with resin because of the fine knitting of this type of fabric; hence, the inter-lamina bond was not appropriately developed. Furthermore, the location of the overlap at the column mid-height resulted in premature failure of the bond in one of the specimens.

5.3 Effects of CFRP Design Configuration on Dynamic Response of Seismic Columns

The mid-height displacement response of seismic Columns S1-A-G1 (as-built), S2-A-G1 (UD $[0^{\circ}/90^{\circ}]$ W $[\pm 45^{\circ}]_2$), S3-A-G1 (W $[0^{\circ}/90^{\circ}]_2$), S4-A-G1 (W $[0^{\circ}/90^{\circ}]_2$ W $[\pm 45^{\circ}]_2$), and S5-G1 ($[0^{\circ}_2/90^{\circ}_2]$) are compared in Fig. 5.10. It can be seen that Columns S2-A-G1 and S5-G1 showed the best structural behaviour. Given that Column S2-A-G1 was subjected to 4 % higher blast load than Columns S5-G1, it can be concluded that the CFRP laminate used in Column S2-A-G1 provided the best dynamic performance among all the CFRP systems utilized in this comparison.

Preliminary design and coupon tests indicated that Columns S2-G1 and S3-G1 would show comparable blast performance since the CFRP laminate of the latter column was expected to

provide additional tensile force and confinement pressure equivalent to those of the former column. However, the dynamic behaviour of Column S3-A-G1 was unsatisfactory compared to that of Column S2-A-G1. This can be explained by the large in-plane deformation capacity of the woven laminas. In addition, it was observed during the wrapping of W [0˚/90˚] CFRP fabric that it was difficult to align fibers in longitudinal and hoop directions. Inevitably, some deviations in fiber alignment were observed during the application process, potentially resulting in less favourable behaviour.

It was additionally observed that the dynamic behaviour of Column S4-A-G1 under high blast pressure was unsatisfactory. This behaviour was expected based on the results of the coupon tests. The poor performance of Column S4-A-G1 was entirely due to the insufficient number of W [0˚/90˚] plies included in the laminate. Increasing the number of W [0˚/90˚] CFRP plies to six, instead of two, could provide much better outcomes.

The mid-height displacement response of Columns S3-B-G1 and S4-B-G1 are compared in Fig. 5.11. These columns were exposed to an equal level of blast pressure. Column S3-B-G1 was wrapped with four CFRP plies of W [0˚/90˚], whereas S4-B-G1 was wrapped with two W [0˚/90˚] CFRP plies followed by two W [±45˚] plies. It can be observed that Column S3-B-G1 behaved quasi-elastically and showed no sign of damage when subjected to 183 kN blast load. Conversely, Column S4-B-G1 experienced permanent damage associated with a relatively large residual mid-height deflection. The reason for the poor performance of Column S4-B-G1 was the rupture of the laminate at maximum mid-height displacement. This sudden rupture drastically reduced flexural capacity. Thus, the residual mid-height deflection of S4-B-G1 was 170.3 % higher than the mid-height deflection of S3-B-G1. Correspondingly, the residual axial load in S4-B-G1 was 28.2 % lower than that in S3-B-G1.

5.4 Effects of Seismic Detailing on Structural Performance of Columns

In this section, two comparisons are made between seismically and non-seismically detailed columns to explain the influence of increasing the number of lateral steel ties both in as-built and CFRP protected columns. In other words, the only variable explored in this section is the center to center spacing between the internal steel ties. Fig. 5.12 compares the dynamic responses of Columns NS1-B-G1 and S1-B-G1. Both columns were investigated under identical blast pressures. It is noted that the maximum and mid-height deflections observed in S1-B-G1 were

lower than those in NS1-B-G1 by 16.95 % and 5.3 %, respectively. Accordingly, the residual axial load measured in S1-B-G1 was 19.4 times the residual axial load obtained in NS1-B-G1. This comparison clearly illustrates that increasing the number of internal steel ties in columns would slightly enhance structural performance. This enhancement in strength is due to the confinement of the concrete core. This strength enhancement observed is accompanied by an increase in the ductility.

Another comparison is made in Fig. 5.13 between two identical columns; Columns NS4-A-G1 and S4-B-G1. Like the previous comparison, these columns were exposed to a nearly equal blast pressure, and they were both protected by exactly the same CFRP laminated system. The maximum and residual mid-height deflections of S4-B-G1 were smaller than those for NS4-A-G1 by 30.65 % and 37.5 %, respectively.

From the two comparisons given above, it can be concluded that as-built and CFRP retrofitted seismically detailed columns behave better than the companion non-seismically detailed columns. However, the enhancement in blast behaviour was more pronounced in CFRP protected columns. This is due to the dual confinement effects provided by the closely spaced steel ties and the CFRP wrapping.

5.5 Influence of Concrete Strength on Structural Performance of Columns

Concrete used for casting the columns came from two batches. The batch used for Group G1 had compressive strength of 33 MPa, whereas the batch for Group G2 had 44 MPa concrete. The comparisons presented herein include columns with different concrete strengths, but otherwise having identical properties.

Column NS1-G2 and Column NS1-A-G1 are compared in Fig. 5.14. It can be seen that when NS1-G2 with a higher concrete strength was subjected to 191 kN blast force, the maximum and the residual mid-height deflections were 112.6 mm and 98.7 mm, respectively. In comparison, when NS1-A-G1 with a lower concrete strength was exposed to about 200 kN blast force, the maximum and residual mid-height deflections were marginally higher, and equal to 127.4 mm and 112.6 mm, respectively. Residual axial loads were equal for both specimens. The lower displacements observed in NS1-G2 is mostly attributed to the lower blast load applied on this column, rather than the higher concrete strength.

A similar comparison was made between seismically detailed columns with two different concrete compressive strengths in Fig. 5.15. When S1-G2 was subjected to 206.7 kN blast load, maximum and residual mid-height deflections were 108.1 mm and 106.7 mm, respectively. On the other hand, Column S1-A-G1 was loaded with 208 kN blast force. This dynamic load generated a maximum and residual mid-height displacement of 130.4 mm and 120.1 mm, respectively. Once again , the lower deflection attained in S1-G2 is likely due to the lower blast load applied rather than the higher concrete compressive strength.

The influence of the concrete compressive strength on CFRP wrapped columns is investigated in Fig. 5.16. It is shown that Column NS2-B-G2 was tested under a blast force 4.6 % higher than the force applied on NS3-A-G1. Yet, the maximum and residual mid-height displacements of Column NS2-B-G2 were 19.5 % lower than the comparable displacements produced in Column NS3-A-G1. Given that the dimensions, longitudinal reinforcement, steel tie diameter and spacing, and CFRP wrapping are identical for both columns, it can be concluded that increasing concrete strength even moderately (i.e. from 33MPa to 44MPa) can alter the blast response. On the other hand, increasing concrete strength had no significant influence on un-retrofitted columns.

The limited results of this investigation suggest that a further study is warranted for investigating the effect of concrete strength in a wider range of variation of concrete strength both on protected and unprotected columns.

5.6 Dynamic Resistance Functions as Derived from Test Data

The significance of different CFRP laminate designs was investigated by comparing experimentally obtained force-deformation relationships in the form of resistance functions. These resistance functions are labelled as “actual” dynamic resistance functions to differentiate from those generated analytically. The actual resistance functions were obtained from the applied force and the inertia force time histories for each test specimen, assuming the dumping force is very small and negligible. The inertia time history is calculated from the mass and the acceleration, which is the second numerical derivation of the measured displacement.

Two laser sensors were used during the experimental program to monitor time histories of mid-height deflection accurately. This highly sensitive measuring technique, together with the ultra-high speed HBM Genesis data acquisition system (records 10^6 points per second), provided very

precise experimental data. This data made it possible to accurately establish velocity and acceleration time profiles for each test. HBM Catman 6.0 software was used to compute the first and second derivatives of the recorded displacement-time relationship as velocity and acceleration functions, respectively. During the blast event, the velocity (v) at column mid-height is the rate of change in mid-height displacement, as shown in Eq. 5.1. Similarly, the rate of change in velocity at column mid-height gives acceleration (a); this is given by Eq. 5.2.

Fig. B-1 to Fig. B-19 in Appendix B, show the velocity and acceleration time histories for most of the columns tested. Then, the time history of the actual dynamic resistance (R_t) for the columns was computed from the equation of motion, shown in its simplest form in Eq. 5.3. Knowing, the applied blast force (F_t) and the inertia force (IF_t), it was a straightforward process to compute the resistance profile. The actual blast force applied was obtained by multiplying the peak reflected pressure by the area of the load application device at the end of the shock tube, which is an area of 2 m by 2.2 m. The peak reflected pressure was estimated with an acceptable accuracy by dividing the maximum value of the measured positive impulse by 0.5 t_d. It was assumed that the reflected pressure decayed linearly from its peak value to zero within a time equal to t_d. Similarly, the inertia force function was found by multiplying the equivalent total mass by the acceleration time history (a_t) generated earlier. The equivalent total mass in this study was the mass (weight of the column plus the weight of the load transfer system) multiplied by an appropriate mass factor (K_{LM}). This factor varied based on the damage level observed. For a simply supported system this factor is equal to 0.78 in the elastic range, and 0.66 in the inelastic range (Biggs 1964). The mass (M) was 400 kg.

$$v = \frac{\Delta x}{\Delta t} = \frac{x_{i+1} - x_i}{t_{i+1} - t_i} \tag{5.1}$$

$$a = \frac{\Delta v}{\Delta t} = \frac{v_{i+1} - v_i}{t_{i+1} - t_i} \tag{5.2}$$

$$F_t = K_{LM} M a_t + R_t \quad (5.3)$$

Figs. C-1 through C-19 in Appendix C illustrate graphically the application of equation of motion and the generation of resistance time histories for 21 columns. In all these figures the difference between the applied force-time history and the inertia force-time history give the actual dynamic resistance-time history function. The readings of Strain Gauge T-3 (strain gauge attached to the tension steel at column's mid-height) are also displayed in these figures to denote yield force and maximum column capacity.

The actual dynamic resistance-displacement curves were also established because of its use in the analysis of equivalent single degree of freedom (SDOF) system. Appendix D, Fig. D-1 through D-19 describe the actual dynamic resistance-displacement relationships combined with the strain profile measured by Strain Gauge T-3 for all the columns tested in this investigation.

Representative resistance functions were produced for columns that experienced large deformations and permanent deformations to demonstrate complete resistance curves. Fig. 5.17 and Fig. 5.18 show the resistance-displacement curves for NS4-G1 and S2-G1 pairs of columns, respectively. Columns NS4-A-G1 and N4-B-G1 were subjected to blast forces of 190.4 kN and 174.5 kN, respectively; and Columns S2-A-G1 and S2-B-G1 were subjected to 221 kN and 232 kN, respectively. The curves indicate that the resistance of NS4-B-G1 and S2-A-G1 increased almost linearly from zero to the yield displacement. Beyond this point, the resistance remained constant while the displacement continued to increase to its maximum limit. However, just before approaching this limit, the resistance curve bounced back with a slope nearly parallel to the initial elastic portion of the resistance curve. On the other hand, the resistance curve of NS4-A-G1 and S2-B-G1 dropped down shortly after passing the yield limit. This is because the blast load applied was higher than the member capacity. This higher load resulted in the rupture of the CFRP protection system at the instant when the mid-height displacement was reached. This rupture dramatically reduced the resistance of the tested specimen.

5.6.1 Effects of CFRP laminate design on non-seismic columns

The resistance functions for non-seismic columns are compared in Fig. 5.19. It can be seen that Columns NS2, NS3 and NS4 developed approximately the same resistance with a maximum

value ranging approximately between 180 and 185 kN. Column NS5 had the highest force resistance of about 220 kN and Column NS1 had the lowest resistance. This observation can be explained by NS5 having the highest longitudinal fibre content, whereas NS1 not having any FRP protection system. Columns that have ± 45 degree fibres generally showed ductile behaviour (NS2, NS3 and NS4). However, Column NS3 was subjected to somewhat higher lateral pressure, which resulted in the rupturing of fibres and consequent failure as evidenced by the development of large permanent deflection. The presence of ± 45 degree fibres controlled inelastic deformations and helped columns recover a significant portion of their inelastic displacements. This is evident in Fig. 5.19, which shows about 20 mm residual deflection for these columns at the end of the test. Similar behaviour was also observed in Column NS5, which had sufficiently high unidirectional fibres, which prevented premature failure of the column, resulting in reduced residual displacement. Among the columns with ± 45 degree fibres, Column NS2 had the highest ductility, maintaining its force resistance up to about 55 mm before it re-bounced back to 20 mm of permanent displacement. This can be attributed to the superior laminate design which consisted of a combination of unidirectional and inclined fibres.

5.6.2 Effects of CFRP laminate design on seismic columns

The resistance functions of seismically detailed Columns S1-G1 through S5-G1 are compared in Fig. 5.20. The findings of this comparison resemble to those of the previous comparison for non-seismically detailed columns. Fig. 5.20 depicts that while all FRP protected columns showed about the same force resistance, Column S2-G1 exhibited significantly improved ductility, with maximum displacement reaching as high as 75 mm before it recovered back to approximately 35 mm. This performance singled out the FRP laminate design used in this column to be the best among all the others considered.

5.6.3 Seismic versus non-seismic columns

Seismic columns were compared against non-seismic columns of the same protective systems to assess the significance of seismic detailing on strength and deformability. Fig. 5.21 compares the resistance functions of Columns NS1-G1 and S1-G1. The results indicate 33% higher resistance in Column S1-G1 shortly after the initial yield point. This enhancement can be attributed to the confining effects provided by the closely spaced steel ties inside the Column. However, the overall behaviour of the two columns was similar.

The non-seismic CFRP protected columns tested were wrapped by five CFRP plies, except for Column NS4-G1, while the seismic columns were wrapped by four CFRP plies. The additional ply in non-seismic columns had unidirectional fibres in the hoop direction. It was initially believed that adding an extra ply of CFRP lamina would substitute for the lack of proper confinement in non-seismic columns.

Figs. 5.22 to 5.24 show the comparisons of companion non-seismic and seismic columns. They indicate that column behaviour is not affected significantly by the presence of closely spaced interior steel ties provided in seismic columns. Fig. 5.22, shows enhanced confinement in Column S2-G1, because of high inelastic displacements developed. However, this is attributed to 11% higher blast pressure applied on this column, which increased maximum displacement, but also resulted in a higher residual deformation. Similar effect can be observed in Fig. 5.24, where Column S5-G1 was subjected to 15 % higher blast pressure than Column NS5-G1.

The above comparisons indicate that the resistance of CFRP protected non-seismic columns can be improved to the level observed in CFRP protected seismic columns by adding an extra CFRP layer in the hoop direction. This additional unidirectional layer is believed to offset the absence of sufficient internal confinement in non-seismic columns.

In all cases, the jacketing of columns with CFRP fabrics improved overall column performance significantly. Columns NS2-G1 and S2-G1 showed the best performance in terms of ductility enhancement. This can be explained by the use of unidirectional fibers oriented in the longitudinal and hoop directions in combination with cross ply woven-angled fibers. This laminate lay-up ensured both strength and ductility enhancements. It can be concluded that the laminas with unidirectional fibers contributed more to the strength, whereas the laminas with woven-angular fibers contributed more to the ductility enhancement. The stresses applied on the CFRP laminate is transferred between different laminas by the inter-laminar shear resistance. The stresses applied on a lamina with woven-angular fibers are resisted by two mechanisms: (i) stretching of the woven fabric where variable stress components are applied in the direction of the fibers; and (ii) planer rotation of the fibers into the principal stress direction. This stress redistribution mechanism, which is not developed in the unidirectional laminas, enables the smoothening of the stresses and holds them below the rupture levels, resulting in larger deformation capacities. Generally, in blast resistant structural members, ductility is more

important than strength. When concrete components possess the required ductility, they have the ability to dissipate higher shock energy.

The second best resistance function was offered by the CFRP laminate installed on column NS5-G1 and Column S5-G1. It was obvious that the strength was improved while the ductility was not as significant as that of Columns NS2-G1 and S2-G2. This is because of the brittle and explosive failures associated with the CFRP systems containing only unidirectional fibers.

The CFRP laminate fabricated by combining woven [0˚/90˚] and woven [±45˚] showed less improvement than the two other laminate types mentioned above. This is because the strength provided by the woven [0˚/90˚] fabric was not equivalent to the strength offered by the unidirectional fabric for two reasons: (i) the amount of the fibers in the woven fabric was less than that in the unidirectional fabric as discussed earlier; and (ii) the woven fabric had less stiffness because of its larger extension capacity without developing higher stresses in the fibers.

5.7 Static versus Dynamic Loading

The actual blast resistance curves of the seismically detailed columns of the current investigation were compared with the corresponding resistance curves produced by static tests under the same loading and boundary conditions. Nine seismically detailed columns, identical to those tested in the present study, were tested statically at the NRC-Construction Structures Laboratory by Hasak (2015). NRC developed a Blast Emulator testing system, which was designed and built to apply uniformly distributed load along the length of an axially loaded column. For the purpose of the comparison, the columns of the current study will be referred as S-Blast while the columns of the static test will be referred as S-QS (for quasi-static loading).

Figs. 5.25 through 5.33 compare static and blast load-displacement curves, as well as the photographs taken at the end of each test. It can be seen that the curves produced by the two loading types are nearly alike, with dynamic blast loads showing marginally higher resistance in most cases. This can be attributed to high strain rates under blast loads and associated increase in material strength. The strain profile measured by Strain Gauge T-3 in each column was also shown in the figures displaying the effect of the strain rate on the yield strain of longitudinal tension reinforcement. The column failure modes shown in the photographs of Figs. 5.26, 5.28, 5.30 and 5.32 show almost identical damage patterns under dynamic and static loads.

5.8 Recorded versus Computed Dynamic Reactions

Column reactions were measured during dynamic blast testing of 12 columns. The average of reactions measured at the top and bottom supports are compared with computed dynamic reactions. The computed reactions (V) were obtained by Eq. 5.4. This equation was first proposed by Biggs (1964) for theoretical estimation of dynamic reaction force for shear design purposes, as well as for the design of the supporting structures.

$$V = c_1 F_t + c_2 R_t \tag{5.4}$$

where,

F_t, and R_t are time varying applied force and column resistance, respectively.

c_1 = 0.38 and 0.39 for elastic and plastic behaviour respectively, and

c_2= 0.12 and 0.11 for elastic and plastic behaviour respectively.

Figs. 5.34 to 5.45 show the time history of applied force, experimentally recorded (actual) resistance force, and experimentally recorded and computed (by Eq. 5.4) dynamic reactions. It is generally observed that up to the member yield, the actual dynamic reaction matches the dynamic reaction computed by Eq. 5.4. However, after yielding, the actual dynamic reaction curve falls down faster than the calculated curve. This is mostly because Eq. 5.4 was based on the assumption that the post yield portion of the resistance curve is flat up to the failure, while in fact the post yield resistance increases due to the strain hardening of tension reinforcement. This development in strength continues until the maximum capacity of the structural member is reached. Subsequently the resistance curve drops owing to the complete failure of the column.

In design, one may only be interested in the maximum value of dynamic reactions. For this reason, Eq. 5.4 proves to be a powerful tool to accurately estimate the value of lateral dynamic reaction initiated at the ends of columns under blast loads.

With less accuracy, the same equation can still be used to predict the entire resistance curve when the reaction forces at the supports and the applied force are given.

5.9 Effect of FRP Laminate Design on Plastic Hinge Length

In RC columns exposed to catastrophic events (e.g., significant earthquake, significant blast or impact) plastic hinges form at maximum moment regions where the most damage occurs. Plastic hinge length (L_p) can be defined as the virtual length over which the plastic curvature is assumed to be constant (Fig. 5.46) (Park and Paulay 1975). The rotation over a cantilever RC member can be computed by integrating curvatures along the member length if L_p is known, from which the tip displacement can be computed; and vice versa. For this reason it is essential to predict the plastic hinge length with acceptable accuracy since it is a key step in correlating the section-level response to the member level response of a concrete column (Bae and Bayrak 2008). Indeed, the plasticity spreads over a larger physical length, referred to as the yield length (L_y). This is shown in Fig. 5.46. The yield length is the distance between the critical section and the location where the tension steel reaches its yield stress (Kheyroddin and Naderpour 2007). The yield length is believed to be related to the plastic hinge length (Zaho et al. 2012). Hence, the plastic hinge can be expressed as $L_p = \beta L_y$, where β is a dimensionless reduction factor for the curvature distribution near the support and it is always smaller than 1.0 (Mortezaei and Ronagh 2012).

While a large number of studies were carried out to estimate the plastic hinge length formed in un-retrofitted RC beams and columns subjected to monotonic or cyclic loading, only a very limited number of studies were conducted to investigate the plastic hinge formation mechanism in FRP jacketed RC columns (Mortezaei and Ronagh 2012, Gu et al. 2012, Jiang et al. 2014). To the knowledge of the author of the present study, no experimental investigation has been conducted so far to compute the plastic hinge length of RC concrete elements exposed to blast effects despite the importance of this parameter in establishing the resistance function. This function in turn is essential in obtaining the blast response of the member using SDOF solution.

The plastic hinge length was established using experimental results. These include measured column mid-height displacements, experimentally established actual column resistance functions, and the longitudinal reinforcement tension profiles.

The variation of tensile strains in column longitudinal reinforcement along the height is shown in Figs. 5.47 through 5.55 for Group 1 Columns. The columns selected for the presentation of strain measurements are those that had strain gauges that survived tests until the attainment of large deformations. The value of the yielding strain at T-3 was also identified for each test specimen.

Note that the yielding strain detected was always higher than 0.0025 (static yield strain) due to the rapid nature of the applied force. The yield length was measured by plotting a horizontal line that intersects the strain profile. The height of this line on the y-axis is equal to the dynamic yielding strain for each test. The length of the line along the column height is equal to the yielding length.

Given that Δ_y (yield displacement) and Δ_u (ultimate displacement) were measured experimentally, $\emptyset_y$ (yield curvature) can be computed using the following equation:

$$\Delta_y = \frac{1}{3}\emptyset_y L^2 \tag{5.5}$$

The ultimate curvature $(\emptyset_u)$ is obtained by the second moment-area theorem of the actual (measured) curvature diagram

$$\Delta = \int_0^L \emptyset_x x dx \tag{5.6}$$

Finally the plastic hinge length of the column is calculated using the following expression for L_p

$$\Delta_u = \frac{1}{3}\emptyset_y L^2 + (\emptyset_u - \emptyset_y)L_p(L - 0.5L_p) \tag{5.7}$$

where, L is the total height of the column.

In the plastic hinge analysis of this study, Δ_y is the column mid-height displacement at the onset of yielding in the tension rebars, and Δ_u is the displacement at which 20 % drop in the maximum lateral load is observed beyond the peak load resistance. Table 5.1 summarizes the plastic hinge length results of selected columns.

Figs. 5.47 to 5.55 and Table 5.1 show the effect of different FRP wrapping on yield length (L_y) and plastic hinge length (L_p). The shortest L_y and L_p lengths were observed in the as-built Un-retrofitted) columns, although as-built seismic columns had relatively longer yielding and plastic

hinge lengths than the as-built non-seismic columns. In contrast, the longest yielding length was observed in Columns NS2, NS3 and S2. The CFRP wrapping system of these columns includes ±45˚ woven CFRP fabric. Columns wrapped with unidirectional fibers only, (e.g., columns NS5 and S5) had shorter yielding lengths than the other CFRP wrapped columns.

The above comparisons show that columns retrofitted with FRP laminate containing woven ±45˚ CFRP fabrics developed longer yield lengths than those that had unidirectional fabrics only when subjected to the same blast loads. In other words, including the woven ±45˚ CFRP fabric in CFRP laminate improved the ductility of the column.

5.10 Effect of CFRP Laminate Design on Columns Post-Blast Axial Capacity

The post-blast axial capacity of selected CFRP protected columns were investigated in the experimental program. Columns tested for residual axial capacity are those that did not experience large residual lateral displacements, and also did not have any visible damage after the blast test.

Fig. 5.56 compares post-blast axial capacities of Columns NS2-B-G1, NS5-G1, S2-A-G1, S3-B-G1, S4-B-G1, and S5-G1. It is important to mention that the residual axial loads were released prior to the application of the post-blast axial loads. These columns were previously subjected to blast effects of varied magnitudes. Hence, the maximum and residual mid-height displacements and the residual axial loads applied were not the same as those attained at the end of the blast test.

It can be seen in Fig. 5.56 that the columns wrapped with CFRP protection systems containing [±45˚] woven fabrics showed more ductile behaviour than those that contained uniaxial fibres. Columns wrapped only with unidirectional or woven [0˚/90˚] fabrics failed abruptly after yielding, whereas the others sustained the applied axial load for relatively high post-yield mid-height displacements.

The highest post-blast axial capacity of 884 kN was recorded in Column NS5-G1. The multi-layer CFRP laminate bonded to this column contained three plies of unidirectional CFRP running in the hoop direction. Therefore, this column was expected to have the highest axial capacity. The next highest post blast axial capacity was offered by Column NS2-B-G1. The recorded post-blast axial capacity for this column was 865 kN. Although, the post-blast axial

capacity of Column NS5-G1 was slightly higher than the capacity of Column NS2-B, the overall axial behaviour of Column NS2-B-G1 was more ductile than Column NS5-G1. Furthermore, Column NS5-G1 was exposed to a blast load that was 11 % smaller than the corresponding load applied to Column NS2-B-G1. It can be concluded that, as in the case of columns subjected to blast pressures, columns tested under monotonically increasing axial compression showed a ductile failure mode when the FRP jacket included fibres oriented in $\pm 45^{\circ}$ orientation.

For the reasons mentioned above, the UD [0˚/90˚] W [$\pm 45^{\circ}_2$] UD [0˚] CFRP laminate applied to Columns NS2-G1 provided the best post-blast axial capacity and response among the columns protected. Column S2-A-G1 had a post-blast axial capacity equal to 582 kN and this was the lowest axial capacity among the columns examined. This is because Column S2-A-G1 was exposed to the worst blast scenario compared to the other columns. The maximum and residual mid-height blast displacements of this column were 81 mm and 38.5 mm, respectively. None of the other columns in Fig. 5.56 experienced such high blast displacements. Despite the relatively low post-blast axial capacity of Column S2-A-G1, this capacity was higher than the initial design axial load capacity of the column.

Table-5.1: Computed plastic hinge lengths of selected columns

Column	L_y (mm)	Δ_y (mm)	Δ_u (mm)	$\emptyset_y$ (1/mm)	$\emptyset_u$ (1/mm)	L_p (mm)
NS1	180	26.7	65	3.3×10^{-5}	0.000216	99.6
NS2	270	27.7	55.3	3.4×10^{-5}	0.000137	171.5
NS3	260	28.6	55.6	3.55×10^{-5}	0.000115	166.3
NS5	225	22.7	44.7	2.8×10^{-5}	0.000105	138
S1	210	22.65	60	2.8×10^{-5}	0.000183	116
S2	265	28.8	61.9	3.566×10^{-5}	0.000136	161.2
S3	240	27.7	49.3	3.433×10^{-5}	0.0001007	159.7
S5	230	31.4	56	2.78×10^{-5}	0.000114	137.6

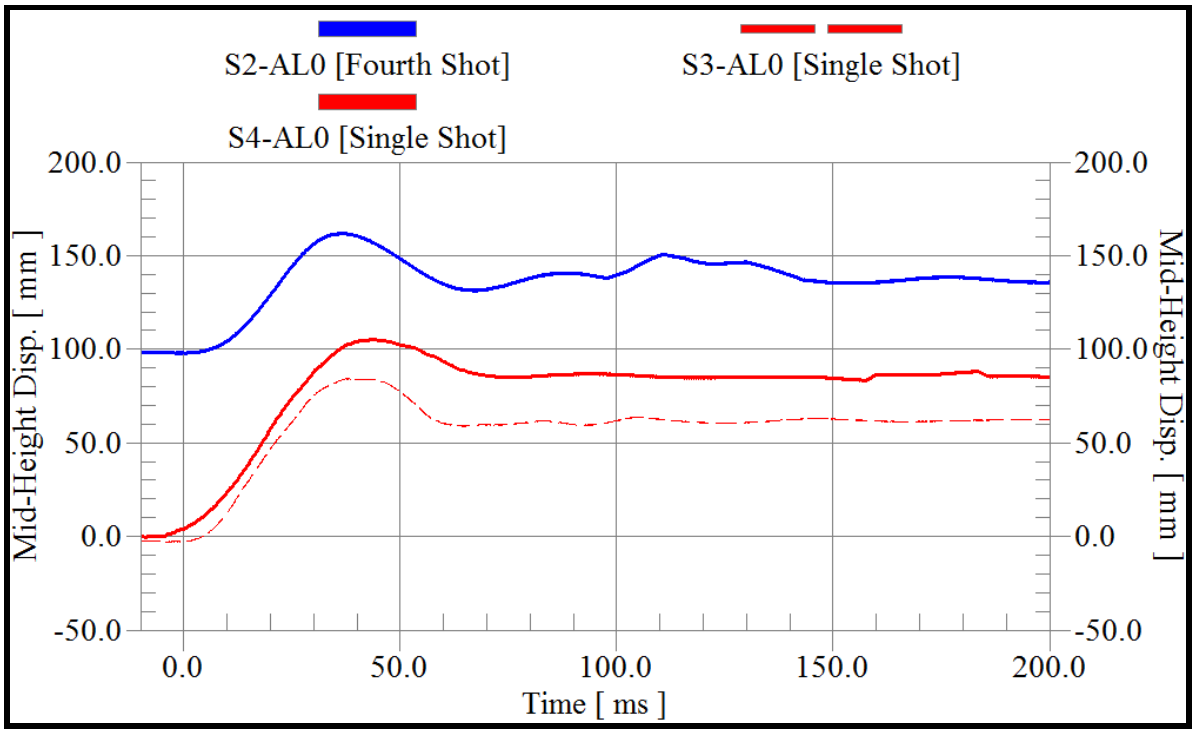

Fig. 5.1 Displacement-time history of S2-AL0 (4th shot), S3-AL0, and S4-AL0

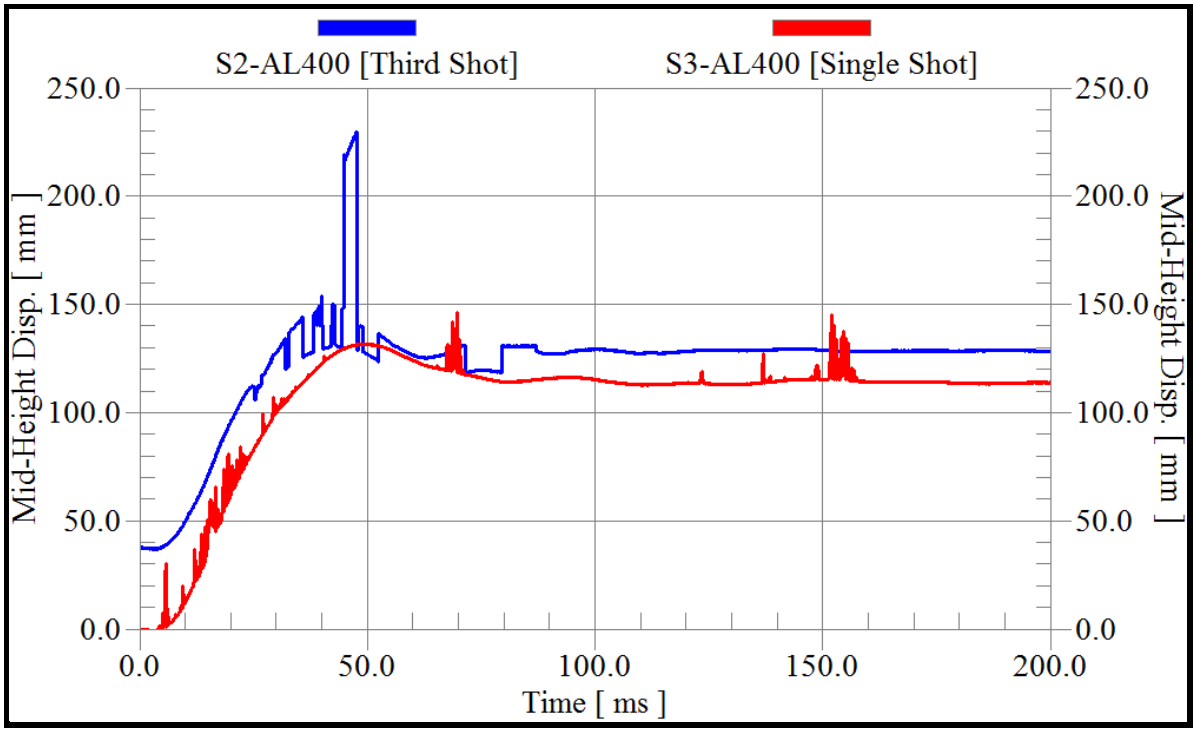

Fig. 5.2 Displacement-time history of S2-AL400 (3rd shot), and S3-AL400

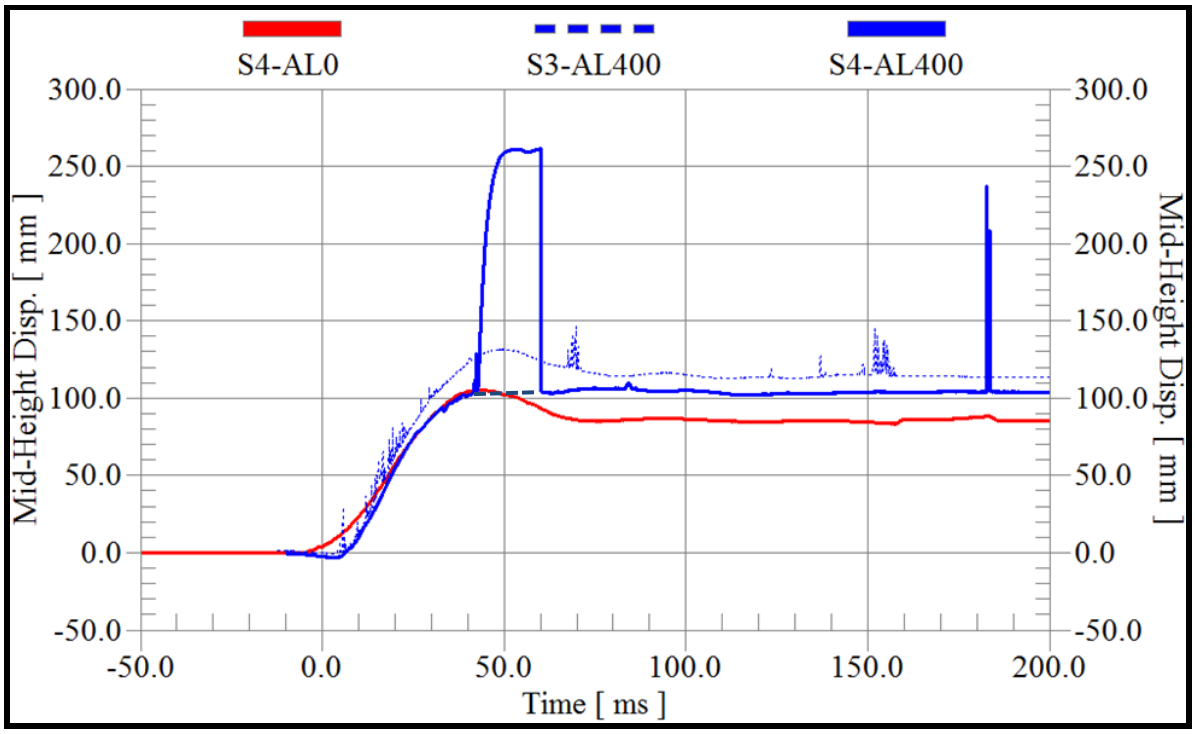

Fig. 5.3 Displacement-time history of S4-AL0, S3-AL400, and S3-AL400

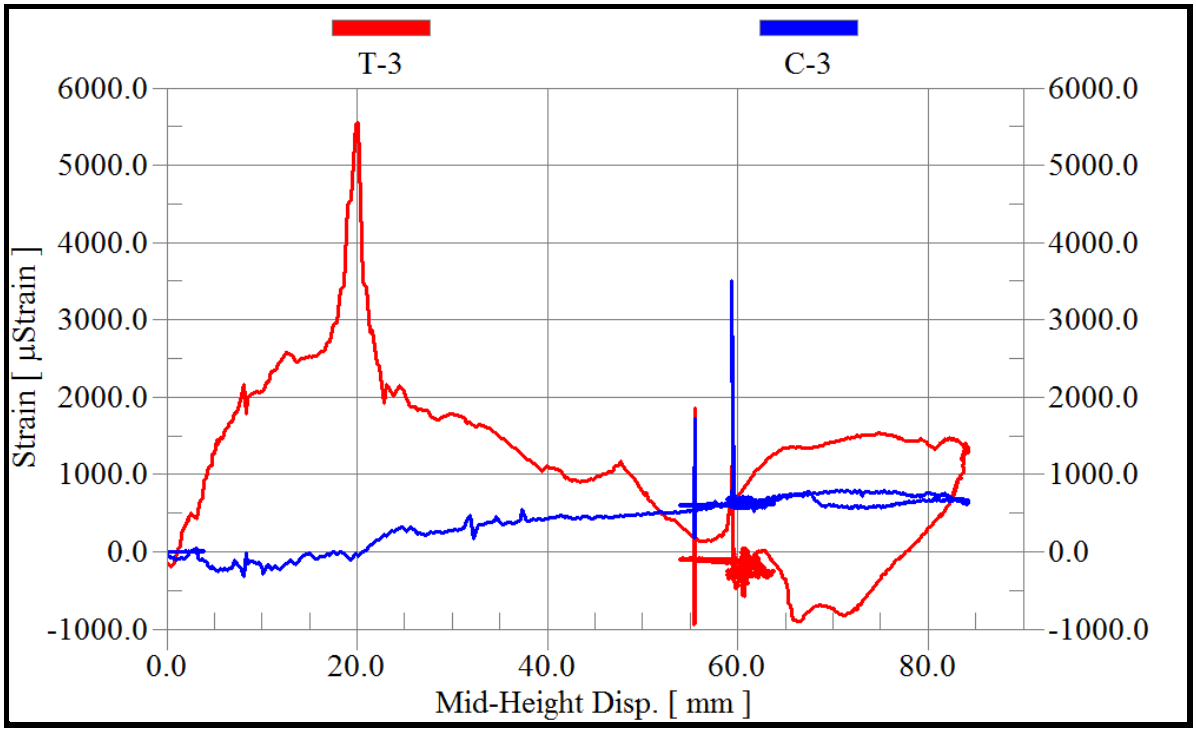

Fig. 5.4 Strains at mid-span vs. mid-height displacement for S3-AL0

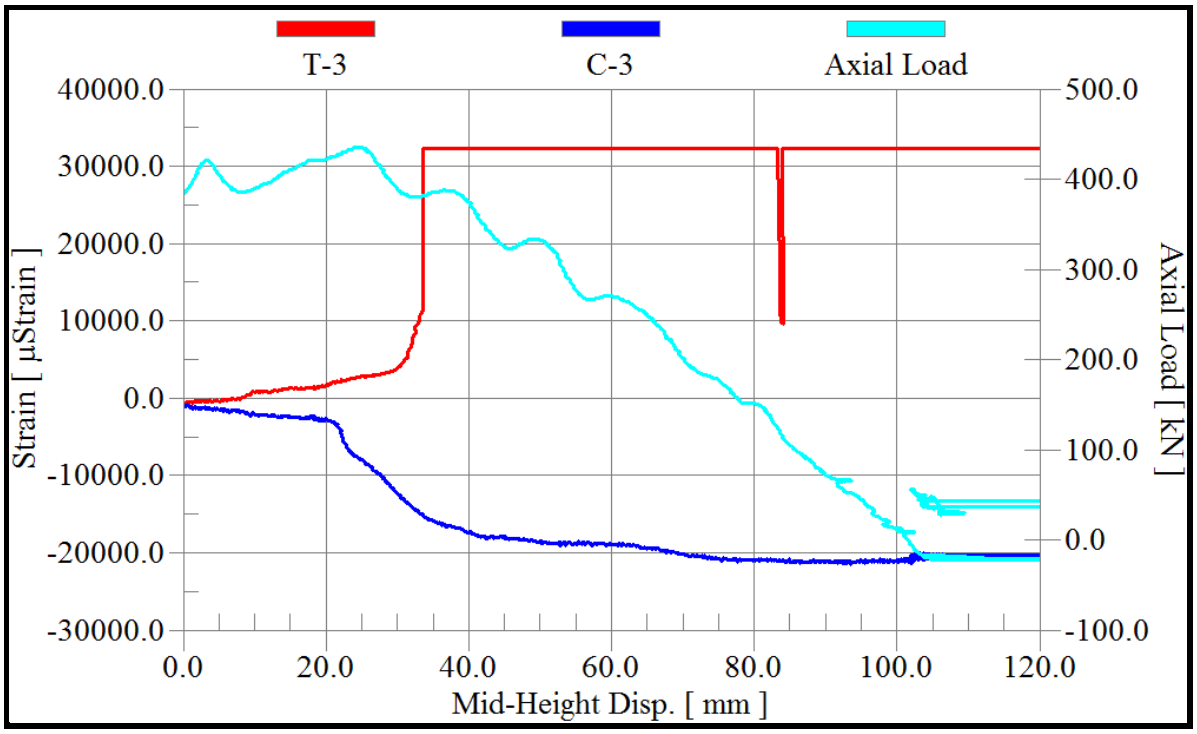

Fig. 5.5 Strains at mid-span and axial load vs. mid-height displacement for S4-AL400

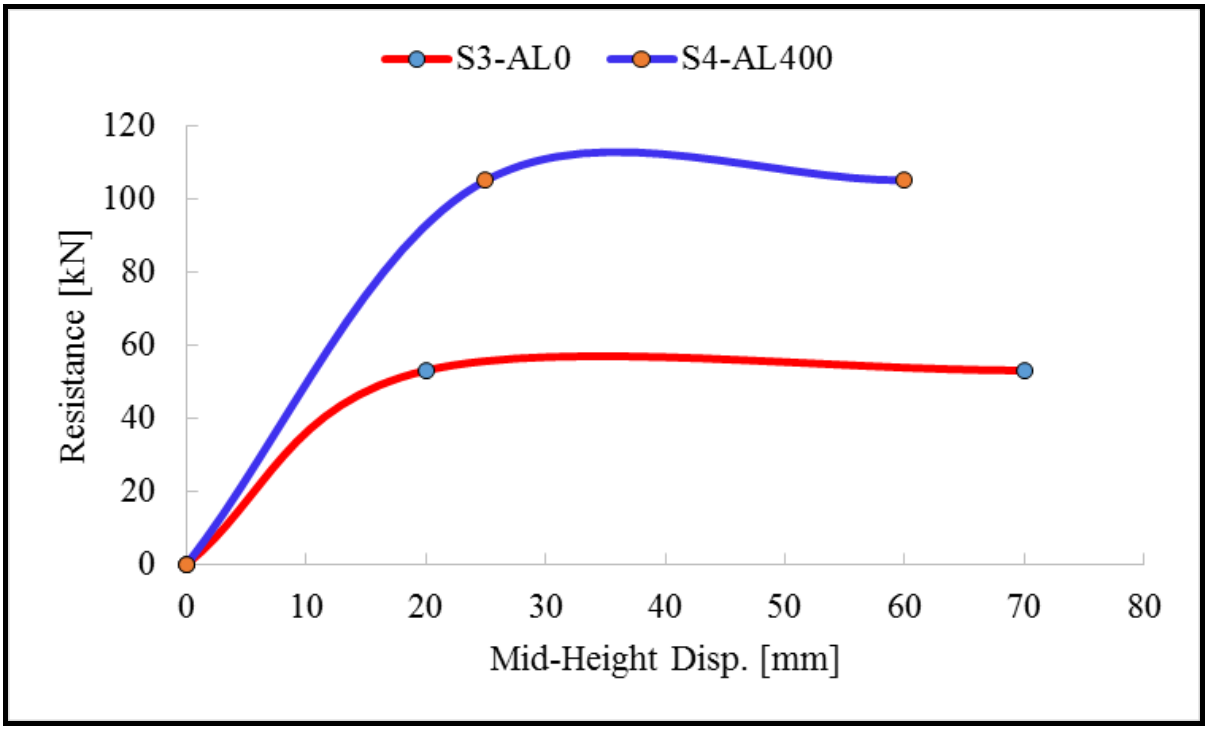

Fig. 5.6 Resistance-displacement functions for S3-AL0 and S4-AL400

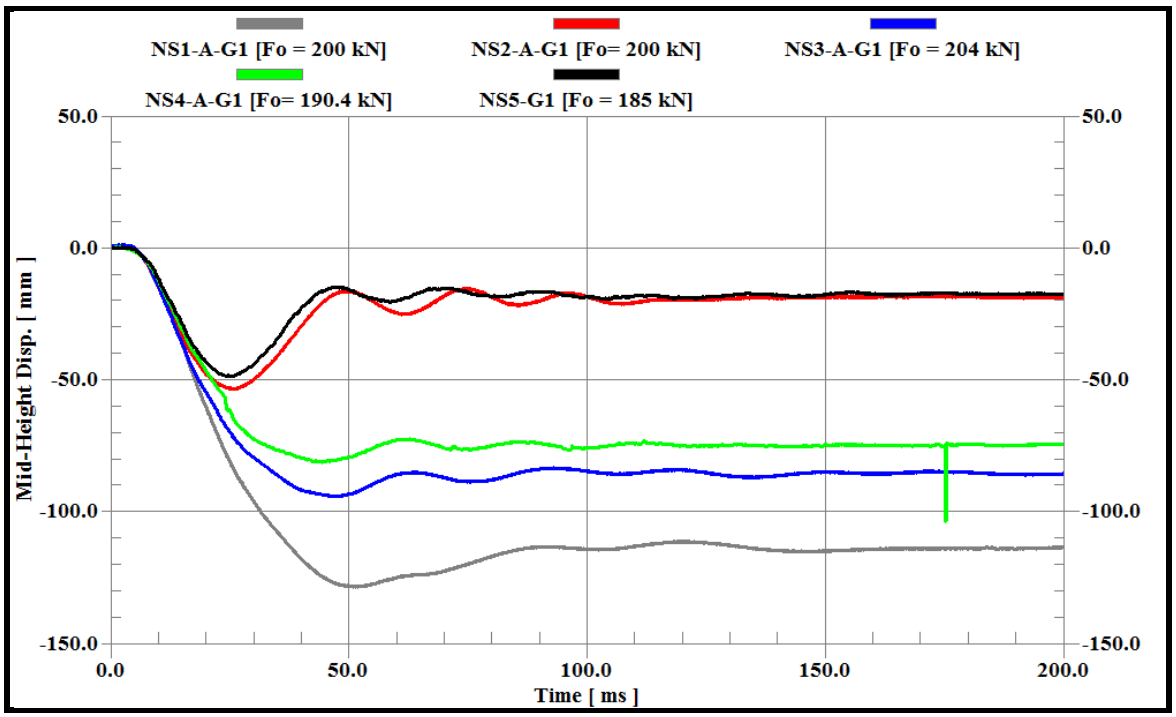

Fig. 5.7 Mid-height deflection time histories of non-seismic columns-Group G1

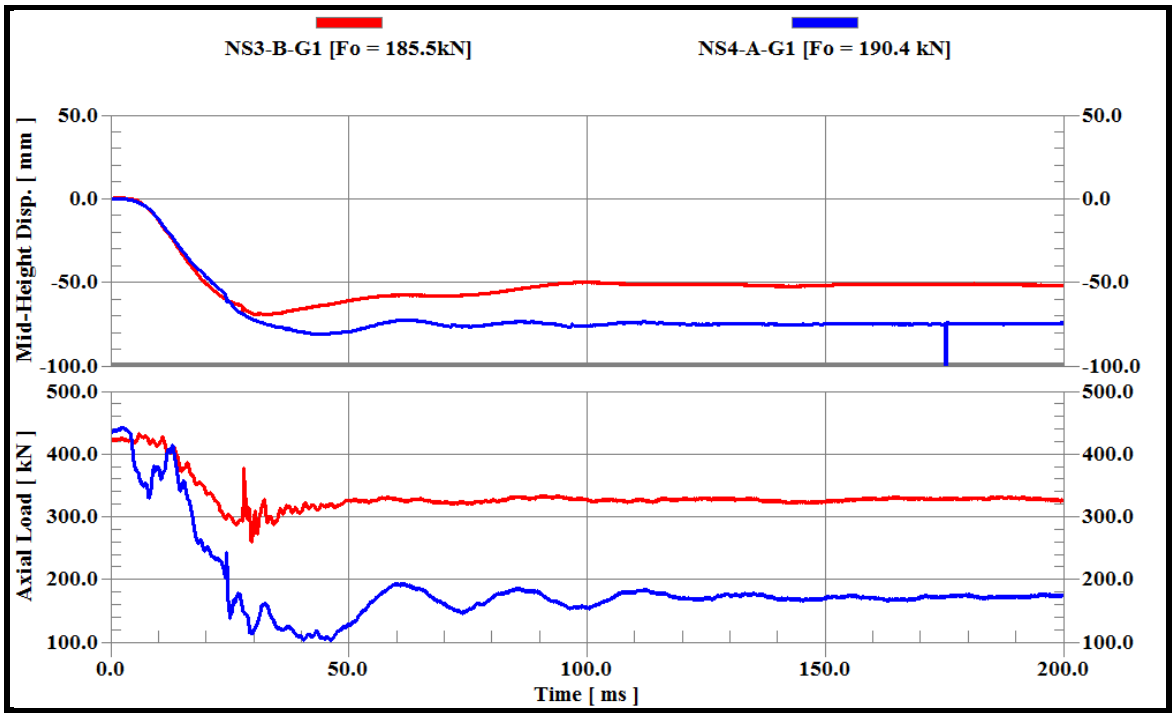

Fig. 5.8 Mid-height deflection and axial load time histories of NS3-B-G1 and NS4-A-G1

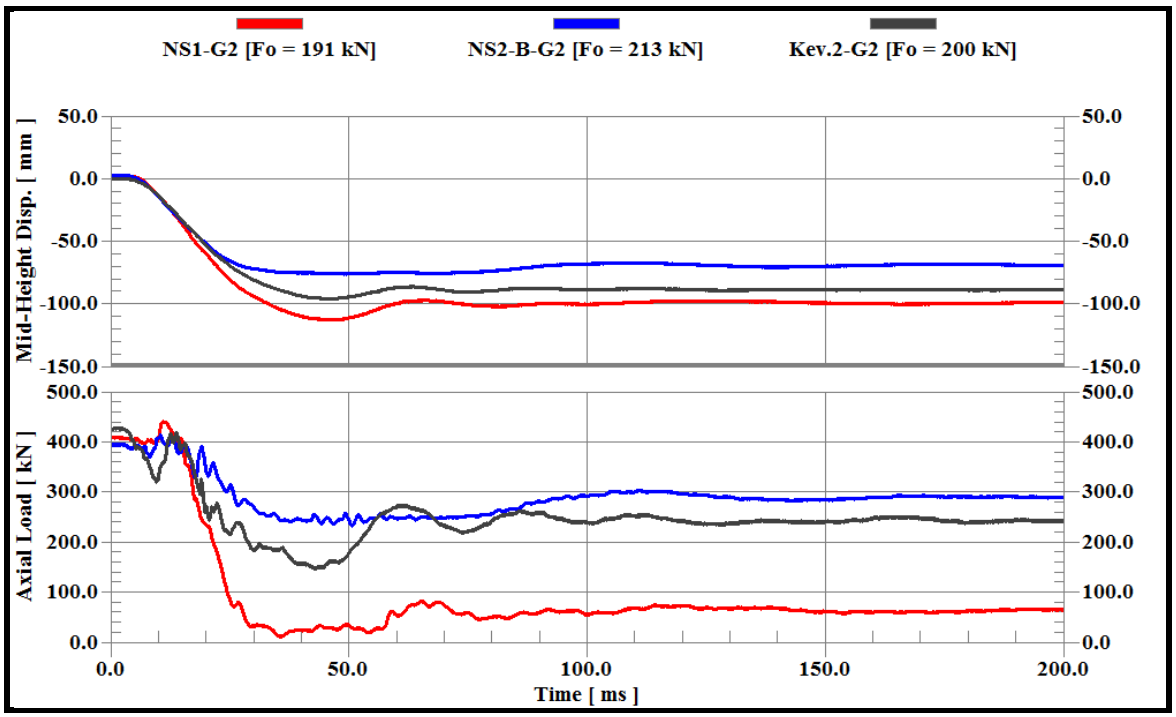

Fig. 5.9 Mid-height deflection and axial load time history for NS1-G2, NS2-G2 and Kev.2

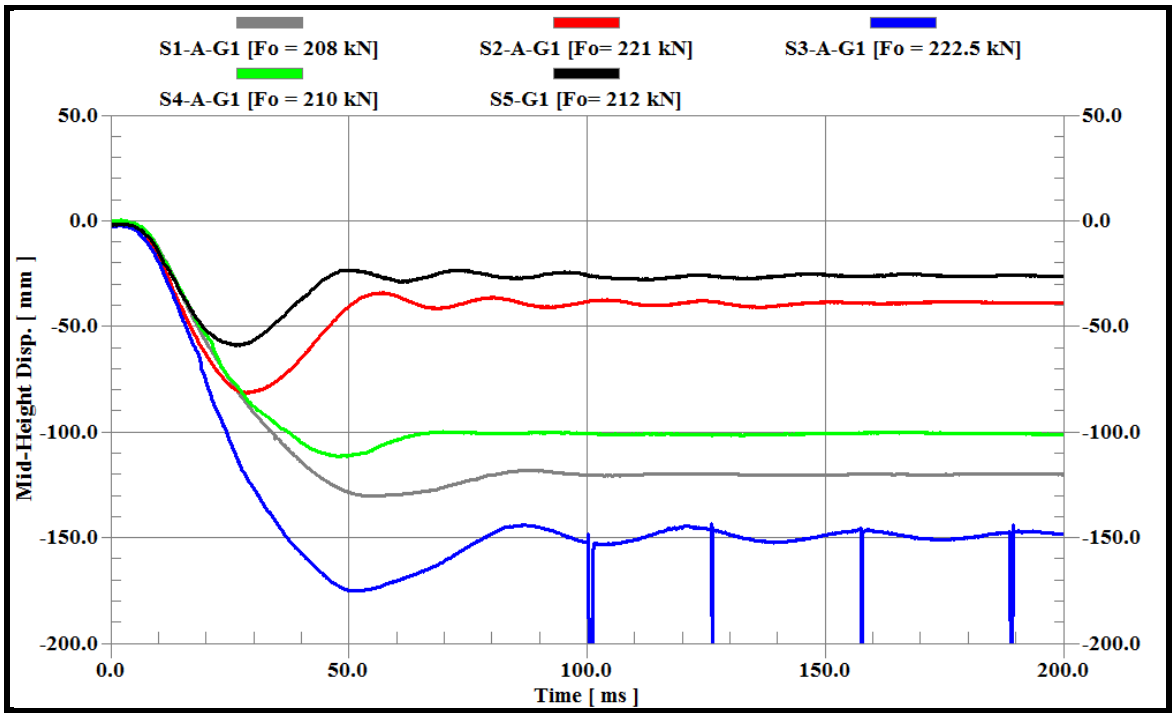

Fig. 5.10 Mid-height displacement time histories of seismic columns

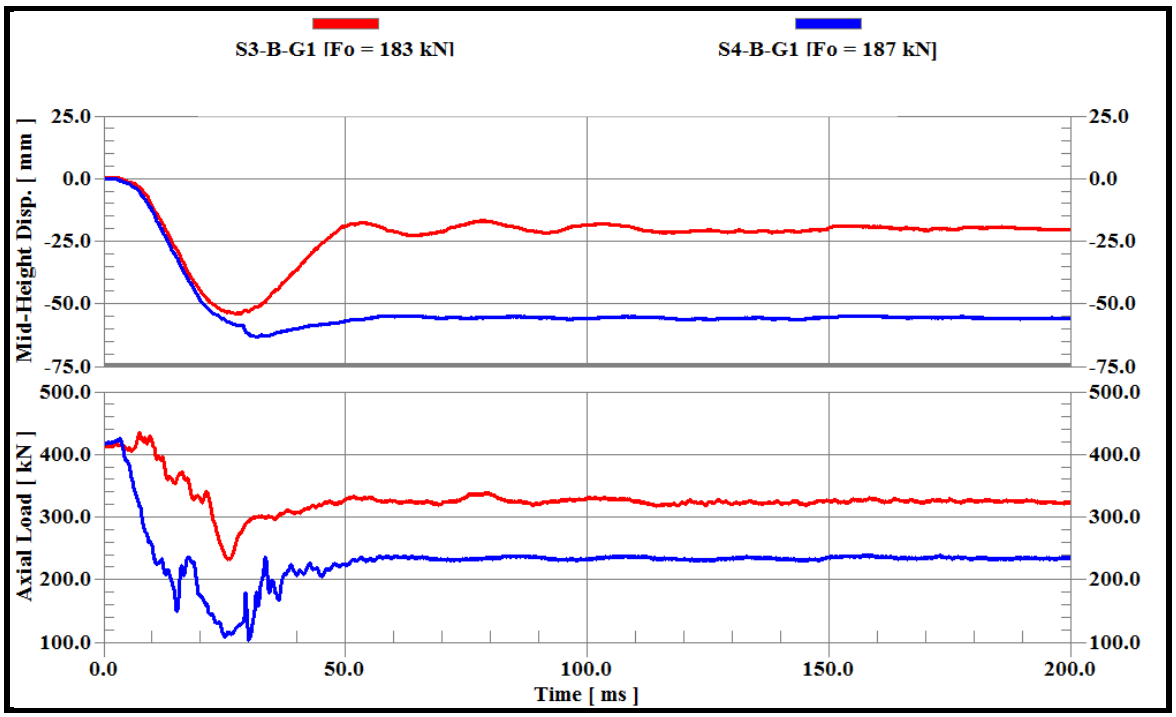

Fig. 5.11 Mid-height displacement time histories of S3-B-G1 and S4-B-G1

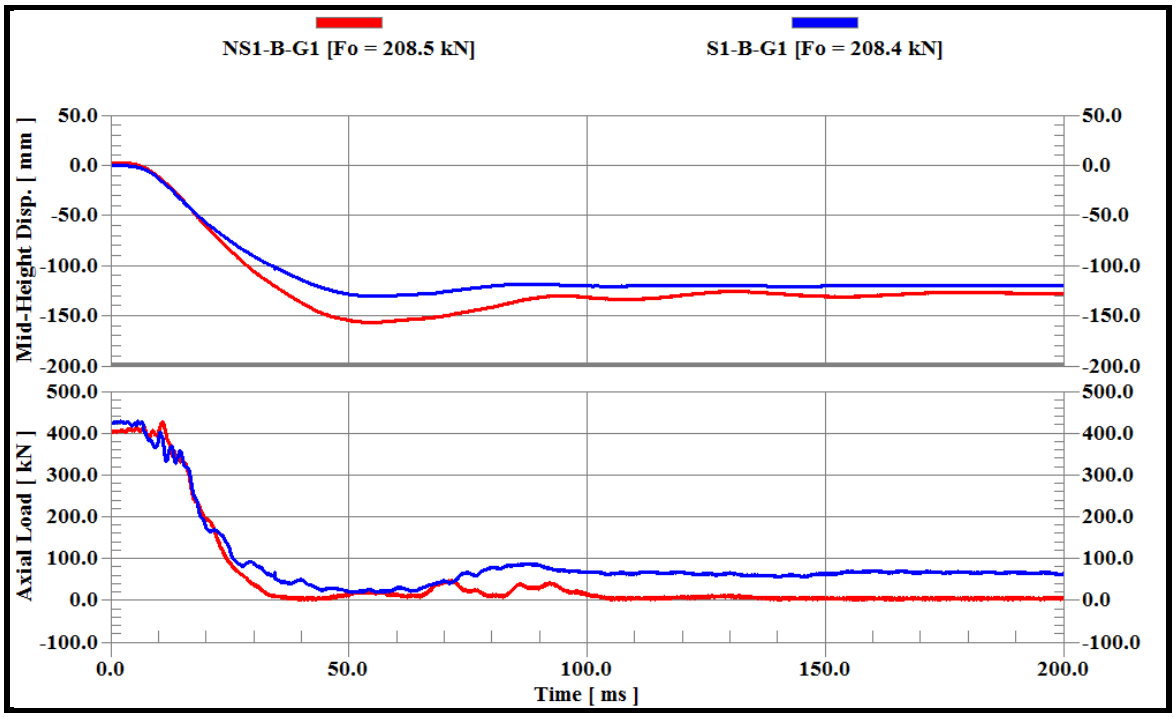

Fig. 5.12 Mid-height deflection and axial load time histories for NS1-B-G1 and S1-B-G1

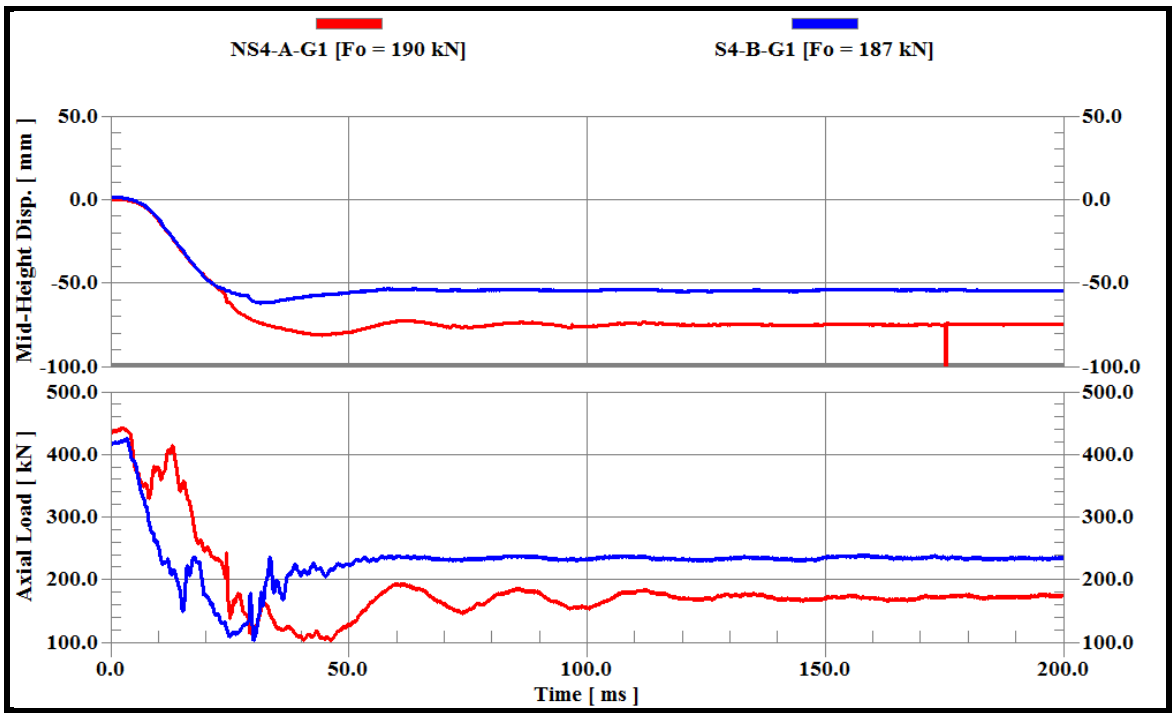

Fig. 5.13 Mid-height deflection and axial load time histories for NS4-A-G1 and S4-B-G1

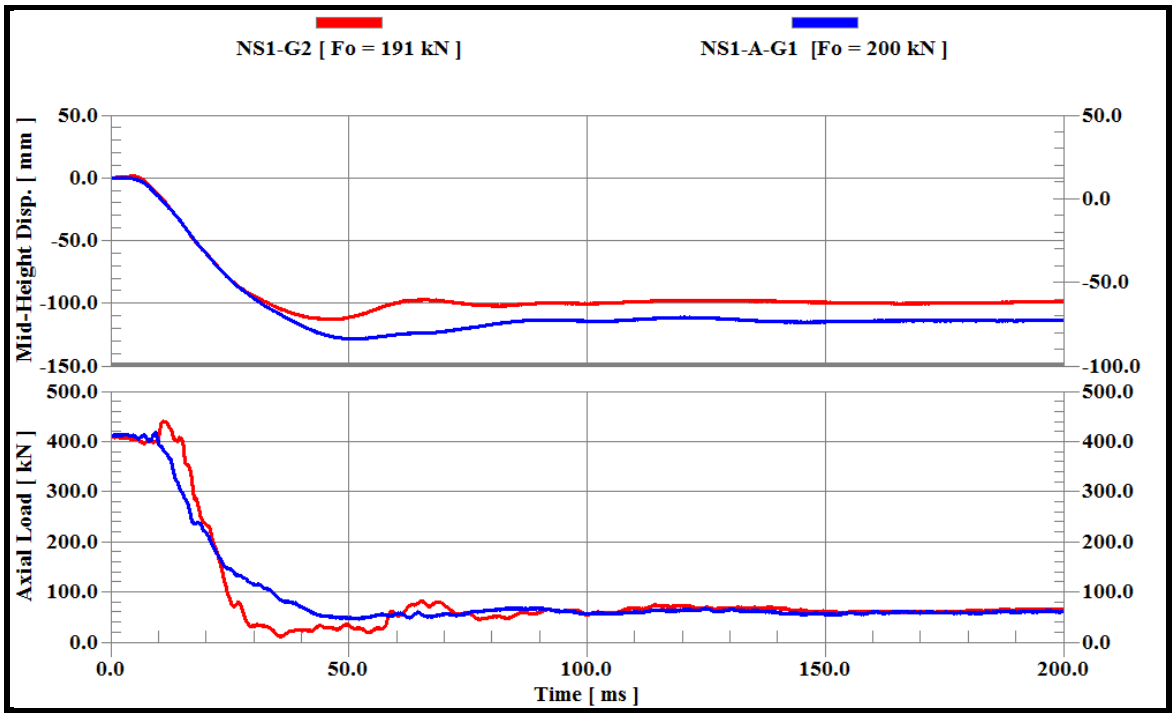

Fig. 5.14 Mid-height deflection and axial load time histories for NS1-G2, and NS1-A-G1

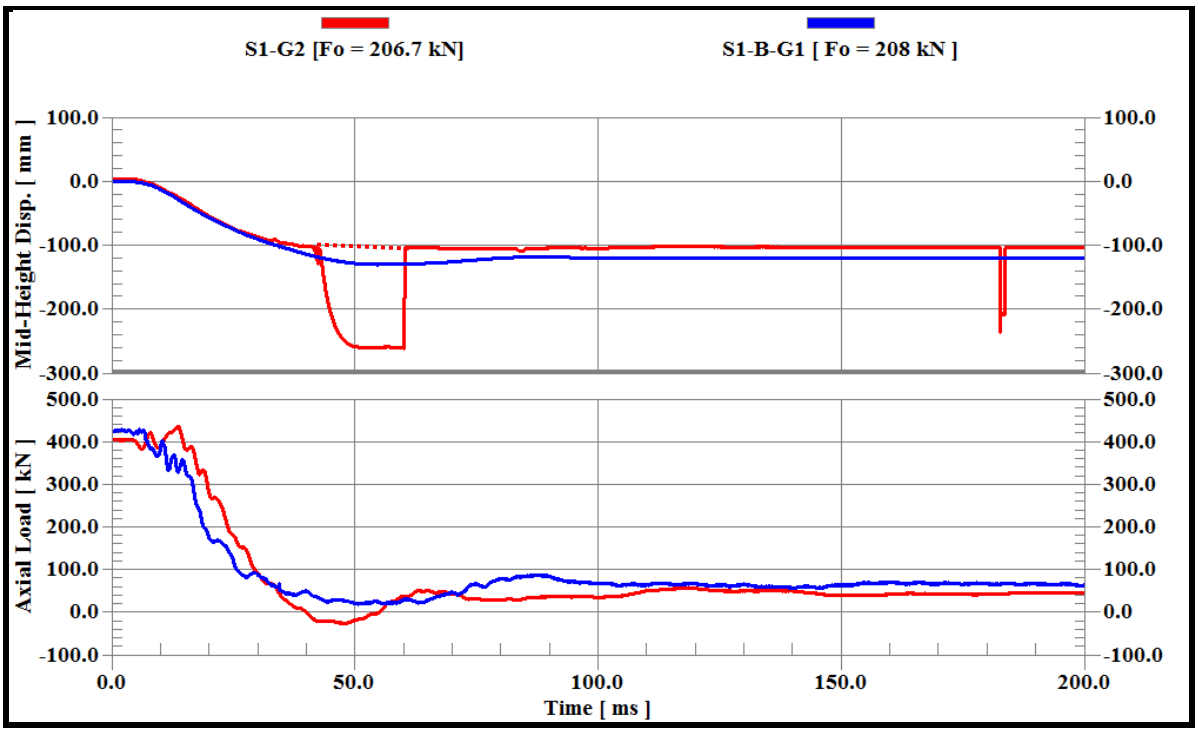

Fig. 5.15 Mid-height deflection and axial load time histories for S1-G2 and S1-B-G1

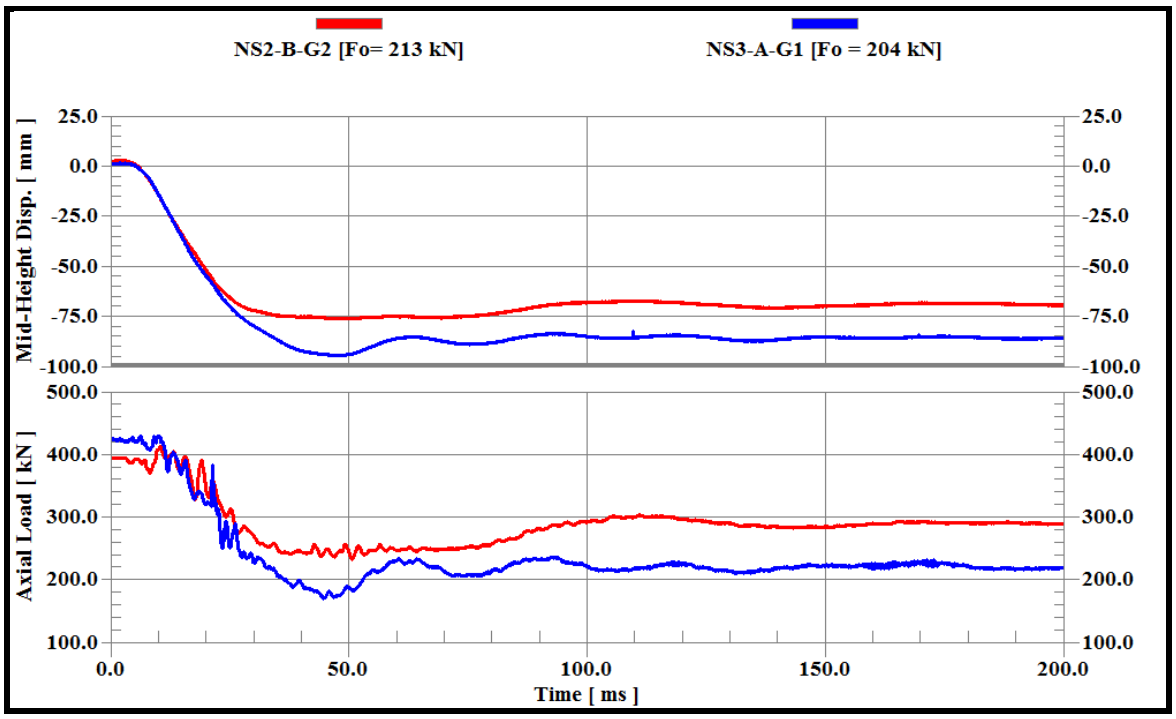

Fig. 5.16 Mid-height deflection and axial load time histories for NS2-B-G2 and NS3-A-G1

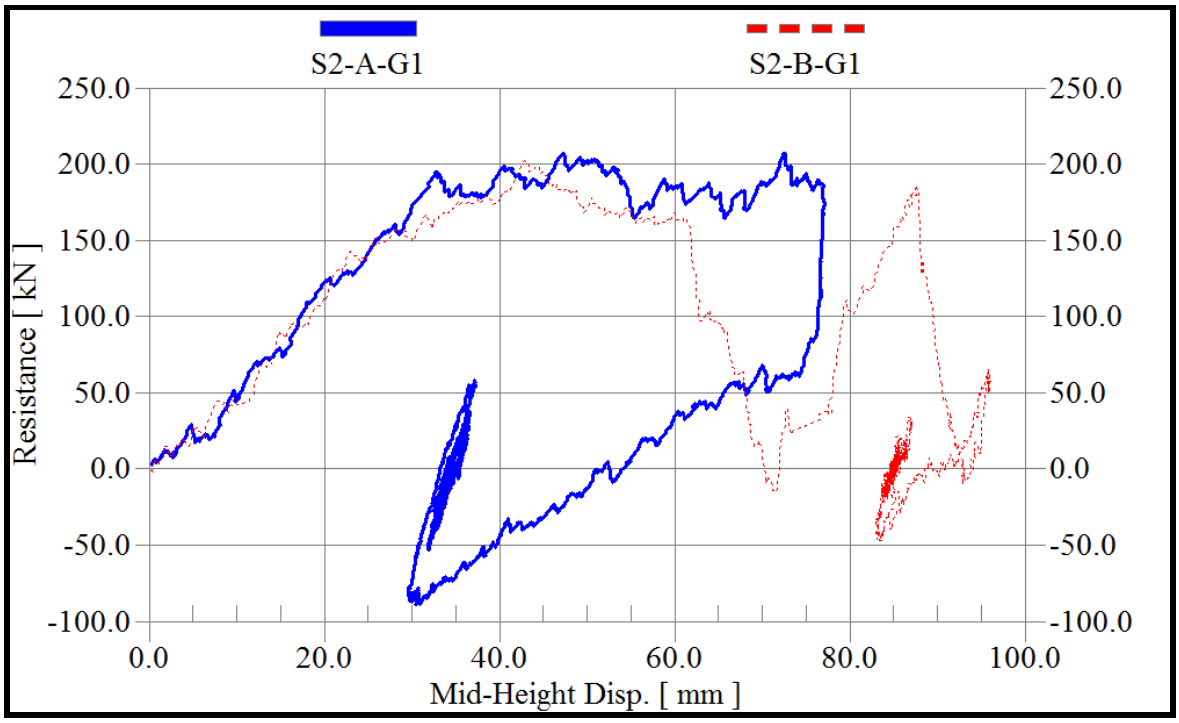

Fig. 5.17 Resistance-displacement function of Columns S2-A-G1 and S2-B-G1

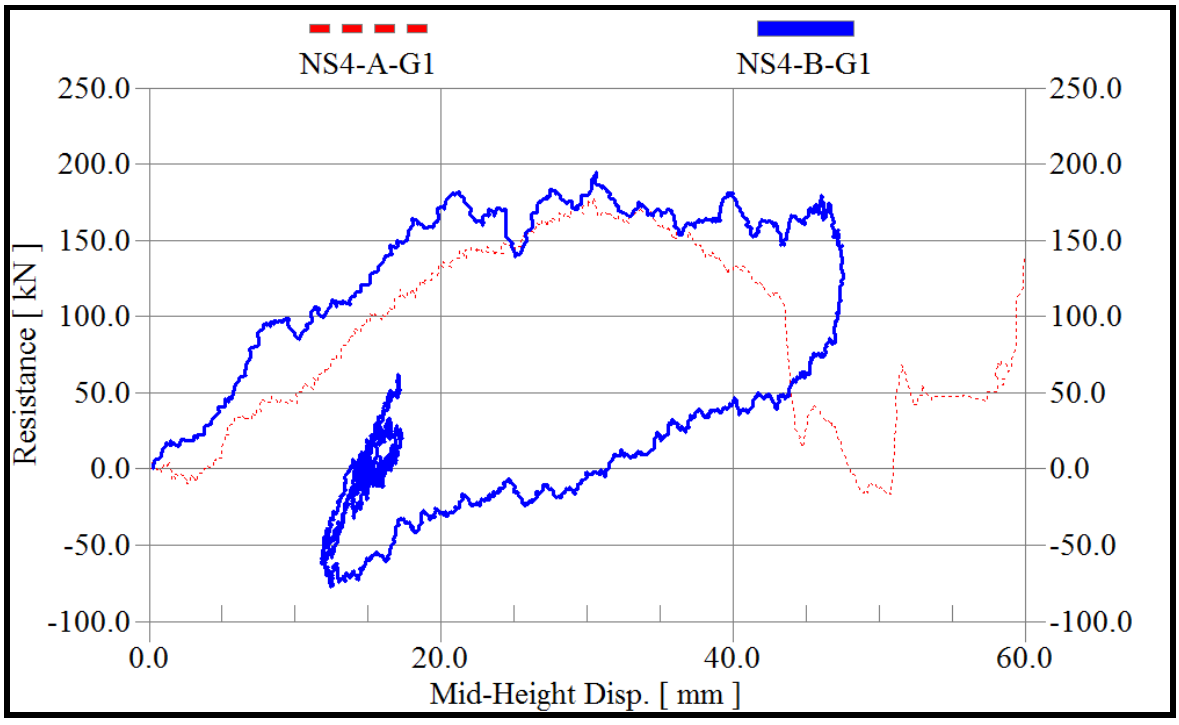

Fig. 5.18 Resistance-displacement function of Columns NS4-A-G1 and NS4-B-G1

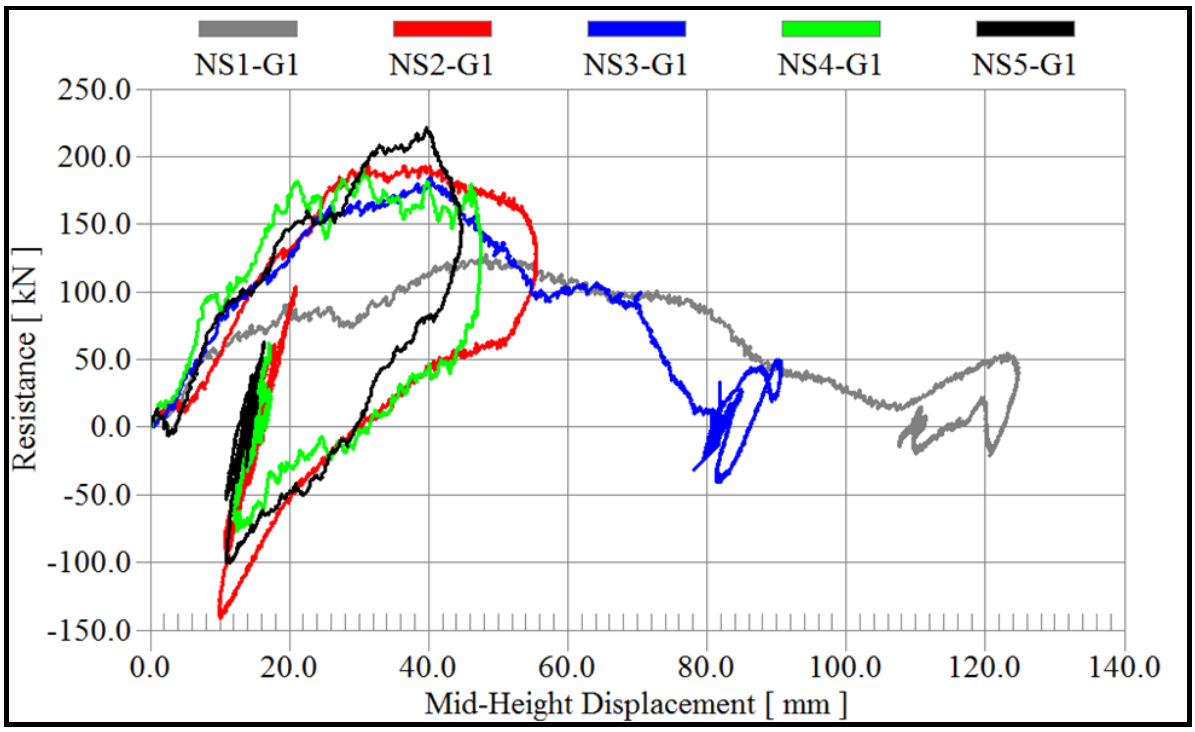

Fig. 5.19 Resistance functions of non-seismic columns

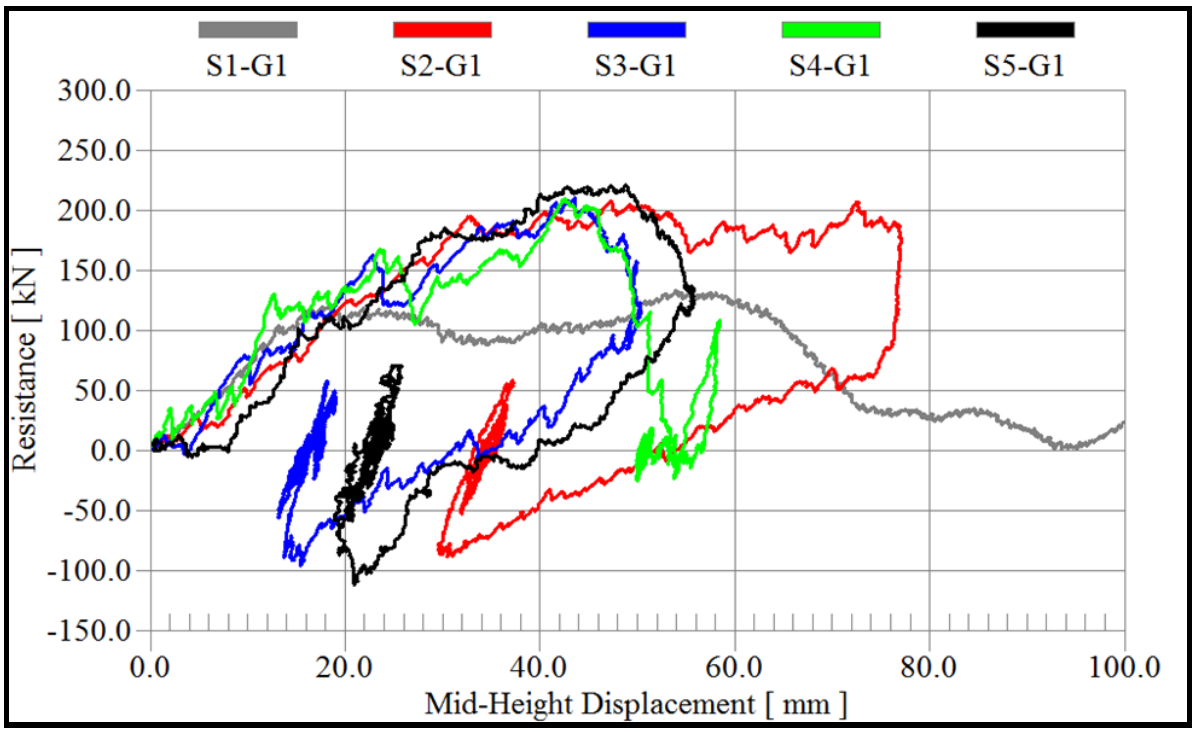

Fig. 5.20 Resistance functions of seismic columns

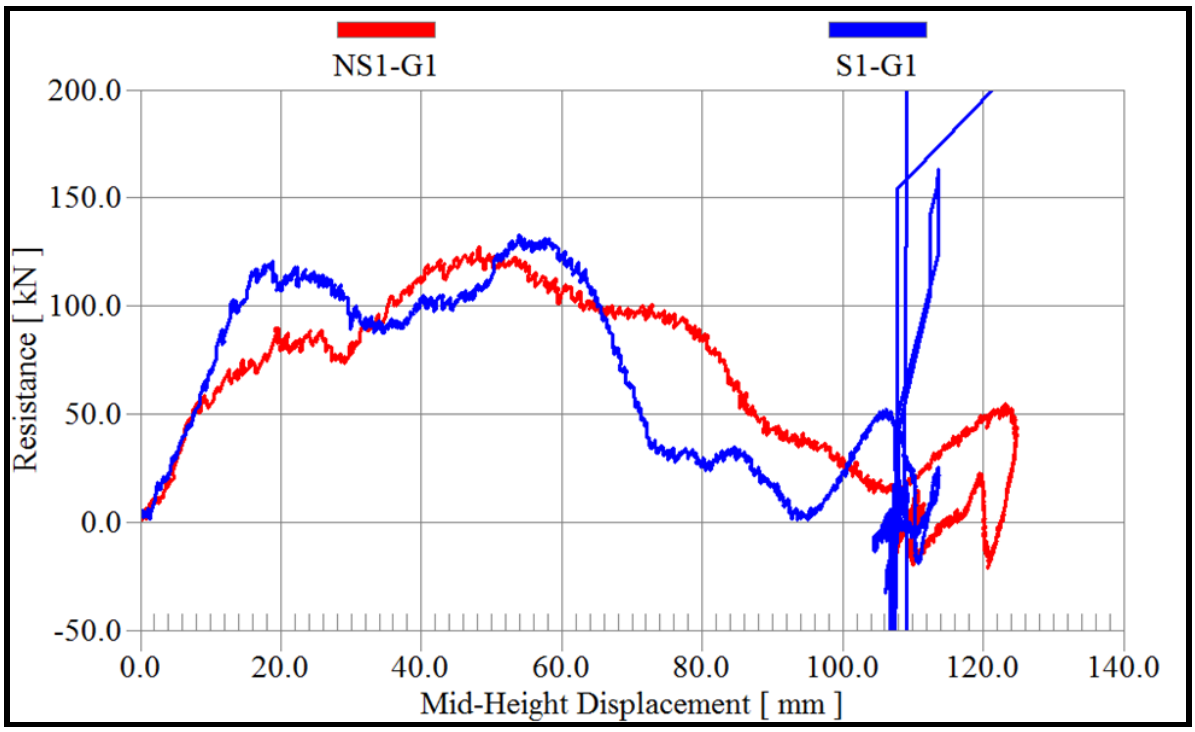

Fig. 5.21 Resistance functions of Columns NS1-G1 and S1-G1

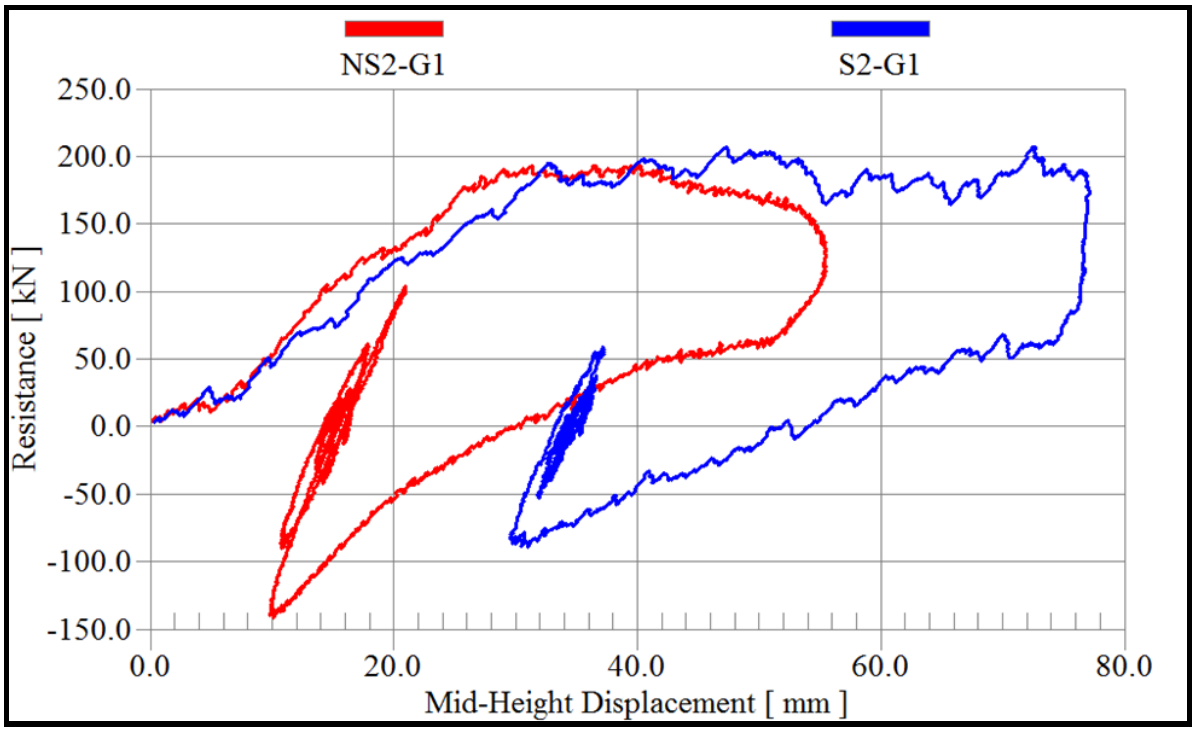

Fig. 5.22 Resistance functions of Columns NS2-G1 and S2-G1

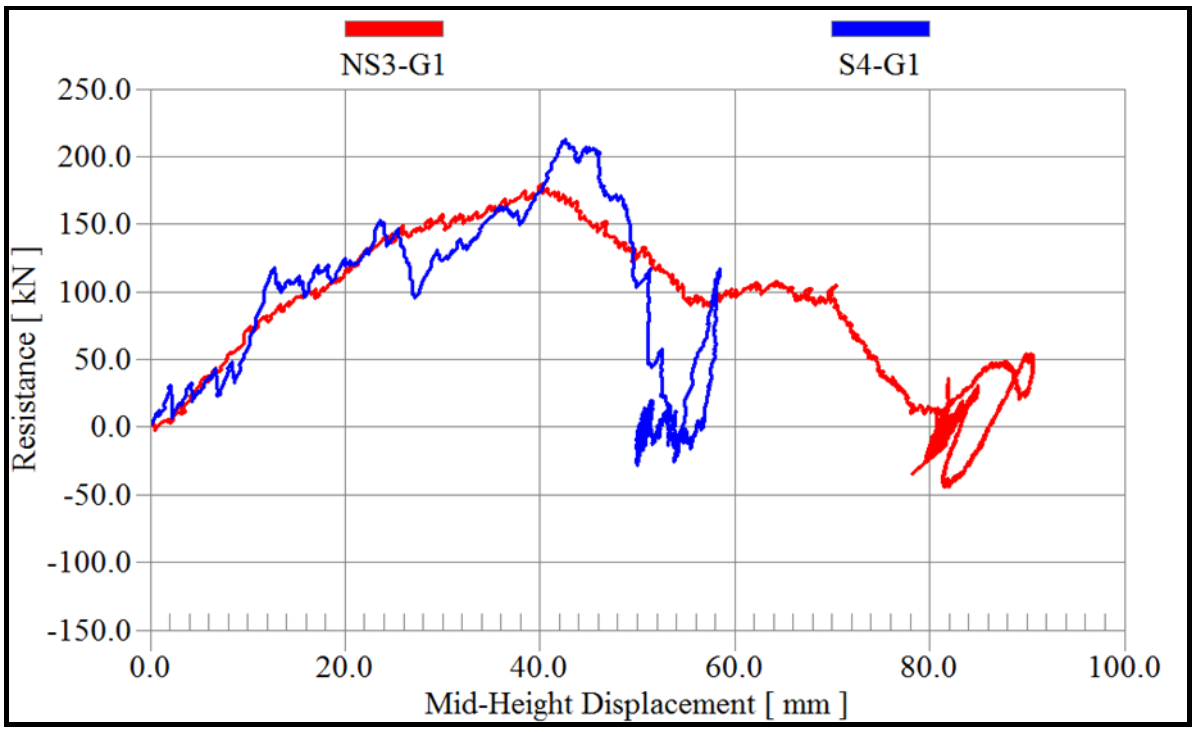

Fig. 5.23 Resistance functions of Columns NS3-G1 and S4-G1

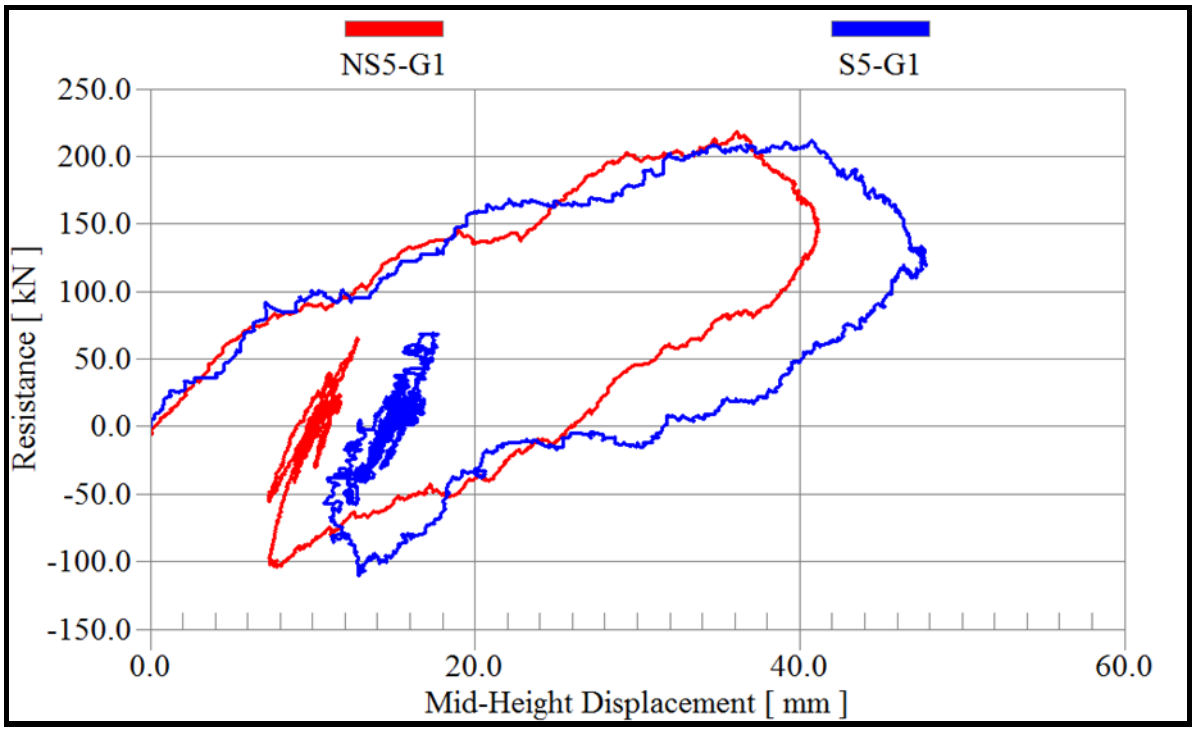

Fig. 5.24 Resistance functions of Columns NS5-G1 and S5-G1

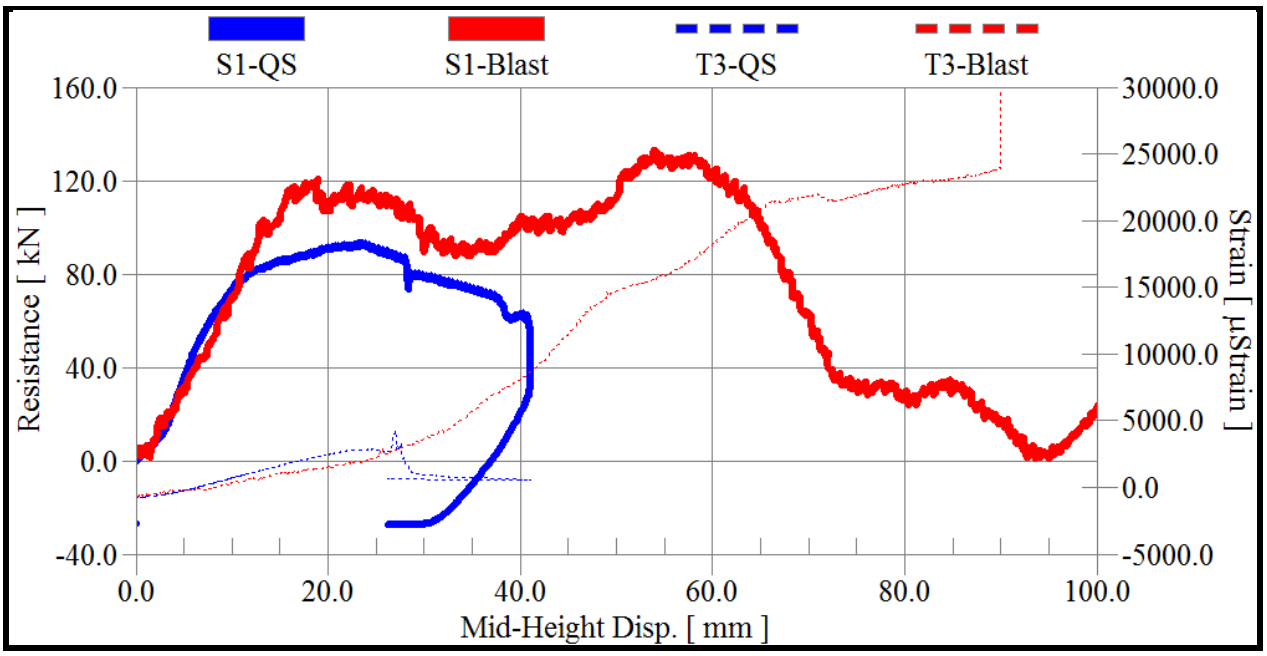

Fig. 5.25 S1 resistance functions - QS vs. Blast

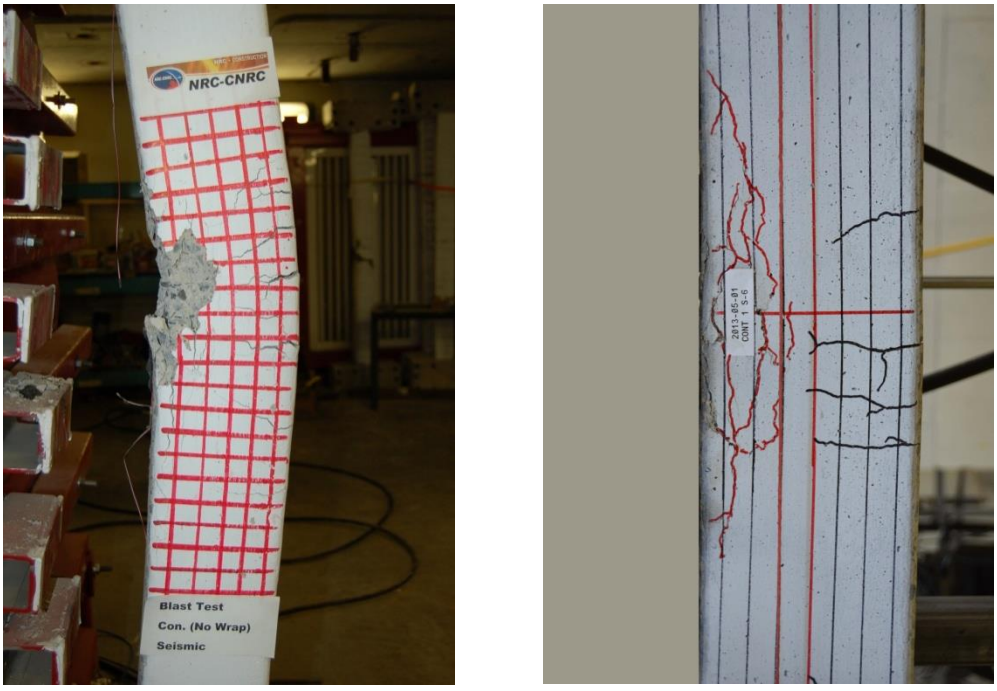

(a) (b)

Fig. 5.26 Damage level of S1- Blast vs. QS

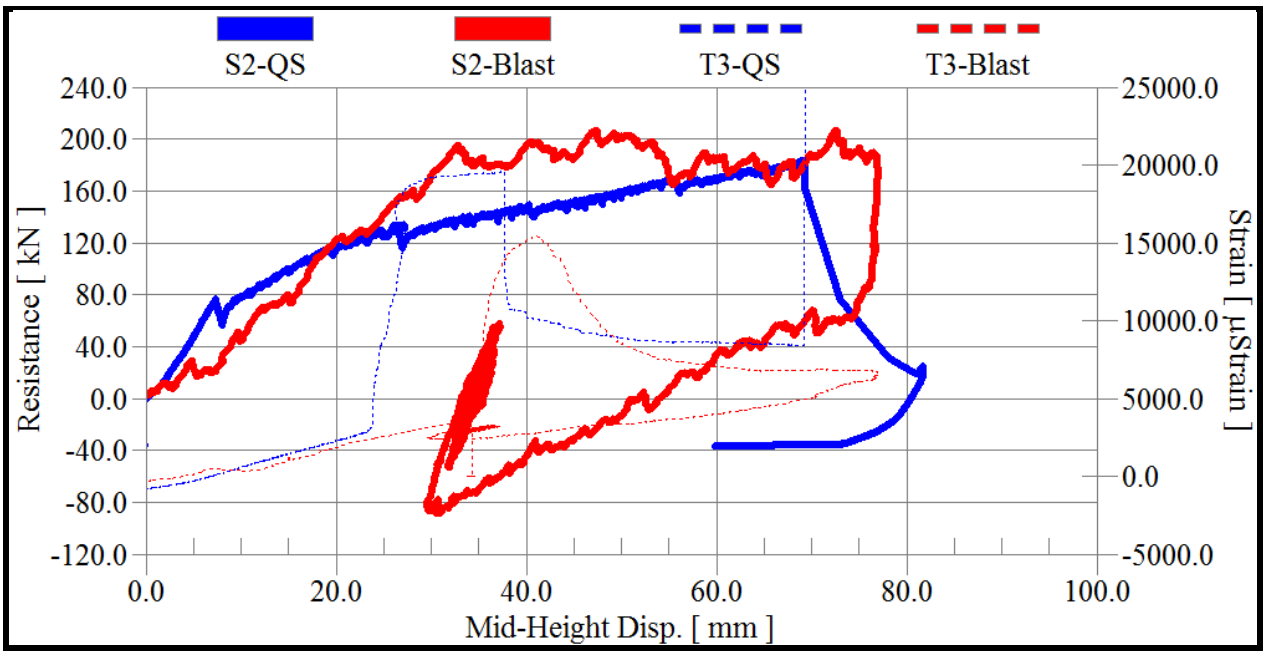

Fig. 5.27 S2 resistance functions - QS vs. Blast

(a) (b)

Fig. 5.28 Damage level of S2 - Blast vs. QS

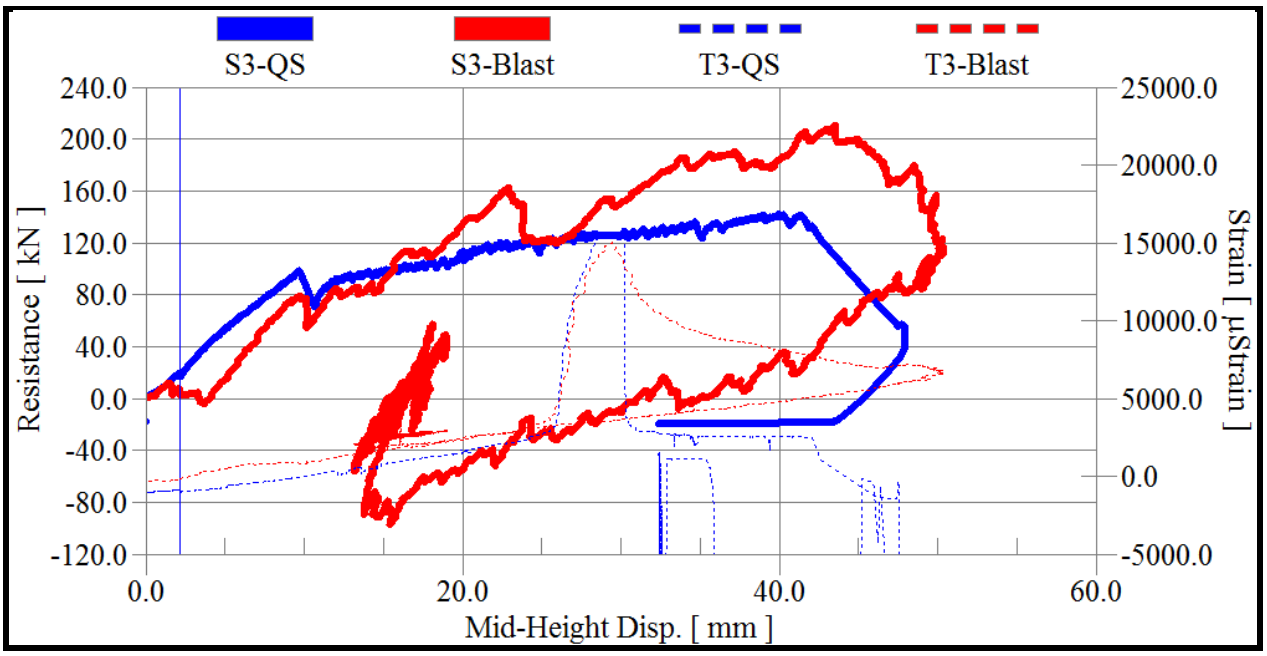

Fig. 5.29 S3 resistance functions - QS vs. Blast

(a) (b)

Fig. 5.30 Damage level of S3 - Blast vs. QS

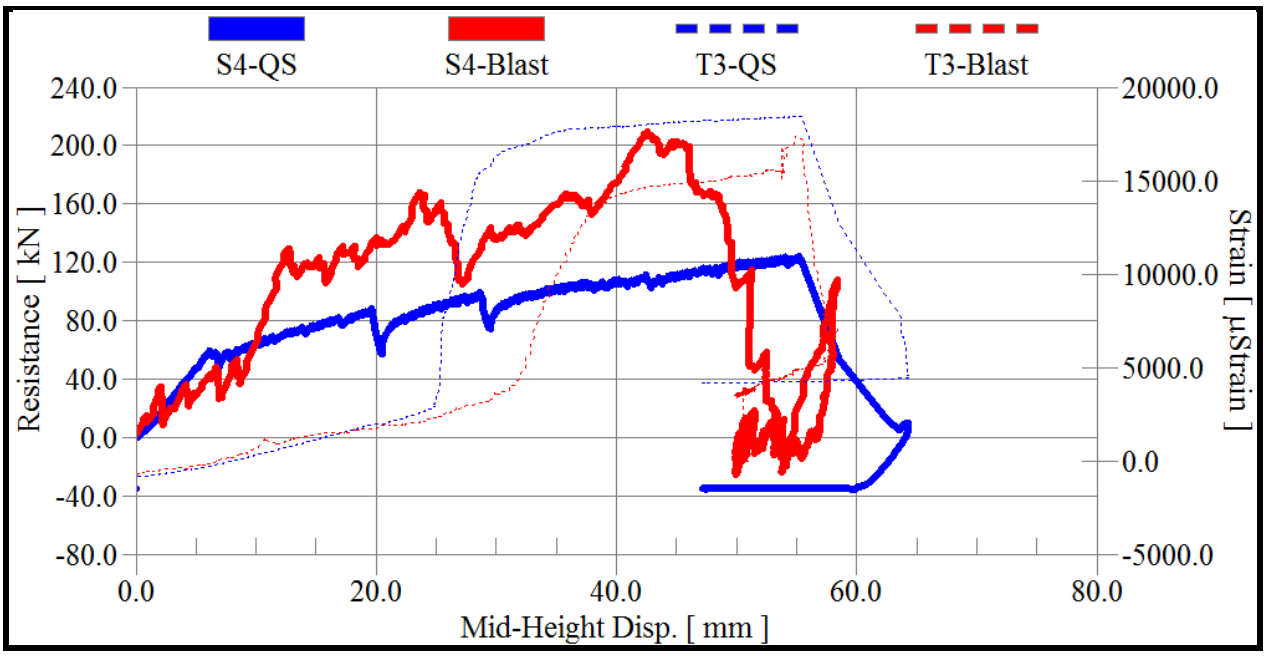

Fig. 5.31 S4 resistance function - QS vs. Blast

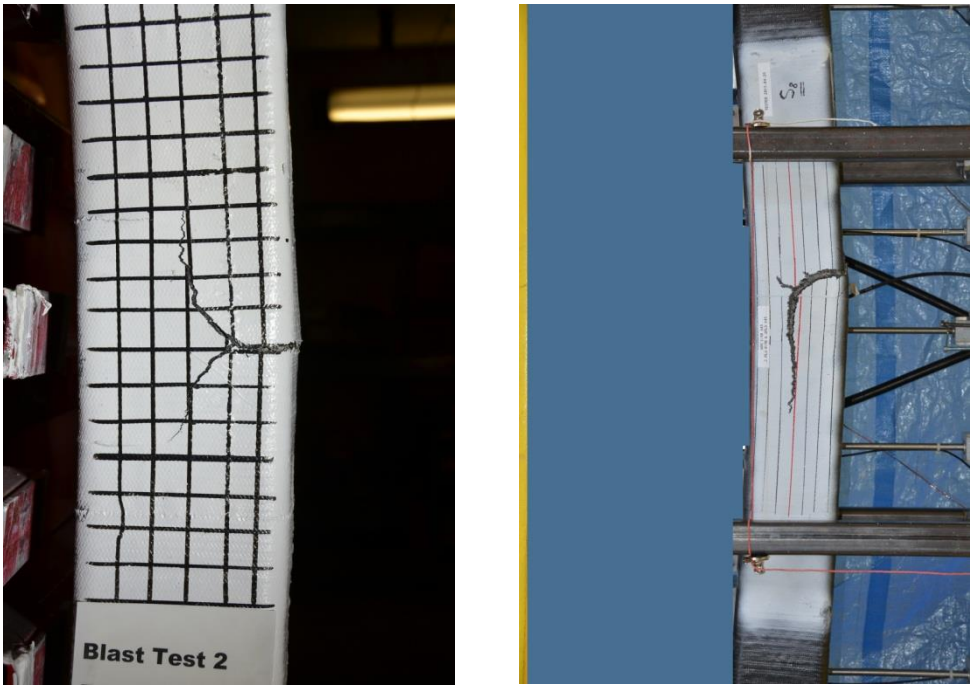

(a) (b)

Fig. 5.32 Damage level of S4 - Blast vs. QS

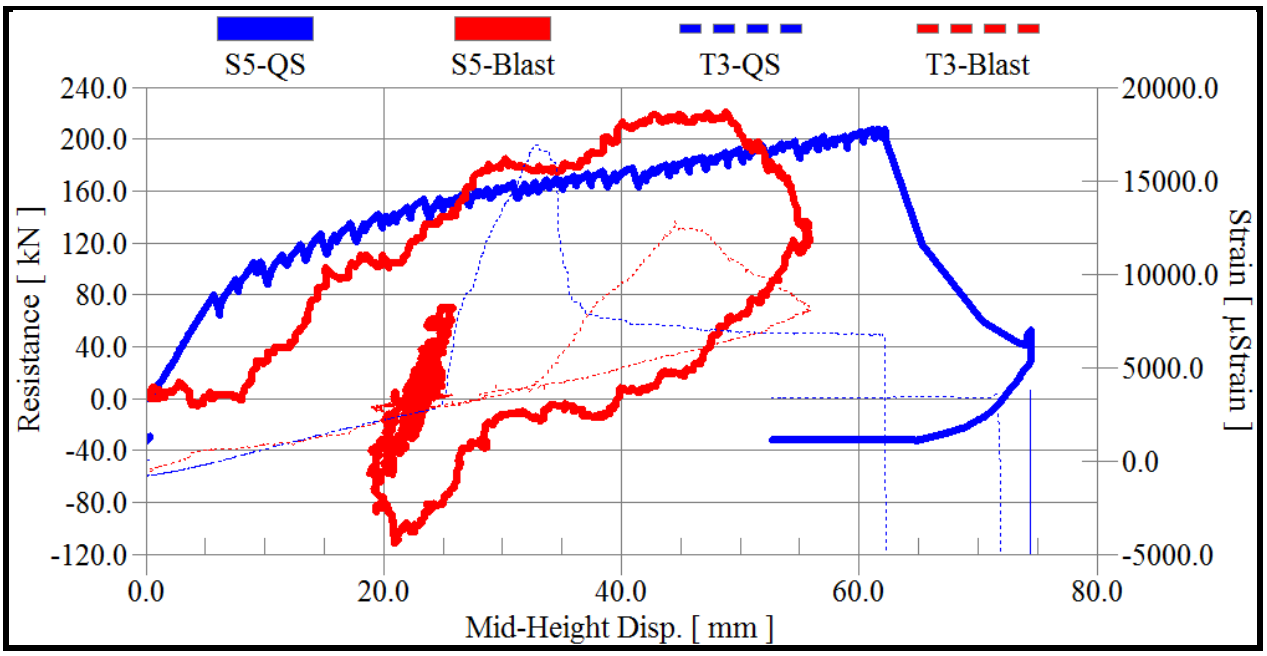

Fig. 5.33 S5 resistance functions - QS vs. Blast

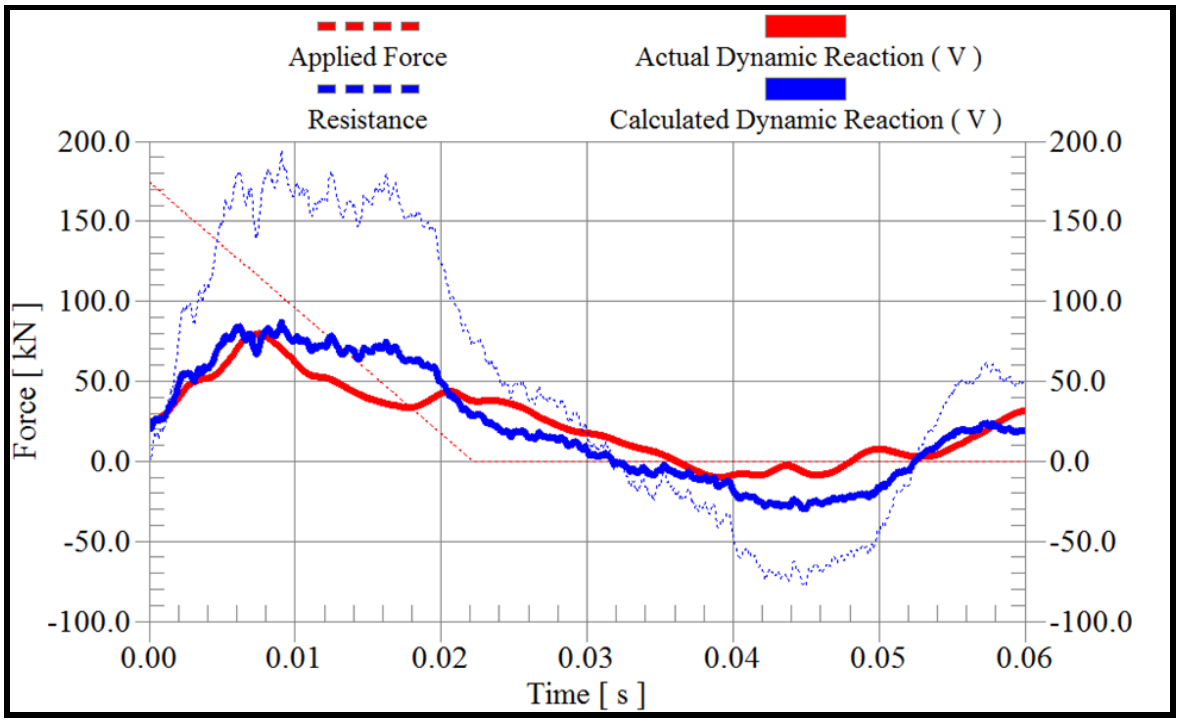

Fig. 5.34 Actual dynamic reaction vs. calculated dynamic reaction for Column NS4-G1

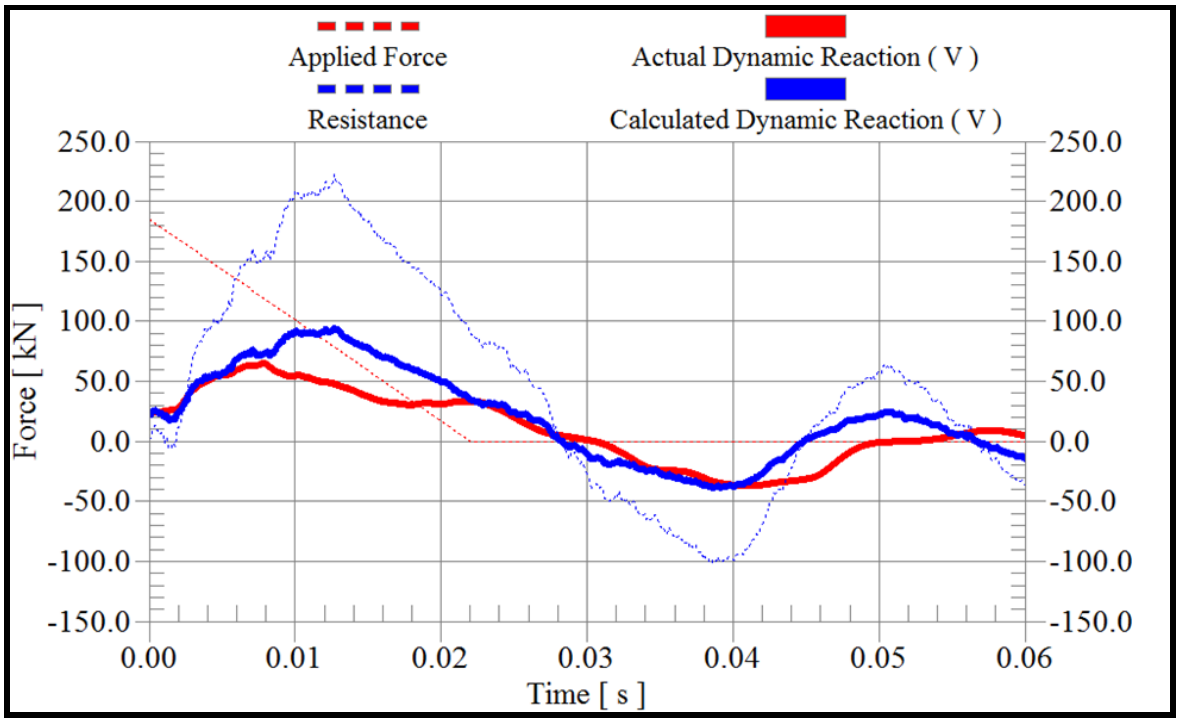

Fig. 5.35 Actual dynamic reaction vs. calculated dynamic reaction for Column NS5-G1

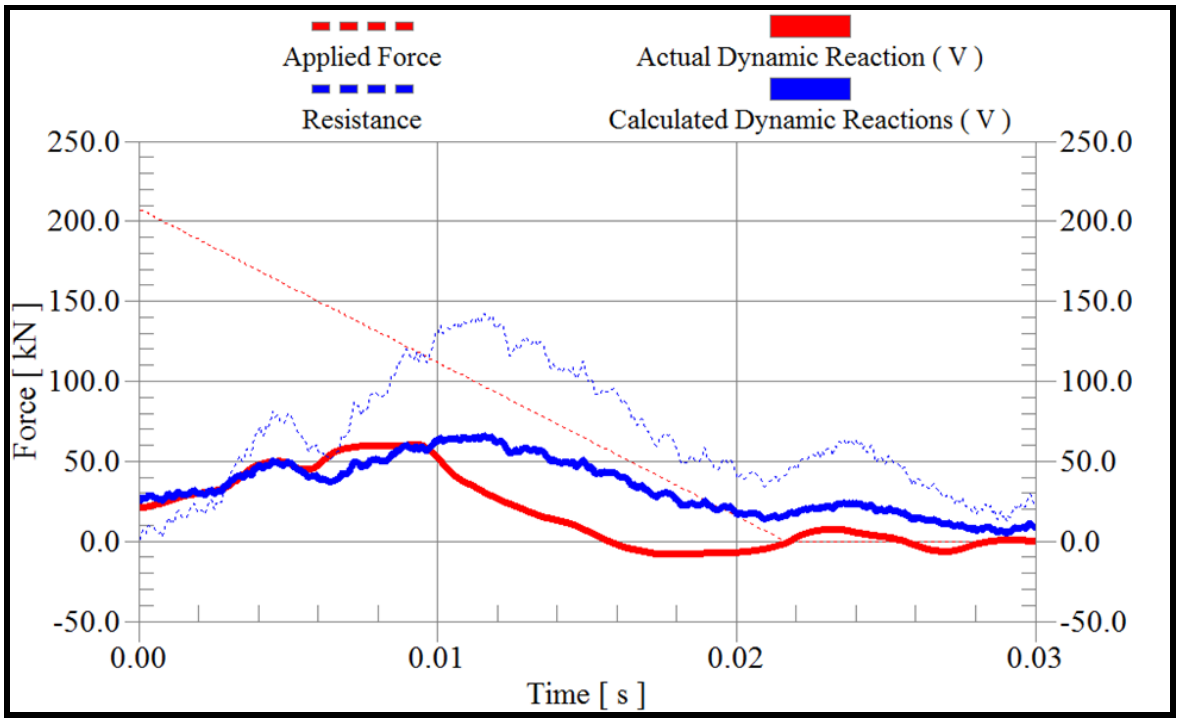

Fig. 5.36 Actual dynamic reaction vs. calculated dynamic reaction for Column S1-C-G1

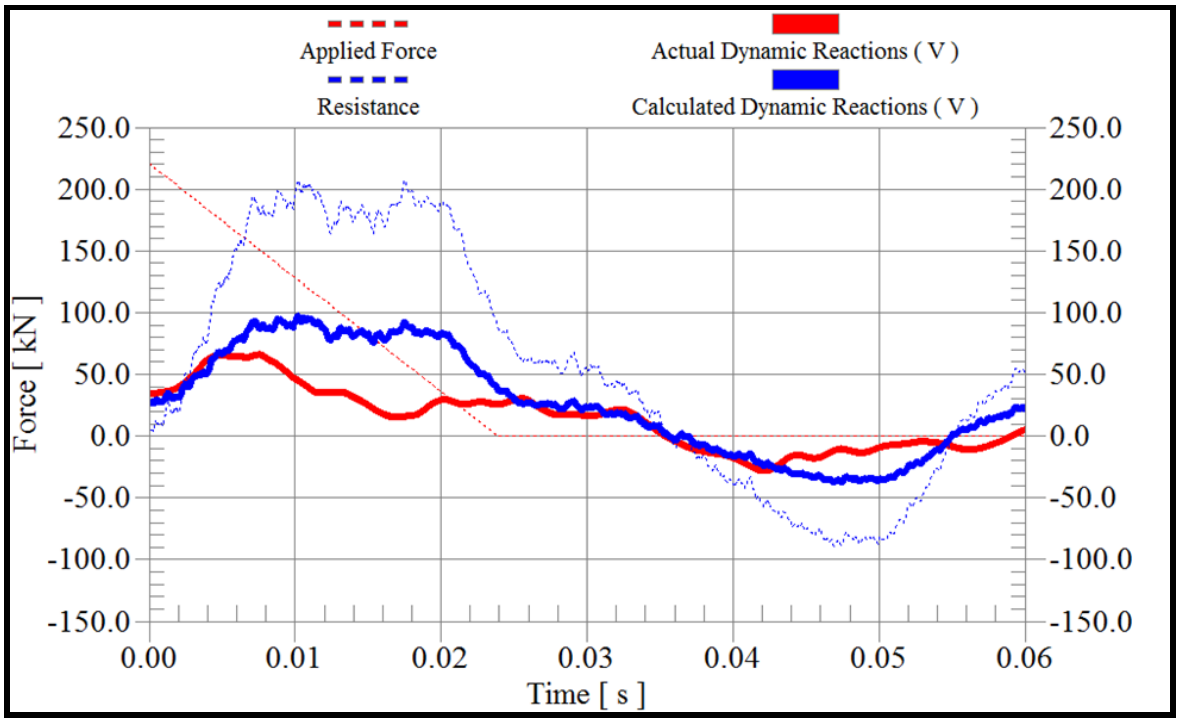

Fig. 5.37 Actual dynamic reaction vs. calculated dynamic reaction for Column S2-A-G1

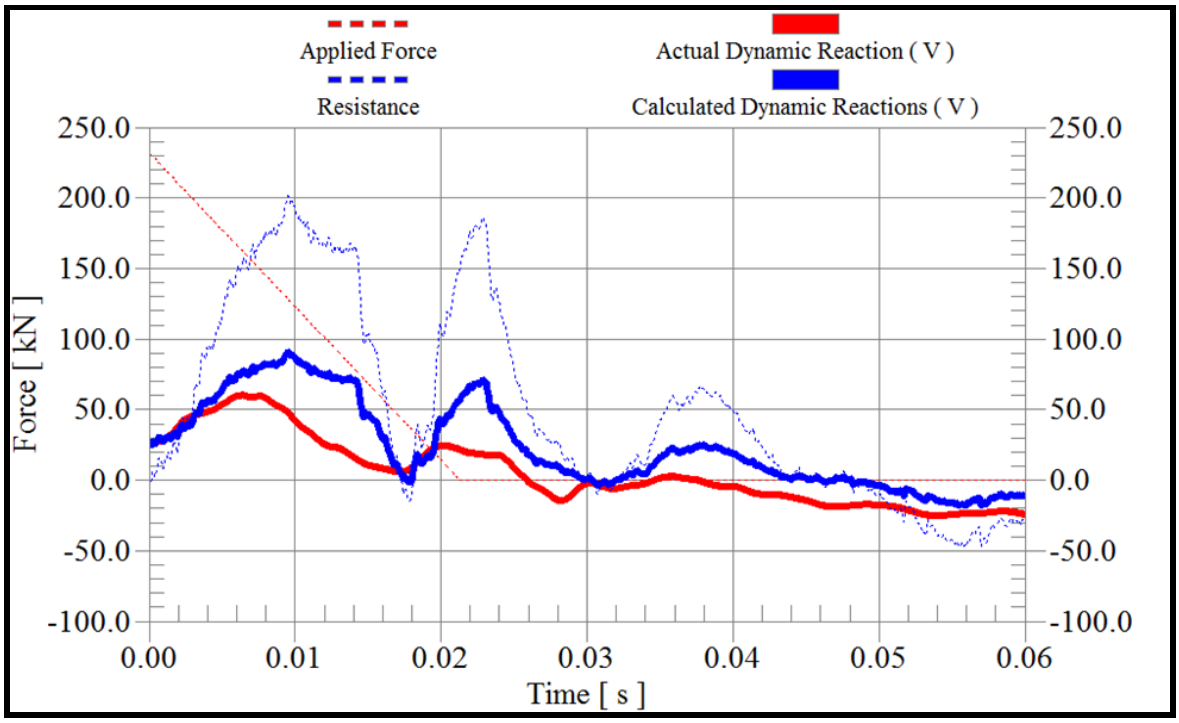

Fig. 5.38 Actual dynamic reaction vs. calculated dynamic reaction for Column S2-B-G1

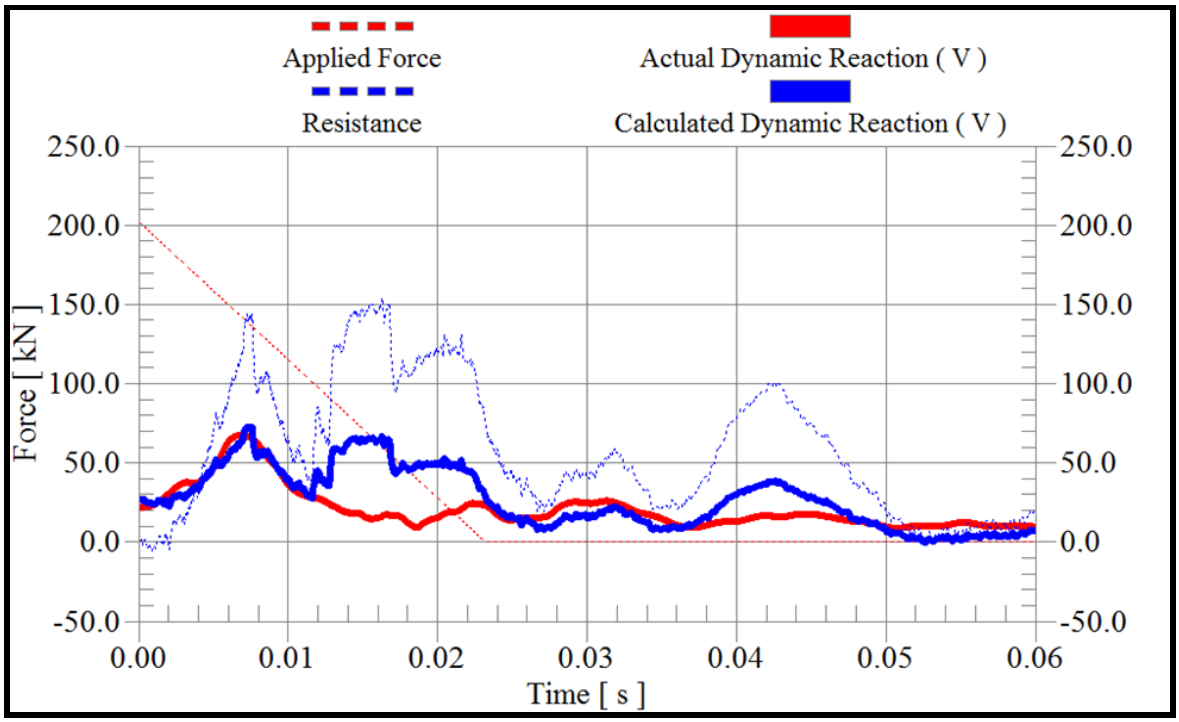

Fig. 5.39 Actual dynamic reaction vs. calculated dynamic reaction for Column S3-A-G1

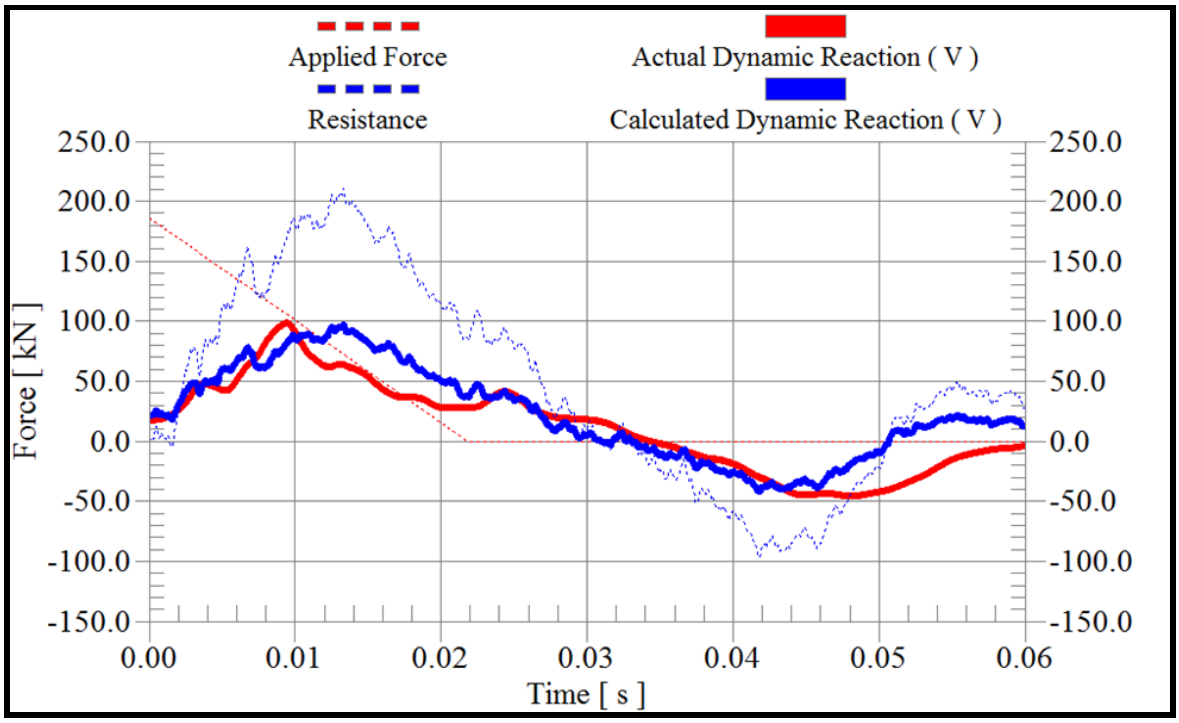

Fig. 5.40 Actual dynamic reaction vs. calculated dynamic reaction for Column S3-B-G1

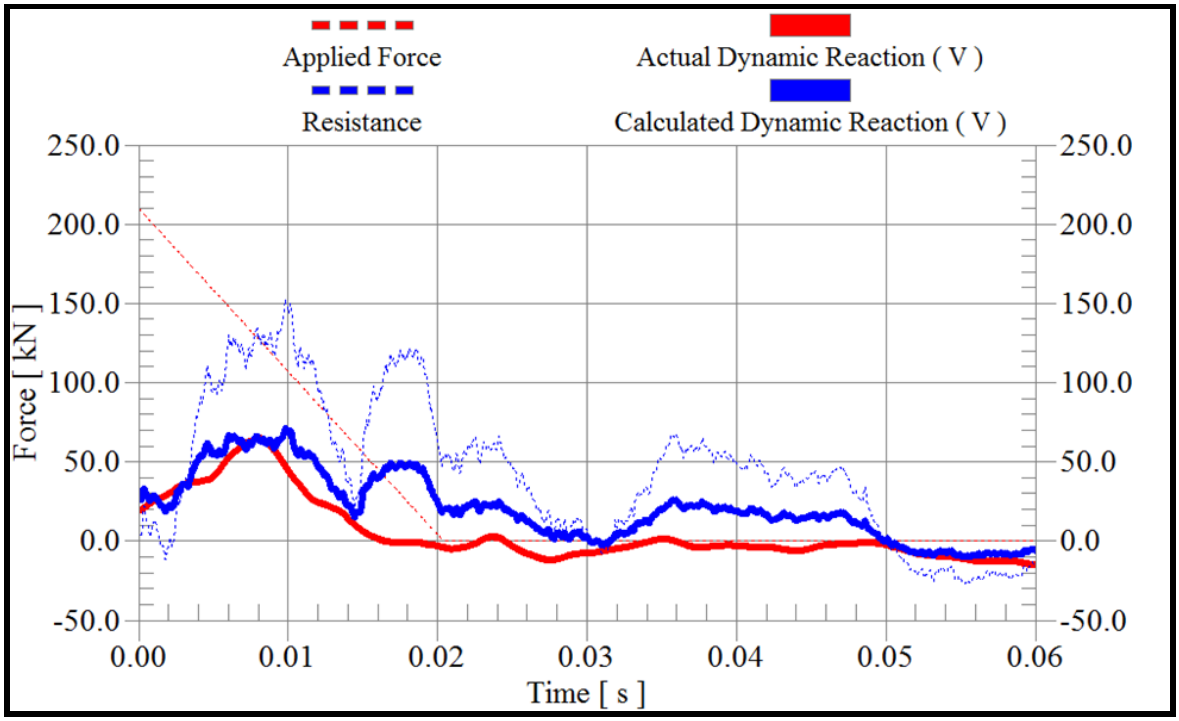

Fig. 5.41 Actual dynamic reaction vs. calculated dynamic reaction for Column S4-A-G1

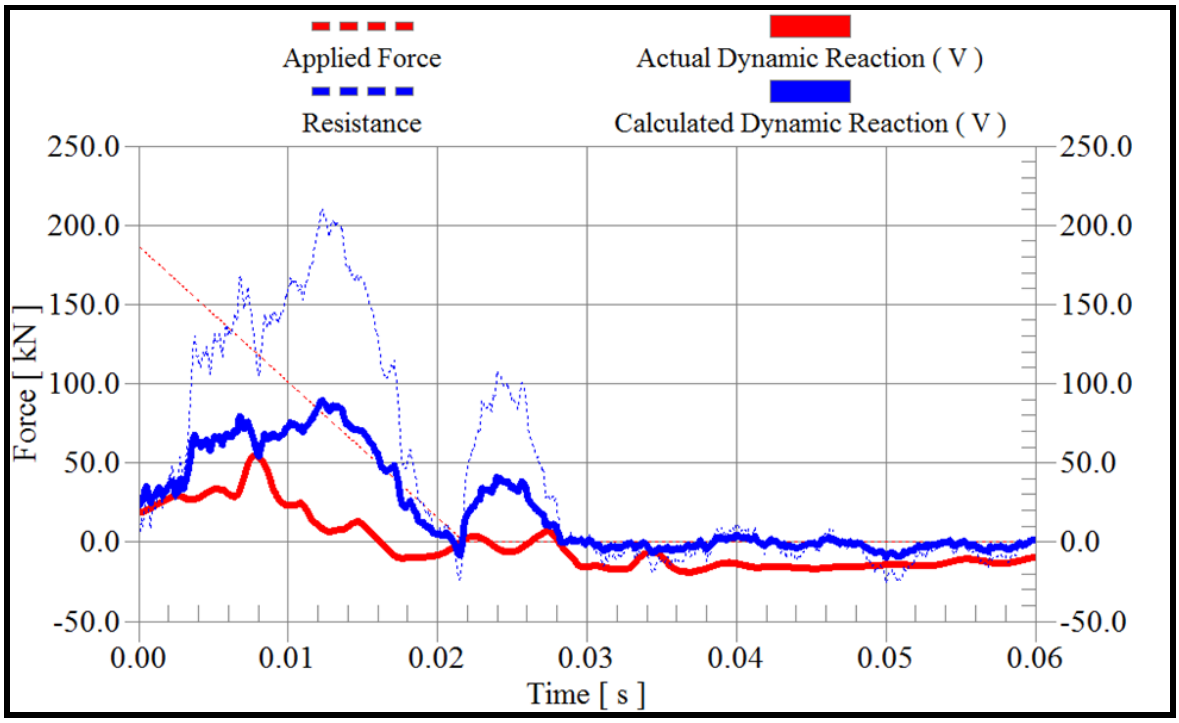

Fig. 5.42 Actual dynamic reaction vs. calculated dynamic reaction for Column S4-B-G1

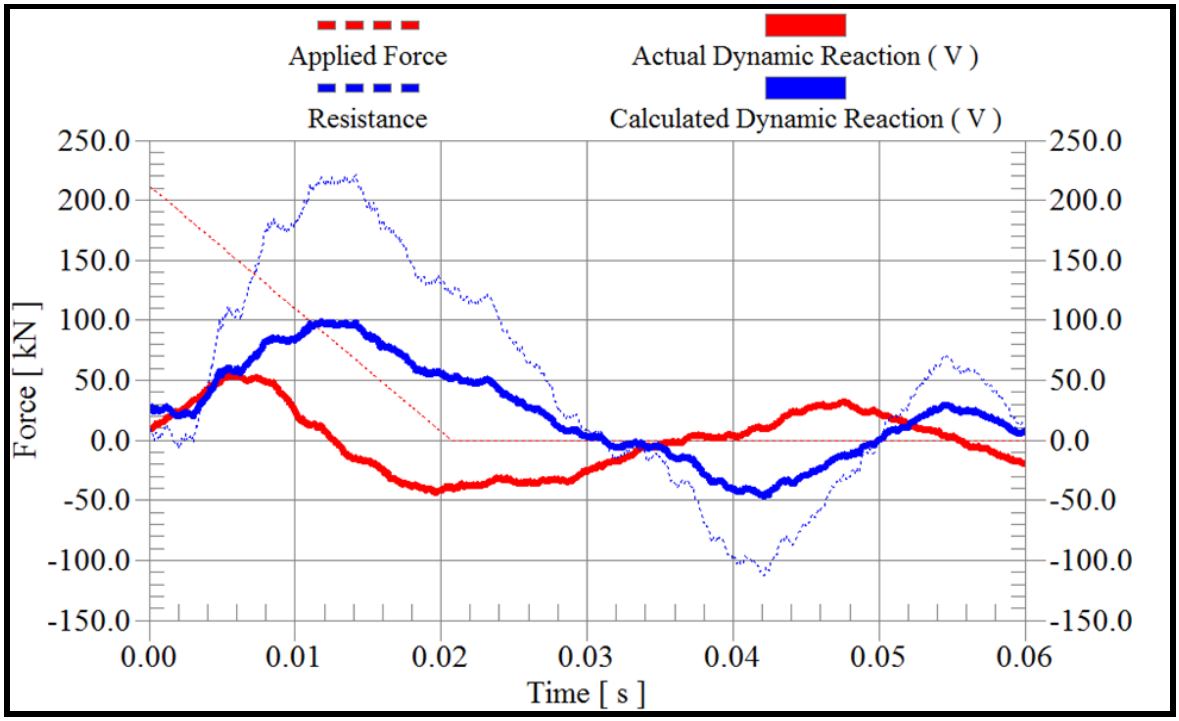

Fig. 5.43 Actual dynamic reaction vs. calculated dynamic reaction for Column S5-G1

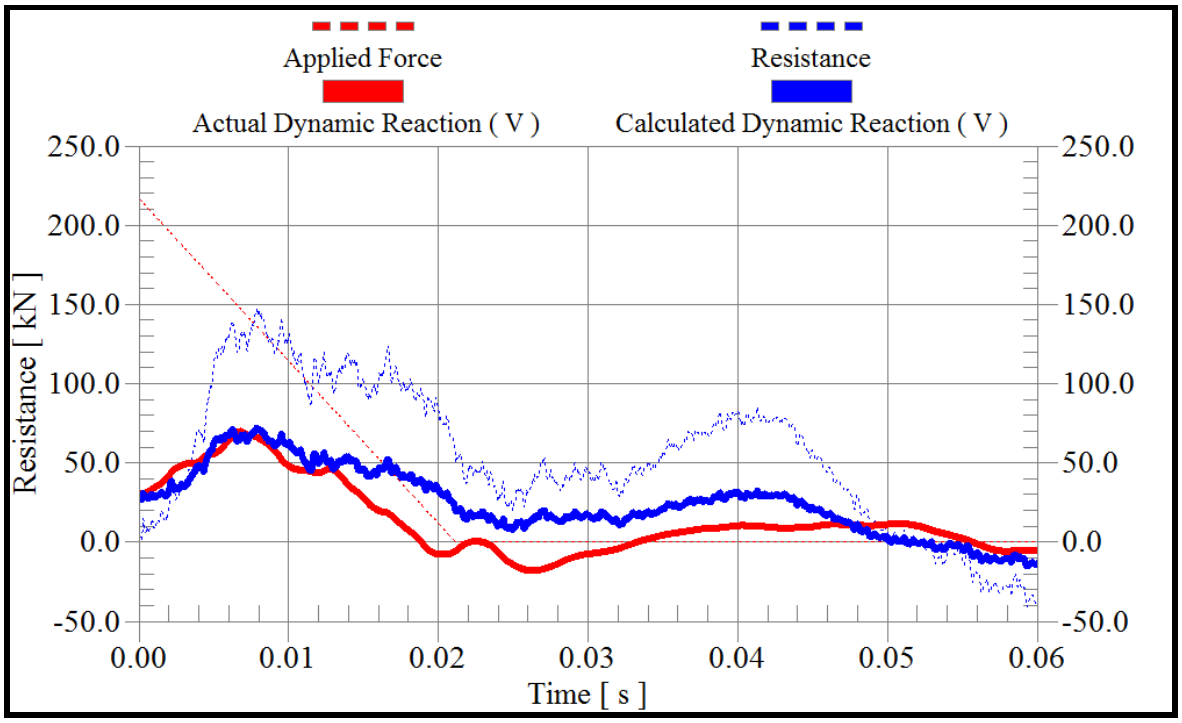

Fig. 5.44 Actual dynamic reaction vs. calculated dynamic reaction for Column KEV.1-G2

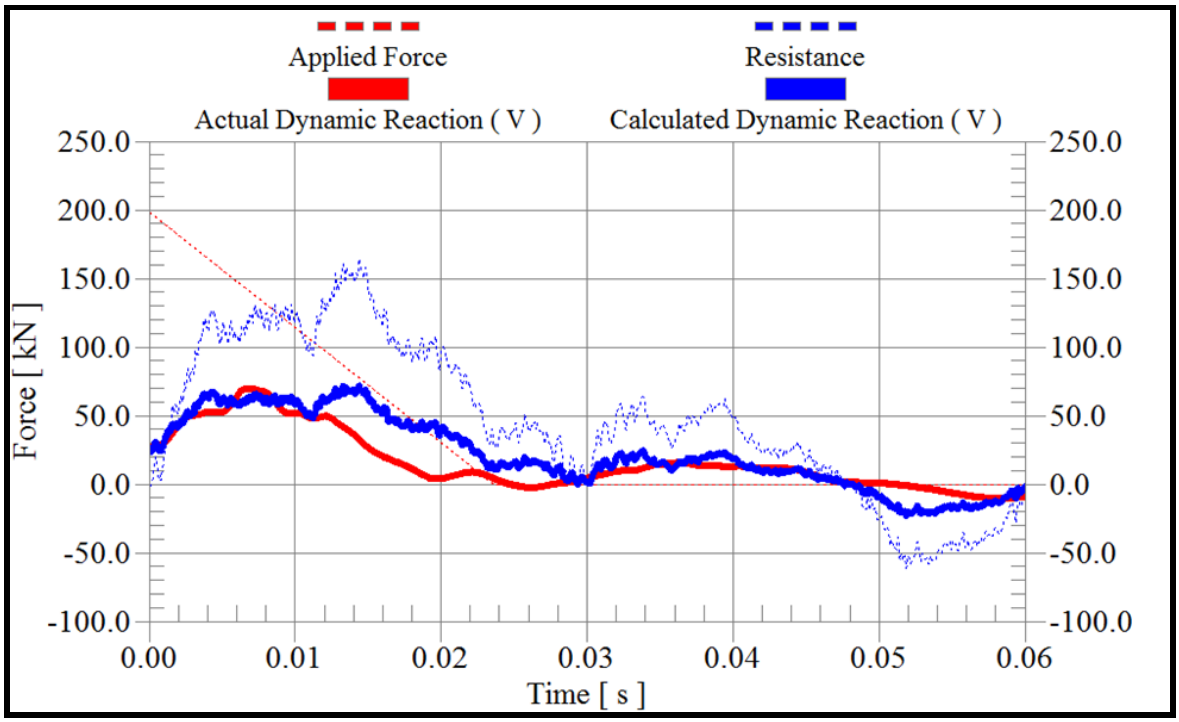

Fig. 5.45 Actual dynamic reaction vs. calculated dynamic reaction for Column KEV.2-G

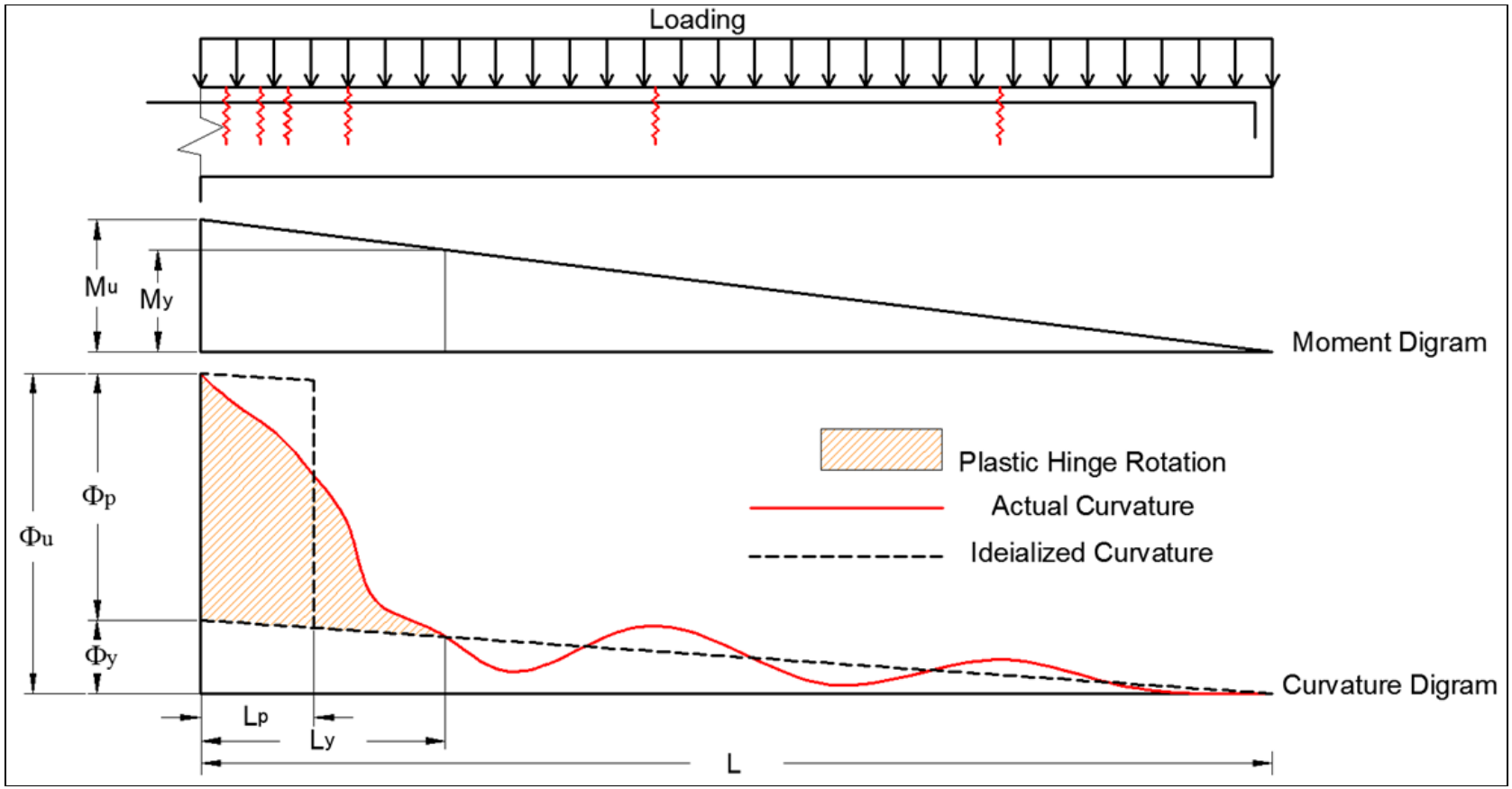

Fig. 5.46 Plastic hinge formation

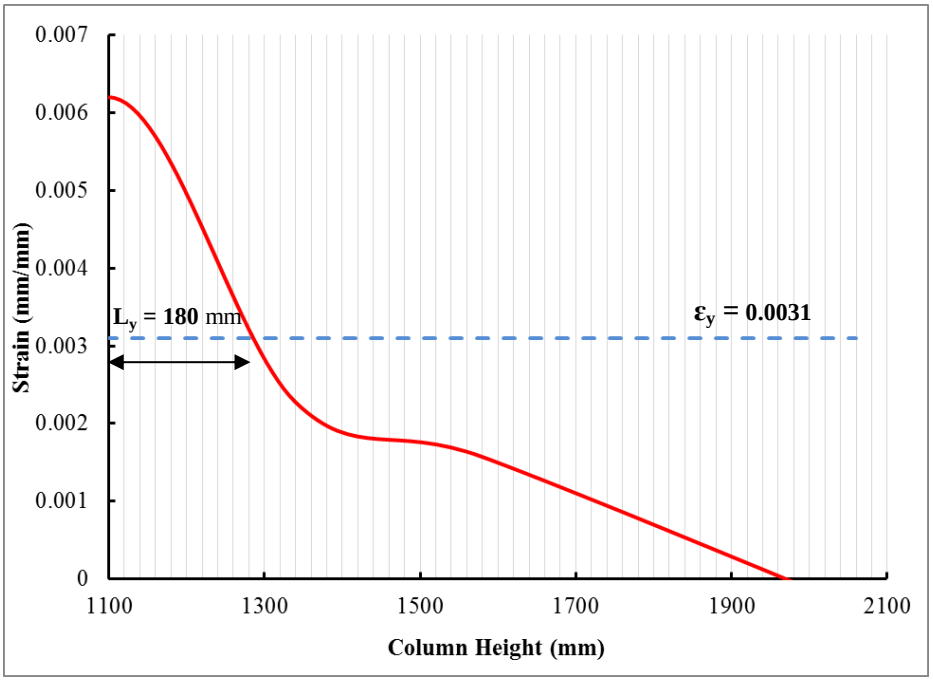

Fig. 5.47 Yielding length for Column NS1-G1

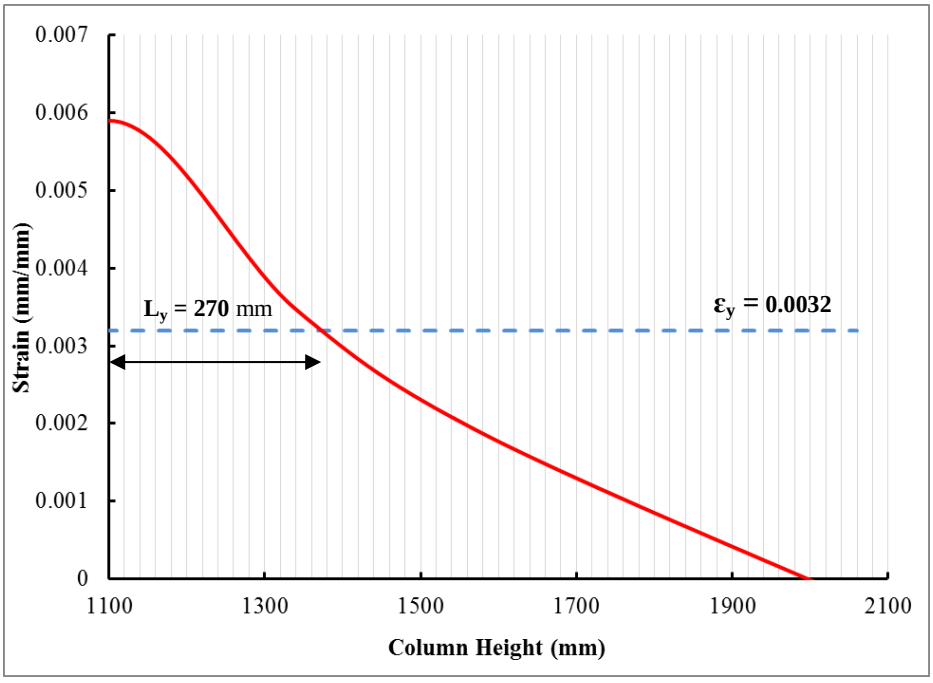

Fig. 5.48 Yielding length for Column NS2-G1

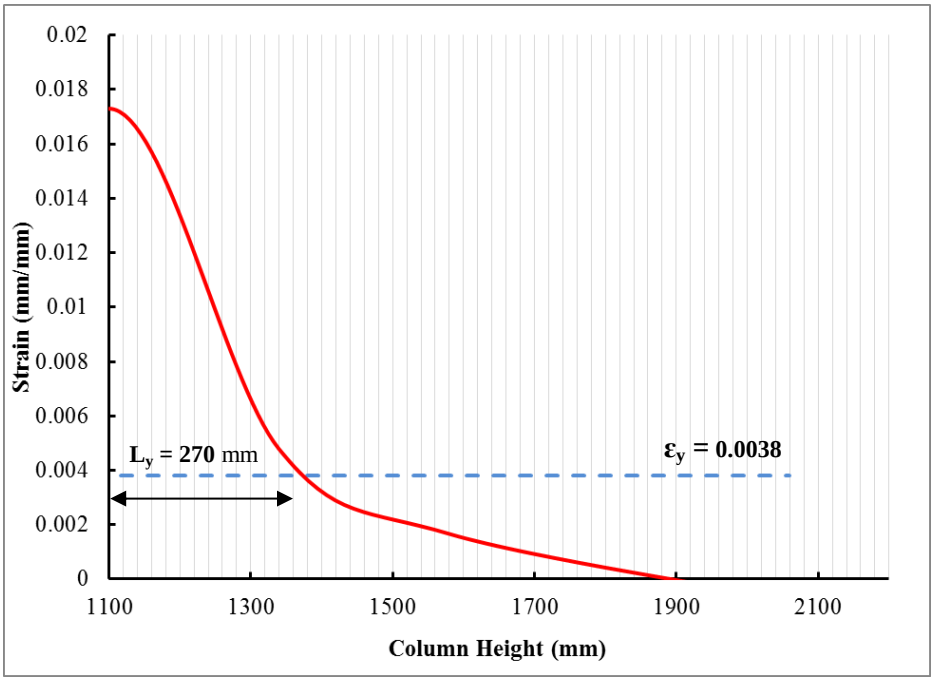

Fig. 5.49 Yielding length for Column NS3-G1

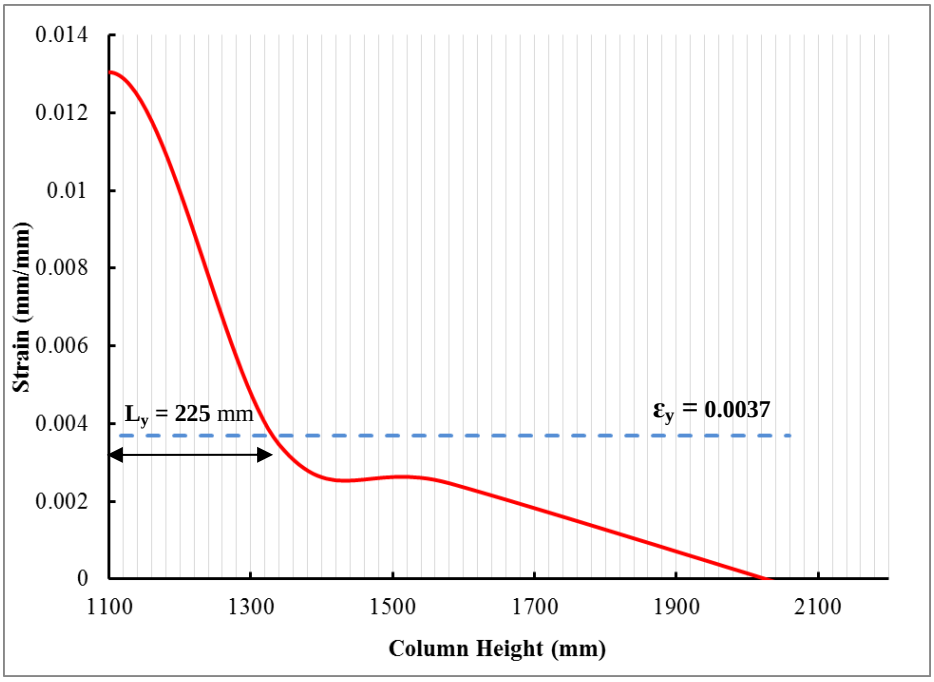

Fig. 5.50 Yielding length for Column NS5-G1

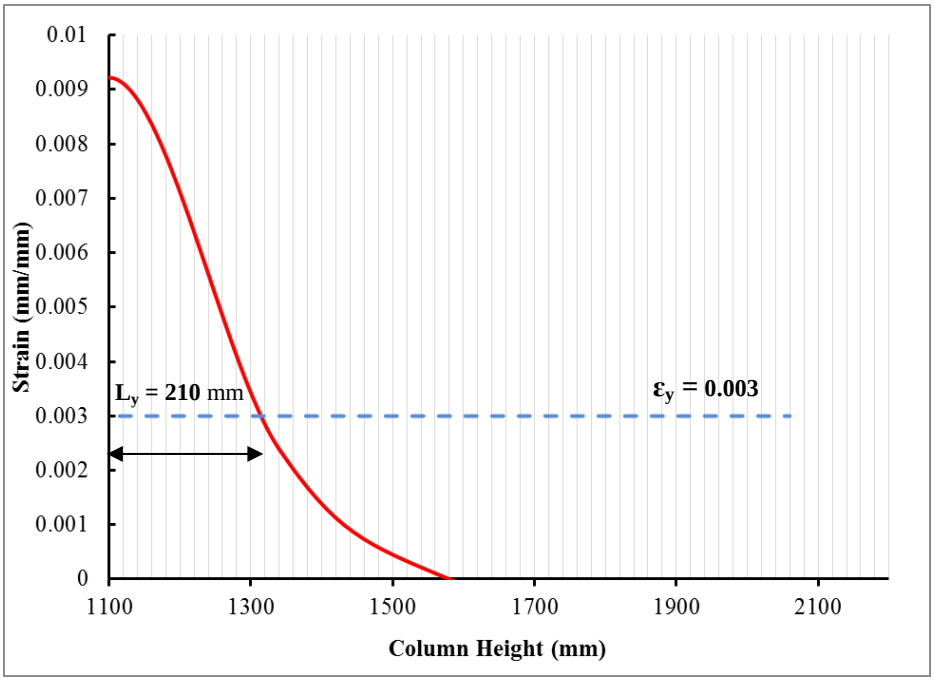

Fig. 5.51 Yielding length for Column S1-G1

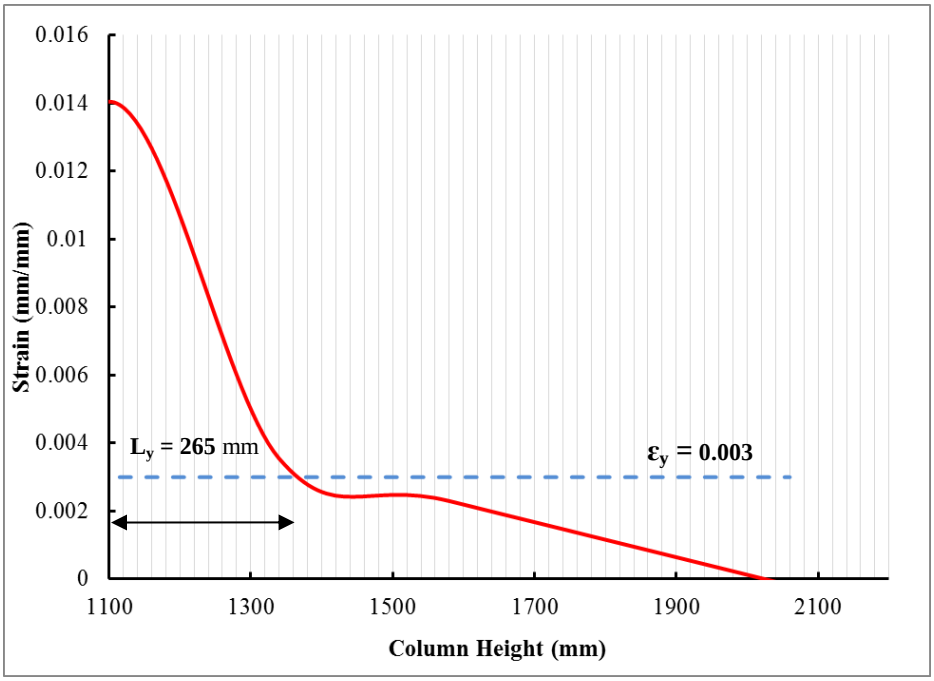

Fig. 5.52 Yielding length for Column S2-G1

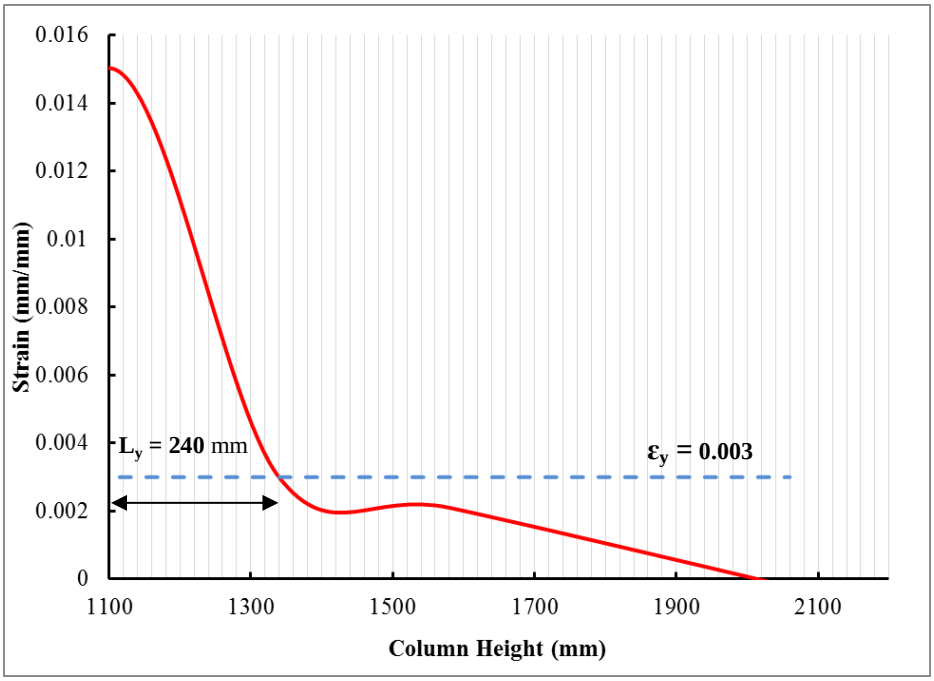

Fig. 5.53 Yielding length for Column S3-G1

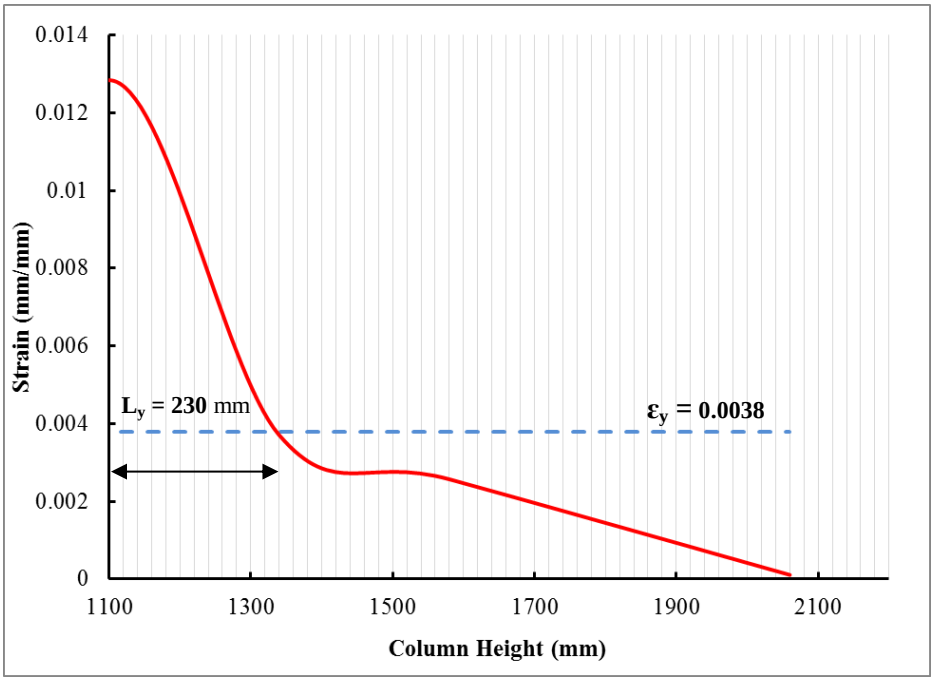

Fig. 5.54 Yielding length for Column S5-G1

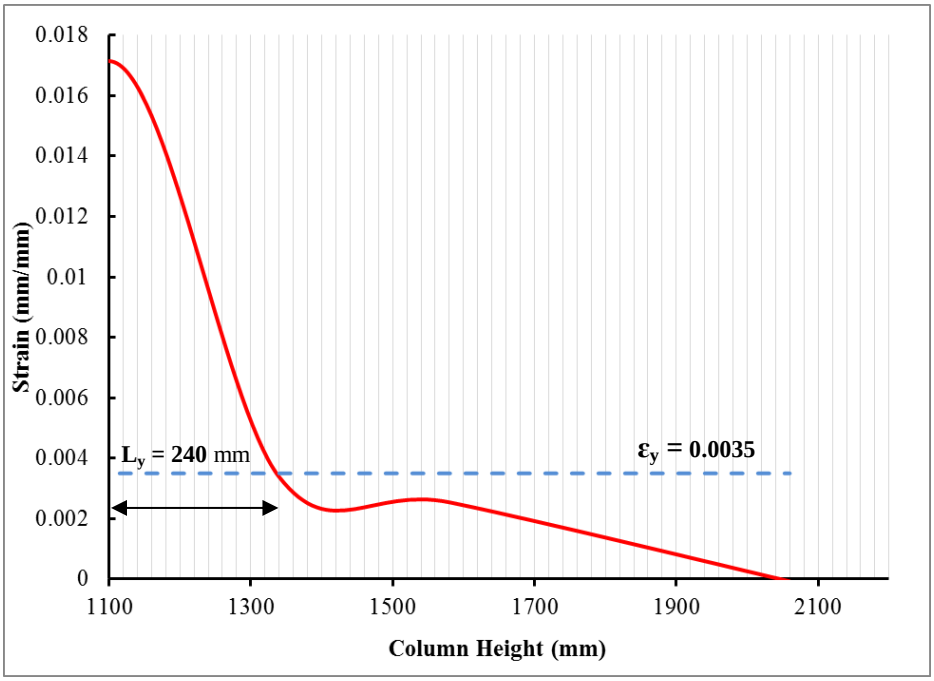

Fig. 5.55 Yielding length for Column KEV.-G1

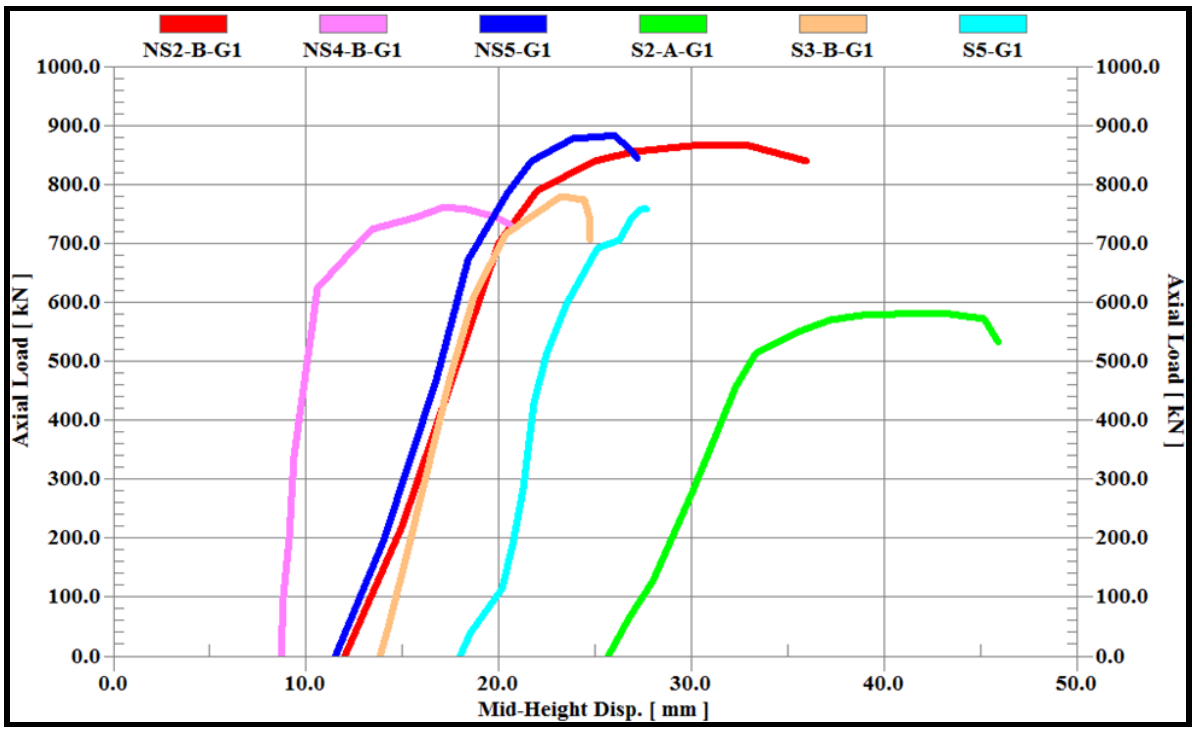

Fig. 5.56 Post-blast axial capacity of CFRP jacketed columns

Chapter Six

Analytical Modeling of Column Blast Response

6.1 Introduction

The columns tested in the experimental phase of the research program were analysed as single-degree-of-freedom (SDOF) elements to compute their dynamic response under the same blast shock waves that they were subjected to during the tests. This chapter presents the analysis procedure employed, material models used, and the resistance functions computed.

The dynamic analysis was conducted using computer software RC-Blast that was developed by Eric Jacques at the University of Ottawa (2014). This software was designed to run inelastic analysis of structural components exposed to the effects of blast loads. The program uses the dynamic resistance function and the impulsive forcing function for a specific structural element as input, and provides the displacement time history of the representative SDOF model, which in this case represents the column mid-height deflection.

An important step in the analysis is the computation of the force-displacement resistance function, based on which the structural characteristics of the element are introduced. The stiffness and strength of the column are obtained from this resistance function. Therefore, a detailed description of the material models, sectional analysis and member analysis are presented for the columns analysed. The analysis results are then compared with those recorded during the experimental phase of the investigation.

6.2 Sectional Analysis

A module was included in the RC-Blast software to compute inelastic sectional behaviour (moment-curvature relationship) of as-built and FRP retrofitted RC members. The first set of data required by the software is cross-sectional geometry and the type of structural element. Also included are the diameter and arrangement of longitudinal steel reinforcement, as well as the width and thickness of externally bonded FRP sheets used as flexural reinforcement (Fig. 6.1). Material models are specified in the form of confined and unconfined concrete and the stress-strain relationships of reinforcing materials. Dynamic increase factors (DIF) for each constituent material are specified as defined in ASCE (2011) and CSA S850 (2012) documents.

The RC-Blast module for RC column sectional analysis includes the effect of accompanying axial force. The magnitude of the axial force is a key input in computing the capacity of the section. Since the axial load on a column may vary during its response to shock waves, the effect of variable axial load is accounted for by considering different levels of axial compression. During the shock tube simulation of blast tests, the pre-blast axial load applied on the RC member drops in magnitude during the response as the mid-height lateral displacements take place. This axial load drop can be very high if the column mid-height lateral displacement becomes very large. The axial loads in columns of buildings subjected to explosions can vary substantially since the projected length decreases faster than the rate at which gravity loads can follow the column (Lloyd 2010 and Jacques et al. 2013). Consequently, both the initial and residual axial loads applied on the test column need to be predefined as input to the software. The users of RC-Blast have the option to run a sectional analysis at multiple levels of axial loading. It is the user's choice to decide on the number of moment-curvature curves to be produced. It was found that generating five moments–curvature curves of gradually decreasing axial load is reasonable when the pre-blast axial load degraded from 400 kN to 0 kN.

RC-Blast establishes moment-curvature diagram for positive and negative bending. Section capacity is reached once the program can no longer achieve equilibrium of internal forces, or if the moment capacity drops significantly (Jacques et al. 2013).

6.2.1 Material properties and material models

The mechanical properties of concrete, reinforcing steel and CFRP laminates used in the current analyses were obtained from the material characterization tests carried out as part of the

experimental program of this study (see Chapter 3). A predefined built-in model was used for each material to establish its stress-strain relationship. A detailed description of the expressions adopted for material modeling is given below.

6.2.1.1 Concrete

a) Unconfined concrete

RC columns include unconfined cover concrete and confined core concrete, if the core concrete is confined with a sufficient amount of closely spaced transverse reinforcement. The confinement effects provided by steel ties in ordinary (non-seismic) columns are negligible due to the relatively large spacing of ties. Therefore, the entire column section may be viewed to have unconfined concrete. The unconfined concrete stress-strain relationship used in RC-Blast was that suggested by Hognestad (1951). This model contains two parts, an ascending part between $0 \leq \varepsilon_c \leq \varepsilon_{o1}$ and descending part when $\varepsilon_c \geq \varepsilon_{o1}$. The ascending branch of the curve is generated by the second degree parabola shown below:

$$f_c = f'_{co}\left[2\frac{\varepsilon_c}{\varepsilon_{o1}} - \left(\frac{\varepsilon_c}{\varepsilon_{o1}}\right)^2\right] \tag{6.1}$$

where,

f_c is the stress in concrete,

f'_{co} is the unconfined concrete compressive strength,

ε_c is the strain in concrete, and

ε_{o1} is the strain at peak stress of unconfined concrete (may be assumed equal to 0.002).

The descending portion of Hognestad's stress-strain model consists of a linear branch between the peak strength and the point of 15% strength decay (or $0.85f'_{co}$) where the strain is set equal to 0.0038. After this point, the linear branch continues to drop down to $0.2f'_{co}$, beyond which it remains constant at $0.2f'_{co}$.

b) Confined concrete

Both the compressive strength and ductility of concrete improve when concrete is adequately confined by closely spaced transverse reinforcement of sufficient volumetric ratio (Fig. 6.2). Generally, column confinement is increased by reducing the spacing between the lateral ties, as well as reducing the spacing of laterally supported longitudinal reinforcement. On the other hand, FRP or steel jacketing is considered as an effective technique for providing different levels of confinement to the concrete. In seismically detailed FRP retrofitted RC columns, concrete confinement results from the dual confining actions offered by the closely spaced internal steel ties and the external FRP jackets. The two concrete confinement models developed by Saatcioglu and Razvi (1992) and Razvi and Saatcioglu (1999) were integrated into the RC-Blast computer program as default models for confined concrete (Jacques et al. 2013).

In the column analysis, concrete confinement was considered in one of three different manners: (i) In as–built (un-retrofitted) seismically detailed columns the core concrete was confined by internal steel ties; (ii) In CFRP retrofitted non-seismic columns the concrete in the entire column section (core + cover) was confined by the CFRP jackets; and (iii) In seismically detailed retrofitted columns the dual action of the steel hoops and the CFRP jackets was considered in the confined core, while the cover concrete was only confined by the CFRP jacket. In all cases Eq. 6.2, given below, was used to determine the confined concrete strength.

$$f'_{cc} = f'_{co} + k_1 f_{le} \qquad (6.2)$$

where,

f'_{cc} is the compressive strength of confined concrete,

f'_{co} is the compressive strength of unconfined concrete, and

f_{le} is the equivalent uniform lateral pressure.

Different procedures were used for different types of columns to obtain the confinement pressure (f_l) for each case:

1) Seismically detailed as-built columns

$$k_1 = 6.7(f_{le})^{-0.17} \quad (6.3)$$

$$f_{le} = k_2 f_l \quad (6.4)$$

$$k_2 = 0.15\sqrt{\frac{b_c b_c}{s_1\, s}} \leq 1.0 \quad (6.5)$$

$$f_l = \frac{A_s f_y}{s\, b_c} \quad (6.6)$$

where,

b_c is the core dimension measured center-to-center of the perimeter hoop,

s is the spacing of transverse reinforcement,

s_1 is the spacing of laterally supported longitudinal reinforcement, and

A_s is the area of transverse steel reinforcement.

2) Non-seismically detailed CFRP retrofitted columns

$$f_l = \frac{2 t_j f_{fj}}{D} \quad (6.7)$$

$$f_{tj} = 0.006\, E_F \quad (6.8)$$

where,

t_j is the thickness of FRP jacket,

f_{fj} is the effective stress of FRP,

D is the column diameter or width in the direction of loading, and

E_F is the elastic modulus of FRP.

$$f_{le} = k_2 f_l \quad (6.9)$$

$k_2 = 1.0$ for circular and oval columns, and

$k_2 = 0.4$ for rectangular or square column

3) Seismically-detailed CFRP column

$$f_{le} = (k_2 f_l)_{Hoop} + (k_2 f_l)_{CFRP} \quad (6.10)$$

The ascending portion of the compressive stress-strain curve of normal strength confined concrete is expressed by:

$$f_c = f'_{cc}\left[2\frac{\varepsilon_c}{\varepsilon_1} - \left(\frac{\varepsilon_c}{\varepsilon_1}\right)^2\right]^{1/(1+2K)} \quad (6.11)$$

$$K = \frac{k_1 f_{le}}{f'_{co}} \quad (6.12)$$

The post peak branch of the confined concrete stress-strain curve in compression is given by the following expressions (Saatcioglu and Razvi 1992).

$$\varepsilon_1 = \varepsilon_{1o} + (1 + 5K) \quad (6.13)$$

$$\varepsilon_{85} = 260\,\rho\varepsilon_1 + \varepsilon_{o85} \quad (6.14)$$

where,

ε_1 is the strain at peak stress of confined concrete,

$\varepsilon_{85}$is the strain corresponding to 85% of peak stress of confined concrete on the descending portion of the compressive stress-strain curve, and

ρ is the volumetric ration of transverse reinforcement.

6.2.1.2 Longitudinal steel reinforcement

a) Reinforcement in tension

The stress-strain relationship of longitudinal steel reinforcement in tension was modelled to include three successive segments; i) elastic segment, ii) yield plateau, and iii) strain hardening. For the first two segments, the relationship was linear, whereas the last part of the curve was expressed by a parabolic function. The equations shown below (Yalcin and Saatcioglu 2000) describe the full stress-strain relationship of longitudinal reinforcement in tension:

when $\varepsilon_s \leq \varepsilon_y$

$$f_s = E_s \varepsilon_s \tag{6.14}$$

where,

f_s is stress in reinforcing steel; ε_s is the corresponding strain, and

E_s is the reinforcing steel modulus of elasticity.

$$\varepsilon_s = \frac{f_y}{E_s} \tag{6.15}$$

when $\varepsilon_y < \varepsilon_s < \varepsilon_{sh}$

$$f_s = f_y + \left(\varepsilon_s - \varepsilon_y\right)\left(\frac{f_{sh} - f_y}{\varepsilon_{sh} - \varepsilon_y}\right) \tag{6.16}$$

when $\varepsilon_{sh} < \varepsilon_s < \varepsilon_u$

$$f_s = f_y + (f_u + f_y)\left[2\frac{\varepsilon_s - \varepsilon_{sh}}{\varepsilon_u - \varepsilon_{sh}} - \left(\frac{\varepsilon_s - \varepsilon_{sh}}{\varepsilon_u - \varepsilon_{sh}}\right)^2\right] \quad (6.17)$$

where f_y, f_{sh}, f_u are yield, strain-hardening and ultimate stresses; ε_y, $\varepsilon_{sh}, \varepsilon_u$ are the corresponding strains, respectively.

b) Reinforcement in compression

The stress-strain relationship of reinforcement in compression is the same as that in tension only if the reinforcement was prevented from buckling. The rebar aspect ratio (rebar unsupported length between column ties/rebar diameter) controlled the behaviour of the material in compression (Yalcin and Saatcioglu 2000, Jacques et al. 2013). When the rebar aspect ratio is larger than 8.0, rebar buckling initiated immediately upon yielding. The stress-strain relationship followed a descending curve immediately after the yield point, resulting in material failure. On the other hand, some strength can still be maintained after yielding if the rebar aspect ratio is equal to 8.0. Compression rebars with an aspect ratio of less than 8.0 can develop limited strain hardening behavior (Yalcin and Saatcioglu, 2000, Jacques et al. 2013).

For simplicity, the elastic and the full post yield behaviour of steel were modeled by a typical simplified bi-linear stress-strain relationship. Equation 6.14 was used to describe the first part of the curve while the post-yield part was represented by a straight line starting from the yield point and extending horizontally up to the ultimate strain.

6.2.1.3 Externally bonded CFRP

Test data collected from FRP tensile coupon tests showed a linear stress-strain relationship for all FRP laminates used in this study. The stress-strain curve of CFRP laminates in tension was modeled as shown in Fig. 6.3. The CFRP input data included modulus of elasticity and ultimate stress and strain (stress and strain at rupture). The failure of CFRP retrofitted columns due to debonding of the externally bonded CFRP laminate was not observed in the present study. This is because all test columns were fully wrapped along their entire length by overlapping CFRP

sheets. Consequently, the debonding strain is always considered much higher than the rupture strain of the CFRP material.

CFRP laminate width or height, actual thickness, and arrangement in the section were defined in the software RC-Blast as part of the input data. The following simplifying assumptions were made in modelling the FRP:

1. The CFRP laminate had no contribution to compression resistance.
2. The additional tension forces provided to the section were generated by the bottom and sides segments of the CFRP jacket.
3. Only the parts of the side CFRP laminates below the centroidal axis were considered in the analysis (see Fig. 6.4).

6.2.2 High strain rate effects on materials

The effect of high strain rates on materials is often characterized with an increase in strength. The strength of a material in a structural element subjected to blast loading can be analytically modelled by using an appropriate dynamic increase factor. For this purpose, designers use tables and equations given by design guidelines or standards, or they use values available in the literature. In the present analysis, the dynamic increase factors (DIF) assumed for concrete compressive strength, and yield and ultimate tensile strengths for steel reinforcement were 1.19, 1.17, and 1.05, respectively. Due to the limited information available, a dynamic increase factor of 1.0 was applied to the CFRP tensile strength.

6.2.3 Strength Increase Factor (SIF)

In the design of blast resistant structures, strength increase factors (SIF) are applied to construction materials since the actual strength of these materials exceeds specified minimums (PCA-EB090, 2009). Concrete compressive strength is typically tested at the age of 28 days; however, over time, concrete keeps gaining strength. In practice the average yield strength of steel rebars or structural sections is approximately 25% higher than the specified minimum values (ASCE-2011). Most codes and standards for structural design against blast suggest SIF values for concrete and steel reinforcement. Unfortunately, there is not enough information in the literature related to the application of SIF to FRP materials. It is usually left to the designer's judgment and experience whether to include such strength increase factors or not.

In the present column analysis, no strength increase factors were applied to concrete and steel reinforcement since the quality of these materials was highly controlled. However, this did not apply to the CFRP materials. This is because during the present blast tests conducted on CFRP strengthened columns, it was observed that the predicted ultimate CFRP jacket tensile strains were higher than the corresponding strains measured by coupon tests. The ultimate tensile strains of the CFRP at column mid-heights were indirectly computed from the section strain compatibility as the rebar tension and compression strains were measured at the columns' critical regions. Note that the rebar maximum tensile strain was always well developed prior to the rupture of the tensile CFRP. Fig. 6.5 shows the time history of the tensile and compression strains and the mid-height displacement of Column NS3-B. From Fig. 6.5 and Fig. 6.6 it can be observed that while the maximum tensile strain of the steel occurred at 17.5 ms from the start of the test, the CFRP rupture was initiated at 26.6 ms from the start of the test. Table-6.1 compares the CFRP maximum tensile strains obtained by static coupon tests to the CFRP dynamic tensile strains determined from strain compatibility of the section. It can be seen that in most cases the tensile strains determined from column blast tests were at least 50 % higher than the CFRP strains obtained from coupon tensile tests. This increase in strength may be attributed to the fact that the concrete column restrains the CFRP laminate wrapped around it from developing out-of-plane deformations or distortion. This results in a better mechanical behaviour of the laminate that can reach very high strengths compared to the laminate behaviour experienced in a state of free-deformation (e.g.the case of uni-directional coupon test of CFRP laminate). All the laminates investigated in this study are asymmetrical. The laminate is symmetrical when exactly the same laminas on the two sides of the centroidal plane are located at same distances from the centroid. For example a laminate with lay-up sequence of (W [±45 ˚] UD [0˚] UD [90˚] UD [90˚] UD [0˚] W [±45 ˚]) is a symmetrical laminate while the laminate with lay-up sequence of (W $[\pm 45\ ^\circ]_2$ UD $[0^\circ]_2$ UD $[90^\circ]_2$) is an asymmetrical laminate. When an asymmetrical laminate is under unidirectional or bi-directional in-plane stresses, it develops an anisotropic behaviour with out of plane stresses together with high extension-extension and shear-extension stress couplings. Depending on different lamina characteristics and their lay-up, this complicated state of stress results in a premature failure of the laminate when low uniaxial stress is applied (see ASTM STP 1383, 2001, Eurocomp Design Code and Handbook, 2005, and Knops 2008). Hence the out of plane deformations of the asymmetrical laminates wrapped around concrete columns are

restrained enabling the laminate to reach much higher strength and in-plane strain capacities. Other researchers observed such increase of the uni-directional tensile strength of the FRP used for strengthening structural elements subjected to blast loads. Myer et al. (2004) suggested a strength increase factor of 1.3 for the FRP in their blast analysis, which is used in the present study.

6.2.4 Variation of axial load

Prior to the column tests, the columns were loaded axially by two hydraulic jacks placed at the bottom of the column. The test results showed that the pre-blast axial loads always decrease at different rates and magnitudes as the columns develop lateral deflections during the application of simulated blast loads. This reduction in the applied axial load is mainly due to the shortening in the projected height of the column along the neutral axis. The decrease in column height provides a space to the hydraulic jack piston to expand and release the oil pressure and hence reduce the applied axial load. Columns in buildings exposed to a real explosion could experience the same pattern of sudden decrease of the axial load. This is because the lateral acceleration of the column due to the blast load is much higher than the gravitational acceleration of the self-weight, super-imposed dead load and live loads that make up the column axial load.

It was stated earlier that for each column section, RC-Blast can perform sectional analysis under different level of axial loads. This feature of the computer program is very efficient in constructing a composite resistance-displacement relationship in which the variation in the axial load applied is integrated. Therefore, the resistance curve formed by RC-Blast represents the corresponding curve of the actual scenarios with reasonable accuracy.

6.3 Resistance Function Development

The development of the dynamic resistance-displacement function by RC-Blast for as-built and CFRP protected columns was based on a lumped inelasticity approach (Jacques and Saatcioglu, 2014). In this method, the non-linear behaviour (crushing of concrete, yielding of steel, and buckling of compression reinforcement) is assumed to occur entirely within the critical section located at mid-height (Jacques et al. 2015). Fig. 6.7 shows that the columns were idealized as simply supported, half-span elastic beam-column with a rotational spring at mid-height. The effective pre-yield slope of the moment-curvature relationship was used to define the flexural rigidity of the member, while the post-yield sectional response was used to construct and idealize

the hinge moment-rotation relationship (Aoude et al. 2015). The equivalent plastic hinge length at column mid-height was assumed to be equal to the column overall depth. The resistance curve was established through solving the force-deflection curve equation shown below at various incremental loads (Jacques et al. 2015).

$$y\,(x) = \frac{wx}{24EI}(x^3 - 2L_o x^2 + 2L_o^3) + \frac{k_s \theta_s x}{EI}\left(\frac{L_o}{2} - \frac{x^2}{6L_o}\right) + \theta_s x \qquad (6.18)$$

where,

$y\,(x)$ is the deflected shape,

w is the distributed load,

k_s is the secant rotational spring stiffness,

θ_s is the corresponding rotation found from moment rotation response, and

L_o is the half length of the member.

6.4 Equivalent SDOF Analysis

RC-Blast runs an equivalent SDOF analysis to determine the entire mid-height displacement-time history of RC columns subjected to blast loading. The dynamic response of a RC member is predicted through the application of the equation of motion shown below.

$$k_{LM}(y)m\ddot{u}(t) + R\big(u(t)\big) = AP_r(t) \qquad (6.19)$$

The value of the load-mass transformation factor (k_{LM}) is specified based on the response type of the member (elastic or plastic). The total mass (m) includes both the weight of the RC column and the weight of the lateral load transfer device. In the current analysis (m) was equal to 400 kg. The theoretical composite resistance function produced by the software in the structural analysis module was incorporated into the solution of the equation of motion. Damping was ignored as in blast analysis its effect is assumed negligible on the response of the member. The reflected

pressure was idealized by assuming a linear variation starting at the peak, and reducing down to zero over a period equal to the positive phase duration (t_d). The peak reflected pressure was estimated by dividing the actual impulse reported in the test over $0.5t_d$. In analysis, the time step used was 0.0001 seconds.

The average constant acceleration numerical integration method was used to solve the equation of motion. This method is particularly useful due to its ease of use and unconditional stability (Jacques et al. 2013, UFC 2008).

6.5 Analytical Results

The analytical results computed using RC-Blast were compared with the results of the different column tests described in previous chapters. The comparisons include the resistance-displacement curves and column mid-height displacement time-histories.

6.5.1 Resistance functions

The actual experimental resistance-displacement relationships were computed from displacements, accelerations, and reflected pressure that were measured with very high accuracy. The resistance-displacement relationships were also produced analytically by RC-Blast. The plastic hinge length in the analysis was assumed to be equal to 150 mm or the overall section depth of the column (Sheik and Khoury 1994, Sheikh et al. 1994, Bayrak and Sheikh 1998, Bae and Bayrak 2008).

Figs. 6.8 to 6.17 compare the actual resistance-displacement relationship with the corresponding analytically derived relationships. The results indicate that RC-Blast has the capability to simulate the actual dynamic resistance curve with reasonable accuracy for most of the tested specimens. Yet, the RC-Blast underestimated the ductile behaviour of Columns NS2 and S2 as clearly shown in Fig. 6.9 and Fig. 6.14. This is due to the relatively short plastic hinge length assumed in the analysis of Columns NS2 and S2. In section 5.10, the calculation conducted for estimating the plastic hinge lengths of the columns investigated showed that Column NS2 and Column S2 had plastic hinge lengths larger than 150 mm. Note that this length was adopted in the analysis of RC-Blast for all columns in this study. To enhance the simulated ductility of NS2 and S2 another run was performed to generate the analytical resistance functions assuming longer plastic hinge lengths as shown in Fig. 6.18 and Fig. 6.19. It is obvious that the ductility

was increased in the analytically predicted resistance functions when the plastic hinge lengths are set equal to 165 mm and 195 mm for Column NS2 and Column S2, respectively. The increase of the plastic hinge length when some laminate designs are used (for instance, with Columns NS2 and S2) results in improved ductility as shown in Chapter 5. Increasing the plastic hinge as input for the analytical prediction of the resistance function resulted in a better fit with the actual resistance-displacement relationships.

6.5.1 Columns mid-height time history

Figs. 6.20 to 6.29 and Table-6.2 show the comparison between measured mid-height displacements and the corresponding computed displacements by RC-Blast. The results show that RC-Blast underestimated the mid-height displacement for all columns. On average, the analytical results are 40% less than the test results. The accuracy of the input data for different parameters, such as materials mechanical properties and their representative stress-strain models, assumed values for dynamic and strength increase factors, assumed values for plastic hinge lengths, and the overall measured mass have all contributed with different levels to the error in the estimation of the displacement time-history. Conducting a detailed sensitivity analysis to evaluate the effects of each of the mentioned parameters on the accuracy of the displacement time history is not considered as part of the scope of this study. However, because the analytically predicted resistance functions using RC-Blast well matched the actual resistance-displacement relationships of the columns, material properties and their incorporated models, the dynamic and strength increase factors are considered as accurate. On the other hand, the sensitivity of RC-Blast results to the weight of the total mass and the length of the plastic hinge will be explored below.

6.5.1.1 Effect of total mass weight on RC-Blast results

The equivalent lumped mass used in the SDOF analysis has a major role on the prediction accuracy of the dynamic displacement time history of the tested column specimens. In the present study, the total mass is a combination of the column mass and the mass of the steel curtain (or the lateral load transfer system). During the shock tube test, the blast pressure is first applied to the steel curtain, which is in contact with the column. The curtain ribs touch the column and the blast pressure is fully transferred to the column through equally spaced contact points distributed over the height of the column. Once this happens, the two mass components

start to accelerate until the blast pressure is vanished. Hence, for the analysis, the column and the curtain are assumed acting as one mass from the point when the blast load is transferred to the column specimen until a later time during the blast event. This is clearly shown in Fig 6.30 (a and b). No separation between column NS1 and the steel curtain was noticed at the instant 50.7 ms (Fig. 6.30-a). It should be noted that at this instant, the mid-height displacement has become maximum. Fig. 6.30-b shows that at the instant 74.8 ms from the start of the test the two loaded components were still attached to each other. The first separation on the other hand was initiated after the instant 81.7 ms as illustrated in Fig. 6.30-c. The gap between the column and the curtain was substantially increased after this moment (Fig. 6.30-d). This phenomenon was observed in all blast tests. It is possible to include a part of the steel curtain mass in the SDOF analysis only when an early uncoupling takes place between the two loaded components.

The effect of changing mass during response was investigated. A new mass, equal to 300 kg, was assumed at the point of detachment of the load application system, as compared to the full mass of 400 kg. Fig. 6.31 and Fig. 6.32 show the influence of decreasing mass on maximum mid-height displacement for Columns NS2 and S3, respectively. It can be seen that reducing the mass from 400 kg to 300 kg increased the maximum displacement of Columns NS2 and S3 by 13.6 % and 11.4 %, respectively. This improves the results of the analysis, yet this increase in the theoretical results is not enough to obtain a perfect fit to the test data.

6.5.1.2 Effect of plastic hinge length on RC-Blast maximum displacement results

It was stated earlier that RC-Blast underestimated the ductility of columns NS2 and S2 when a plastic hinge length, Lp, equal to 150 mm was assumed in the analysis. It was also shown that the ductility produced by the computer program was notably improved when Lp was increased to 165 mm and 195 mm for Columns NS2 and S2, respectively.

In this section, the effect of increasing the plastic hinge length on the maximum mid-height displacement predicted by RC-Blast for Columns NS2 and S2 is further examined. Fig. 6.33 and Fig. 6.34 clearly show the effect of increasing the plastic hinge length on the mid-height time history for Columns NS2 and S2. It can be seen from these figures that increasing the plastic hinge in the present analysis state has a negligible effect on increasing the maximum mid-height displacements for these columns.

6.5.3 P-Δ effects

In the current investigation the level of applied axial load is relatively high (40-45% of column concentric capacities). Furthermore, lateral displacements caused by blast loads are substantial in all tests. Hence, the second order effects of axial loads (P-Δ effects) must be considered in the SDOF analysis to accurately predict theoretical mid-height displacements.

Fig. 6.35 and Fig. 6.36 show time history of P-Δ moments measured for the non-seismic and seismic columns, respectively. The two figures prove that the secondary moments generated during the loading process are very high and should be included in the analysis. Unfortunately, the present version of RC-Blast does not consider the second order analysis or the P-Δ effects.

Including the P-Δ effect requires modifying the step-by-step integration procedure of the equation of motion in RC-Blast SDOF analysis, which is beyond the scope of this investigation. Instead, the Equivalent Lateral Load Method suggested by Oswald (2010) is applied to account for P-Δ moments as described in the following sub-section.

6.5.3.1 Equivalent lateral load method (ELLM)

In the equivalent lateral load method (ELLM) the effect of a secondary moment is substituted by an equivalent dynamic lateral load. ELLM method for calculating P-Δ effects is incorporated into the current version (version 4.1) of SBEDS (Single-Degree-of-Freedom-Blast Effects Design Spreadsheets) (Oswald 2010). The equivalent blast pressure can be calculated as follows:

$$p_{(t)} = P_{(t)}\left[\Delta_{(t)} + e\right]\left(\frac{C}{L^2}\right) \tag{6.20}$$

$$C = K_1 K_2 \tag{6.21}$$

where,

$p_{(t)}$ is the equivalent lateral load (ELLM) (psi),

$P_{(t)}$ is the axial load (lb) divided by the width of the loaded element,

$\Delta_{(t)}$ is the maximum mid-height displacement obtained by SDOF analysis not including P-Δ effects,

e is the axial load eccentricity relative to the centroid of the column (e =0 in the current study),

L^2 is the column height (in),

C is a constant related to load distribution and boundary condition,

K_1 see Table-6.3, and

K_2 is equal to 1.0 for one way system and 0.64 for two way system.

From the first run of the SDOF analysis conducted by RC-Blast (where P-Δ effects are not included), $\Delta_{(t)}$ and $P_{(t)}$ are specified. Equation 6.20 is then applied to compute the equivalent reflected pressure; this pressure is added to the initial blast pressure (Table-6.4). Another cycle of the analysis is conducted using RC-Blast with the modified pressures being applied to predict the maximum mid-height displacement for each of the investigated column.

Figs. 6.37 through 6.46 compare test data with computed mid-height displacement time histories with and without the P-Δ effects. The figures show that the analytical results of the maximum lateral displacements are significantly improved with a very good match with the experimentally recorded results when the ELLM approach is used. Table-6.5 gives the ratio of modified RC-Blast maximum mid-height displacement to the experimentally measured maximum mid-height displacement (Max. $\text{Disp.}_{\text{RC Blast}}$/Max. $\text{Dip.}_{\text{Test Data}}$). The average (Max. $\text{Disp.}_{\text{RC Blast}}$/Max. $\text{Dip.}_{\text{Test Data}}$) ratio and percent error are 0.93 % and 11.67 %, respectively.

Table-6.1: CFRP tensile strains in shock tube tests

Column	T-3	C-3	ε_{frp} (actual)	C	ε_{frp} (coupon test)	ε_{frp} (actual)/ ε_{frp} (coupon test)
	%	%	%	mm	%	
NS2	1.63	-	-	-	1.26	-
NS3	1.59	1.2	2.18	68.4	0.96	2.27
NS4	1.74	1.2	2.35	65.3	1.22	1.92
NS5	1.31	1.15	1.82	71.7	1.22	1.49
S2	1.59	-	-	-	1.28	-
S3	1.5	0.511	1.92	48.8	1.23	1.5
S4	1.94	1.12	2.58	61.6	1.22	2.11
S5	1.28	1.155	1.79	72.1	1.17	1.53

Table-6.2: Summary of experimental and analytical results

Column	Shock Wave Properties			Experimental Response		RC-Blast Response		
	Pressure	Impulse	Duration	Maximum Disp.	Time to max. Disp.	Maximum Disp.	Time to max. Disp.	Max.Disp.$_{RC\ Blast}$/Max. Disp.$_{Experimental}$
	kPa	kPa-ms	ms	mm	ms	mm	mm	
NS1	45.5	477.4	21	125.3	50.8	80.5	33.7	0.64
NS2	45.5	472.9	20.8	53.5	25.6	36.3	18.9	0.68
NS3	42.15	437.5	20.76	69.1	32.9	38.6	18.4	0.56
NS4	43	440	21.8	81	44.1	45	27.9	0.55
NS5	42	463	22	51.3	23.9	33.3	18.6	0.65
S1	47.33	509.3	21.52	114.9	73.3	68.4	29.5	0.6
S2	52.7	561.4	21.3	100.3	43.7	49.2	22.5	0.49
S3	41.65	456	21.9	54.7	28.4	35.9	19.6	0.66
S4	47.7	486.6	20.4	111.3	47.3	85.9	54.6	0.53
S5	48.2	499	20.7	58.7	26.7	38.2	18.7	0.65
							Average	0.601

Table-6.3: Values for K1 (Oswald 2010-reproduced)

Case	Boundary Locations	Blast Load Distribution	K_1	Example
1	At both ends of component in direction of axial load	Uniform	8	Uniformly loaded column or one-way spanning wall with top and bottom supports. Supports may be fixed and/ or simple
2	At both ends of component in direction of axial load	Concentrated at mid-span	4	Column with beam applying blast load as concentrated load at mid-span. Supports may fixed and/or simple
3	At one end of component in direction of axial load	Uniform	2	Cantilevered column that is not supported at top where axial load is applied (i.e. supported on two or three sides, not including top of wall). Uniform blast load in both cases.
4	At one ends of component in direction of axial load(unloaded end)	Concentrated at free end	1	Cantilevered column with blast load applied by supported beam as concentrated load at free end.

Table-6.4: Equivalent lateral load pressures

Column	RC Blast Results (first run)			Reflected Pressure		
	t	$P_{(t)}$	$\Delta_{(t)}$	$p_{r(ELLM)}$	$p_{r(initial)}$	$p_{r(total)}$
	ms	kN	mm	kPa	kPa	kPa
NS1	33.7	140	80.5	9.3	45.5	54.8
NS2	18.9	300	36.3	9	45.5	54.5
NS3	18.4	376	38.6	12	42.15	54.15
NS4	43	100	45	3.7	43	46.7
NS5	18.6	350	33.3	9.6	42	51.6
S1	29.5	150	68.4	8.5	47.33	55.8
S2	22.5	160	49.2	6.5	52.7	59.2
S3	19.6	300	35.9	8.8	41.65	50.45
S4	54.6	100	85.9	5.55	47.7	53.25
S5	18.7	350	38.2	11	48.2	59.2

Table-6.5: Summary of experimental and modified analytical results

Column	Experimental Response		RC-Blast Response		Max.Disp.$_{\text{RC Blast}}$/Max. Disp.$_{\text{Test Data}}$	% Error
	Maximum Disp. mm	Time to max. Disp. ms	Maximum Disp. mm	Time to max. Disp. mm		
NS1	125.3	50.8	119.2	33.8	0.95	4.86
NS2	53.5	25.6	46.5	21	0.87	13.1
NS3	69.1	32.9	51.7	23.3	0.75	25.2
NS4	81	44.1	89	52.8	1.1	9.9
NS5	51.3	23.9	45.1	20.1	0.87	12.1
S1	114.9	73.3	98.5	33.7	0.86	14.7
S2	100.3	43.7	85	36.5	0.85	15.25
S3	54.7	28.4	56.6	31.3	1.03	3.5
S4	111.3	47.3	122.5	44.1	1.1	10.06
S5	58.7	26.7	54	21.2	0.92	8.0
				Average	0.93	11.67

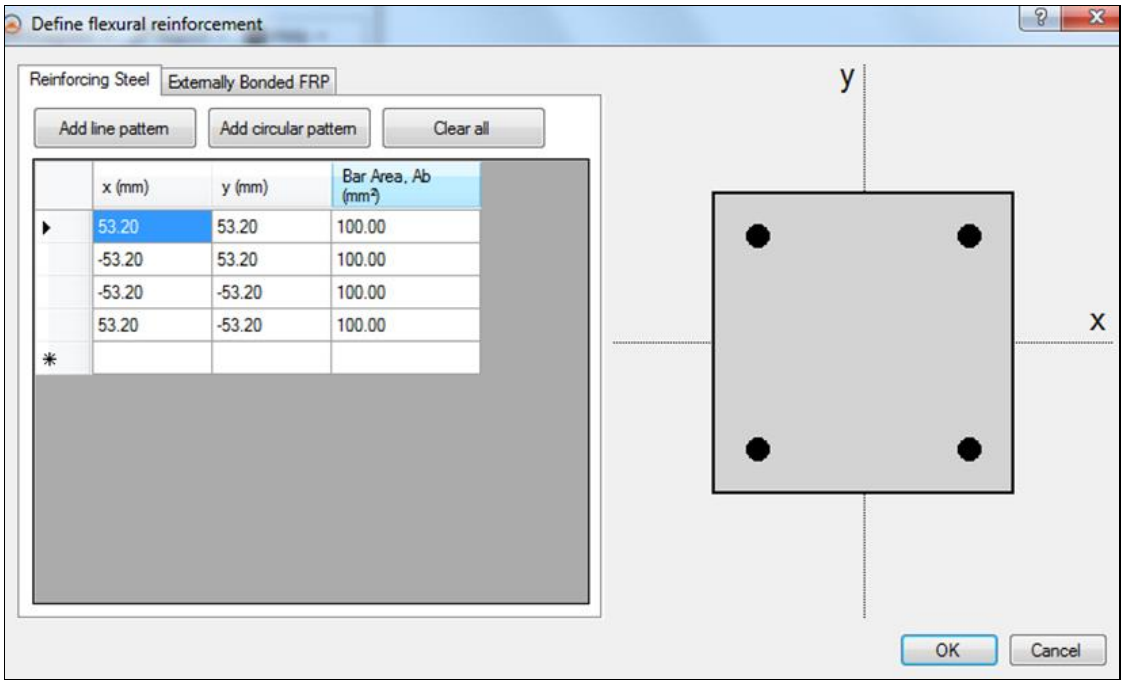

Fig. 6.1 Diameter and arrangement of rebars defined in RC Blast software

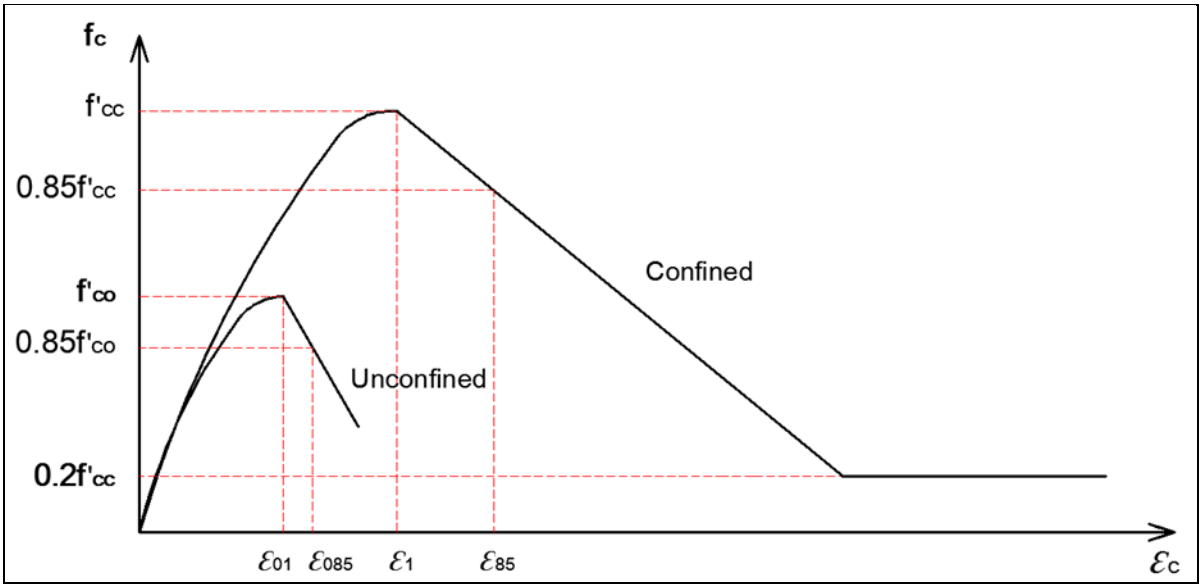

Fig. 6.2 Confined and unconfined concrete compressive stress-strain relationships

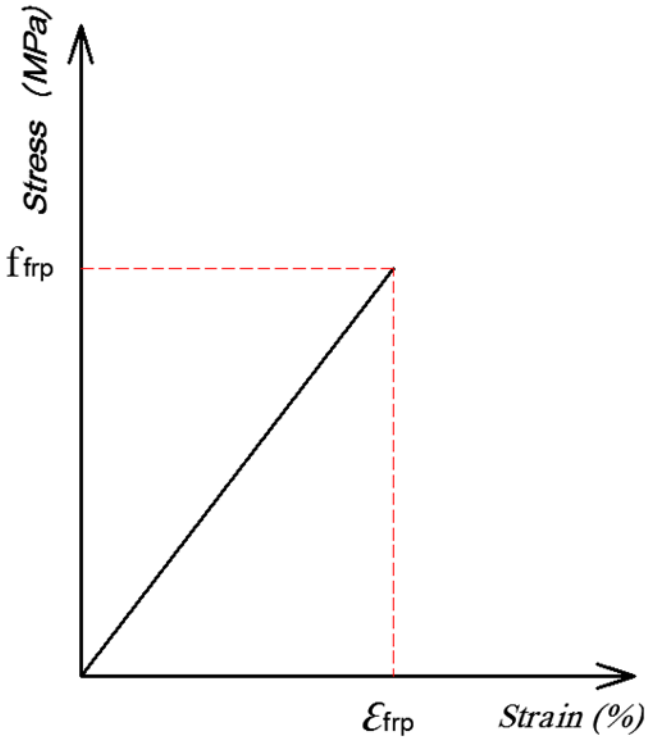

Fig. 6.3 CFRP tensile stress-strain relationship

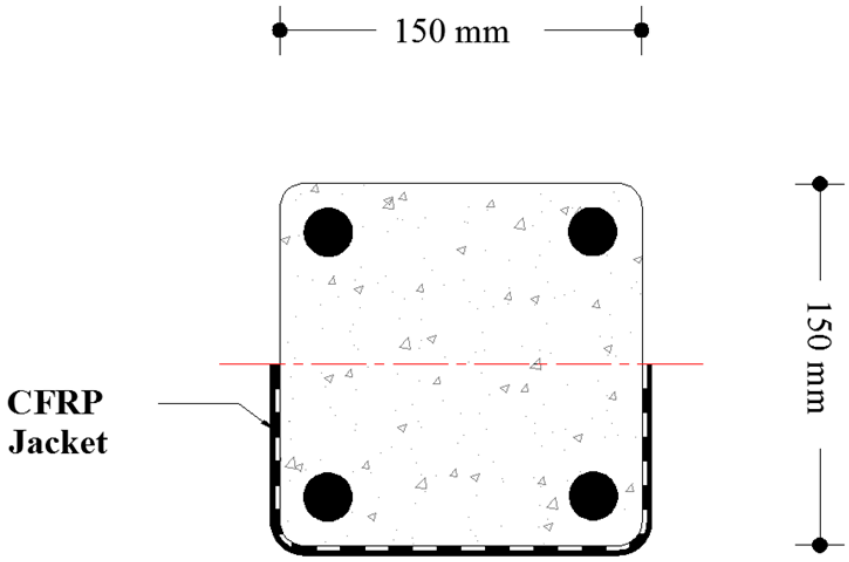

Fig. 6.4 CFRP configuration assumed for flexural analysis

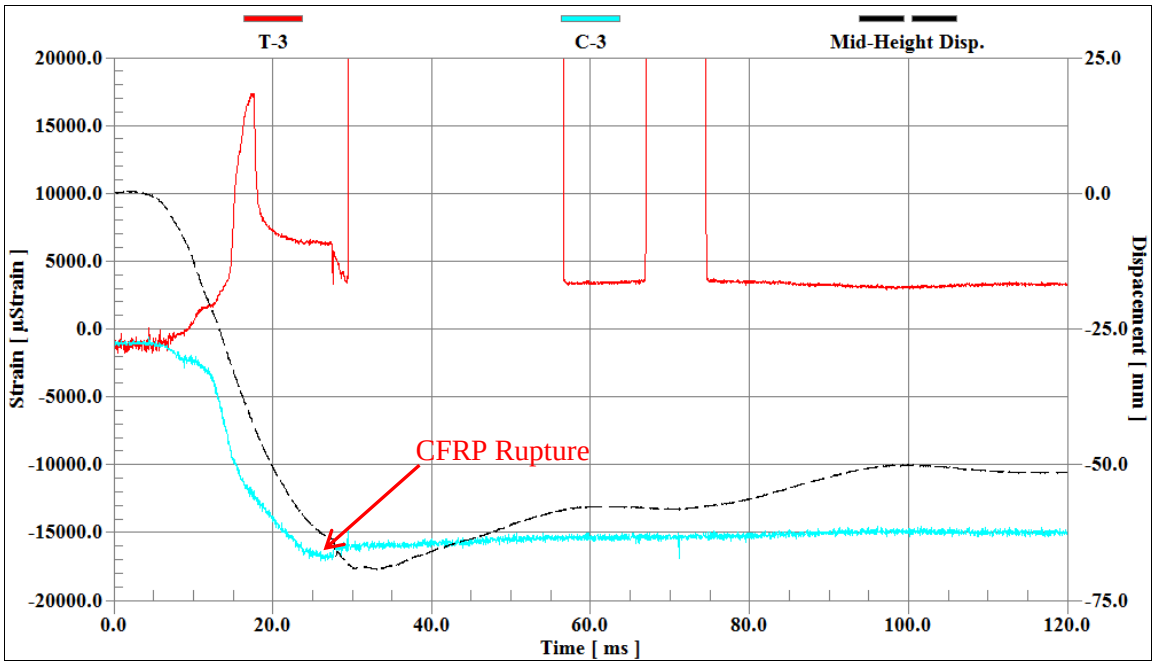

Fig. 6.5 Time history of tension and compression strains at column's mid-height –NS3-B

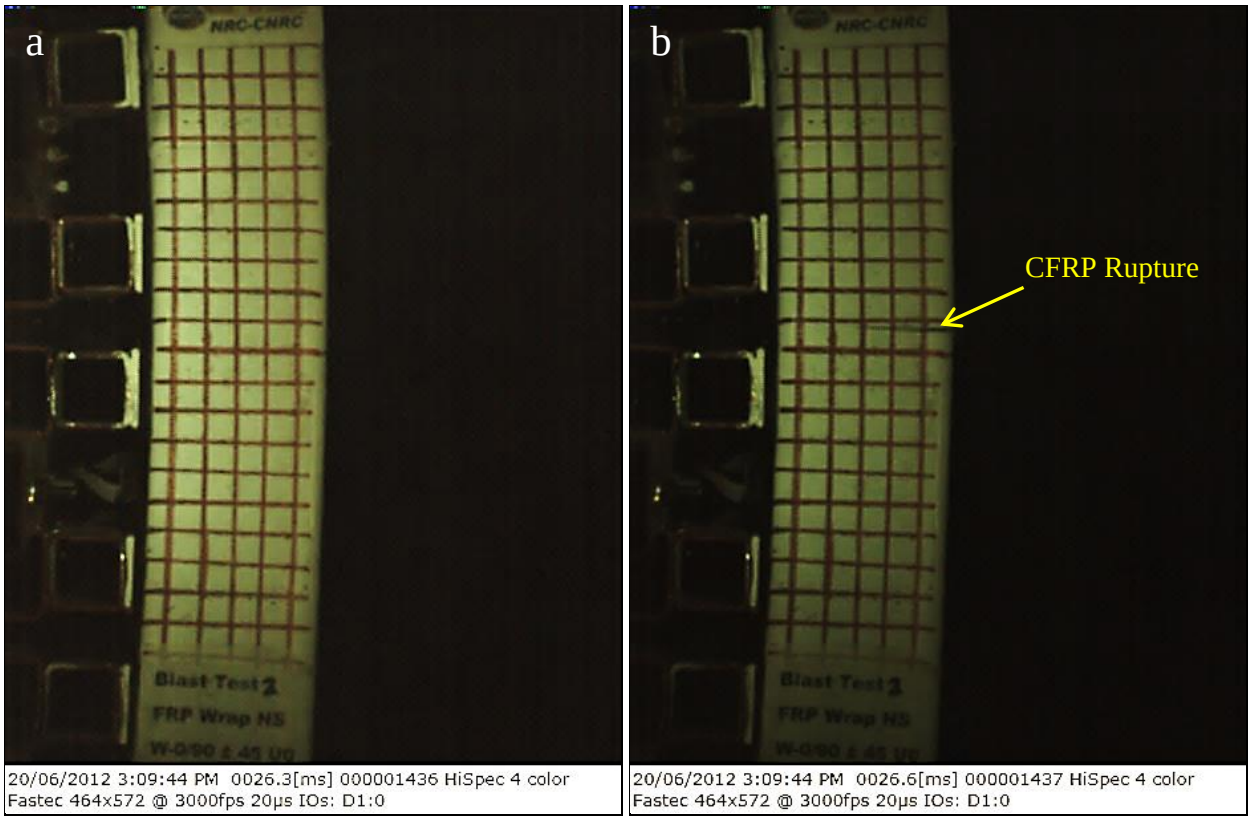

Fig. 6.6 CFRP rupture-NS3-B: a) Prior to rupture at 26.3 ms

b) CFRP rupture is initiated 26.6 ms

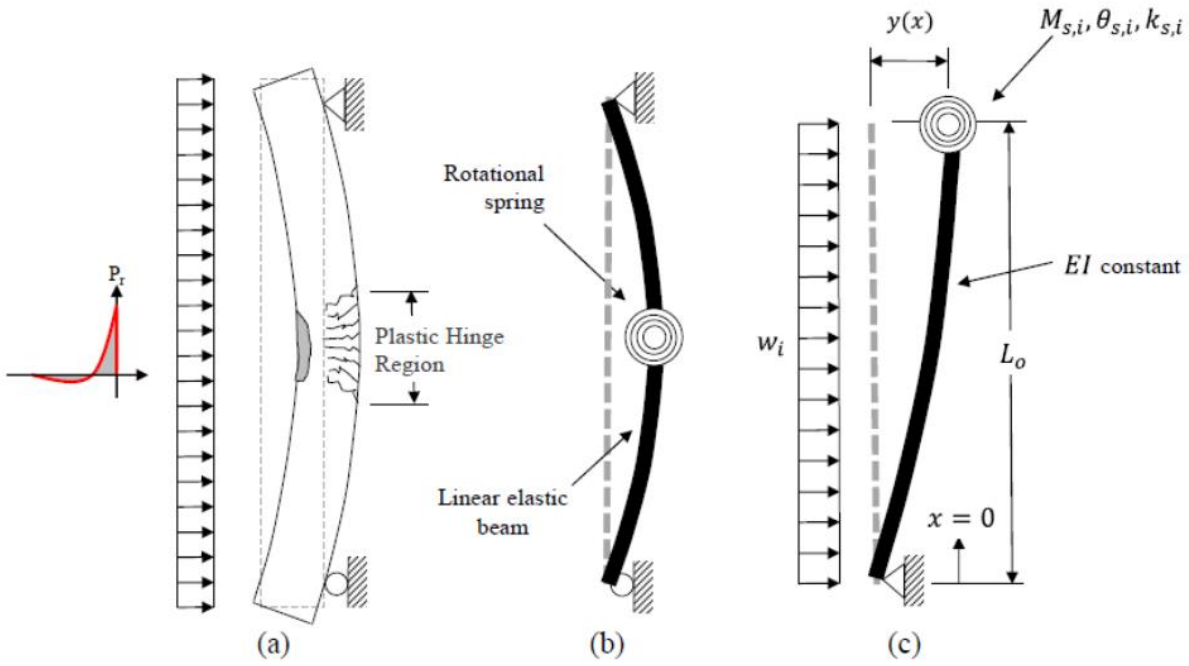

Fig. 6.7 Reinforced concrete column forming the basis of lumped inelasticity approach: a) actual column; b) idealized column; and c) half span idealized column (Jacques and Saatcioglu, 2015)

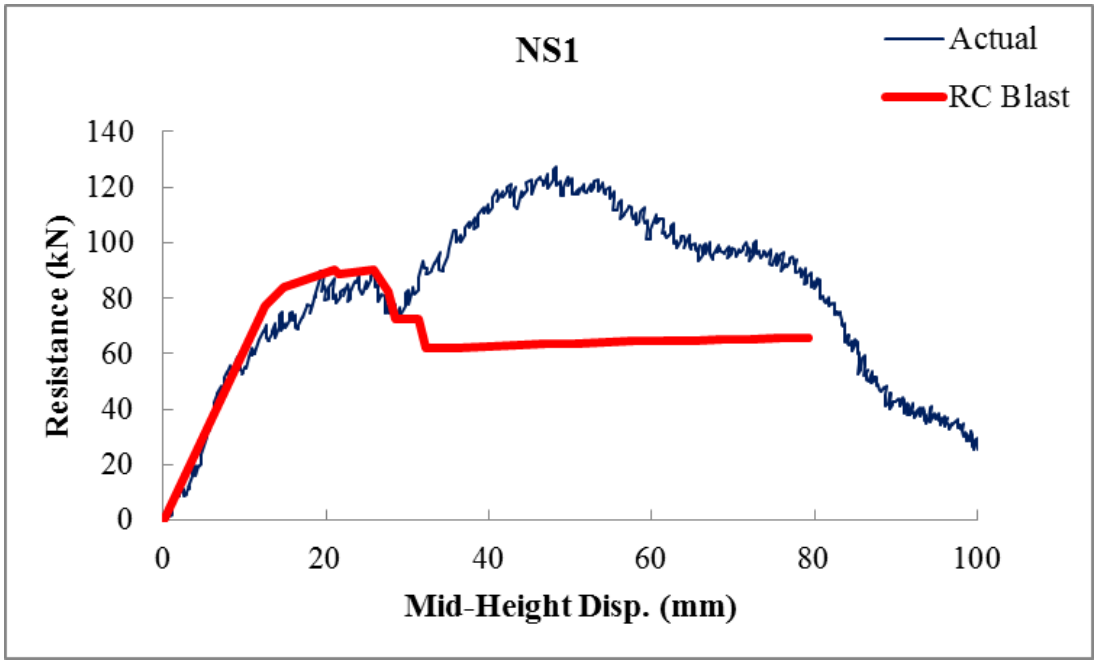

Fig. 6.8 Actual and theoretical resistance functions - Column NS1

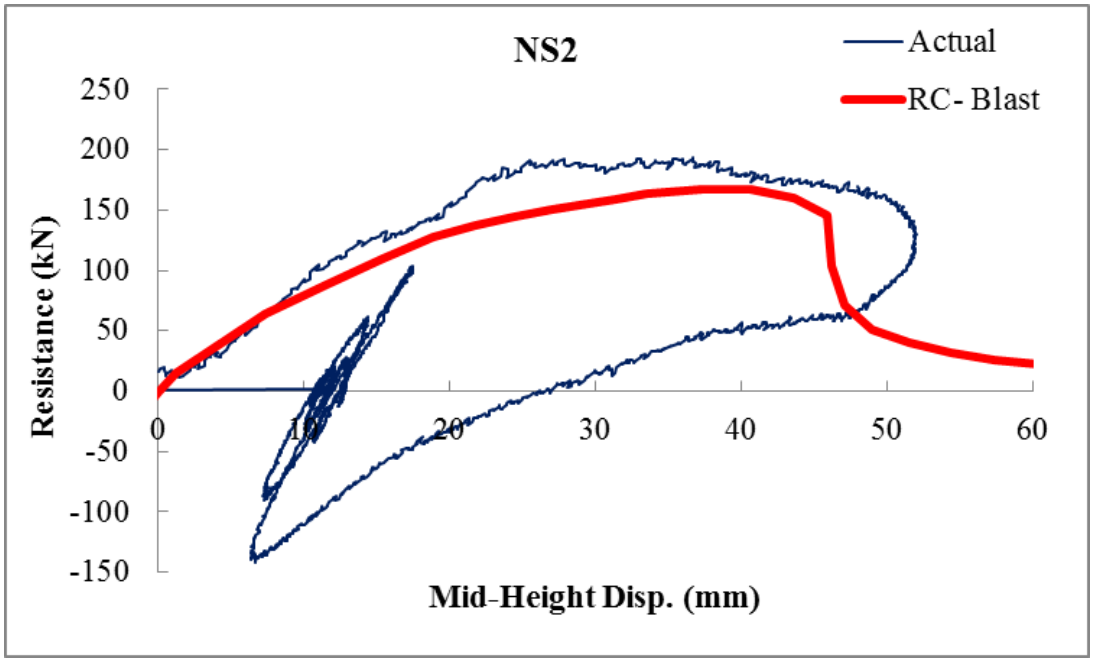

Fig. 6.9 Actual and theoretical resistance functions - Column NS2

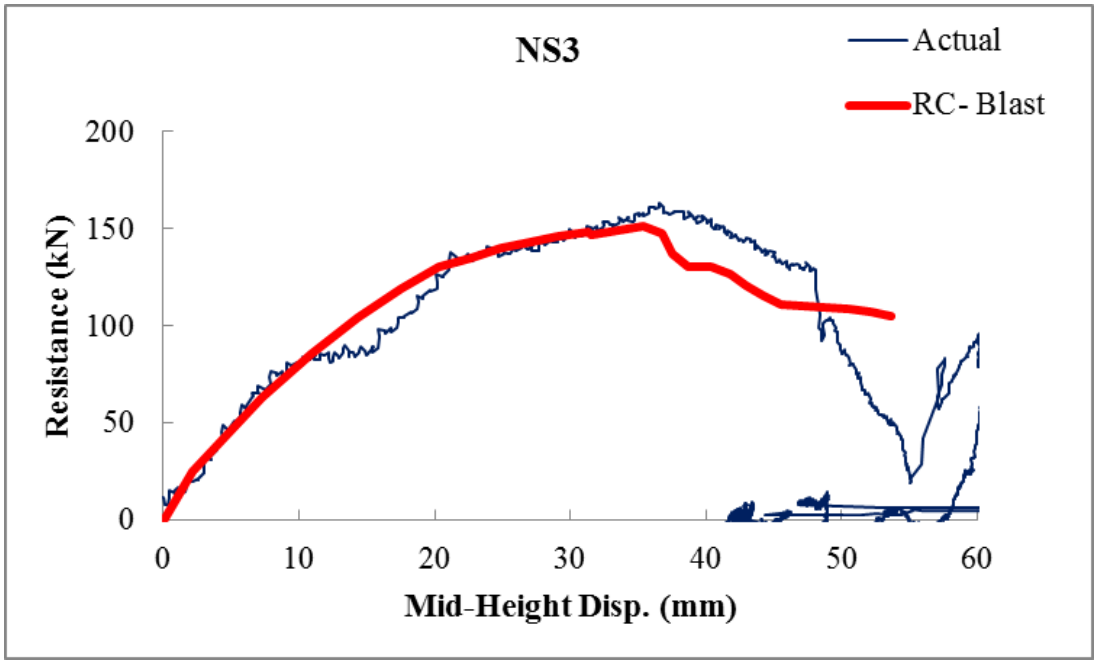

Fig. 6.10 Actual and theoretical resistance functions - Column NS3

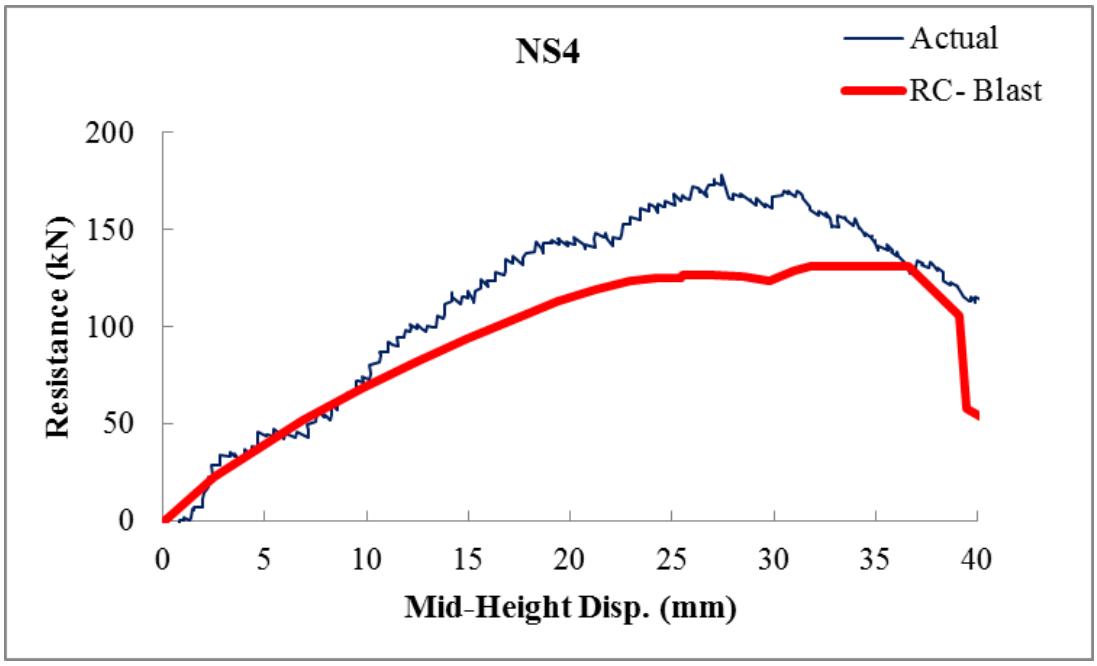

Fig. 6.11 Actual and theoretical resistance functions - Column NS4

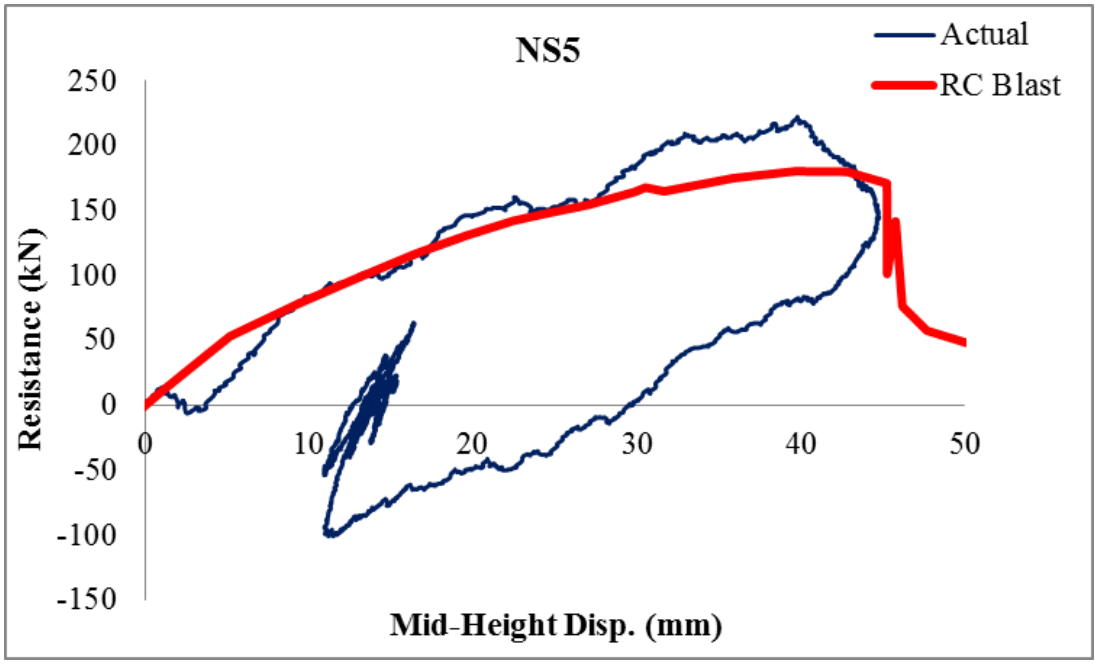

Fig. 6.12 Actual and theoretical resistance functions - Column NS5

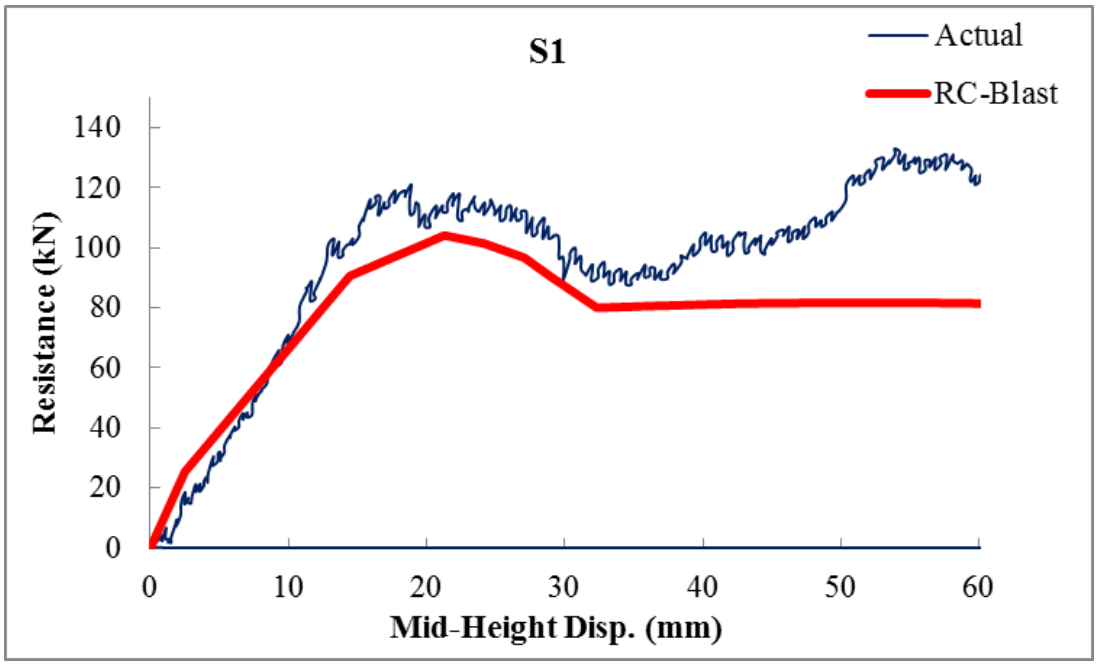

Fig. 6.13 Actual and theoretical resistance functions - Column S1

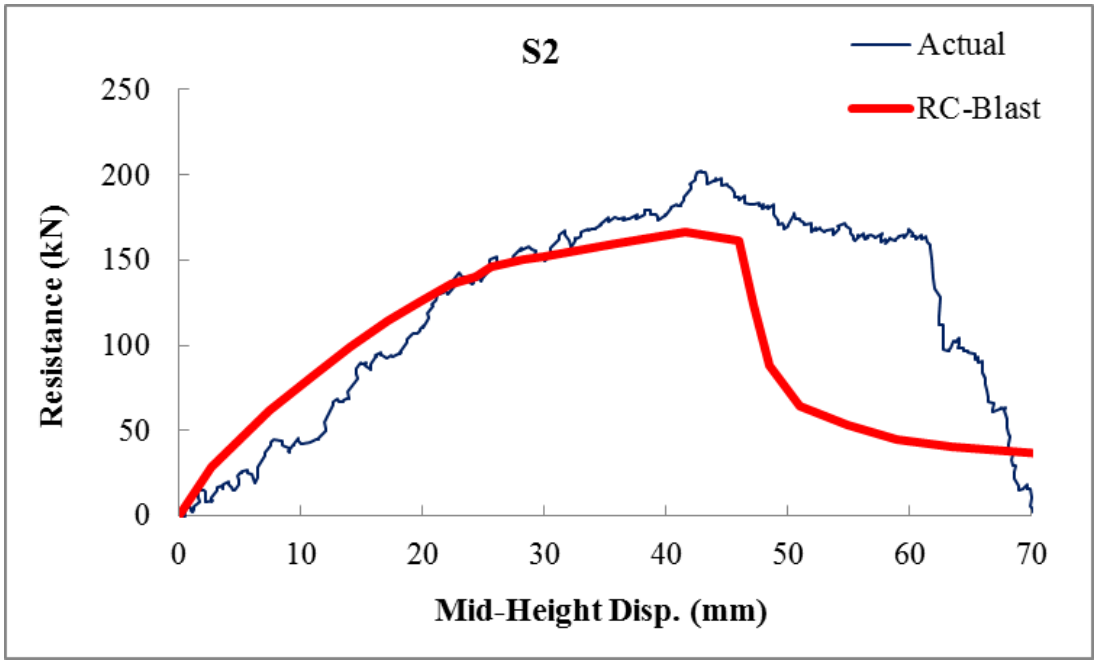

Fig. 6.14 Actual and theoretical resistance functions - Column S2

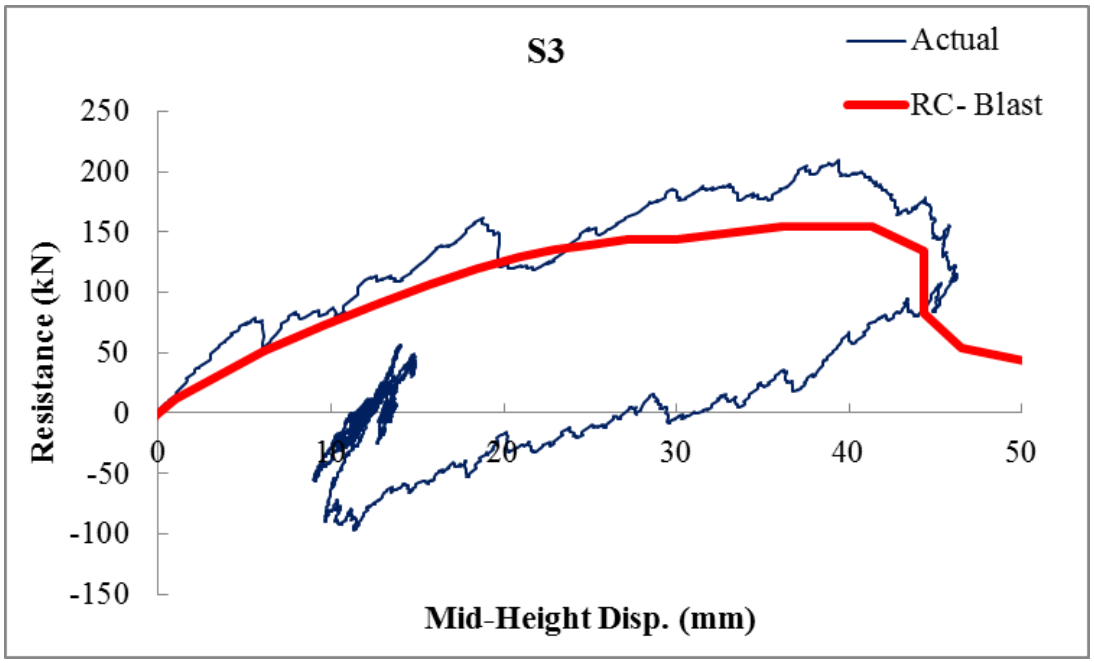

Fig. 6.15 Actual and theoretical resistance functions - Column S3

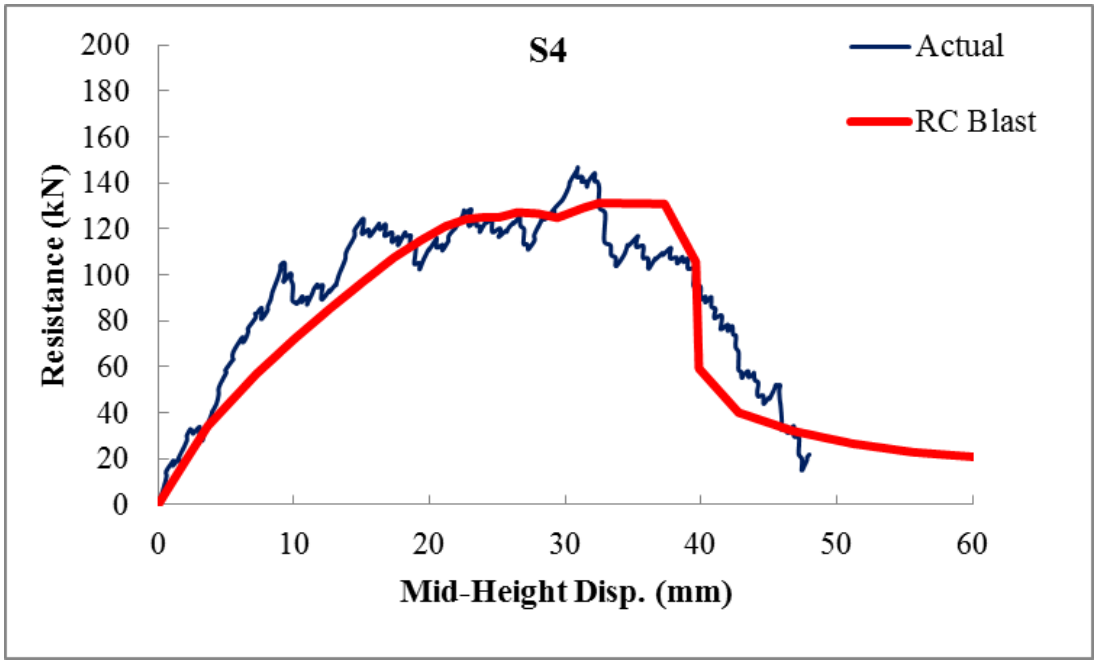

Fig. 6.16 Actual and theoretical resistance functions - Column S4

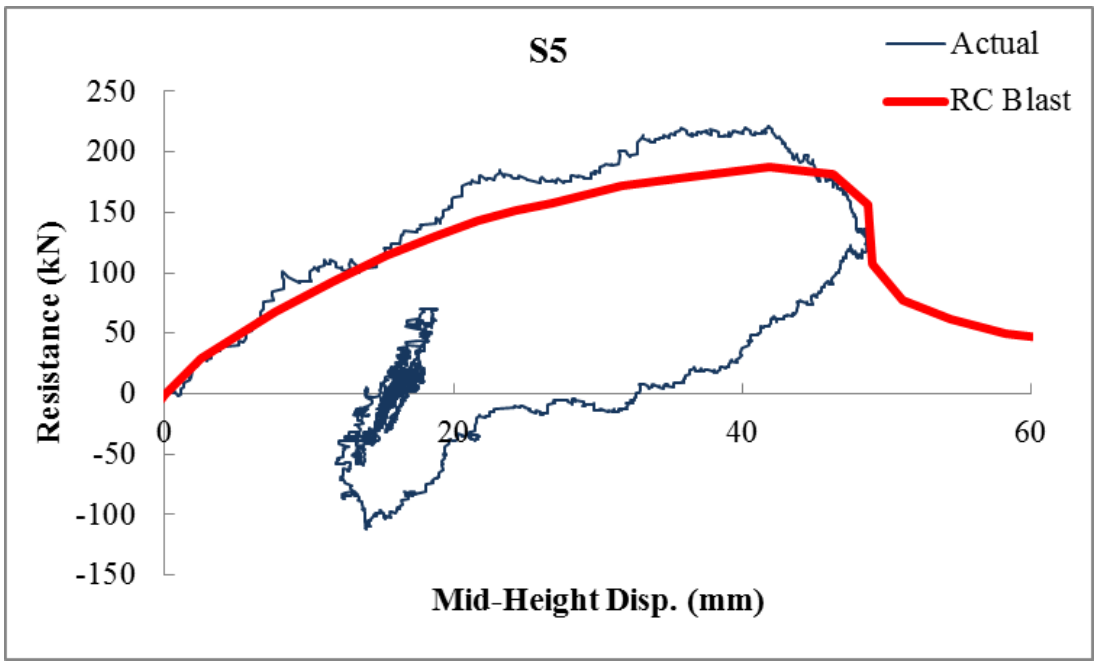

Fig. 6.17 Actual and theoretical resistance functions - Column S5

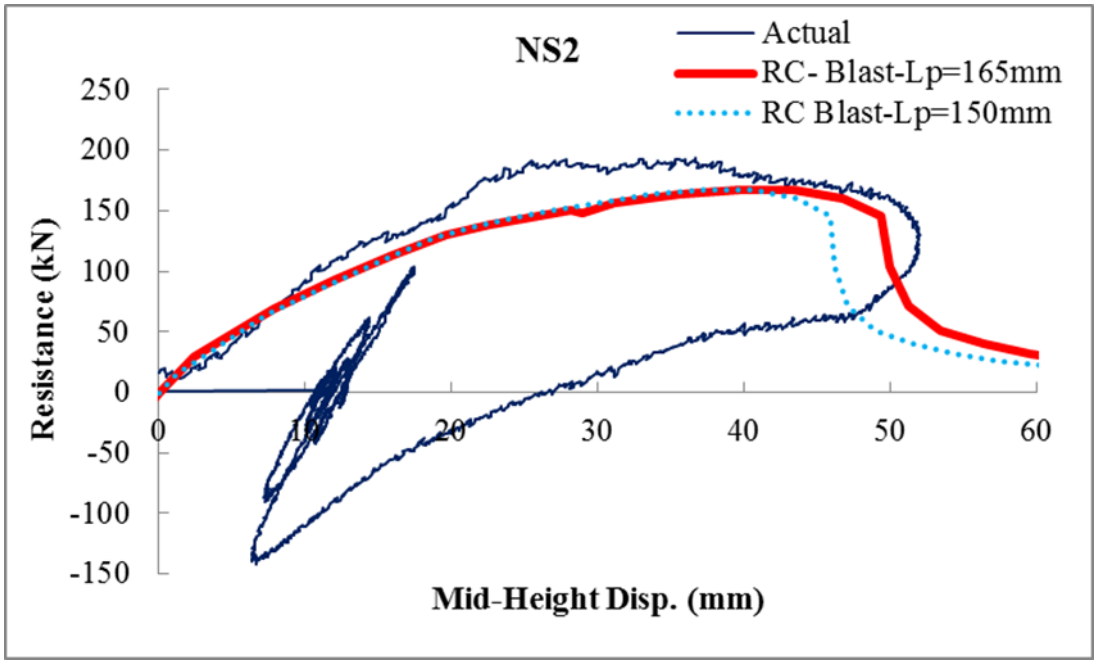

Fig. 6.18 Effect of plastic hinge length on theoretical resistance function - Column NS2

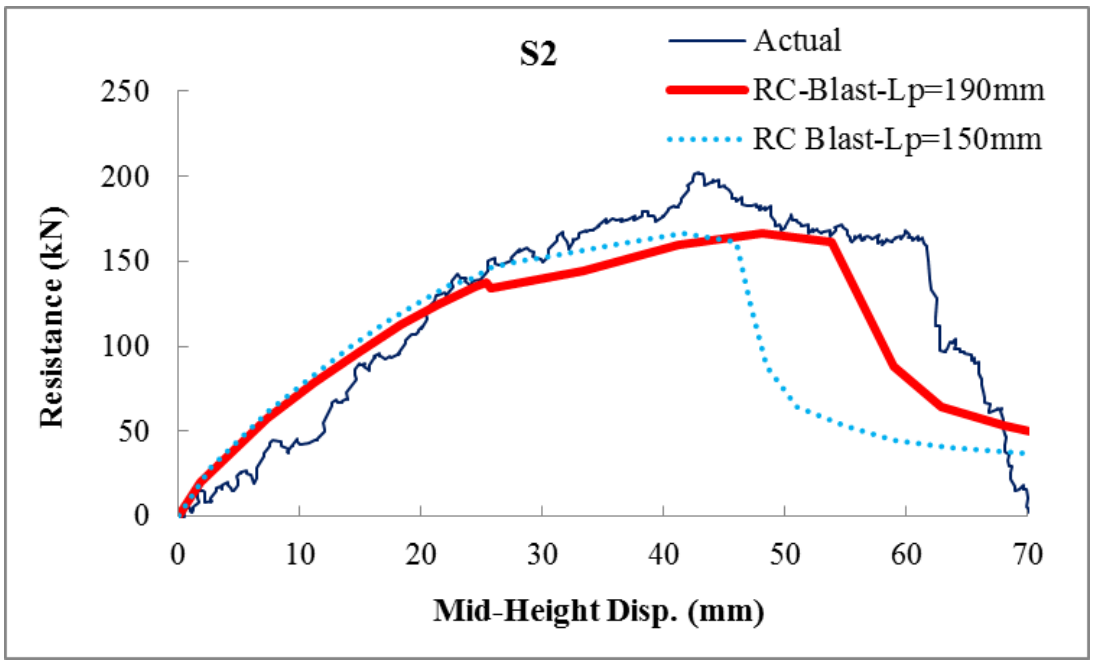

Fig. 6.19 Effect of plastic hinge length on theoretical resistance function - Column S2

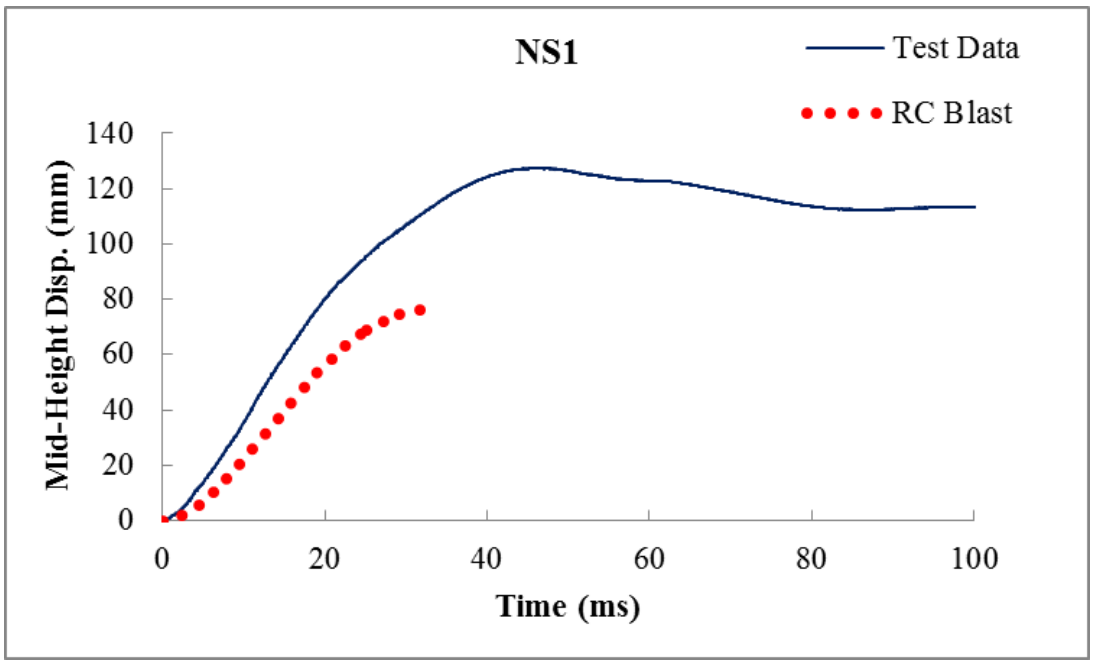

Fig. 6.20 Mid-height displacement time history – NS1; RC-Blast vs. test data

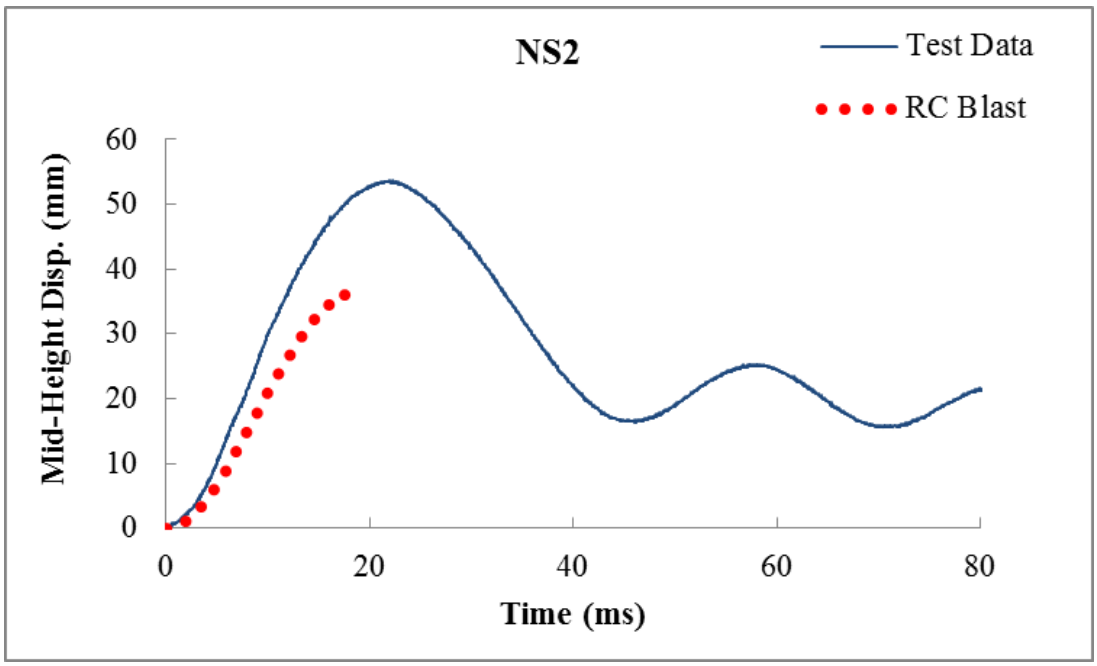

Fig. 6.21 Mid-height displacement time history - NS2; RC-Blast vs. test data

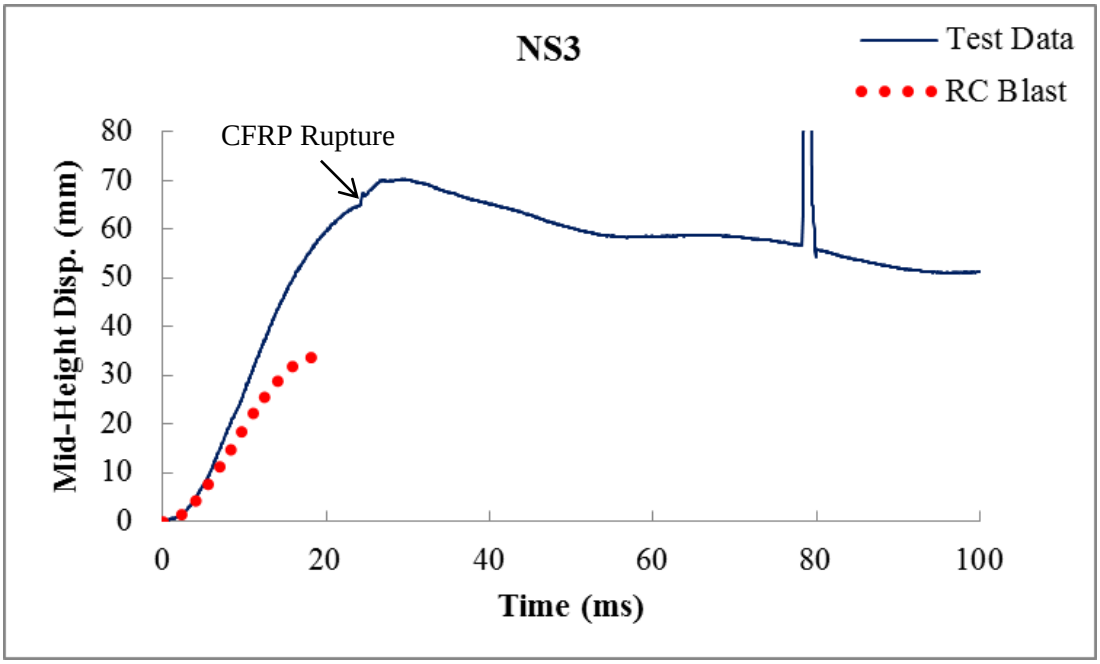

Fig. 6.22 Mid-height displacement time history - NS3; RC-Blast vs. test data

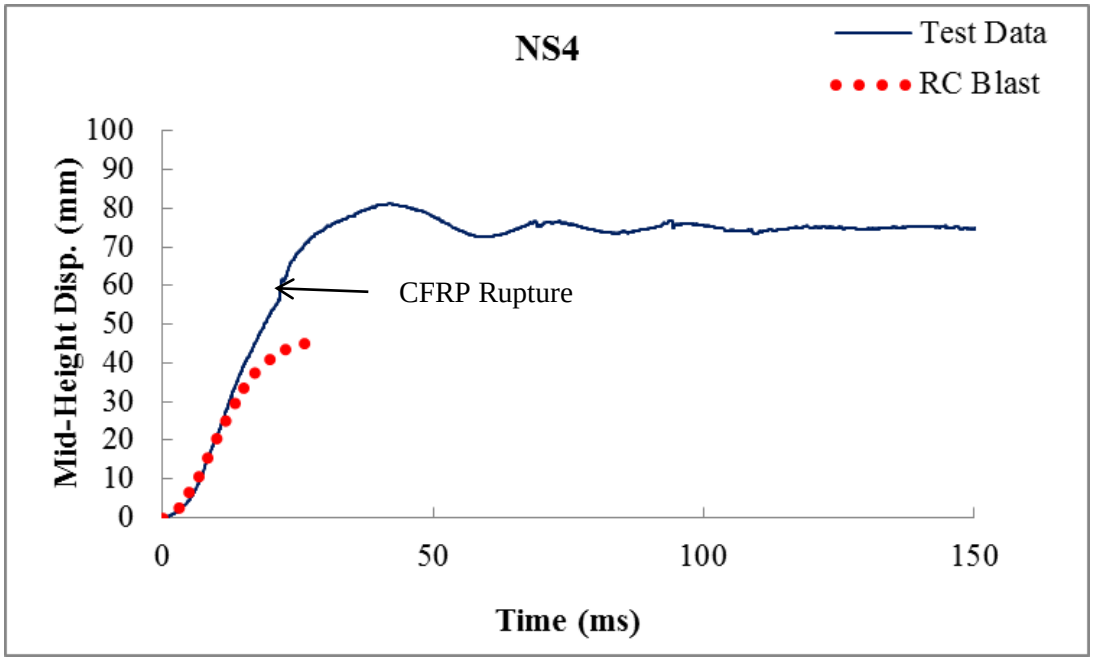

Fig. 6.23 Mid-height displacement time history - NS4; RC-Blast vs. test data

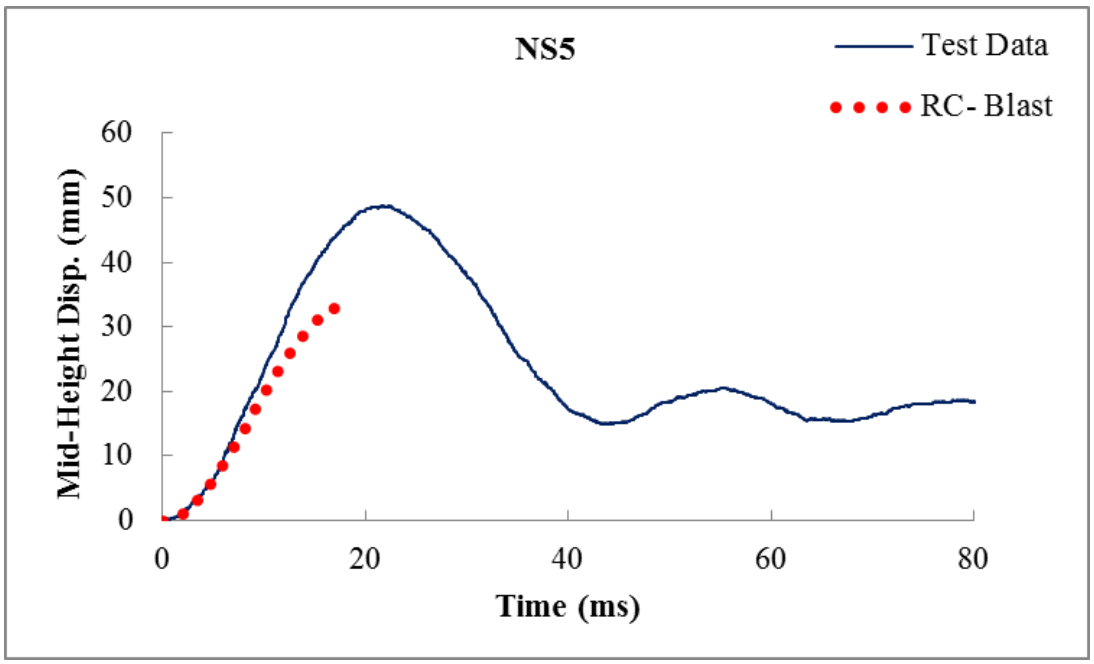

Fig. 6.24 Mid-height displacement time history - NS5; RC-Blast vs. test data

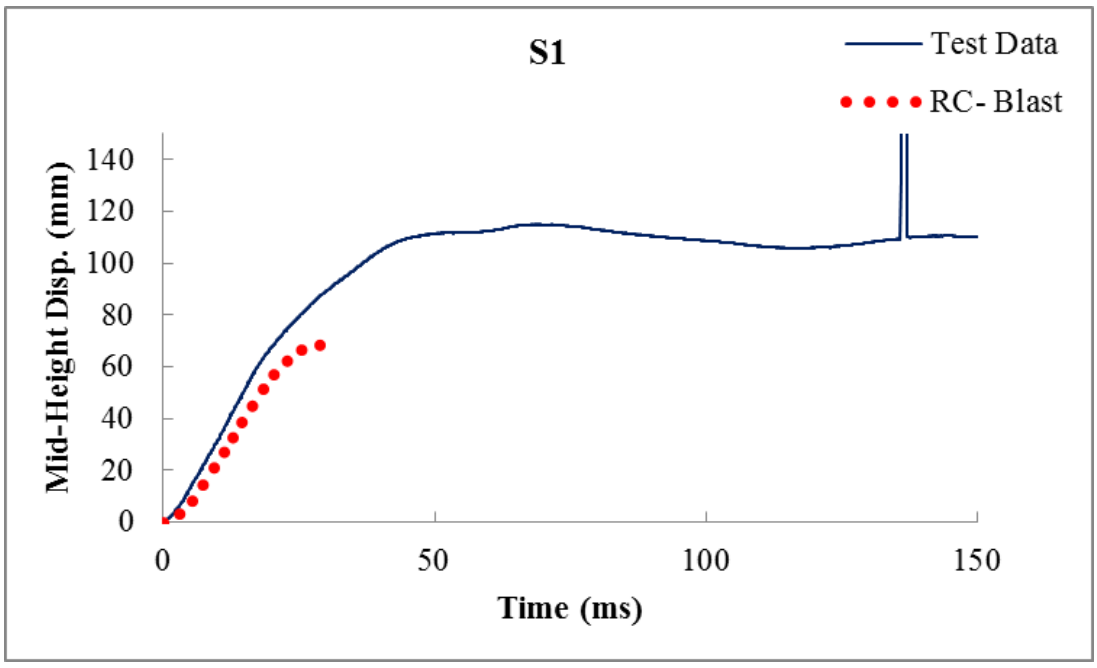

Fig. 6.25 Mid-height displacement time history - S1; RC-Blast vs. test data

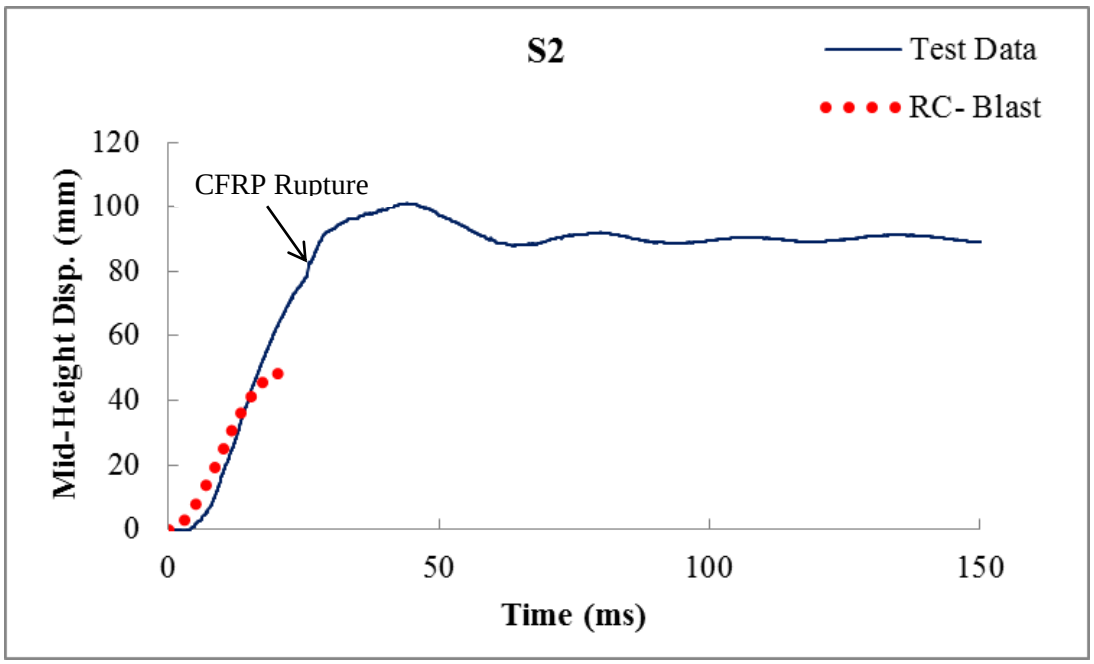

Fig. 6.26 Mid-height displacement time history - S2; RC-Blast vs. test data

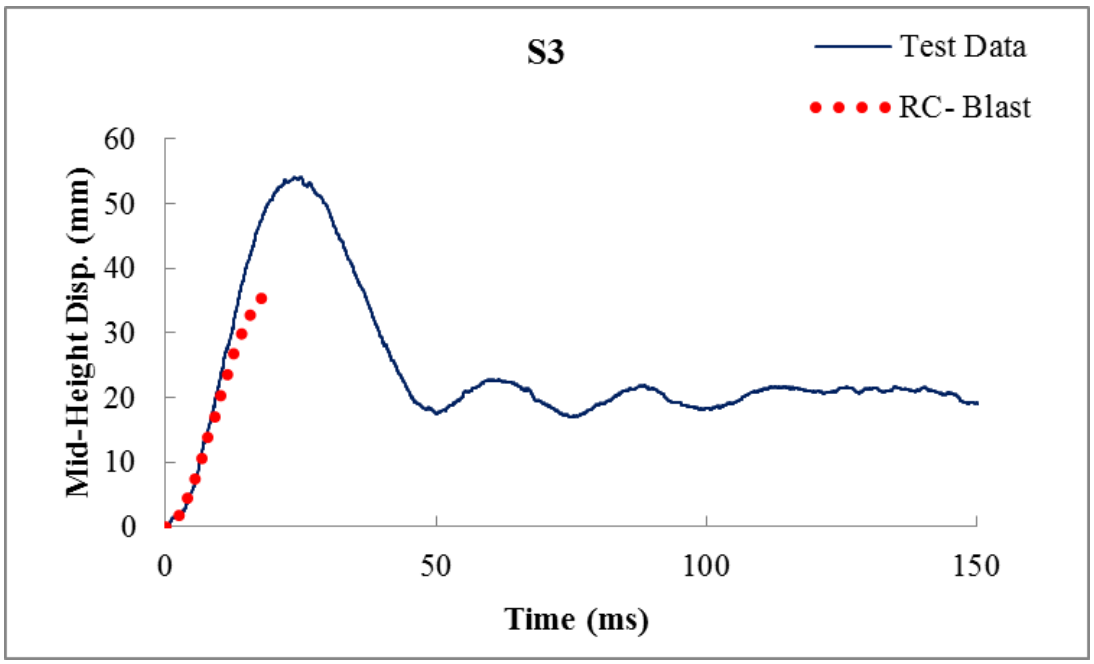

Fig. 6.27 Mid-height displacement time history - S3; RC-Blast vs. test data

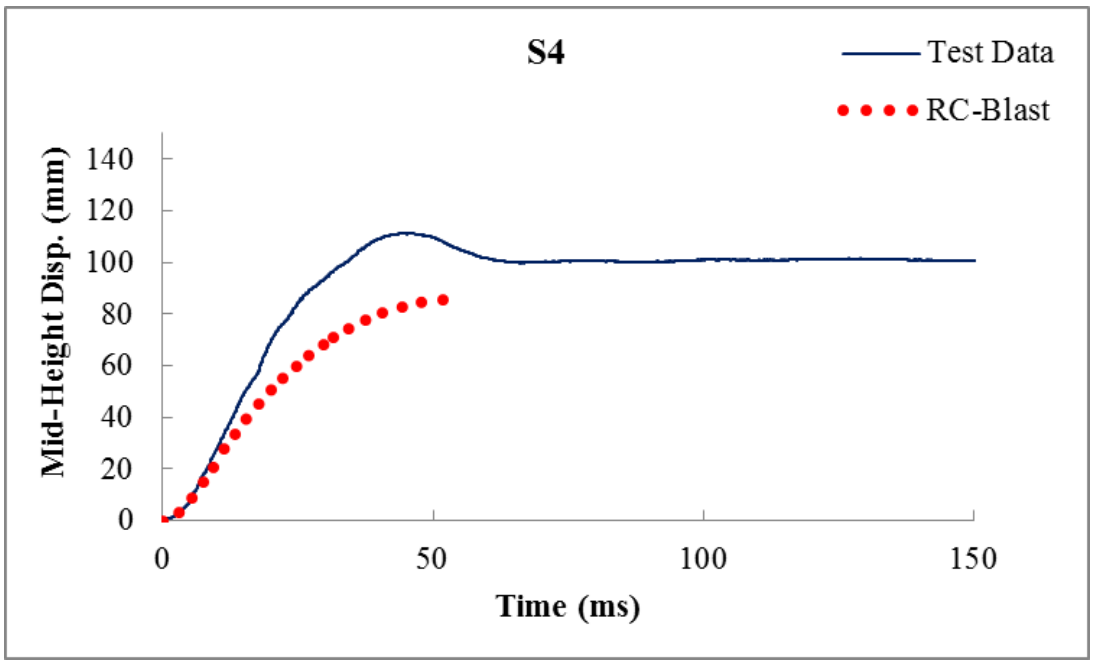

Fig. 6.28 Mid-height displacement time history - S4; RC-Blast vs. test data

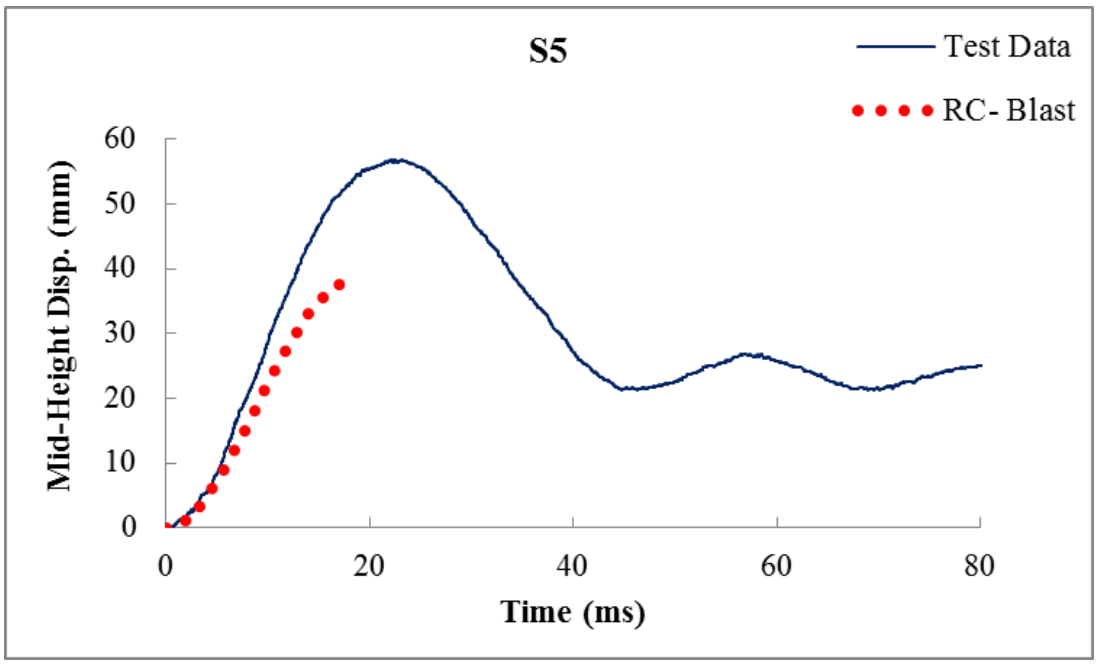

Fig. 6.29 Mid-height displacement time history - S5; RC-Blast vs. test data

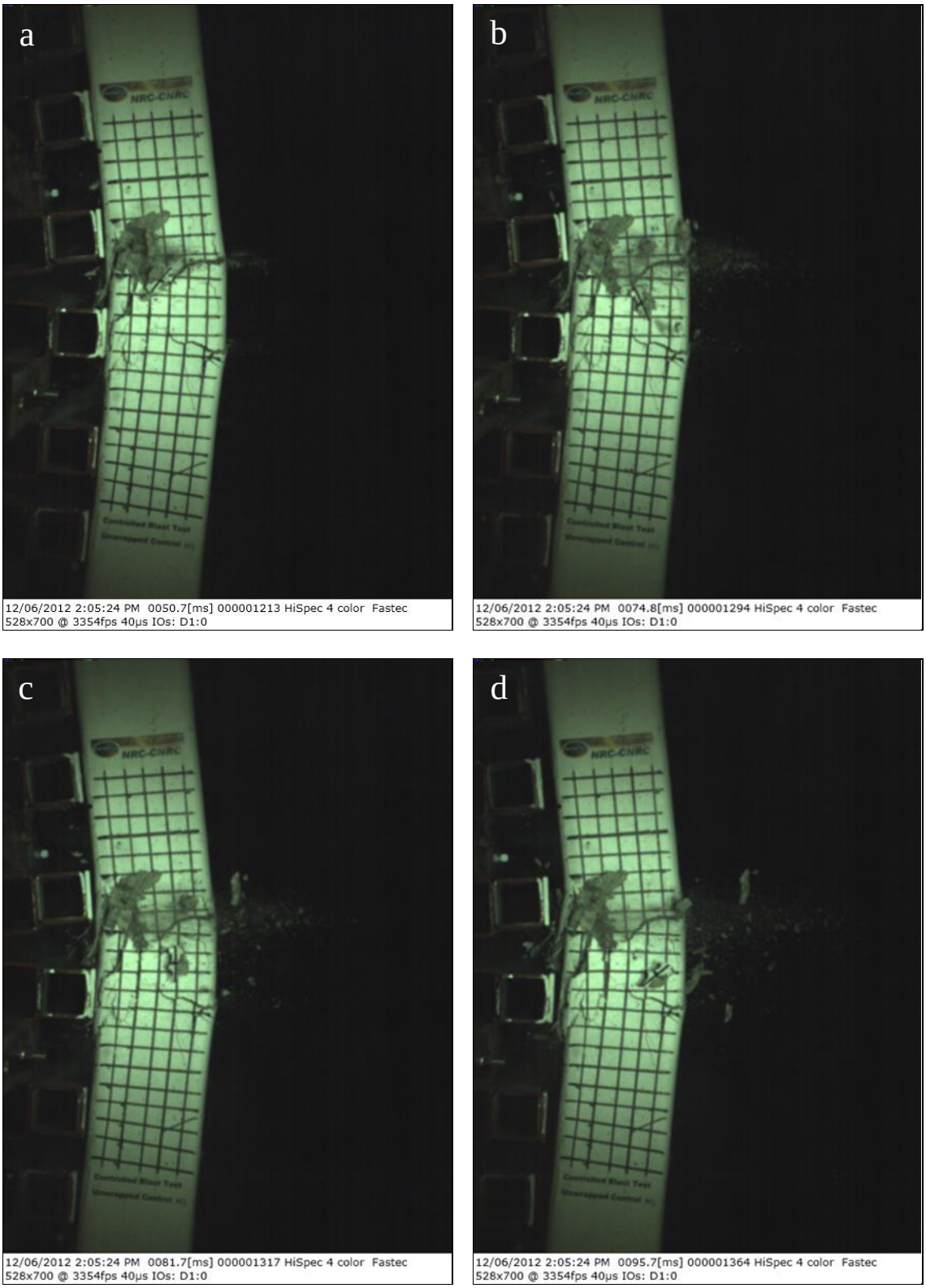

Fig. 6.30 Combined loading system at instants: a) 50.7 ms; b) 74.8 ms; c) 81.7 ms; and d) 95.7 ms

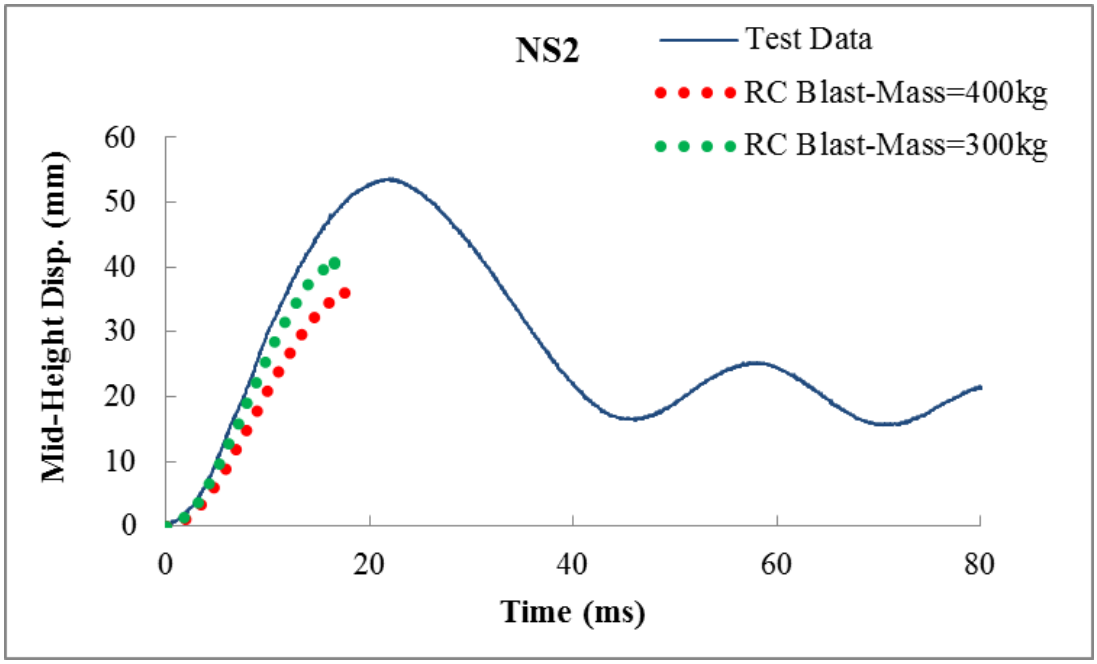

Fig. 6.31 Influence of mass on displacement response of Column NS2

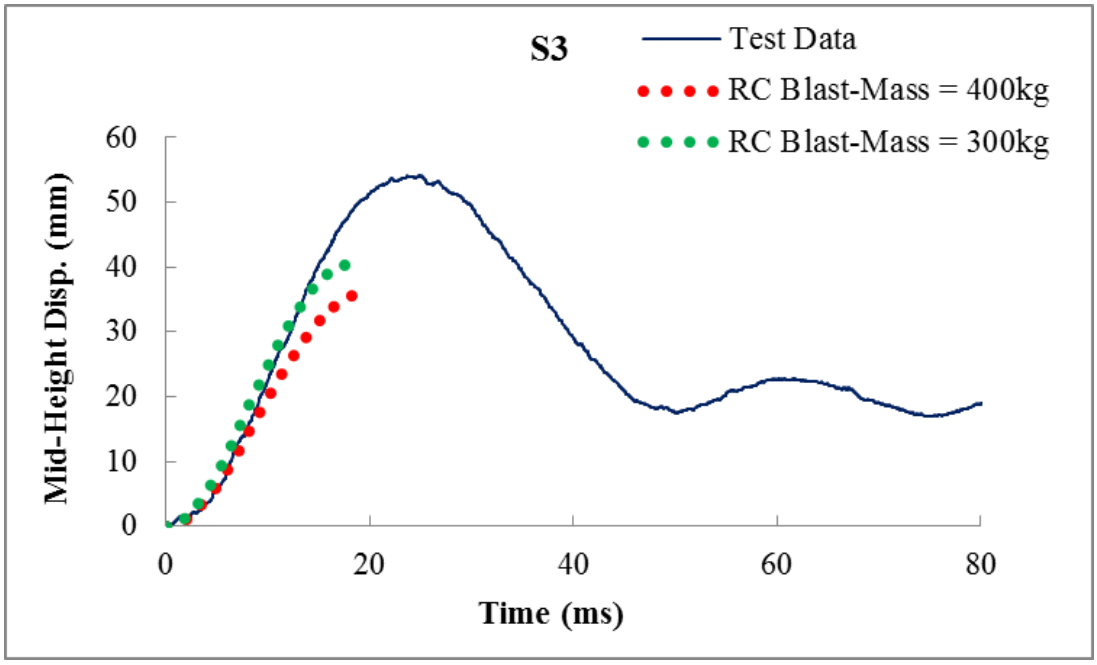

Fig. 6.32 Influence of mass on displacement response of Column S3

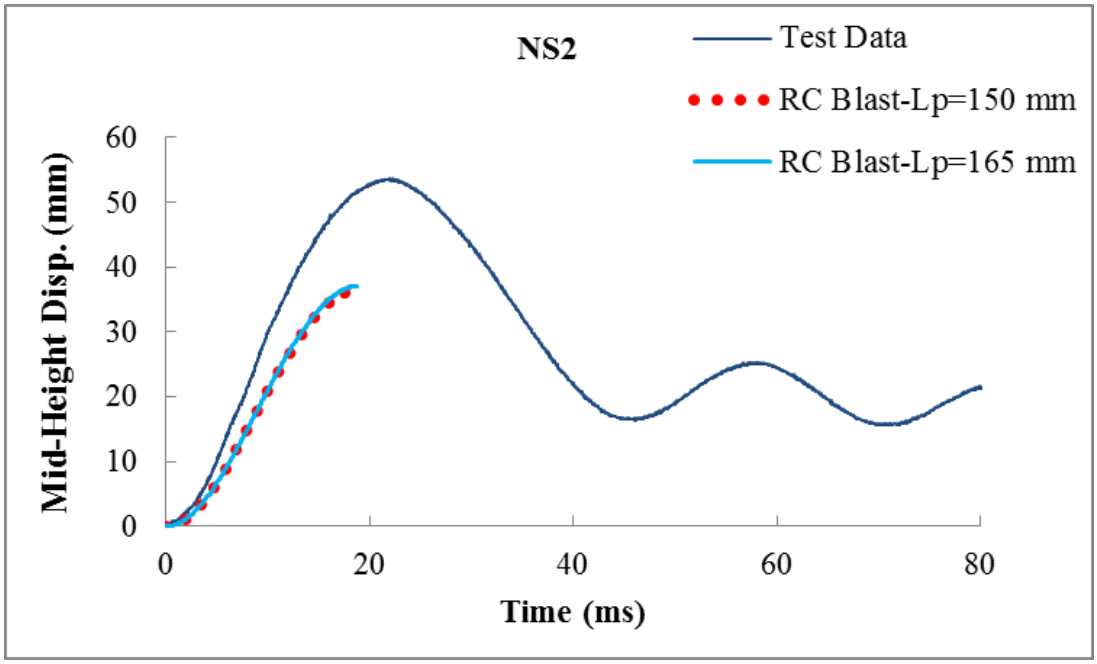

Fig. 6.33 Influence of plastic hinge length on RC Blast displacement for Column NS2

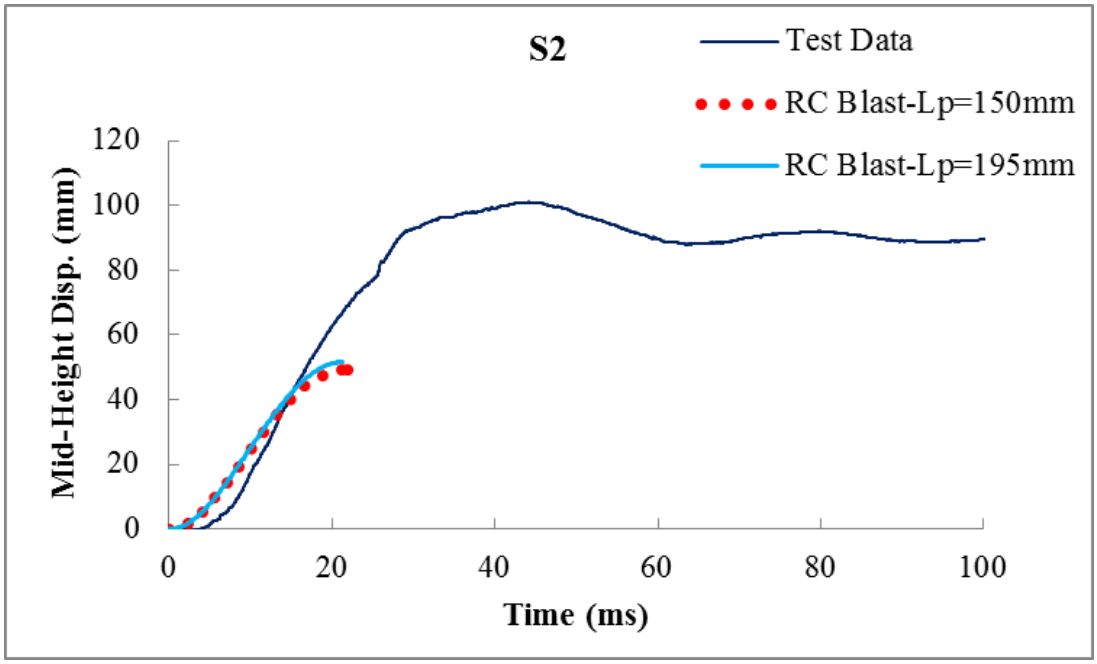

Fig. 6.34 Influence of plastic hinge length on RC Blast displacement for Column S2

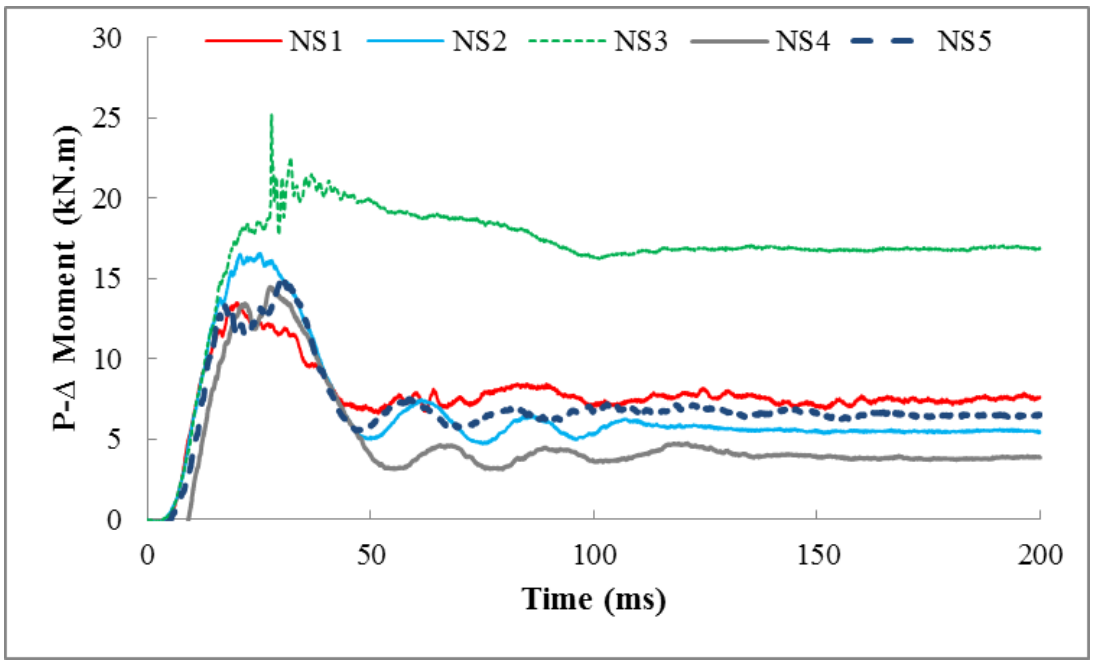

Fig. 6.35 P-Δ measured moments for non-seismic columns

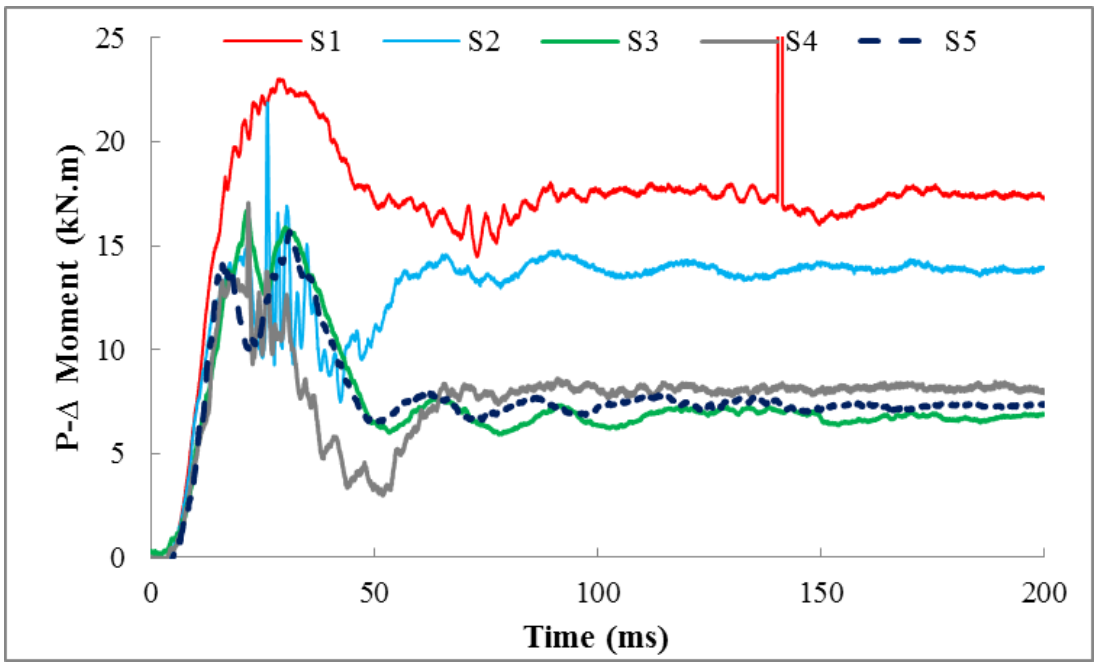

Fig. 6.36 P-Δ measured moments for seismic columns

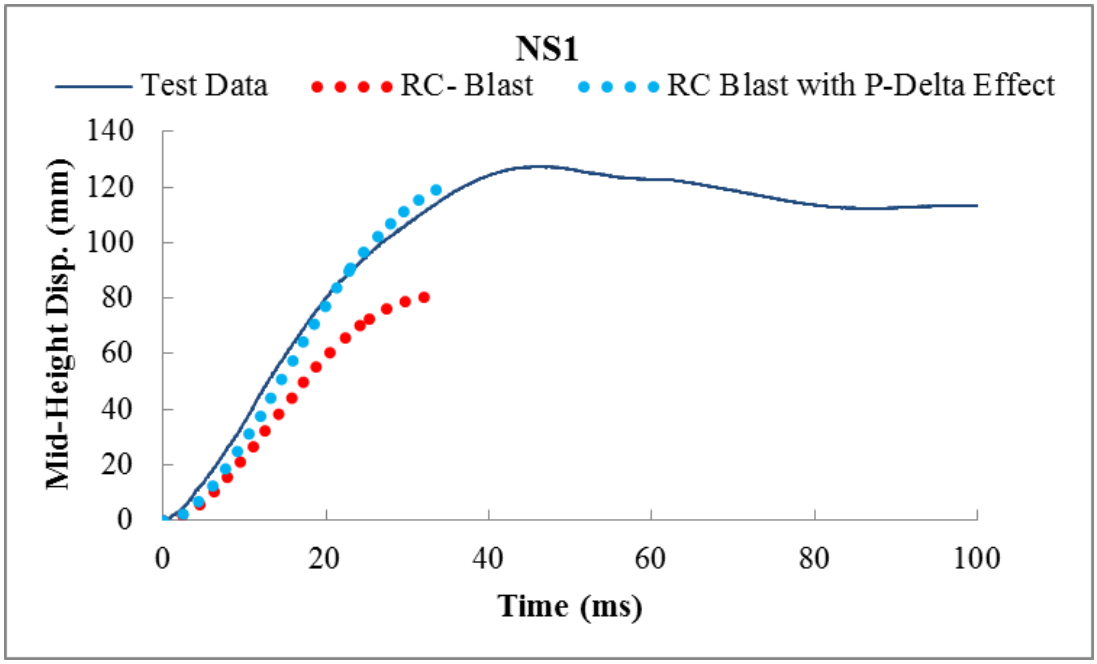

Fig. 6.37 P-Delta effects on maximum mid-height displacement - Column NS1

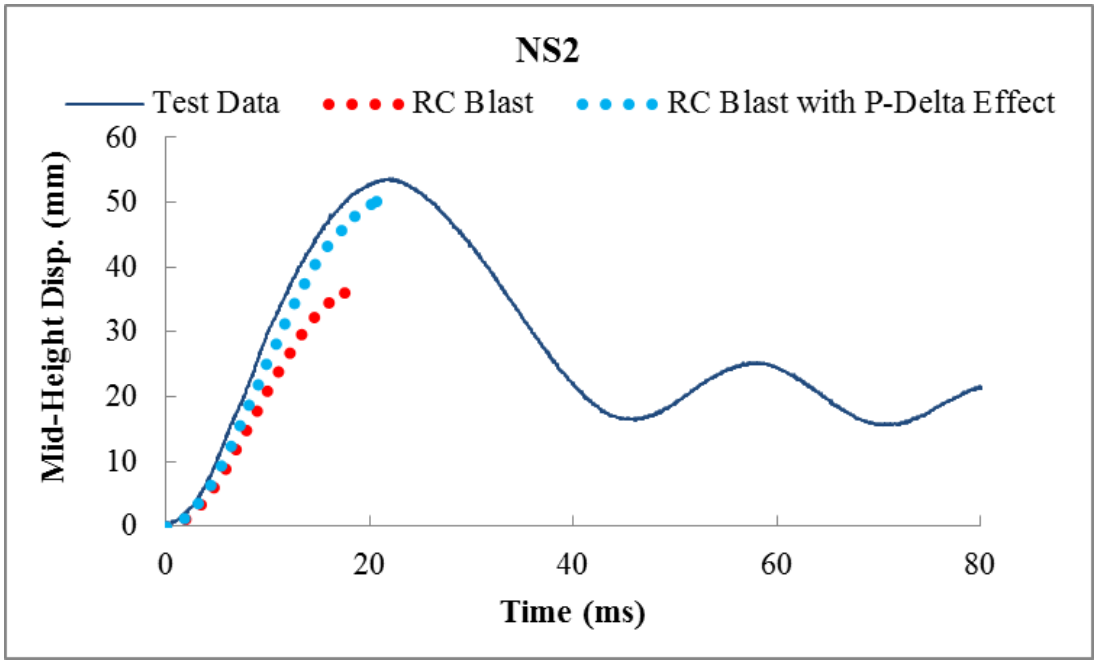

Fig. 6.38 P-Delta effects on maximum mid-height displacement - Column NS2

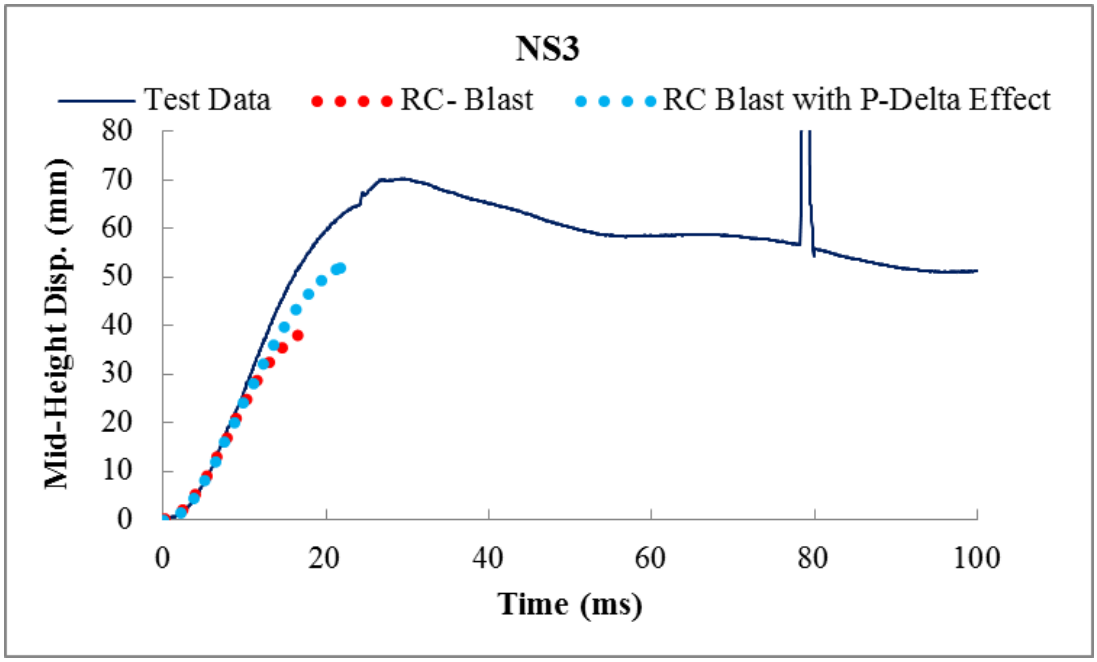

Fig. 6.39 P-Delta effects on maximum mid-height displacement - Column NS3

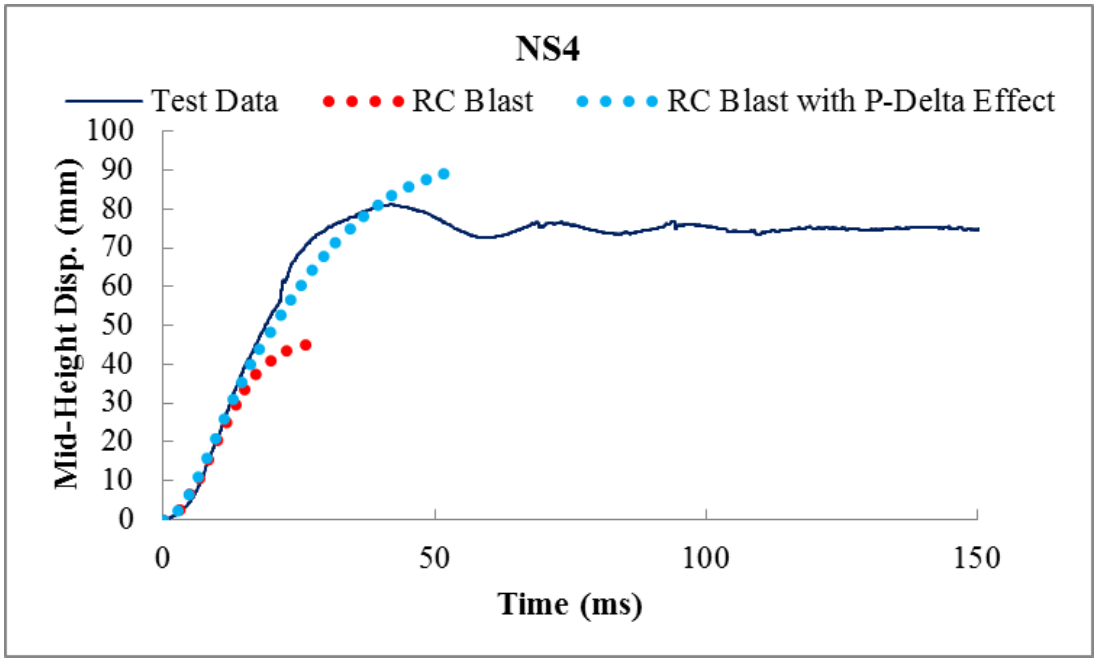

Fig. 6.40 P-Delta effects on maximum mid-height displacement - Column NS4

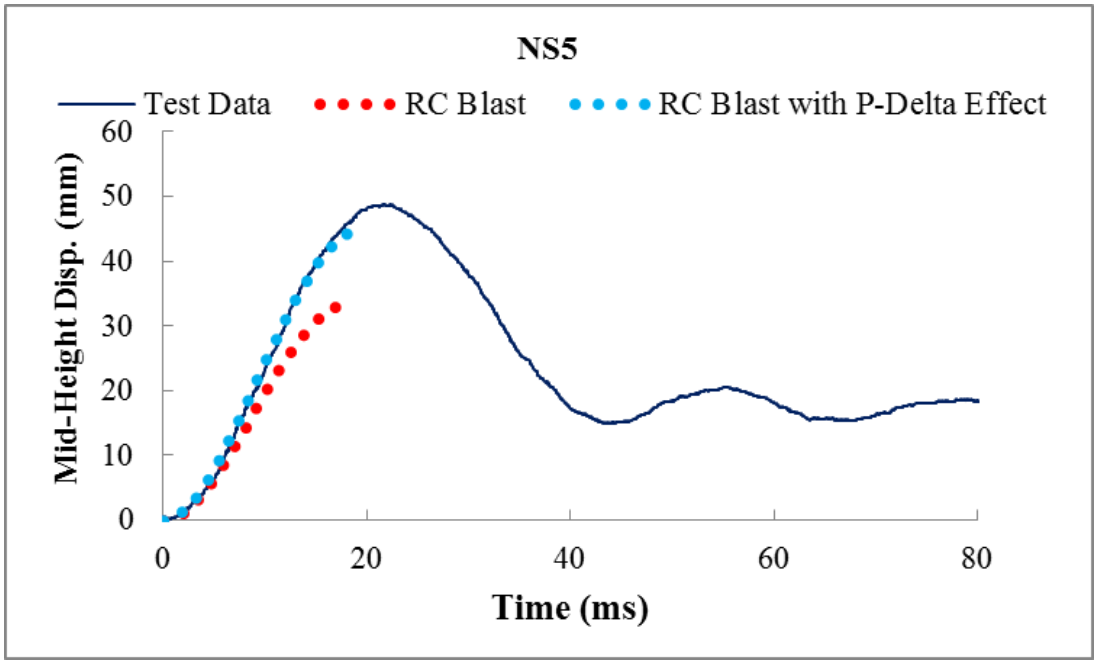

Fig. 6.41 P-Delta effects on maximum mid-height displacement - Column NS5

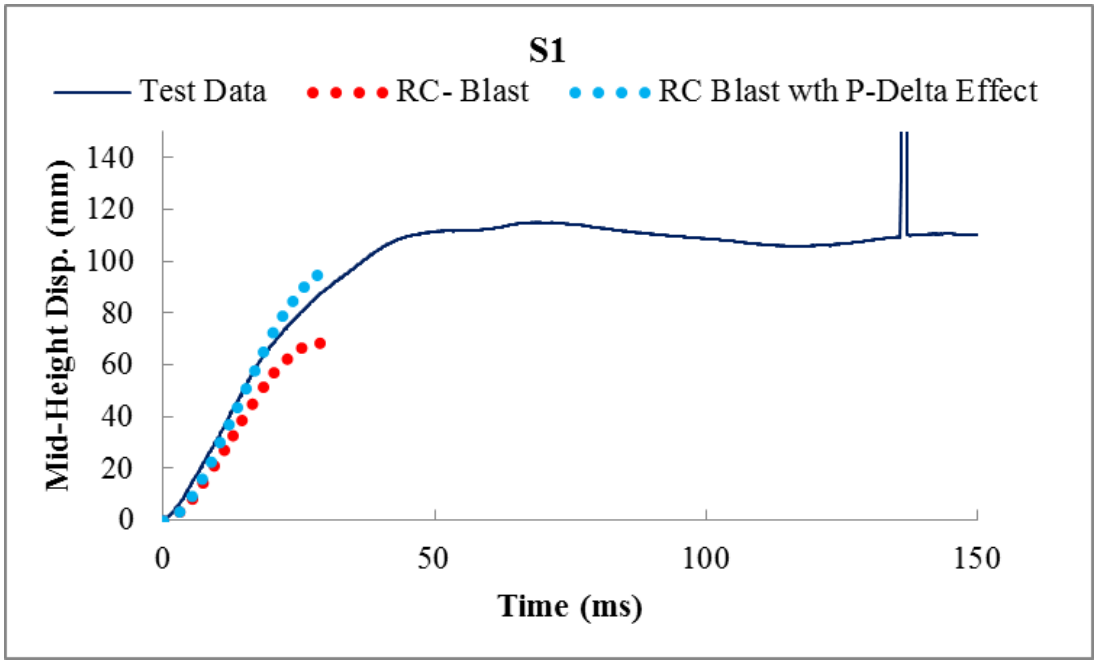

Fig. 6.42 P-Delta effects on maximum mid-height displacement - Column S1

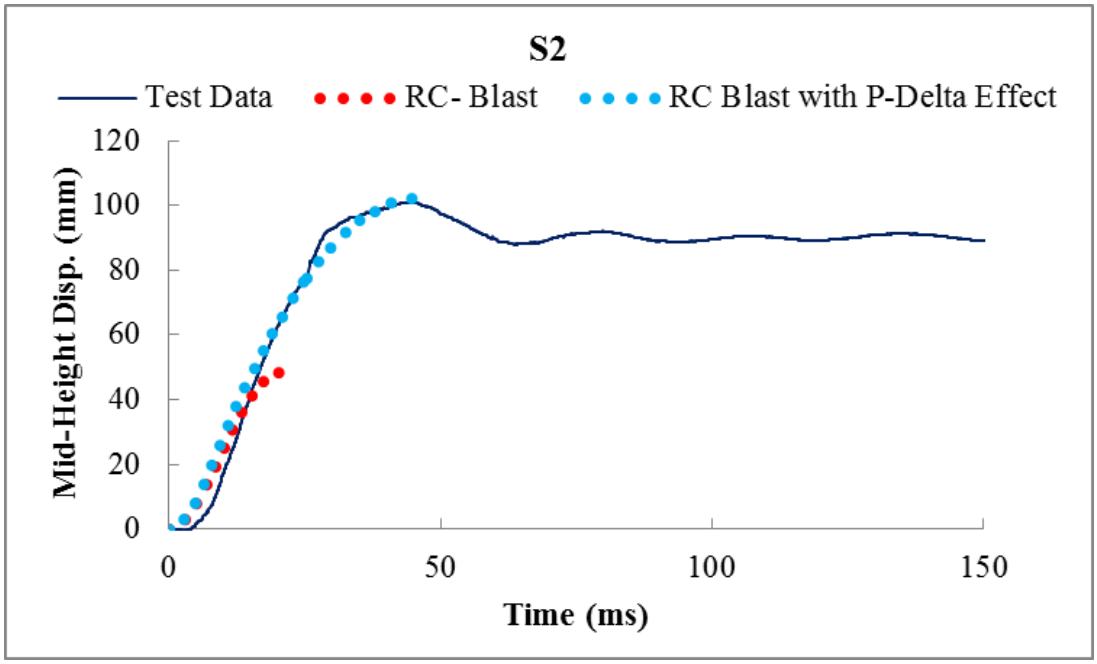

Fig. 6.43 P-Delta effects on maximum mid-height displacement - Column S2

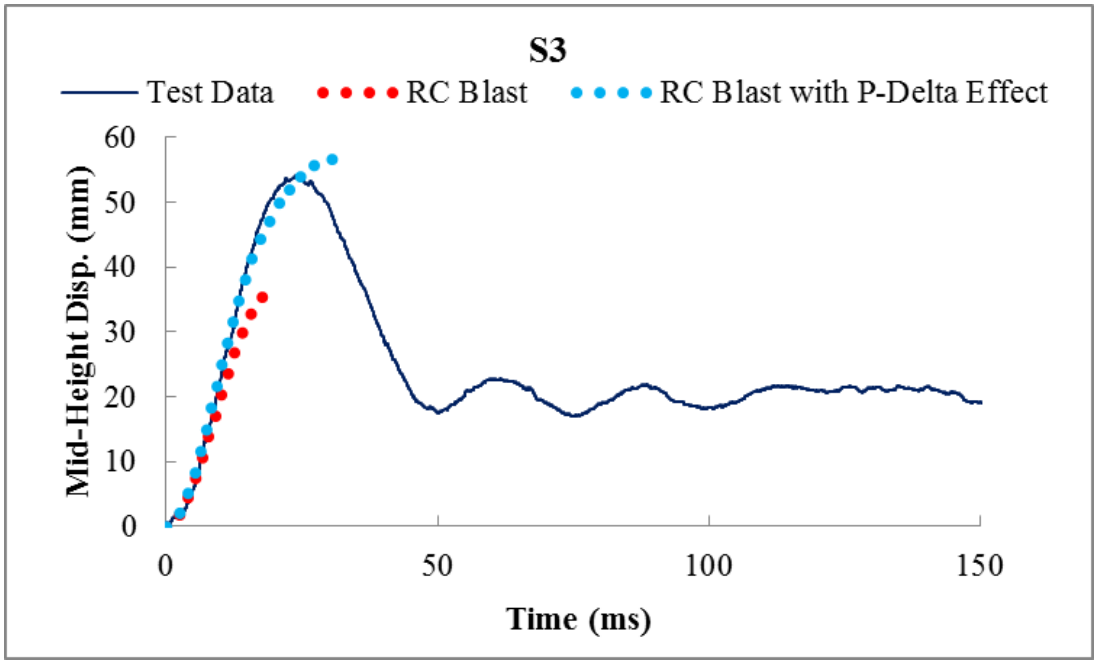

Fig. 6.44 P-Delta effects on maximum mid-height displacement - Column S3

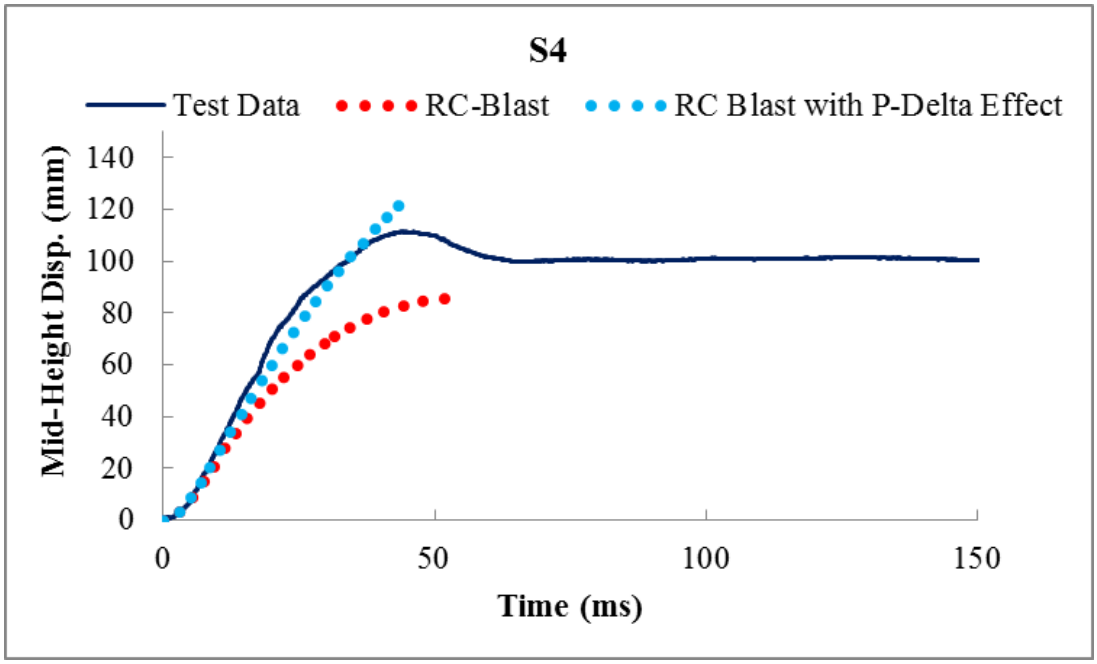

Fig. 6.45 P-Delta effects on maximum mid-height displacement - Column S4

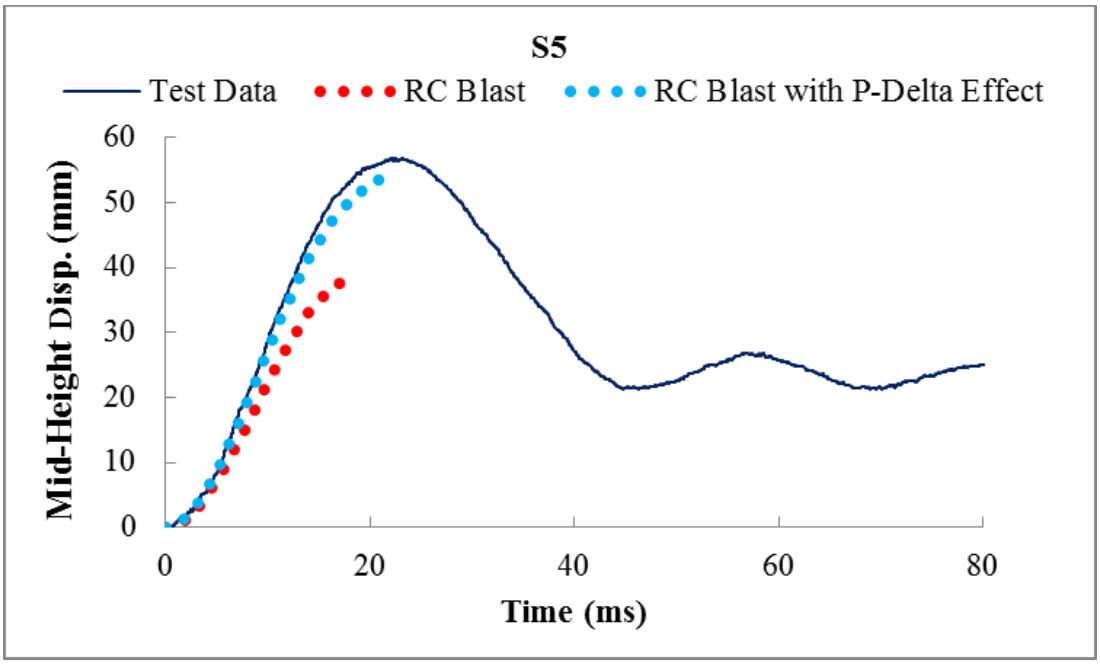

Fig. 6.46 P-Delta effects on maximum mid-height displacement - Column S5

Chapter Seven

Summary, Design Recommendations and Conclusions

7.1 Summary

A comprehensive experimental and analytical investigation was performed to explore the effects of selected structural and blast shock wave parameters on the dynamic response of reinforced concrete columns with and without CFRP jackets. Of particular interest was the CFRP laminate design on blast behaviour of CFRP jacketed columns. Blast loads were simulated using the University of Ottawa Shock Tube. All columns in this research program had 150 mm x 150 mm x 2438 mm dimensions. Two types of columns were considered; i) ordinary gravity load columns without confined concrete in the core, and ii) seismically detailed columns with confined core. Each column was reinforced longitudinally with four 10M rebars and laterally with 6.3 mm closed steel ties at either 37.5 mm or 100 mm c/c spacing for seismic and non-seismic columns, respectively. The work was divided into two phases. Phase-I (sub-study) included blast tests of eight as-built seismic columns for studying the effects of applying single or multiple blast shots with and without the application of pre-blast axial loads. Phase-II (main-study) involved the investigation of the influence of different CFRP wrapping designs on dynamic response of twenty three seismic and non-seismic columns. The performance of each column test was presented and discussed with detailed experimental results consisting of applied shock waves, impulsive forcing functions, displacement and support reaction time histories. Improved experimental measurement techniques were employed to obtain accurate

displacements from which response accelerations were computed. Column support reactions were also measured, allowing the construction of experimental resistance functions together with experimental accelerations. The effects of the test parameters were assessed through extensive comparisons of experimental results and observations. The design of each CFRP laminate was investigated, with particular emphasis on fibre orientation and the characteristics of the fibre sheets utilized. Emphasis was placed on the effects of variable axial loads during response and the progression of plastic hinging in columns, especially for CFRP retrofitted columns.

The analytical research consisted of extensive SDOF non-linear dynamic analyses of columns with and without the CFRP jackets. Parameters contributing to the accuracy of the analysis were identified and studied further with a view of making recommendations for use in research and practice. A design procedure was developed for blast retrofit of columns with CFRP jackets of different laminate designs.

7.2 Design Recommendations

Civilian infrastructure in Canada is not designed for blast loads, with the exception of special facilities and some government assets like important buildings and embassies. Therefore, the National Building Code of Canada does not address blast design for civilian buildings. However, the Canadian Standards Association developed a new Standard in 2012 for the design and assessment of buildings subjected to blast loads (CSA S850 2012).

Considering the needs for blast retrofitting of existing buildings, a retrofit design procedure is developed for FRP jacketing of reinforced concrete columns as part of the current research project. The design procedure utilizes the results of the experimental and analytical research conducted in the project. The basic performance-based design principles outlined in CSA S850 are also utilized. It is intended for flexure dominant columns, subjected to far-field explosions, with sufficient shear capacity.

The following provides a step-by-step approach for the recommended design procedure:

1. The first step involves the determination of the design basis threat (DBT), which identifies the charge weight and standoff distance for the explosion, for which the building column is to be retrofitted. These two parameters define the forcing function to be used in design, where the charge weight plays a prominent role on the magnitude of

the design blast pressure and the standoff distance plays a major role on the duration of the positive phase of pressure. As often is the case, using an idealized triangular forcing function, linearly varying between the maximum reflected blast pressure at zero time and zero pressure at the end of the positive phase duration provides sufficiently accurate designs.

2. The second step involves a decision to be made by the building owner or the authority having jurisdiction over the building for the level of protection required. This depends on the importance of the building and the consequence of damage. Table 7.1 provides the levels of protection (LOP) and corresponding performance levels and associated damage levels to choose from.
3. Once the LOP is selected, the column must be designed to remain within the deformation limits specified as response limits in CSA S850 (2012). Response limits for primary RC column elements that are responsible for overall strength and stability of columns are expressed in terms of maximum displacement ductility factors (μ_{max}). Displacement ductility demands will be established through a SDOF dynamic analysis, as outlined in Step 4 below for comparison with response limits given in Table 7.2. The initial analysis should be conducted for the existing column with its prevalent site conditions and material properties, prior to the retrofit, to assess its capacity and the requirements for possible enhancements in strength and ductility.
4. SDOF dynamic analysis requires three sets of data; i) impulsive forcing function that is obtained from the DBT established in Step 1, ii) column mass that can be computed and the load-mass transformation factors that are available for columns with different support conditions in elastic and inelastic regions of response, and iii) the resistance function that defines strength and stiffness. The first two sets of data are readily available for any structural element. Step 5 provides guidelines for the computation of column resistance function utilizing the results of the current investigation.
5. The resistance function can be computed in the form of a column force resistance-column displacement relationship. It can be constructed starting with sectional analyses of critical sections where plastic hinges are expected to form.
    a. The sectional analysis can be done by performing a strain compatibility analysis, with Bernoulli's principle on "plane sections before bending remaining plane after

bending." It is important to use the appropriate material constitutive models for the analysis. The confinement of concrete for the core concrete, potentially caused by the additive effects of internal transverse reinforcement and external FRP jacket should be accounted for in retrofitted columns. Similarly, the confinement effect of the FRP jacket on the cover concrete should be incorporated. The strain hardening of reinforcement in tension and the potential buckling of longitudinal bars in compression should be modelled. The stress-strain relationship of FRP jacket should be established carefully by coupon tests. These relationships are linear for typical FRP laminates; but it is important to test the FRP coupons in the direction of stresses for which the FRP is used; for flexural strength calculations the coupon test results should reflect the stress-strain characteristics of FRP in the column longitudinal direction, and for the purpose of confinement pressure calculations it should reflect the material behaviour in the column transverse direction. Once the material strengths are attained, Dynamic Increase Factors (DIF) should be applied. The DIFs specified in CSA S850, also given in Table 7.3 may be used for this purpose. It is also recommended to use the Strength Increase Factors specified in Table 7.4.

b. The sectional analysis should be conducted under different levels of constant axial load. The columns tested in the current investigation were initially subjected to 40% of their concentric compressive capacity. During testing, they experienced a drop in the level of axial compression because of lateral column deflections. It was argued earlier that the rate at which the columns deformed laterally under lateral blast loads was faster than the rate at which the gravity load was applied. Depending on the magnitude of lateral deflections, columns experienced varying degrees of losses in axial load, some of which was recovered subsequently as lateral deflections were recovered. The columns tested in the current investigation lost their axial loads almost entirely when they developed a support rotation of 8 degrees and higher momentarily, before the axial loads were recovered to their residual levels. While the amount of variation in axial load depends on many factors, including the level of protection sought for design, reduced level of axial

load may be considered in the second iteration of analysis if the computed deflections under the initial axial load level are high.

c. Once the sectional characteristics are computed as described above, the resulting moment-curvature relationship can be idealized as a bilinear relationship where the first line segment connects the origin with a point on the curve at 70% of the moment capacity, extending to intersect with a horizontal line drawn at moment capacity, which forms the second line segment. The ultimate curvature, beyond which the section is considered to have failed, may be taken as the curvature on the descending branch of the moment-curvature relationship at 20% strength decay point.

d. The bi-linear moment-curvature relationship can be used to compute the column mid-height deflection by employing the second moment area theorem (moment of the area under M/EI = ϕ diagram). The plastic hinge length (L_p) for columns, defined as the length within which the ultimate curvature is assumed to be constant, can be used as established in the experimental phase of the current investigation. Accordingly, for columns without external FRP jacketing: $L_p = 0.7h$ (in the experimental program it varied between 0.67h for non-seismic columns to 0.77h for seismic columns); for columns with FRP jackets containing unidirectional fibres only: $L_p = 0.9h$ and jackets containing $\pm 45^\circ$ degree fibres $L_p = 1.1h$, where h is the column cross-sectional dimension in the direction of blast loading. It should be noted that, columns with simply supported end supports are expected to develop their plastic hinges at the maximum moment location at mid-height. However, columns with end fixities may experience multiple hinges, with moment redistribution taking place beyond the first yielding, while the column continues sustaining additional deformations until a collapse mechanism is formed, necessitating plastic analysis. In lieu of such vigorous plastic analysis, column deflection at the formation of first complete plastic hinge may be used as a conservative deflection value. This deflection divided by the deflection at first yield gives the ductility demand, which has to be compared with the ductility capacity assumed as the response limit specified in Table 7.2 for the LOP sought.

e. The accuracy of the resistance function described above can be improved by incorporating secondary moments associated with P-Δ effects. This can be done by implementing the Equivalent Lateral Load Method described in Section 6.5.3.1.

f. If the ductility demand is within the response limit for the LOP sought, then the design is acceptable. Otherwise, the column flexural capacity must be increased by increasing the FRP jacket thickness and/or the FRP laminate design. The entire Step 5 has to be repeated with the new FRP jacket design until the ductility demand falls within the respective response limit for the LOP selected in design.

7.2 Conclusions

The following key conclusions can be drawn from the present experimental and analytical investigations:

- RC members experience lower deflections when exposed to a single blast shot of a specific magnitude, compared to multiple shots gradually increasing up to the same pressure magnitude.
- When subjected to blast loads; axially loaded columns develop lower displacements and higher resistances compared to the companion columns under zero axial load. The initial axial load on columns drop significantly as columns deform laterally under blast loads. The reduction in axial load is proportional to the increase in lateral deflection. For the columns tested in the current investigation the entire axial load was lost at about 9˚ support rotation. Recovery of elastic deflections resulted in a residual deflection and residual axial load on columns.
- Among the various FRP laminates investigated for column jacketing, the laminate that contained fibres oriented in ±45˚ directions, in combination with unidirectional fibres placed in longitudinal and transverse directions, showed the best performance with the most ductile response. Those that contained only the unidirectional fibres showed second best performance.
- Seismically detailed columns, with and without CFRP retrofitting show better performance than corresponding non-seismic columns with and without CFRP jacketing. However, the enhancement in behaviour was more pronounced in the CFRP protected

columns. This can be explained by the dual confinement provided in these columns by the closely spaced internal steel ties and the externally placed CFRP wrapping.

- Increasing concrete compressive strength (from f'_c = 33 MPa to 44 MPa) improved blast response of CFRP protected columns, albeit marginally. However, this effect was found to be negligible for un-retrofitted columns.
- FRP laminate lay-up has a noticeable influence on the length of the plastic hinge generated at column mid-height. In the experimental program the use of FRP laminates with unidirectional fibres resulted in an increase in the plastic hinge length from 0.7h for unretrofitted columns to 0.9h for retrofitted columns. The use of ±45˚ fibres in the laminates further increased the plastic hinge length to 1.1h.
- The residual axial load capacity and ductility of columns, established under monotonically increasing static loading improve with FRP jacketing. The column tests indicated that columns with CFRP jackets, especially those with ±45˚ fibres showed more favourable behaviour than those that did not have CFRP jacketing.
- Accurate measurements of mid-height displacement using laser displacement sensors and high-speed data acquisition system enable accurate monitoring of the inertia force, facilitating the construction of experimental resistance functions.
- Behaviour of columns tested under dynamic shock waves can be reproduced under equivalent static pressures, provided that the strain rate effects on materials are accounted for. This observation has been verified by comparing some of the columns tested in the current investigation with identical companion columns tested in another phase of the investigation under incrementally increasing static pressure for both unretrfoitted and CFRP retrofitted columns.
- SDOF analysis can be used effectively to estimate the response of columns to blast-induced shock waves. The analysis must include appropriate material models for concrete confinement, reinforcement strain hardening and buckling of longitudinal reinforcement in compression, while also incorporating the effects of high strain rates on materials.
- SDOF results can be improved by considering the effects of variable axial loads, variation in plastic hinge length with different laminate designs, and the P-Δ effect during response to blast loads.

- The design procedure formulated for FRP retrofit of columns against blast load effects, as a results of the column tests and analytical verifications conducted as part of the current research project, can be used to design blast-resistant concrete columns.

7.3 Recommendations for Future Work

The following topics are recommended for future research projects:

- Investigation of the effects of column dimensions, column slenderness and end fixity (or boundary condition) on blast performance of "full scale" RC columns wrapped with CFRP laminate design of choice (with lay-up UD $[0^{\circ}/90^{\circ}/0^{\circ}]$ W $[\pm 45^{\circ}]_2$).
- Further investigation of the effects of concrete compressive strength on dynamic behaviour of RC columns, using a wider range of concrete strengths.
- Development of a risk-based optimization process for CFRP laminate design. This may require conducting series of field blast tests, finite element modeling, and quasi-static tests to demonstrate the effectiveness of the selected CFRP laminate lay-up.
- Optimize the CFRP laminate materials and its integration with other safety and security technologies for best performance under the effects of fragmentation and fire.
- A comprehensive experimental study that is entirely devoted to investigating the influence of CFRP laminate design on plastic hinge length under blast loading.
- Development of a multiple-degree of freedom non-linear dynamic analysis tools for blast analysis of structural elements that account for second order effects (or P-Δ).

Table-7.1: Levels of protection, building performance, column damage and associated response limits (CSA S850 2012)

Level of Protection	Building Performance	Column Damage	Response Limits
Unacceptable	Hazardous failure	Severe Damage	Between B3 and B4
Very Low	Collapse prevention	Heavy	Between B2 and B3
Low	Life safety	Moderate	Between B1 and B2
Medium	Immediate occupancy	Superficial	Less than B1
High	Operational	Superficial	Less than B1

Table-7.2: Response limits in terms of maximum ductility factors for reinforced concrete columns (CSA S850 2012)

Column Type	B1	B2	B3	B4
Seismic Columns	0.9	1	2	3
Non-Seismic Columns	0.7	0.8	0.9	1
CFRP Jacketed Columns	0.9	1	2	3

Table-7.3: Dynamic Increase Factors (DIF) (CSA S850 2012)

Material Property	Flexural failure mode	Compression failure mode
Concrete compressive strength	1.2	1.1
Yield strength of steel	1.2	1.1
Ultimate strength of steel	1.1	-
CFRP	1.0	1.0

Table-7.4: Strength Increase Factors (SIF) (CSA S850 2012)

Compressive strength of concrete	1.1
Yield strength of reinforcing steel	1.1
Ultimate strength of steel	1.0
CFRP	1.3

References

1. Abdelrahman, K., and Al-Hacha, R., “Behaviour of Large-Scale Concrete Columns Wrapped with CFRP and SFRP Sheets”, Journal of Composite for Construction, ASCE, July-August, 2012.
2. Agnew, E., Majanishvili, S., and Gallant, S., “Concrete Detailing for Blast”, Structure Magazine, January, 2007.
3. Agnew, E., Marjnishvili, S., Gallant, S., “Concrete Detailing for Blast” Structure Magazine, January 2007.
4. Aoude, H., Dagenais, F. P., Burrell, R.P., and Saatcioglu, M., “Behaviour of Ultra-High Performance Fiber Reinforced Concrete Columns”, International Journal of Impact Engineering, 80-2015.
5. Arndt, M. C., “FRP Rehabilitation of Blast and Impact Damaged Reinforced Concrete”, MS Thesis, Faculty of the Royal Military College of Canada, Civil Engineering Department, August 2009.
6. ASCE. (1996). “The Oklahoma City Bombing: Improving Building Performance through Multi-Hazard Mitigation”, Federal Emergency Management Agency, FEMA 277, ASCE, Reston, VA.
7. ASCE. (2010). “Minimum Design Loads for Buildings and other Structures”, ASCE/SEI 7, Reston, VA.
8. ASCE. (2011). “Design of Blast-Resistant Buildings in Petrochemical Facilities”, Reston, VA.
9. Au, C., and Buykozturk, O., “Effect of Fiber Orientation and Ply Mix on Fiber Reinforced Polymer-Confined Concrete”, Journal of Composite for Construction, September, 2005.
10. Bae, S., and Bayrak, O., “Plastic Hinge Length of Reinforced Concrete Columns”, ACI Structural Journal, May-June, 2008.
11. Ballinger, C., Maeda, T., and Hoshijima, T., “Strengthen of Reinforced Concrete Chimneys, Columns and Beams with Carbon Fiber Reinforced Plastic”, Proceedings of the International Symposium on Fiber-Reinforced-Plastic Reinforcement for Concrete Structures, ACI SP-138, 1993.

12. Bank, L. C., “Composites for Construction: Structural Design with FRP Materials”, John Wiley & Sons, Inc., New Jersey, USA, 2006.
13. Bao, X., and Li, B., “Residual Strength of Blast Damaged Reinforced Concrete Columns”, International Journal of Impact Engineering, April, 2009.
14. Berger, J.O., Heffernan, P.J., and Wight, R.G., “Blast Testing of CFRP and SRP strengthened RC Columns”, Design against Blast, pp. 189-198, WIT Press, UK, 2013.
15. Biggs, J. M., “Introduction to Structural Dynamic”, McGraw-Hill, Inc., 1964.
16. Buchan, P. A., and Chen, J. F., “Blast Resistance of FRP Composites and Polymer Strengthened Concrete and Masonry Structures- A state of-the-art review”, Composites: Part B38 (2007) 509-522.
17. Buchan, P.A., and Chen, J. F., “Blast Protection of Buildings Using Fiber-Reinforced Polymer (FRP) composites/ Blast Protection of Civil Infrastructures and Vehicles Using Composites”, Woodhead Publishing Limited, 2010.
18. Burrell, R., “Performance of Steel Fiber Reinforced Concrete Columns under Shock Tube Induced Shock Wave Loading”, MS Thesis, Department of Civil Engineering, University of Ottawa, February 2012.
19. Carrier, M., Heffernan, P.J., Wight, R.G., and Braimah, A., “Behaviour of Steel Reinforced (SRP) Strengthening RC members under Blast Load”, Canadian Journal of Civil Engineering, 36, 2009.
20. Chen, J. F., Li, S. Q., and Bisby, L. A. “Factors Affecting the Ultimate Condition of FRP-Wrapper Concrete Columns”, Journal of Composite Construction, ASCE, January-February, 2013.
21. Cormie, D., Mays, G. and Smith, P., “Blast Effects on Buildings”, Thomas Telford Limited, 2009.
22. Crawford, J. E., Malvar, L. J., Dunn, B. D.,and Gee, D. J., “ Retrofit of Reinforced Concrete Columns Using Composite Wraps to Resisit Blast Loads”, TR, Karagozian and Case Structural Engineers , Burbank , Claif, Aug.-1996.
23. Crawford, J. E., Malvar, L. J., Morrill, K. B., and Ferritto, J. M., “ Composite Retrofits To Increase the Blast Resistance of Reinforced Concrete Buildings” TR-P-01-13, 10th International Symposium on Interaction of the Effects of Munitions with Structures, 1-13 May 2001, San Diego, CA.

24. Crawford, J. E., Malvar, L. J., Wesevich, J. W., Valancius, J., and Reynolds, A. D., " Retrofit of Reinforced Concrete Structures to Resist Blast Effects", ACI Structural Journal, Vol. 94, No. 4, July-August 1997.
25. CSA. CSA A23.3-04 "Design of Concrete Structures", Canadian Standard Association, Mississauga, 2004.
26. CSA S850-2012 "Design and Assessment of Buildings Subjected to Blast Loads", Canadian Standard Association, Mississauga, 2012.
27. Department of Defense, Unified Facilities Code (UFC) 03-340-02), "Structures to Resist the Effects of Accidental Explosions," United States of America Department of Defence, Washington, DC, 2008.
28. Dusenberry, D. O., "Hand Book for Blast Resistant Design of Buildings", John Wiley&Sons, Inc, USA, 2010.
29. Gram, M.M., Clark, A. J., Hegemier, G. A., and Seible, F., "Laboratory Simulation of Blast Loading on Building and Bridge Structures", WIT Structures on the Built Environment, Vol. 87, 2006.
30. Gu, D., Wu, Y., Wu, G., and Wu, Z., "Plastic Hinge Analysis of FRP Confined Circular Concrete Columns", Journal of Construction and Building Martials, 2012.
31. Hasak, A., "Performance of FRP Strengthened Concrete Columns Under Simulated Blast Loading", MS Thesis, Department of Civil Engineering, University of Ottawa, February 2015.
32. Hemmatie, A., Kheyroddin, A., and Shartada M. K., "Plastic Hinge Rotation Capacity of Reinforced HPFRCC Beams.
33. ISIS (2008), "FRP Rehabilitation of Reinforced Concrete Structures", Design Manual No.4.
34. Jacques, E., Lloyd, A., and Saatcioglu, M., " Predicting Reinforced Concrete Response to Blast Loads", Canadian Journal of Civil Engineering, Vol. 40, Issue 5, April,2013.
35. Jaing, C., Wu, Y., and Wu, G., "Plastic Hinge Length of FRP-Confined Square Columns", Journal of Composite Construction, ASCE, 2014.
36. Johan-EK, K., and Mattason, P., "Design with Regard to Blast-and Fragment Loading", MS Thesis , Department of Civil and Environmental Engineering, Chalmers university of technology , Sweden , 2009.

37. Kazaz, İ., “Analytical Study on Plastic Hinge Length of Structural Walls”, Journal of Structural Engineering ASCE, November, 2013.
38. Kheyroddin, A., and Naderpour, H., “ Plastic Hinge Capacity of Reinforced Concrete Beams”, International Journal of Civil Engineering , Vol. 5, No. 1, 2007.
39. Li, G., Maricherla, D., Singh, K., Pang, S., and John, M., “Effect of Fiber Orientation on Structural Behaviour of FRP Wrapped Concrete Cylinders”, Journal of Composite Structures, June, 2005.
40. Lloyd, A., “ Performance of Reinforced Concrete Columns Under Shock Tubes Induced Shock Wave Loading”, MS Thesis , Department of Civil Engineering, University of Ottawa, February 2010.
41. Lloyd, A., “Blast Retrofit of Reinforced Concrete Columns”, PhD Thesis, Department of Civil Engineering, University of Ottawa, February 2015.
42. Malvar, L. J., Crawford, J. E., and Morrill, K. B., “Use of Composites to Resist Blast” Journal of Composites for construction, ASCE ,November-December 2007.
43. Malvar, L. J., Ross, C. A., “Review of Strain Rate Effects for Concrete in Tension”, ACI Materials Journal, November-December 1998.
44. Mirmiran, A., and Shahawy, M., “Behaviour of Concrete Columns Confined by Fiber Composites”, Journal of Structural Engineering, May, 1997.
45. Morrill, K. B., Malvar, L. J., Crawford, J. E., and Attaway, S. T., “ RC Columns and Slabs Retrofit to Survive Blast Loads”, Proc., Congress 2000, ASCE, Reston, Va.
46. Morrill, K. B., Malvar, L. J., Crawford, J. E., and Ferritto, J. M., “ Blast Resistant Design of Reinforced Concrete Columns and Walls”, Proc., Congress 2004, ASCE, Reston, Va.
47. Mortezaei, A., and Ronagh, H.R., “Plastic Hinge Length of FRP Strengthened Reinforced Concrete Columns Subjected to Both Far-Fault and Near-Fault Ground Motions”, Scientia Iranica, 19, 6, 2012.
48. Myers, J. J., Belarbi, A., and K. A. El-Domiaty “Blast Resistance of FRP Retrofitted Un-Reinforced Masonry (URM) Walls with and without Arching Action”, TMS Journal, September, 2004.
49. Oswald, C. J., “Comparison of Response from Combined Axial and Blast Loads Calculated with SDOF and Finite Methods”, Department of Defense Explosive Safety Board Seminar, 34th, Portland, Oregon, July, 2010.

50. Ou, Y. and Nguyen, N. D., “Plastic Hinge Length of Corroded Reinforced Concrete Beams”, ACI Structural Journal, Sept.-Oct. 2014.
51. Park, R., and Paulay, T., “Reinforced Concrete Structures”, John Wiley & Sons, Inc., USA, 1975.
52. Parvin, A., and Jamwal, A. S., “Effects of Wrap Thickness and Ply Configuration on Composite-Confined Concrete Cylinders”, Journal of Composite Structures, March, 2004.
53. Paulay, T., and Priestly, M. J. N., “Seismic Design of Reinforced Concrete and Masonry Buildings”, John Wiley & Sons, Inc., USA, 1992.
54. Pessiki, S., Harries, K. A., Kestner, J. T., Sause, R., and Ricles, J. M., “Axial Behaviour of Reinforced Concrete Columns Confined with FRP Jackets” Journal of Composite for Construction, November, 2001.
55. Priestley, M. J. N. and Park, R., “Strength and Ductility of Concrete Bridge Columns under Seismic Loading”, ACI Structural Journal, Jan.-Feb., 1987.
56. Razvi, S. R., and Saatcioglu, M., “Stress-Strain Relationship for Confined High Strength Concrete”, ASCE Journal of Structural Engineering, 125(3), 1999.
57. Rochette, P., and Labossiere, P., “Axial Testing of Rectangular Column Models Confined with Composite”, Journal of Composite for Construction, August, 2000.
58. Rodriguze-Nikle, T., “Experimental Simulation of Explosive Loading on Structural Components: Reinforced Concrete Columns with Advanced Composite Jackets”, PhD thesis, University of California, San Diego, USA, 2006.
59. Rodriguze-Nikle, T., Lee, C., Hegemier, G. A., and Seible, F., “Experimental Performance of Concrete Columns Composite Jackets under Blast Loading”, Journal of Structural Engineering, 138, pp. 81-89, 2012.
60. Rong, H., and Li, B., “Deformation–Controlled Design of Reinforced Concrete Flexural Members Subjected of Blast Loadings”, Journal of Structural Engineering, ASCE, October, 2008.
61. Saatcioglu, M. and Razvi, S. R. “Strength and Ductility of Confined Concrete”, ASCE Journal of Structural Engineering, 118(6), 1992.

62. Sadeghian, P., and Ehsani, M. R., "Numerical Modeling of Concrete Cylinders Confined with CFRP Composite", Journal of Reinforced Plastic and Composites, Vol.27, No.12, 2008.
63. Sadeghian, P., Rahi, A. R., and Ehsani, M. R., "Effect of Fiber Orientation on Nonlinear Behaviour of CFRP Compsite", Journal of Reinforced Plastic and Composites, Vol.28, No.18, 2009.
64. Sadeghian, P., Rahi, A. R.,and Ehsani, M.R., "Effect of Fiber Orientation on Compressive Behaviour of CFRP-Confined Concrete Columns", Journal of Reinforced Plastic and Composites, Vol.29, No.9, 2010.
65. Sadeghian, P., Shekari, A. H., and Mousavi, F., "Stress-Strain Behaviour of Slender Concrete Columns Retrofitted with CFRP Composites", Journal of Reinforced Plastic and Composites, Vol.28, No.19, 2009.
66. Sasani, M., Kazemi, A., Sagiroglu, S., and Forest, S., "Progressive Collapse of an Actual 11-Story Structure Subjected to Severe Initial Damage", Journal of Structural Engineering, ASCE, September, 2011.
67. Smith, P. D., and Hetherington, J. G. "Blast and Ballistic Loading of Structures", Butterworth Heinemann Ltd., Great Brittan, 1994.
68. Teng, J. G., Chen, J. F., Smith, S. T., and Lam, L., "Behaviour and Strength of FRP-Strengthened RC Structures: A State-of-the-Art Review", Structures and Buildings, 156, 2003.
69. Teng, J. G., Chen, J. F., Smith, S. T., and Lam, L., "FRP Strengthened RC Structures", John and Wiley, 2002.
70. Williamson, E. B., Bayrak, O., Marchand, K. A., Davis, C., Williams G., Holland, and C., "Performance of Bridge Columns Subjected to Blast Loads I", Journal of Bridge Engineering, ASCE, 2011.
71. Wu, C. Y., and Wu, G., "Plastic Hinge Length of FRP-Confined Square RC Columns", Journal of Composite and Construction, 18, 2014.
72. Wu, D. Y., and Wu, Z., "Plastic Hinge analysis of FRP Confined Circular Concrete Columns", Construction and Building Martials, 27, 2012.
73. Yalcin, C., and Saatcioglu, M., "Inelastic Analysis of Reinforced Concrete Columns", Computers and Structures, 77, 2000.

74. Zhao, X., Wu, Y., and Leung, A., “Analysis of Plastic Hinge Regions in Reinforced Concrete Beams under Monotonic Loading”, Engineering Structures, 34, 2012.

APPENDIX -A
STRAIN DATA

All columns investigated in this study were instrumented with sixteen internal general purpose electric strain gauges. These strain gauges were placed at different locations on the steel reinforcement. Fig. A-0 clearly shows the position of the strain gauges used. Figs. A-1 to A-33 depict the time history of tensile and compression strains monitored for most of the tests carried out in this experiment.

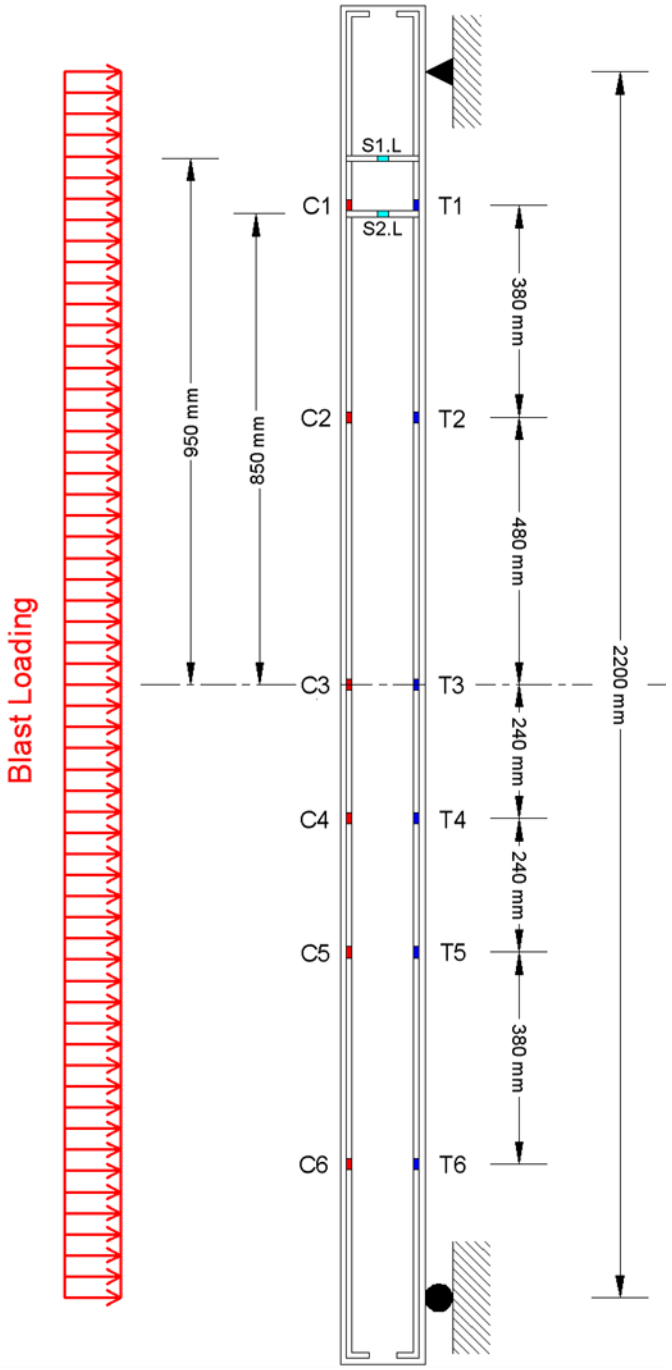

Fig. A-0 positions of the internal strain gauges

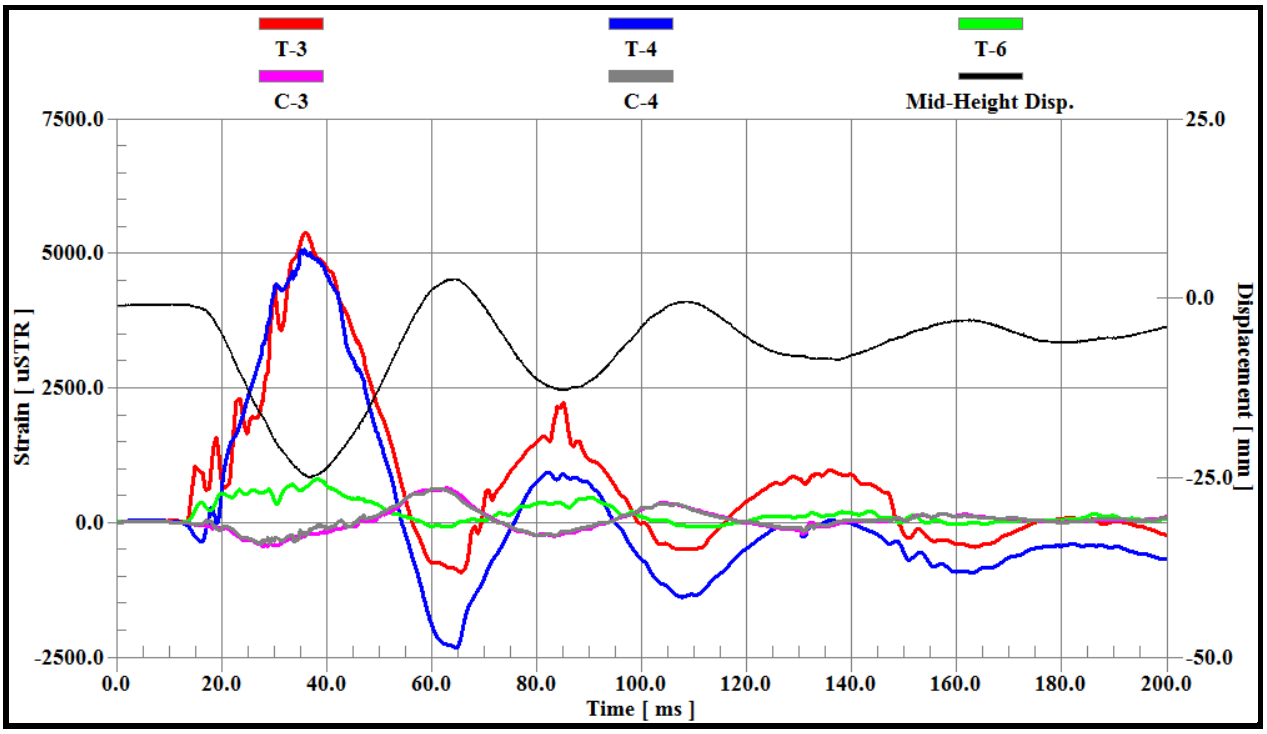

Fig. A-1 Time history of strains and mid-height displacement for column S1-AL0 (2nd shot)

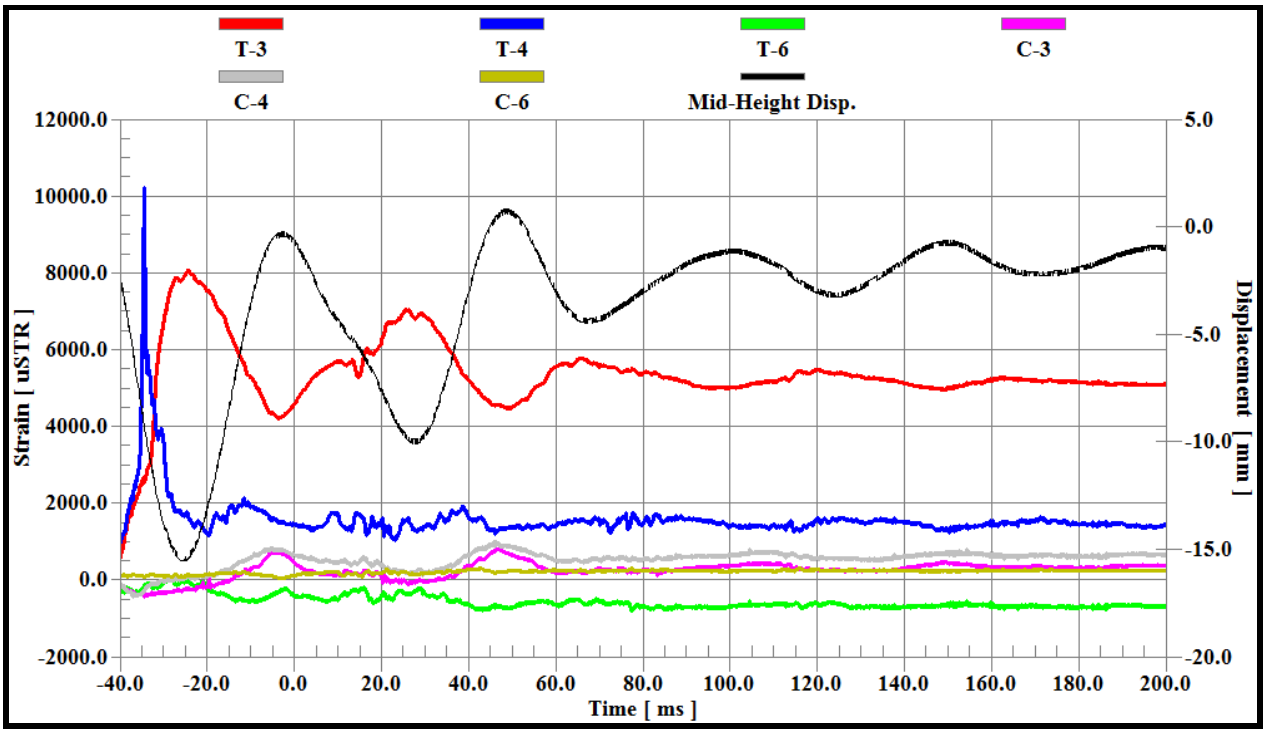

Fig. A-2 Time history of strains and mid-height displacement for column S2-AL0 (1st shot)

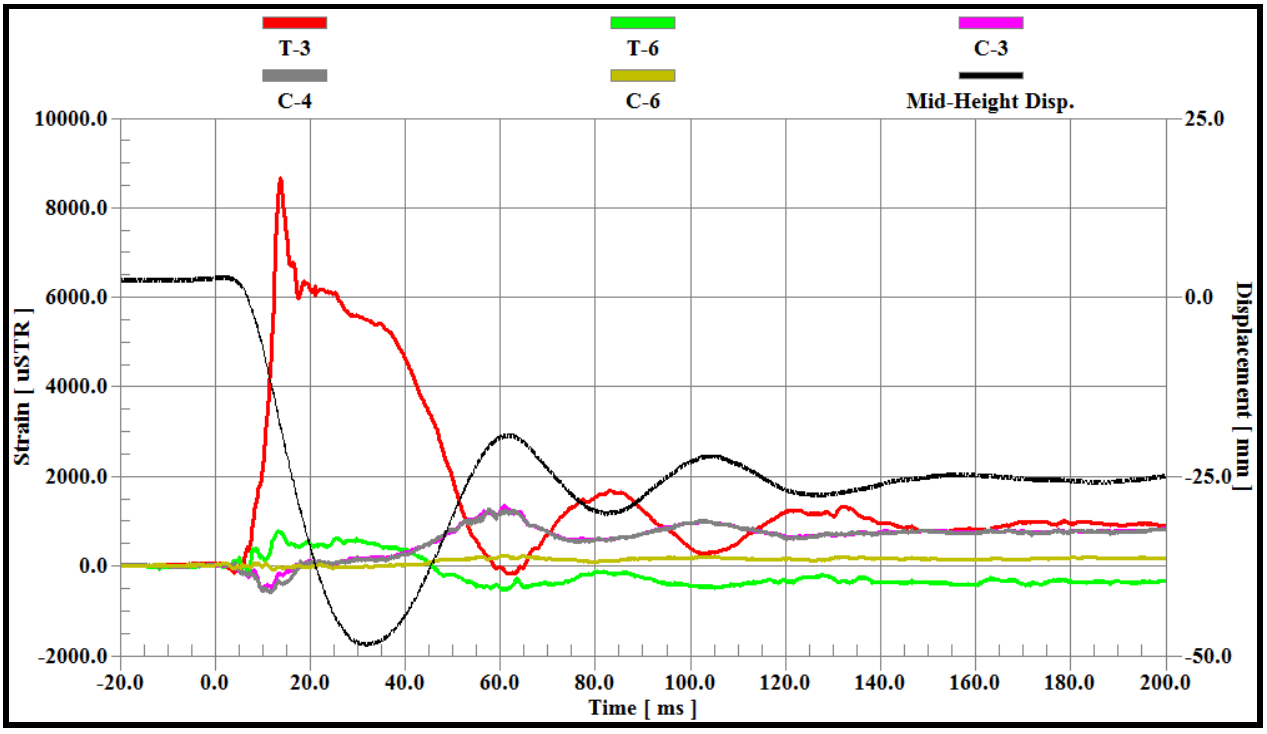

Fig. A-3 Time history of strains and mid-height displacement for column S2-AL0 (2nd shot)

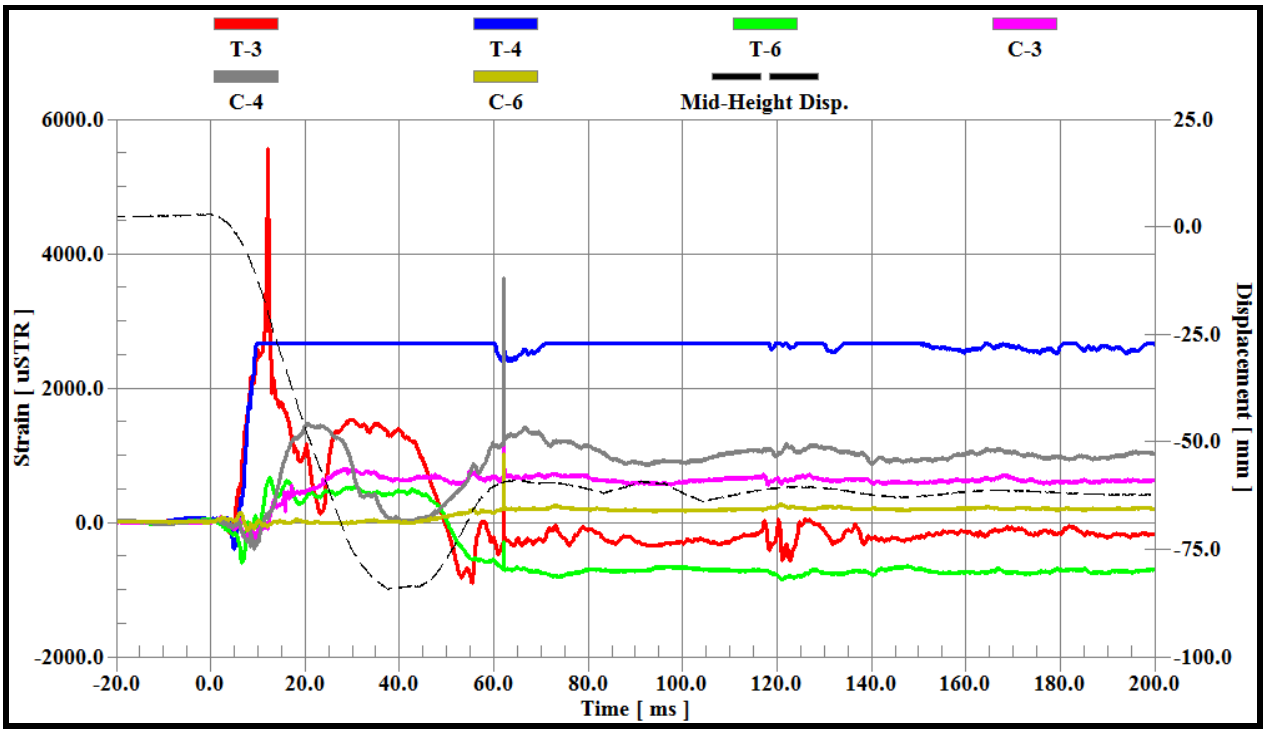

Fig. A-4 Time history of strains and mid-height displacement for column S3-AL0 (single shot)

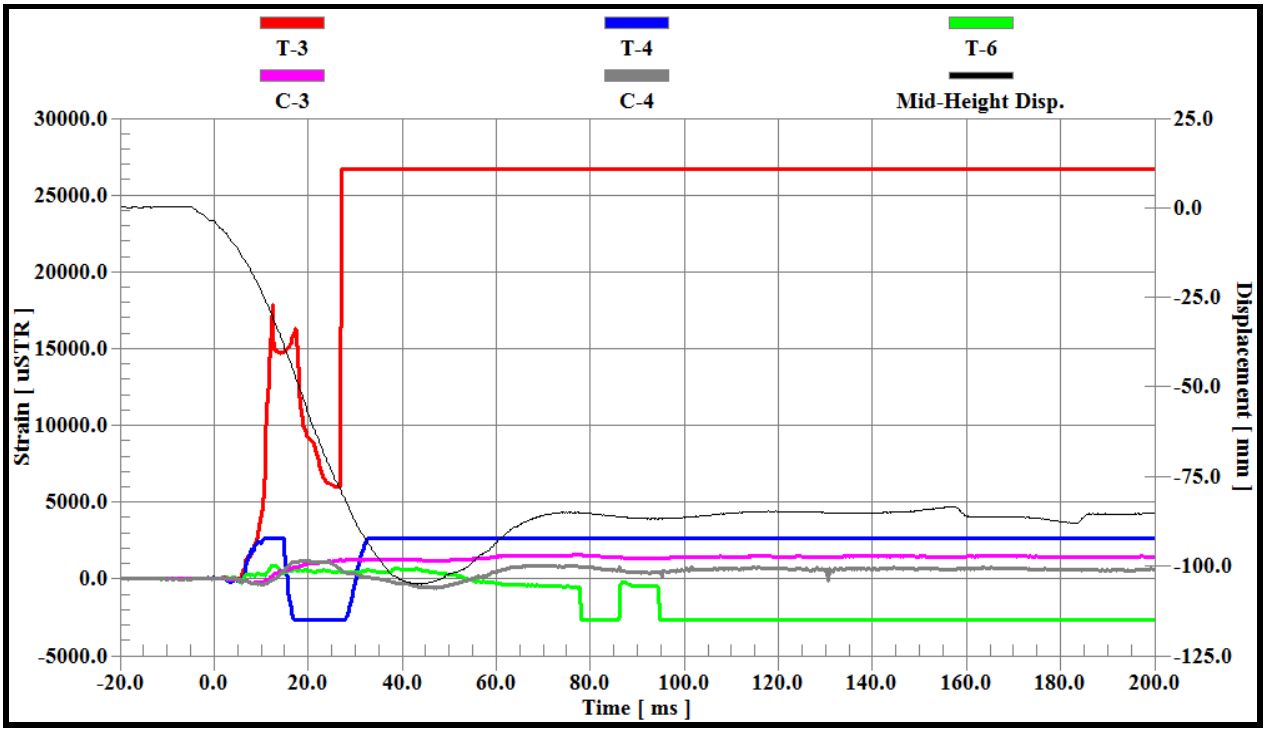

Fig. A-5 Time history of strains and mid-height displacement for column S4-AL0 (single shot)

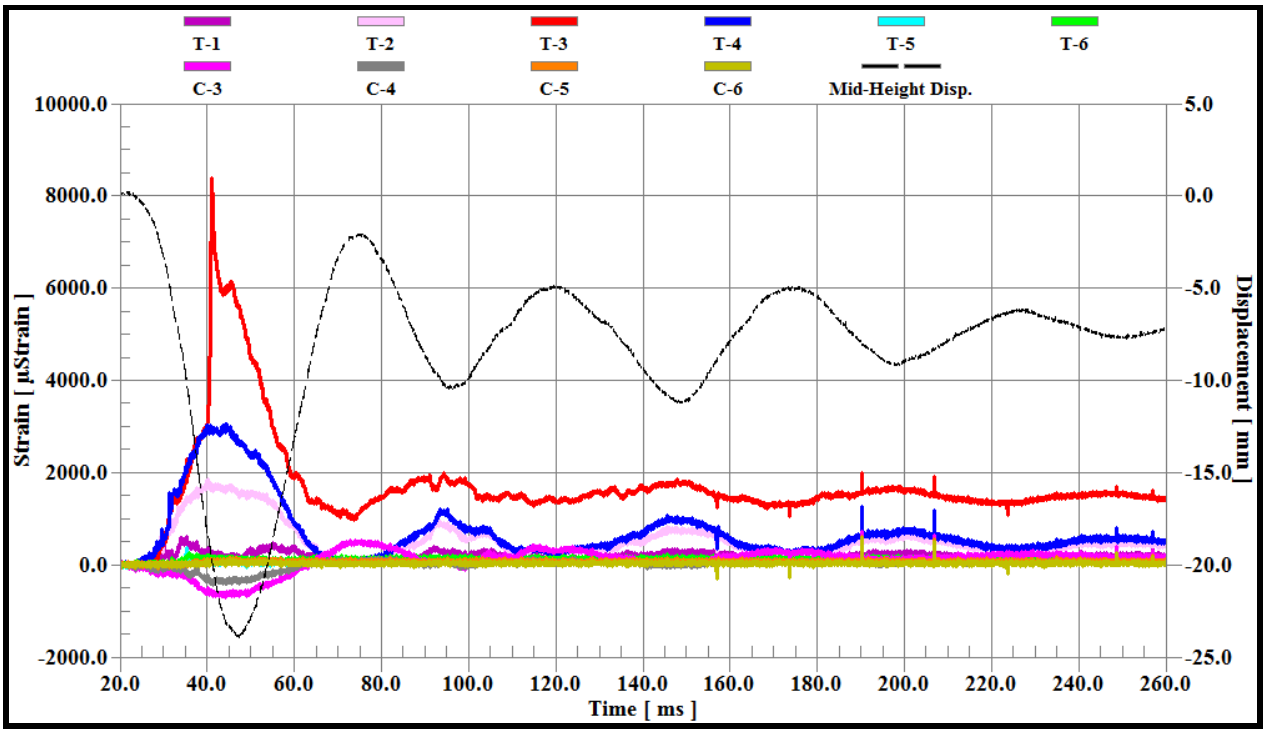

Fig. A-6 Time history of strains and mid-height displacement for column S1-AL400 (1st shot)

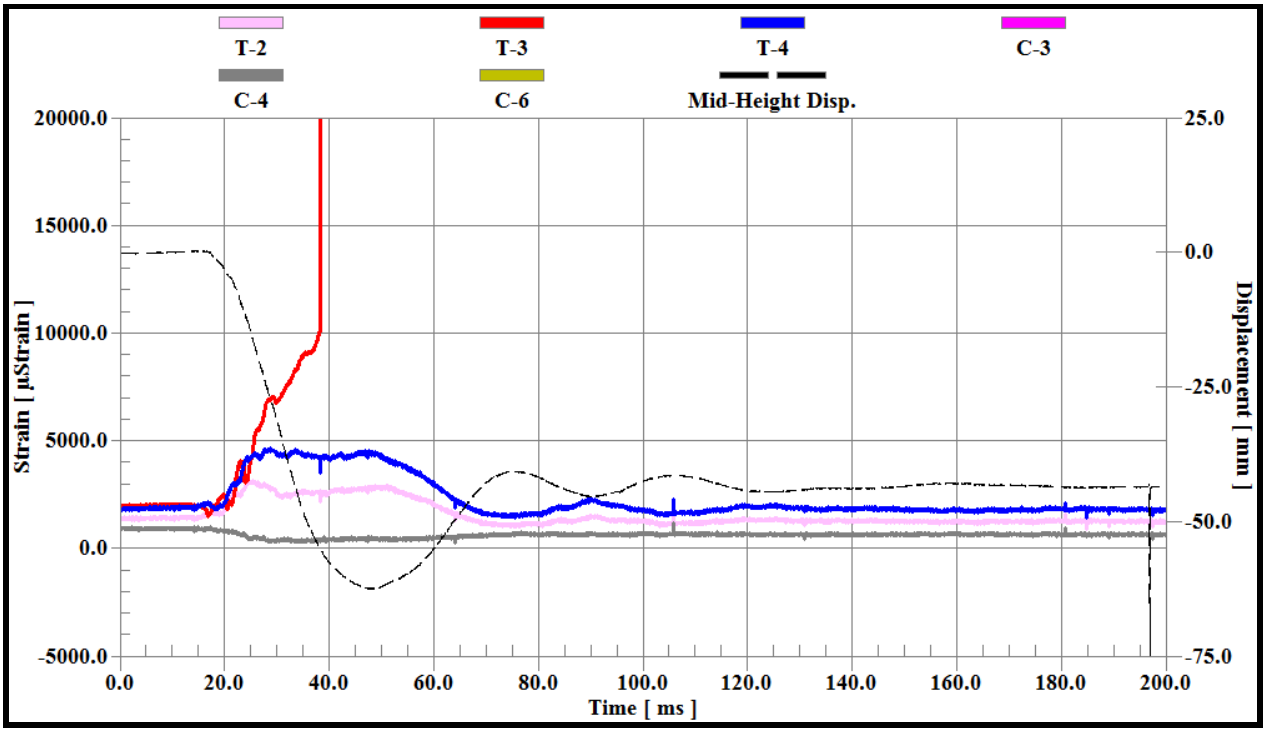

Fig. A-7 Time history of strains and mid-height displacement for column S1-AL400 (2nd shot)

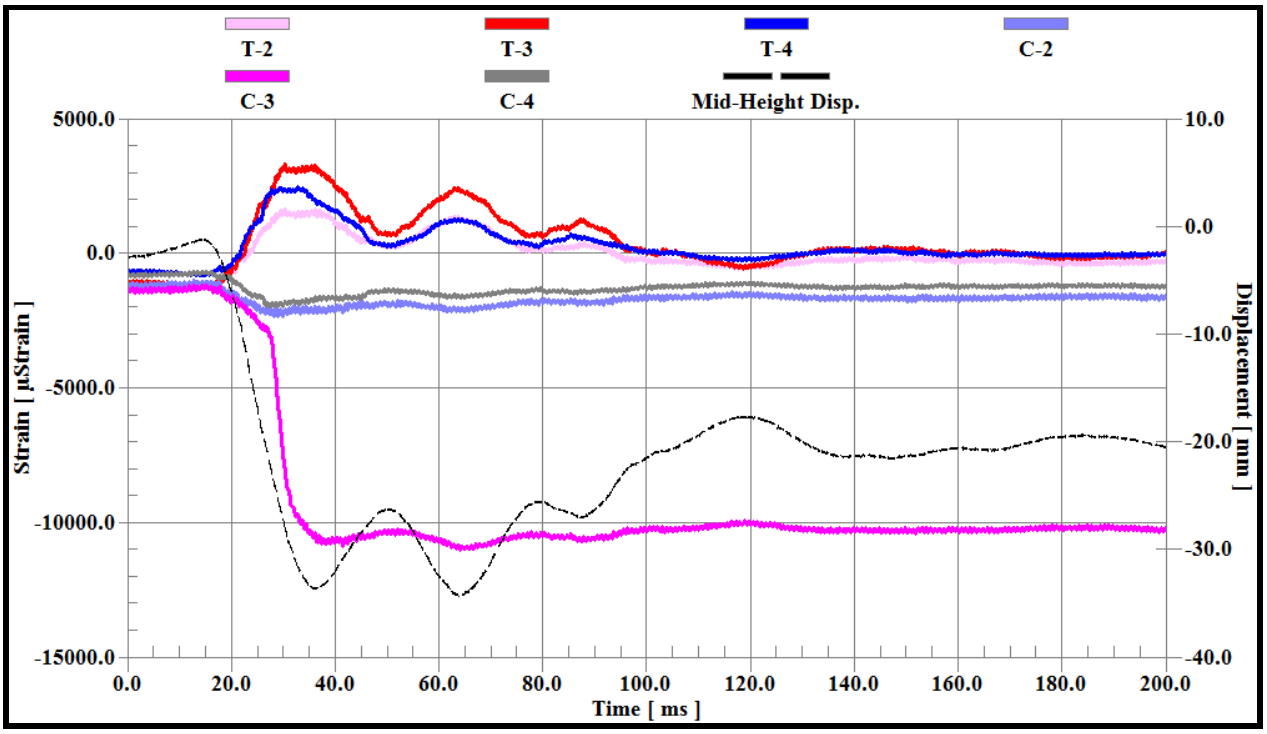

Fig. A-8 Time history of strains and mid-height displacement for column S2-AL400 (2nd shot)

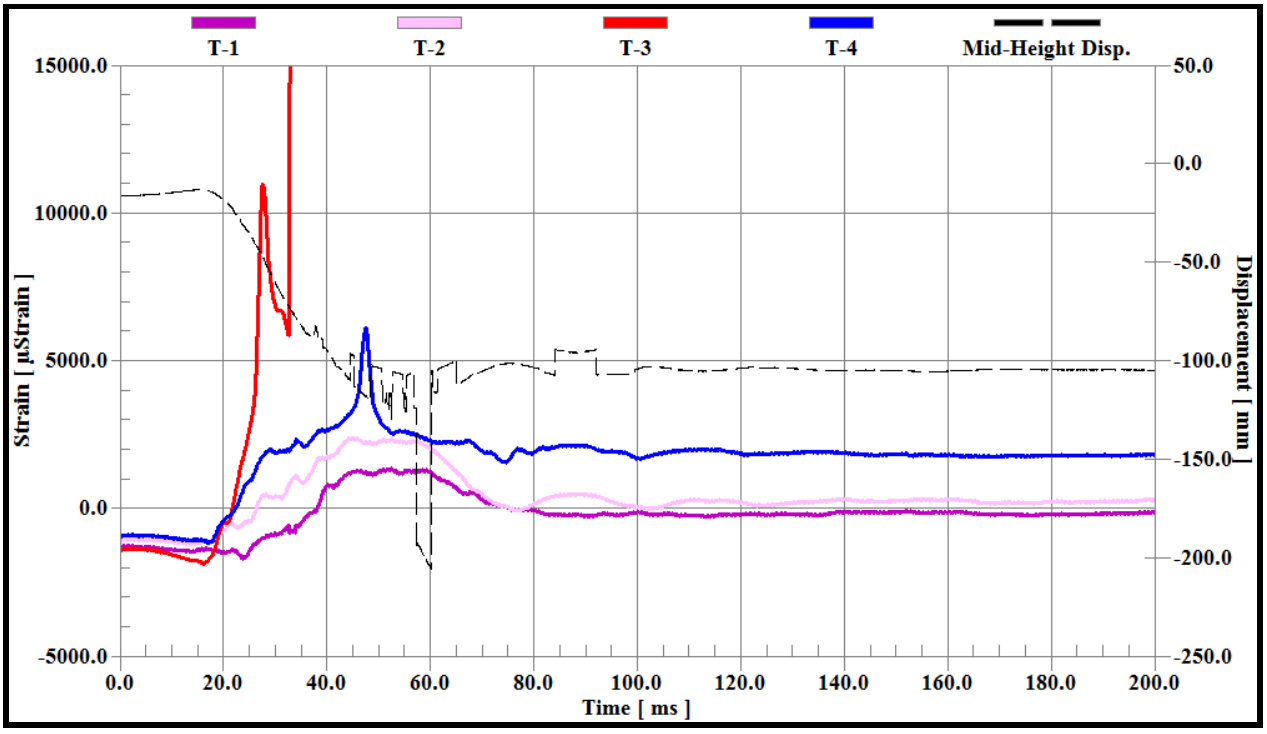

Fig. A-9 Time history of strains and mid-height displacement for column S2-AL400 (3rd shot)

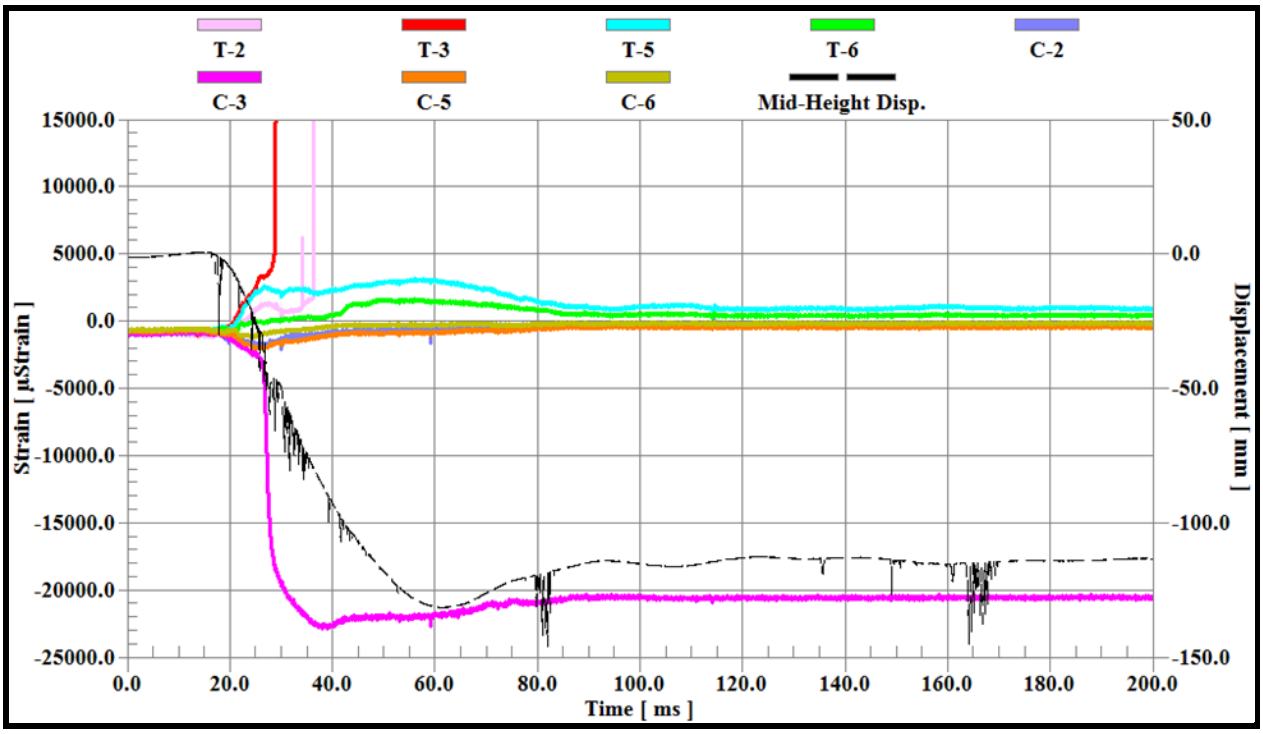

Fig. A-10 Time history of strains and mid-height displacement for column S3-AL400 (single shot)

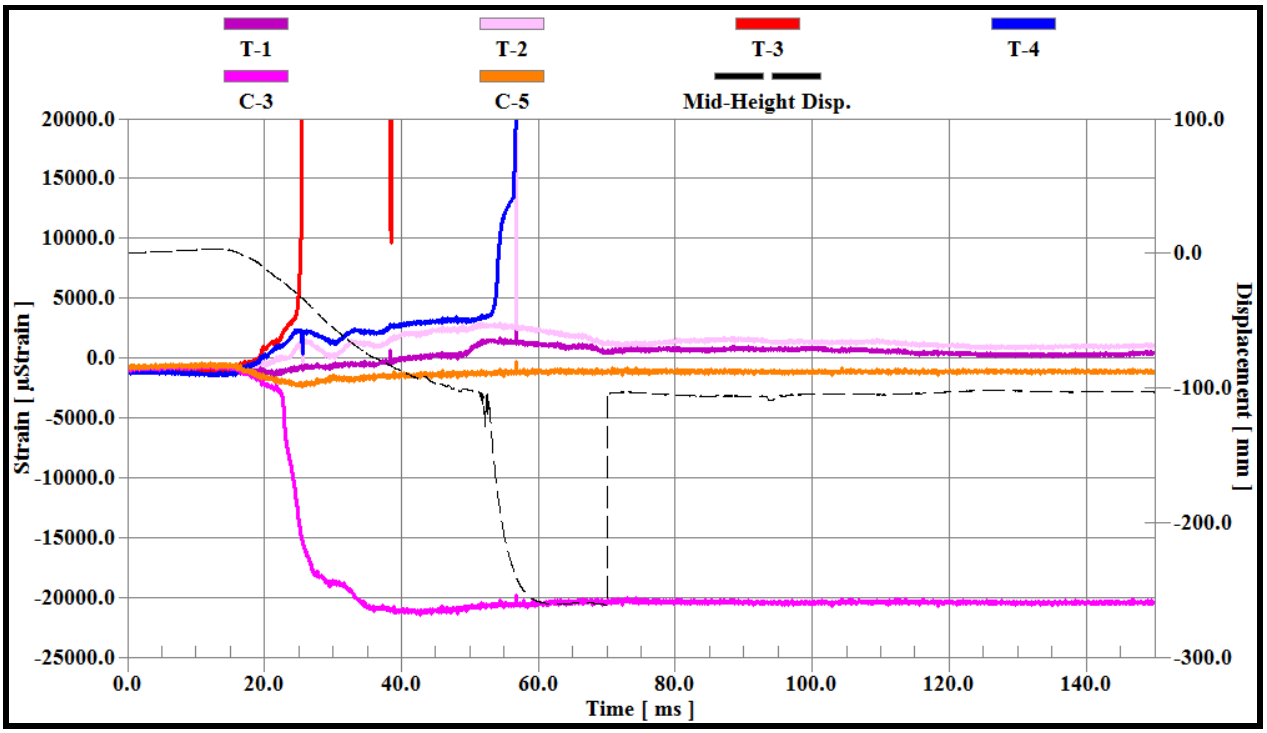

Fig. A-11 Time history of strains and mid-height displacement for column S4-AL400 (single shot)

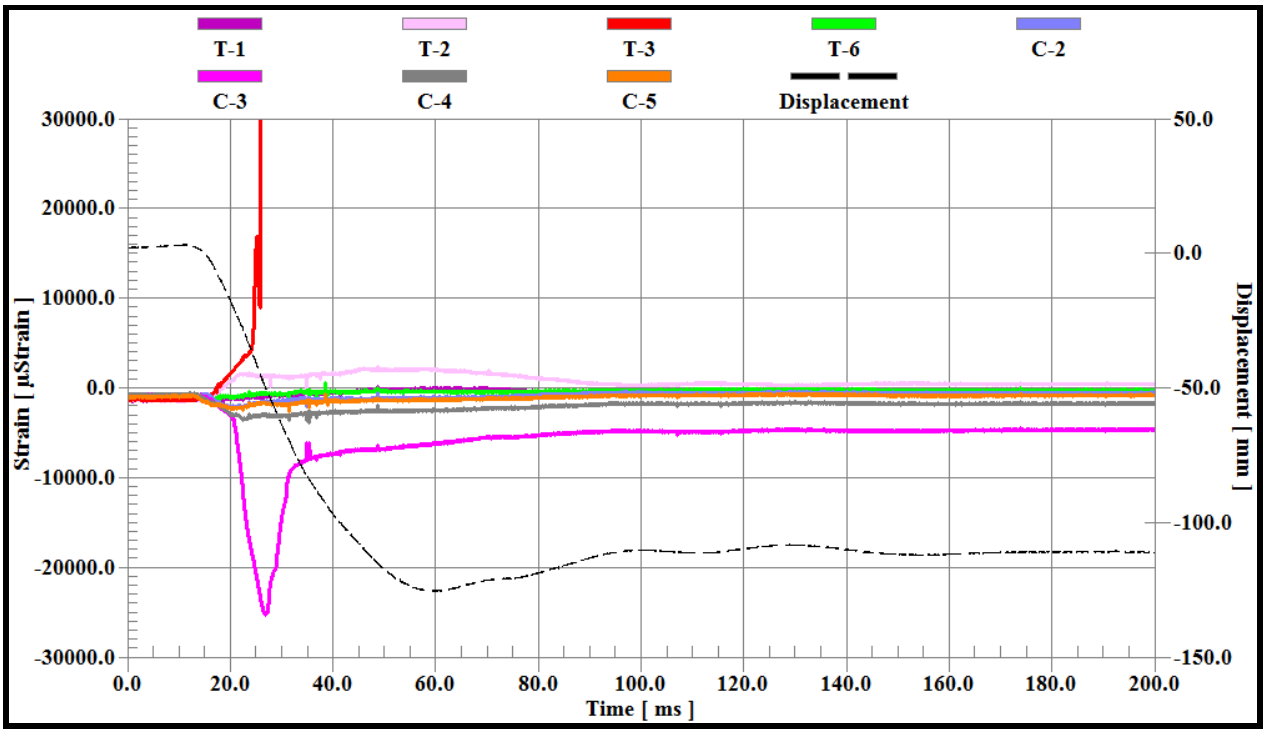

Fig. A-12 Time history of strains and mid-height displacement for column NS1-A-G1

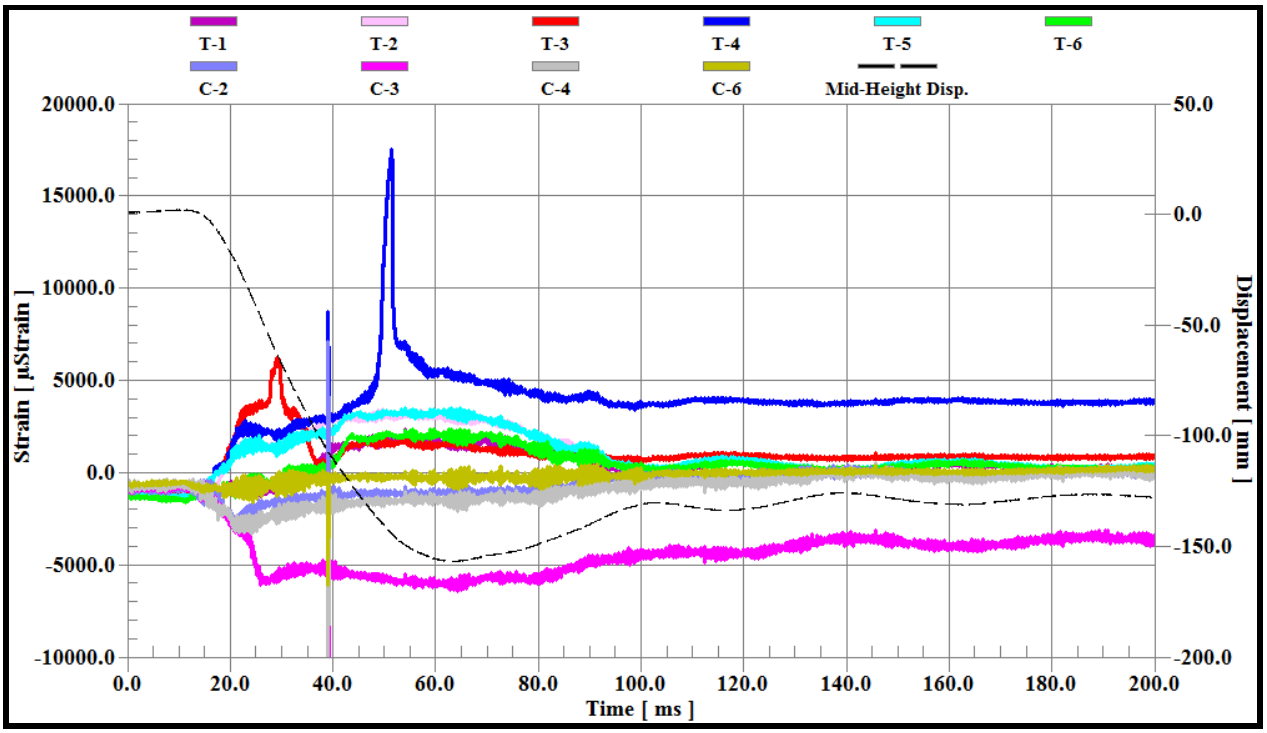

Fig. A-13 Time history of strains and mid-height displacement for column NS1-B-G1

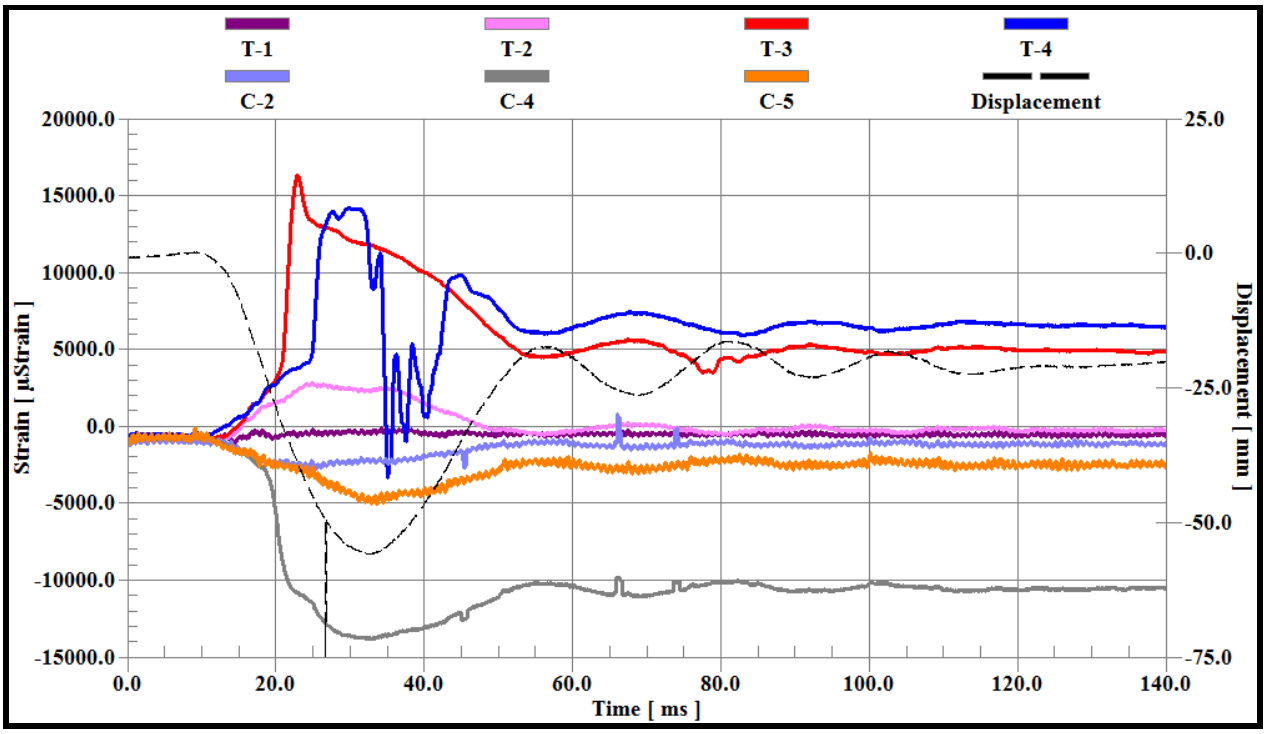

Fig. A-14 Time history of strains and mid-height displacement for column NS2-A-G1

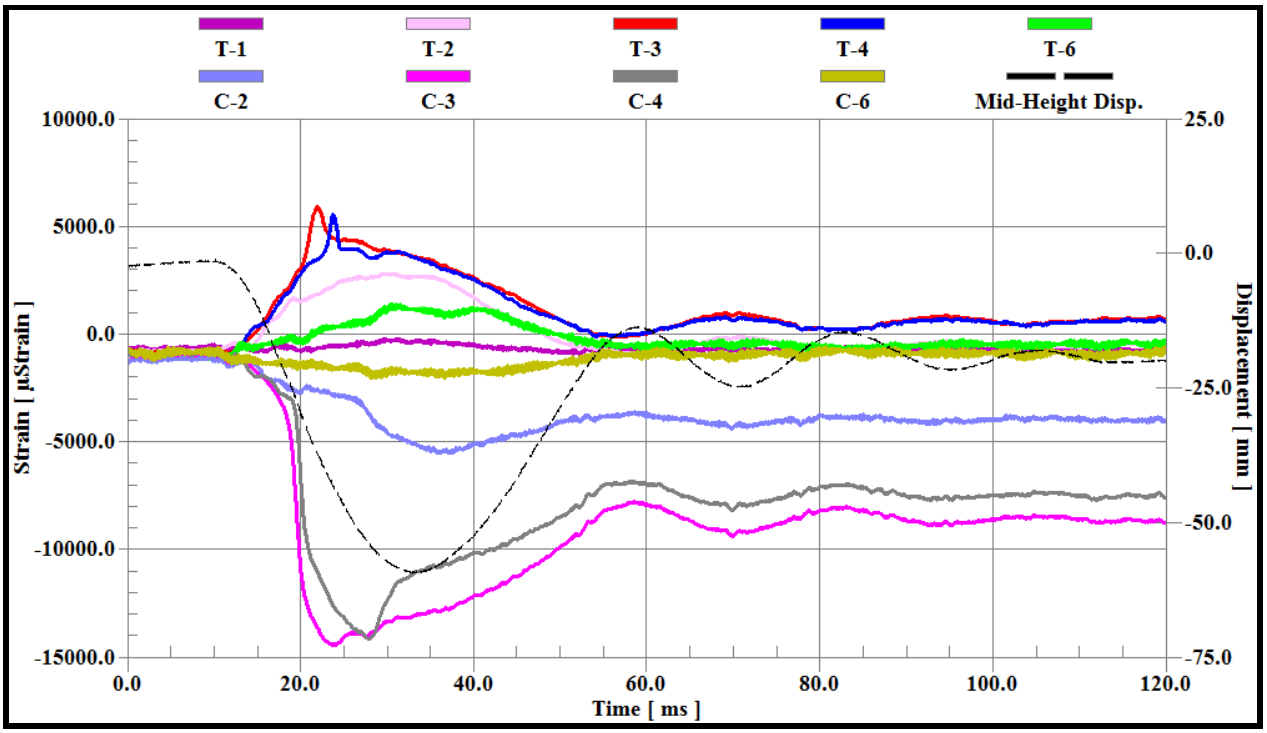

Fig. A-15 Time history of strains and mid-height displacement for column NS2-B-G1

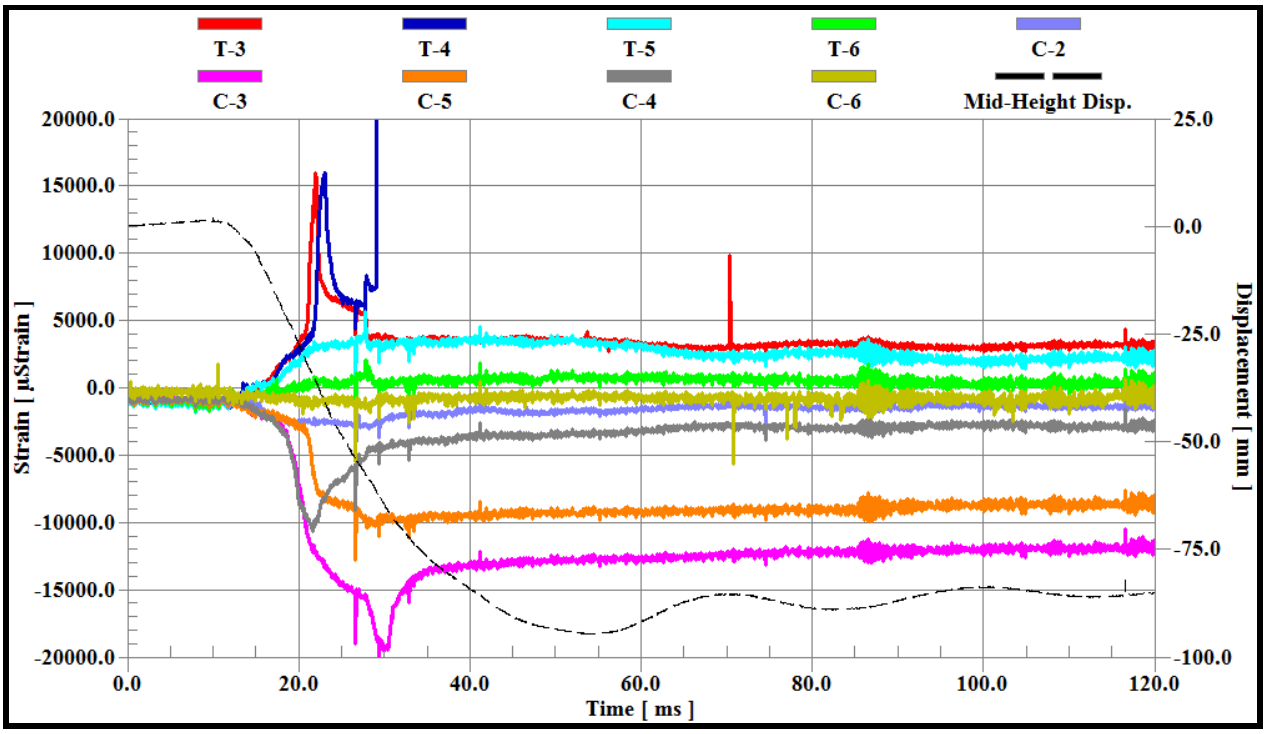

Fig. A-16 Time history of strains and mid-height displacement for column NS3-A-G1

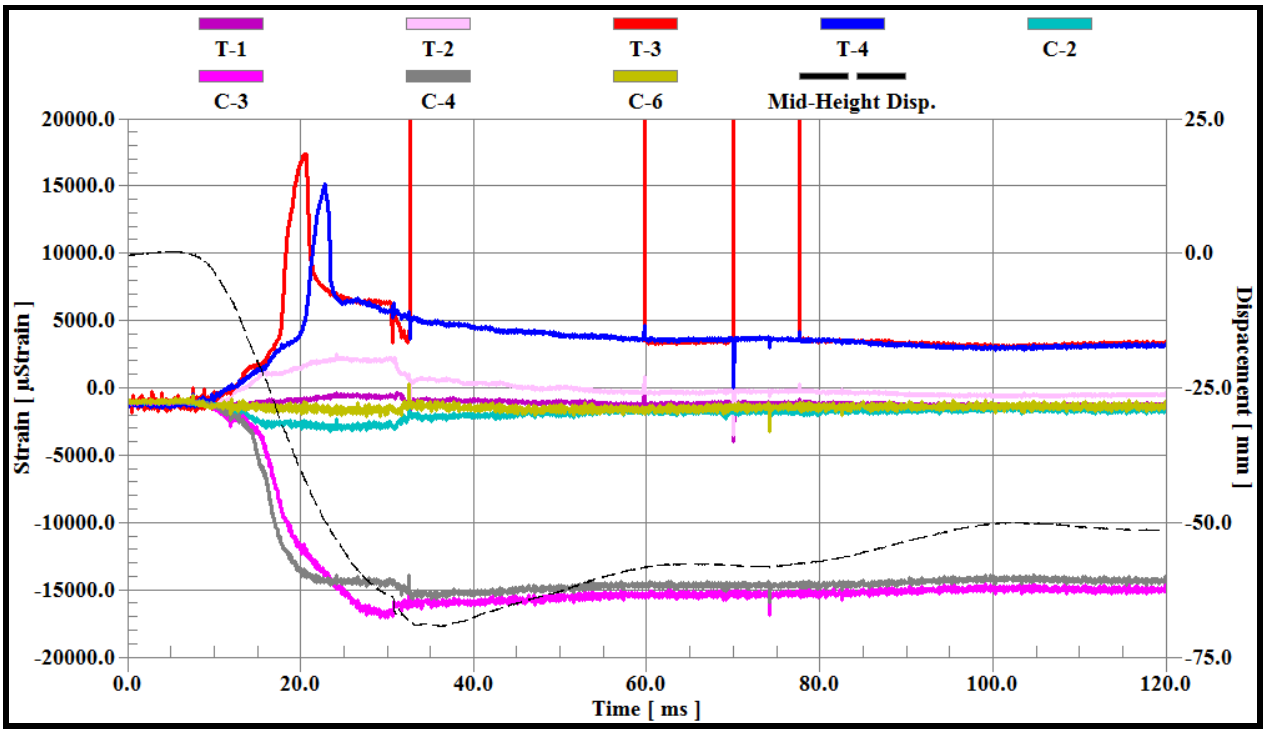

Fig. A-17 Time history of strains and mid-height displacement for column NS3-B-G1

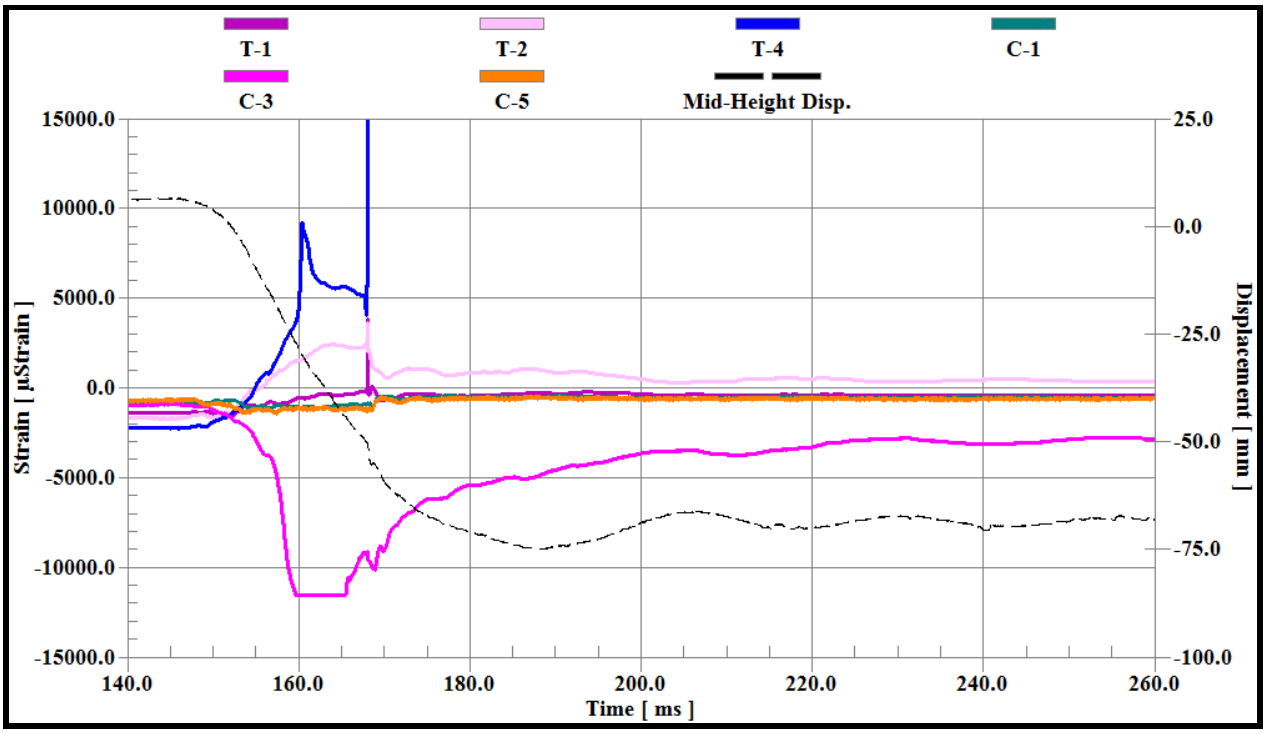

Fig. A-18 Time history of strains and mid-height displacement for column NS4-A-G1

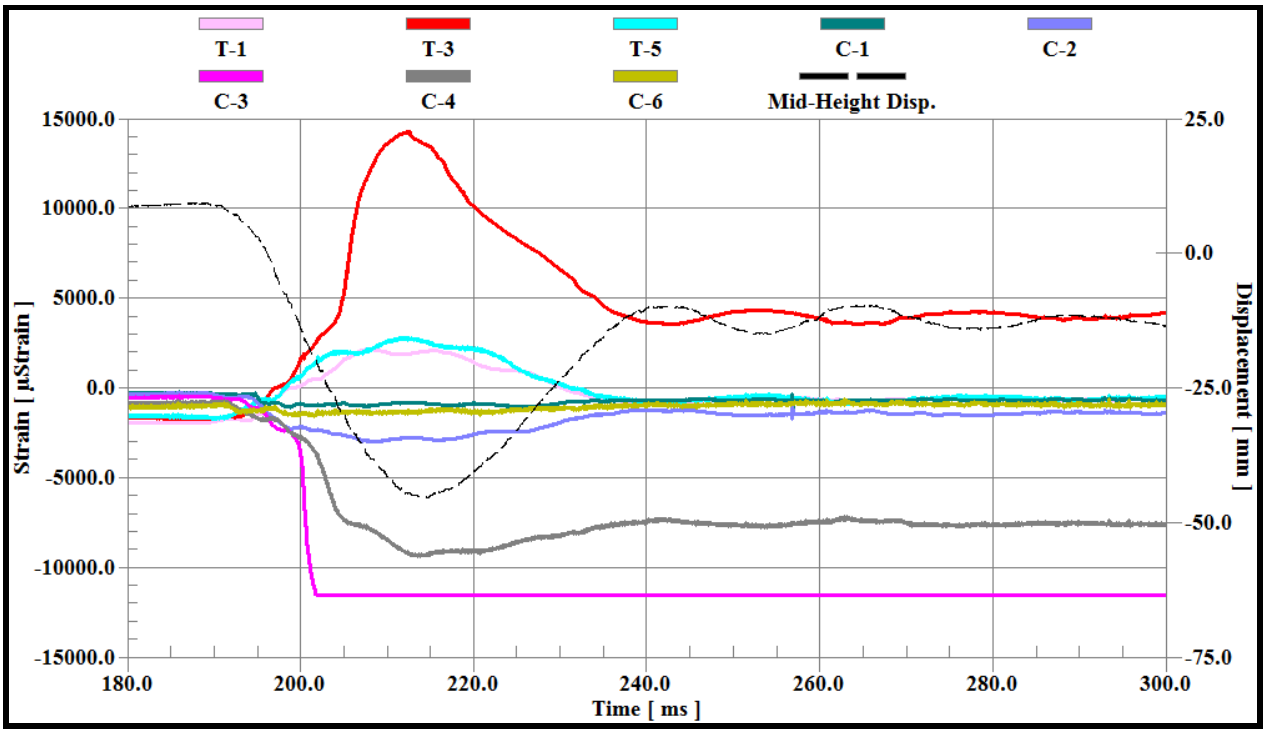

Fig. A-19 Time history of strains and mid-height displacement for column NS4-B-G1

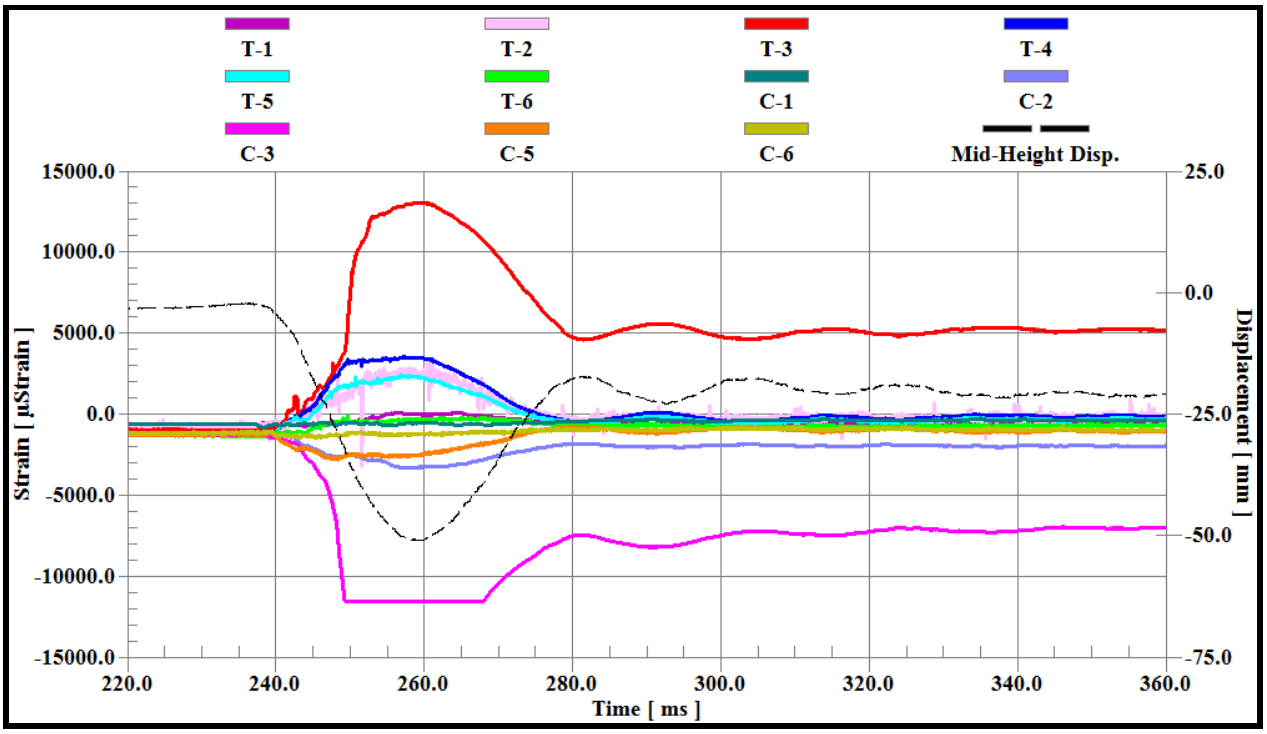

Fig. A-20 Time history of strains and mid-height displacement for column NS5-G1

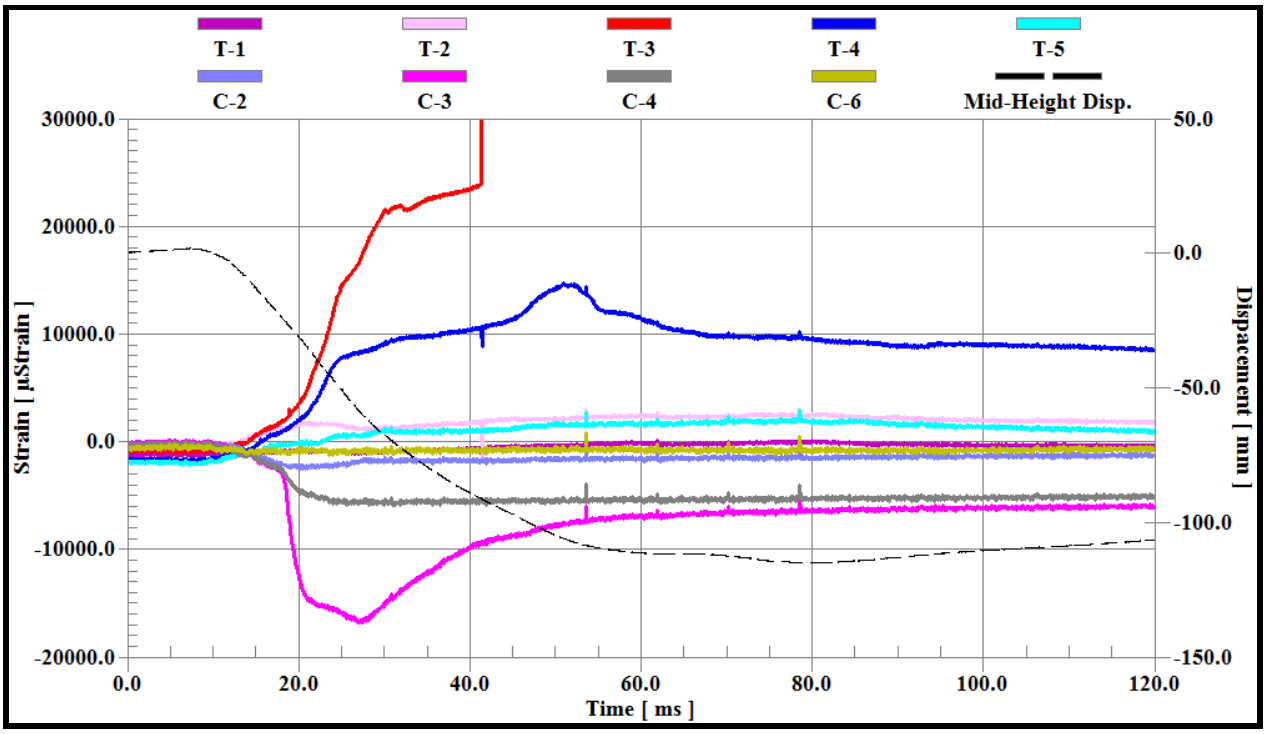

Fig. A-21 Time history of strains and mid-height displacement for column S1-A-G1

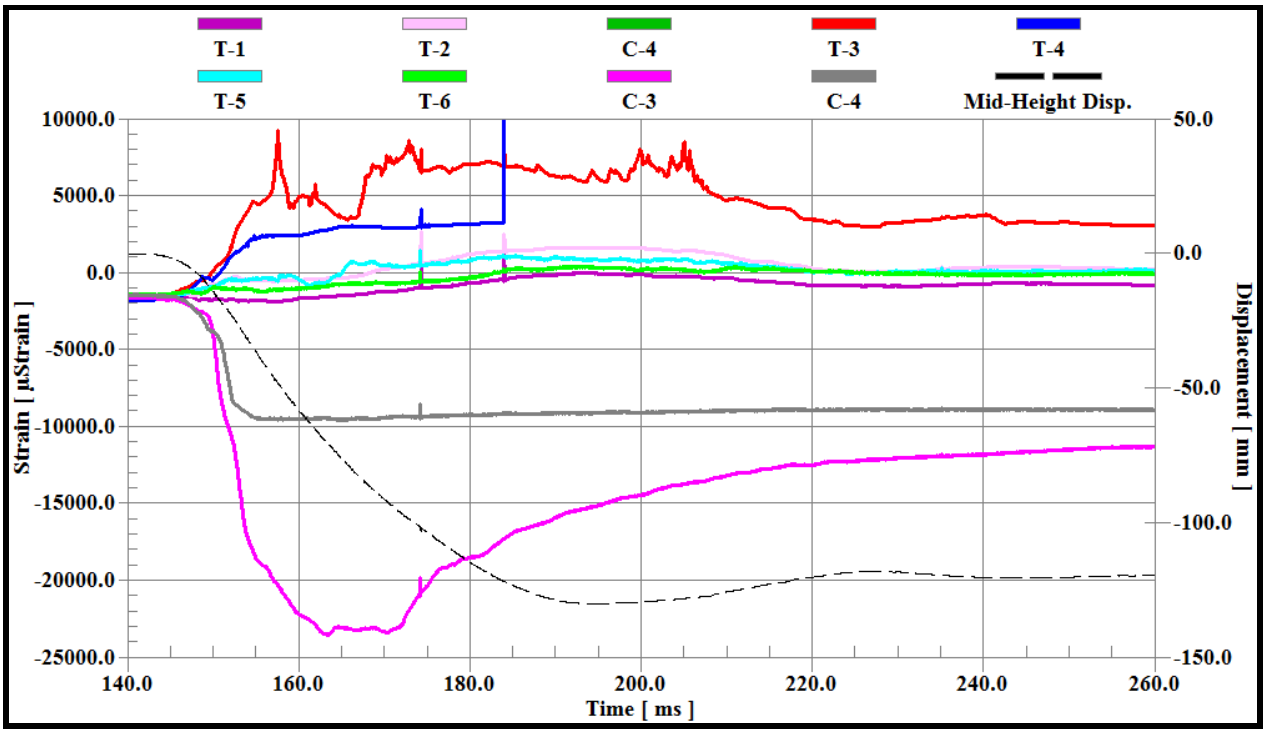

Fig. A-22 Time history of strains and mid-height displacement for column S1-B-G1

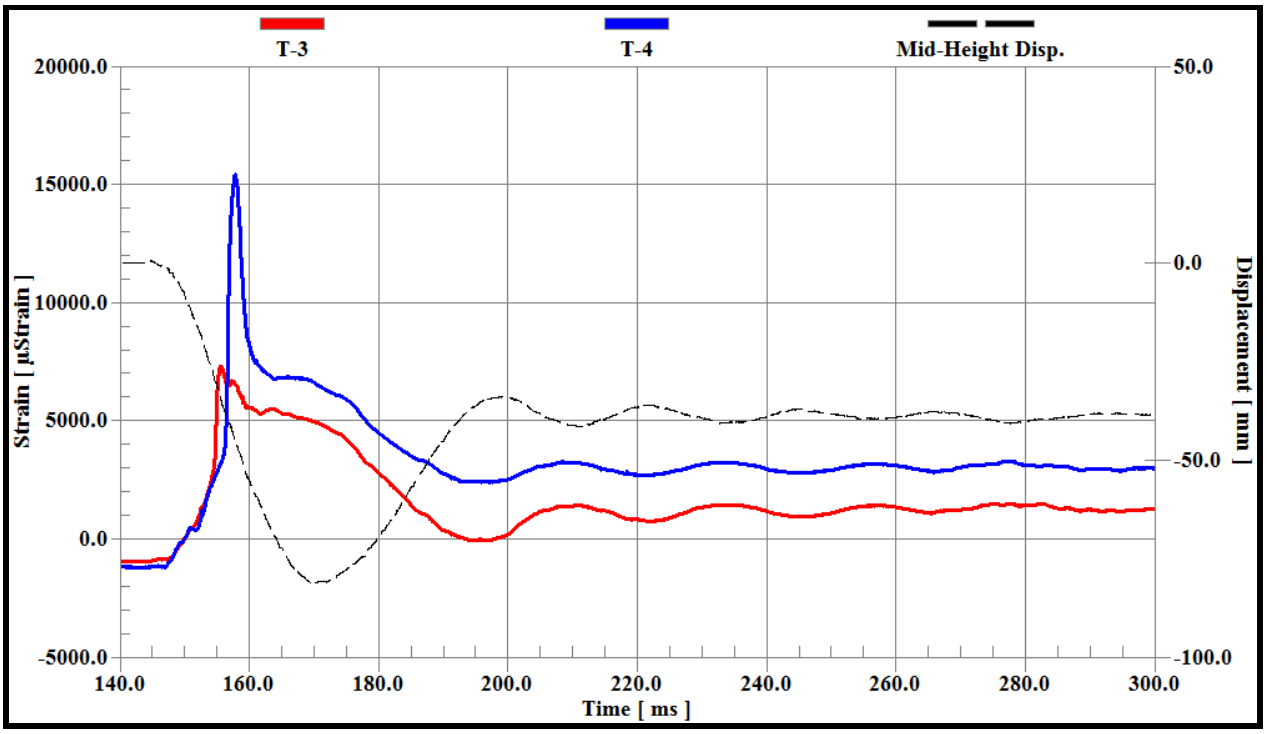

Fig. A-23 Time history of strains and mid-height displacement for column S2-A-G1

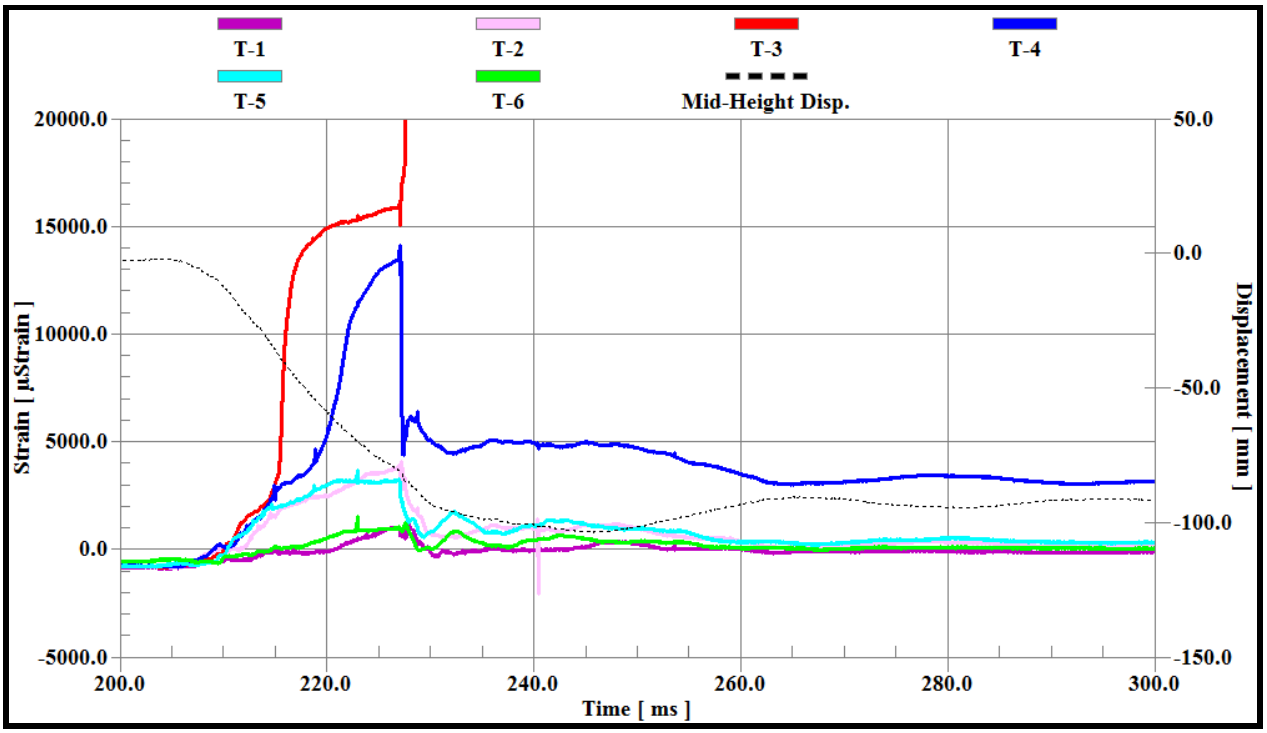

Fig. A-24 Time history of strains and mid-height displacement for column S2-B-G1

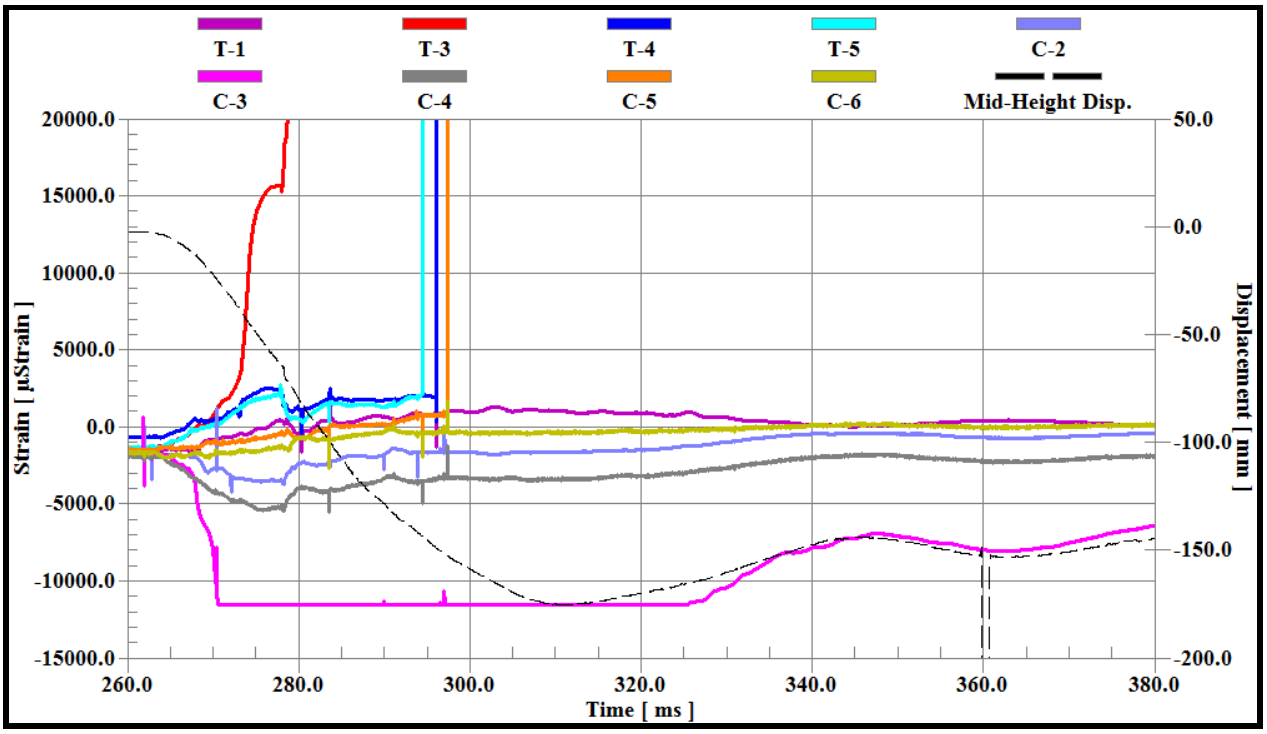

Fig. A-25 Time history of strains and mid-height displacement for column S3-A-G1

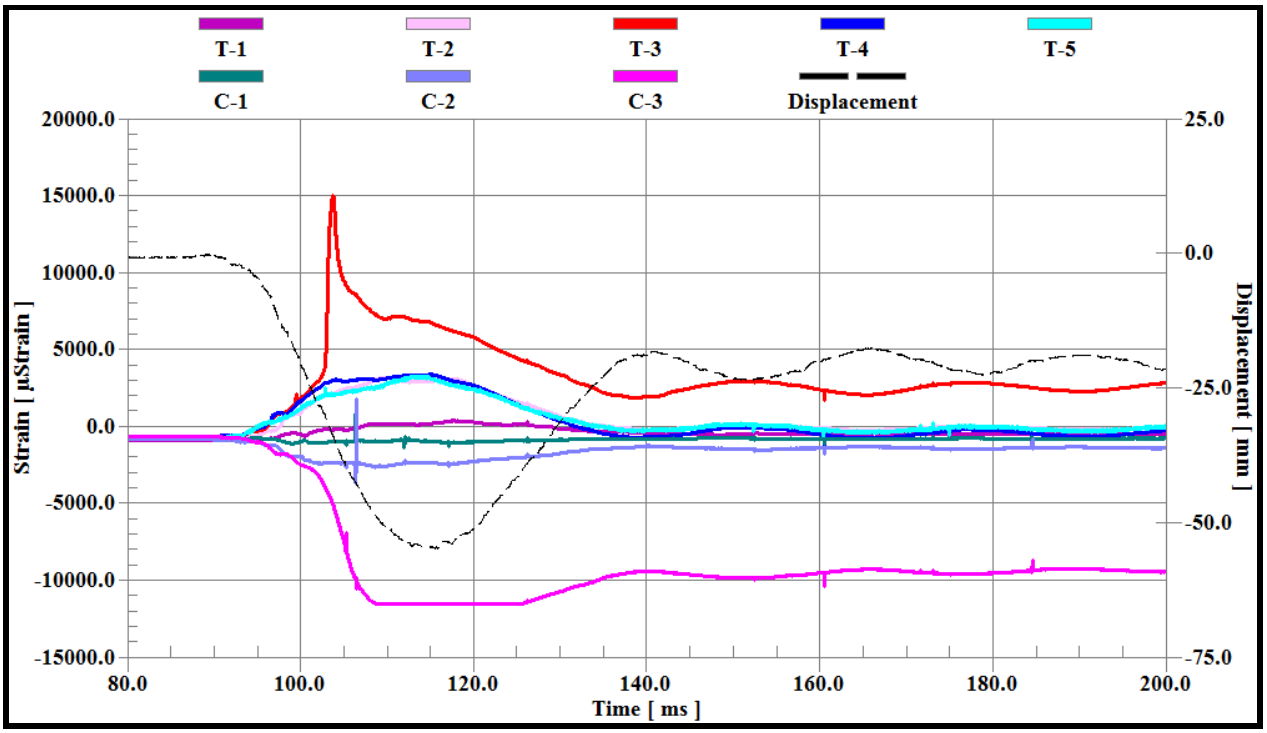

Fig. A-26 Time history of strains and mid-height displacement for column S3-B-G1

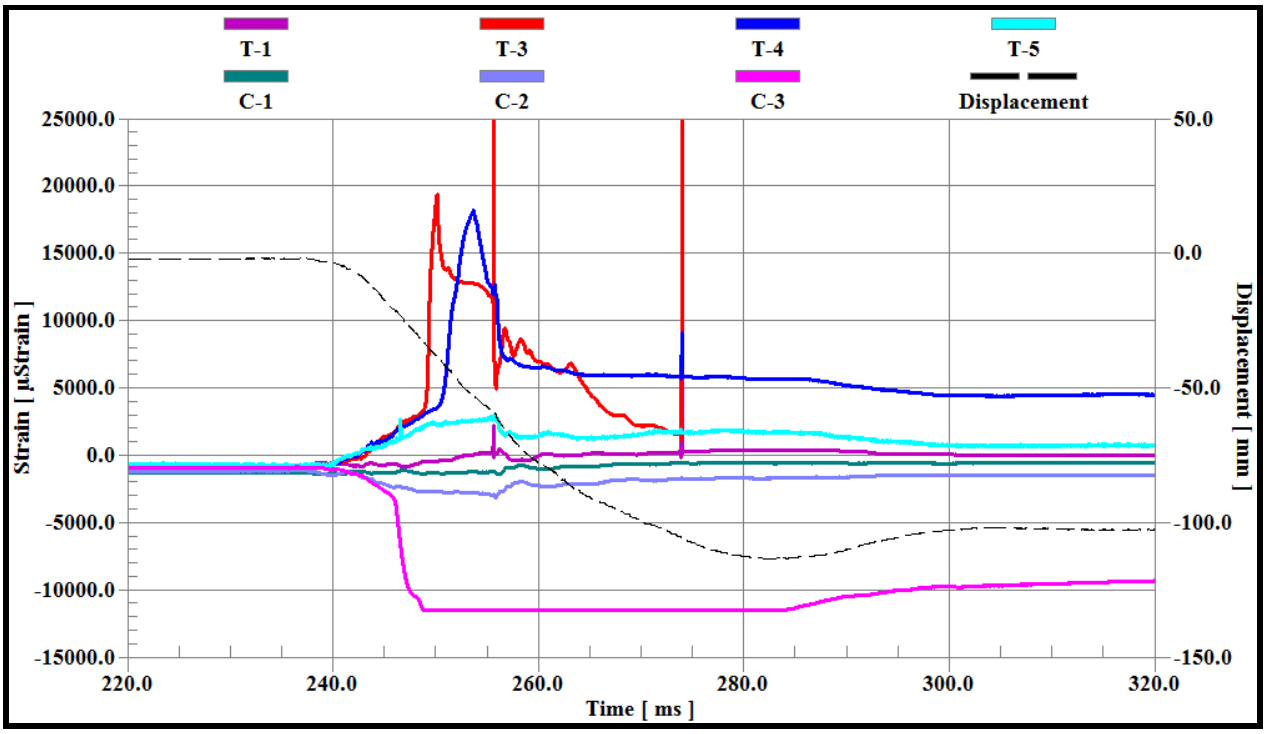

Fig. A-27 Time history of strains and mid-height displacement for column S4-A-G1

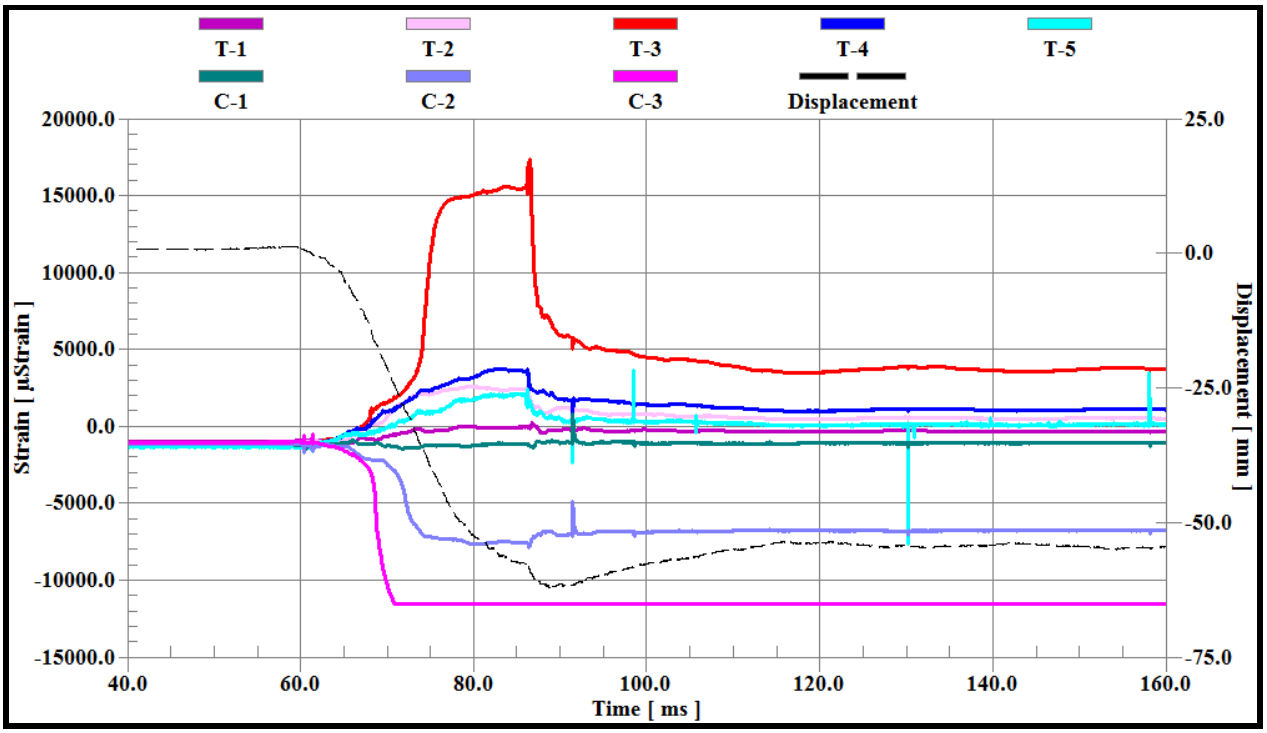

Fig. A-28 Time history of strains and mid-height displacement for column S4-B-G1

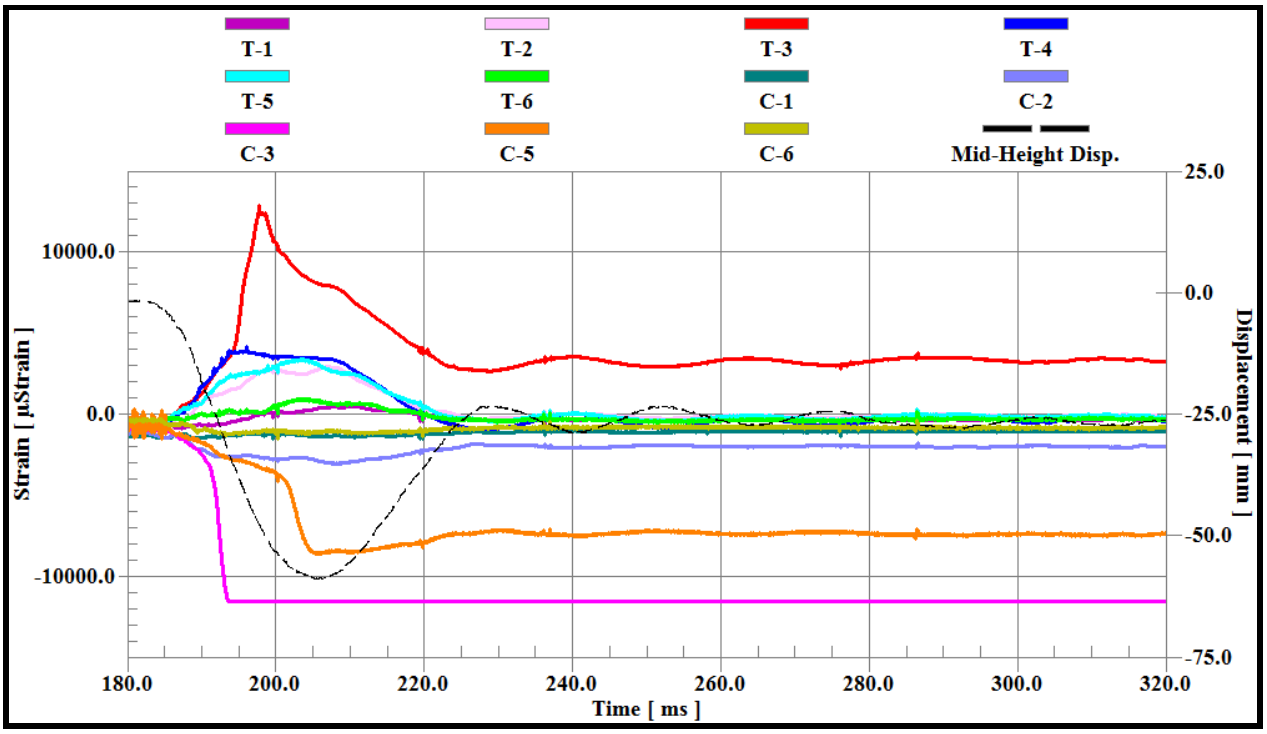

Fig. A-29 Time history of strains and mid-height displacement for column S5-G1

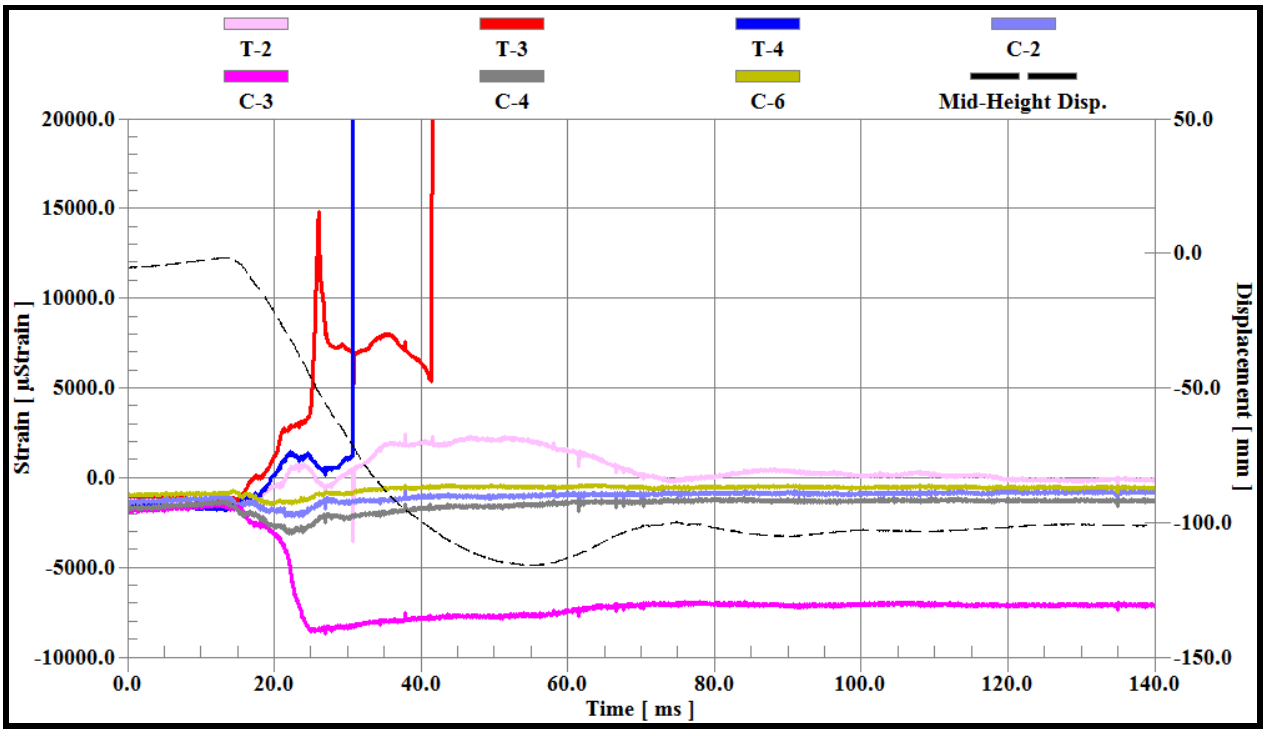

Fig. A-30 Time history of strains and mid-height displacement for column NS1-G2

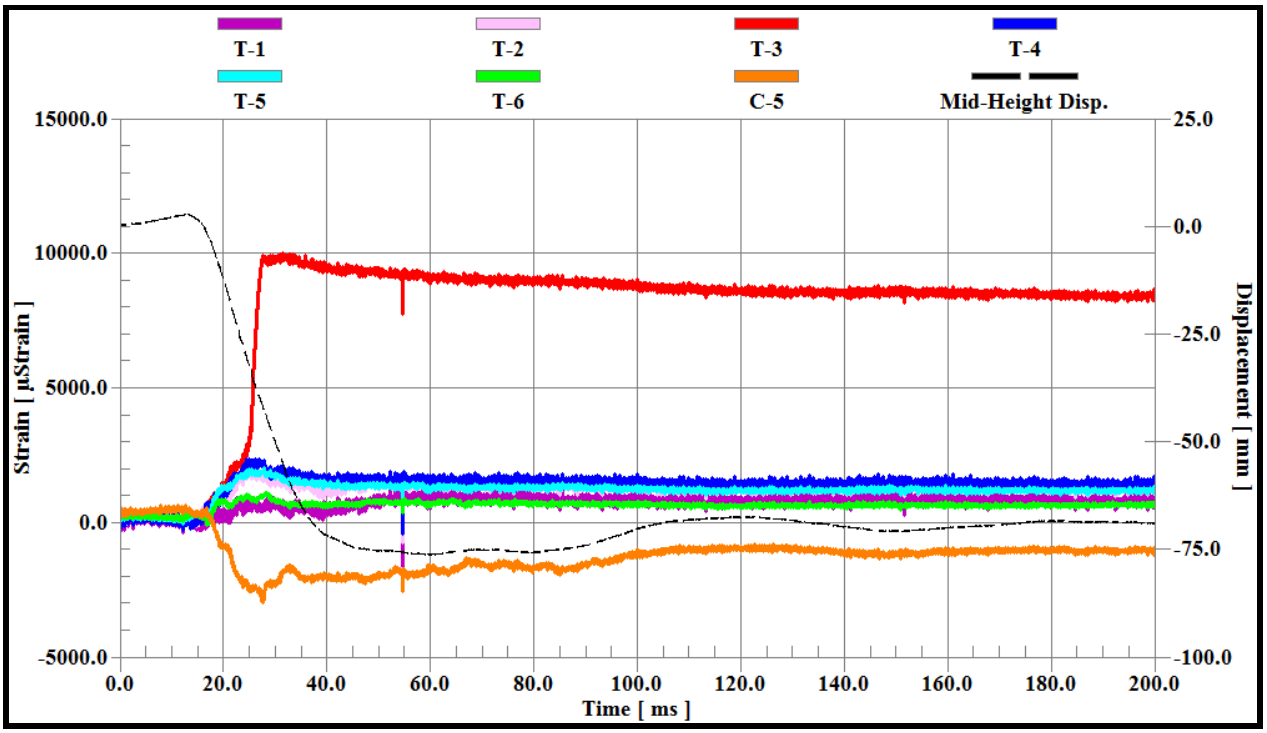

Fig. A-31 Time history of strains and mid-height displacement for column NS2-B-G2

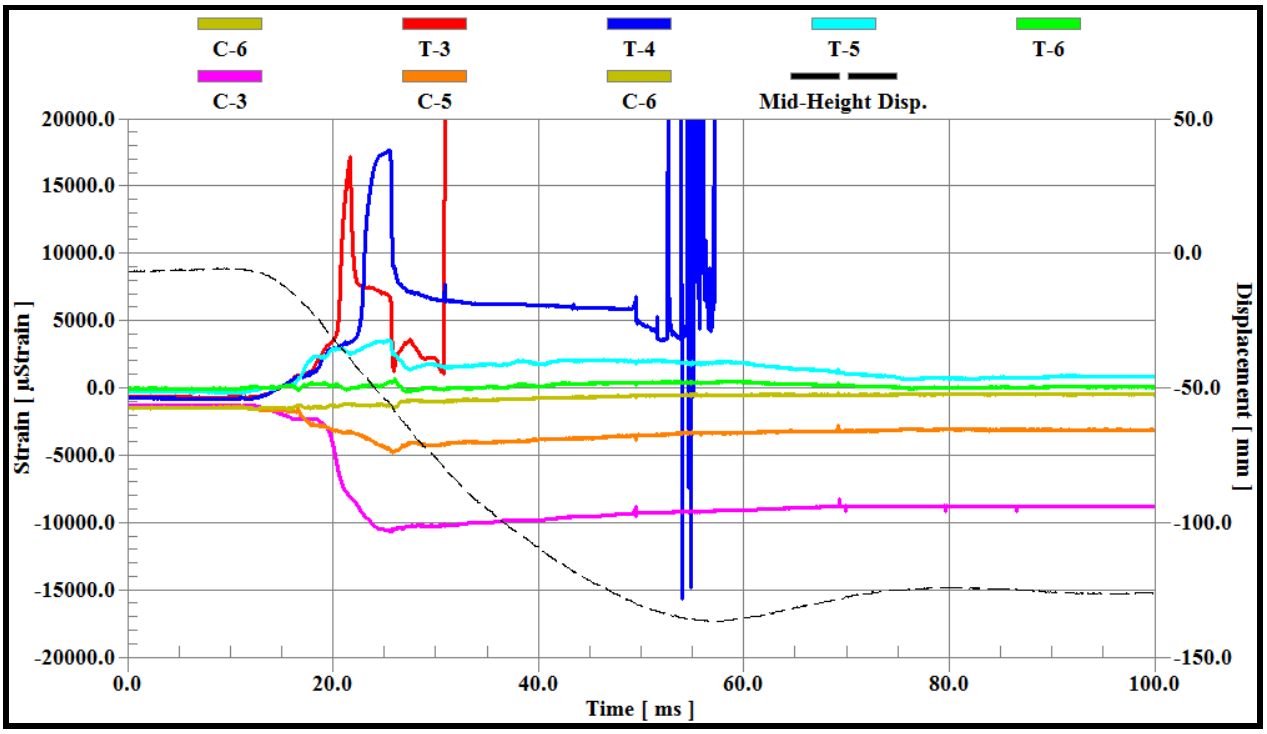

Fig. A-32 Time history of strains and mid-height displacement for column KEV-1-G2

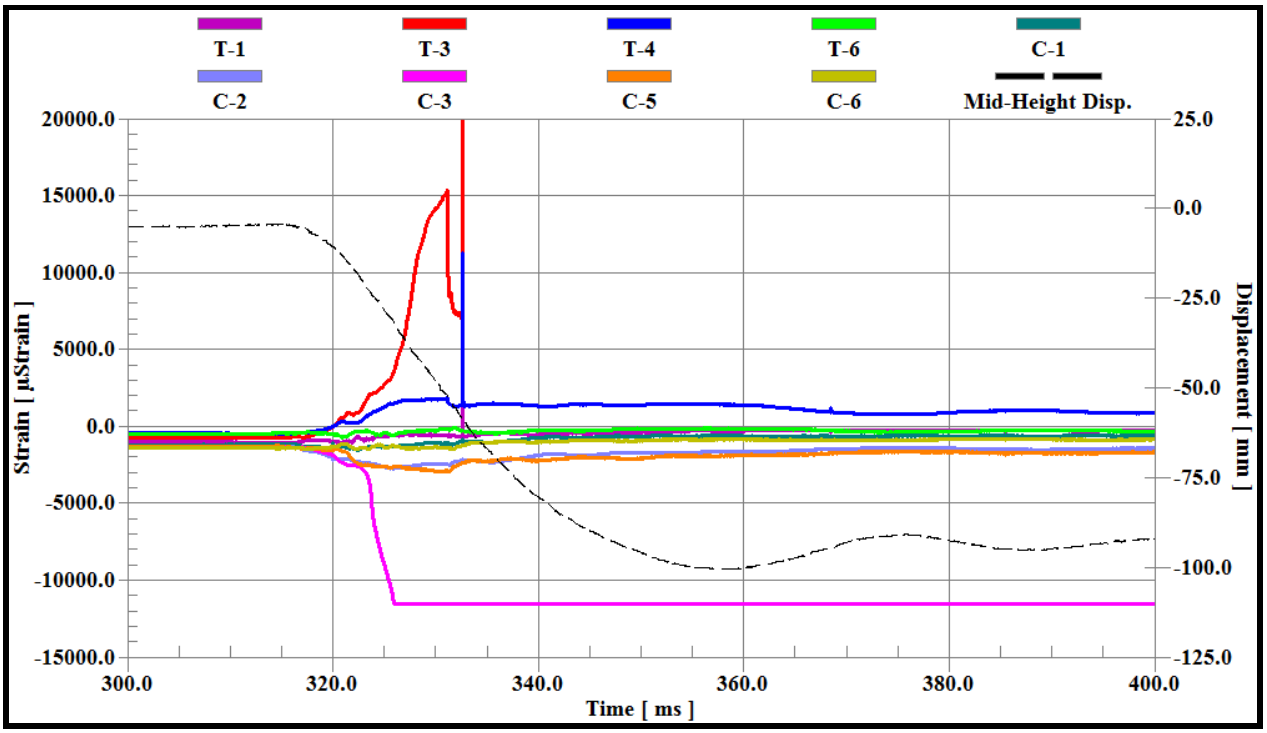

Fig. A-33 Time history of strains and mid-height displacement for column KEV-2-G2

APPENDIX –B

VELOCITY & ACCELERATION PROFILES

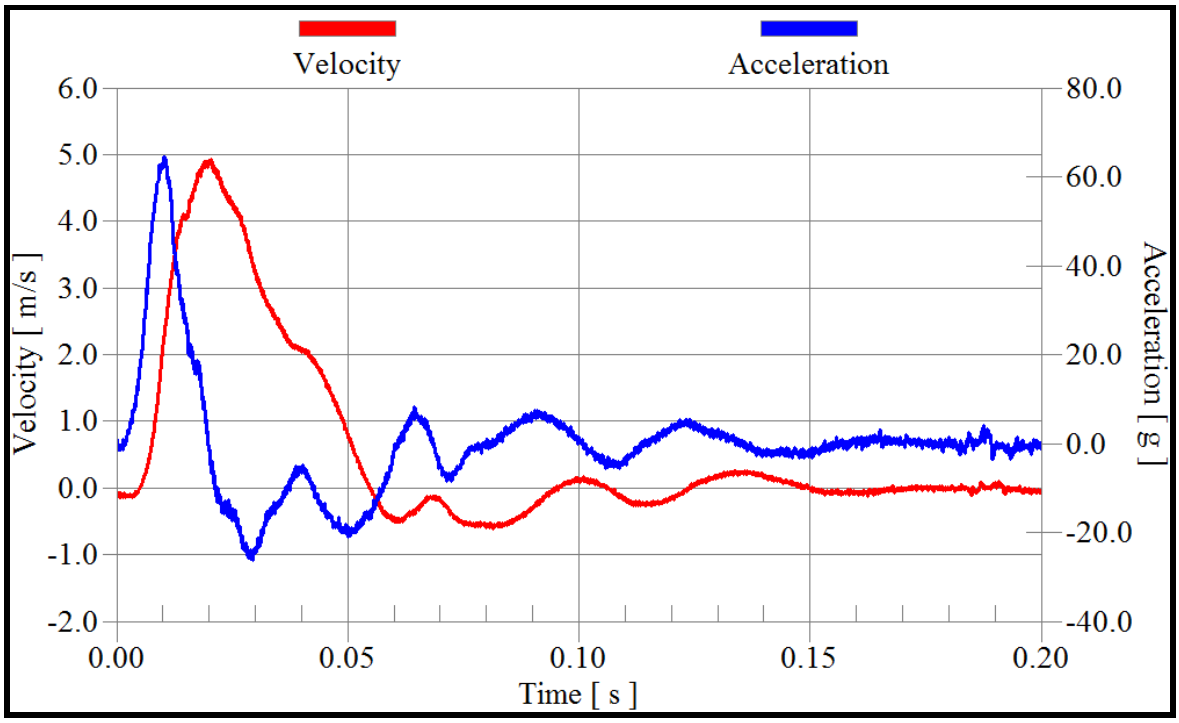

Fig. B-1 Time history of velocity and acceleration of column NS1-A-G1

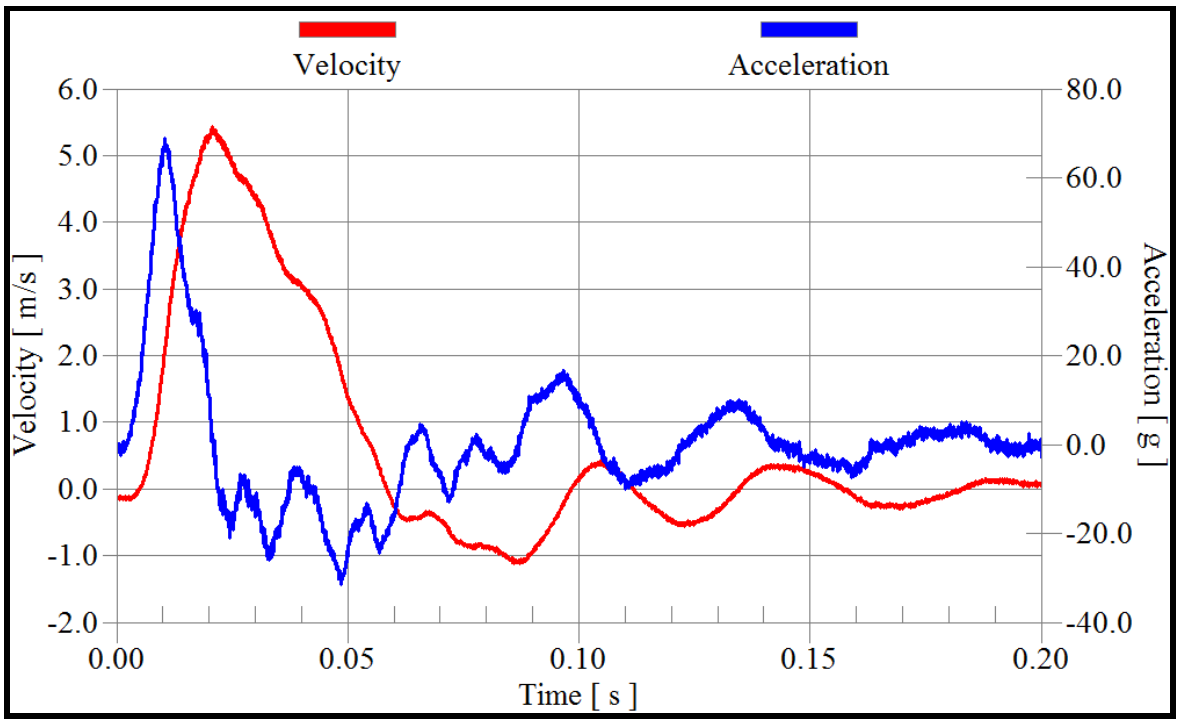

Fig. B-2 Time history of velocity and acceleration of column NS1-B-G1

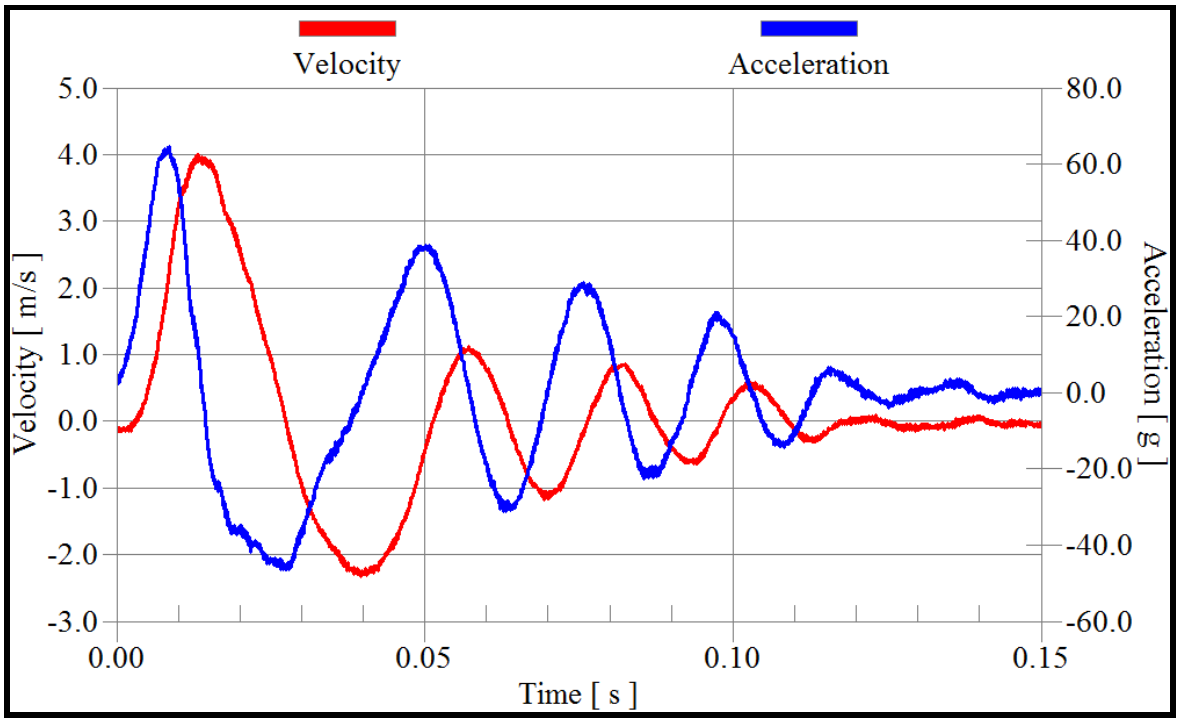

Fig. B-3 Time history of velocity and acceleration of column NS2-A-G1

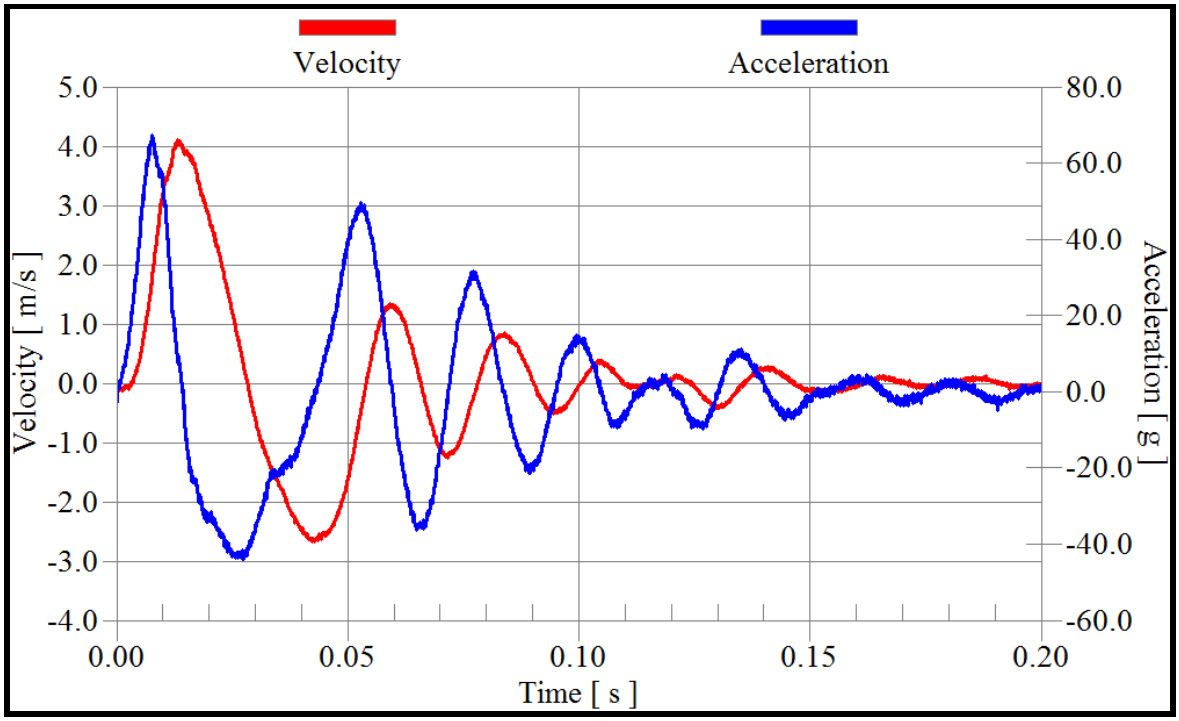

Fig. B-4 Time history of velocity and acceleration of column NS2-B-G1

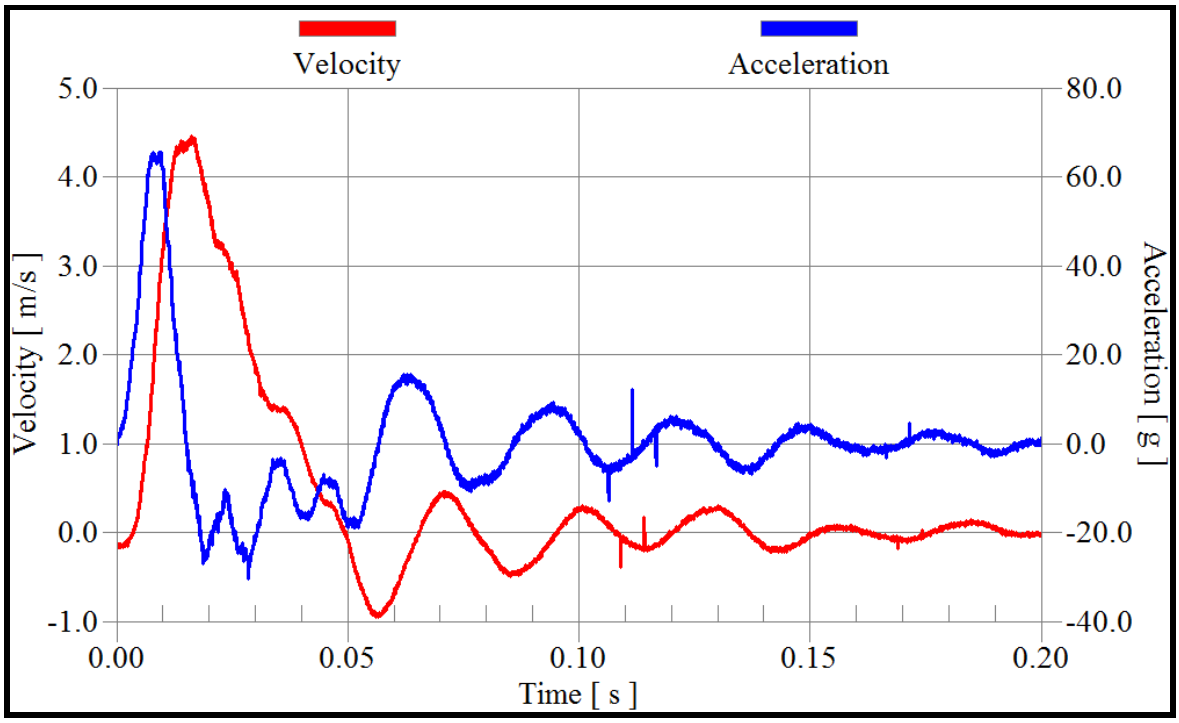

Fig. B-5 Time history of velocity and acceleration of column NS3-A-G1

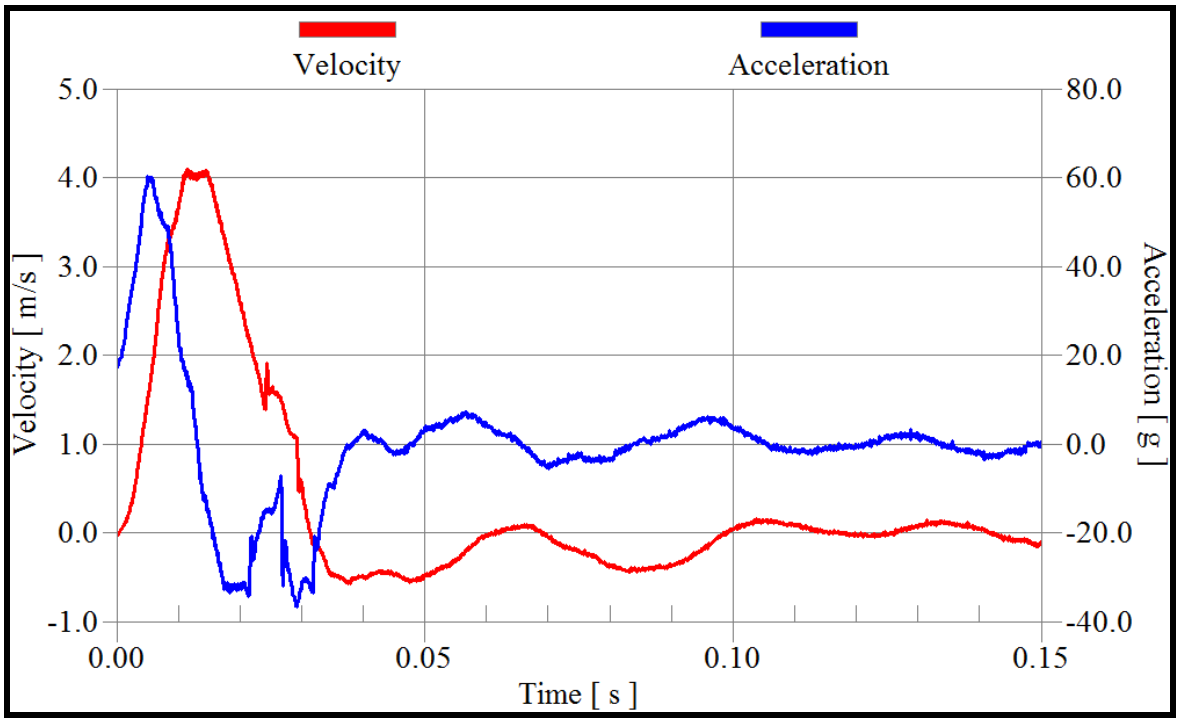

Fig. B-6 Time history of velocity and acceleration of column NS3-B-G1

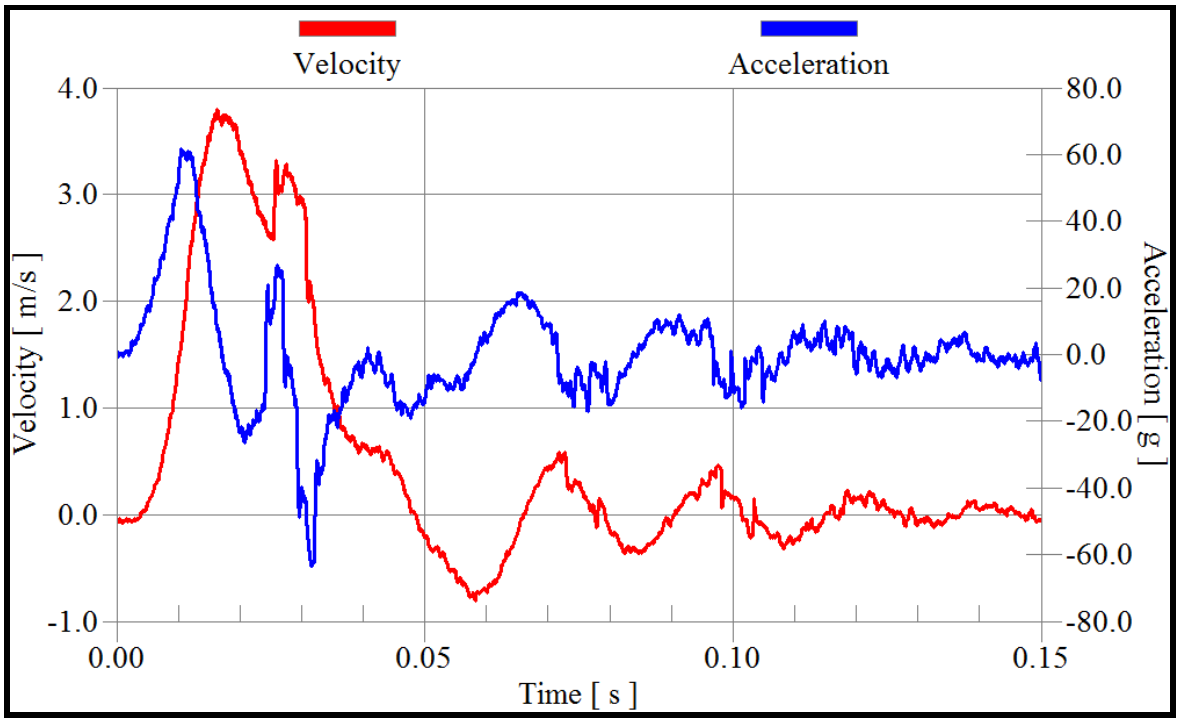

Fig. B-7 Time history of velocity and acceleration of column NS4-A-G1

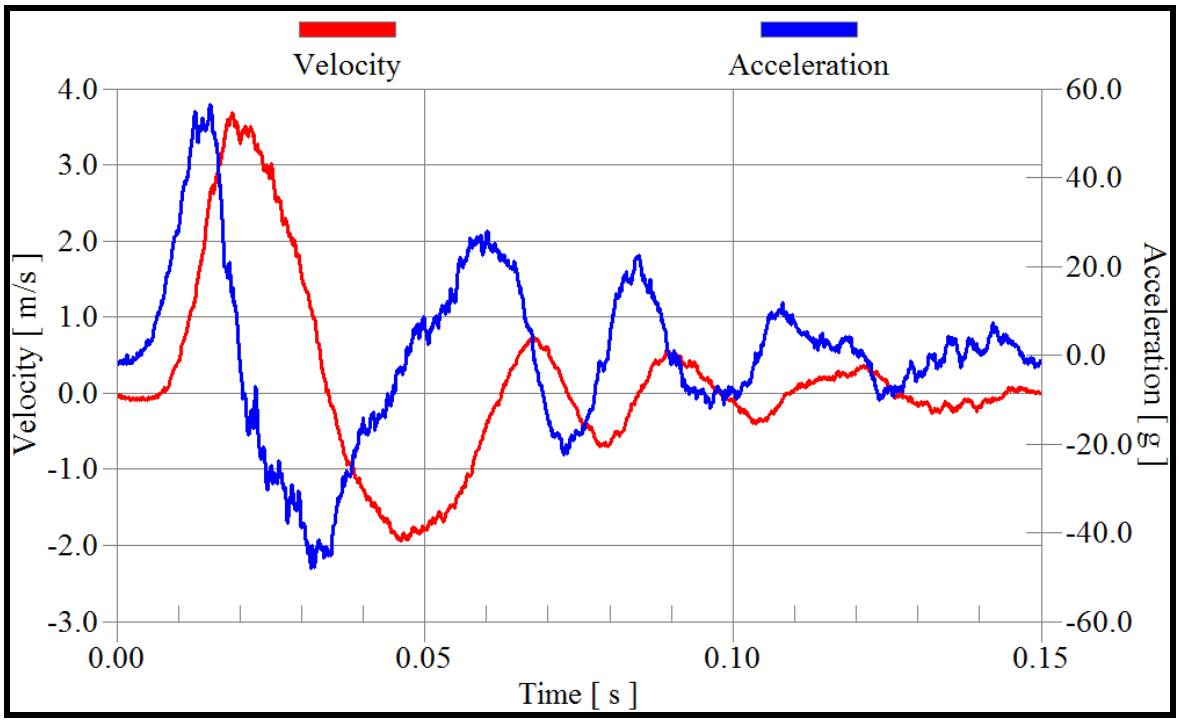

Fig. B-8 Time history of velocity and acceleration of column NS4-B-G1

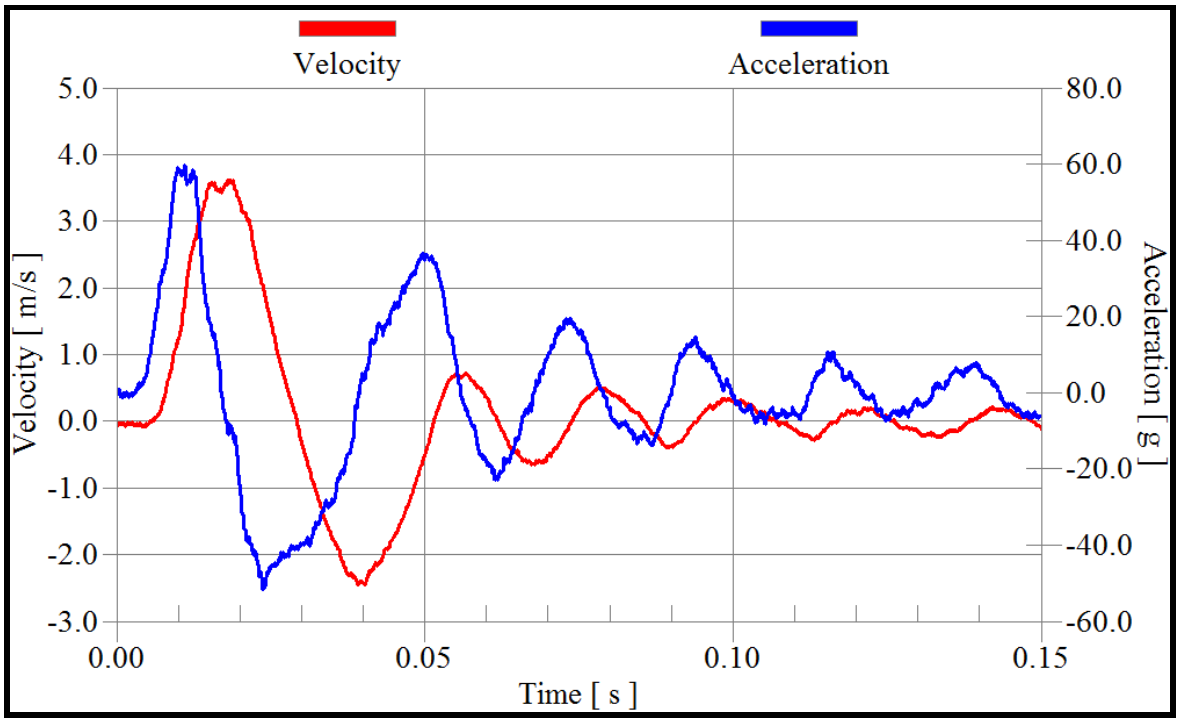

Fig. B-9 Time history of velocity and acceleration of column NS5-G1

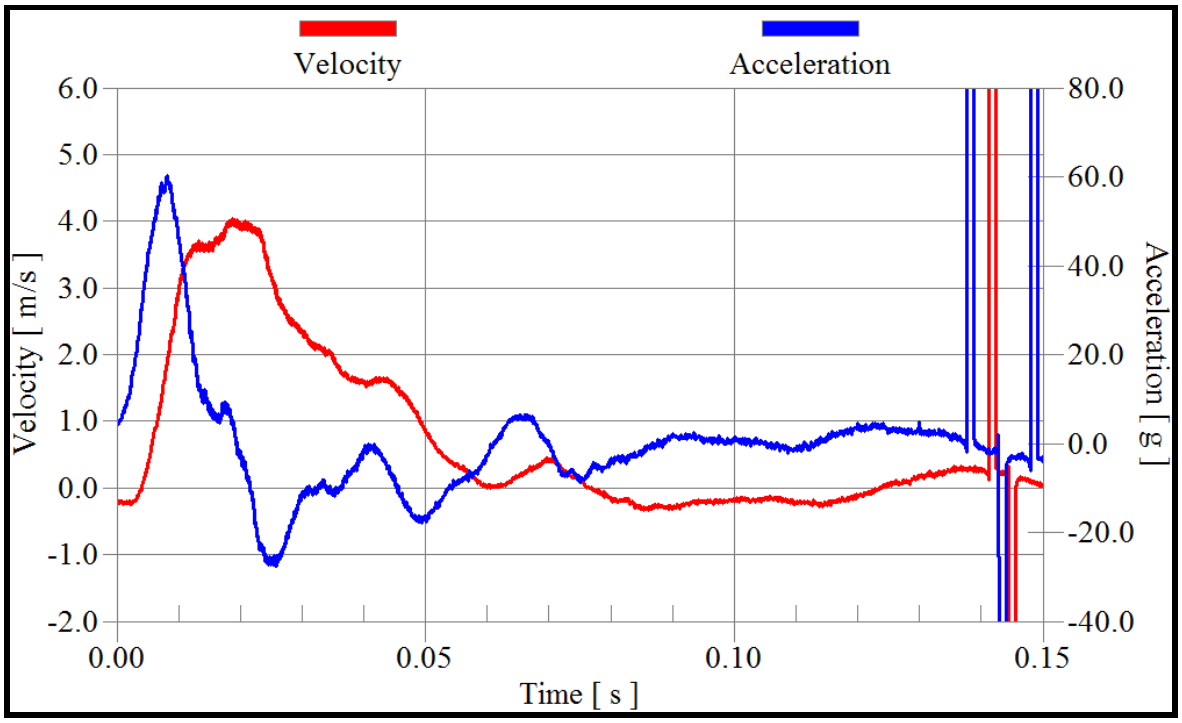

Fig. B-10 Time history of velocity and acceleration of column S1-A-G1

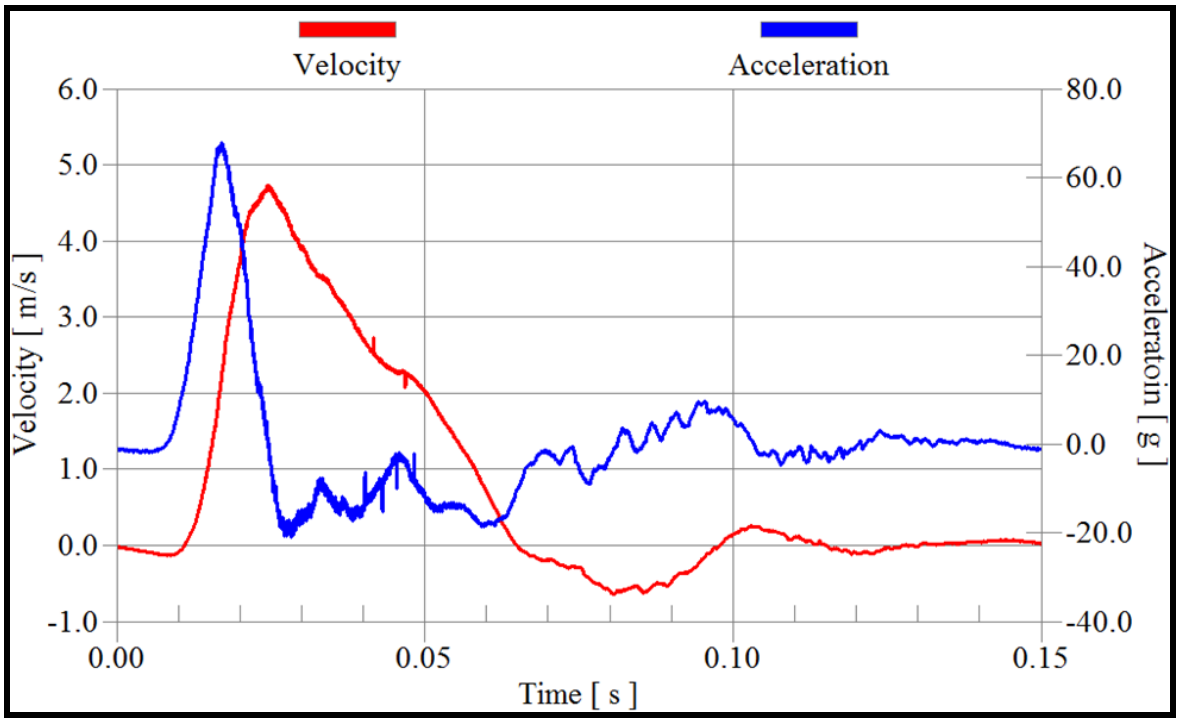

Fig. B-11 Time history of velocity and acceleration of column S1-B-G1

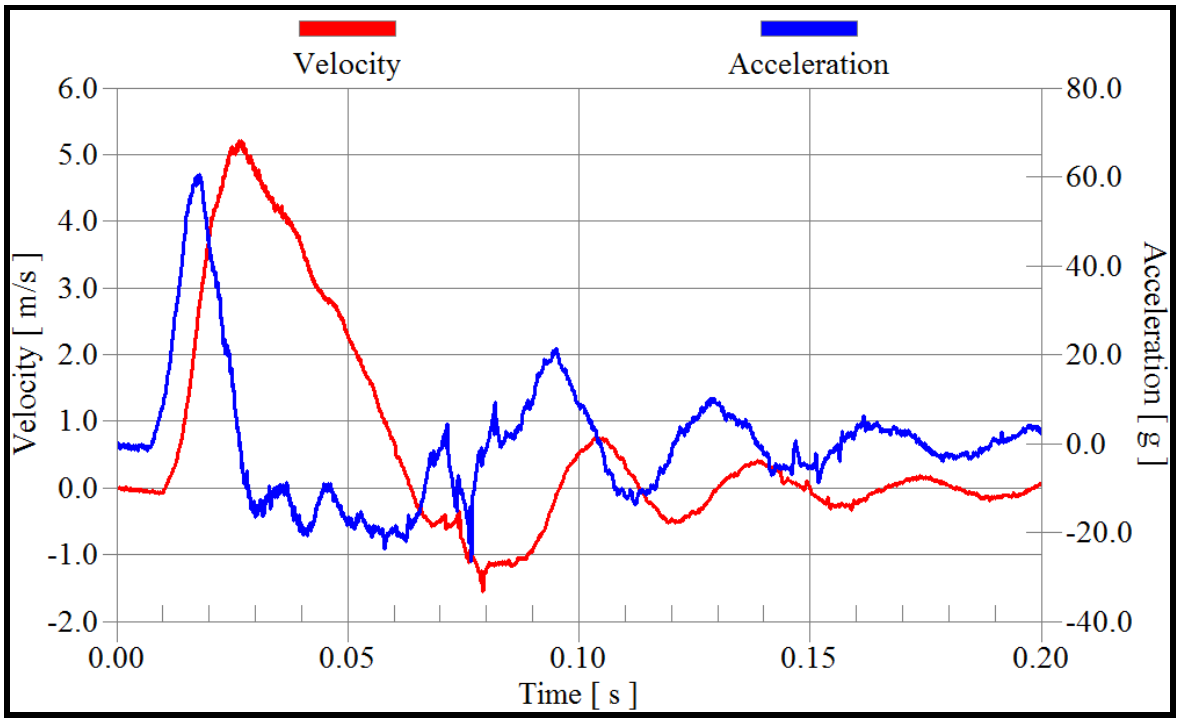

Fig. B-12 Time history of velocity and acceleration of column S1-C-G1

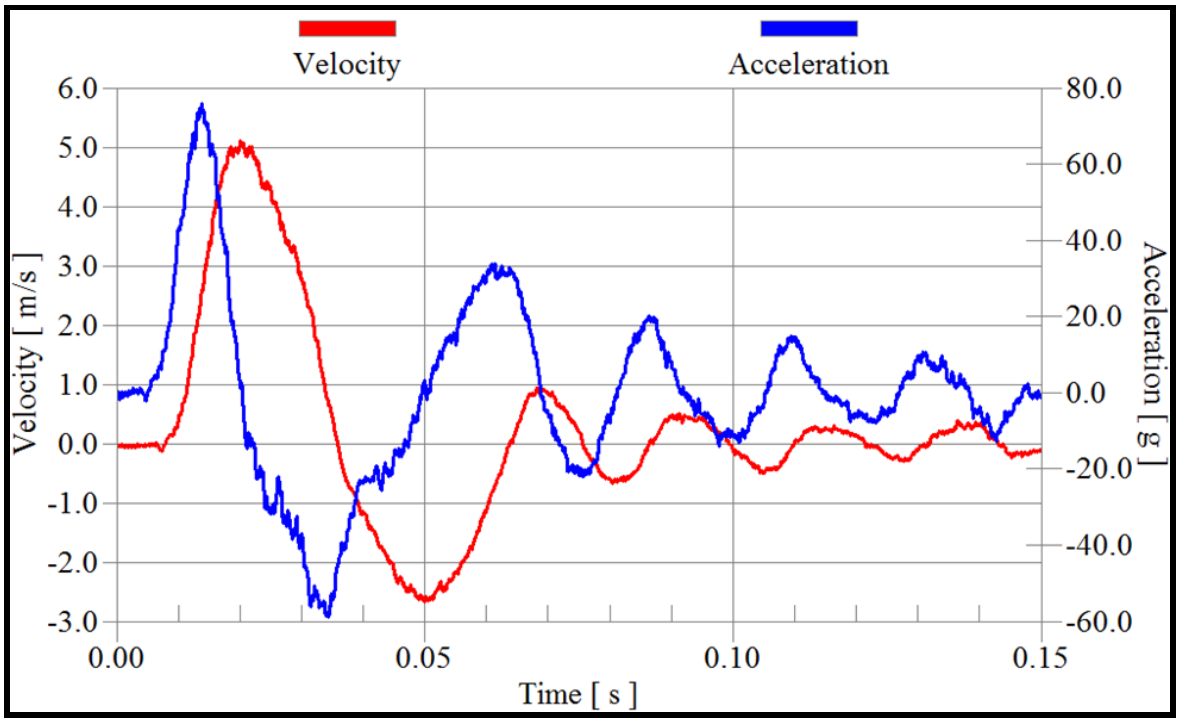

Fig. B-13 Time history of velocity and acceleration of column S2-A-G1

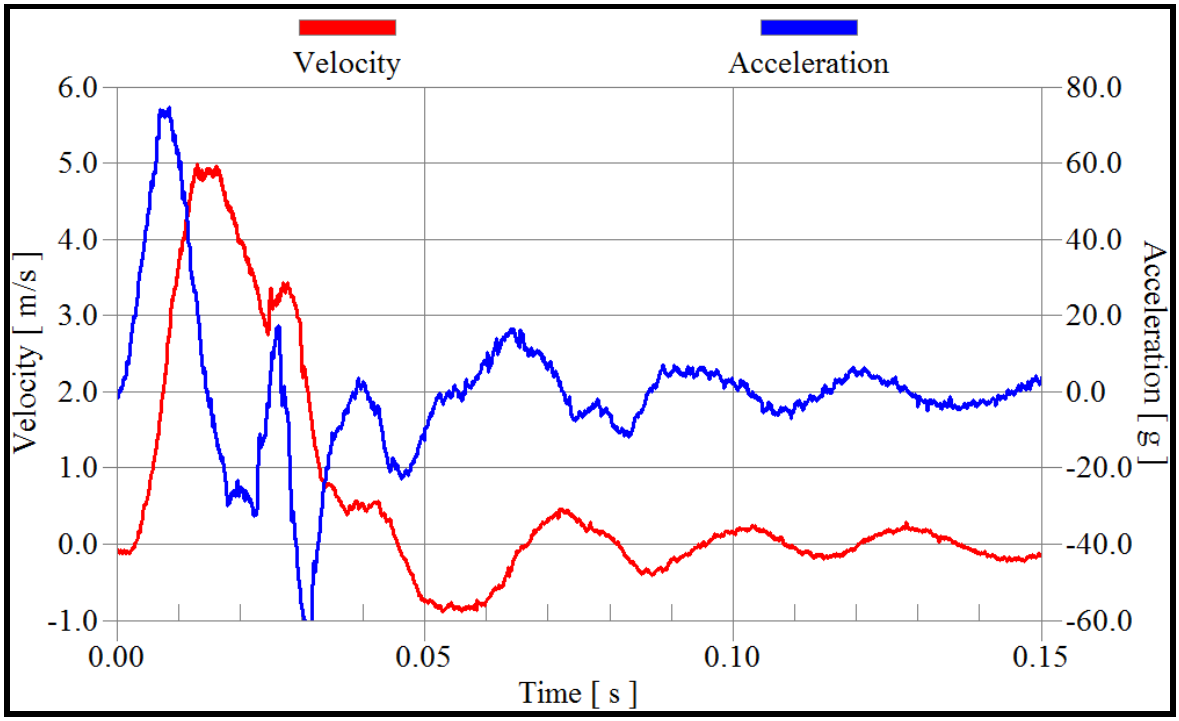

Fig. B-14 Time history of velocity and acceleration of column S2-B-G1

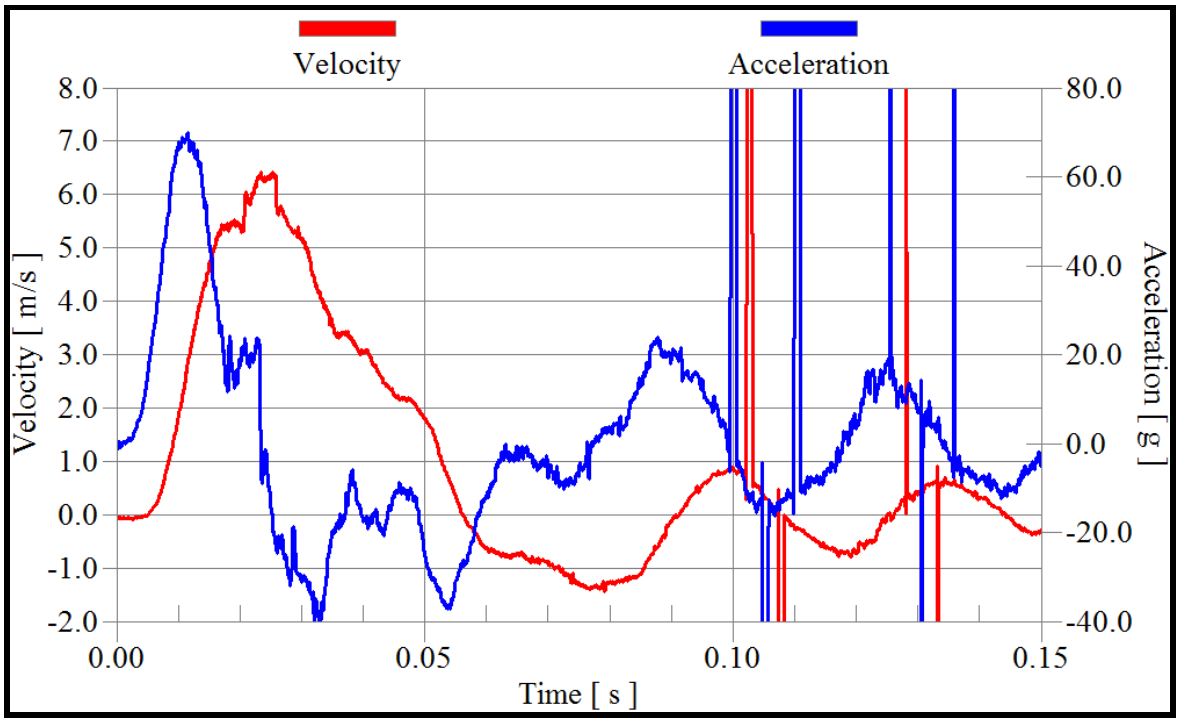

Fig. B-15 Time history of velocity and acceleration of column S3-A-G1

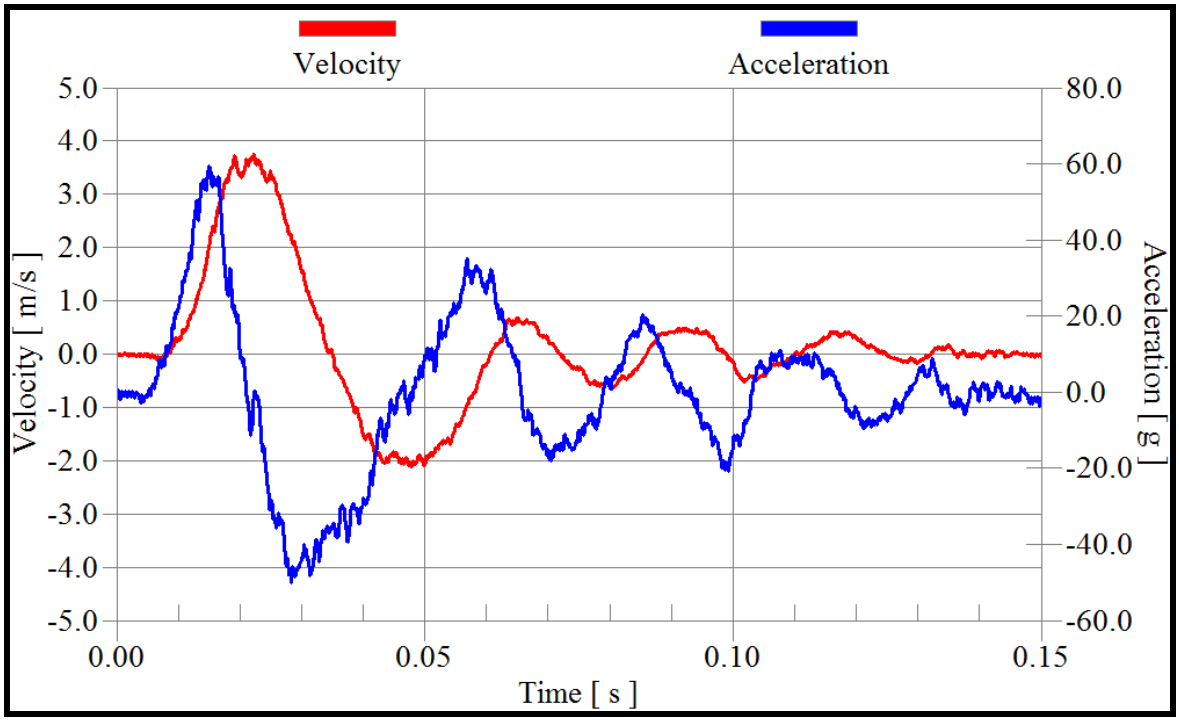

Fig. B-16 Time history of velocity and acceleration of column S3-B-G1

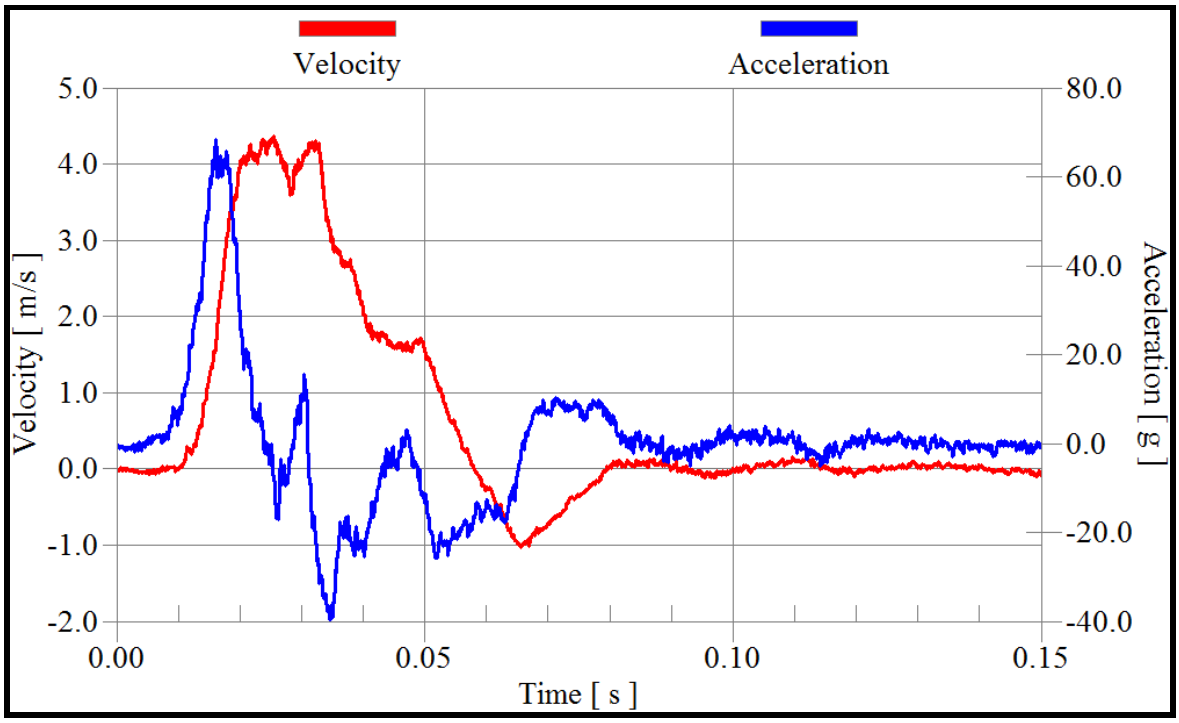

Fig. B-17 Time history of velocity and acceleration of column S4-A-G1

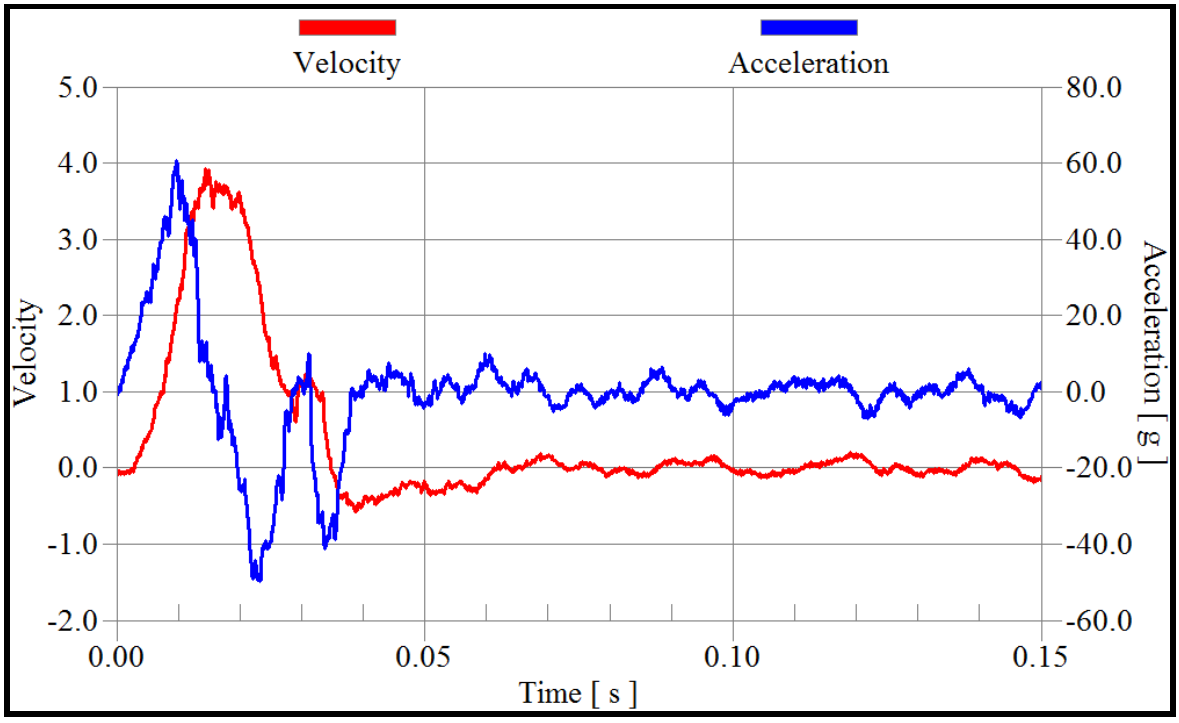

Fig. B-18 Time history of velocity and acceleration of column S4-B-G1

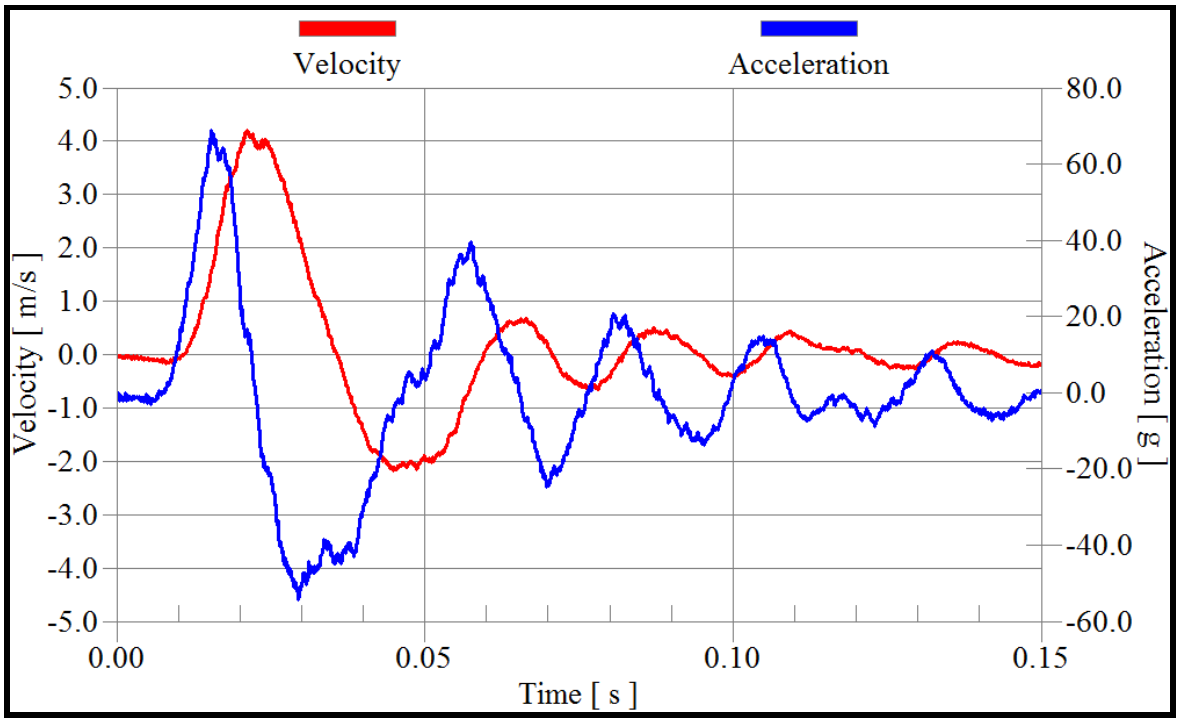

Fig. B-19 Time history of velocity and acceleration of column S5-G1

APPENDIX -C

MEASURED DYNAMIC RESISTANCE TIME HISTORIES

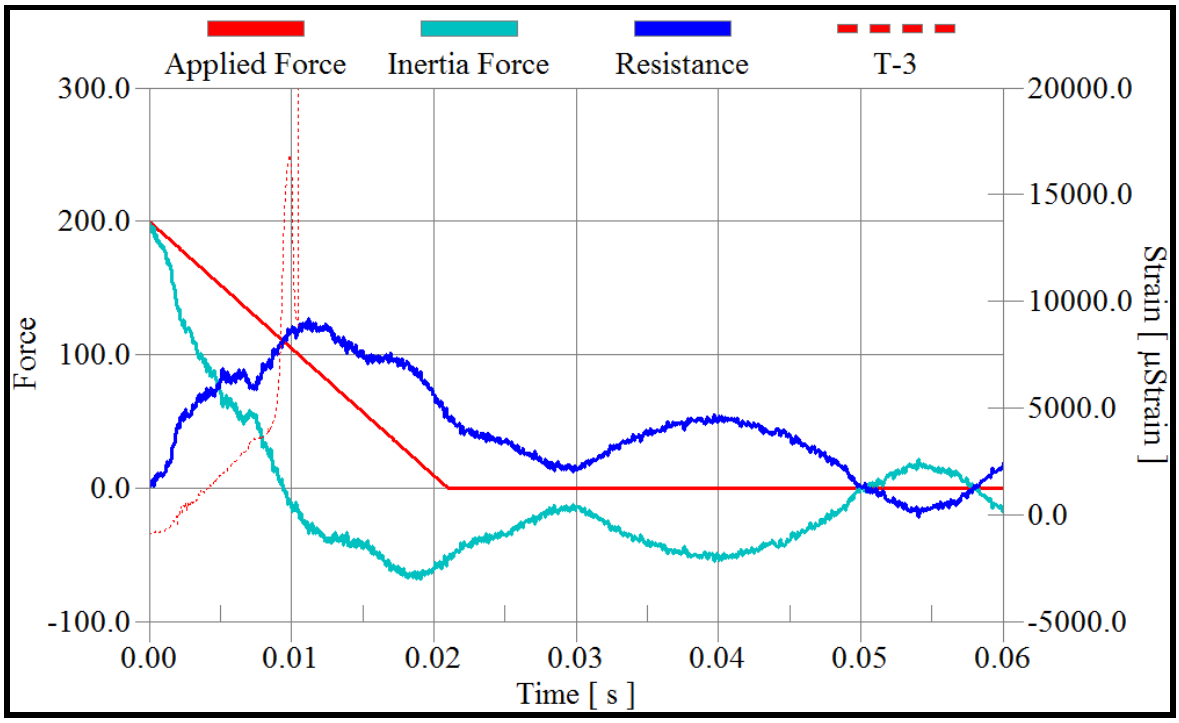

Fig. C-1 Applied force, inertial force, and resistance time history of column NS1-A-G1

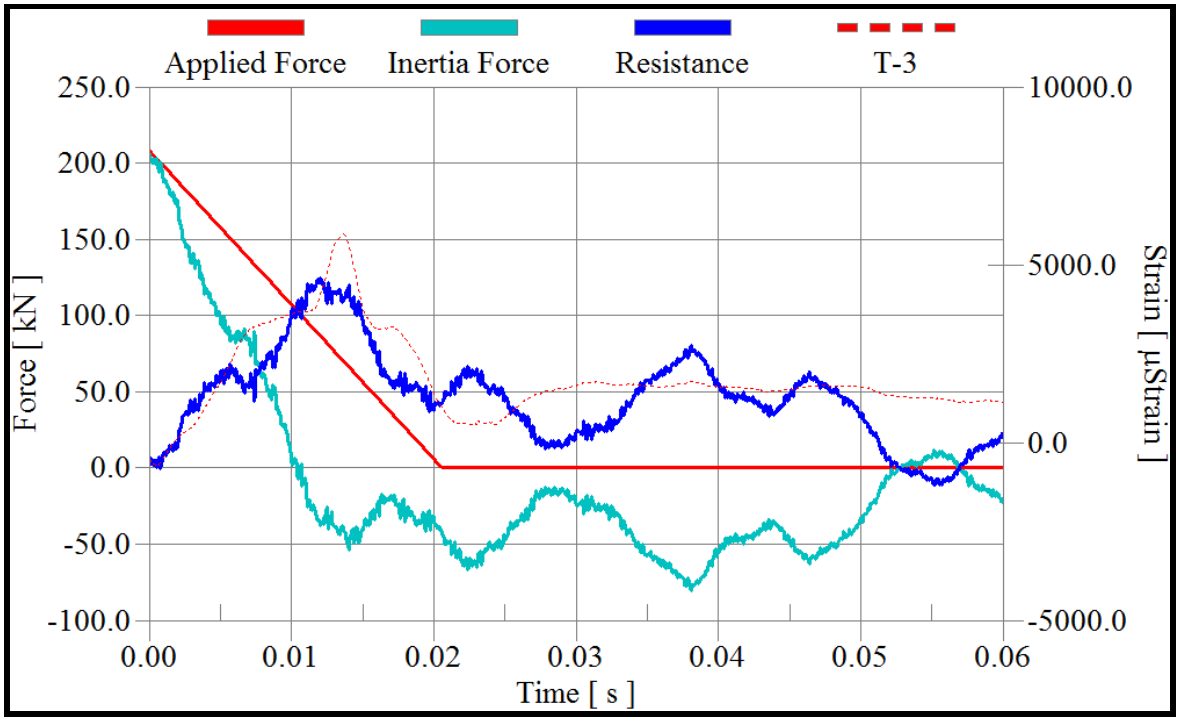

Fig. C-2 Applied force, inertial force, and resistance time history of column NS1-B-G1

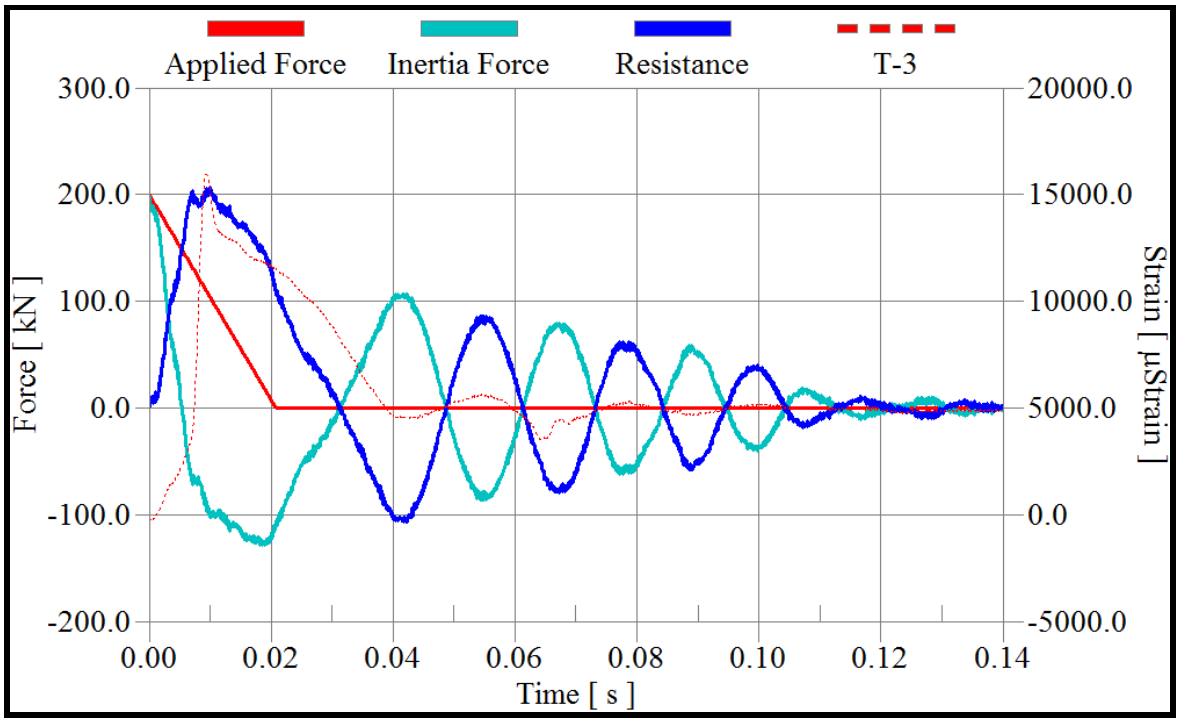

Fig. C-3 Applied force, inertial force, and resistance time history of column NS2-A-G1

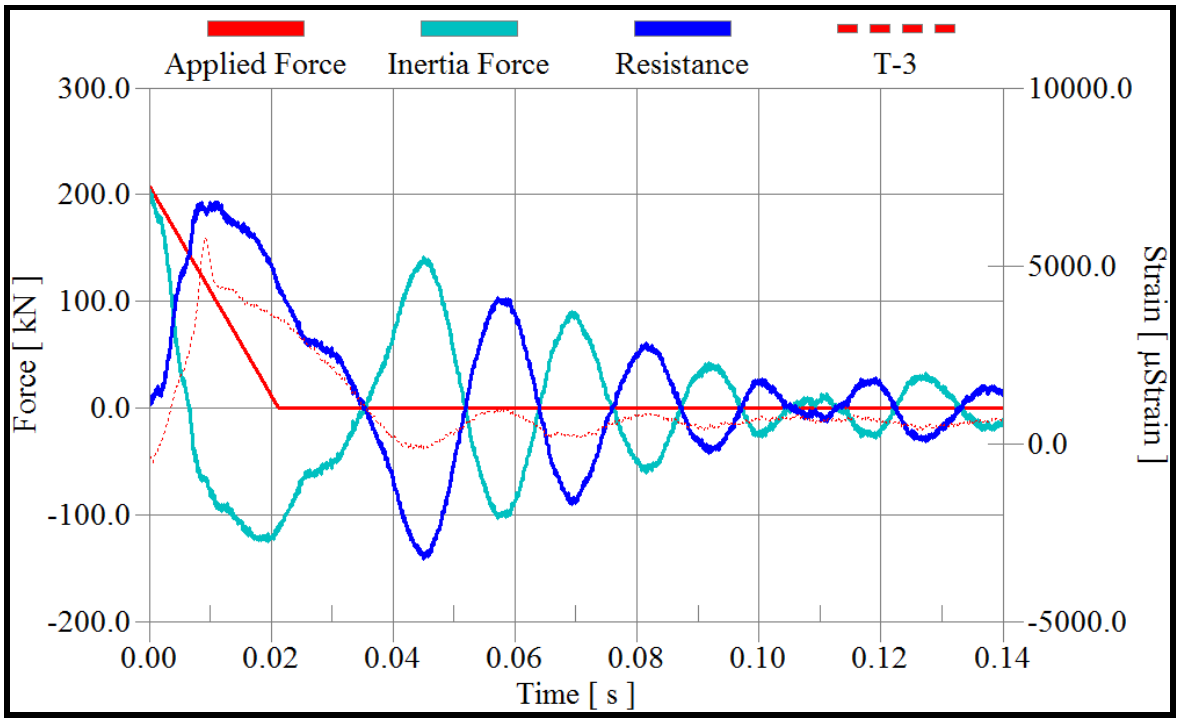

Fig. C-4 Applied force, inertial force, and resistance time history of column NS2-B-G1

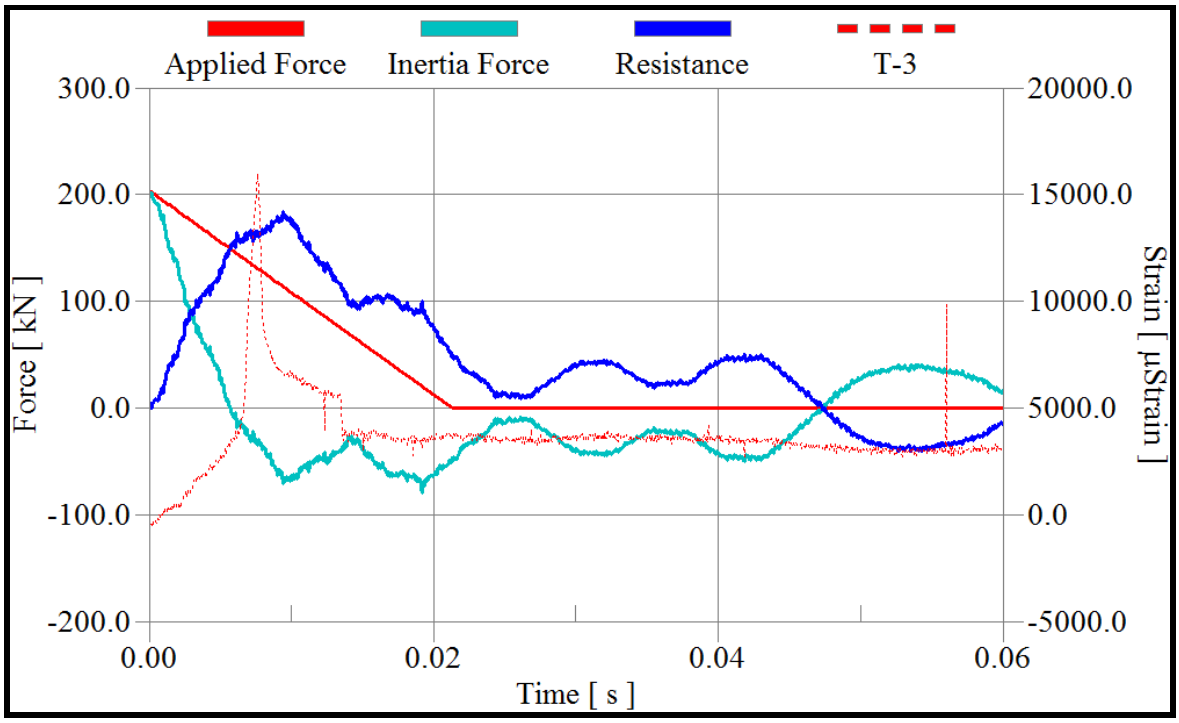

Fig. C-5 Applied force, inertial force, and resistance time history of column NS3-A-G1

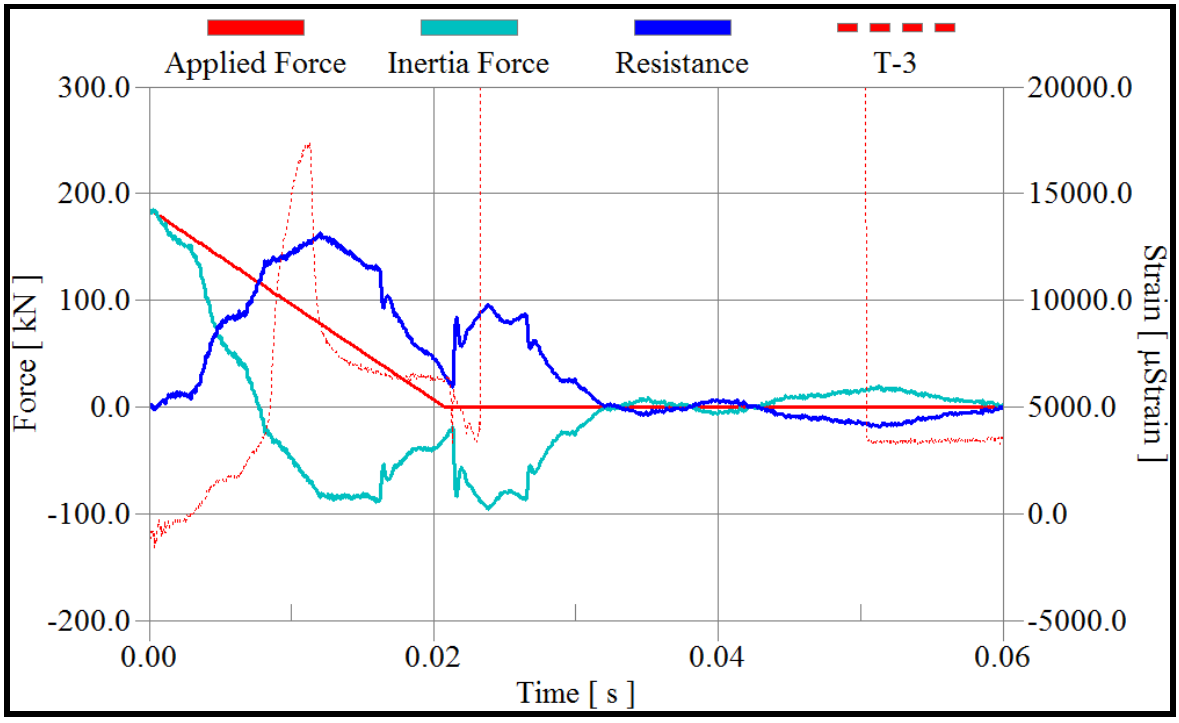

Fig. C-6 Applied force, inertial force, and resistance time history of column NS3-B-G1

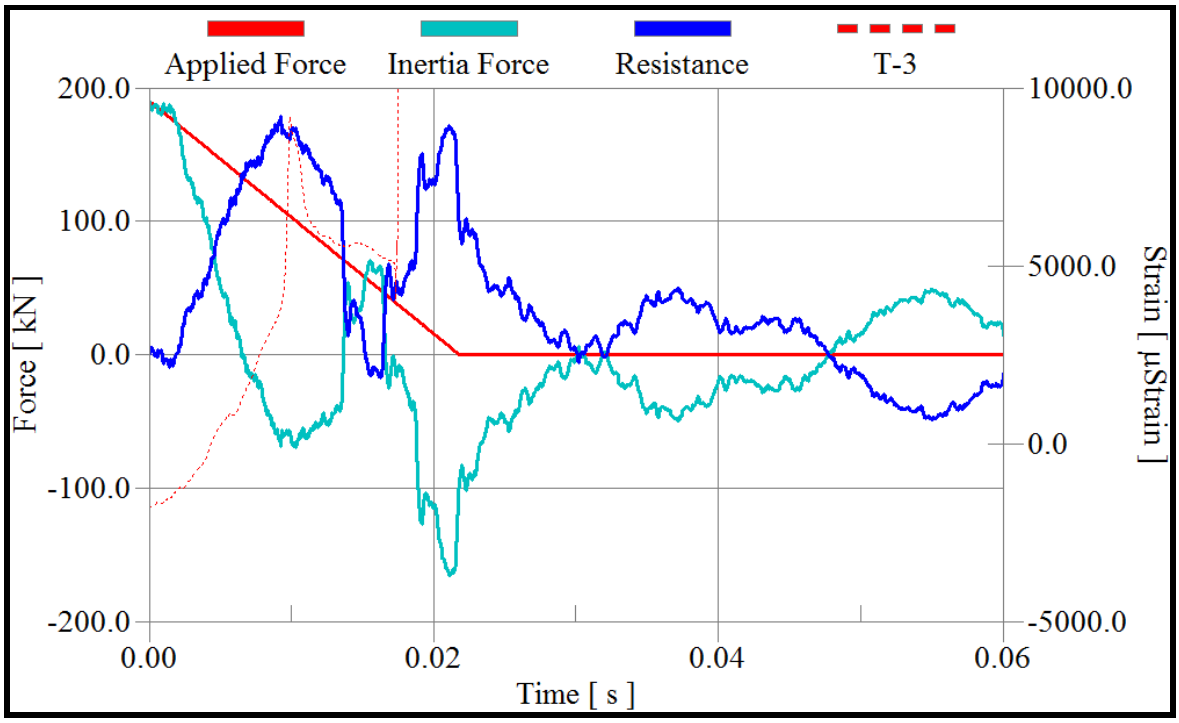

Fig. C-7 Applied force, inertial force, and resistance time history of column NS4-A-G1

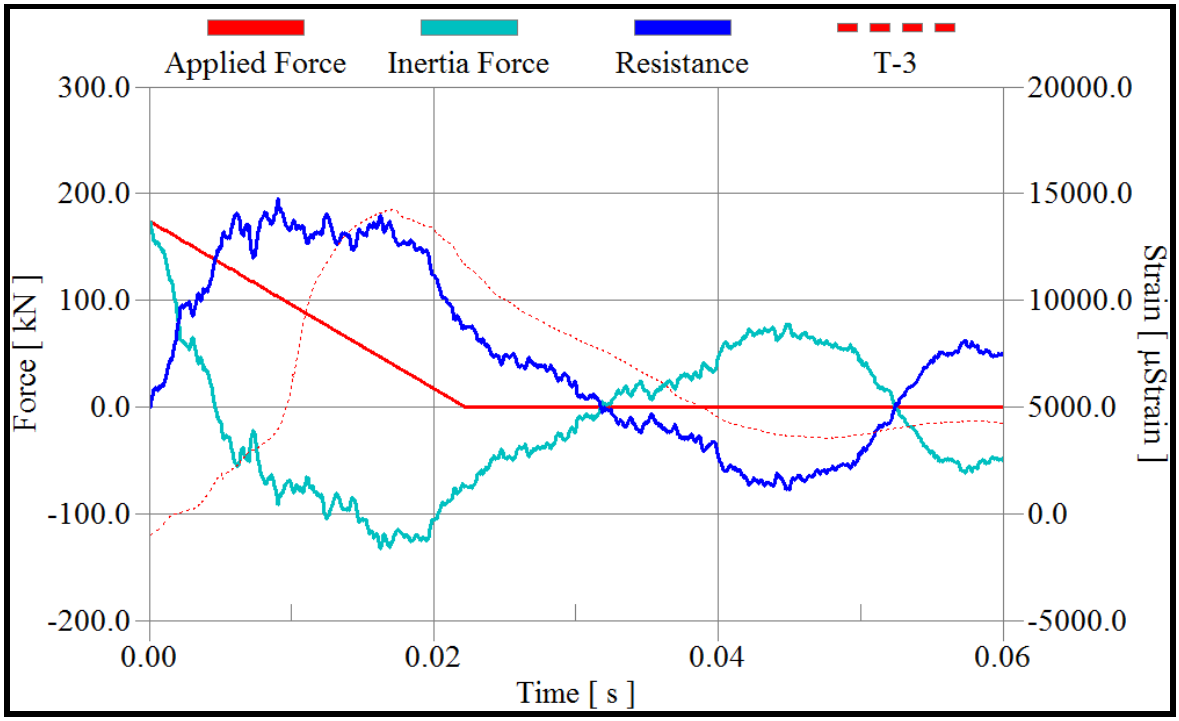

Fig. C-8 Applied force, inertial force, and resistance time history of column NS4-B-G1

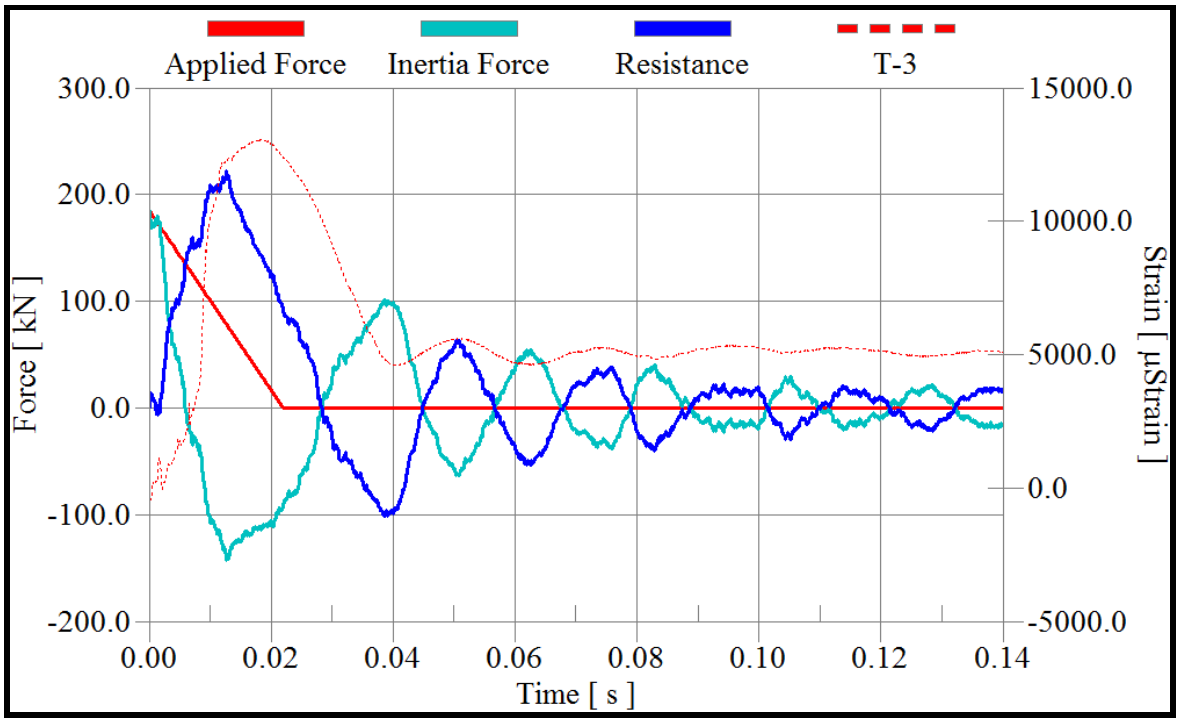

Fig. C-9 Applied force, inertial force, and resistance time history of column NS5-G1

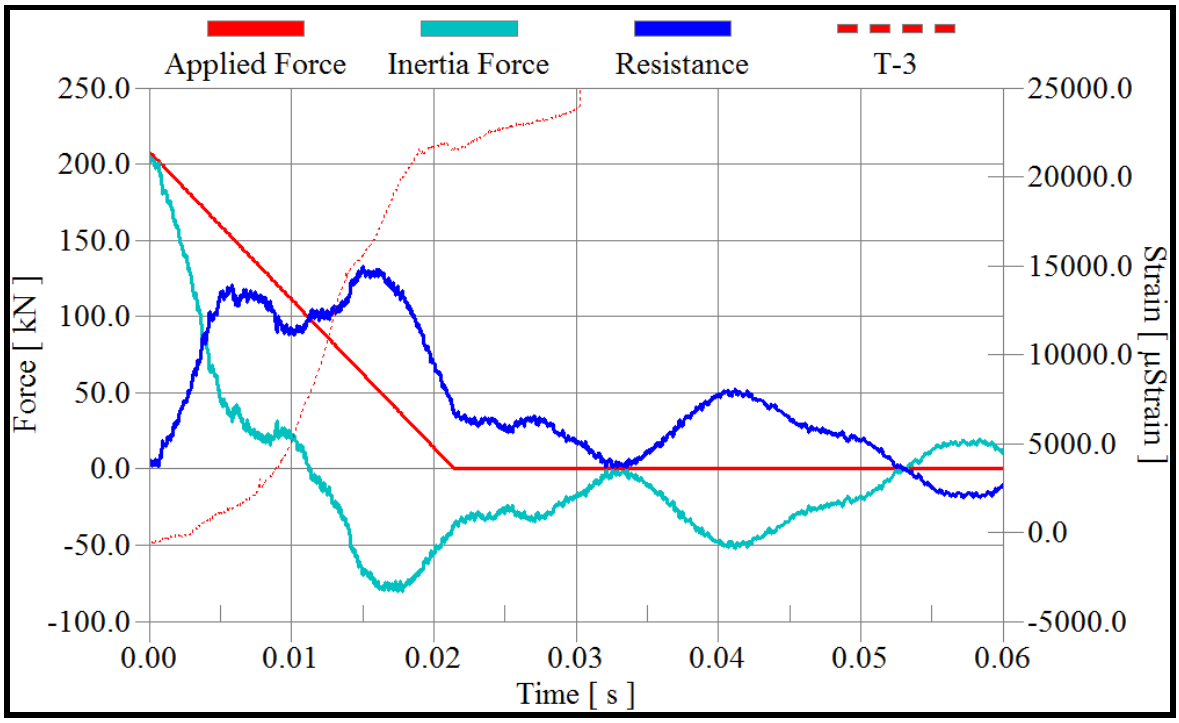

Fig. C-10 Applied force, inertial force, and resistance time history of column S1-A-G1

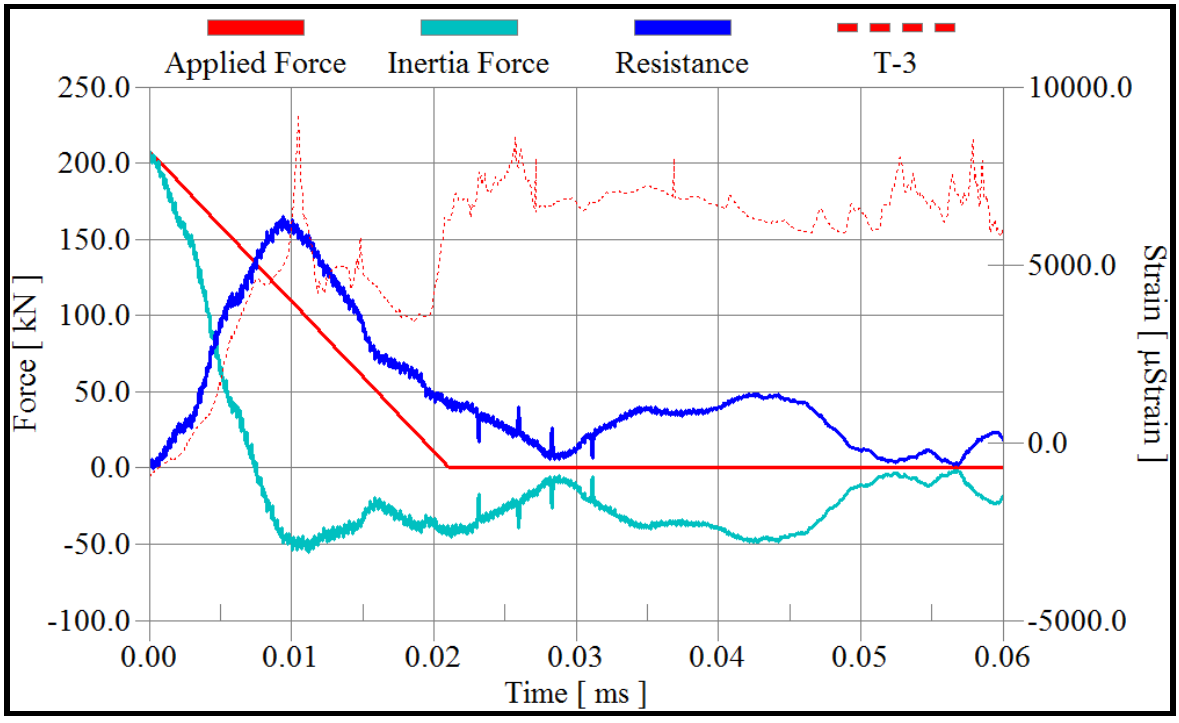

Fig. C-11 Applied force, inertial force, and resistance time history of column S1-B-G1

Fig. C-12 Applied force, inertial force, and resistance time history of column S1-C-G1

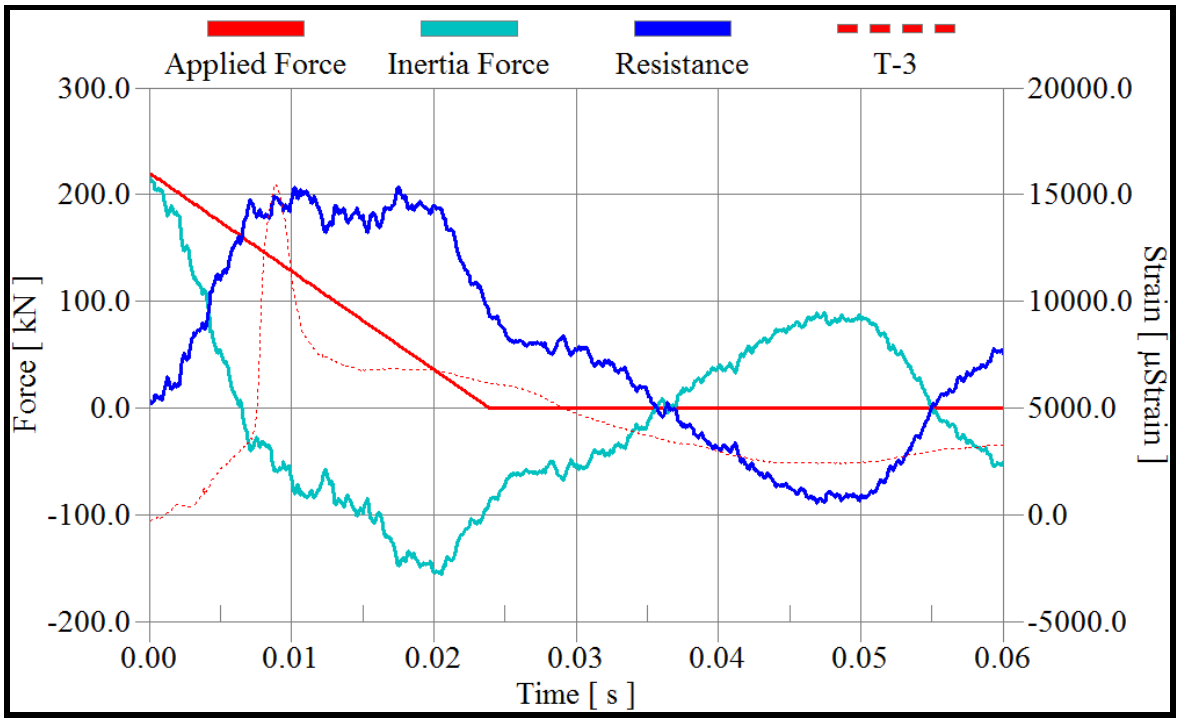

Fig. C-13 Applied force, inertial force, and resistance time history of column S2-A-G1

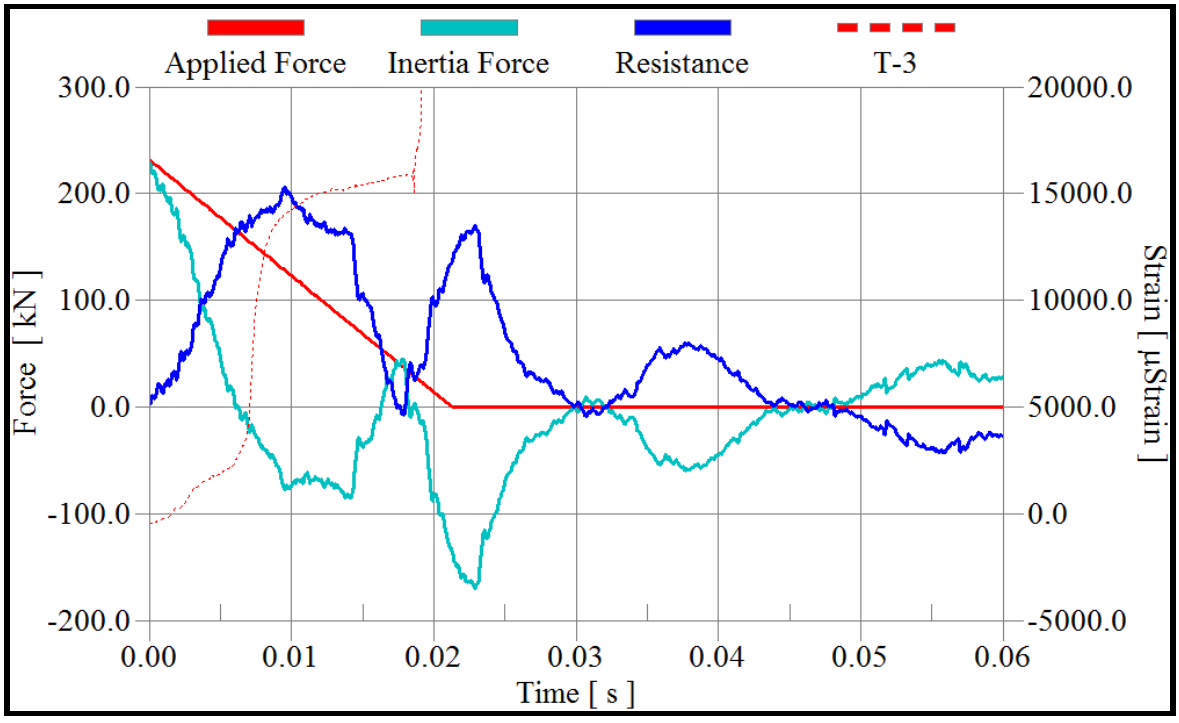

Fig. C-14 Applied force, inertial force, and resistance time history of column S2-B-G1

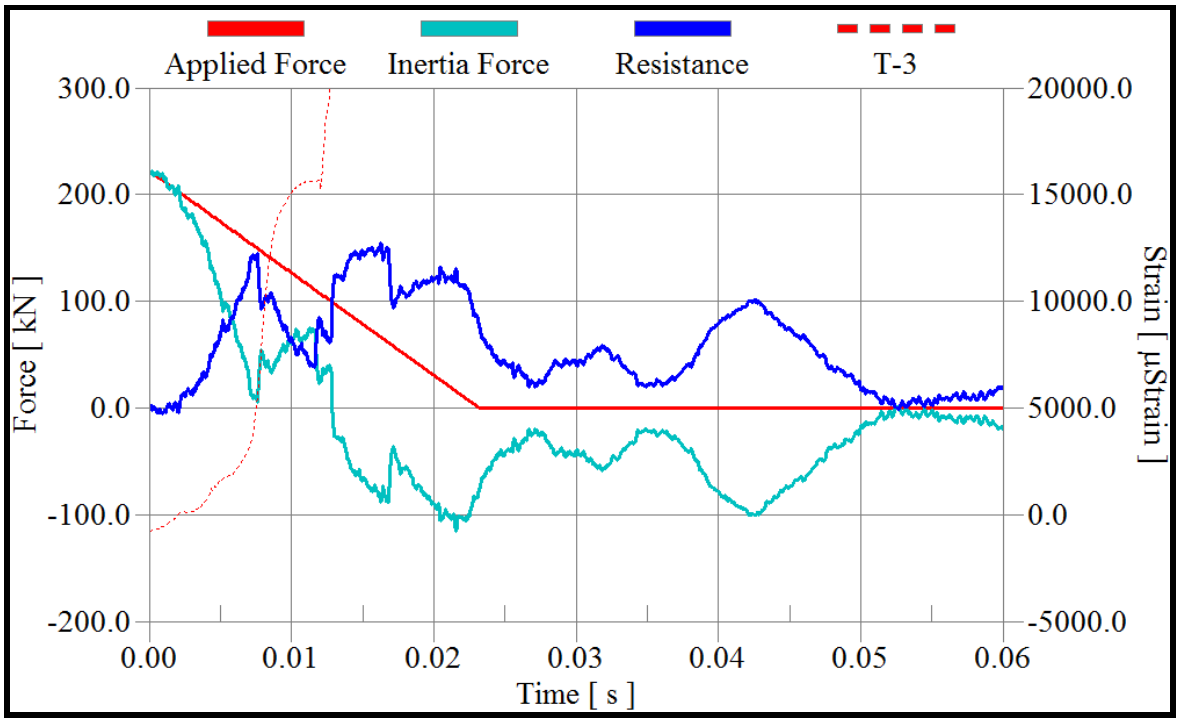

Fig. C-15 Applied force, inertial force, and resistance time history of column S3-A-G1

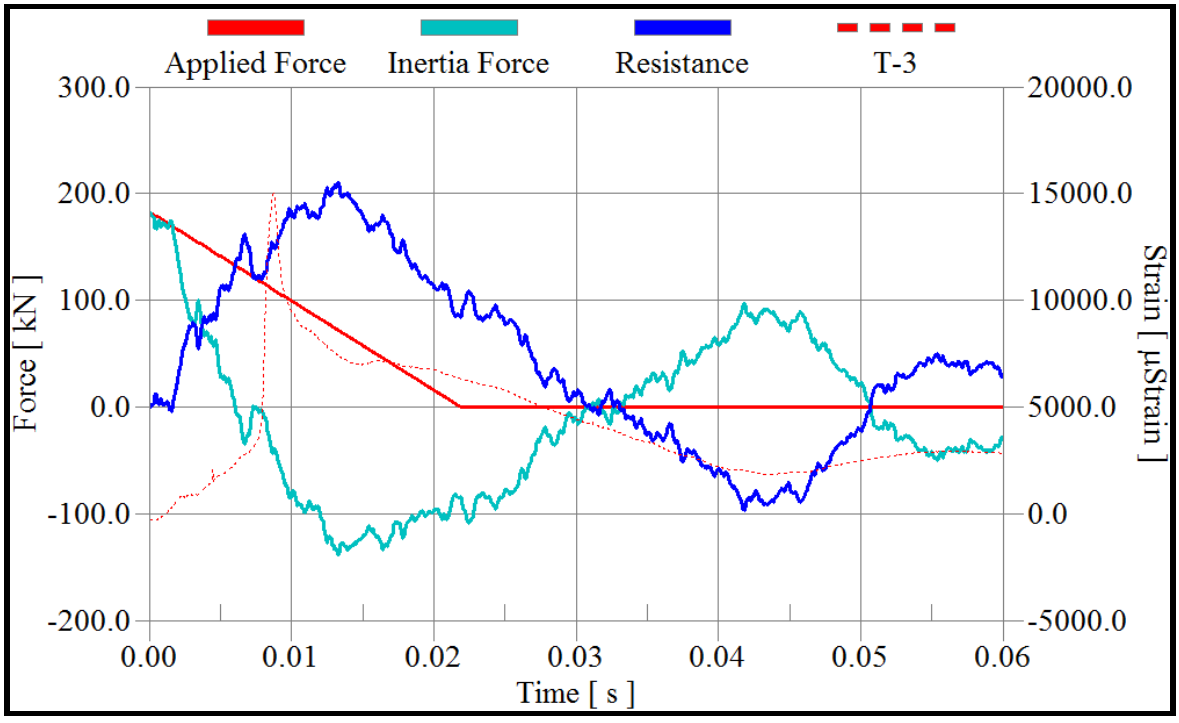

Fig. C-16 Applied force, inertial force, and resistance time history of column S3-B-G1

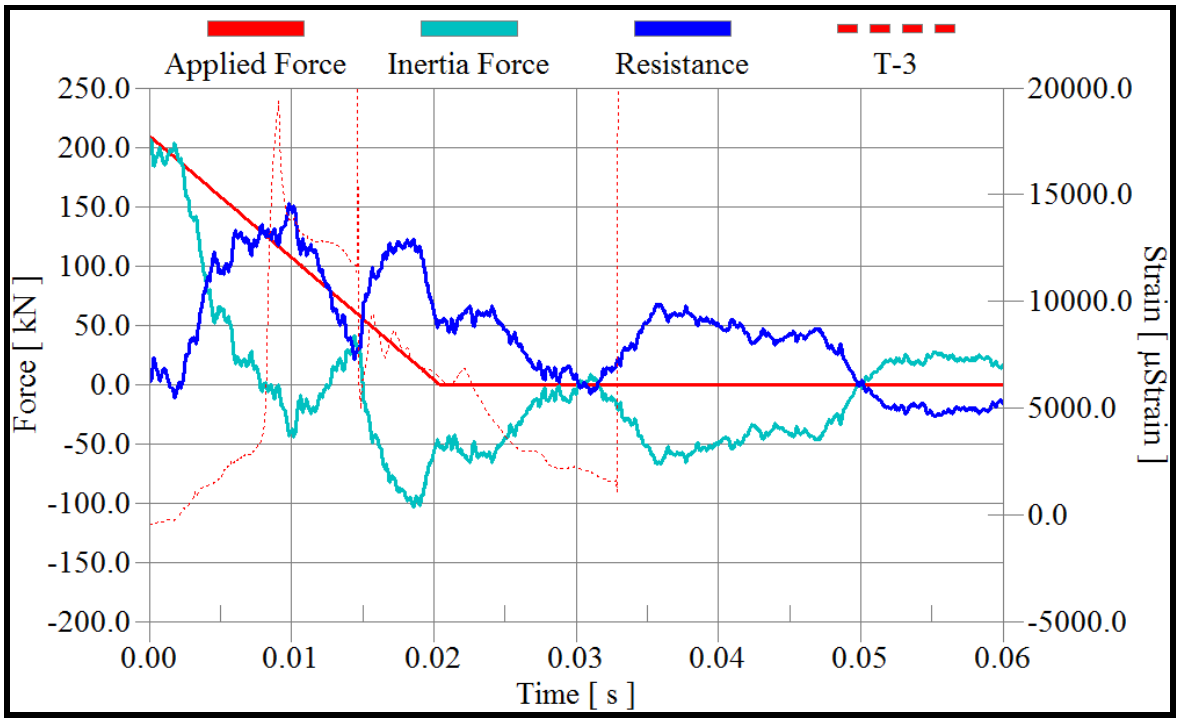

Fig. C-17 Applied force, inertial force, and resistance time history of column S4-A-G1

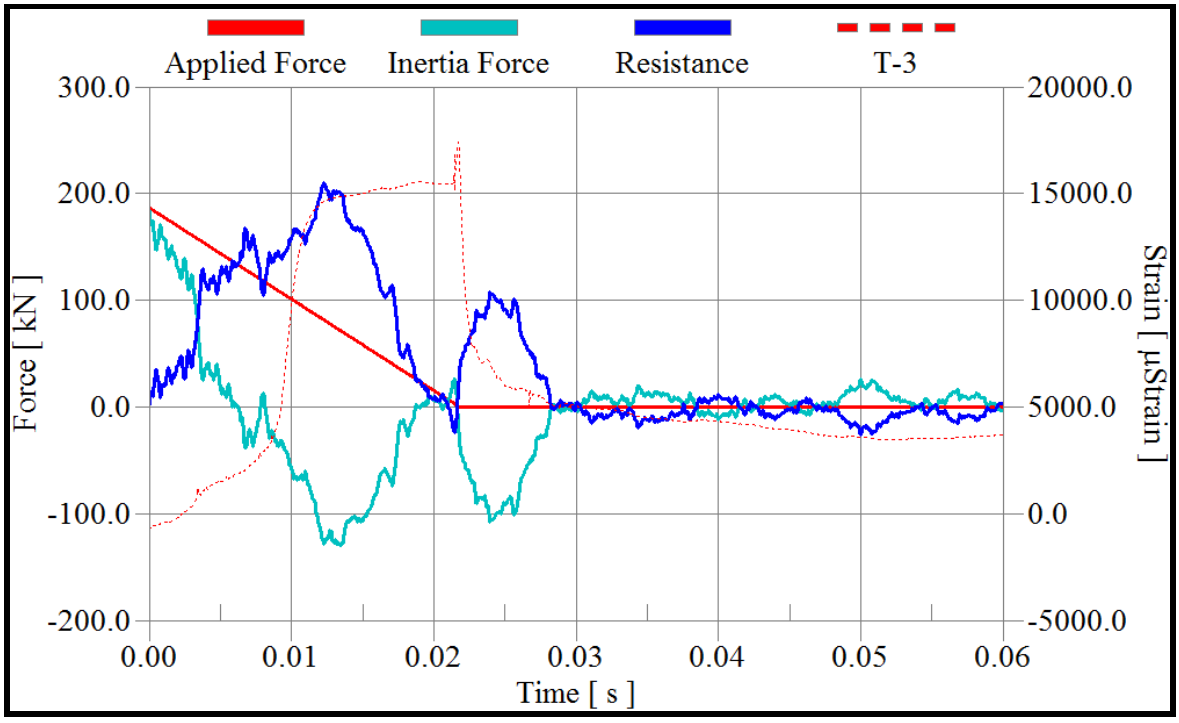

Fig. C-18 Applied force, inertial force, and resistance time history of column S4-B-G1

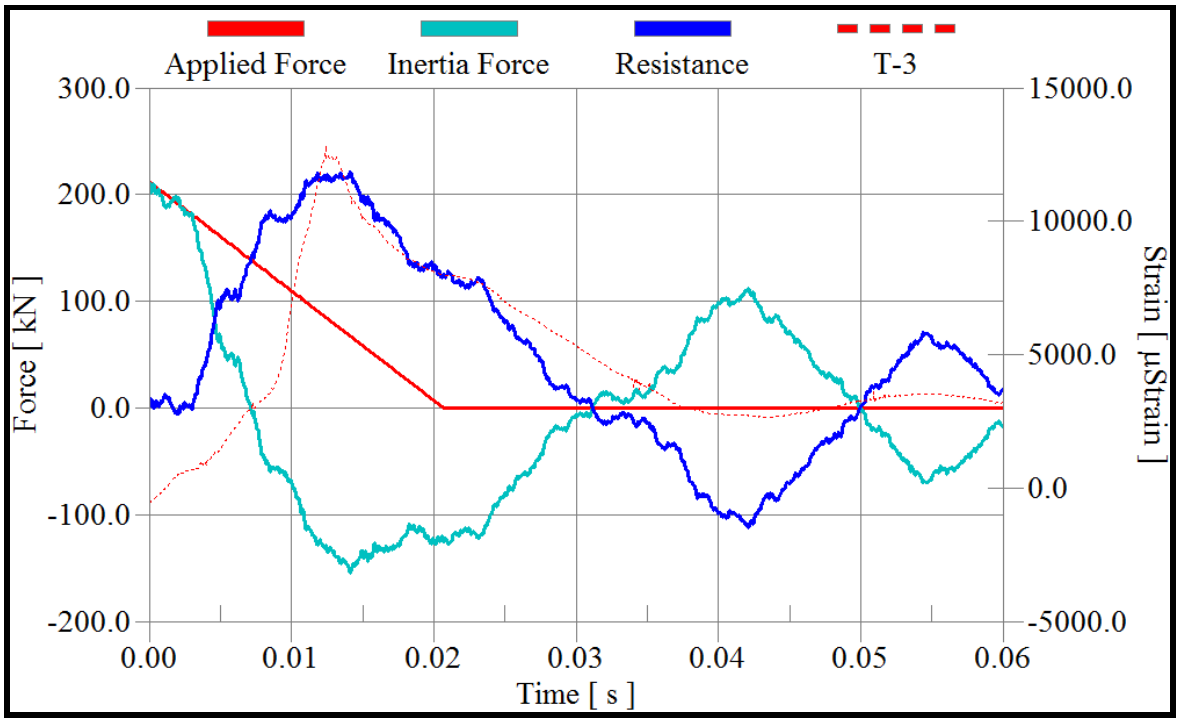

Fig. C-19 Applied force, inertial force, resistance, and T-3 time history of column S5-G1

APPENDIX-D

MEASURED RESISTANCE FUNCTIONS

(FORCE-DISPLACEMENT RELATIONSHIPS)

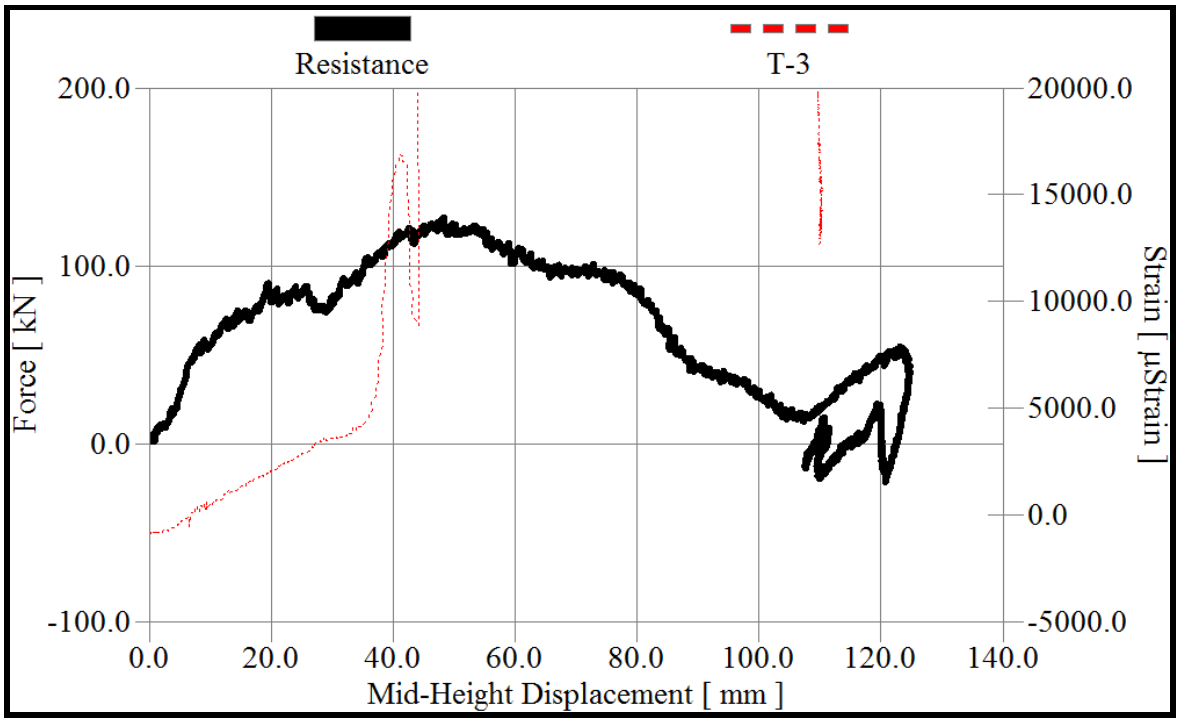

Fig. D-1 Resistance-displacement function of column NS1-A-G1

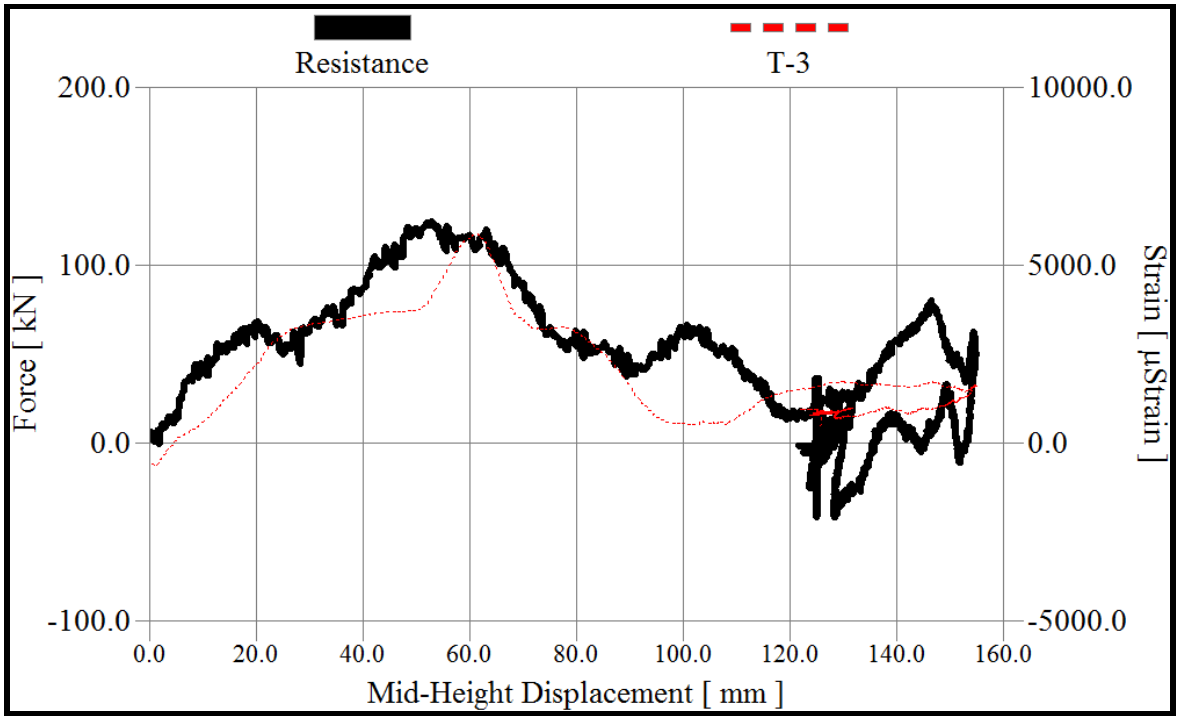

Fig. D-2 Resistance-displacement function of column NS1-B-G1

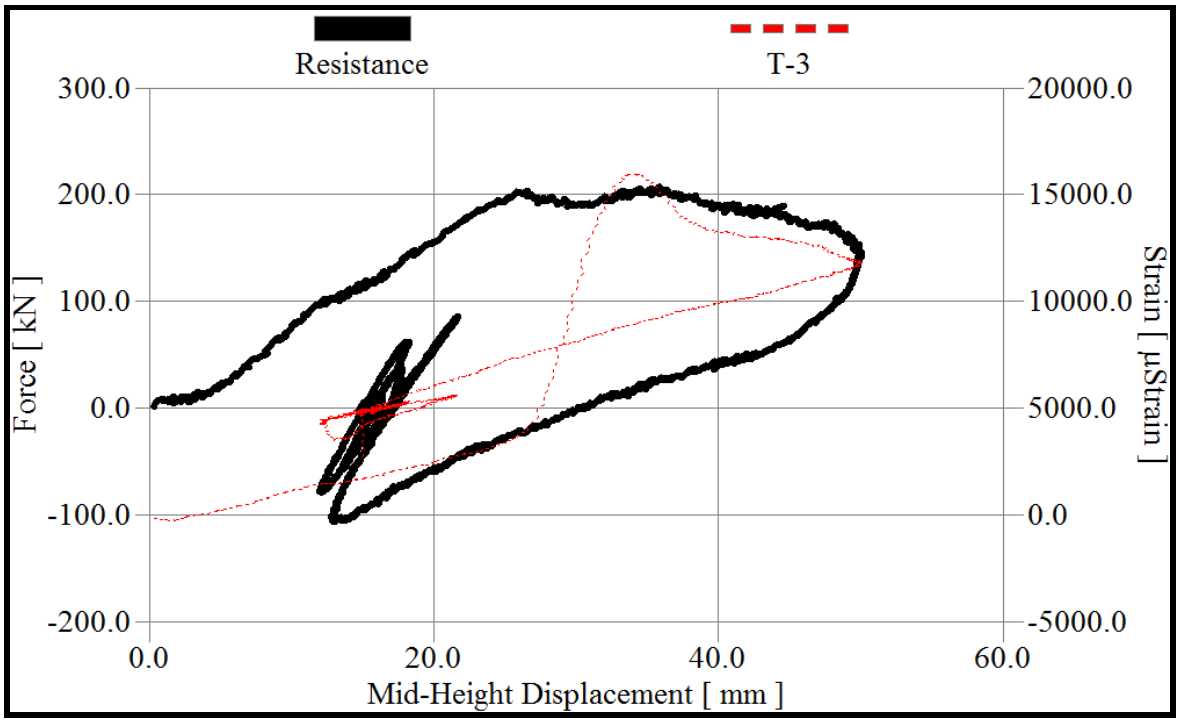

Fig. D-3 Resistance-displacement function of column NS2-A-G1

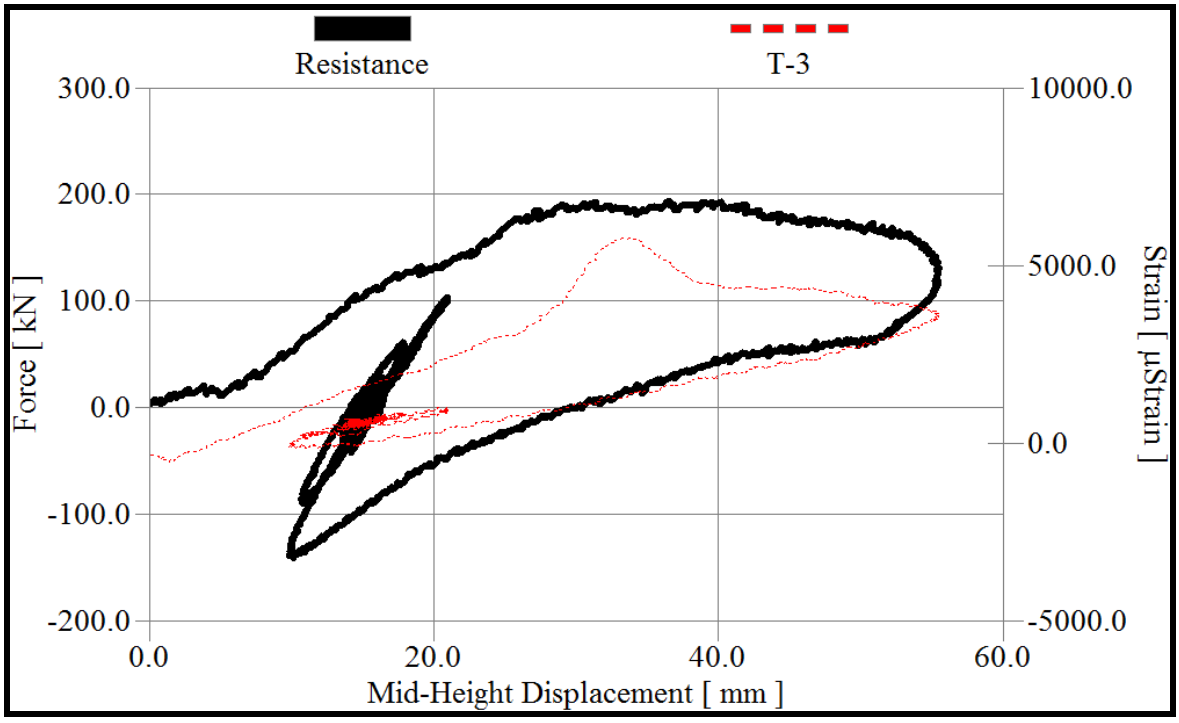

Fig. D-4 Resistance-displacement function of column NS2-B-G1

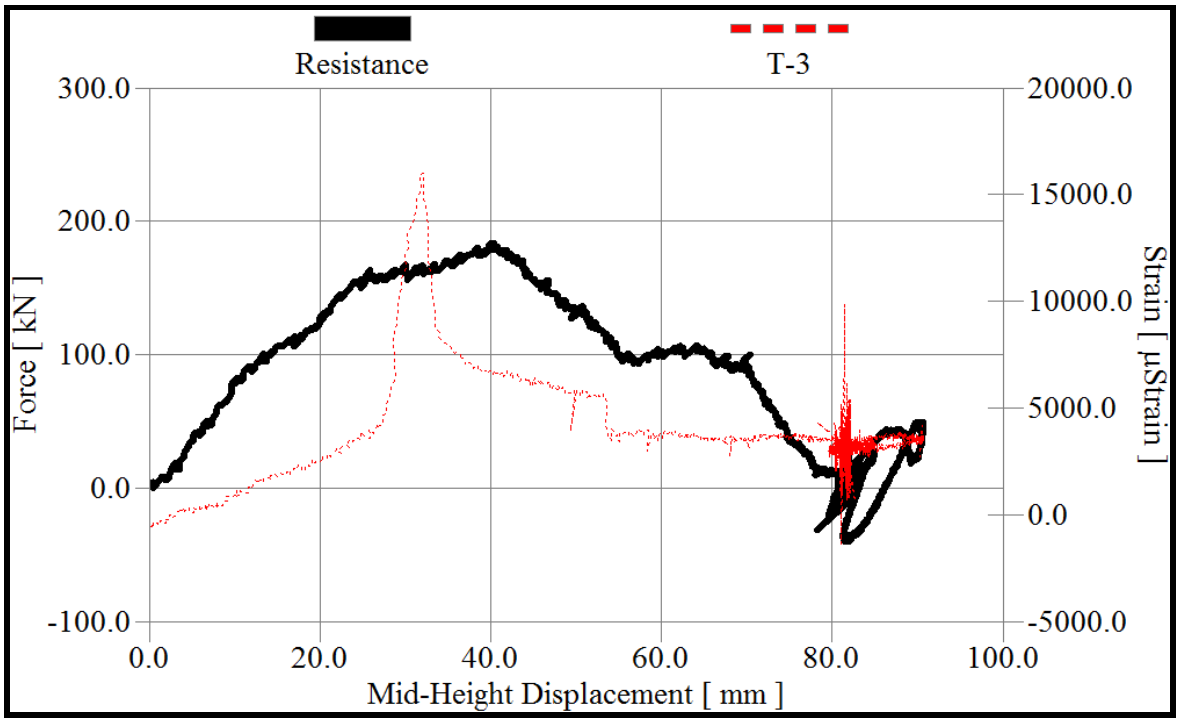

Fig. D-5 Resistance-displacement function of column NS3-A-G1

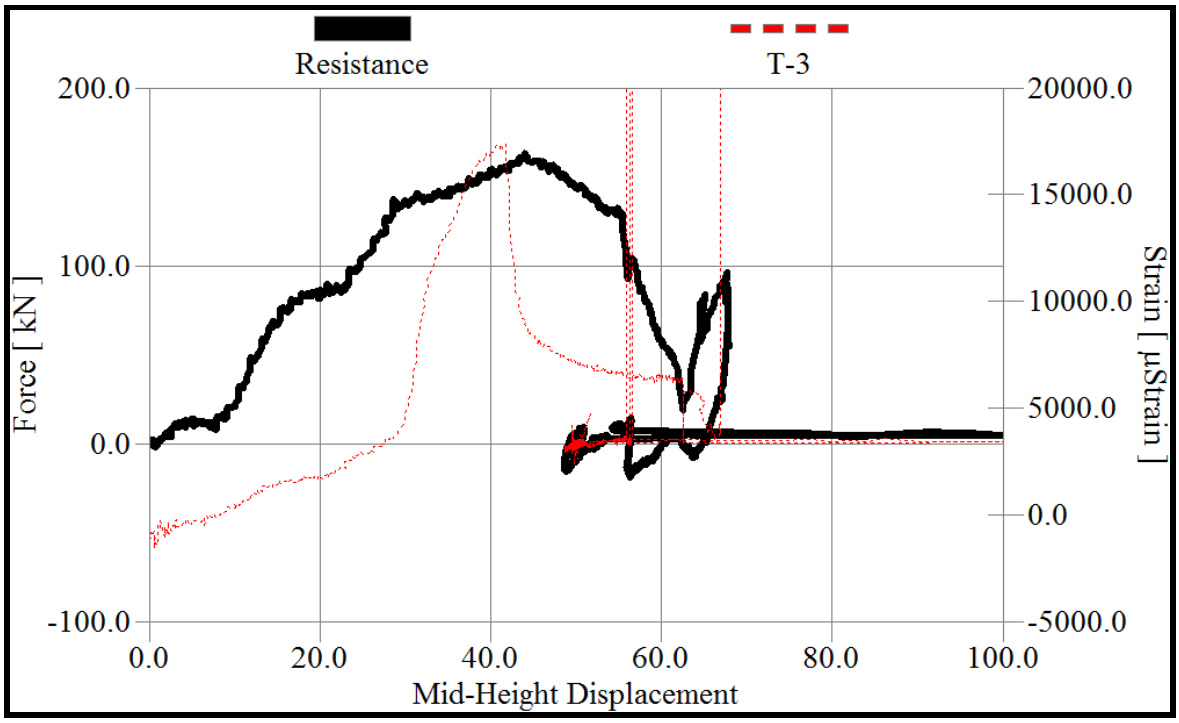

Fig. D-6 Resistance-displacement function of column NS3-B-G1

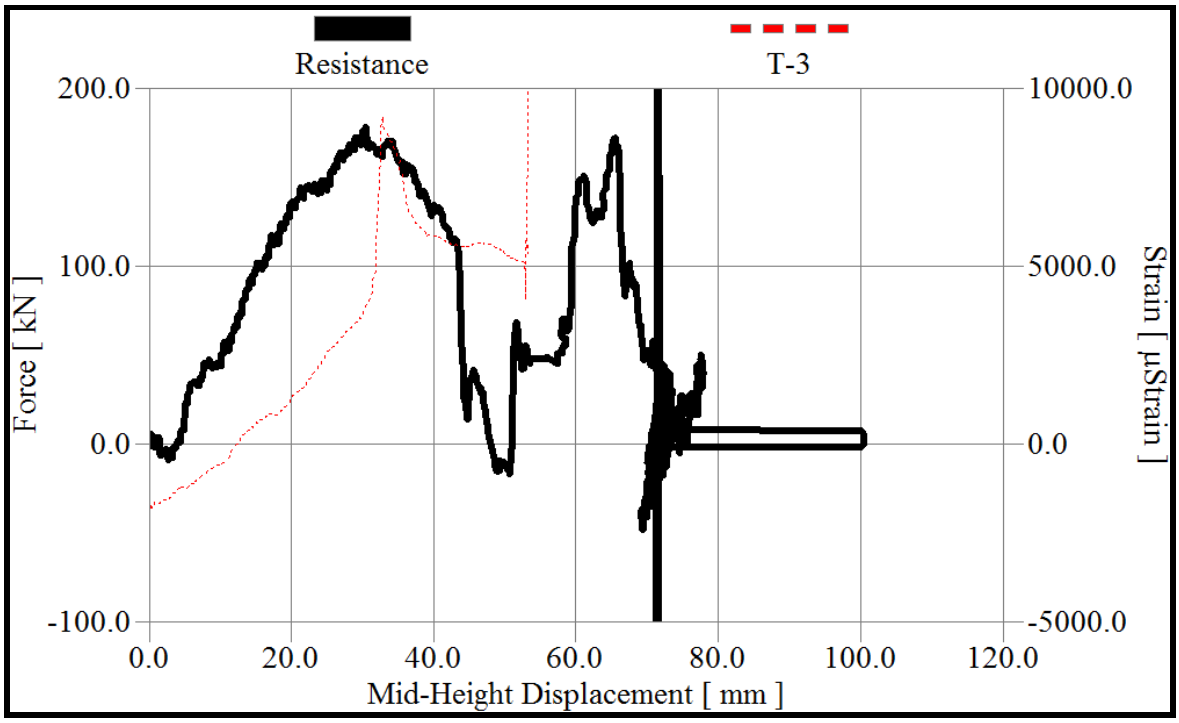

Fig. D-7 Resistance-displacement function of column NS4-A-G1

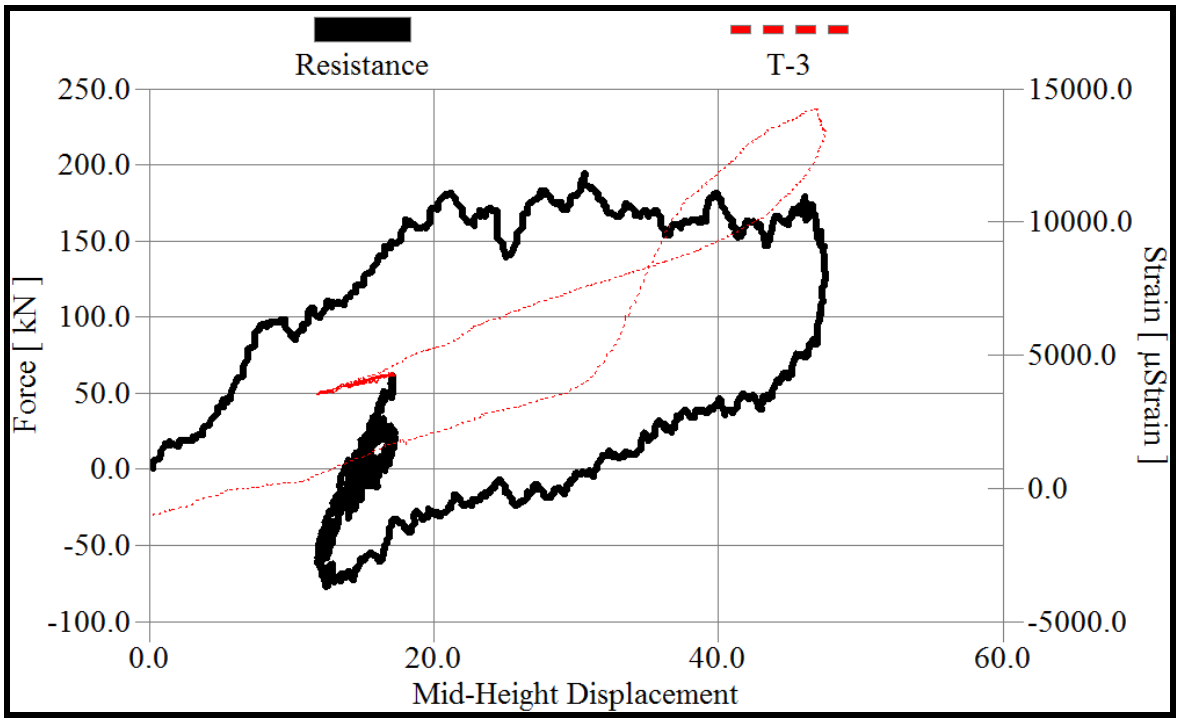

Fig. D-8 Resistance-displacement function of column NS4-B-G1

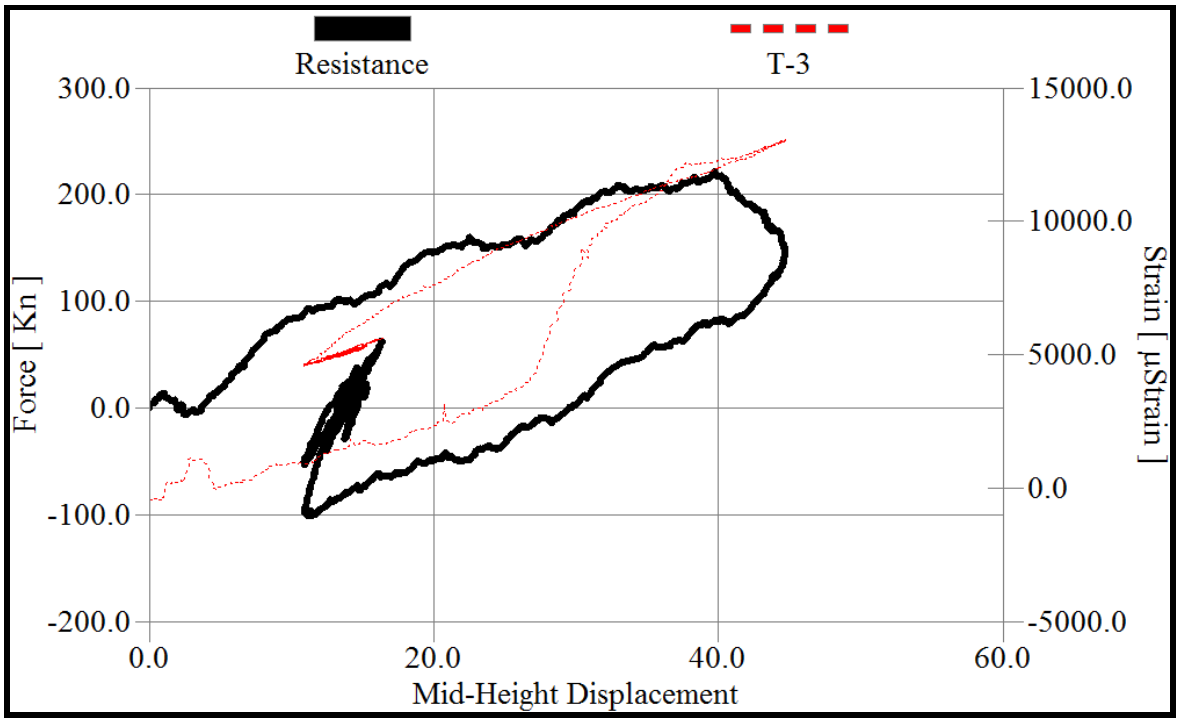

Fig. D-9 Resistance-displacement function of column NS5-G1

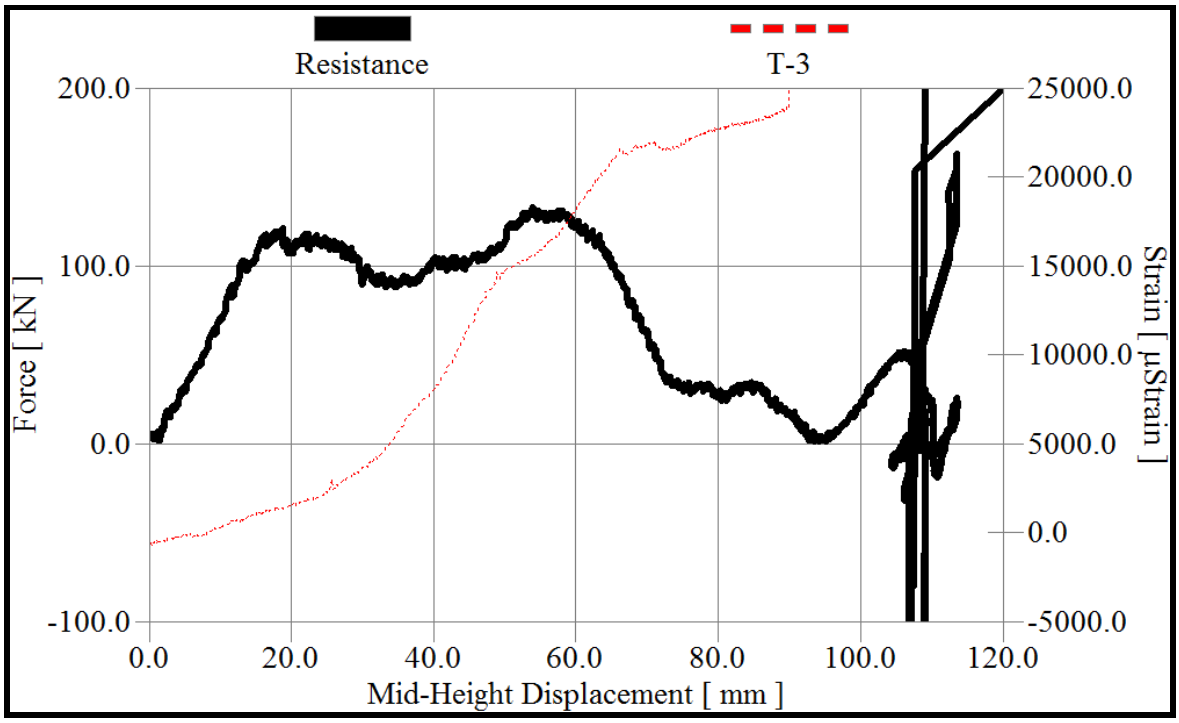

Fig. D-10 Resistance-displacement function of column S1-A-G1

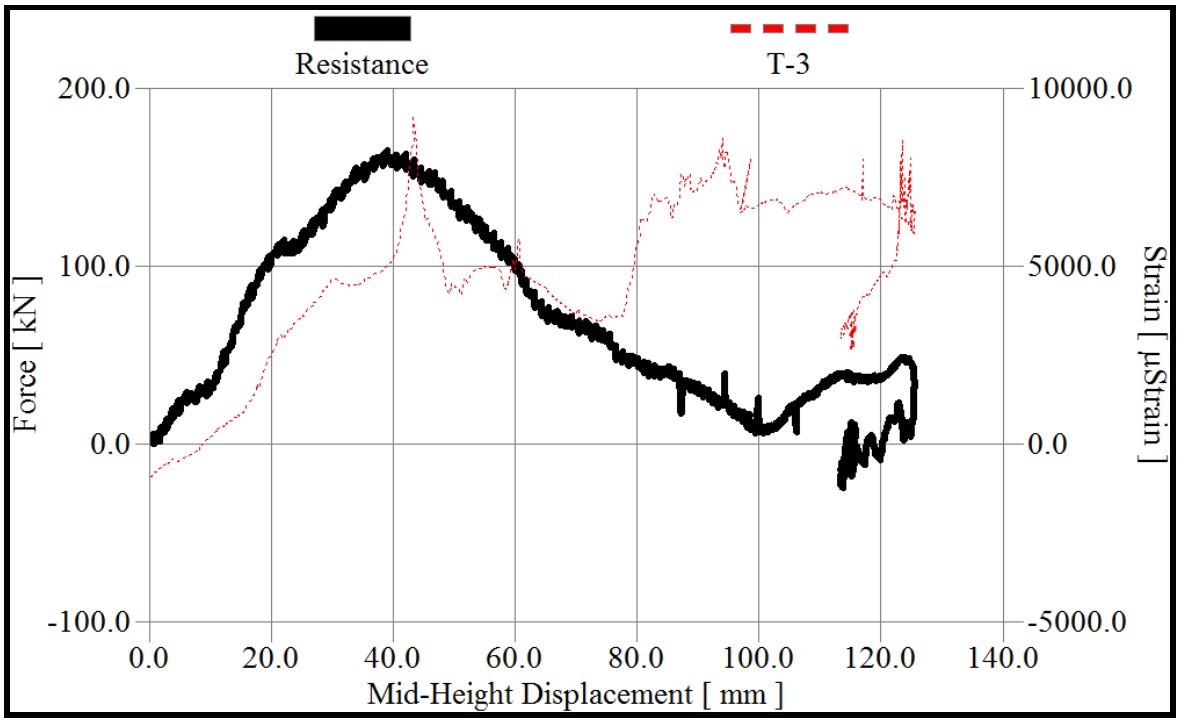

Fig. D-11 Resistance-displacement function of column S1-B-G1

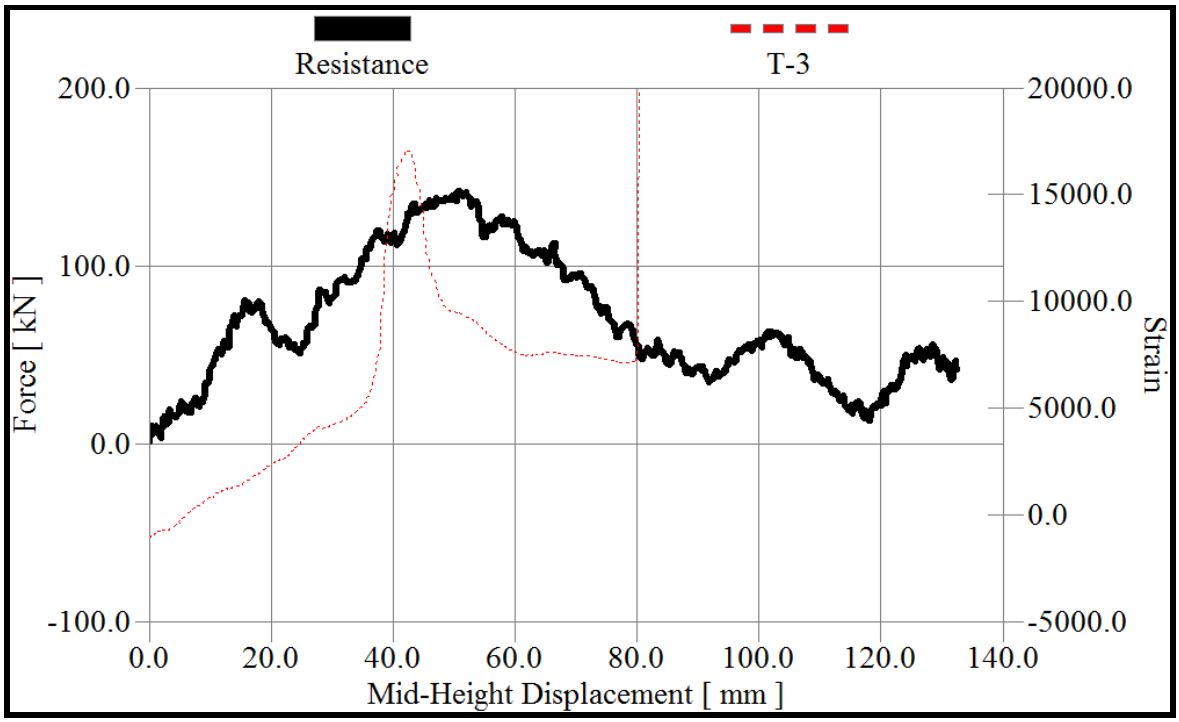

Fig. D-12 Resistance-displacement function of column S1-C-G1

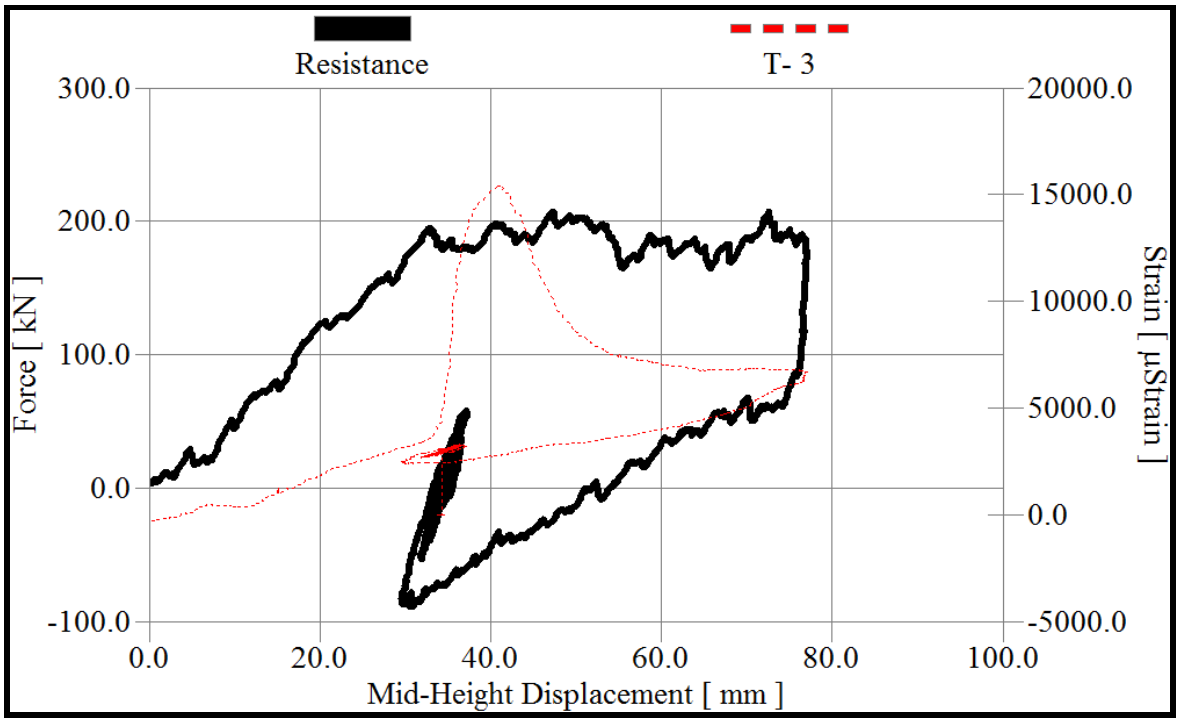

Fig. D-13 Resistance-displacement function of column S2-A-G1

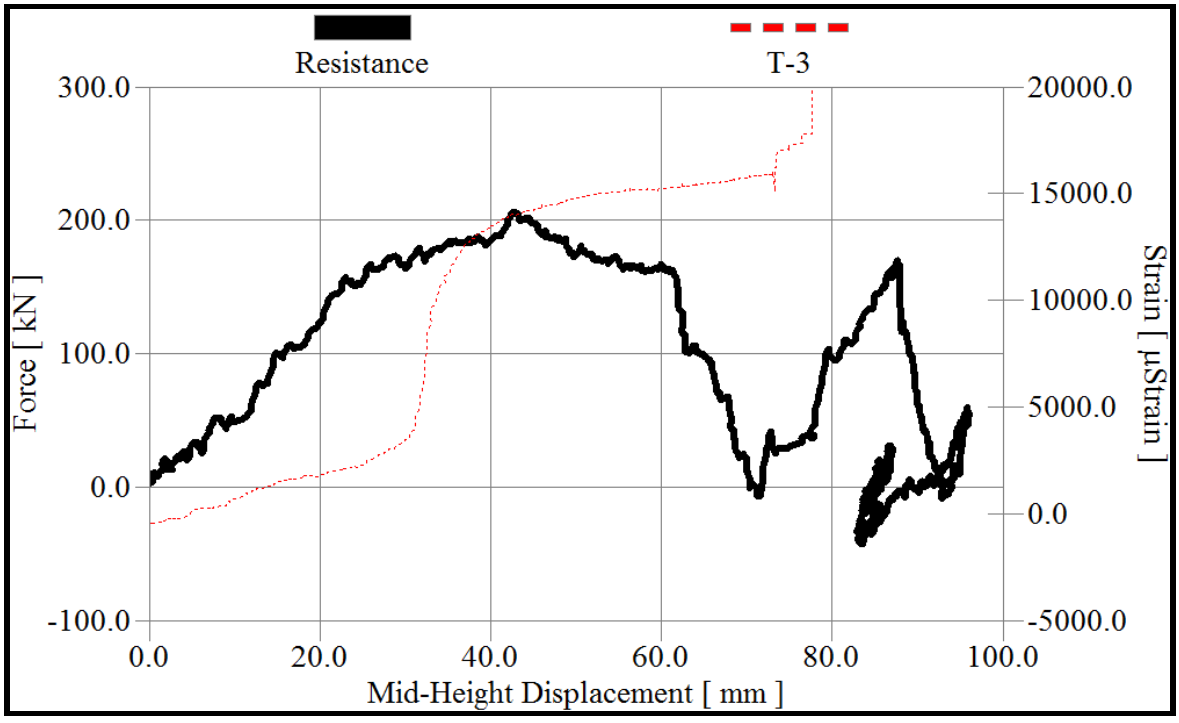

Fig. D-14 Resistance-displacement function of column S2-B-G1

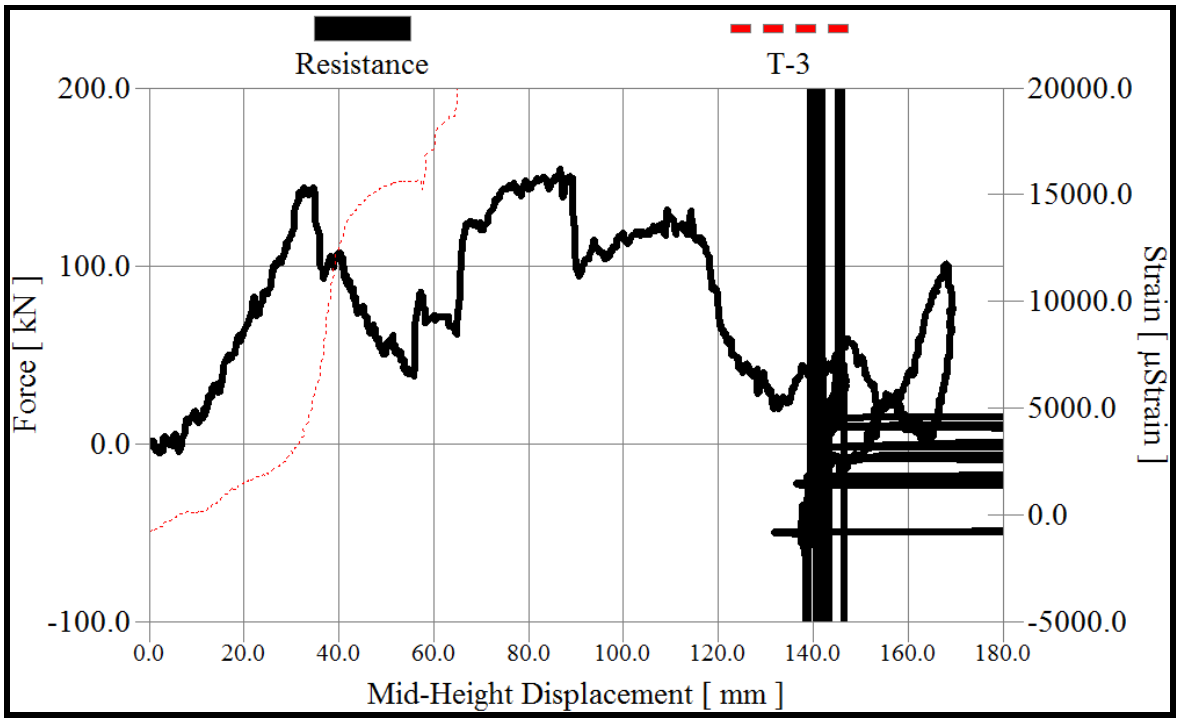

Fig. D-15 Resistance-displacement function of column S3-A-G1

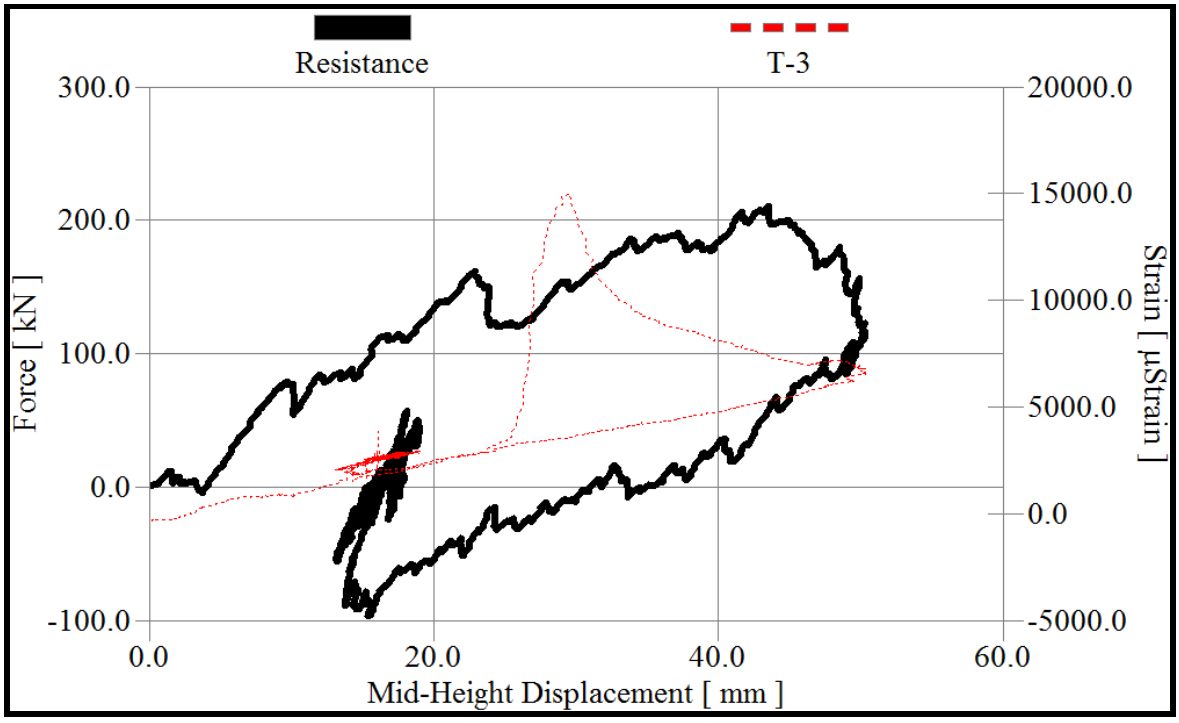

Fig. D-16 Resistance-displacement function of column S3-B-G1

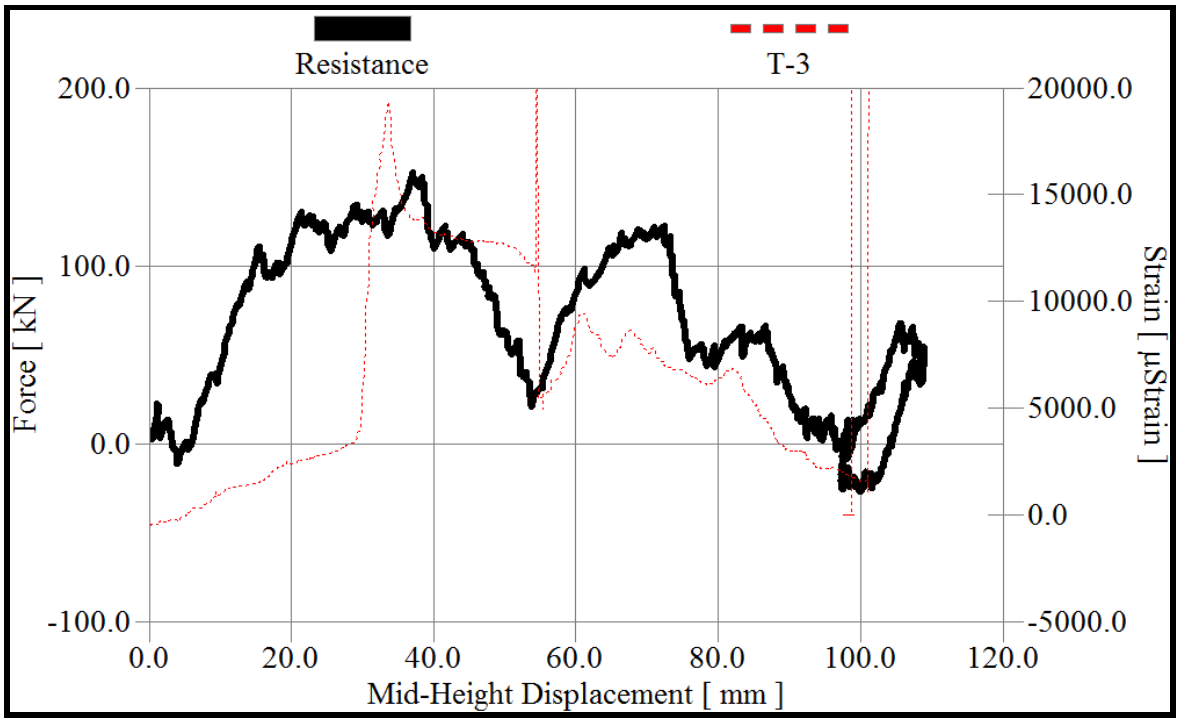

Fig. D-17 Resistance-displacement function of column S4-A-G1

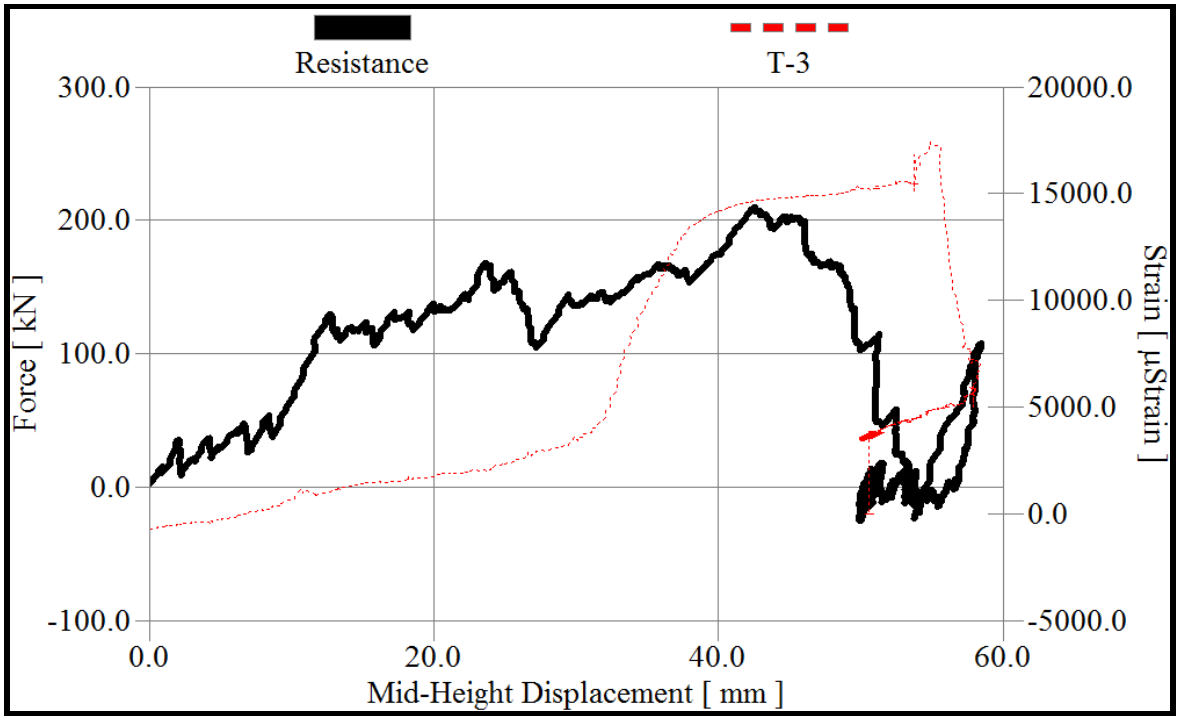

Fig. D-18 Resistance-displacement function of column S4-B-G1

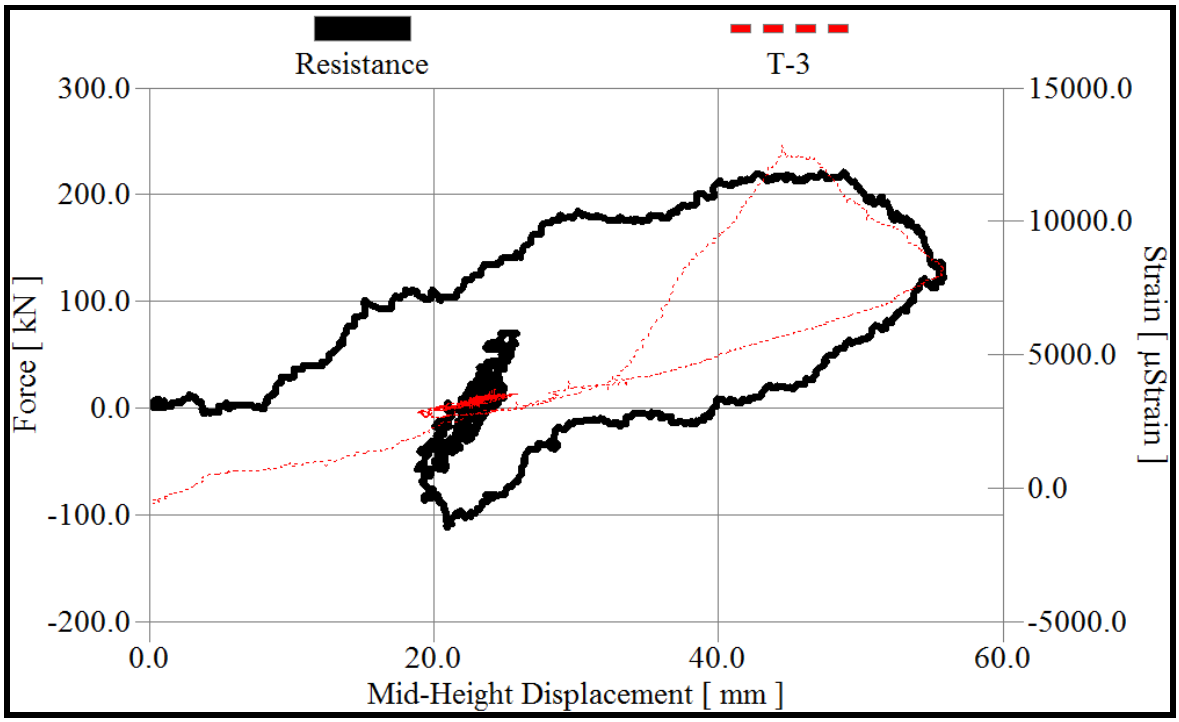

Fig. D-19 Resistance-displacement function of column S5-G1